Mathematical modelling and electrophysiological monitoring of the regulation of cochlear amplification

Greg A. O'Beirne
B.Sc. (Hons.)

This thesis is presented in partial fulfilment of the requirements of the degree of Master of Clinical Audiology / Doctor of Philosophy of The University of Western Australia

Physiology
School of Biomedical and Chemical Sciences
2005

Abstract

The cochlea presumably possesses a number of regulatory mechanisms to maintain cochlear sensitivity in the face of disturbances to its function. Evidence for such mechanisms can be found in the time-course of the recovery of CAP thresholds during experimental manipulations, and in observations of slow oscillations in cochlear micromechanics following exposure to low-frequency tones (the "bounce phenomenon") and other perturbations. To increase our understanding of the these oscillatory processes within the cochlea, and OHCs in particular, investigations into cochlear regulation were carried out using a combination of mathematical modelling of the ionic and mechanical interactions likely to exist within the OHCs, and electrophysiological experiments conducted in guinea pigs.

The electrophysiological experiments consisted of electrocochleographic recordings and, in some cases, measurement of otoacoustic emissions, during a variety of experimental perturbations, including the application of force to the cochlear wall, exposure to very-low-frequency tones, injection of direct current into scala tympani, and intracochlear perfusions of artificial perilymph containing altered concentrations of potassium, sodium, and sucrose. To obtain a panoramic view of cochlear regulation under these conditions, software was written to enable the interleaved and near-simultaneous measurement of multiple indicators of cochlear function, including the compound action potential (CAP) threshold, amplitude and waveshape at multiple frequencies, the OHC transfer curves derived from low-frequency cochlear microphonic (CM) waveforms, distortion-product otoacoustic emissions (DPOAEs), the spectrum of the round-window neural noise (SNN), and the endocochlear potential (EP).

The mathematical model takes into account the known electrical properties of OHC, and includes the effect of fast and slow-motility of the cell body on transducer operating point and apical conductance. Central to the operation of the model is a putative intracellular 2nd-messenger system based on cytosolic calcium, which is involved in regulation of i) the operating point of OHC MET channels via slow motility and axial stiffness; ii) the permeability of the basolateral wall to potassium (via calcium-sensitive potassium channels); and iii) the cytosolic concentration of calcium itself, via modulation of its own sequestration into (and release from) intracellular storage organelles, and extrusion from the cell. The model was constructed in a manner which allowed simulation of different cochlear perturbations, and the comparison of results from these simulations to experimental data.

The mathematical model we have developed provided a physiologically-plausible and internally-consistent explanation for the time-courses of the cochlear changes observed during a number of different perturbations. We show that much of the oscillatory behaviour within the cochlea is consistent with underlying oscillations in cytosolic calcium concentration. We conclude that a number of the discrepancies between the simulation results and the experimental data can be resolved if the cytosolic calcium functions as two distinct pools: one which controls basolateral permeability and one which controls slow motility. This two-calcium-pool model is discussed.

Acknowledgements

I owe an enormous debt of gratitude to my supervisor and mentor, Dr Robert Patuzzi, for his guidance, support, and friendship. He is an inspirational teacher with tremendous insight, and has done more to influence my thinking and my choice of career more than anyone else. Thanks Rob.

I would like to thank my colleagues in the Auditory Laboratory of the University of Western Australia. In particular, for their friendship and camaraderie, I'd like to thank Mr Daniel Brown, Dr Catherine McMahon, Dr Susmita Thomson, and Mr Neil Wareing, all of whom I worked closely with, and from whom I learned a great deal, and Mr Simon Marcon, whose data provided a foundation for this work. For their friendship, collegiality, and expertise, I'd like to thank Prof. Don Robertson, Dr Peter Sellick, Dr Helmy Mulders, Dr Maria Layton, Mr Greg Nancarrow, Mr Bardia Paki, Mr Norman Zakaria, Dr Jérôme Ruel, Dr Takayuki Sueta, Dr Takafumi Yamano, Dr Kumar Seluakumaran, and Mr Andrew Garrett. I would also like to thank Dr Helmy Mulders and Ms Beatrice Birkner for providing much-appreciated transport to a "poor student".

Sadly, two of our colleagues, Dr Graeme Yates and Dr Des Kirk, died during the early stages of this work. Their presence in the Lab, and their contribution to Auditory Physiology, is sorely missed.

I wish to thank Richard Ludwig, John Newbury, and Brian Cameron, for helping me get this far. I would also like to thank Ms Peta Monley and the staff of IHear Australia, particularly Vanessa Wedge, Dee Hadrill, Carl Chase, and Vesna Maric, for their friendship and for providing an enjoyable and flexible work environment. I would like to thank Professor Michael Robb and the Department of Communication Disorders, University of Canterbury, for providing an environment in which I was able to finish writing this thesis while preparing Audiology lectures.

I am sincerely grateful for the support of my family, particularly Brad and Frances (for their helpful badgering!), Mum and Chris, Dad and Marie, Doug and Mary, and Mollie and Blue. I'd also like to thank Scott Lewis for his friendship and moral support.

This thesis is dedicated with love and heartfelt gratitude to my wonderful partner Donna. I thank her for her unstinting encouragement, love, good humour, and for her incredible patience. She supported me every step of the way, and I could not have done it without her.

The author was supported financially by an Australian Postgraduate Award from 2000 to 2003. The University of Western Australia's Postgraduate Research Student Travel Award scheme, and Professor Tony Gummer and the European Commission, generously provided financial support enabling the author to attend the "Biophysics of the Cochlea: Molecules to Models" conference in Titisee, Germany, in July/August 2002. The Auditory Laboratory also provided funds for travel to the IUPS Auditory Satellite Symposium in Auckland, New Zealand, in August 2001, and the Australasian Auditory Neuroscience Workshop in Melbourne, Australia, in January 2004.

Statement of candidate contribution

The central idea for the project was provided by Dr Robert Patuzzi, who developed the schematic model of outer hair cell homeostasis. The modification and development of this schematic model into the mathematical model was the combined work of the author and Dr Patuzzi. The LabVIEW software for electrophysiological measurement and mathematical modelling was written almost solely by the present author, in collaboration with Dr Patuzzi in the earlier stages of design. The author designed the majority of the physiological experiments, usually following discussion with Dr Patuzzi. The majority of the experimentation, including animal preparation, surgery, and measurement, was carried out by the author, with the occasional surgical assistance of Mr Daniel Brown and Dr Peter Sellick. The interpretation of the results was developed through extensive discussion between the author and Dr Patuzzi.

Abbreviations

ABR	auditory brainstem response
AC	alternating current
ACh	acetylcholine
ADP	adenosine diphosphate
ATP	adenosine triphosphate
AP	artificial perilymph
B&K	Brüel & Kjær
BM	basilar membrane
CAP	compound action potential
CF	characteristic frequency
CM	cochlear microphonic
CRO	cathode ray oscilloscope
DC	direct current
DP	dendritic potential
DPOAE	distortion-product otoacoustic emission
ECochG	electrocochleography
EMT	electromechanical transduction
Eo	operating point
EP	endocochlear potential
GHK	Goldman-Hodgkin-Katz
GPHL	guinea pig hearing level
HL	hearing level
IHC	inner hair cell
IO	input/output
IP3	inositol 1,4,5-trisphosphate
LF	low frequency
ME	middle ear
MET	mechanoelectrical transduction
OAE	otoacoustic emission
OHC	outer hair cell
OW	oval window
P_i	inorganic phosphate
pp	peak-to-peak
RC	resistor/capacitor
RL	reticular lamina
RM	Reissner's membrane
RMS	root mean square
RW	round window
SC	synaptic cisternae
SM	scala media
SNN	spectrum of neural noise
SP	summating potential
SSC	subsurface cisternae
ST	scala tympani
SV	scala vestibuli
TEOAE	transient-evoked otoacoustic emission
TM	tectorial membrane
TTX	tetrodotoxin
VI	virtual instrument
VLF	very low frequency
Vsat	saturating current
Z	sensitivity

Units

S.I. units are used in the text, with the exception of the electron volt (eV), which is approximately 1.602176×10^{-19} J.

Table of contents

Chapter 1
Introduction

1. Introduction

The aim of the present study was to develop methods to investigate and characterise the homeostatic mechanisms within the outer hair cells (OHCs) of the organ of Corti. In particular, the ways in which the cochlea maintains its exquisite auditory sensitivity over long periods, despite the daily perturbations to which it is exposed. These investigations were carried out using a combination of mathematical modelling of the ionic and mechanical interactions likely to exist within the OHCs, and electrophysiological experiments conducted in guinea pigs.

The electrophysiological experiments consisted of electrocochleographic recordings and, in some cases, measurement of otoacoustic emissions, during a variety of experimental perturbations, including the application of force to the cochlear wall, exposure to very-low-frequency tones, injection of direct current into scala tympani, and intracochlear perfusions of artificial perilymph containing altered concentrations of potassium, sodium, and sucrose. To obtain a panoramic view of cochlear regulation under these conditions, software was written to enable the interleaved and near-simultaneous measurement of multiple indicators of cochlear function, including the compound action potential (CAP) threshold, amplitude and waveshape at multiple frequencies, the OHC transfer curves derived from low-frequency cochlear microphonic (CM) waveforms, distortion-product otoacoustic emissions (DPOAEs), the spectrum of the round-window neural noise (SNN), and the endocochlear potential (EP).

The main aim of the project was to create a mathematical model of the outer hair cells that was capable of explaining much of the experimental data obtained using the above techniques. It was clear from the outset that for such a model to provide realistic predictions of experimental data, it must incorporate not only what is known about the electrophysiology of the OHCs, but also include their motile properties, as this motility directly influences a major component of the conductance at their apical membranes. It was believed that such a model would enable the results from a wide variety of experiments to be explained within a single framework, consistent both internally and externally, which would improve our understanding of cochlear function, regulation, and pathology.

A major impetus for the creation of the hair cell model was to develop an understanding of the cochlear processes responsible for the so-called “bounce phenomenon”, where cochlear gain slowly oscillates (usually displaying a transient improvement in sensitivity) following exposure to a low-frequency (LF) tone.

Exposures to intense LF tones also trigger and enhance oscillations in other cochlear parameters, such as otoacoustic emissions, the EP, and the Boltzmann parameters describing the distortion of the CM.

The central hypothesis of the present project was that oscillatory behaviours (such as the bounce) could be produced in the cochlea by underlying oscillations in the cytosolic calcium concentration of the outer hair cells, as these cells are the source of much of the exquisite auditory sensitivity of mammals.

1.1.1 Regulation of cochlear sensitivity and the impetus for the study

The mammalian cochlea is capable of detecting displacements of molecular dimensions (Sellick et al., 1982), it has a million-fold range of energy sensitivity from threshold of detection to threshold of pain, and it can perform for decades with sometimes only minor degradation in performance over this time. The only way for this to be possible is for its environment and component parts to be tightly regulated, and in most biological systems this regulation is achieved by the use of negative feedback.

The regulation of cochlear function can be divided into a number of categories, some of which are examined in this thesis, and others which are not. Falling into the latter division are topics such as the regulation of the ionic concentrations of endolymph and perilymph, intracellular and extracellular pH, and the functioning of stria vascularis. Regulation of these factors is vital, not only for the proper functioning of the cochlea, but also for the survival of the cells within it. However, the primary focus of this thesis is the mechanisms existing within the OHCs to achieve regulation of stereociliary operating point, basolateral permeability, AC receptor potential, active gain, and the control of spontaneous neural firing by shunt-regulation of the endocochlear potential. Evidence for the existence of such mechanisms within the OHCs themselves has come from observations of a number of cochlear phenomena. These are briefly listed below, and are discussed in the following sections.

1) The “bounce” phenomenon: Following exposure to an intense low-frequency tone, hearing thresholds can display an oscillatory recovery time-course, consisting of an initial threshold elevation, followed by a transient hypersensitivity approximately one minute after cessation of the exposure. This oscillatory behaviour is also observed in DPOAEs, Boltzmann parameters, and psychophysical measures of tinnitus, but are often out of phase with one another.

2) Oscillations in Boltzmann parameters: Marcon and Patuzzi (in preparation) found that a number of transient cochlear perturbations occasionally trigger slow, damped oscillations in the Boltzmann parameters (with a period of between 200 and 500 seconds) that persist for several cycles.

3) Oscillations in CAP threshold following potassium perfusion: following perfusion of artificial perilymph containing an elevated concentration of potassium, the CAP threshold often displays a multi-phasic, rather than monotonic, recovery.

4) Hydrostatic-induced active movement of the organ of Corti: under certain measurement conditions, the transient hydrostatic movement of the organ of Corti towards scala vestibuli during various cochlear perfusions (including control perfusions of artificial perilymph) triggers a larger, rapid movement of the outer hair cell operating point in the opposite direction, towards scala tympani.

The mathematical model was based on the schematic model of OHC regulation that had been developed by Patuzzi (2003), which showed how a number of oscillatory phenomena could originate from the operation of a set of interlocked feedback loops, with different perturbations acting at different parts of the loop. This schematic model was modified and quantified during the present project, resulting in the mathematical model of outer hair cell regulation presented in Chapter Two. The aim was to see what the mathematical model could (and, importantly, could not) do. The success or otherwise of the mathematical model was judged by its ability to account for, or replicate (sometimes to varying degrees of accuracy) the changes observed experimentally.

This process of designing and programming the model, and then testing it experimentally, took several years. During this time, an attempt was made to settle on a *single set of parameters* that provided a reasonable match to as many of the results of the experimental perturbations examined in the present project as possible. Arriving at this single set of parameters was necessarily an iterative process, and in most cases, the results of the modelling provided results that were consistent with experimental observations: for individual perturbations, further adjustment of the model could provide closer matches in some cases.

However, after many experiments and iterations of the modelling process, there were a number of key results which the model was incapable of replicating. Rather than indicating that further fine-tuning of the mathematical model was required, these “exceptions” to the model indicated that some basic changes to the underlying

schematic model of the OHC were required to fully account for the observed experimental behaviours. This thesis will first show the mathematical model in its present state, and then, following presentation and discussion of the experimental data from a range of different perturbations, and the ability of the model to account for these behaviours, the revised schematic model of OHC will be proposed in Chapter Nine.

Within this introductory chapter, in the interests of readability, a brief summary of what is known of the ionic transport mechanisms of the OHCs will be presented first, followed by a discussion of the significance and implications of each of the above oscillatory phenomena. Then follows a discussion of the role of regulatory processes within the OHC, and a description of the schematic model of OHC regulation (Patuzzi, 2003). Finally, the rationale for the inclusion of the calcium-based second-messenger cascade that is responsible for much of the behaviour of the model is discussed, followed by a brief outline of the structure of this thesis.

1.1.2 Known cellular components of the OHC

Figure 1.1 shows a schematic diagram of the main ionic transport mechanisms of the OHCs. These components are discussed in great detail in Chapter Two, but briefly, the apical membrane of the OHC (the endolymphatic face of the hair cell) contains the displacement-sensitive MET channels and an ATP-sensitive conductance, while the basolateral wall (the perilymphatic face) contains voltage-sensitive, calcium-sensitive, and stretch-sensitive potassium channels, potassium leakage channels, ACh-sensitive and voltage-sensitive calcium channels, physiologically-silent voltage-sensitive sodium channels, chloride leakage channels, sodium-calcium antiports, plasma-membrane calcium-ATPases (or PMCAs), and sodium-potassium-ATPases (Na^+/K^+/ATPases). Two intracellular cisternae are also shown – the subsurface cisternae and the synaptic (or synaptoplasmic) cisternae, both of which are likely to function as calcium stores, and contain sarcoplasmic/endoplasmic calcium ATPases (or SERCAs), calcium leakage channels, and a calcium-sensitive calcium channel involved in calcium-induced calcium release (or CICR).

Two motile mechanisms are included in Figure 1.1 - the calcium-dependent “slow-motility’ (Zenner, 1986b; Dulon et al., 1990), and the voltage-dependent “fast-motility”, or somatic electromotility, which is due to conformational changes in the motor protein prestin (Zheng et al., 2000). What is *not* included, is any form of hair-cell motility arising from the stereocilia, as will be discussed in Section 1.4.1 below.

Many of the ionic pathways through the OHC, and the directions of ionic fluxes, are indicated with arrows in Figure 1.1. These include the entry of potassium through the apex of the cell and its exit through the basolateral wall, the cycling of calcium and sodium through the basolateral wall, and the influence of calcium within the OHC. What may not be clear from this diagram is the way in which these pathways interact to influence each other's behaviour. It is precisely these interactions which form the basis of the homeostatic model presented here, and which will be discussed in later sections.

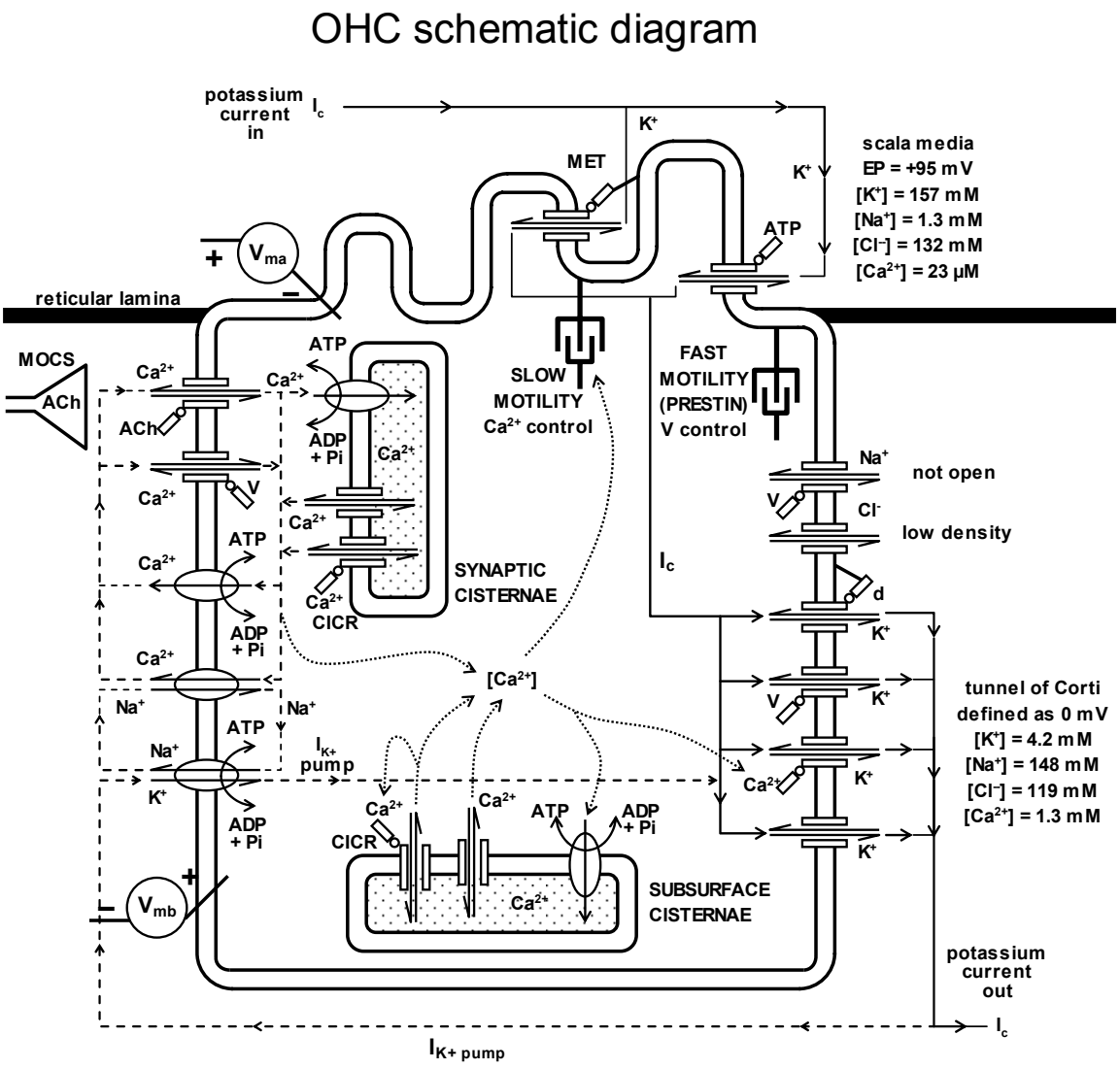

Figure 1.1: A summary of the main ionic transport pathways through the OHCs (adapted from Patuzzi, 1998), discussed in detail in Chapters One and Two. Also shown are representations of fast and slow somatic motility, the apical and basolateral transmembrane voltages (V_{ma} and V_{mb} respectively), and the presumed ionic concentrations of scala media and the tunnel of Corti.

1.2 Observations of oscillatory behaviour in the cochlea

As the homeostatic model was developed with the aim of accounting for many oscillatory processes within the cochlea, a brief introduction to some of these oscillations is presented below.

1.2.1 The "bounce" phenomenon[1]

More than fifty years ago, Hirsch and Ward (1952) found that the recovery of hearing thresholds following exposure to an intense low-frequency tone can display an oscillatory, rather than monotonic, time-course. The initial period of threshold elevation following exposure can be followed by a transient hypersensitivity (a net threshold decrease) occurring approximately one minute after exposure, after which time thresholds again increase transiently before recovering towards normal. An example of this oscillatory threshold behaviour is shown in Figure 1.2.

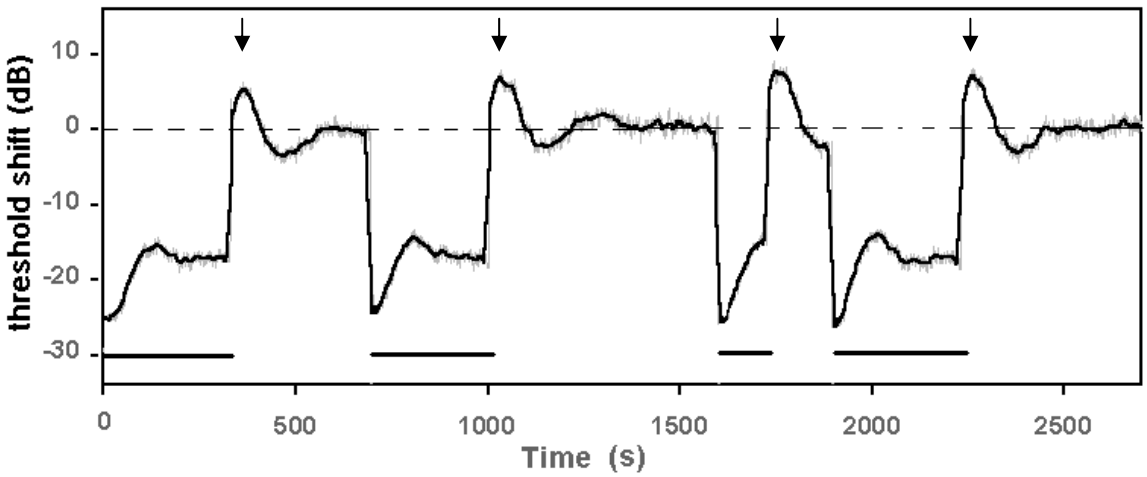

Figure 1.2: Damped sinusoidal oscillations in human audiometric threshold (tracked with Békésy audiometry) at onset and offset of exposures (black bars) to a 126 dB SPL 40 Hz tone. Transient hypersensitivities (bounces) are marked with an arrow. Figure adapted from Wareing (2001).

The observation that transient otoacoustic emissions (TEOAEs) followed a similar post-exposure time-course (Kemp, 1982; 1986) indicated that the threshold oscillation was mechanical, rather than solely neural, in origin. As such, the bounce phenomenon is also reflected in a number of other indicators of cochlear function. Subsequent work has shown the bounce to be associated not only with increases in neural sensitivity (Hughes, 1954; Hirsch and Bilger, 1955; Zwicker and Hesse, 1984; Patuzzi and Wareing, 2002),

[1] While the term "bounce" was used by Hirsch and Ward to describe the transient worsening of thresholds at two-minutes post-exposure, we follow here the terminology of Kemp (1986) and Kirk and Patuzzi (1997), in which "bounce" is used to describe the transient *improvement* in sensitivity occurring one-minute post-exposure.

but with changes in f_2-f_1 DPOAEs (Kirk and Patuzzi, 1997), an increase in EP (Kirk, 1972; Kirk and Patuzzi, 1997), and transient tinnitus (Kemp, 1986; Wareing, 2001; Patuzzi and Wareing, 2002). By analysing the cochlear microphonic (CM) waveform using a technique known as Boltzmann analysis (discussed in detail in Chapter Three), Kirk et al. (1997) showed this EP rise was most likely due to a reduction in the current shunt through the outer hair cells (caused by a hair bundle operating point shift in the direction that causes closure of MET channels), rather than from any change in the pumping of stria vascularis.

Patuzzi and Wareing (2001; 2002) studied the bounce phenomenon in human subjects using Békésy audiometry to track psychophysical threshold, and to match the loudness of a synthesised "tinnitus" in the contralateral ear to that of the transient tinnitus evoked by the LF tone. Comparison of the time-course of the threshold shifts and the tinnitus revealed significant phase delays between the two measures, with the peak of the tinnitus loudness occurring around 30-40 seconds after the peak threshold enhancement, as shown in Figure 1.3.

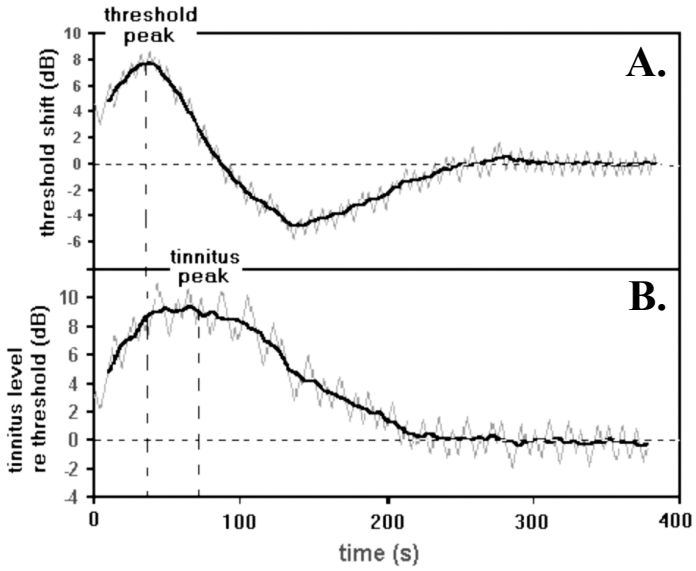

Figure 1.3: Békésy audiometry results from Patuzzi and Wareing (2002) showing **A.** psychophysical threshold oscillations and **B.** the contralaterally-matched loudness of transient tinnitus following 3 minute exposures to 116 dB SPL 100 Hz tones in a single subject.

As will be discussed in Chapter Six, the form of tinnitus tracked in Figure 1.3B is likely to be "rate tinnitus" - the result of an increase in the spontaneous firing rate of the primary afferent neurons that occurs with depolarisation of the IHCs, probably caused by elevation of EP (Patuzzi, 2002; Patuzzi and Wareing, 2002).

As will be described in detail in Chapter Six, the bounce phenomenon is interesting in that it indicates that i) active gain is *not* the only "design" consideration within the cochlea (if it were regulated at the expense of everything else, it would presumably not be maintained at a sub-optimal level), and ii) such regulatory mechanisms can be perturbed in a way that allows us to make inferences about them.

1.2.2 Slow oscillations in Boltzmann parameters describing MET

As mentioned above, Boltzmann analysis of the CM provides a technique for detecting small changes in the mechanoelectrical transduction of the outer hair cells, and can be used to infer changes in cochlear micromechanics using a simple round-window electrode and an intense low-frequency tone. As the technique forms the basis for the majority of the results presented in this thesis, a detailed description is presented in the Methods section (Chapter Three).

Briefly, the CM potential is the extracellular analogue of the OHC receptor current. As the opening probability of the MET channels at the apex of the hair cell can be approximated by a 1st-order Boltzmann activation function (Holton and Hudspeth, 1986; however, see discussion in Chapter Three), the relationship between the angular displacement of the hair bundle and the current through the OHC follows a similar function. An intense, non-traumatic, low-frequency tone (for example, around 200 Hz) can be used to drive the basal OHCs into partial saturation, enabling the characteristics of this nonlinear distortion of the CM to be analysed using a curve-fitting process.

The parameters of the distortion obtained from the Boltzmann analysis are i) Vsat – proportional to the maximal OHC receptor current for maximal excursions of the hair bundle, ii) Z – a sensitivity parameter (in units of meV/Pa) giving the slope of the transduction curve, and iii) Eo, an offset parameter (in units of meV) accounting for the fact that the current through the OHC is non-zero for a zero-pressure stimulus in the ear canal. The Eo parameter gives the operating point of the MET channels on the transfer curve, and is used to indicate the quiescent angle of the OHC stereocilia. Because the tips of the stereocilia are embedded in the overlying TM, the operating point is partially determined by the position of the reticular lamina relative to the TM, and so can provide an indication of the degree of contraction or elongation of the hair cell. Because movement of the reticular lamina towards SV causes displacement of hair bundles in the direction that causes opening of the MET channels (i.e. in the direction of the basal body), this shift is commonly referred to as “a movement in the SV direction”, or as “an SV operating point shift”. Conversely, movement in the direction that closes MET channels will be referred to here as a “movement in the ST direction”, or as “an ST operating point shift”.

Marcon (1995) researched the effects of altered perilymphatic potassium concentration on cochlear function using a combination of Boltzmann analysis, EP measurement, and CAP threshold determination. The 1995 study, as well as work

carried out by Marcon and Patuzzi between 1995 and 1998, found the presence of slow oscillations in the Boltzmann parameters, not only following exposure to an intense low-frequency tone (the bounce phenomenon, described above), but during a range of other experimental perturbations, including transient hypoxia, hydrostatic bias, and perfusion of artificial perilymph containing elevated concentrations of potassium, gadolinium, and mercury (Marcon, 1995; Marcon and Patuzzi, in preparation). These oscillations were remarkably slow, with periods ranging from 200 to 500 s.

Examples of these oscillations are shown in Figure 1.4. The changes in Boltzmann parameters shown in columns one and two were induced by onset of an intense low-frequency (207 Hz) tone. In the second column (GP#SM186), there was a rapid initial operating shift (panel E) towards scala tympani, followed by a slower shift in the same direction, consistent with contraction of the OHC.

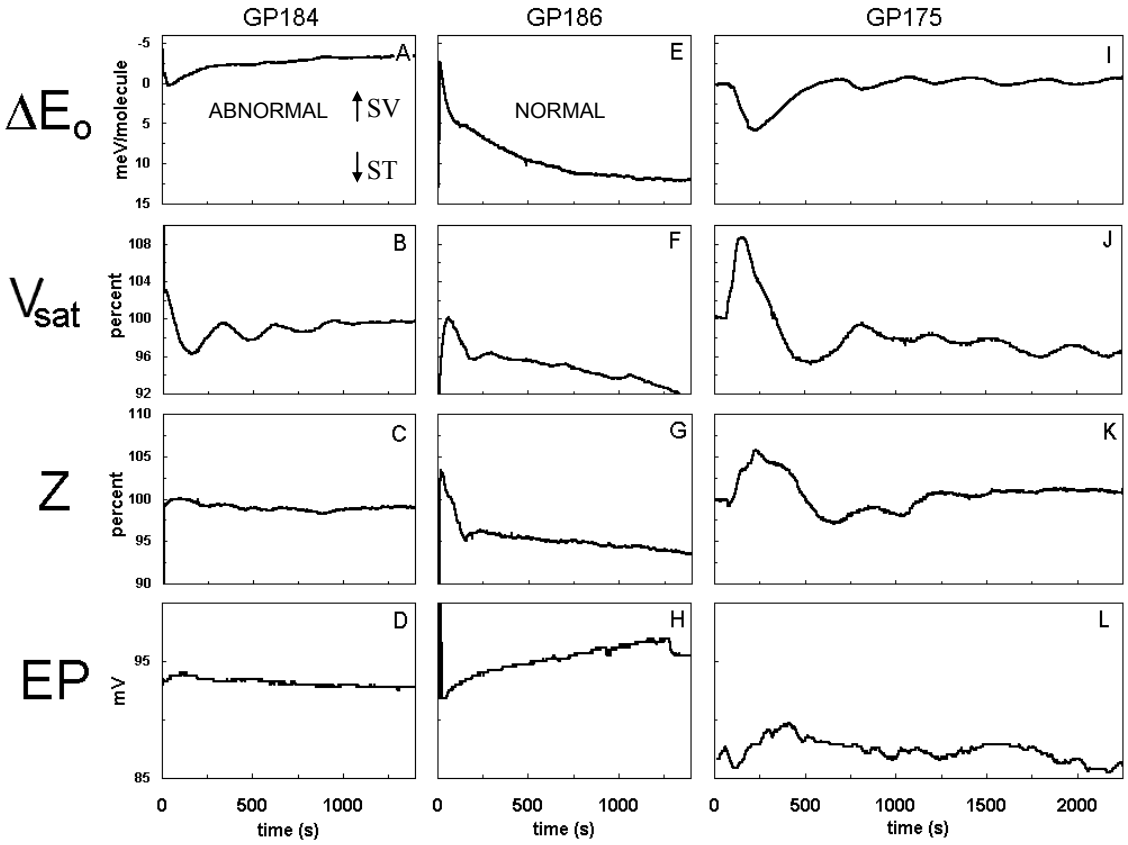

Figure 1.4: Data from Marcon and Patuzzi (in preparation) showing slow oscillations in the Boltzmann parameters and the endocochlear potential in response to experimental perturbations (GP#SM184 & GP#SM186 – onset of LF tone, GP#SM175 – hydrostatic bias).

The EP was observed to rise during this period (panel H), consistent with a reduction in the OHC shunt current due to the scala tympani operating-point shift. The initial rapid component of this operating-point shift was concurrent with a transient

increase in Vsat (panel F), which was then followed by a slower oscillatory decrease with a period of around 400 s. The Z parameter (panel G) also decreased with an initial rapid component followed by a slower one. While this was a normal adaptation response to a low-frequency tone, the results from GP#SM184 (first column) were abnormal. Instead of a scala tympani operating-point shift, in this animal the low-frequency tone resulted in a small operating-point shift towards scala vestibuli (panel A), and a pronounced oscillation in the Vsat parameter (period of about 300 s; panel B), which was accompanied by smaller amplitude oscillations in the Z parameter (panel C) and the EP (panel D).

The perturbation in the third column (GP#SM175) was a hydrostatic bias created by a control perfusion of artificial perilymph. The perfusion caused an immediate scala tympani operating-point shift (panel I) which recovered over the next eight minutes, accompanied by prolonged oscillations in all three Boltzmann parameters (period of about 390 s; panels I, J, and K). Damped oscillations are also visible in the EP (panel L).

1.2.3 Multi-phasic threshold recovery following potassium perfusion

As will be shown in Chapter Eight, perfusion of artificial perilymph containing high concentrations of potassium usually causes a rapid elevation of CAP threshold. Cessation of the perfusion usually allows the recovery of hearing threshold, but in many cases this recovery does not follow what is assumed to be the time-course for the return of perilymph potassium concentration to normal levels, but instead shows a multi-phasic time-course. An example of this time-course is shown in Figure 1.5 below, recorded by Marcon (1995; Marcon and Patuzzi, in preparation).

At the offset of the two-minute perfusion (the duration of which is indicated by the black bar in Figure 1.5) , the CAP thresholds recovered from the maximal loss of 30 dB to around 12 dB, before increasing again to show local maxima of 25 dB and 10 dB at around the 500 and 1000-second marks, respectively. Concurrent measurement of the SP threshold showed a very similar pattern, indicating that the oscillations were also occurring at the hair-cell level, rather than being a solely neural phenomenon. The possible origins of this oscillatory pattern of threshold recovery will be discussed further in Chapter Eight.

1.2.4 Cochlear oscillations occur at the hair-cell level

The above phenomena indicate that oscillatory processes can occur in the cochlea, and that they occur *at the hair cell level*. These oscillations are visible in measures of the operating point of the OHC MET channels, in the permeability of the basolateral wall of the OHCs, in the sensitivity of the MET process, and in the active gain produced by the OHCs.

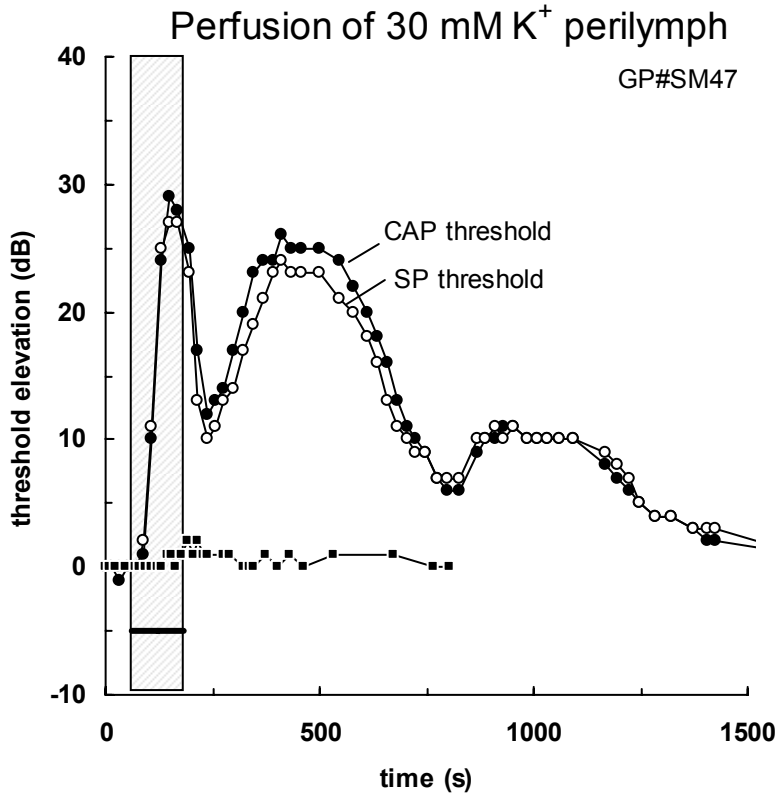

Figure 1.5: Data from Marcon (1995) showing the multiphasic recovery of CAP thresholds following two-minute perfusion of artificial perilymph containing 30 mM K^+. The near 1:1 tracking of the SP and CAP thresholds indicates the observed effects of the perfusion were mechanical, rather than solely neural, in origin.

Before discussing how such oscillations can arise from regulatory feedback processes, we must first consider the role of the outer hair cells in cochlear regulation. Discussed in Section 1.3 below is the need to control the operating point of the outer hair cell and the mechanisms (in the OHCs and elsewhere) for achieving this. Section 1.4 discusses the importance of the permeability of the OHC membranes (both apical and basolateral), and the role of the OHCs in contributing to the active gain of the cochlea and in control of the EP. Both of these sections highlight the importance of cytosolic calcium in OHC regulation, a point which is developed further in Sections 1.5 and 1.5.3 below.

1.3 Displacement coupling and the need to control operating point

Optimal transduction of auditory stimuli requires that the OHC hair bundles are maintained in their most sensitive region. Because the hair bundles of the OHCs are displacement-coupled, they are vulnerable to slow or static changes to the relative positions of the reticular lamina and the tectorial membrane that can bias the MET channels out of this region of maximum sensitivity. In addition, the resting hair bundle angle (and therefore the degree to which the population of MET channels are open or closed at rest) directly influences the DC membrane potential of the OHC itself, as the MET conductance is a significant component of the potassium flux at the apex of the cell. The factors influencing this regulation of operating point are discussed below.

1.3.1 External, middle, and inner-ear high-pass filter mechanisms

The task of optimising the ability of the cochlea to detect sound (an AC stimulus) is made considerably easier by limiting its exposure to DC stimuli in the first place. High-pass filter mechanisms exist at numerous points within the cochlea to reduce the effect of DC stimulation in order to maintain sensitivity to AC stimulation. From the external ear inwards, these mechanisms include:

i) *Shunting of atmospheric pressure at the eardrum:* The first high-pass filtering stage occurs with the common mode rejection of atmospheric pressure by the tympanic membrane, which is deflected according to the pressure difference between the ear canal and the middle-ear cavity. As a percentage of atmospheric pressure, the amplitude of a 0 dB SPL tone (approximately equal to the standard human audiometric threshold at 1 kHz) is extremely small, representing a pressure fluctuation of just over $1/200{,}000^{th}$ of a percent of atmospheric pressure. However, the DC component of this signal is minimised by the shunting of slow pressure imbalances through the periodic opening of the Eustachian tube, allowing the vibration of the tympanic membrane to be dominated by the AC component of this signal, sound.

ii) *The malleoincudal joint of the middle ear:* The next stage of high-pass filtering occurs at the slip-joint between the malleus and the incus, which shields the cochlea from the full effects of large static pressures, such as the ± 200 daPa biases applied to the ear drum during acoustic impedance audiometry (tympanometry).

iii) *The helicotrema:* In the inner ear, the junction between scala vestibuli and scala tympani in the extreme apex of the cochlea, the helicotrema, acts as a pressure shunt in parallel with the cochlear partition, limiting the ability of low frequency stimuli to displace the basilar membrane (Dallos, 1970; Ruggero et al., 1986). In the guinea pig, the high-pass-filter corner frequency is around 300 Hz.

In addition to the above, further mechanisms exist at the level of the hair cells themselves to maintain the hair-bundle in the region of maximum sensitivity. Discussed below, these are: i) transducer adaptation, ii) calcium-dependent slow motility, and iii) slow-acting fast electromotility.

1.3.2 Transducer adaptation

Many types of hair cell display adaptation, whereby the current passing through the MET channel decreases during a sustained deflection of the hair bundle (for a review, see Eatock, 2000). These adaptation processes are dependent on extracellular calcium (Eatock et al., 1987), and are abolished completely when calcium is removed (Assad et al., 1989; Crawford et al., 1989; Crawford et al., 1991). The two forms of transducer adaptation present in some cochlear hair cells in some species are "fast" and "slow" adaptation, which are distinguished from each other by the time scale over which they operate, and their underlying mechanism of operation (Wu et al., 1999).

"Fast adaptation" occurs with millisecond time-constants and requires the binding of calcium to sites on or near the transduction channel, and may enhance cochlear amplification and frequency selectivity in lower vertebrates, such as the turtle (Ricci and Fettiplace, 1997). There is evidence from *in vitro* experiments that fast adaptation is also present in mammalian hair cells under some conditions (Kros et al., 1992; Kennedy et al., 2003), but its contribution to OHC motility is still debated (Allen, 2003). "Slow adaptation" operates over tens or hundreds of milliseconds, and involves the action of an unconventional myosin motor, myosin-1c, to alter the tension of so-called gating springs in the stereocilia (Holt et al., 2002; Gillespie and Cyr, 2004).

The experimental evidence for *in vivo* adaptation of the OHC MET channels in guinea pigs is currently limited. Infrasonic bias experiments by Salt and DeMott (1999) found no indication of low-frequency attenuation of CM waveforms, with stimulation at frequencies as low as 1 Hz producing large responses. Furthermore, experiments by Konishi and Nielsen (1978) in which the guinea-pig helicotrema had been surgically blocked, triangular displacement of the round window produced trapezoidal CM

waveforms with displacement plateaus as long as 200 ms, indicating a lack of adaptation over that time-scale, or that any transducer-adaptation that did occur was so small as to not significantly affect the current through the OHC.

1.3.3 Calcium-dependent slow motility and modulation of axial stiffness

The term "slow motility" describes the length changes of outer hair cells that occur on a time-scale of tens of seconds, in response to changes in cytosolic calcium concentration (Zenner, 1986b; Dulon et al., 1990; Pou et al., 1991; Pujol et al., 1991). The motile response can be initiated in a number of ways, including the application of solutions containing elevated extracellular K^+ (Zenner et al., 1985; Zenner, 1986a), ATP (Zenner, 1986a), and the calcium ionophore ionomycin (Dulon et al., 1990).

The OHC cortical lattice consists of circumferential actin filaments, cross-linked by spectrin (Holley, 1996). In isolated OHCs *in vitro*, the motile response is manifested as a circumferential contraction, with either an axial contraction (if the cell is permeabilised; Schacht and Zenner, 1987) or an axial elongation (if the cell is intact; Dulon et al., 1990). Dulon et al. (1990) and Coling et al. (1998) suggested that the difference in the axial length change between the intact and permeabilised cells is most likely due to the lack of a constant-volume restraint in the latter case, in which the circumferential contractions fail to increase the hydrostatic pressure which causes elongation in the intact isolated cell.

As for the mechanism, slow motility is known to involve cytoskeletal reorganization (Slepecky, 1989; Dulon and Schacht, 1992), and is mediated by phosphorylation reactions catalyzed by either myosin light chain kinase (MLCK) and/or calcium/calmodulin-dependent protein kinase II (CaMKII; Puschner and Schacht, 1997; Sziklai et al., 2001).

In addition to the active contractile mechanism above, the slow-motile OHC length changes could also be brought about by a modulation of axial stiffness (Frolenkov et al., 2003). In the presence of a tonic force, this decrease in axial stiffness could result in an apparent contraction or elongation, depending on whether the hair cell *in situ* is under compression or tension, respectively. Therefore, while the unloaded OHCs *in vitro* may elongate with increased Ca^{2+}_i, the *in vivo* situation is more complicated: whether the cell length increases or decrease will depend on the balance between the positive intracellular turgor pressure (Chertoff and Brownell, 1994) and the compressive forces imposed by the reticular lamina and the Deiters' cells.

Regardless of its underlying mechanism (i.e. an active contraction or a modulation of axial stiffness), evidence from our experiments, presented in Chapters Seven and Eight, suggest that *in vivo* the conditions which would result in an increase in intracellular calcium are likely to result in a movement of the hair-bundle in the direction that closes MET channels, consistent with a longitudinal shortening of the hair cell.

1.3.4 Slow-acting electromotility

The OHCs are able to generate mechanical forces that counteract viscous damping by the cochlear fluids, thereby enhancing the vibration of the basilar membrane by around 60 dB (for a review, see Geisler, 1998). The exact mechanism of this force production is still the subject of debate (see, for example, Allen, 2003), but there is a strong likelihood that somatic motility is the main force-generating component of the active process, driven by voltage-dependent conformational changes of the motor protein, prestin, in the basolateral membrane of the OHCs (Zheng et al., 2000).

While fast electromotility is capable of acting on a cycle-by-cycle basis up to many tens of kilohertz (Frank et al., 1999), it also responds to slow changes in transmembrane voltage, producing a slow, graded change in cell length (Ashmore, 1987). This has been referred to by Frolenkov et al. (2003) as "activating fast OHC electromotility slowly", and has been incorporated into the mathematical model of the OHC described in the Section 1.5 below.

1.3.5 Competing mechanisms to change operating point in OHCs

From the above, it can be seen that the operating point of the OHC can be moved towards scala tympani by a depolarisation of the hair cell (acting via prestin), or by an increase in cytosolic calcium (acting via slow motility). However, from a causative point of view, increasing cytosolic calcium *in vivo* will cause a slow-motile contraction of the OHC, but will also open Ca^{2+}-dependent K^{+} channels, which will cause hyperpolarisation of the OHC and a prestin-mediated *elongation* of cell length. It appears that these two motile mechanisms are essentially independent and additive, with the resulting operating point shift being the sum of the contributions from both.

1.4 Cytosolic calcium and the need to control basolateral permeability

In addition to influencing the operating point of the OHC MET channels via slow motility, cytosolic calcium concentration also affects the permeability of the basolateral wall to potassium, via the calcium-sensitive potassium channels (Ashmore and Meech,

1986). As a resistive element of the voltage divider between the EP and the tunnel of Corti potential, the basolateral permeability of the OHCs determines the basolateral membrane potential of the OHC, the standing current through the OHCs, and, in the presence of sound, determines the magnitude of the AC receptor current and receptor potential.

1.4.1 AC receptor potential and fast electromotility

As discussed above, we make the assumption here that somatic motility is the main force-generating component of the active process, driven by voltage-dependent conformational changes of the motor protein, prestin, in the basolateral membrane of the OHCs (Zheng et al., 2000). At this point in the discussion it should be mentioned explicitly that the mathematical model presented here was developed with the aim of investigating the possible role of cytosolic calcium in regulating *somatic* electromotility: any degree of OHC electromotility which may arise from the stereocilia was not within the scope of the present project, and so was not considered in the modelling, but will be discussed later in Chapter Nine.

The voltage driving the conformational changes of prestin on a cycle-by-cycle basis is the AC receptor potential, produced by the flow of ions (the receptor current) through mechanoelectrical transduction (MET) channels with movement of the hair bundle at the apex of the cell. The relationship between receptor current and receptor potential is determined by the resistance to current flow at the apex and the base of the cell, and the capacitance of the cell membrane. The capacitance of the OHC membrane limits the amplitude of the receptor potential at higher frequencies, with some measurements on isolated outer hair cells indicating a cut-off frequency of around 400 Hz (Housley and Ashmore, 1992). Many authors have suggested compensatory mechanisms by which this "RC time constant problem" could be resolved, including fast-acting K^+ (Ospeck et al., 2003) or Cl^- fluxes (Rybalchenko and Santos-Sacchi, 2003), and resonant electromechanical forces arising from the tympanic membrane (Zwislocki and Kletsky, 1979; Scherer and Gummer, 2004) or the piezoelectric properties of the OHC cell wall (Spector et al., 2003).

If we assume that the AC receptor potential *is* responsible for driving somatic electromotility, then any mechanism which decreases its magnitude is likely to result in a reduction of the ability of electromotile contractions to contribute to BM motion, thereby reducing the active gain of the cochlea. In the outer hair cells, most ionic current is carried by K^+ (Johnstone et al., 1989), and (as shown in the schematic

diagram in Figure 1.1) the basolateral potassium permeability is controlled by the basolateral membrane potential itself (via voltage-dependent potassium channels), and by cytosolic calcium (via calcium-dependent potassium channels). An increase in cytosolic calcium concentration causes opening of the calcium-dependent potassium channels, decreasing the resistance of the basolateral wall, which results in an increase in the AC receptor current and a decrease in the AC receptor potential (that drives prestin). The cytosolic calcium concentration is therefore able to exert a strong influence on the potassium permeability of the basolateral wall of the OHC, and therefore somatic electromotility, because elevated cytosolic calcium essentially "short-circuits" the basolateral wall (at low frequencies, at least).

1.4.2 Standing current, the EP, and rate tinnitus

The standing current through the OHC is inversely proportional to the sum of resistances of its apical and basolateral membranes. The apical resistance is determined in part by the operating point, while a major component of the basolateral resistance (as described above) is also controlled by intracellular calcium. As the outer hair cells are a major current shunt from scala media, the endocochlear potential is directly affected by changes to either of the OHC resistances. As discussed by Patuzzi (2002), an increase in the EP (due to a reduction in the current shunt provided by the OHCs) can depolarise the resting membrane potential of the nearby inner hair cells (IHCs), resulting in an increased release of neurotransmitter onto the primary afferent neurones. This increase is presumed to underlie at least one form of tinnitus, which can be called "rate tinnitus" (McMahon and Patuzzi, 2002; McMahon, 2004; Searchfield et al., 2004). It is this form of tinnitus that is presumed to occur during the low-frequency bounce in humans (Patuzzi and Wareing, 2002), corresponding to increases in the EP in the guinea pig (Kirk, 1972), and which will be discussed further in Chapter Six.

1.5 The Model

1.5.1 The schematic model of OHC regulation – omissions and additions

In order to model the homeostatic mechanisms within the OHCs, it was necessary to make a number of simplifications, including the removal of certain cellular components, and consolidation of the intracellular Ca^{2+} storage compartments. The rationale behind each of the simplifications will be presented in detail in Chapter Two, but for the moment the changes can be viewed at a glance by the comparison of Figures 1.6A and 1.6B. Removed from the basolateral wall of the OHC schematic diagram (Figure 1.6A) were the voltage-gated sodium channel, the chloride leakage channel, the stretch-

sensitive K^+ channel, and the plasma-membrane calcium channel (PMCA), while the synaptic cisternae were incorporated into the subsurface cisternae (SSC). There are also some inclusions to the diagram: namely, a putative intracellular second-messenger system (consisting of Ca^{2+}, and its intracellular messenger cascade M2, M3 and M4). This intracellular messenger system is central to the functioning of the model, and so will be discussed in detail in later sections, but briefly, it has been incorporated into the cell model to account for the phase delays between the presumed rise in cytosolic calcium, the action of calcium-dependent slow-motility, and the accelerated sequestration of calcium into the SSC. The phase delays provided by the second-messenger system were required in order to allow the intracellular calcium concentration feedback loop to oscillate, in accordance with our hypothesis that many of the cochlear oscillations described above can be attributed to oscillations in cytosolic calcium concentration. The schematic model described here has been presented previously by O'Beirne and Patuzzi (2002; 2003) and Patuzzi (2003).

Figure 1.7 shows a different representation of the OHC, arranged so that the relationship between cellular components and ions are more clearly visible. Essentially, Figure 1.7 shows the five major components of the model: a) a voltage divider which determines the OHC resting potential from its apical and basolateral conductances, the intracellular and extracellular ionic concentrations, and the potentials within scala media and the tunnel of Corti; b) a basolateral Ca^{2+} transport system, consisting of a voltage-controlled Ca^{2+} channel, a ligand-mediated (acetylcholine or ACh) Ca^{2+} channel, a Na^+/Ca^{2+} antiport, and a Ca^{2+}-ATPase pump; c) an intracellular-messenger cascade consisting of the cytosolic Ca^{2+} concentration, and three additional putative intracellular messengers (M2, M3, and M4); d) somatic electromotility, which produces an OHC length change proportional to the voltage (V_{mb}) across the basolateral wall; and e) slow Ca^{2+}-dependent motility, which produces an OHC length change proportional to the level of the intracellular messenger M4. The transmembrane voltage across the apical wall of the OHC is indicated by V_{ma} in Figure 1.6, while the basolateral transmembrane voltage is indicated by V_{mb} in Figure 1.6 and simply V_m in Figure 1.7. Also shown in Figure 1.7 are the four *negative feedback loops* of the model, indicated by shaded arrows labelled I to IV.

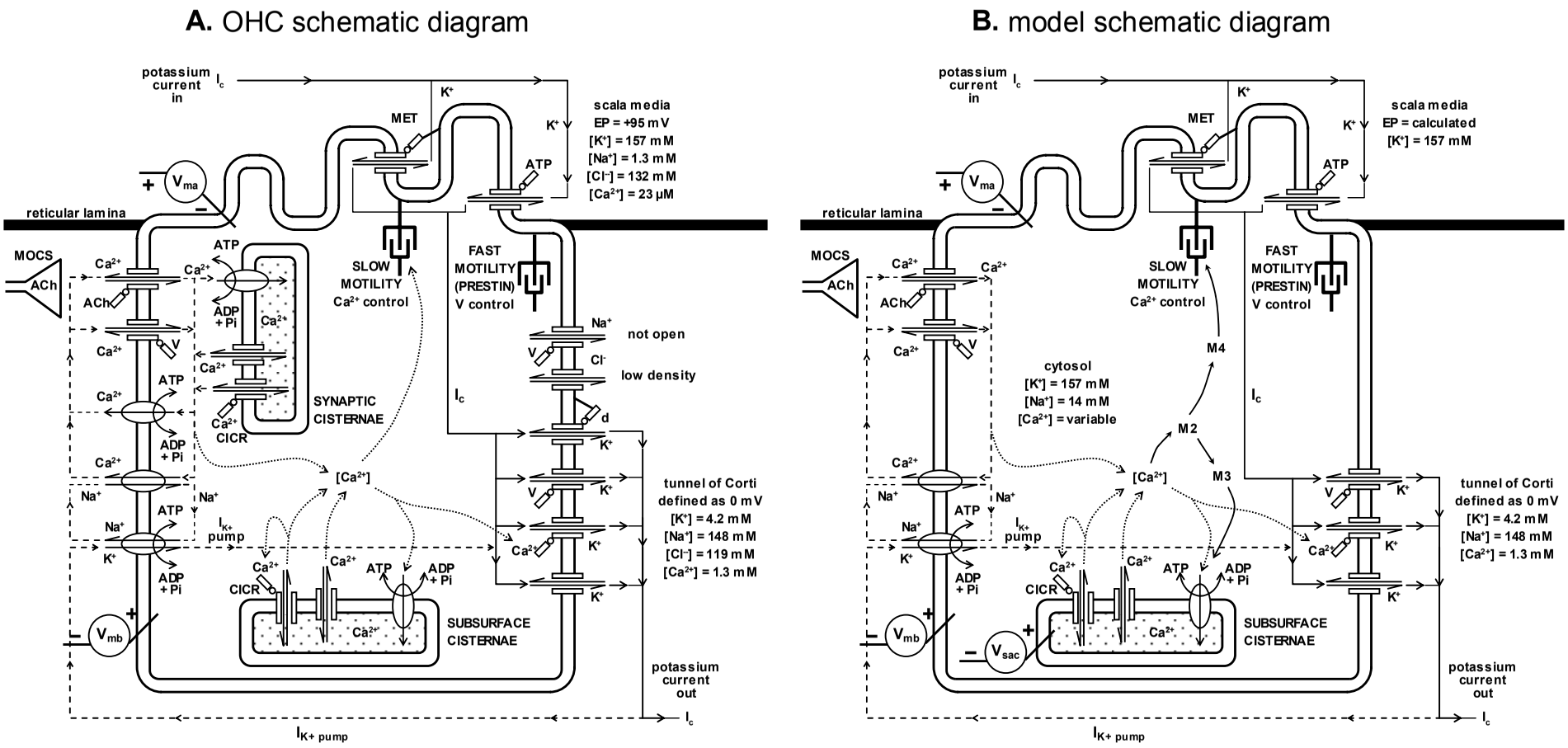

Figure 1.6: A. This figure was shown previously in this chapter as Figure 1.1, but is presented again at this point in the text to allow comparison with panel B. It is a summary (adapted from Patuzzi, 1998) of the main ionic transport pathways through the OHCs, with representations of fast and slow somatic motility, the apical and basolateral transmembrane voltages (V_{ma} and V_{mb} respectively), and the presumed ionic concentrations of scala media and the tunnel of Corti. **B.** The mathematical model of OHC regulation contains a subset of the ionic transport mechanisms shown in panel A, and includes the putative second-messenger system controlling calcium extrusion and slow motility (Ca^{2+}/M2/M3-M4). A full discussion of these model components (and the omissions) is presented in Chapter Two.

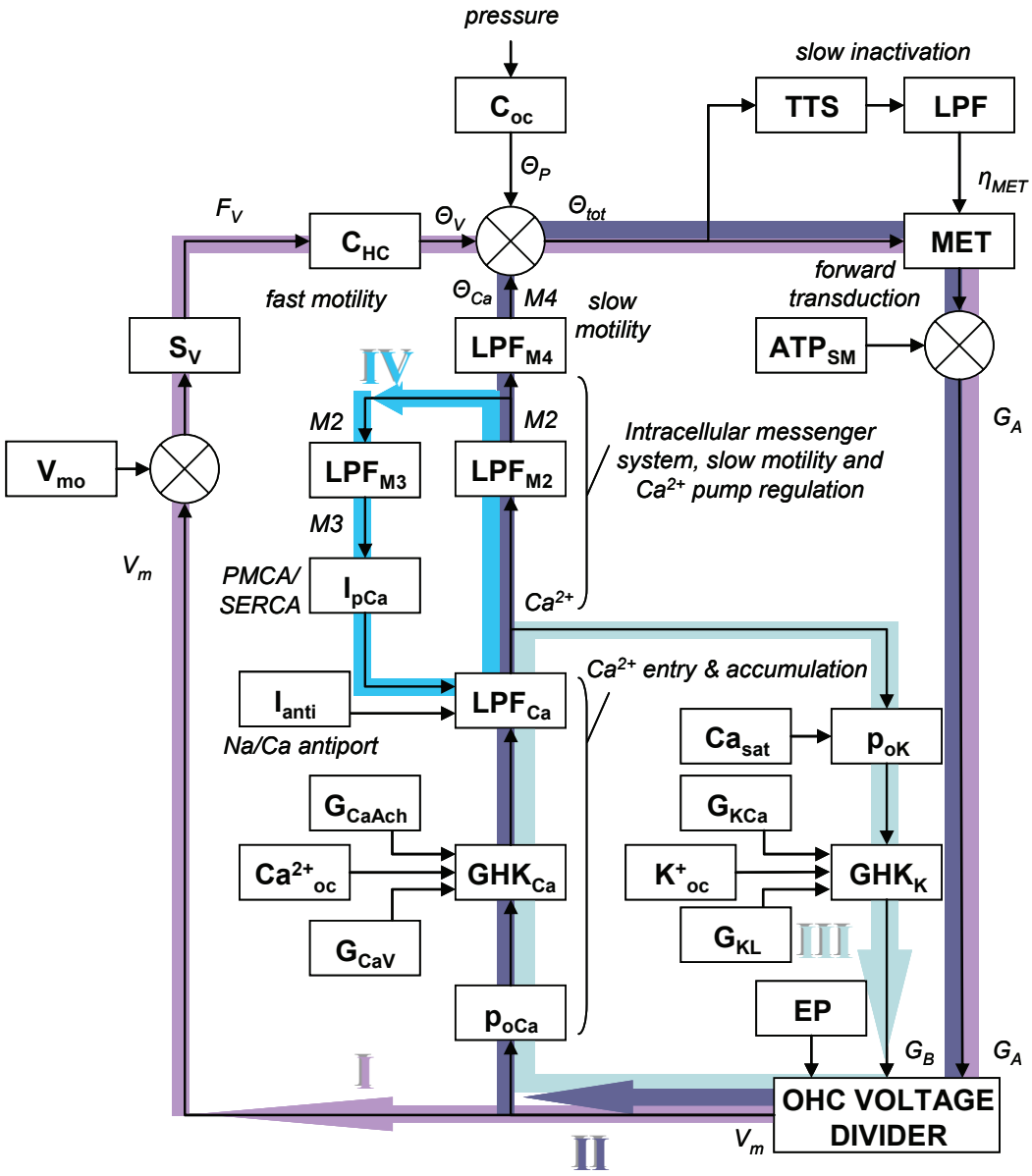

Figure 1.7: Schematic diagram of OHC homeostasis, illustrating the interactions between the cellular components and mechanisms shown in Figure 1.6B (see text for explanation).

Legend:

ATP_{SM}	endolymphatic ATP concentration
Ca^{2+}	cytosolic calcium concentration
Ca^{2+}_{oc}	Ca^{2+} concentration in the tunnel of Corti
Ca_{sat}	binding constant of Ca^{2+} to Ca^{2+}-controlled basolateral K^+ conductance
C_{HC}	combined compliance of OHC and organ of Corti
C_{oc}	mechanical compliance of organ of Corti
EP	endocochlear potential
F_V	force generated by electromotile process
G_A	total OHC apical conductance
G_B	total OHC basal conductance
G_{CaACh}	Ca^{2+} conductance in basolateral wall (leakage & ACh-controlled channel)
G_{CaV}	maximal voltage-controlled Ca^{2+} conductance of basolateral wall
GHK_{Ca}	Goldman-Hodgkin-Katz equation describing Ca^{2+}-channel current
GHK_K	Goldman-Hodgkin-Katz equation describing K^+-channel current
G_{KCa}	maximal conductance of Ca^{2+}- controlled K^+ basolateral channel
G_{KL}	leakage K^+ conductance of OHC base
I_{anti}	Ca^{2+} flux through basolateral Na^+/Ca^{2+} antiport
I_{pCa}	Ca^{2+} ATPase pump (e.g. PMCA or SERCA)
K^+_{oc}	K^+ concentration in the tunnel of Corti
LPF	Low pass filter (slow integration of preceding variable)
M2	intracellular messenger 2
M3	intracellular messenger 3
M4	intracellular messenger 4
MET	mechano-electrical transduction
Po_{Ca}	activation probability of voltage-controlled Ca^{2+} channel
Po_K	activation probability of Ca^{2+}-controlled K^+ channel
S_V	sensitivity of OHC electromotile process (nm/mV)
TTS	temporary threshold shift (slow inactivation of MET channels)
V_m	membrane potential within OHC relative to extracellular space beneath cell
V_{mo}	membrane potential reference level defining set-point of OHC electromotility
ΘV	OHC operating point change due to fast electromotility (voltage-mediated)
ΘCa	OHC operating point change due to slow electromotility (calcium-mediated)
Θp	OHC operating point change due to an input pressure stimulus
Θtot	total change in OHC operating point

It should be emphasised that the schematic diagrams shown in Figures 1.6B and 1.7 are intended to represent the same system. However, there are some important differences between the diagrams that should be pointed out: for simplicity, only the potassium and calcium ions are represented in Figure 1.7 (the "loop" diagram). Also, the sodium ionic pathways have been omitted, as have the synaptic and subsurface cisternae.

1.5.2 Demonstration of the negative feedback loops

To demonstrate how the feedback loops shown in Figure 1.7 would function within the OHC, let us consider the application of a positive hydrostatic bias to scala tympani, and track the effects of this perturbation through each of these feedback loops. Firstly,

i) the pressure stimulus would result in an OHC operating point change towards scala vestibuli, with magnitude dependent on the overall compliance of the organ of Corti.

Beginning with Feedback Loop I, we would expect:

ii) an increase in the OHC apical conductance via the MET channels;

iii) a depolarisation of the cell via the OHC voltage divider, causing a fast-electromotility-induced operating point shift towards scala tympani, of a magnitude dependent on the sensitivity of the reverse-transduction process and the combined compliance of the OHC and organ of Corti, *thereby partially compensating for the initial operating point shift towards scala vestibuli*.

Following Loop III from the depolarisation event in point iii) above, we would see:

iv) an increase in the activation probability of the basolateral voltage-sensitive Ca^{2+} channels, resulting in increased entry of Ca^{2+} into the cell, in accordance with the Goldman-Hodgkin-Katz (GHK) equation;

v) this increased Ca^{2+} flux integrate to produce an increased cytosolic Ca^{2+} concentration;

vi) an increase in the activation probability of the calcium-sensitive K^+ channels in the OHC basolateral membrane, resulting in increased K^+ efflux from the cell;

vii) a hyperpolarisation of the cell via the OHC voltage divider, *thereby partially compensating for the depolarisation above*.

If we then observe Loop IV from the increased cytosolic Ca^{2+} concentration in point v) above, we would see:

viii) a slow increase in the activity of the putative second messenger M2, followed by a similarly slow increase in the third messenger M3;

ix) the increased M3 activity cause an increase in the rate of Ca^{2+} extrusion from the OHC via the Ca^{2+}/ATPase pump, and increased Ca^{2+} sequestration into the SSC (not shown);

x) this increased Ca^{2+} efflux and sequestration integrate to produce a decreased cytosolic Ca^{2+} concentration, *partially compensating for the above increase in Ca^{2+} concentration*.

Finally, if we follow Loop II from the increased M2 activity in point viii) above, we see:

xi) a slow increase in the activity of the messenger M4, which would cause a contraction of the cell due to the operation of the calcium-dependent slow motility mechanism; and

xii) a scala tympani operating point shift, *thereby partially compensating for the initial scala vestibuli operating point shift produced by the hydrostatic bias in point i) above.*

It is clear from this simple (and, indeed, somewhat simplistic) demonstration that the presence of these feedback loops serves to buffer the model against perturbations, and in this sense the overall system can be described as homeostatic. However, while the system as a whole may be stable in the long-term, there is strong evidence that it is susceptible to transient oscillatory behaviour, such as that demonstrated during the "bounce phenomenon". Such oscillatory behaviour could arise in OHCs as a consequence of phase shifts between variables, as described below.

The slow integration of preceding variables to influence others (such as the intracellular messenger cascades in the model) effectively results in these elements acting as low-pass filters, each of which contributes a phase shift to the system. The theoretical maximum phase shift any single stage of filtering can contribute is 90º. To determine whether this negative feedback loop is able to oscillate, we must refer to the Nyquist stability criteria (Nyquist, 1932), which state that a negative feedback system will become unstable at a particular frequency (that is, negative feedback will become positive feedback) when the loop has a net phase shift of 180º (which becomes 360º

when the inversion due to the negative feedback is added) and a total loop gain greater than one (Ogata, 1997). The inclusion of multiple stages of filtering in a single loop of the homeostatic model (for example, the integration stages between Ca^{2+}, M2, and M3 in Loop III) therefore helps to satisfy the Nyquist criteria, increasing the likelihood that a perturbation of this loop may cause transient instability and oscillatory behaviour.

1.5.3 Calcium in outer hair cells

Calcium was proposed as an integral component of the oscillations due to its involvement in slow motility, and its ability to affect cochlear gain via modulation of basolateral permeability and axial stiffness. Ca^{2+} is uniquely placed to influence all three of these components.

The cytosolic calcium concentration of a typical cell is generally of the order of 100 nM, rising to around 5 μM when the cell is activated by an extracellular signal, and reaching dangerous levels above 10 μM (Alberts et al., 2002). The Ca^{2+} concentration of endolymph is extremely low (around 23μM), but is somewhat higher (around 1.3 mM) in scala tympani perilymph (Lumpkin et al., 1997).

Calcium enters the OHCs through voltage-sensitive and ACh-sensitive Ca^{2+} channels in the basolateral wall, and through the MET channels (Housley et al., 1992; Wang et al., 2003) and ATP-sensitive non-specific cation channels present in the apical membrane (Crawford and Fettiplace, 1985; Howard and Ashmore, 1986). In eukaryotic cells, cytosolic calcium concentration is tightly regulated by a range of mechanisms, including extrusion from the cell by the plasma membrane Ca^{2+}-ATPase (PMCA) and the Na^{+}/Ca^{2+} antiport, buffering by intracellular proteins, and sequestration into internal compartments – the cell nucleus, the mitochondria, and the endoplasmic reticulum (ER) / sarcoplasmic reticulum (SR) of muscle cells. These intracellular compartments act as reservoirs for the storage and release of Ca^{2+}.

Once the Ca^{2+} has been transported into the compartment by the sarcoplasmic/endoplasmic Ca^{2+}-ATPase (or SERCA), it is buffered by luminal proteins such as calreticulin in the ER and calsequestrin in the SR (Lytton and MacLennan, 1992). Release of Ca^{2+} from the compartment occurs via the action of the ryanodine receptor (RyR) and/or the inositol 1,4,5-trisphosphate (IP3) receptor Ca^{2+}-release channels (Berridge, 1998). Both the IP3-sensitive release channels and the RyRs are sensitive to Ca^{2+} itself, providing mechanisms for the amplification of calcium signals in a process known as calcium-induced calcium release (CICR).

There exist two structures in the OHC that are analogous to the ER/SR compartments – the subsurface cisternae (SSC) and the synaptic cisternae (or SC; Lioudyno et al., 2004). The subsurface cisternae (SSC) of the OHCs share a number of the same morphological and functional characteristics of the ER/SR (Pollice and Brownell, 1993), including a high calcium concentration (Schulte, 1993), and the presence of the Ca^{2+}-ATPase pump (particularly in the innermost layer of the SSC; Schulte, 1993; Zine and Schweitzer, 1996).

As shown in Figure 1.8, the close proximity of the SC to the olivocochlear efferent terminals indicates that they may mediate the effects of efferent stimulation on the OHCs. These effects include an increase in basolateral permeability (as evidenced by an increase in CM magnitude and a reduction in the EP), a reduction in active gain, and a reduction in axial stiffness (Guinan, 1996; Dallos et al., 1997). This is likely to take place in a two-step process, with a fast efferent effect due to the direct effect of Ca^{2+} influx on the Ca^{2+}-sensitive K^{+} channels, with a slower efferent effect (following a delay of around 10 seconds) that is consistent with a release of Ca^{2+} from intracellular stores (Shigemoto and Ohmori, 1991; Dallos et al., 1997).

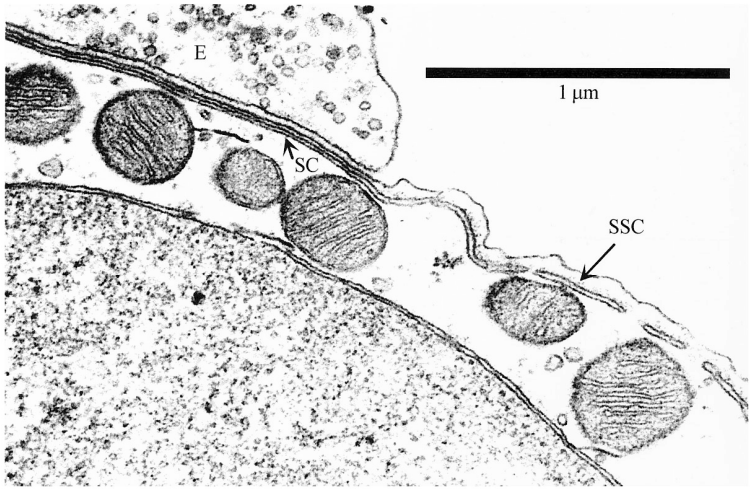

Figure 1.8: A transmission electromicrograph of the subsurface cisternae (SSC) and synaptic cisternae (SC) in a guinea pig OHC near an olivocochlear efferent terminal (E), showing the proximity of the SSC to the OHC lateral membrane (Kimura, 1975; Sridhar et al., 1997).

In terms of the role of calcium in the schematic model of OHC regulation, the cytosolic calcium level in the model is controlled via a negative feedback loop, whereby a rise in calcium concentration causes an increase in the concentration of the messenger M2, which in turn causes an increase in M3, which acts to reduce the cytosolic calcium concentration. The M4-sidebranch of this loop is used in the model to cause the slow-motility contraction of the OHC, resulting in a scala tympani operating point shift. This is summarised in Figure 1.9 below.

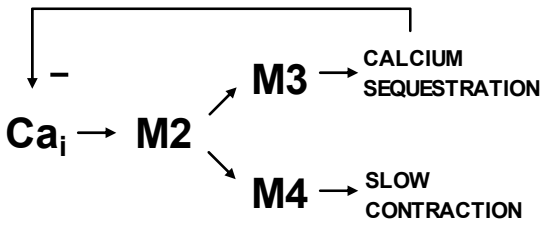

Figure 1.9: A schematic representation of the intracellular 2nd-messenger cascade of the homeostatic model. M4 acts as a side-arm from the overall negative feedback loop shown as Loop IV in Figure 1.7.

The decision to include the messenger M4 as a slow-motile side-branch of this loop (rather than using an intermediate such as M3 to control slow-contractions) was made after an examination of accumulated experimental evidence that indicated that while oscillations in basolateral permeability (manifested in the Vsat Boltzmann parameter, described in Section 1.2.2 above) can occur without an oscillation in the operating point, *the reverse is never observed*. That is, oscillations in the operating point have not been observed in the absence of oscillations in Vsat. If the operating point were controlled by M3, the oscillation of the calcium loop would also be visible in the operating point. As discussed later, this observation of Vsat oscillation without substantial operating-point oscillation may be partly explained by a two Ca^{2+}-compartment model.

In any case, does this system of 2nd-messengers have any physiological basis? Are there known biochemical correlates within the OHCs which could carry out the roles assigned to M2, M3, and M4 in the outer hair cell model? The final stage of the negative feedback loop shown in Figure 1.9 requires that a rise in the second messenger M3 acts to lower intracellular calcium concentration.

1.5.4 Possible biochemical correlates of the 2nd messengers

Possible intermediates in this process (referred to as M2 and M3) are the calcium-calmodulin complex, and calcium-calmodulin-dependent protein kinase II (CaM-kinase II), as discussed below.

Calmodulin is found in virtually all eukaryotic cells, and can constitute up to 1% of the total protein mass of a typical animal cell (Alberts et al., 2002). In OHCs, it is present in the hair bundles (Walker et al., 1993), cuticular plate and cell body (Pack and Slepecky, 1995) and is co-localised with actin (Slepecky et al., 1988). It acts as a high-affinity intracellular receptor and mediates many cell processes by binding to other proteins. Two such proteins are the plasma membrane Ca^{2+}-ATPase (PMCA; Furuta et al., 1998), and the SR Ca^{2+}-ATPase (Xu and Narayanan, 2000).

In addition to this modulation of the activity of the Ca^{2+}-ATPases by the calcium-calmodulin complex, the activity of the Ca^{2+}-ATPases can also be altered by calcium itself (Wu et al., 2001). However, as these two means of modulating the activity of the Ca^{2+}-ATPase consist of either only one step (calcium to the pump) or two steps (calcium to calcium-calmodulin to the pump), they cannot impart the necessary phase delays for oscillation, as each low-pass filter step can add a maximum of 90 degrees phase shift, as described above. Therefore, while we assume that these processes occur, they do not form part of the oscillations of interest and are therefore excluded from the model.

However, as mentioned above, another regulatory mechanism involves CaM-kinase II, which increases Ca^{2+}-ATPase activity by phosphorylation. In studies of the SERCA-2A isoform (found in cardiac muscle cells and slow-twitch skeletal muscle), Xu and Narayanan (1999) found that phosphorylation by CaM-kinase II exerted two effects on SERCA-2A: the first was a 50-70% increase in the maximal pumping rate of the Ca^{2+}-ATPase, while the second was phosphorylation of the intrinsic SR protein phospholamban[2], which increased the affinity of the SERCA for Ca^{2+} (Xu and Narayanan, 1999, and references therein). In addition, because CaM-kinase II is activated by calcium-calmodulin complex, this provides the additional intermediate required to satisfy our oscillation criteria. The result of such a cascade in the OHC would be that an increase in cytosolic Ca^{2+} would cause an increase in calcium-calmodulin concentration, which would cause an increase in CaM-kinase II, which increases the sequestration of Ca^{2+}, thereby lowering free cytosolic Ca^{2+} levels.

Therefore, to summarise, we believe that M2 may be the calcium-calmodulin complex, and M3 is CaM-kinase II. Whether M4 is a distinct entity, or a separate pool of one of the other messengers in the cascade, will be considered in Chapter Nine.

1.6 Structure of the project and thesis organisation

The genesis of the project was the development of the schematic model by Patuzzi. This was developed further in conjunction with the present author, and the preliminary versions of the mathematical model were constructed. The preliminary modelling used the results of Marcon and Patuzzi (Marcon, 1995; Marcon and Patuzzi, in preparation) as a reference. However, as well constructed and performed as those experiments were, the available technology meant that usually (with the exception of the EP) only one set of parameters could be recorded during any one perturbation (that is, Boltzmann data or

DPOAE/CAP/SP, but not both). In order to elucidate the mechanisms of the changes observed experimentally, it was clear that more data was needed, particularly that which showed the correspondences between the Boltzmann data and the CAP thresholds.

The hardware Boltzmann analysis technique used by Marcon and Patuzzi (and described in Chapter Four) extracted the Boltzmann parameters from CM waveforms evoked by a continuous 207 Hz tone, but the presence of the tone itself caused alterations to the cochlear behaviour (such as a hydrops; Salt, 2004). The different behaviours of the cochlea under these conditions made it more difficult to compare the time-courses for the Boltzmann data for a given perturbation with the measurements of SP or CAP threshold, which were necessarily recorded in the absence of the 207 Hz tone. A similar conflict arose when attempting to compare DPOAE results with other measurements.

To resolve this dilemma, it was decided to develop software to enable the near-simultaneous measurement of multiple indicators of cochlear function, so that the interactions between the various cochlear components could be inferred from one set of time-courses. This programming was carried out by the author, in collaboration with Dr. Robert Patuzzi during the earlier stages of the software design. The software included a method of extracting the Boltzmann data from CM waveforms evoked by 50 ms 207 Hz tone-bursts. This had the advantage of allowing co-measurement of other cochlear indicators, and greatly improved the experimental recordings, including the simultaneously measurement of seven different CAP thresholds at different frequencies. As far as we know, experimental results of this type have not been previously published, or are extremely rare. A detailed discussion of The Cricket software that made it possible to obtain the data required for the present study is presented in Chapter Four.

In hindsight, however, the lack of a continuous LF tone during the measurement procedures could have back-fired: it almost eliminated the highly oscillatory responses that the project was designed to model! The potentiation of these oscillations by low-frequency tones will be discussed further in Chapter Six. Nevertheless, once the measurement software had been designed and programmed, a series of guinea-pig experiments were undertaken. The strategy adopted was to perturb the cochlea in a variety of different ways, and then to monitor as many aspects of cochlear function at once, in order to establish the time-courses and study the interactions between the

[2] Phospholamban is also phosphorylated by cAMP dependent protein kinase (PKA).

various components. The results of the experimental data obtained using the custom-written software were then used to refine and modify the mathematical model, with further model development and consolidation occurring in the latter stages of the project. As will be described in the coming chapters, the mathematical model was capable of replicating most of the key features of the experimental data. However, there were some important differences between the model predictions and the experiment results that provided an insight into the shortcomings of the single-calcium-pool model described here. These will be discussed in detail in later sections of this report.

The overall structure of the report is as follows:

a) Chapter Two contains the details of the mathematical model of the outer hair cell, including the model equations and parameters, and some of the insights from the modelling process.

b) The general methods are presented in Chapter Three. Additional procedures or techniques that were used only in subsets of the experiments are presented in the relevant Chapters.

c) Chapter Four describes custom software we developed for the monitoring of cochlear regulation, and details the CAP-tracking measurement techniques employed in this study.

d) Chapter Five contains results from experiments involving a novel perturbation that produced lasting operating point shifts: the application of force to the cochlear wall.

e) The cochlear oscillations produced during low-frequency bounce experiments are examined in Chapter Six, as well as the simulation results for mathematical modelling of the bounce phenomenon.

f) Chapter Seven presents the experimental results of injections of direct current into scala tympani, and compares these data with the mathematical modelling results for EP biases.

g) Chapter Eight contains the results of perilymphatic perfusion experiments (and corresponding modelling data) for changes in the concentration of perilymphatic sodium and potassium, and for increases in perilymphatic osmolarity.

Finally, a general discussion of the project findings and conclusions is presented in Chapter Nine, with preliminary details of the revised two-pool calcium model and its implications.

Chapter 2
Mathematical modelling of cochlear regulation

2. Mathematical modelling of cochlear regulation

2.1 Introduction

A mathematic model of the outer hair cell was created in an attempt to explain within one framework the results obtained from a range of experiments on cochlear regulation. In particular, the model was used to examine the possibility (described in Chapter 1) that the very slow oscillations in cochlear gain measured by Marcon (1995) and others following various cochlear perturbations were caused by a regulatory feedback loop involving calcium. The model attempts to replicate the electrochemical and mechanical characteristics of an OHC (or an homogenous population of OHCs) from the basal turn of the cochlea, and can be used to predict the response of these hair cells to given perturbations, and to allow examination of the time-course of the subsequent changes in basolateral membrane potential, ionic fluxes and concentrations, and hair-bundle angle. Predictions of the effect of hair cell parameters on the active gain of the cochlea are also generated, under the assumption that the force-generation ability of a hair cell is largely dependent on the conformational changes of the motor protein prestin driven by the small-signal AC receptor potential. Any electromotility arising from the stereocilia is not included in the model.

The model successfully replicates, and provides a feasible explanation for, a number of the effects of a variety of cochlear perturbations, including i) the low-frequency bounce, ii) EP bias, iii) potassium perfusion, iv) sodium perfusion, v) hydrostatic bias, and vi) efferent stimulation. The results from the model are presented in Chapters Six, Seven, and Eight for ease of comparison with the experimental data. Some of the model predictions were *not* consistent with the experimental data, and these are discussed as and when they arise in the text. A full discussion of the suggested changes to the present model appears in Chapter Nine.

The model is defined by the equations and parameters described in Section 2.8, and experimental perturbations were simulated by systematic and timed variation of one or more of these parameters, as described in Section 2.10 below. There are two main outputs from the model: the first is the membrane potential and intracellular ionic concentrations which, along with the fixed parameters of the system, form the matrix of almost 100 values that defines the state of the cell at any point in time. The second source of output is from the IV-curve section of the model, described in Section 2.5.1 below, which is essentially separate from the main body of the model, and uses load-

line analysis to estimate the receptor current and potential during a simulated high-frequency tone (Patuzzi, 1998).

The model was programmed in G-code using LabVIEW (v5.1 to 7.0; National Instruments Corp., TX, USA). The details of the model that are independent of the specific implementation are presented in this chapter, while the computational issues that pertained solely to the LabVIEW implementation are presented in the Appendix.

2.1.1 Outline of the model

The necessary simplifications, omissions and assumptions made in the formulation of the OHC model are detailed in Section 2.7 , but many of these can also be seen at a glance in Figures 1.6A and 1.6B of Chapter One, which compares a schematic diagram of the cellular components documented in OHCs with those included in the model. For convenience, Figure 1.6B is reprinted below.

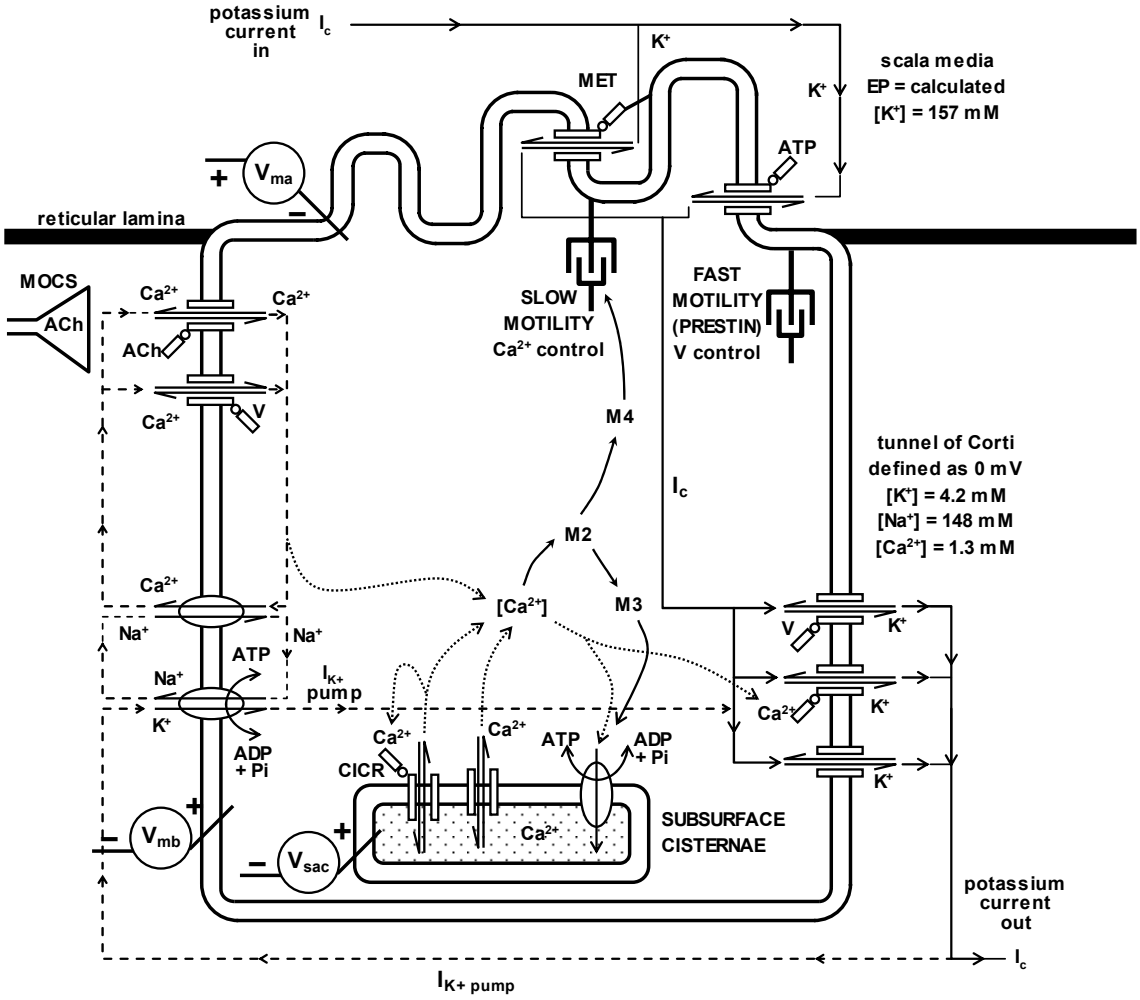

Figure 2.1: A summary (modified from Patuzzi, 1998) of the main ionic transport pathways included in the mathematical model of the OHC, reproduced from Figure 1.6B of Chapter 1. Also shown are the fast and slow motility and the apical and basolateral transmembrane voltages (V_{ma} and V_{mb}).

The model hair cell is assumed to have two external membranes: an apical membrane facing onto scala media and bathed in endolymph (defined as 157 mM K^+), and a basolateral membrane facing into the organ of Corti and bathed in perilymph (defined as 4.2 mM K^+, 148 mM Na^+, and 1.3 mM Ca^{2+}). The intracellular environment of the model cell is divided into two compartments: the cytoplasm (157 mM K^+, 14 mM Na^+, and variable concentrations of Ca^{2+}, M2, M3 and M4), and the subsurface cisternae (SSC) which function as calcium stores. The intracellular K^+ and Na^+ concentrations were derived from assumptions of i) the lack of an apical K^+ concentration gradient, and ii) a ratio of intracellular K^+ to Na^+ of 11:1, based on X-ray microanalysis of shock-frozen mouse cochleae (Anniko et al., 1984). The cytosolic calcium concentration in the model cell was generally of the order of 100 - 200 nM. The *in vivo* free (unbound) $[Ca^{2+}]_i$ in most cell types is generally of the order of 100 nM, rising to around 5 μM when the cell is activated by an extracellular signal, and reaching dangerous levels above 10 μM (Alberts et al., 2002). Isolated OHCs *in vitro* have $[Ca^{2+}]_i$ of around 60-220 nM (Wangemann and Schacht, 1996; Frolenkov et al., 2003).

Each membrane of the modelled OHC (apical, basolateral, and cisternal) contains a number of ionic transport mechanisms, described in greater depth in Section 2.8 below. The apex of the cell contains the MET channel and a leakage conductance simulating an ATP-sensitive channel, while the base of the cell contains voltage-sensitive and Ca^{2+}-sensitive K^+ channels, a K^+-leakage channel, voltage-sensitive and ACh-sensitive Ca^{2+} channels, a Ca^{2+}/Na^+ antiport, and a Na^+/K^+/ATPase pump. The model also contains Ca^{2+} transport into and out of the SSC in the form of a Ca^{2+}-ATPase pump, Ca^{2+} leakage and Ca^{2+}-induced Ca^{2+} release (CICR). The final element of the model is the Ca^{2+}/M2/M3-M4 second messenger cascade described in Chapter 1, in which M3 accelerates the pumping of Ca^{2+} into the SSC, and M4 causes contraction of the cell via the slow-motility mechanism. With the exception of the antiport, pumps, and Ca^{2+}/M2/M3-M4 cascade, the functioning of these ionic transport mechanisms is approximated using variants of the modified Goldman-Hodgkin-Katz (GHK) current equation described in Section 2.2 below.

2.1.2 Front panel (graphical user interface) of the model

To provide a reference for the reader, the main operating controls and outputs of the LabVIEW implementation of the mathematical model are shown in Figure 2.2. While the model equations were not editable from the front panel, the model parameters (listed in Section 2.8 below) were. Further screenshots are presented in the Appendix.

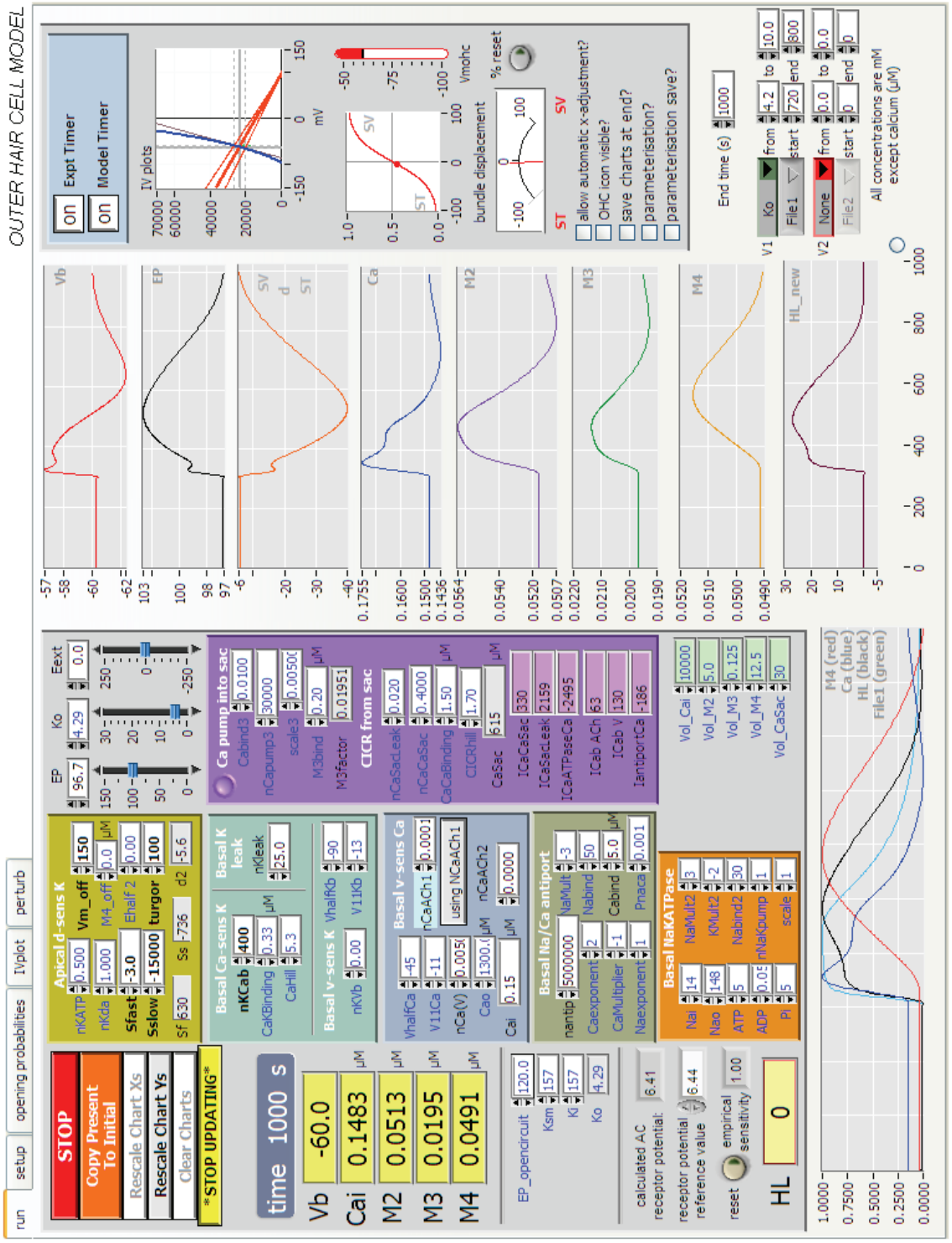

Figure 2.2: A screenshot of the front panel of the LabVIEW implementation of the mathematical model.

2.2 The modified Goldman-Hodgkin-Katz (GHK) current equation

The modified version of the GHK current equation (Patuzzi, 1998) provides useful approximations to the behaviours of many of the channel types present in the OHC. The equation (Hodgkin and Katz, 1949) states that the current of a particular ion through a membrane is equal to the permeability of the membrane to that ion, multiplied by a nonlinear function of voltage (Hille, 1992).

2.2.1 Permeability and opening probability

For an ion x passing through a particular channel j, the permeability P_{xj} is given by the simple product of the single-channel (unitary) conductance g_{xj}, the number of channels present in the membrane n_{xj} (with the assumption that their lateral position in the membrane is irrelevant), and the probability of opening of the channel p_{oj} (with the assumption that the channel has zero conductance in its closed state), such that:

$$P_{xj} = \left(g_{xj} \cdot n_{xj} \cdot p_{oj}\right) \qquad \textbf{[1]}$$

The opening probability p_{oj} shown above can take different forms, depending on the type of channel and opening characteristics. The form that is applicable for most two-state channels is the first-order Boltzmann equation, described below.

Let us assume that a channel whose permeability is sensitive to a particular quantity X (such as voltage or displacement) can, for a particular value of that parameter, be in one of two states – an open, conducting state, or closed, non-conducting state. For a given population of these X-sensitive channels, the probability p_{oX} of opening can be described by a first-order Boltzmann equation, such that:

$$p_{oX} = \frac{1}{\left(1 + 10^{\left((X - X_{½})/X_{11}\right)}\right)} \qquad \textbf{[2]}$$

where X is the instantaneous value of the parameter, $X_{½}$ is the value of X for which the probability of opening is 0.5, and X_{11} is the value of X away from $X_{½}$ required to increase the opening probability of the channel from 0.5 to $^{10}/_{11}$, or to decrease it from 0.5 to $^{1}/_{11}$.

In the case of many ligands, the p_{oX} can also be described using an alternative form of saturating function, such as the Hill equation:

$$p_{oX} = \frac{\left(X_i\right)^{Hill}}{\left(X_i\right)^{Hill} + \left(k_{half}\right)^{Hill}}$$

where X_i is the concentration of X, *Hill* is the Hill coefficient describing the cooperativity of the binding process, and k_{half} is the concentration of X where $p_{oX} = 0.5$.

2.2.2 Driving potential

Given that a membrane is permeable to an ion, for the ion to move from one side to the other there must be an electrochemical potential energy difference μ_x across the membrane – the so-called "driving potential" – which is dependent on the voltage across the membrane (V), the valence of the ion (z), and the activities of the ion inside (c_{xi}) and outside (c_{xo}) the cell, such that:

$$\mu_x = zV + \frac{kT}{q} \cdot \ln\left(\frac{c_{xo}}{c_{xi}}\right) \quad \textbf{[3]}$$

where k is the Boltzmann constant, T is the absolute temperature (in Kelvin), and q is the elementary charge on a proton (in Coulomb). To simplify the calculations presented below, we can substitute a multiplier E_{10}, such that:

$$E_{10} = \ln(10) \cdot \frac{kT}{q} = \frac{2.303kT}{q} \quad \textbf{[4]}$$

E_{10} is approximately equal to 60 mV at mammalian temperatures (around 38º C)[1]. The driving potential μ_x can then be written as:

$$\mu_x = zV + E_{10} \log_{10}\left(\frac{c_{xo}}{c_{xi}}\right) \quad \textbf{[5]}$$

The driving potential equals zero when the statistical or diffusion component, $E_{10} \log_{10}(c_{xo}/c_{xi})$, is balanced by the electrostatic component of the potential energy difference (zV). This voltage at which this occurs is the *equilibrium potential* of the ion at that concentration gradient[2].

2.2.3 The current equation

Taking into account the permeability component $(g_{xj} \cdot n_{xj} \cdot p_{oj})$ described above, we can use the modified GHK equation[3], shown in Equation 6 below, to calculate the current I_{xj} that would flow at a particular transmembrane voltage V. For a particular transmembrane voltage V, the current, I_{xj}, can be approximated by:

---

[1] The multiplier E_{10} can also be expressed as RT/F, where R is the universal gas constant, T is absolute temperature in Kelvin, and F is the Faraday constant.

[2] From this equation it is apparent that the ion's equilibrium potential would be equal to -60 mV if the extracellular concentration of a univalent cation were 10 times higher than the intracellular concentration.

[3] The derivation of the equation is described in detail elsewhere (Hille, 1992; Patuzzi, 1998).

$$I_{xj} = \underbrace{\left(g_{xj} \cdot n_{xj} \cdot p_{oj}\right)}_{\text{CONDUCTANCE}} \cdot \underbrace{\left(\frac{2.3z^2q}{E_{10}}\right) \cdot V \cdot \left[\frac{c_{xi} - c_{xo} \cdot 10^{(-zV/E_{10})}}{1 - 10^{(-zV/E_{10})}}\right]}_{\text{GHK}} \quad \textbf{[6]}$$

2.2.4 Modelling of active transport mechanisms

While the GHK equation provides an adequate approximation to passive fluxes of single ions across semi-permeable membranes, a different class of equation is required for active transport mechanisms. The equations reflect the facts that i) the ability of pumps (such as the Na^+/K^+/ATPase and Ca^{2+}-ATPase) to transport ions across membranes is a saturating function of voltage (Gadsby et al., 1985), and ii) the energy for moving Na^+, K^+, and Ca^{2+} against their concentration gradients is provided by the hydrolysis of ATP to ADP and inorganic phosphate (P_i). This class of equations is discussed further in Section 2.8.6.

2.3 Modelling of the second-messenger cascades

While several candidates exist, the identities of the putative second messengers M2, M3 and M4 are not known. In modelling the second-messenger cascades (from Ca^{2+} to M2, and from M2 to M3 and M4), the activation of each component is assumed to be a saturating function of the precursor concentration, without specifying the actual mechanism: for example, in the model, an increase in Ca^{2+} concentration causes an increase in the activity of the M2, but whether this occurs by phosphorylation, hydrolysis, or some other mechanism is uncertain.

The inactivation of the product is assumed to occur at a constant rate, $k_{reverse}$. The concentration of M2 reaches a steady state (i.e. the net production equals zero) when the rate of production is balanced by the rate of breakdown. The equations defining each stage of the cascade are presented later in Section 2.8 .

2.4 Modelling of hair cell motility

As shown in Equation 7 below, the equivalent energy bias acting to displace the stereocilia is calculated as the sum of three components: i) an internal energy bias due to fast and slow OHC motility; ii) an intracellular turgor pressure; and iii) an external energy bias (E_{ext}) that is used to model movement due to hydrostatic bias or sound.

$$E = \underbrace{E_{ext} + turgor}_{\substack{\text{EXTERNAL BIAS AND} \\ \text{CELL TURGOR}}} + \underbrace{c \cdot \left[\left\{S_{fast} \cdot \left(V - V_{off}\right)\right\} + \left\{S_{slow} \cdot \left(M4 - M4_{off}\right)\right\}\right]}_{\text{MOTILITY}} \quad \textbf{[7]}$$

These three components are described below.

Representation of motility: Both fast and slow motilities are modelled according to their effects on the operating point of the hair bundle. Fast motility is a function of the difference between the basolateral membrane potential, V_m, and an offset parameter, V_{off}, while slow motility is a function of the difference between the M4 concentration and the offset parameter $M4_{off}$ (although this parameter was usually set to zero).

The relative contributions of each motility bias is determined by the scaling factors S_{fast} and S_{slow}, while the combined influence of the motile biases is scaled by the *in situ* compliance of the cell, c.

Intracellular turgor: The turgor of the OHC is a requirement for electromotility (Brownell, 1990; Shehata et al., 1991). *In vitro* studies have shown that the sensitivity of the electromotile process to the AC receptor potential depends directly on the tension of the cell membrane (Kakehata and Santos-Sacchi, 1995; Takahashi and Santos-Sacchi, 2001; He, 2003). In the model, OHC turgor pressure is not used to modify the electromotile sensitivity directly, but can be used by the modeller to bias the hair bundle into its most sensitive range, counteracting the combined tonic slow and fast motile contractions.

External energy bias: The movement of the hair bundle to the presence of a hydrostatic bias or sound was simulated by changing the E_{ext} value directly, and will be discussed in Sections 2.10 , 2.11.1 and 2.11.1 below.

2.5 Membrane potential and load-line analysis

OHCs are in a voltage steady state (i.e. the cell is not charging or discharging) when the current entering through the apical membrane is equal to the current exiting through the basolateral wall. This steady-state occurs for a particular combination of apical and basolateral transmembrane voltages that can be determined using load-line analysis.

The load-line analysis technique, described in detail for OHCs by Patuzzi (1998), is possible because the apical and basolateral membranes share a common current[4] (they are connected in series). As illustrated in Figure 2.3, when the apical IV curve is expressed as a function of the basolateral (rather than apical) membrane potential, the intersection point of the two IV curves gives both the resting membrane potential and the quiescent current. *In vivo*, the resting membrane potential of the OHCs has been measured at approximately –70 mV (Dallos et al., 1982; Russell and Sellick, 1983). However, the reliability of these estimates is questionable: the OHCs are displacement-

[4] This current is shown as the solid line I_c in Figure 1.

coupled, and the process of impaling them with a microelectrode is bound to cause movement of the hair bundle and alteration of membrane potential. Russell and Sellick (1983) successfully measured membrane potentials in two OHCs, recording values of -65 and -70 mV. Similarly, Oesterle and Dallos (1989) measured the membrane potentials of three OHCs, recording values of -66, -70 and -84 mV. They described the OHC's "*tendency toward brief and unstable impalements*", and their characteristic resistance to being impaled, possibly due to their cortical cytoskeleton. This difficulty in puncturing the cell increases the likelihood of large hair-bundle movements during measurement. For want of a better estimate, the quiescent membrane potential (i.e. without perturbations) used in the model was between -60 and -70 mV.

The model employs this load-line analysis technique to solve for the quiescent membrane potential using a custom-written algorithm[5] (described in Appendix One) that iteratively "hunts" for the voltage at which the apical and basolateral currents are equal. The membrane potential found by the algorithm is then used in the transport equations to calculate the transmembrane fluxes, as described in Section 2.6 below.

2.5.1 Output from the IV-curve section of the model

While the primary output from the mathematical model is the state vector itself, the second source of output comes from the IV-curve section of the model, which is essentially independent of the main body of the model. In addition to the use of the load-line technique to find the DC membrane potential, the IV-curve section of the model uses load-line analysis to estimate the AC receptor current and receptor potential (both small-signal and saturated) during a simulated high-frequency tone (Patuzzi, 1998). The small-signal AC receptor potential enables an estimate of motor-induced threshold shifts to be made, as described below, while the saturated AC receptor current provides a correlate of the Vsat parameter extracted from the Boltzmann analysis of the low-frequency cochlear microphonic. In addition, the IV-curve display also provides a valuable graphical representation of the electrical state of the cell.

The basolateral IV curve shown in Figure 2.3 below is the sum of the potassium IV curves that contribute to the calculation of the membrane potential. The contributing channels are the voltage-sensitive K^+ channel, the Ca^{2+}-sensitive K^+ channel, K^+ leakage channel, and the Na^+/K^+/ATPase, described in Section 2.8 in equations 10, 11, 12 and 14b respectively.

[5] If the model were implemented in Microsoft Excel, the "Solver" routine could be used for this purpose.

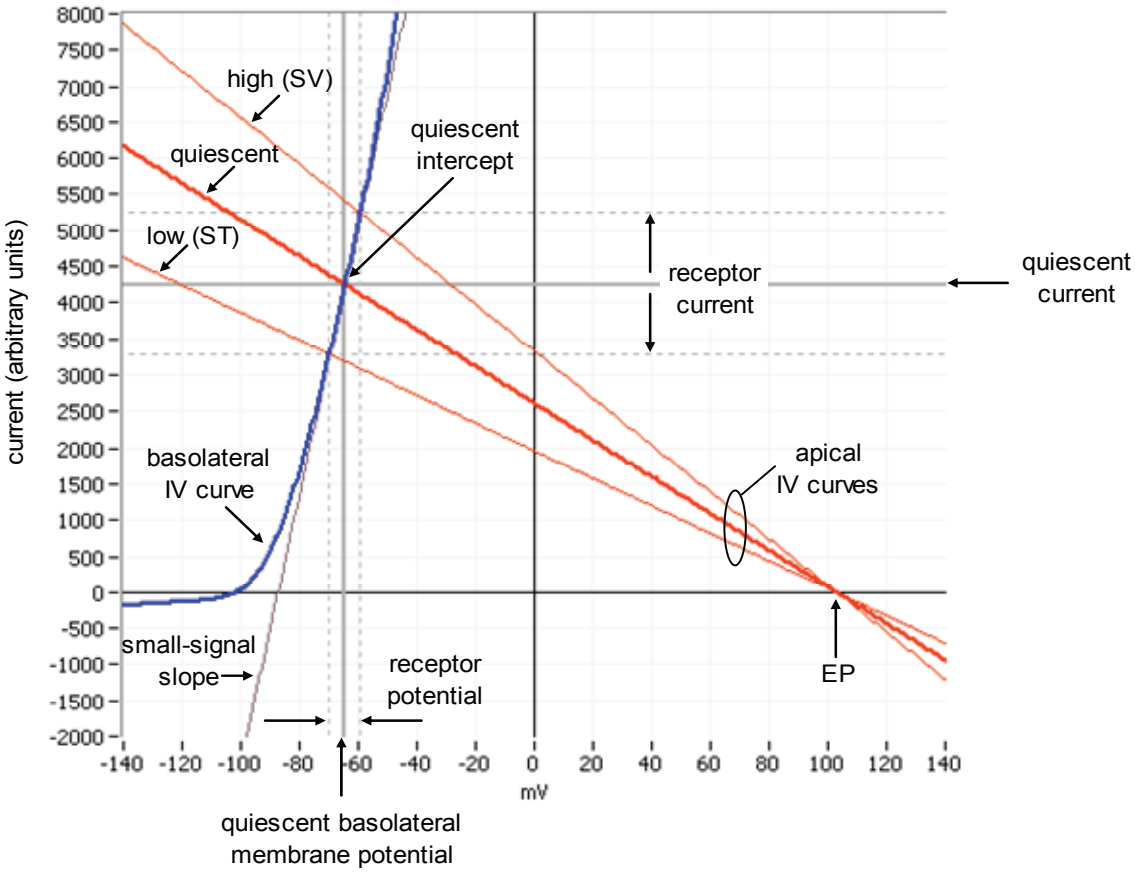

Figure 2.3: Diagram illustrating the process of load-line analysis for the calculation of OHC basolateral membrane potential, and for the calculation of receptor potential and receptor current in response to a simulated high-frequency tone (see text). [Note: The IV-curves shown here are for illustration only, and do not represent those produced by the final version of the model].

Shown in Figure 2.3 is a family of three IV curves representing the current passing through the apex of the OHC when the hair bundles are at their resting operating point (bold trace) and at the extremes of the hair bundle displacement during a simulated tone (lighter traces). The apical conductance (*Ga*) is assumed to be insensitive to voltage. The shape of the apical IV curve is determined by this apical conductance at each value of the apical membrane potential (V_{ma}). If the internal and SM concentrations of K^+ (K_i and K_{sm}) are not equal, G_a varies with V_{ma}, and the apical IV characteristic is curved. However, under normal conditions – when K_i and K_{sm} are equal – the apical IV curve is linear[6], and a single G_a is applicable for all values of V_{ma}.

As mentioned above, even though it was not computationally feasible to constantly generate tones at high frequencies in this particular model, plotting these apical IV curves allows the receptor current and receptor potential to be estimated. These

estimates are made by calculating the intersection of the basolateral IV curve with the IV curves representing the maximum and minimum apical conductances during the sound stimulus, as shown in Figure 2.3. The same basolateral IV curve was used for all three apical IV-curves as it was assumed that significant intracellular concentration changes did not occur during the time taken for one cycle of the high-frequency hair bundle oscillation. The apical IV curves, and the associated intercepts, were labelled "*low"* for hair bundle displacements toward scala tympani, "*quiescent"* for zero displacement, and "*high"* for displacements toward scala vestibuli. This simulated HF displacement was adjusted to a low amplitude (below 10 meV pp) for "small-signal" analysis, and high amplitudes (over 100 meV pp) for "saturated" analysis.

It is worth emphasising the fact that no reactive electrical components were included in the model. As such, the load-line approach used here is only applicable to tones that are well below the low-pass filter imposed by the capacitance of the membrane – in the case of the OHCs, this RC cut-off frequency has been estimated at around 400 Hz for a basal OHC (Housley and Ashmore, 1992; Preyer et al., 1996). Above this cut-off, the capacitive current causes the basolateral IV curve to become elliptical, reducing the magnitude of the receptor potential until it approaches zero.

2.5.2 Receptor potential, active gain, and estimated threshold elevation

As discussed in Chapter 1, there is a strong body of evidence to suggest that somatic motility is the main force-generating component of the active process, driven by voltage-dependent conformational changes of the motor protein, prestin, in the basolateral membrane of the OHCs. The AC voltage driving these conformational changes on a cycle-by-cycle basis is the AC receptor potential (Dallos et al., 1991), produced by the pulsatile flow of ions (the receptor current) that occurs with movement of the hair bundle at the apex of the cell. The production of this AC receptor potential in response to a sound stimulus is dependent on each step in the feedback loop describing the active process, as shown in Figure 2.4.

---

[6] When these concentrations are equal, there is no concentration component to the driving potential, and the K^+ current entering through the apex falls to zero when V_a equals the EP.

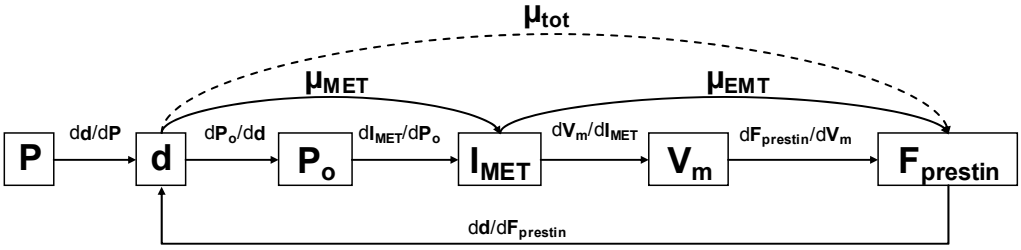

Figure 2.4: Schematic diagram of the active process. The μ_{tot} measure denotes the total efficiency of the mechanoelectrical and electromechanical transduction processes (MET and EMT respectively). *Legend:* P = pressure, d = displacement of the hair bundle, P_o = probability of opening of the MET channels, I_{MET} = the current through the MET channels, V_m = the basolateral membrane potential, $F_{prestin}$ = the force generated by prestin that causes movement of the hair bundle at the apex of the cell. μ_{tot} is the total efficiency of this process, and is the product of μ_{MET} and μ_{EMT}.

The efficiency with which displacement of the hair bundle (d) produces an AC receptor potential, and the subsequent force generation by prestin ($F_{prestin}$), is used in the model to provide an estimate of the changes in active gain of the cochlea, as will be described below. In the real OHC, the relationship between receptor current and receptor potential (V_m/dI_{MET} in Figure 2.4) is determined by the permeabilities of the apex and the base of the cell, and the capacitance of the cell membrane. However, in the model, reactive electrical components were excluded, and reactive mechanical components were included implicitly in the gain equation below.

Patuzzi and colleagues derived an empirical formula to describe the hearing loss (HL) resulting from a given percentage reduction in the active process (Patuzzi et al., 1989a; Patuzzi and Rajan, 1992). The formula relating threshold shift to the percentage loss of CM amplitude following acoustic over-stimulation is

$$HL = \frac{101\,\mathrm{dB}\cdot\left(1-\mu_{tot}\right)}{\left[1+0.85\cdot\left(1-\mu_{tot}\right)\right]} \qquad \textbf{[8]}$$

where μ_{tot} is a fraction of the closed loop gain of the active process. The significance of this μ_{tot} parameter was shown in the Figure 2.4. The 101 dB and 0.85 terms in the numerator and denominator respectively were derived empirically from the relationship between the drop in CM amplitude and neural sensitivity, shown in Figure 2.5 below. The acoustic over-stimulation used to derive the function would have affected the dP_o/dd component of Figure 2.4. The relationship shown in Figure 2.5 gives a maximum threshold elevation due to loss of the active process of around 55 dB,

implying that threshold elevation in excess of this is due to additional neural or IHC disruption.

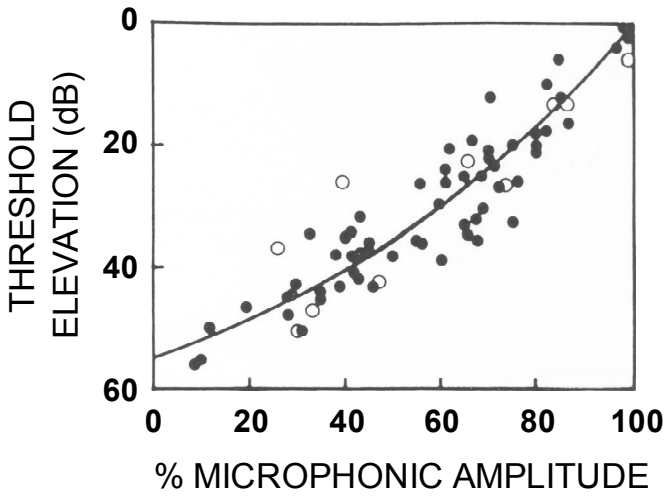

Figure 2.5: Figure adapted from Patuzzi and Rajan (Patuzzi et al., 1989; Patuzzi and Rajan, 1992) showing the correlation between the average elevation of CAP threshold (between 10 kHz and 20 kHz) and the reduction in amplitude of the low-frequency CM (relative to just prior to the initial acoustic trauma), recorded from 18 animals. Dark circles indicate 115 dB SPL exposures, while open circles indicate longer exposures at 105 dB SPL.

Some caveats must be kept in mind when using this empirical equation to provide an estimate of the threshold elevation produced by manipulations within the model. Firstly, the data shown in Figure 2.5 was recorded some 4 minutes after the exposure to the TTS stimuli (once the thresholds had stabilised) in order to avoid synaptic issues. This means that the hearing loss measured was that which would be expected once any second-order effects had run their course, whereas, in the model, it is used to provide an estimate of the threshold elevation at that instant in time.

One of the assumptions of the formula given above is that reductions of the active process due to different manipulations are independent and multiplicative. In the model, this means that any perturbations that affect any part of the loop shown in Figure 2.4 will influence auditory thresholds by the degree to which they reduce the small-signal AC receptor potential of the OHC. As such, in the model, the μ_{tot} parameter of Equation 8 is approximated by the fraction of AC receptor potential relative to a reference value.

2.6 Computational framework

The time-domain operation of the model is an extension of the steady-state solution described above. The model is essentially an “initial value problem”. In the absence of any continuing perturbation, the deterministic nature of the mathematical model means

that the state vector for iteration "*n*" is the only input required to the model to allow the simulation of the cell at iteration "*n+1*".

The basic functioning of the model can be divided into three steps, as shown in Figure 2.6 below.

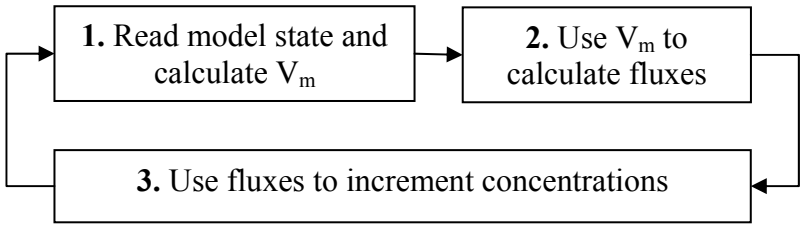

Figure 2.6: Simplified flow-chart of the calculations during one iteration of the model. The arrow between step 3 and step 1 represents the flow of information from one iteration to the next.

In the first step, the membrane potential (V_m) is determined using load-line analysis based on the state of the cell at iteration "*n-1*". This takes into account all of the factors present at iteration "*n-1*" that influence the apical and basal K^+ conductances, the most important being the cytosolic Ca^{2+} concentration. In the second step, the membrane potential determined at iteration "*n*" is then fed into the relevant transport equations to calculate the fluxes of all ionic species in the model. These transport equations are presented in detail in Section 2.8 below.

In the third step, the Ca^{2+} fluxes across the basolateral wall and lateral sac, and the amount of M2, M3 and M4 activated or inactivated, are each divided by the particular volumes they occupy to calculate a concentration increment. Using simple finite difference integration, these increments are added to their existing concentrations to form new concentrations, which are then passed via shift register from iteration "*n*" of the model to iteration "*n+1*". All other parameters and concentrations are either fixed or are calculated rather than carried over. These include the membrane potential (V_m) described above, and the EP, which is calculated from the apical potassium flux from the previous iteration (as shown in Equation 9e of Section 2.8.1).

The values chosen for each "volume" mentioned above were not derived from any published physiological quantity – rather they were used to adjust the rate-of-change of the parameter, and therefore the gain and phase of the feedback loop, to match the experimental data. The volumes were Ca_i = 10000, M2 = 5, M3 = 0.125, M4 = 12, and Ca_{sac} = 30. As described in Section 2.7.1 below, the unitary conductances and transmembrane ionic fluxes are relative, and so these volumes are in arbitrary units.

2.6.1 Coarse time-step simulation

The model was designed to simulate the slow homeostatic mechanisms that regulate hair cell function over periods of seconds, minutes, and hours. For this purpose, it was too computationally-intensive and time-consuming to always calculate the model with time-steps small enough to resolve the cycle-by-cycle movement of stereocilia at high audio frequencies. The time-step (dT) is used when incrementing the intracellular concentrations within the model: as the ionic flux is the movement of ions per unit time, the calculated fluxes were multiplied by this dT and added to the previous ionic concentration.

While increasing the dT reduces the time-resolution of the model, it can also affect the model's numerical stability, and reduce the numerical accuracy of the modelled time-course due to accumulated error. Under normal rest conditions (when the cell was in a steady state), a dT of $^1/_5$ s provided an appropriate compromise between calculation speed and numerical accuracy: reduction of this dT by a factor of 10 produced identical results. However, when the rate of change of parameters was expected to be large (e.g. during the onset or offset of an experimental perturbation, or when settling into a new set of initial values), a finer time increment was used, such as $^1/_{15}$ or $^1/_{20}$ s. One exception to this coarseness of time-step was in the modelling of exposures to very-low-frequency tones (see Chapter Six), which were able to be computed within a reasonable time-frame when a dT of $^1/_{100}$ was used.

Of the almost 100 parameters that define the OHC, only 8 are updated automatically with each iteration: the membrane potential (V_m), the endocochlear potential (EP), the operating point (d), the concentrations of calcium in the cytosol and lateral sac (Ca_i and Ca_{sac}), and the concentrations of the messengers M2, M3, and M4. The results of any perturbation to the model will cause time-variant changes in these values, which can be saved to a file, along with reference values such as the model time (s), and the value of the particular perturbation (such as the external energy bias applied, or the extracellular K^+ during a perfusion). This forms the primary output of the model for comparison with the results from real-world experiments.

2.7 Model assumptions and simplifications

In addition to the intracellular second-messenger cascade described in Chapter One and Section 2.3 above, a number of assumptions were required to allow the modelling to be performed, either because certain physiological values or behaviours were unknown, or because certain cellular components were judged to be of limited

importance to the behaviours that were being modelled. Many of these assumptions and simplifications, described below, also served to reduce the computation times of the model, increasing the efficiency of the modelling process.

2.7.1 Ionic fluxes and permeabilities are relative

While absolute voltages and ionic concentrations have been used, the magnitude of the fluxes described in the model are relative. This has been done in order to reduce quantisation and floating-point-truncation errors, and to make numbers more manageable in the calculations. For example, the $\left(2.3z^2q/E_{10}\right)$ component of Equation 6 above can represented by the term *F*, which is equal to 6.1479 x 10^{-20} multiplied by the square of the valence of the ion. However, to simplify the calculations in the GHK-based equations, the value of F in the model has been set to the square of the valence of the ion.

In addition, as the channel density (*n*) and unitary conductance (*g*) are always multiplied by each other, the unitary conductance has been set at 1 to enable easier comparison of permeabilities. The *n* term used in the equations is therefore effectively the product of *n* and *g*.

2.7.2 Cytosolic homogeneity and instantaneous diffusion

The composition of solutions within the cytosol and the intracellular compartments (the lateral sac) was assumed to be homogenous, in that there were assumed to be no concentration gradients within each compartment and diffusion of solutes within a solution was assumed to occur instantaneously.

2.7.3 No Ca^{2+} buffering by sequestration proteins

Intracellular calcium is buffered in OHCs by endogenous buffering proteins such as calbindin, calreticulin, and parvalbumin (Pack and Slepecky, 1995; Heller et al., 2002). In the intracellular storage compartments of most cells, calcium is buffered by luminal proteins such as calreticulin in the endoplasmic reticulum and calsequestrin in the sarcoplasmic reticulum (Lytton and MacLennan, 1992).

Such buffering is not included in either the cytosol or the SSC of the model OHC, as the assumption is made that the cytosolic free calcium is proportional to the influx of calcium and the efflux into intracellular storage compartments and the extracellular space.

2.7.4 Receptor current carried solely by potassium

In vivo, most ionic current is carried by K^+ entering the OHC through the apical MET channels and exiting through the basolateral K^+ channels (Johnstone et al., 1989). In the model, the assumption was made that when calculating the basolateral membrane potential of the OHC in the model this K^+ current was dominant, and the contribution of all other currents (for example, Na^+ or Ca^{2+}) to the basolateral membrane potential were low enough to ignore.

2.7.5 Exclusion of certain channels

Some of the channel types that have been documented in OHCs have been excluded from the model, as they are assumed to be closed or insignificant under normal physiological conditions in the mature cell. These include a voltage-gated Na^+ channel that is closed at physiological membrane potentials (Witt et al., 1994).

The chloride channel shown in Figure 1.1 of Chapter One was also excluded from the model. There is little evidence for significant chloride permeability in OHCs (Ashmore and Meech, 1986; Sunose et al., 1992). Recently, a stretch-activated non-selective conductance has been reported in the lateral membrane of OHCs that is permeable to chloride *in vitro* (Rybalchenko and Santos-Sacchi, 2003). It seems unlikely that any significant chloride permeability would exist in the basolateral wall *in vivo*, as this would render the OHCs vulnerable to osmotic pressures, given their high water permeability.

The effects of ATP-γ-S on the perilymphatic face of the OHC have also been disregarded. ATP-γ-S has been found to cause a movement of the operating point toward scala tympani when perfused in scala tympani perilymph (Bobbin and Salt, in press).

In addition, no stretch-sensitive channels were included in the basolateral wall of the model, although such channels have been identified in the OHCs (Ding et al., 1991; Iwasa et al., 1991; Harada et al., 1993). These were eliminated because the movement of water was not included explicitly in the model, as described below.

2.7.6 Limited osmotic effects and no calculation of water movement

The outer hair cell is highly permeable to water. The osmotic water permeability coefficient of the basolateral wall of isolated guinea pig OHCs was estimated by Belyantseva et al. (2000) to be approximately 10^{-2} cm/sec: a value which is sufficiently high to suggest the involvement of aquaporins. The flow of water across the basolateral

wall is also inhibited by $HgCl_2$, a known blocker of aquaporin-mediated water transport (Verkman et al., 1996; Marcon and Patuzzi, in preparation).

As a simplification, the model described here does not calculate the movement of water across the cell membranes, and the volume of the cell is fixed, eliminating the concentration or dilution of intracellular solutes by water movement. Despite this, the effects of an osmotic perturbation on the hair bundle and operating point can be simulated by specifying the time-course of an external energy bias (E_{ext}) to the hair bundle in Equation 7, described in Section 2.8.1 below.

2.7.7 Channel kinetics and instantaneous activation times

Because the present model has a much coarser time resolution than that of most channel-gating time-constants, the channel opening kinetics have not been considered in the model, and all channels have been assumed to gate instantaneously. The opening probability of a channel in the model, whether it is sensitive to voltage, displacement, or to a particular ligand, is assumed to be in pseudo-equilibrium, following the steady-state Boltzmann curve.

2.7.8 No transducer adaptation

Slow adaptation of the MET channel (described in Section 1.3.2 of Chapter One) was not included in the model, as one of the aims of the model was to determine whether calcium-mediated slow motility and prestin-mediated electromotility were sufficient to account for the homeostatic regulation of operating point.

2.7.9 Electromotility operating in linear range

In the model, electromotility is represented by a simple linear approximation to the Boltzmann function governing the relationship between OHC length and the basolateral membrane potential (Santos-Sacchi, 1992). The equations governing electromotility in the model were presented in Section 2.4 above.

2.7.10 Endocochlear potential and scala media ATP

In the model, the stria vascularis is modelled as a simple voltage source with a series resistance (R_{sm}). The voltage source provided by stria vascularis is assumed to be fixed (unless perturbed using hypoxia or current injection),

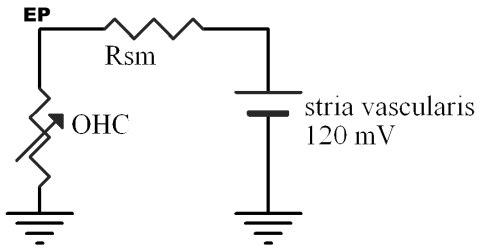

Figure 2.7: Equivalent circuit for EP calculation in the model.

and the EP is determined by the scala media resistance, which is dominated by the apical MET and ATP-sensitive K^+ channels described in Section 2.8.1 below.

The access resistance of scala media in the guinea pig is generally between 3 and 3.5 kΩ (Asakuma et al., 1978; Thorne et al, 2004). However, as the ionic fluxes used in the model are arbitrary, a value for R_{sm} of 0.001 was used, such that a doubling of the K^+ flux through the OHC resulted in a 23 mV decrease in the EP.

Although the scala media ATP concentration is known to increase following exposure to loud noise and other perturbations (Munoz et al., 2001), this concentration is assumed to be fixed in the model. However, these ATP-perturbations may be simulated by systematically altering the n_{KATP} parameter (also described in Section 2.8.1).

2.8 Model equations and parameters

The ionic transport mechanisms identified on the apical and basolateral membranes of the outer hair cell (shown in Figure 2.1) have been characterised primarily using data derived from patch-clamp studies carried out *in vitro* on isolated outer hair cells, and so caution must be exercised in assuming that currents described *in vitro* are present and active *in vivo*. In most cases, adequate data on the *in vivo* electrophysiological characteristics of the channels have not been published. Where available, the published opening characteristics for particular channels have been used (such as $V_{½}$ and V_{11} for voltage-gated channels, or Hill coefficients for ligand-gated channels), but in other cases it has been necessary to make educated guesses about likely values for these parameters.

Values for unitary conductance *g* and number of channels *n* have in most cases been chosen in order to match the model behaviour to the experimental data, as described in Section 2.9 below. In most cases, the strategy has been to set the unitary conductances to 1, and alter the *number* of channels only, enabling a simple comparison of conductances.

The equations forming the mathematical model are described below.

2.8.1 Apical MET and ATP-sensitive K^+ channels

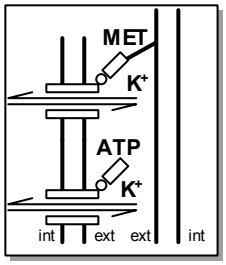

On deflection of the hair cell stereocilia in the direction of the basal body, the MET channels located in the stereocilia open, allowing the flow of cations into the cell. Most of this cation current

is carried by potassium (Johnstone et al., 1989), but the hair-cell MET channel is also highly permeable to Ca^{2+} (Lumpkin et al., 1997). However, as the Ca^{2+} concentration of scala media is exceedingly low (around 23-30 μM; Bosher and Warren, 1978; Wangemann and Schacht, 1996), the apical Ca^{2+} current in the model has been ignored as a direct determinant of the receptor current (although its possible role in determining cytosolic Ca^{2+} and/or MET conductance will be discussed later).

The molecular identity of the displacement-sensitive hair-cell MET channel is currently unknown, although several candidates exist (for a review, see Strassmaier and Gillespie, 2002), including TRPA1 (Corey et al., 2004). The net potassium flux through channels at the apex of the hair cell is given by Equation 9a below.

$$I_{KDA} = -\left(g_{KATP} \cdot n_{KATP} + g_{KDA} \cdot n_{KDA} \cdot p_{od}\right) \cdot F \cdot \left(-V_a\right) \cdot \left[\frac{K_i - K_{sm} \cdot 10^{(V_a/E_{10})}}{1 - 10^{(V_a/E_{10})}}\right] \quad \textbf{[9a]}$$

where:

$$p_{od} = \frac{1}{(1 + 10^{(-(E - E_{½})/E_{10})})} \quad \textbf{[9b]}$$

$$E = E_{ext} + turgor + c \cdot \left[\left\{S_{fast} \cdot \left(V - V_{off}\right)\right\} + \left\{S_{slow} \cdot \left(M4 - M4_{off}\right)\right\}\right] \quad \textbf{[9c]}$$

$$V_a = EP - V \quad \textbf{[9d]}$$

$$EP_{(n+1)} = EP_{opencircuit} - R_{sm} \cdot I_{KDA(n)} \quad \textbf{[9e]}$$

using values:

g_{KATP} = 1	$EP_{opencircuit}$ = 120 mV	c = 1
n_{KATP} = 0.5	R_{sm} = 0.001	V_{off} = 150 mV
g_{KDA} = 1	E_{ext} = 0 meV	S_{fast} = -3
n_{KDA} = 1	$E_{½}$ = 0 meV	$M4_{off}$ = 0
K_i = 157 mM	E_{10} = 60 mV	S_{slow} = -15000
K_{sm} = 157 mM	F = 1	$turgor$ = 100 meV

As well as the displacement sensitive conductance, Equation 9a also contains the terms for an additional fixed conductance that is not sensitive to displacement of the stereocilia. This conductance is a simplified representation of the ATP-sensitive non-specific cation channel present in the apical membrane (Housley et al., 1992; Wang et al., 2003), made because the concentration of ATP in scala media is fixed in this model.

As discussed in Chapter One, a first-order Boltzmann activation function is used here to described the opening probability of the displacement-sensitive channels (Holton and Hudspeth, 1986), as shown in Equation 9b. The displacement is described

in terms of an equivalent energy bias, E, such that 50% of the channels are open when E is equal to the half-activation energy value $E_{½}$.

As described in Section 2.4 above, this equivalent energy bias acting to displace the stereocilia is calculated as the sum of an external energy bias (E_{ext}) that is used to model movement due to hydrostatic bias or sound, an intracellular turgor pressure, and an internal energy bias due to fast and slow OHC motility.

Because both the endocochlear potential (EP) and the basolateral membrane potential, V_m, are defined relative to the tunnel of Corti potential (0 mV), the voltage across the apical membrane of the cell is simply the difference between V_m and EP.

The unitary conductance of the MET channel, g_{KDA}, can be reduced in the model to simulate pharmacological block of the channels by substances such as aminoglycosides (Hudspeth and Kroese, 1983; Kroese et al., 1989; Meyer et al., 1998), gadolinium (Kimitsuki et al., 1996), and cisplatin (Kimitsuki et al., 1993; Ernst and Zenner, 1995).

2.8.2 Basolateral voltage-sensitive K^+ channel

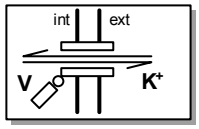

Three voltage-dependent potassium channels present in the basolateral wall of OHCs have been characterised (Kros, 1996). They are K_s channels, K_n channels, and a Ca^{2+}-sensitive K^+ channel that is described in more detail in Section 2.8.3 below.

K_s channels are slow-acting (τ = 2 - 10 ms; Kros and Crawford, 1990), low-conductance (20 pS) channels that are insensitive to internal Ca^{2+}. The channel opens on depolarisation, with a half-activation voltage of –15 mV. The channel is insensitive to internal calcium, and is inhibited by 4AP (van den Abbeele et al., 1999).

K_n channels are small-conductance (45 pS) channels that are highly selective for K^+ (P_K:P_{Na} = 30:1), and are blocked by 5mM extracellular Cs^+. They have a half-activation voltage of –90 mV, and a $V_{11} \approx$ –13 mV (Housley and Ashmore, 1992). The channels are likely to contain the KCNQ4 subunit (Marcotti and Kros, 1999), mutation of which is found in an autosomal-dominant form of non-syndromic progressive hearing loss in humans (Kubisch et al., 1999). There is also evidence that K_n-type channels are inactivated by elevated $[Ca^{2+}]_i$ (Chambard and Ashmore, 2005), but this effect is likely to be masked *in vivo* by the activation of the calcium-sensitive K^+ channels described in Section 2.8.3 below.

These channels have been disabled in the version of the OHC model presented here, primarily because the membrane potential of the model OHC was too positive for the

voltage-sensitive characteristics of the channels to be of relevance: the opening probability of these voltage-sensitive channels follows a Boltzmann activation function, shown in Equation 10b below, and is characterised using the $V_{½}$ and V_{11} values. For completeness, the net potassium flux through voltage-sensitive channels in the basolateral membrane of the hair cell is given by Equation 10a below.

$$I_{KVB} = -\left(g_{KVB} \cdot n_{KVB} \cdot p_{ov}\right) \cdot F \cdot V \cdot \left[\frac{K_i - K_o \cdot 10^{(-V/E_{10})}}{1 - 10^{(-V/E_{10})}} \right] \qquad \textbf{[10a]}$$

where:

$$p_{ov} = \frac{1}{(1 + 10^{((V - V_{½})/V_{11})})} \qquad \textbf{[10b]}$$

using values:

$g_{KVB} = 1$	$K_i = 157$ mM	$E_{10} = 60$ mV
$n_{KVB} = 0$	$K_o = 4.2$ mM	$F = 1$
$V_{½} = -90$ mV	$V_{11} = -13$ mV	

2.8.3 Basolateral Ca^{2+}-sensitive K^+ channel

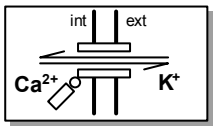

Two main types of calcium-sensitive potassium channels – BK and SK channels – have been found in mammalian outer hair cells.

BK channels, also known as maxi-channels or KCNMA1 channels, are large-conductance (220 - 240 pS) channels which are sensitive to both Ca^{2+} and voltage (Ashmore and Meech, 1986; Gitter et al., 1992; van den Abbeele et al., 1999). Although undoubtedly present in both OHCs and IHCs, the opening characteristics of the BK channels make it unlikely that they would be open in any significant quantities under normal OHC conditions (approx. 1 µM Ca^{2+} and -70 mV V_m): In patch-clamp studies conducted in rat muscle cells, Barrett et al. (1982) showed a half-activation voltage of +34 mV for 1 µM Ca^{2+}, while in studies in IHCs, Oliver et al. (2003) showed a half activation voltages of +7 mV for 1 µM and +39 mV for 0 µM.

SK channels, also known as KCNN2 channels, are small conductance (45 pS) channels that are formed as heteromeric complexes of SK-α subunits and calmodulin (Xia et al., 1998). *In vitro*, the channels are blocked by apamin, suggesting that the SK channels of OHCs are primarily the SK2 sub-type (Soh and Park, 2001). These SK2 channels have been proposed to be the most likely end-target for the rise in Ca^{2+}_i with efferent innervation (Nenov et al., 1996; Dulon et al., 1998; Oliver et al., 2000). They are relatively insensitive to voltage (Nenov et al., 1996), and are typically activated by

Ca^{2+} in the high nanomolar range – when fitted with the Hill equation, the Ca^{2+} activation of the SK2 subunit showed a $K_{½}$ of 330 nM and a Hill co-efficient of 5.3 (Xia et al., 1998).

For these reasons, the Ca^{2+}-sensitive K^+ channels modelled here are based on the SK channel characteristics. The net potassium flux through these channels is given by Equation 11a below.

$$I_{KCaB} = -\left(g_{KCaB} \cdot n_{KCaB} \cdot Ca_{sat}\right) \cdot F \cdot V \cdot \left[\frac{K_i - K_o \cdot 10^{(-V/E_{10})}}{1 - 10^{(-V/E_{10})}}\right] \qquad \textbf{[11a]}$$

where:

$$Ca_{sat} = \frac{\left(Ca_i\right)^{Hill}}{\left(Ca_i\right)^{Hill} + \left(Ca_{Khalf}\right)^{Hill}} \qquad \textbf{[11b]}$$

using values:

$g_{KCaB} = 1$	$K_i = 157$ mM	$F = 1$
$n_{KCaB} = 400$	$K_o = 4.2$ mM	$Hill = 5.3$
$Ca_{Khalf} = 0.33$ µM	$E_{10} = 60.00$ mV	

2.8.4 Basolateral K^+-leakage channel

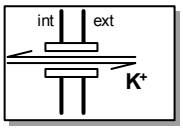

As the voltage-sensitive K^+ channels (described in Section 2.8.2 above) were essentially open at most membrane potentials encountered in the model, they were replaced by potassium leakage channels. Both types of channels could be used interchangeably to limit the sensitivity of the membrane potential to intracellular Ca^{2+} under the influence of the calcium-sensitive potassium channels. In particular, their inclusion prevented a form of instability (most likely unphysiological) in which falling calcium levels could cause the basolateral wall of the cell to "shut off" entirely.

As leakage channels, their permeability is not dependent on voltage, displacement, or ligands, and so the net potassium flux through these channels in the basolateral membrane of the OHCs is given by Equation 12 below.

$$I_{Kleak} = -g_{Kleak} \cdot n_{Kleak} \cdot F \cdot V \cdot \left[\frac{K_i - K_o \cdot 10^{(-V/E_{10})}}{1 - 10^{(-V/E_{10})}}\right] \qquad \textbf{[12]}$$

using values:

$g_{Kleak} = 1$	$K_i = 157$ mM	$F = 1$
$n_{Kleak} = 25$	$K_o = 4.2$ mM	$E_{10} = 60$ mV

2.8.5 Basolateral voltage- and ACh-sensitive Ca^{2+} channels

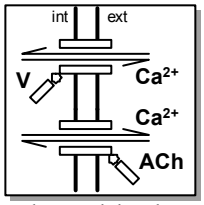

The majority of voltage-sensitive Ca^{2+} channels found in guinea pig OHCs are L-type channels (Nakagawa et al., 1991), but N-type channels are also present (Chen et al., 1995). L-type channels in the OHC are formed by α1D subunits, and are blocked by nifedipine. Gd^{3+} is also a blocker of both L-type and N-type Ca^{2+} channels (Lacampagne et al., 1994). In the presence of 1.6 mM Ca^{2+}, the L-type channels display a half-activation voltage of -45 mV, and a V_{11} of approximately -11 mV (Rodriguez-Contreras and Yamoah, 2003).

The efferent neurotransmitter, acetylcholine (ACh), causes the influx of calcium into the OHC, acting through either the homomeric α9 nicotinic receptor subunit (Yoshida et al., 2001), or more probably a heterometric nicotinic receptor assembled from both α9 and α10 subunits (Vetter et al., 1999; Elgoyhen et al., 2001).

Although the dose-response characteristics of the ACh receptors have been published (e.g. Housley and Ashmore, 1991; Shigemoto and Ohmori, 1991), the effect of ACh has been simply modelled as a Ca^{2+}-leakage conductance additional to the voltage-dependent Ca^{2+} conductance. Elevated efferent activity can then be modelled by increasing the Ca^{2+} conductance via the n_{CaACh} parameter.

The combined flux through these two channels is given by Equation 13a below.

$$I_{Cab} = -\left(g_{CaACh} \cdot n_{CaACh} + g_{Ca} \cdot n_{CaV} \cdot p_{ov}\right) \cdot F \cdot 2V \cdot \left[\frac{Ca_i - Ca_o \cdot 10^{(-2V/E_{10})}}{1 - 10^{(-2V/E_{10})}}\right] \qquad \textbf{[13a]}$$

where:

$$p_{ov} = \frac{1}{(1 + 10^{((V - V_{½})/V_{11})})} \qquad \textbf{[13b]}$$

using values:

$g_{CaACh} = 1$	$g_{Ca} = 1$	$Ca_o = 1300$ µM
$n_{CaACh} = 0.0001$	$n_{CaV} = 0.005$	$F = 4$
$E_{10} = 60$ mV	$V_{½} = -45$ mV	$V_{11} = -11$ mV

The ratio of voltage-controlled to ACh-controlled Ca^{2+} conductances was a major determinant of the oscillatory behaviour of the model, as will be discussed in Section 2.9.1 below.

2.8.6 Basolateral Na^+/K^+/ATPase

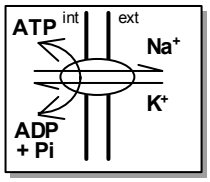

The Na^+/K^+/ATPase pump is ubiquitous, found in virtually all animal cells (Alberts et al., 2002). It is present in the basolateral wall of the OHCs (Sunose et al., 1992; Sunose et al., 1993).

The Na^+/K^+/ATPase pump has a Na:K stoichiometry ratio of 3:2 – for every molecule of ATP hydrolysed, three sodium ions are pumped out of the cell and two potassium ions are pumped in (Sen and Post, 1964). This ratio is enforced by the multiplier terms in Equations 14a and 14b, which define the Na^+ and K^+ flux of the pump:

$$I_{NaKATPaseSodium} = Na_{multiplier} \cdot I_{NaKATPase} \quad \textbf{[14a]}$$

$$I_{NaKATPasePotassium} = K_{multiplier} \cdot I_{NaKATPase} \quad \textbf{[14b]}$$

where:

$$I_{NaKATPase} = n_{NaKATPase} \cdot \left(\frac{Na_i^3}{(Na_i + Na_{Binding})^3} \right) \cdot \arctan(scale \cdot \mu) \quad \textbf{[14c]}$$

$$\mu = E_{10} \cdot \log\left[\left(\frac{K_o}{K_i} \right)^2 \cdot \left(\frac{Na_i}{Na_o} \right)^3 \cdot \left(\frac{\gamma_{ATP}}{K_{ATP}} \right) \right] - V \quad \textbf{[14d]}$$

$$\gamma_{ATP} = \frac{ADP \cdot P_i}{ATP} \quad \textbf{[14e]}$$

using values:

$Na_{multiplier} = 3$	$K_{ATP} = 1\text{x}10^8$	$K_{multiplier} = -2$
$Na_{binding} = 30$	$ATP = 5$ mM	$K_i = 157$ mM
$Na_i = 14$ mM	$ADP = 0.05$ mM	$K_o = 4.2$ mM
$Na_o = 148$mM	$P_i = 5$ mM	$scale = 1$
$n_{NaKATPase} = 1$	$E_{10} = 60$ mV	

The term $\left(Na_i^3 / (Na_i + Na_{Binding})^3\right)$ in Equation 14c provides a kinetic limit to the action of the pump, as intracellular sodium is the limiting substrate. Given an intracellular sodium concentration of 14 mM and a Michaelis constant of 20 mM (Beagué, 1984), this term scales the resulting flux by approximately 0.07. For simplicity, the corresponding term for potassium $\left(K_o^2 / (K_o + K_{Binding})^2\right)$ has been omitted, as the Michaelis constant for potassium is only 1-2 mM (Garrahan and Glynn, 1967a), resulting in a multiplication of only 0.98.

The arctan term of Equation 14c is saturating function used to approximate the hyperbolic IV characteristic of the Na^+/K^+/ATPase (Gadsby et al., 1985), while also providing for the reversal of the ATPase pumping that occurs in the absence of intracellular ATP (Garrahan and Glynn, 1967b). This reversal is usually only hypothetical, as the pump is normally operating well into its saturated mode.

The Gibbs free energy of the pump, μ, was defined as the sum of the free energy used in moving potassium and sodium against their concentration gradients, and the energy provided by the hydrolysis of ATP, given by the mass action ratio for cytoplasmic ATP (γ_{ATP}; Equation 14e) divided by the equilibrium constant for the hydrolysis of ATP to ADP and P_i. (approx 1 x 10^{-8}; Nicholls, 1982).

Although present, the activity of the Na^+/K^+/ATPase is low in OHCs (Schmiedt et al., 2002). The blockage of the pump by ouabain, which binds to the potassium binding site, may be simulated in the present model by reducing $n_{NaKATPase}$.

2.8.7 Basolateral Ca^{2+}/Na^+ antiport

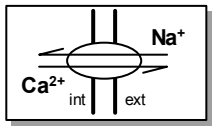

The basolateral wall of the OHC is likely to contain a Na^+/Ca^{2+} exchange mechanism, whereby one Ca^{2+} ion is extruded from the OHC by the flow of three Na^+ ions into the cell down its electrochemical gradient from perilymph. In isolated OHCs, Ikeda et al. (1992a) found that i) $[Ca^{2+}]_i$ reversibly increased when $[Na^+]_o$ was decreased, and ii) elevated $[Ca^{2+}]_o$ resulted in a decrease in $[Na^+]_i$. Both findings support the presence of a Na^+/Ca^{2+} antiport in OHCs. Such a mechanism is not present in IHCs (Kennedy, 2002). Na^+/Ca^{2+} exchange in ventricular myocytes is blocked by gadolinium (Zhang and Hancox, 2000), but whether this occurs in the OHC is uncertain.

The structure of the equations for the antiport is similar to that of the Na^+/K^+/ATPase, with the exception that it is not driven by ATP. These equations are given below.

$$I_{antiportCalcium} = Ca_{multiplier} \cdot I_{antiport} \quad \textbf{[15a]}$$

$$I_{antiportSodium} = Na_{multiplier} \cdot I_{antiport} \quad \textbf{[15b]}$$

where:

$$I_{antiport} = n_{antiport} \cdot \left(\frac{Ca_i}{Ca_i + Ca_{binding}} \right)^p \cdot \left(\frac{Na_o}{Na_o + Na_{binding}} \right)^q \cdot \arctan\left(scale_{NaCa} \cdot \mu\right) \quad \textbf{[15c]}$$

and

$$\mu = E_{10} \cdot \log\left[\left(\frac{Ca_i}{Ca_o}\right)^p \cdot \left(\frac{Na_o}{Na_i}\right)^q\right] - V \qquad \textbf{[15d]}$$

using values:

$Ca_{multiplier} = -1$	$Ca_{binding} = 5\ \mu M$	$p = 2 \qquad q = 1$
$Na_{multiplier} = 3$	$Na_{binding} = 50$	$n_{antiport} = 5000000$
$Na_i = 14$ mM	$Na_o = 148$ mM	$Scale_{NaCa} = 0.001$

Although the $1.Ca^{2+} : 3.Na^+$ ratio means the antiport is electrogenic, the Ca^{2+} flux of the antiport under normal conditions is only around 1% of the K^+ flux through the basolateral wall, and has therefore been ignored in the calculation of the membrane potential.

2.8.8 Basolateral Ca^{2+}-ATPase (PMCA)

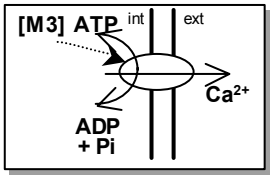

The basolateral plasma membrane Ca^{2+}-ATPase (PMCA) in the OHC has been identified as the PMCA2 isoform (Furuta et al., 1998) – an isoform with a high affinity for calmodulin. Stimulation of the PMCA by calmodulin increases both the calcium-affinity and maximum pumping velocity of the pump (for a review, see Monteith and Roufogalis, 1995). In the model, the rate of calcium extrusion from the cell is accelerated by M3.

$$I_{PMCA} = n_{PMCA} \cdot \left(\frac{M3}{(M3 + M3_{Binding})}\right) \cdot \left(\frac{Ca_i}{(Ca_i + Ca_{Binding})}\right) \cdot \arctan(scale \cdot \mu) \qquad \textbf{[16a]}$$

where:

$$\mu = E_{10} \cdot \log\left[\left(\frac{Ca_o}{Ca_i}\right) \cdot \left(\frac{\gamma_{ATP}}{K_{ATP}}\right)\right] + V \qquad \textbf{[16b]}$$

$$\gamma_{ATP} = \frac{ADP \cdot P_i}{ATP} \qquad \textbf{[16c]}$$

using values:

$N_{PMCA} = 0$	$K_{ATP} = 10^8$	$ATP = 5$ mM
$M3_{binding} = 0.20\ \mu M$	$E_{10} = 60$ mV	$ADP = 0.05$ mM
$Ca_{binding} = 0.01\ \mu M$	$scale = 0.005$	$P_i = 5$ mM

2.8.9 Ca^{2+}-ATPase pump into subsurface cisternae (SERCA)

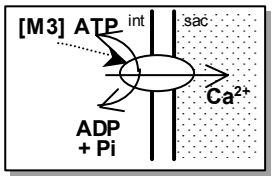

The sarcoplasmic/endoplasmic reticulum Ca^{2+}-ATPase (SERCA) is an ATP-driven calcium extrusion pump that has been

identified in the OHCs (Schulte, 1993). It has been localised to the innermost layer of the subsurface cisternae (Zine and Schweitzer, 1996).

The Ca^{2+}-ATPase is inhibited by thapsigargin, cyclopiazonic acid (CPA), 2,4-di-(t-butyl)hydroquinone (BHQ) and vanadate (Seidler et al., 1989; Tucker and Fettiplace, 1996; Bobbin et al., 2003). Perilymphatic application of 1 µM thapsigargin increased the magnitude of the slow efferent effect (Sridhar et al., 1997) indicating the activity of the SERCA in sequestering the elevated intracellular calcium during efferent stimulation. The perilymphatic and chronic application of higher concentrations of thapsigargin (10 µM) also suppressed sound-evoked cochlear potentials and both high- and low-level $2f_1$-f_2 DPOAEs (Bobbin et al., 2003).

The maximal pumping rate of SERCAs is increased by phosphorylation by CaM-Kinase II (Xu and Narayanan, 1999). In the model, the rate of calcium extrusion into the lateral sac is accelerated by M3.

$$I_{SERCA} = n_{SERCA} \cdot \left(\frac{M3}{(M3 + M3_{Binding})} \right) \cdot \left(\frac{Ca_i}{(Ca_i + Ca_{Binding})} \right) \cdot \arctan(scale \cdot \mu) \qquad \textbf{[17a]}$$

where:

$$\mu = E_{10} \cdot \log\left[\left(\frac{Ca_{sac}}{Ca_i} \right) \cdot \left(\frac{\gamma_{ATP}}{K_{ATP}} \right) \right] + V_{sac} \qquad \textbf{[17b]}$$

$$\gamma_{ATP} = \frac{ADP \cdot P_i}{ATP} \qquad \textbf{[17c]}$$

using values:

N_{SERCA} = 30000	K_{ATP} = 10^8	ATP = 5 mM
$M3_{binding}$ = 0.20 µM	E_{10} = 60 mV	ADP = 0.05 mM
$Ca_{binding}$ = 0.01 µM	$scale$ = 0.005	P_i = 5 mM
V_{sac} = 30 mV		

2.8.10 Ca^{2+} leakage from subsurface cisternae

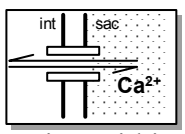

A fixed-conductance calcium leakage channel was incorporated into the SSC of the model as a means of controlling the resting calcium concentration within the SSC. The ratio of the SERCA pumping rate to the leakage of Ca^{2+} from the sac was adjusted so that the $[Ca^{2+}]_{sac}$ was maintained at around 600 µM at rest. Leakage from the sac is described by the following equation:

$$I_{CaSacLeak} = g_{CaSacLeak} \cdot n_{CaSacLeak} \cdot F \cdot V \cdot \left[\frac{Ca_{sac} - Ca_i \cdot 10^{(-V/E_{10})}}{1 - 10^{(-V/E_{10})}} \right] \quad \textbf{[18]}$$

using values:

$g_{CaSacLeak} = 1$ $\quad F = 4$ $\quad E_{10} = 60$ mM
$n_{CaSacLeak} = 0.02$ $\quad V_{sac} = 30$ mV

2.8.11 Ca^{2+}-induced Ca^{2+} release from subsurface cisternae

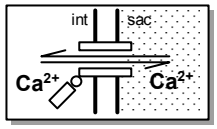

The calcium-induced calcium release (CICR) from the intracellular calcium stores serves to amplify any transient elevations in cytosolic calcium. Type I ryanodine receptors (RyRs) involved in CICR have been found in OHCs (Lioudyno et al., 2004). Evidence supporting the presence of CICR in the OHCs comes from the observations that compounds that act on intracellular calcium stores – namely ryanodine, caffeine, and cADPR, increase the amplitude of the calcium-sensitive potassium currents[7] that result from application of extracellular ACh (Sridhar et al., 1997; Lioudyno et al., 2004). While the unaltered time-course is suggestive of a tightly spatially-coupled store release (from the synaptoplasmic rather than subsurface cisternae), these two cisternae are merged in the present model.

In the model, the CICR is described by Equations 19a below, in which the efflux of calcium from the SSC (down its concentration gradient) is scaled by a saturating function of intracellular calcium, given by the Hill equation in Equation 19b.

$$I_{CaCaSac} = g_{CaCaSac} \cdot n_{CaCaSac} \cdot Ca_{sat} \cdot F \cdot V_{sac} \cdot \left[\frac{Ca_{sac} - Ca_i \cdot 10^{(-V_{sac}/E_{10})}}{1 - 10^{(-V_{sac}/E_{10})}} \right] \quad \textbf{[19a]}$$

where:

$$Ca_{sat} = \frac{(Ca_i)^{Hill}}{(Ca_i)^{Hill} + (Ca_{CaBinding})^4} \quad \textbf{[19b]}$$

using values:

$g_{CaCaSac} = 1$ $\quad Ca_{CaBinding} = 1.5$ µM $\quad E_{10} = 60$ mM
$n_{CaCaSac} = 0.4$ $\quad Hill = 1.7$ $\quad F = 4$
$V_{sac} = 30$ mV

[7] via the SK channels described in Section 2.8.3 above.

The values for the Hill coefficient, and the calcium-binding constant and exponent, were chosen to ensure the CICR channels opened with large increases of cytosolic calcium. Under normal rest conditions in the model, CICR accounted for around 13% of the efflux of calcium from the SSC, with the other 87% coming from the leakage channel described below. However, during rapid increases in cytosolic calcium (such as during efferent stimulation), the CICR percentage could increase markedly, causing a lowering of the sac calcium concentration and a further increase in cytosolic calcium.

2.8.12 Ca^{2+}/M2/M3-M4 messenger cascade

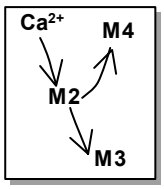

The equations below describe the calculation of the concentrations of the intracellular second messengers to be used in the next iteration of the model, based on the forward and reverse reaction rates for the activation of M2 by Ca^{2+}, and the subsequent activation of M3 and M4 by M2. The forward reaction rates are saturating functions of the precursor, with the degree of saturation depending on the size of the *z* denominator.

$$M2_{(n+1)} = M2_{(n)} + \frac{\left[\left(k_{M2} - M2_n\right)\cdot kM2_{forward}\cdot x_{M2}\cdot\left(\frac{Ca_i}{Ca_i + z_{M2}}\right)^{y_{M2}} - M2_n\cdot kM2_{reverse}\right]\cdot dT}{Vol_{M2}} \quad \textbf{[20a]}$$

$$M3_{(n+1)} = M3_{(n)} + \frac{\left[\left(k_{M3} - M3_n\right)\cdot kM3_{forward}\cdot x_{M3}\cdot\left(\frac{M2}{M2 + z_{M3}}\right)^{y_{M3}} - M3_n\cdot kM3_{reverse}\right]\cdot dT}{Vol_{M3}} \quad \textbf{[20b]}$$

$$M4_{(n+1)} = M4_{(n)} + \frac{\left[\left(k_{M4} - M4_n\right)\cdot kM4_{forward}\cdot x_{M4}\cdot\left(\frac{M2}{M2 + z_{M4}}\right)^{y_{M4}} - M4_n\cdot kM4_{reverse}\right]\cdot dT}{Vol_{M4}} \quad \textbf{[20c]}$$

using values:

$k_{M2} = 1.00$	$kM2_{forward} = 0.3$	$kM2_{reverse} = 0.3$
$x_{M2} = 0.4$	$y_{M2} = 1.00$ µM	$z_{M2} = 1.00$
$k_{M3} = 1.00$	$kM3_{forward} = 0.3$	$kM3_{reverse} = 0.3$
$x_{M3} = 0.4$	$y_{M3} = 1.00$ µM	$z_{M3} = 1.00$
$k_{M4} = 1.00$	$kM4_{forward} = 0.3$	$kM4_{reverse} = 0.3$
$x_{M4} = 1.00$	$y_{M4} = 1.00$ µM	$z_{M4} = 1.00$
$Vol_{M2} = 5$	$Vol_{M3} = 0.125$	$Vol_{M4} = 12.5$

The equation parameters chosen are such that the concentrations of M2 and M3 are equivalent to first-order low-pass-filtered and scaled versions of their precursors. M4 is also a low-pass filtered and scaled version of M2, but differs from M3 in the x_{M4}

parameter, and in the volume the messenger inhabits. As will be discussed in Section 2.9 , the choice of model parameters means that although the scale and offset value of M3 is different from that of M2, the phase shift between the M2 and M3 parameters is minimal. By contrast, the M4 parameter is substantially more low-pass filtered than M3. This is illustrated in Figure 2.8 below.

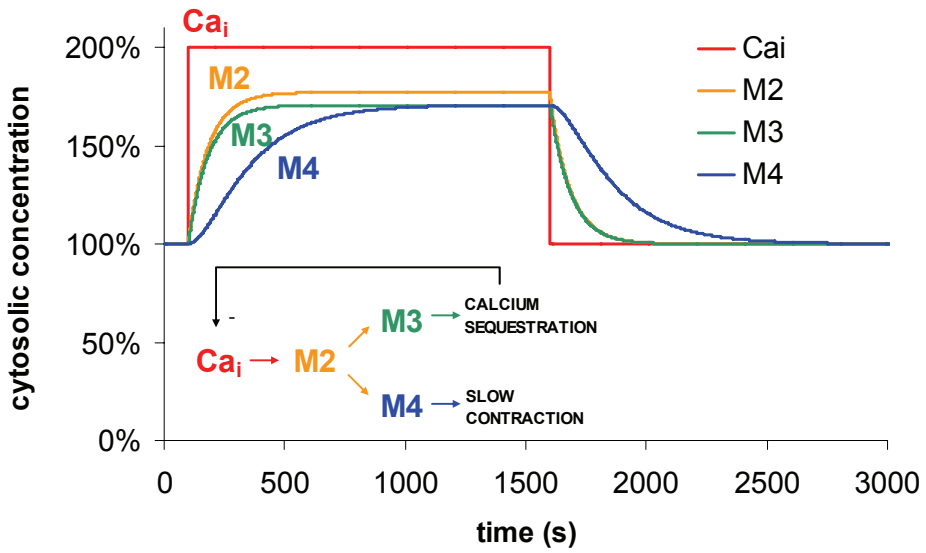

Figure 2.8: The time-course of the percentage increases in the intracellular second-messenger concentrations in response to a step-change in intracellular calcium concentration, as given by Equations 20a, b, and c alone (i.e. in the absence of other model mechanisms affecting calcium concentration). The 100% increase in $[Ca]_i$ produced a steady-state increase in [M2] of 77%, with increases of 71% in [M3] and [M4]. The normalised time-courses of the M2 and M3 increases were similar because of the low "volume" for the M3 concentration.

2.8.13 Finite-difference integration of calcium concentrations

The cytosolic and cisternal calcium concentrations for the next model iteration were calculated according to the following equations:

$$Ca_{i(n+1)} = Ca_{i(n)} + \frac{\left(I_{Cab} + I_{SERCA} + I_{antiportCalcium} + I_{CaSacLeak} + I_{CaCaSac}\right)\cdot dT}{Vol_{Cai}} \qquad \textbf{[21a]}$$

$$Ca_{Sac(n+1)} = Ca_{Sac(n)} - \frac{\left(I_{SERCA} + I_{CaSacLeak} + I_{CaCaSac}\right)\cdot dT}{Vol_{CaSac}} \qquad \textbf{[21b]}$$

using values:

$$Vol_{Cai} = 10000 \qquad Vol_{CaSac} = 30$$

The subtraction sign is used in Equation 21b because the calcium fluxes are described relative to the cytosolic concentration. For example, a positive value for $I_{CaSacLeak}$ produces an increase in cytosolic calcium but a decrease in sac calcium.

2.9 Selection of model parameters

If a model has *n* free parameters that affect its output, and each parameter can be one of *x* values, then there are essentially x^n potential variants on the model's output. The task of selecting the location in "multi-dimensional parameter space" that best achieves the desired model behaviour can therefore be made less arduous by reducing *n*, the number of free parameters. In this study, the first step in this process was to use published estimates of the characteristics of particular channels, ports and pumps, where these values were available. Once the decision was made to use a particular channel type (e.g. an SK potassium channel, or an L-type calcium channel), the number of free parameters describing that part of the model was often reduced by 50% or more.

The selection of appropriate values for the remaining parameters was an iterative process that was begun using a version of the model that had a number of components disabled, such as motility, voltage-dependence, and a variable EP. This simplified version was progressively complicated as each of the disabled components was restored and adjusted. In addition to ensuring that each added component displayed the appropriate behaviour, the model was adjusted at each stage of the iterative process according to three main criteria:

i) intracellular concentrations should be in the physiological range for an OHC;

ii) the resting basolateral membrane potential should be around -70 mV; and

iii) the operating point of the hair bundle should be reasonably close to 0 meV[8];

With regard to the second of these three criteria, the basolateral membrane potential was defined as the voltage at which the current entering the apex of the cell was balanced by the current exiting through the basolateral wall. By setting the number of other channels and pumps to zero, the cell was set up to have a single conductance in each membrane: the MET channel (at its half-activation point, or central quiescent point on the MET transfer curve) in the apical membrane (see Section 2.8.1 above), and a potassium leakage channel in the basolateral membrane (Section 2.8.4 above). Given a fixed EP of 95 mV, no apical potassium concentration gradient (i.e. SM and cytosolic

[8] As will be discussed in Chapter Six, there is evidence that the operating point of the hair bundle is not at the point of maximum sensitivity at rest.

[K^+] equal), and a basolateral K^+ concentration gradient of 157 mM internal to 4.2 mM external, a membrane potential of -69 mV was achieved when the simple conductance ratio of apical to basolateral membranes was set to 1:50. Moving the hair bundle to completely turn off or on the MET conductance (i.e. 0% opening probability and 100% opening probability) changed the membrane potential from -94 mV to -55 mV respectively, resulting in a maximum receptor potential of around 40 mV.

With regard to the third criterion, the operating point could be adjusted using a number of different techniques. For example, to cause a long-term shift in the operating point towards ST, the modeller could:

i) reduce the turgor of the cell.

ii) increase the slow-motile tonic contraction by

- increasing the resting Ca_i (for example, by reducing its extrusion via the Na^+/Ca^{2+} antiport or increasing its entry through the voltage-sensitive or ACh-sensitive Ca^{2+} channels);
- increasing either the cytosolic activity of M4 (via adjustment of the 2nd-messenger cascade), or increasing the sensitivity of the slow-contraction process to M4 (using the $M4_{off}$ parameter or the slow motility scaling factor, S_{slow}); or,
- increasing the *in situ* compliance of the cell if the operating point is already on the ST side of the mid-point.

or, iii) increase the electromotile tonic contraction by

- depolarising the cell (for example, by increasing the K^+ influx at the apex or reducing the K^+ efflux across the basolateral wall);
- increasing the sensitivity of the electromotility to voltage, by reducing the Vm offset factor (Vm_{off}) or increasing the fast motility scaling factor (S_{fast}); or,
- increasing the *in situ* compliance of the cell if the operating point is already on the ST side of the mid-point.

The intracellular turgor and the motility factors were described in Equation 9c above. These slow- and fast-motile contraction methods could sometimes be counterproductive: for example, increasing intracellular calcium might cause a slow-motile contraction (via M4), but a fast-motile relaxation (due to hyperpolarisation of the

OHC via the SK-channels), with the resulting ST or SV shift depending on the relative sensitivities of both processes.

In summary, the density of the selected channels are presented in the table below. However, the utility of the density measures is somewhat limited without some indication of the sensitivity of each of the channels to their precursor.

Transport mechanism	Type	Equation	Density (n)
Apical MET K^+ channel		9	1
Apical ATP-sensitive K^+ channel		9	0.5
Voltage-sensitive K^+ channel	K_n	10	0
Ca^{2+}-sensitive K^+ channel	SK2	11	400
K^+ leakage channel		12	25
Voltage-sensitive Ca^{2+} channel	L-type	13	0.005
ACh-sensitive Ca^{2+} channel		13	0.0001
Na^+/K^+/ATPase pump		14	1
Ca^{2+}/Na^+ antiport		15	5000000
PMCA Ca^{2+} pump		16	0
SERCA Ca^{2+} pump		17	30000
Ca^{2+} leak from SSC		18	0.02
Ca^{2+} induced Ca^{2+} release from SSC		19	0.4

Table 2.1: The densities of the selected membrane transport mechanisms. Published data was found for the transport characteristics of three of the channels and the Na+/K+/ATPase pump, with the characteristics of the other components chosen to shape the behaviour of the OHC model.

2.9.1 Adjustment of the frequency and damping of calcium oscillations

The parameters of the model were adjusted so that the oscillatory behaviour of the model was dominated by the Ca^{2+}/M2/M3 cascade (Loop IV in Figure 1.7 of Chapter One). The loop gain and phase delay around this loop could be adjusted according to the Nyquist criteria (Nyquist, 1932) to control the degree of damping and the frequency of the calcium oscillations, enabling the changes in basolateral permeability (via calcium) and the operating point (via M4) to match the experimental data. The loop gain could be reduced by reducing the density or rate of the calcium pumps, or reducing the sensitivity of each messenger to its precursor (via Equations 20a, b, and c). The phase delay of the loop could be increased by enlarging the "volumes" occupied by cytosolic calcium and the messengers M2 and M3, which decreased the frequency of any oscillation. The gain of each step in the cascade was also affected by the volume size, as a large volume for a messenger served to buffer it against incremental changes in messenger activity caused

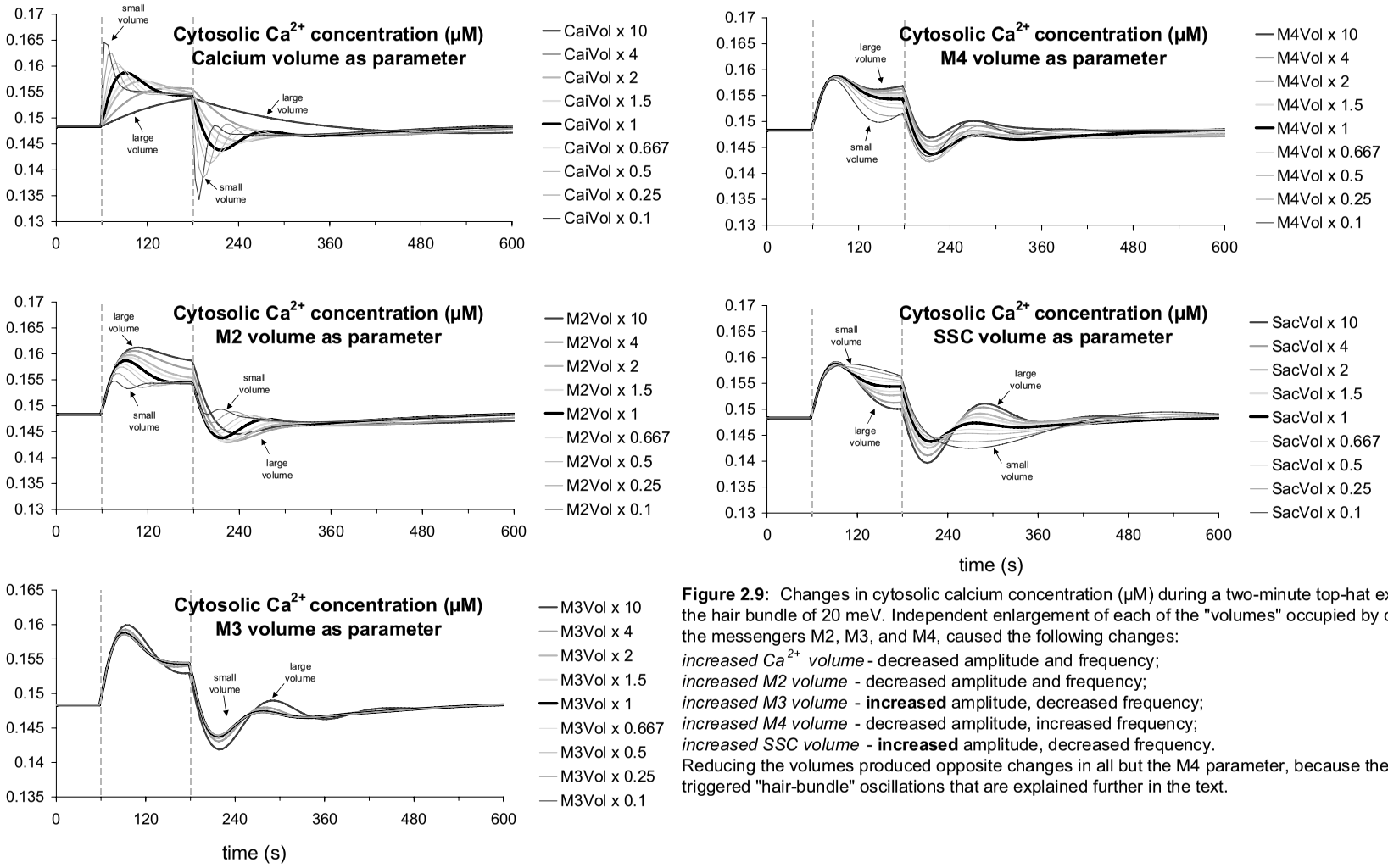

Figure 2.9: Changes in cytosolic calcium concentration (μM) during a two-minute top-hat external energy bias to the hair bundle of 20 meV. Independent enlargement of each of the "volumes" occupied by cytosolic calcium and the messengers M2, M3, and M4, caused the following changes:
increased Ca^{2+} volume - decreased amplitude and frequency;
increased M2 volume - decreased amplitude and frequency;
increased M3 volume - **increased** amplitude, decreased frequency;
increased M4 volume - decreased amplitude, increased frequency;
increased SSC volume - **increased** amplitude, decreased frequency.
Reducing the volumes produced opposite changes in all but the M4 parameter, because the reduced M4 volume triggered "hair-bundle" oscillations that are explained further in the text.

by its precursors. However, whether the amplitude of the calcium oscillations was increased or decreased by a volume change was dependent on both loop-gain and phase. The effect of volume changes is illustrated in Figure 2.9, which shows the cytosolic calcium changes in response to a step-bias of the hair bundle during parameterisation simulations in which the volumes of each of the messengers were systematically altered (see the figure legend for a description of these changes).

In addition to the dominant M3-driven oscillation, a "hair-bundle-oscillation" could be produced by the calcium-driven changes in M4 acting on the hair bundles (shown as Loop II in Figure 1.7 of Chapter One). Decreasing the volume of the M4 messenger in Figure 2.9 caused just such a hair-bundle oscillation to occur. Examination of the M4 panel in Figure 2.9 showed that increasing the M4 volume increased the frequency of the cytosolic calcium oscillation but reduced its amplitude, while *reducing* the M4 volume increased both the oscillation frequency and amplitude. The oscillations in operating point during the same parameterisation simulation (shown in Figure 2.10 below), showed the operating point oscillations increasing in amplitude (and frequency) as M4 volume was reduced, but decreasing as M4 volume was increased. This indicates that the larger Ca^{2+} oscillations with increasing M4 volume were produced by Loop IV, while the larger Ca^{2+} oscillations with *decreasing* M4 volume were produced by Loop II.

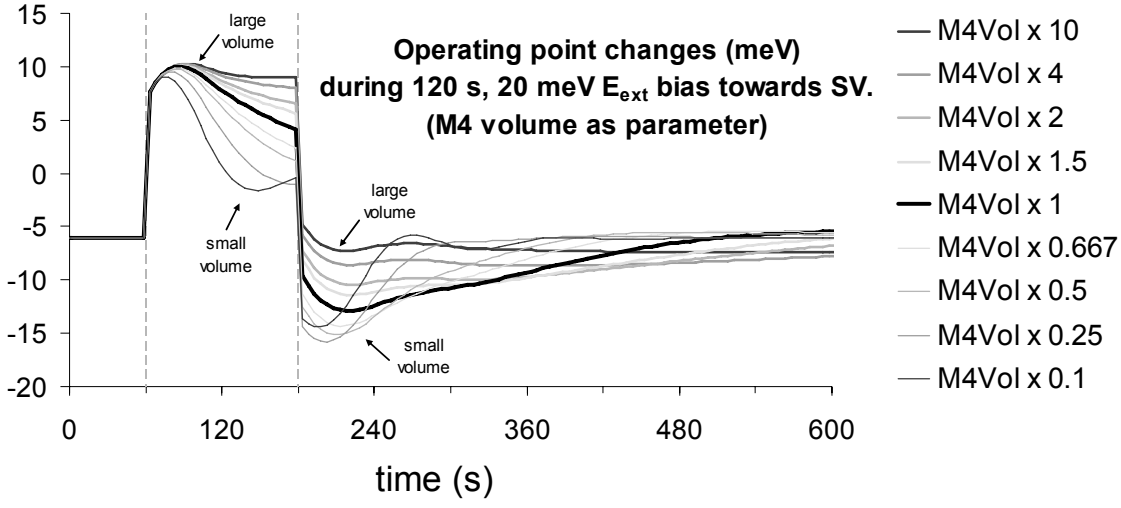

Figure 2.10: Decreasing the M4 compartment volume caused an increase in the amplitude and frequency of operating point oscillations triggered by a 20 meV step-bias towards SV, while increasing the M4 volume did the opposite. Given that changing M4 volume in either direction produced increases in the amplitude of cytosolic calcium oscillations (as shown in Figure 2.9), this indicates that these operating point oscillations arose from Loop II of the schematic OHC model shown in Figure 1.7 of Chapter One.

Because the experimental data suggests that the Ca^{2+}/M2/M3 oscillation dominates under most circumstances, the above checks were undertaken to ensure that the oscillations produced during the modelling of experimental perturbations were *not* due to hair-bundle oscillations.

One method of prolonging the oscillations was to decrease the level of damping provided by the voltage-controlled calcium channels. In this way, the ratio of ACh-dependent to voltage-dependent calcium channels was a tool for adjusting the damping. If the membrane potential is oscillating, the amount of calcium entering through fixed (or ACh) channels will also oscillate proportional to the electrical gradient for Ca^{2+} entry, with the largest influx occurring when the OHC is hyperpolarised. By contrast, the L-type voltage-controlled calcium channels open on depolarisation, *increasing* cytosolic calcium on depolarisation, thereby quenching the oscillations in intracellular calcium.

The phase of the oscillations produced by the 2nd-messenger cascade was critical in determining the ability of the model to match the experimental data. The extent to which oscillations in cytosolic calcium were manifest in the EP was dependent on the phase of M4 relative to Ca^{2+}. For example, if M4 and Ca^{2+} were 180° out of phase, EP oscillations were visible due to the additive effects of elevated $[Ca^{2+}]_i$ and reduced [M4], as both conditions resulted in an increased potassium shunt through the OHCs and therefore a lower EP (with calcium increasing basolateral permeability via the SK channels and the low M4 concentration causing a slow-motile operating point shift towards SV, thereby increasing apical permeability). Conversely, altering the phase delays so that a peak in $[Ca^{2+}]_i$ corresponded to a peak in [M4] would act to reduce that amplitude of any oscillations in the EP.

2.9.2 Functioning of the SSC

As shown in Figure 2.9, increasing the volume of the SSC caused an increase in the amplitude of the oscillations in *cytosoli*c calcium, because the larger SSC volume served to buffer the SSC calcium concentration against changes in calcium influx (due to the SERCA), or efflux (due to leakage or CICR). Leakage or release of calcium from the SSC decreased the effectiveness of the M3-sensitive sequestration[9], and therefore reduced the loop gain.

[9] This is because a small sac volume would mean that Ca^{2+} would leak out as fast as it was pumped in.

Calcium is a minority ion within the OHC. The intracellular store is able to parasitically sequester calcium in the background using the SERCA. Once the sac has reached a steady state, with influx and efflux being equal, we could assume that the sac would not influence cell function until the calcium release is triggered. This provides a mechanism for amplifying transient calcium signals that enable its use as an intracellular signal molecule. If we assume that the operating point and basolateral permeability of the OHC are dependent on the long-term $[Ca^{2+}]_i$, then the sac does not, and cannot, regulate the operating point or basolateral permeability *in the long term*. For that reason, altering the rate of flux into and out of the sac (by simultaneously changing both the pump rate and leakage conductance) is a mechanism for changing the time-course of calcium changes without altering the steady-state $[Ca^{2+}]_i$ or $[Ca^{2+}]_{sac}$. Increasing this flux can cause high-pass filtering of calcium transients which reduces the magnitude of any changes in the low-pass-filtered M4 parameter, and therefore the slow-motile contractions.

In general, the ratio of the SERCA pumping rate to the leakage of Ca^{2+} from the sac was adjusted so that the $[Ca^{2+}]_{sac}$ was maintained at around 600 μM at rest. The volume of the sac was set at 30 units (compared to the 10000 units for Ca_i), which limited the absolute quantity of Ca^{2+} the sac could dump into the cytosol during the peak of CICR[10]. This disparity in volumes was partially a method of compensating for the concentration gradient of approximately 1:4200 (cytosol:SSC). The calcium-binding constant for CICR had to be larger than the maximal $[Ca^{2+}]_i$ reached otherwise the release would be self-quenching. For there to be positive feedback to high-pass filter calcium transients, the amount of calcium released from the sac has to increase when the extracellular calcium increases.

The voltage inside the sac was assumed to be a fixed +30 mV relative to the cytosol, independent of cytosolic and sac calcium concentrations. Given a concentration gradient of approximately 1:4200 (cytosol:SSC), the total driving potential for calcium out of the sac was +280 mV.

2.10 Modelling of experimental perturbations

While the model parameters could be adjusted by hand in a free-form manner, experimental perturbations were more often simulated by the systematic and timed variation of a particular parameter or parameters. The choice of parameters to vary was

[10] Another influence on the CICR function was how quickly the calcium was evacuated from the OHC by the antiport following a CICR disgorgement.

made using selectors on the front panel (labelled V1 and V2), as was shown in Figure 2.2. Those most commonly used were the open-circuit EP (to simulate DC current injection), extracellular potassium or sodium (to simulate perilymphatic perfusions), external energy bias (to displace the hair bundle with sound or osmotic bias), and nCaACh (to simulate the effect of efferent stimulation).

The shape and amplitude of perturbations were treated separately. That is, a particular timing and shape could be applied simultaneously to two separate parameters, but at two different amplitudes. The perturbations were generated as a normalised time-course with a peak magnitude of 1, which were then scaled and offset by the pre-specified perturbation parameters.

The simplest perturbation was a step-change in a particular parameter. This form of perturbation was most applicable to DC current injection and efferent stimulation, where a "top-hat" function was used. However, for many perturbations it was more appropriate to use a less-abrupt change, which could be achieved by low-pass filtering of the step-change.

In some cases, data defining the shape of the perturbation could be read from an external file as a look-up table. This allowed more freedom in the design of the time-course of the perturbations, which could be created by external sources, or even measured experimental data. A particularly useful application of this feature was the importation of data produced by the Washington University Cochlear Fluids Simulator (v1.6h; Salt, 2002). The Cochlear Fluids Simulator allowed more accurate simulation of cochlear perfusions by providing estimates of perfusate concentration at appropriate locations in scala tympani, taking into account factors such as the flow rate of the perfusion pump, the passive perilymph flow rate of the guinea pig cochlea, and the diffusion co-efficient of the perfusate. The importance of these factors in interpreting the results of cochlear perfusions is discussed further in Chapter Eight.

The data were imported in the form of X-Y pairs representing time and magnitude, respectively. Any mismatch between the sample rate of the imported data and the time-step of the model was resolved by the use of cubic spline interpolation to generate the appropriate data points for a given time co-ordinate. In cases where step-transients were important to the sampled perturbation, a thresholding (i.e. non-interpolating) mechanism could be selected.

2.11 Results from the mathematical model

All simulation examples presented within this Chapter, and in the rest of the thesis, were generated by the model using the "standard parameter values" that were listed with each Equation in Section 2.8 above. As described in Section 2.9 above, the selection of a generalised set of model parameters was a time-consuming and highly iterative task, involving continuous comparisons between model output and experimental data. Inevitably some compromise is involved. A closer match to experimental data could be achieved by further alteration of one or more of the parameters, and where this produced in a markedly better match to experimental data, these special cases are also presented.

The bulk of the results for mathematical modelling are presented in the chapters containing the experimental results for the perturbations being modelled: the low-frequency bounce, DC current injection, and perilymphatic perfusion are presented in Chapters 6, 7, and 8, respectively. An additional result for the model is presented below.

2.11.1 Resistance of model OHC to external hair bundle bias

As discussed in Chapter One, the stereocilia of the OHCs are displacement-coupled to the overlying tectorial membrane, and are therefore vulnerable to static displacements. Such displacements can shift the operating point out of the most sensitive region of the MET transfer curve and therefore cause hearing loss.

Mechanisms which are likely to minimise the effects of such displacements in the long-term include transducer adaptation and somatic motility (both voltage- and calcium-dependent). As transducer adaptation mechanisms are not included in this model, a parameterisation simulation was performed on the model to characterise the model OHC's ability to reduce the effect of a static displacement using somatic electromotility and calcium-dependent slow-motility alone.

Figure 2.11 shows a plot of the long-term operating point that results from static displacements of hair-bundle of between -500 meV and 500 meV. Between approximately -200 meV and +100 meV, the resulting operating point shift was limited to approximately a quarter of the imposed bias after 2400 seconds. The dotted line showing proportionality represented the operating point that would result if this negative feedback on the operating point were absent. With energy biases of beyond -250 meV or +150 meV, the negative feedback mechanisms of the hair cell were at the limit of their ability to provide any further operating point compensation, and the slope of the curve returned to 45º.

The compensation provided was the equivalent of a net reduction in the external energy bias by 225 meV for scala tympani displacements, but only 140 meV for scala vestibuli displacements. That the model was more capable of adapting to displacements towards scala tympani than those towards scala vestibuli is most likely due simply to the range of possible calcium fluctuations with this perturbation: large operating point biases in the ST direction can result in a decrease of cytosolic calcium of up to 28%, while those in the SV direction only result in an increase of cytosolic calcium concentration of up to 21%, due to the action of the second-messenger cascade on calcium sequestration.

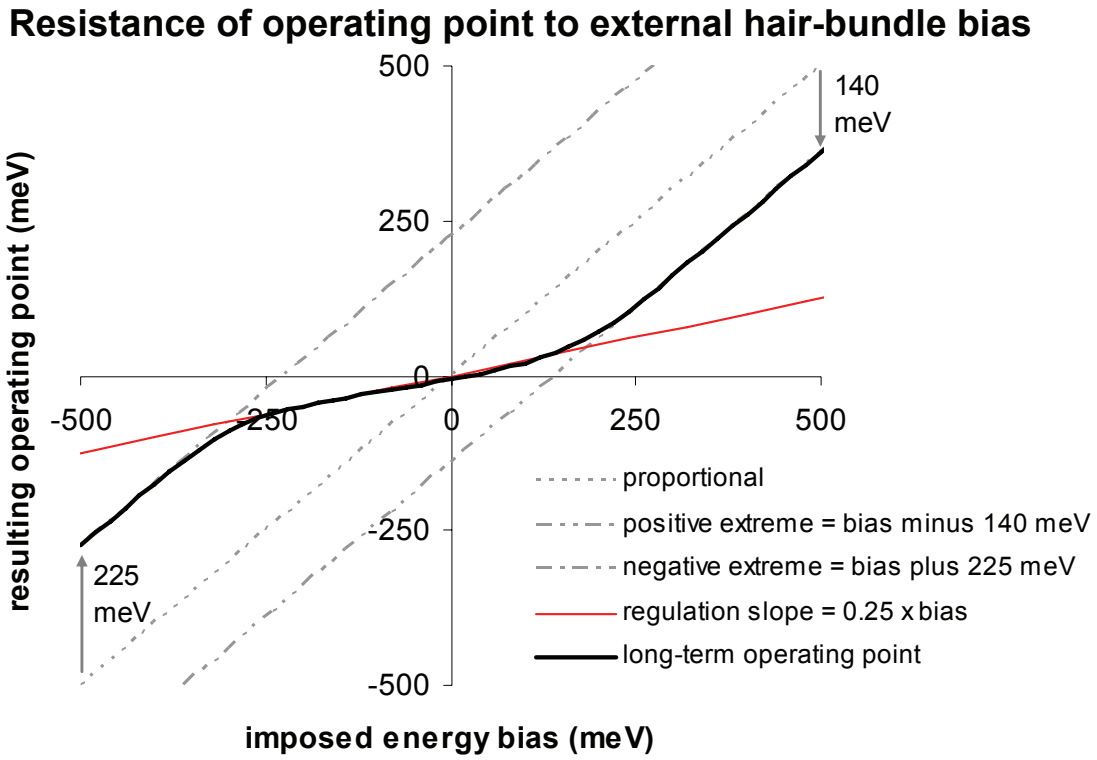

Figure 2.11: A plot of the long-term operating point that results from an imposed external energy bias in the direction of scala tympani (negative values) and scala vestibuli (positive values).

2.12 Discussion

To the best of our knowledge, the mathematical model presented here is the first that incorporates both the electrophysiology of the hair cell *and* its mechanical properties into a single framework. The outer hair cell is uniquely capable of both electromechanical and mechanoelectrical transduction, and as such, any modelling of its electrophysiology requires the inclusion of both of these elements in some form. As will be demonstrated in the following chapters, the model presented here provides a valuable conceptual tool for understanding how manipulation of the ionic and electrical environment of the cochlea can result in hearing loss and tinnitus.

In Chapters Six, Seven, and Eight, the results of the mathematical model for different types of perturbation are presented. These results were systematically compared with the experimental data, and are accompanied by detailed descriptions of the model functioning. For readability, the discussions relating to these issues are to be found in Chapters Six, Seven, Eight, and in the general discussion chapter, Chapter Nine.

In addition to the insights provided by the model itself (i.e. the set of equations presented in this chapter), the LabVIEW software that was developed to carry out the model calculations and perturbations has a number of other applications in both research and as a teaching tool.

By turning off the hair cell motility, eliminating the second messenger cascade, and changing some channel densities (such as removal of the Na^{+}/Ca^{2+} antiport and the SSC), the OHC model becomes an IHC model. Because the model features time-course simulation as well as steady-state values, the hair bundle can be velocity-coupled, instead of displacement-coupled as it is in the present OHC model, allowing simulation of inner hair cell receptor potentials and receptor currents.

With some minor reprogramming, the OHC model becomes a general cell model that can be used to dynamically calculate the effect of ionic concentrations, voltage bias, or channel blockade on many types of cell, both symmetric and asymmetric, with the advantage of informative graphical outputs of load-line analysis and a user-friendly interface. The modular nature of the LabVIEW programming environment means that multiple cell models could be cascaded relatively easily to simulate multi-layer epithelia, such as stria vascularis.

Screenshots and a description of the LabVIEW implementation of the OHC model are presented in the following appendix.

2.13 Appendix: Front panel of the model

2.13.1 The "run" tab

The "run" tab is the main screen of the model program (shown in Figure 2.1), which contains the most important controls defining the cell and the experimental perturbations, displays the main time-course outputs, and contains many of the "administrative" and "housekeeping" functions, such as file-saving. For convenience, it is displayed again here as Figure 2.12. It can be divided into five columns:

The first column contains (from the top) the **stop button**, which causes the model to finish the iteration it was on and halt execution, saving the generated model output if this option was selected. Below the stop button is the **copy present to initial** button, which sets the starting state vector (i.e the initial values of the cytosolic concentrations of Ca^{2+}, M2, M3, M4, the SSC concentration of Ca^{2+}, and the EP) to match the state-vector at that moment. This helped eliminate startup-transients in the model. Below this are three **graphing controls** to autoscale the time and value axes of the time-traces, and to clear them of data. The **graph updating** buttons below this were used to set whether the time-trace charts were updated, primarily as a method of speeding up the execution of the VI. Below the main **time display** are digital readouts of the **basolateral membrane potential**, and the concentrations of cytosolic calcium and the messengers M2, M3 and M4. Below these are controls for the **open-circuit EP** and the **potassium concentrations** for scala media, inside the OHC, and scala tympani. The controls for the calculation of the **hearing loss** predicted by the model (see Section 2.5.2 above) are also shown. The "reset" button allows the present receptor potential value to be used as a reference for subsequent hearing loss calculations.

The second column contains the main controls for the **Apical MET** and **ATP-sensitive K^+** channels, the basolateral **Ca^{2+}-sensitive**, **voltage-sensitive**, and **leakage K^+** channels, the basolateral **Na^+/Ca^{2+} antiport** and **Na^+/K^+/ATPase**.

The third column contains controls for the **EP** (if manual control was selected), **scala tympani potassium**, and the **external energy bias** for the hair bundle. The controls for the main **calcium transport mechanisms** appear below this, with readouts of the different calcium fluxes, along with the controls for the "**volumes**" for calcium and each of the intracellular messengers.

A key objective of the model was to observe the interactions and feedback between various hair cell measures and to examine their detailed time-courses. To that end, the time-traces for the basolateral membrane potential, EP, intracellular Ca^{2+}, M2, & M3, predicted hearing loss, and hair bundle displacement were displayed on this tab. At the base of the bottom plot was the x-scale for the seven time-traces on this tab, as well as for the four time-traces shown on the IVplot tab. For better comparison of the M4, Ca^{2+}, HL, and perturbation time-courses, these plots were overlayed on the trace beneath the first three columns of controls.

At the top of the rightmost column are switches for the **experiment timer** and the **model timer**, which selected whether the "End Time" and timed perturbations were used, respectively. If the model timer is "on", the model is perturbed according to the settings in the bottom right of the tab and on the "perturb" tab itself. Beneath the two switches at the top of the column are thumbnail versions of the IV and transfer curve plots shown in full on the "IVplot" tab, and indicators showing graphical displays of the membrane potential and hair-bundle angle. Beneath these are tick-boxes controlling i) the auto-scaling of the x-axis on the time-course displays, ii) the presence or absence of an animated icon of the OHC, iii) file-saving, iv) parameterisation experiments (which require block-diagram changes at this stage), and v) file-saving for these parameterisation experiments.

The most commonly-used perturbation controls are shown at the bottom of this column. Two timed perturbations could be controlled at once. The variables (named V1 and V2) that could be selected were i) open-circuit EP, ii) extracellular potassium, iii) external hair-bundle bias, iv) the number of ACh-sensitive Ca^{2+} channels (for modelling efferent stimulation), and v) extracellular sodium. The "from" and "to" controls indicated the resting level and maximal perturbation level, while the "start" and "end" controls indicated the onset and offset times for the perturbation, if a simple step-perturbation was used. The "start" and "end" times were ignored if the perturbation was loaded from an external file (using either the File1 or File2 selectors).

2.13.2 Other tabs

The "setup" tab (Figure 2.13) contained diagnostic information about the functioning of the "voltage solver" that hunted for the basolateral membrane potential at which the basolateral K^+ current was zero, and also contained other settings, including those for the intracellular second-messenger cascade, and the initial-value "state vector" for the OHC model.

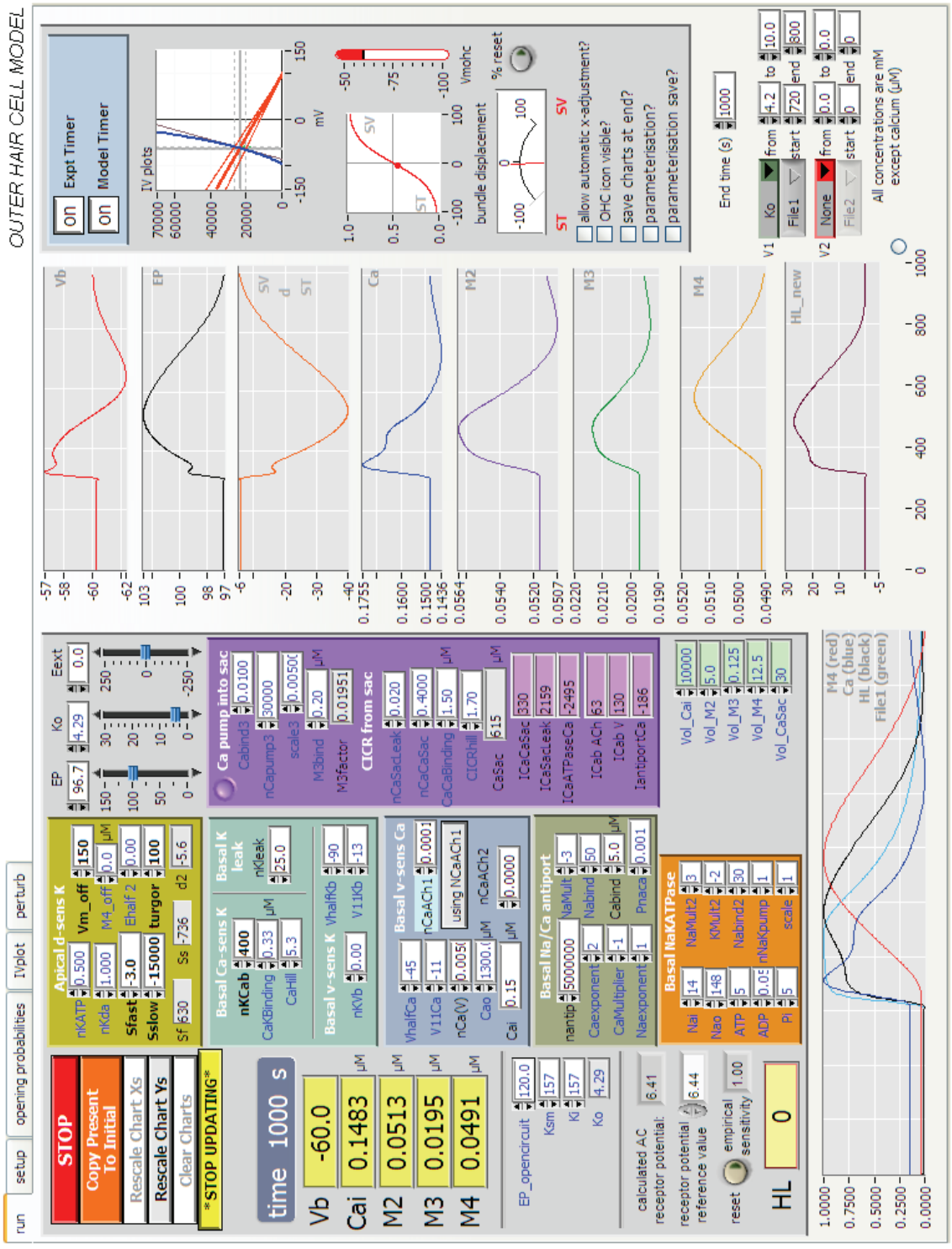

Figure 2.12: The "run" tab of the mathematical model (see text).

The “opening probabilities” tab (Figure 2.14) showed graphical displays of the way a number of channels opened as a function of either voltage, calcium, sodium, or M3, depending on the channel.

Red dots on the probability curves indicated the present state of the channel. Also shown was the dependence of fast motility and slow motility on voltage and M4, respectively.

The “IVplot” tab (Figure 2.15) contained the MET transfer curve and a large IV plot display for the OHC, in addition to controls for the load-line analysis using AC displacement of the hair bundle. The choice of whether small-signal or saturated AC displacements were used was made using the “imposed dp” control, in units of meV. In the following chapters, the small-signal, near-saturated, and fully-saturated AC displacements were produced using 1 meV, 100 meV, and 150 meV displacements, respectively. The resulting receptor potential and receptor current were displayed in time-traces on the right of the panel.

The two main methods of perturbing the cell model were controlled from the “Perturb” tab (Figure 2.16). They were the Filters sub-tab (contents not shown), which contained the settings to control the low-pass filtering of the step-perturbations defined on the “Run” tab of the front panel (i.e. the filter-order and cut-off frequency). The File sub-tab controlled the external perturbation “shapes” that could be imported for use in experiments with the model. The paths for the tab-delimited text files containing the perturbation data were selected using the two “File Path” controls, and the relevant columns of the file containing the “time” and “perturbation data” were selected using the controls provided. The loaded perturbation shapes were then plotted in the “Perturbations From File” graph for reference. The data points within the perturbation files were usually numbers between zero and one defining the *relative* amplitudes of the perturbation: A “0” in the file corresponded to the value of the “from” selector on the front panel, while a “1” corresponded to the value of the “to” selector. The method of interpolating the perturbation data points between those included in the file (either cubic spline interpolation or a simple thresholding method) could be selected, as described in Section 2.10 above. A “mute” function was available to eliminate onset artefacts from the spline interpolation process, as shown in Figure 2.17 below.

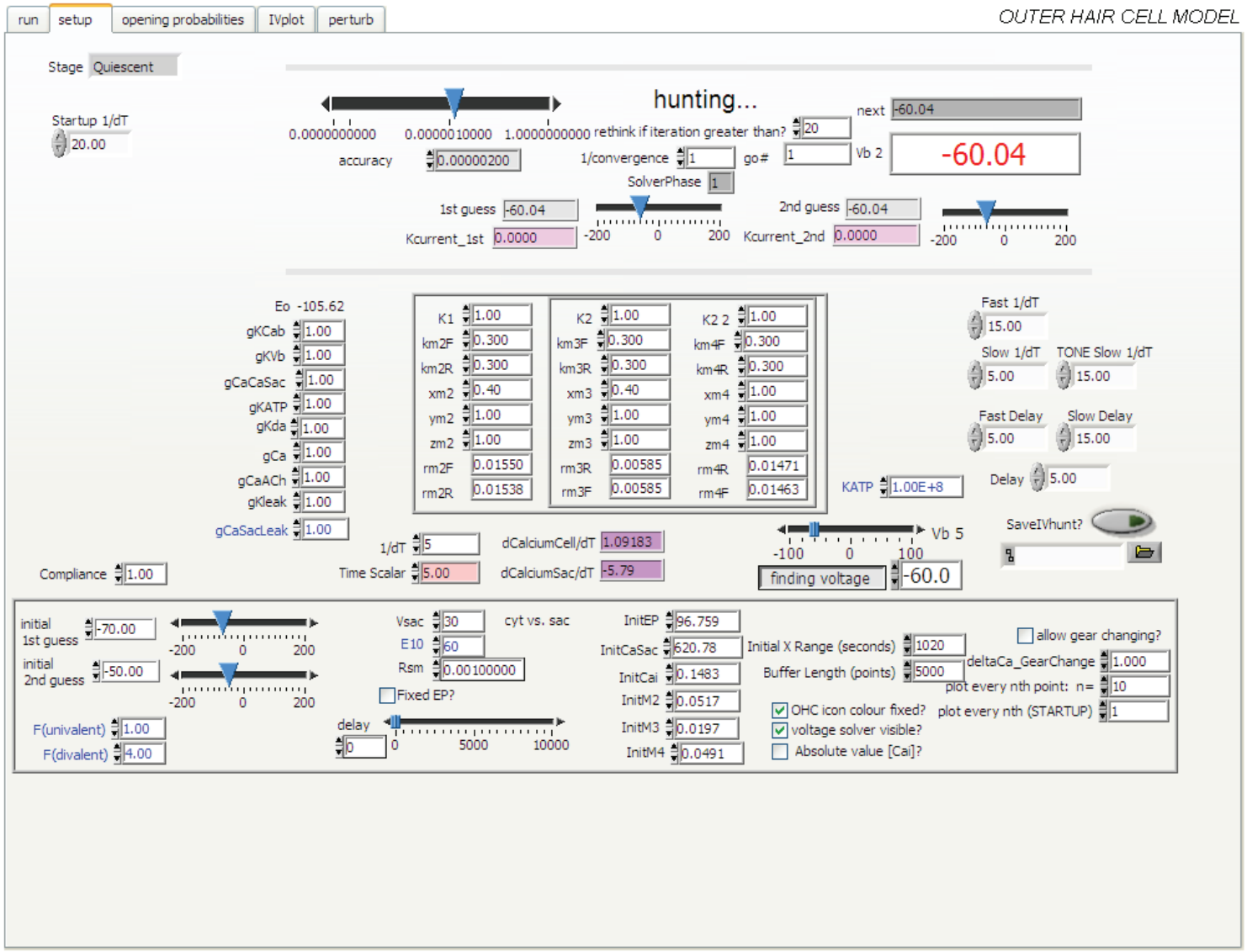

Figure 2.13: The "setup" tab of the mathematical model (see text).

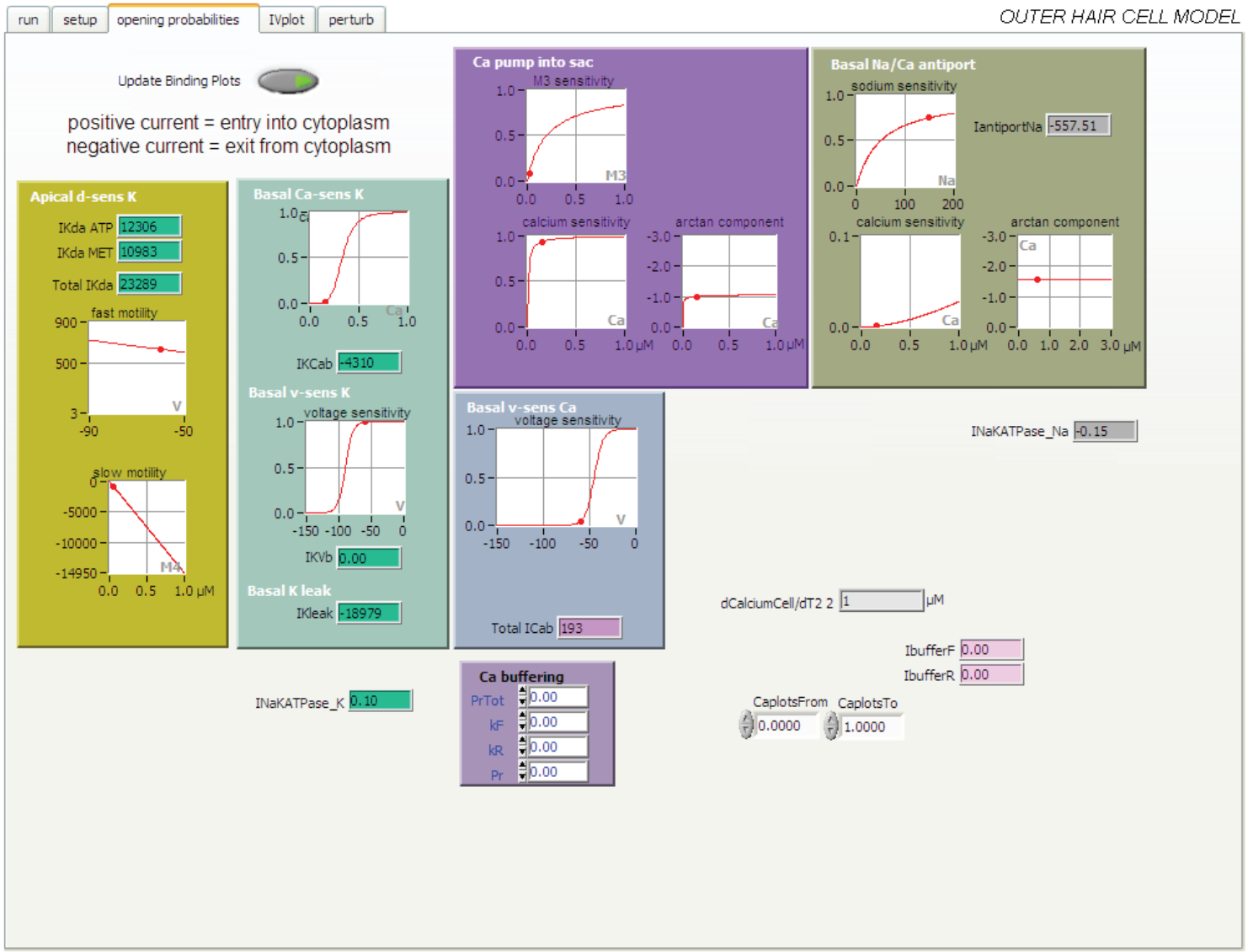

Figure 2.14: The "opening probabilities" tab of the mathematical model (see text).

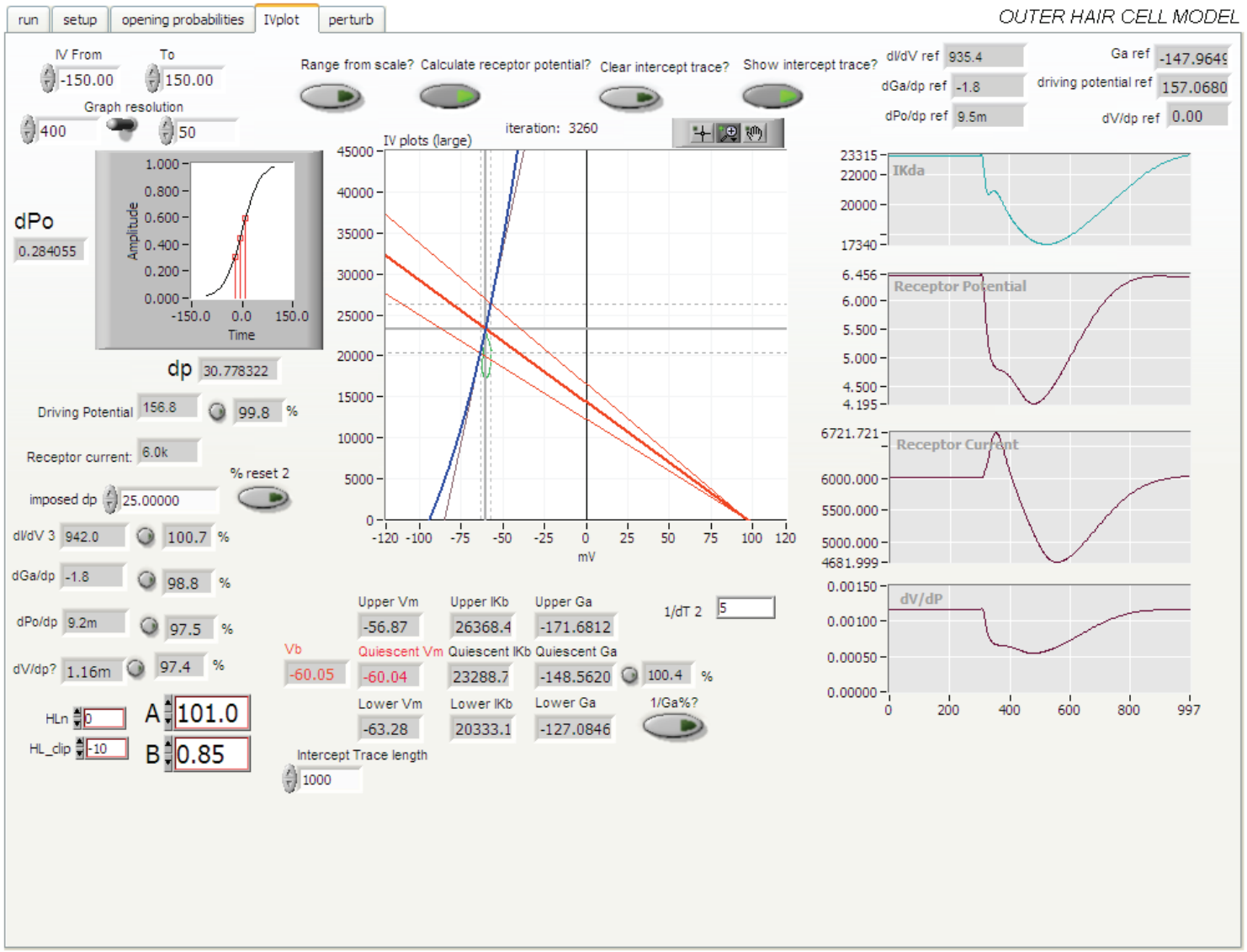

Figure 2.15: The "IVplot" tab of the mathematical model (see text).

Figure 2.16: The "perturb" tab of the mathematical model (see text).

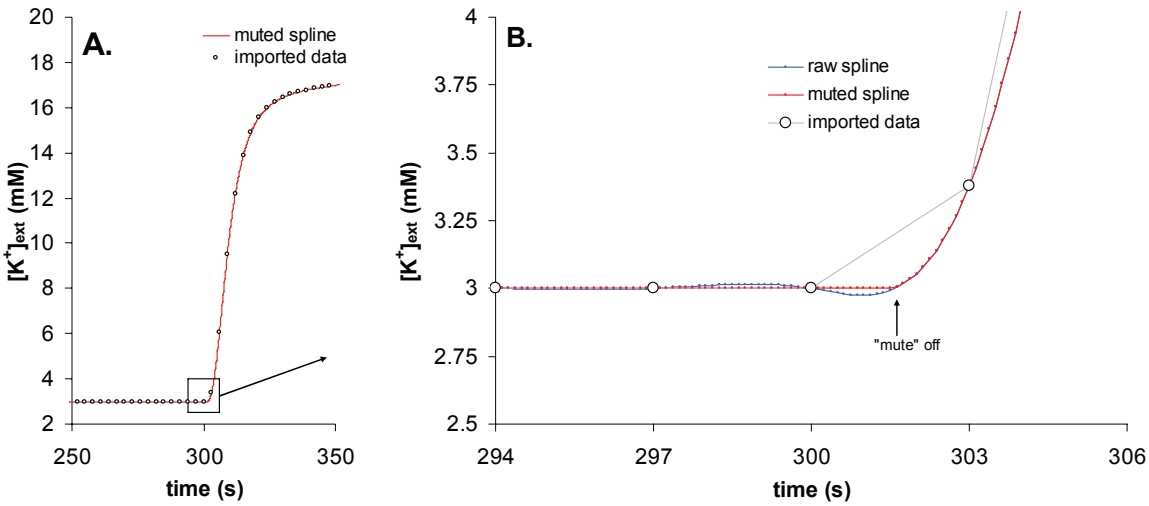

Figure 2.17: An example of the cubic-spline interpolation of imported perturbation data, showing how the use of the "mute" function could prevent onset artefacts caused by the interpolation process (see text).

Chapter 3
General methods

3. General Methods

3.1 Animal preparation

105 adult pigmented guinea pigs (*Cavia porcellus*) with normal hearing thresholds (Patuzzi et al., 1989b), external ears free of debris, and body weights from 200 – 470 g were used[1]. Guinea pigs were obtained from the Biological Sciences Animal Unit at the University of Western Australia, and most were fasted overnight prior to experimentation. All anaesthetic and surgical protocols were approved by the Animal Ethics Committee of the University of Western Australia (Approval No. 02/100/184).

3.1.1 Anaesthetic regime

Following premedication with a subcutaneous injection of 0.1 mL atropine sulphate (0.6 mg/mL; Apex Laboratories, NSW), guinea pigs were anaesthetised with 30 mg/kg body weight Nembutal (60 mg/mL pentobarbitone sodium; Merial Australia, NSW) and 0.15 mL Hypnorm (0.315 mg/ml fentanyl citrate and 10mg/mL fluanisone; Janssen Pharmaceutica, Belgium). Anaesthesia was subsequently maintained by 15 mg/kg Nembutal given every two hours, and 0.15 mL Hypnorm given every hour. Incision sites were anaesthetized locally with lignocaine hydrochloride (20 mg/mL; Troy Laboratories, NSW).

Once surgical anaesthesia was obtained (indicated by the absence of a pedal-withdrawal reflex), animals were paralysed with 0.1 mL pancuronium bromide (2 mg/mL; AstraZeneca, NSW, Australia) to eliminate middle-ear muscle activity and extraneous myogenic potentials. As this also eliminated foot-withdrawal, adequate depth of anaesthesia was determined by monitoring of the electrocardiogram (ECG): animals were given further doses of either Hypnorm or Nembutal if the heart rate increased to a period of less than 175 ms.

Due to supply difficulties, a different anaesthetic regime was used for eight animals (GP#102 to GP#109), which were anaesthetized with 1.5 g/kg urethane (Sigma-Aldrich Chemie, Germany), with hourly doses of 0.15 mL Hypnorm. These animals were also paralysed with pancuronium, and their ECG was monitored as above.

[1] Some collaborative experiments required differing animal identification schemes. Guinea pigs that were part of this project were numbered (in order): 1-24, 31-34, 52-115, PS91-PS92, PS99, and 116-125.

3.1.2 Surgery

All experiments were conducted in electrically-shielded sound-proof rooms. Following surgical anaesthesia, the trachea was cannulated and the animals were artificially ventilated with Carbogen (95% O_2, 5% CO_2) using a Bioscience 8000-1 ventilator (6 cubic cm tidal volume, 51 cycles/minute; Bioscience, Sheerness, Kent, UK). Both tragi were removed and the head was mounted between hollow ear cones, with head position stabilised by a bite-bar and nasal clamp. The ear cones were placed at an angle that allowed a clear and unobstructed view of the tympanic membrane through the cone.

Body temperature was maintained at 38º C by a heating pad controlled by rectal thermostat. Air temperature in the sound-proof room was approximately 22º C for GP#01 to GP#57. To prevent cooling of the exposed cochlea (Brown et al., 1983), a 12 V DC light globe was placed near the head of the guinea pigs numbered GP#58 to GP#81. A room heater was used to maintain sound-proof room air temperature between 30º C and 38º C for all subsequent animals.

Following removal of the right pinna, a small hole was made in the bulla using a scalpel, allowing a dorsolateral approach to the round window and first-turn of the cochlea. In the event that the right cochlea was damaged or deafened, surgery and experimentation were carried out in the left cochlea.

3.1.3 Cochleostomy

For experiments involving cochlear perfusions or DC current injections, a hole was drilled in the first-turn, approximately 1 mm from the round window, using either a hand-held twist drill (0.11 mm diameter; Titex Plus, Germany), or the bevelled end of a 27-gauge needle (Terumo Medical Corp., MD, USA) which created a hole of similar diameter. For perfusion experiments, a small exit hole was made in the otic capsule at the apex of the cochlea using a sharp wire hook. A drop of Heparin Injection BP (heparin sodium – porcine mucous; David Bull Laboratories, VIC, Australia) was applied to this apical opening to prevent its blockage by blood clots[2].

3.1.4 Electrode placement

Electrical signals were recorded using Teflon-coated silver wire (0.008” bare wire diameter; A-M Systems, Inc., WA, USA). Prior to use, the Teflon coating was removed

[2] Although intracellular heparin is a potent blocker of IP3 receptors (Nilsson et al., 1988; Sugasawa et al., 1996), the perilymph flow in the opened cochlea is in the base-to-apex direction (Salt et al., 1991), ensuring diffusion of heparin to the basal regions of the cochlea would be limited.

from the final 1 mm of the wire, and the exposed end was chlorided in a saline solution by applying a 20 μA current for two to five minutes.

The active electrode was placed on (or occasionally through) the round window with the aid of a micromanipulator (Narishige Co. Ltd., Tokyo, Japan). Recordings were made with reference to an indifferent electrode placed in the temporalis muscle overlying the temporal bone. An earth electrode, wrapped in saline-soaked tissue, was placed in the neck. The exposed and chlorided portions of the indifferent and earth electrodes were 1 – 2 cm long. In some of the later perfusion experiments, the active electrode was placed within the perfusion pipette. In these cases, the Teflon coating was removed from the final 1 cm of the wire, and the exposed end was etched in a potassium cyanide solution to produce a sharpened tip that could be placed close to the pulled end of the pipette.

For the experiments investigating the application of force to the cochlear wall conducted with Dr. Peter Sellick (see Chapter 5), electrical signals were recorded from etched wires placed in scala tympani and scala media through first-turn cochleostomies. Small beads of silicone (RTV-734, Dow Corning, MI, USA; RTV-102, GE Plastics, VIC, Australia) were placed along the shank of the electrode to prevent the leakage of cochlear fluids.

ECG signals were recorded from two 26-gauge needles (Terumo Medical Corp., MD, USA) inserted between the digits of the left fore-paw and hind-paw.

3.2 Recording system

Experiments presented here were conducted using two experimental setups within the Auditory Laboratory of the University of Western Australia. Most experimentation was carried out in SPR2, while those involving measurement of otoacoustic emissions were carried out in SPR4. The recording systems for both setups are described below.

For experiments conducted in SPR2, electrical signals from the round window were amplified using a custom-built pre-amplifier (40 dB gain), and low-pass filtered at 5 kHz using a Stanford SR650 programmable filter (Stanford Research Systems, Inc., CA, USA) which provided an additional 10 dB gain. Use of the low-pass-filter at the 5 kHz setting introduced a delay of around 0.14 ms to CAP latencies. The amplified and filtered signals were then passed to the line input of the soundcard (Creative Ensoniq AudioPCI CT4810, Creative Labs, NSW, Australia) and recorded using the Cricket data

acquisition software described in Chapter 4. The soundcard line-input had a flat frequency response (less than ± 2 dB variation) in the range of 6 Hz to 19 kHz.

For experiments conducted in SPR4, electrical signals from the cochlea were amplified and filtered using a DAM 50 differential amplifier (0.1 Hz - 10 kHz pass-band, 40 dB gain; World Precision Instruments Inc., FL, USA), before being passed via a custom-built relay to the line input of the soundcard (CardDeluxe, Digital Audio Labs, MN, USA) and recorded using the Cricket data acquisition software described in Chapter 10. For measurement of otoacoustic emissions, ear-canal sound pressure was monitored with a Brüel & Kjær 4134 ½-inch condenser microphone, amplified by a Brüel & Kjær 2609 measurement amplifier with an A-weighted filter, and analysed using the Cricket software. The A-weighted spectra were then mathematically converted to dB SPL.

3.3 Data Acquisition Software

Stimulus-generation and data acquisition were controlled by The Cricket, custom-written software that enabled automated and rapidly-interleaved measurements of i) the CAP thresholds at multiple frequencies, ii) the CAP waveforms elicited by supra-threshold stimuli, iii) low-frequency (207 Hz) CM waveforms for online Boltzmann analysis, iv) the spectrum of the neural noise (both spontaneous and driven), and v) distortion-product otoacoustic emissions. Details of the software are presented in Chapter 4.

3.4 Acoustic stimuli

The Cricket used custom-generated sound stimuli for eliciting CAPs, the CM, and DPOAEs. These stimuli will be discussed in detail in Chapter 4.

3.4.1 Stimulus delivery methods differed between setups

For experiments conducted in SPR2, the stimuli used for eliciting CAPs were delivered using a reverse-driven Brüel & Kjær 4134 ½-inch condenser microphone (Brüel & Kjær, Denmark) coupled to the external ear through the hollow ear-cone. Low-frequency acoustic stimulation for CM analysis was delivered using a Beyerdynamic DT48 headphone (Beyerdynamic, Heilbronn, Germany) for animals GP#GOB01 to GP#GOB23, and a low-frequency driver (of unspecified origin) for subsequent animals. The low-frequency driver was used in preference to the Beyer headphone because it was lighter and less cumbersome to place, and was able to produce a more intense 207 Hz pure tone for the same electrical drive. Both the Beyer

headphone and the low-frequency driver were coupled to the ear canal using a 3 cm length of polyethylene tubing.

For experiments conducted in SPR4, both the CAP and CM stimuli were delivered using a Beyerdynamic DT48 phone coupled to the cones in the ear canal using a 3 cm length of polyethylene tubing. High-level distortion-product otoacoustic emissions were evoked by primary tones delivered using a pair of Beyerdynamic DT48 phones that were also coupled to the ear canal by 3 cm polyethylene tubes.

3.4.2 Calibration

Low-frequency sound-pressure levels were calibrated at 207 Hz using a Brüel & Kjær 4192 ½-inch condenser microphone with a probe-tube cone to monitor the ear-drum sound-pressure produced by the low-frequency driver used in these experiments. The electrical output of the B&K microphone in this configuration was calibrated against the output produced when the microphone was coupled to a Brüel & Kjær 4230 Sound Level Calibrator, which produced a 1 kHz tone at 94 dB SPL. An unattenuated signal from the soundcard produced 115 dB SPL at the ear drum with the low-frequency driver.

A biological reference was used for high-frequency sound-pressure levels. The tracked thresholds of the ten guinea pigs that had the best overall hearing levels were averaged at each frequency and were used to derive a correction factor to convert the tracked attenuation levels (specific to the SPR2 setup) into a biological reference that could be used to compare the thresholds of individual guinea pigs to those of the rest of the population used in this study, and allowed quicker assessment of the state of an animal during an experiment. This reference scale was referred to as “guinea pig hearing level” (dB GPHL), akin to the “hearing level” (dB HL) used in human audiometry. The GPHL correction factors are presented in Chapter 4.

3.5 Experimental manipulations

The surgical aspects of the experimental manipulations are described in Section 3.1 above. The techniques used to perturb cochlear function are described in the Methods sections of the relevant chapters.

3.6 Issues relating to the Boltzmann analysis of CM waveforms

Boltzmann analysis of the CM was discussed in Section 1.2.2 of Chapter One, and will be discussed further in Chapter Four. Results obtained using the Boltzmann analysis technique are presented in Chapters Five, Six, Seven, and Eight. As mentioned

earlier, the transfer curve relating the OHC receptor current to the assumed angular displacement of the hair bundle can be estimated from the Lissajous figure obtained by plotting the CM potential against the instantaneous phase-shifted sound pressure level in the ear canal (Nieder and Nieder, 1971; Avan and Legouix, 1988; Patuzzi and Rajan, 1990).

The low-frequency CM recorded in the first turn of the guinea pig cochlea has been shown to be proportional to stapes velocity (Dallos, 1973), which phase-leads the ear canal sound pressure by 90º. As the stapes velocity increases at 6 dB/octave relative to sound pressure, the ability of an instantaneous ear canal sound pressure to displace the basilar membrane also increases by 6 dB/octave. However, at any given (fixed) frequency, the angular displacement of the hair bundle can be assumed to be proportional to the instantaneous phase-shifted sound pressure level in the ear canal.

3.6.1 Use of a 1st-order Boltzmann function

The opening probability of the MET channels has been described by a first-order Boltzmann function (Holton and Hudspeth, 1986; Patuzzi, 1995; Sirjani et al., 2004), a second-order Boltzmann function (for example, Kros et al., 1992), and other, more empirical, functions, such as polynomials (Chertoff et al., 2000). The use of a *first-order* Boltzmann function derived initially from noise-analysis studies of the MET channels from the bullfrog sacculus: Holton and Hudspeth (1986) found the relationship between the angular displacement of the hair bundle and the current through the transduction channels to be consistent with a two-conductance-state model, following a sigmoidal first-order Boltzmann activation function. The first-order Boltzmann activation function describes a population of independent and identical channels that have two conductance states – an open (conducting) state, and a closed (non-conducting) state. The stochastic flickering of the population of channels may be biased by displacement of the hair bundle.

In the two-state model (1st-order Boltzmann function), the channels may redistribute between the open and closed states with given rates of transition, as follows:

$$closed \underset{kco}{\overset{koc}{\rightleftharpoons}} open \qquad \textbf{[1]}$$

where k_{co} and k_{oc} are the rate constants for opening and closing transitions, respectively.

In the three-state model (2nd-order Boltzmann function), the channels may redistribute between the open and closed states with given rates of transition, as follows:

$$closed1 \underset{kc1o}{\overset{koc1}{\rightleftarrows}} closed2 \underset{kc2o}{\overset{koc2}{\rightleftarrows}} open \qquad \textbf{[2]}$$

where k_{co} and k_{oc} are the rate constants for opening and closing transitions, respectively.

Kros et al. (1992) found the transfer function of cultured neonatal mouse OHCs to be well described by a 2nd-order Boltzmann activation function. However, the transfer curves obtained in that study (shown in Figure 3.1) were grossly asymmetric, and bear little resemblance to the derived transfer curves obtained from CM Lissajous figures (shown in Figure 3.2), or from microelectrode recordings from OHCs *in vivo*.

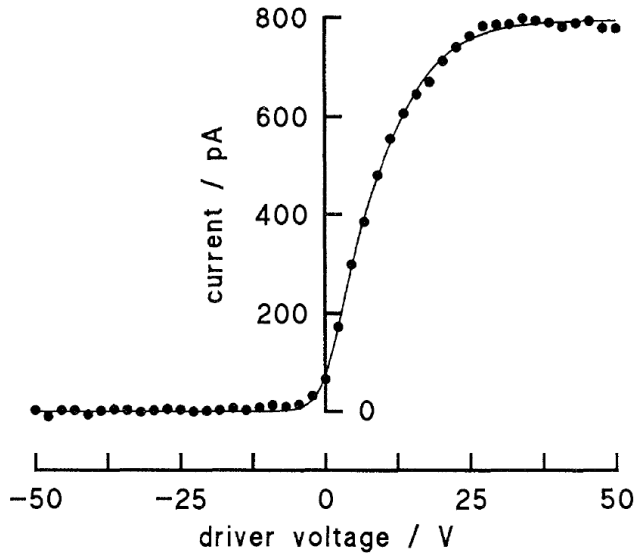

Figure 3.1: A transfer curve from an isolated outer hair cell from the apical turn, recorded by Kros et al. (1992) (see text).

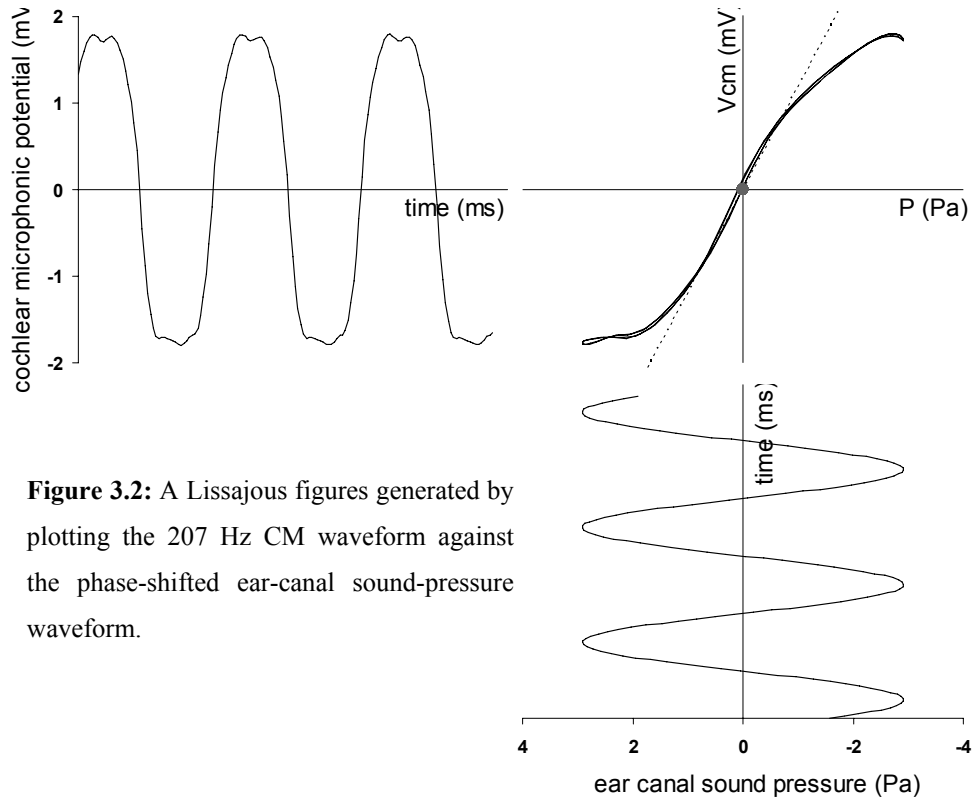

Figure 3.2: A Lissajous figures generated by plotting the 207 Hz CM waveform against the phase-shifted ear-canal sound-pressure waveform.

Cody and Russell (1987) carried out such microelectrode experiments and found an absence of DC receptor potentials for tones above 2 kHz in basal turn OHCs *in vivo*, suggesting that the OHCs operate relatively symmetrically around the steepest part of their transduction curves. Kros et al. suggested the difference between their asymmetric transfer curves and the symmetry implied in Cody and Russell's results may have been due to an external force acting on the hair bundle (such as from the insertion of the hair bundle into the TM), rather than an intrinsic property of the hair bundle itself.

Regardless of the *cause* of the symmetry, and because Boltzmann analysis of CM waveforms is necessarily carried out *in vivo* where OHC transfer curves are relatively symmetric, the 1st-order Boltzmann function produces an adequate description of OHC MET. Patuzzi and Moleirinho (1998) calculated that any errors arising from the fitting of a 1st-order Boltzmann function to CM waveforms produced by a 2nd-order transfer curve would be minimal in comparison to the changes in the parameters they observed experimentally.

Chapter 4
Software for electrophysiological monitoring of cochlear regulation

4. Software for electrophysiological monitoring of cochlear regulation

This chapter describes the main software developed for the project – the evoked-response averager named "The Cricket"[1]. Results obtained using this software are presented in Chapters 5, 6, 7 and 8. Modified versions of the software have been used successfully in a number of other studies[2].

Other programs written for this project are described in the Methods sections of the relevant chapters. These include software for Boltzmann analysis of CM waveforms at multiple probe-tone sound levels (see Chapter 5) and Boltzmann analysis of CM waveforms evoked with a 207 Hz probe and a 13 Hz bias tone (see Chapter 6).

4.1 Overview

In order to study the regulatory mechanisms of the cochlea under experimental conditions, custom-written software was developed to enable the simultaneous measurement of multiple indicators of cochlear function over extended periods.

The software was designed to enable automated and rapidly-interleaved measurement and analysis of:

i) the CAP thresholds at seven representative frequencies;

ii) the averaged CAP waveforms elicited by supra-threshold stimuli;

iii) the outer-hair-cell transfer curves derived from low-frequency CM waveforms;

iv) the spectrum of the neural noise (both spontaneous and sound-evoked);

v) the endocochlear potential; and

vi) distortion-product otoacoustic emissions.

The automated nature of the software had the advantage of freeing the experimenter from repetitive measurement tasks, allowing more time for the preparation and delivery of the various cochlear perturbations. This not only reduced the number of people needed to carry out the experiment to one, but also increased the amount of data that could be obtained from each animal.

The aim of the experimental series was to gather panoramic data about the response of the cochlea to various perturbations and disruptions to its functioning, to inform the development of a mathematical model of cochlear regulation. The model, described in

[1] Named after the chirp-like sound of the stimuli it produces.

[2] See, for example, Clack and Patuzzi (2001), Purdy et al. (2001), Purdy et al. (2002), Purdy et al. (in press [a]), Purdy et al. (in press [b]), Mulders and Robertson (2005),and Sellick et al. (in preparation).

Chapter 2, was concerned with the interactions between various hair cell measures (such as receptor current, receptor potential, and gain), and so the type of data that was anticipated to be most useful for modelling purposes was the detailed time-courses and the co-variation of the available cochlear indicators.

The software presented here, written using LabVIEW (v5.1 to 7.0; National Instruments Corp., TX, USA), enabled the co-variation of these indicators to be studied in great detail, and allowed cochlear function to be assayed at the hair cell and neural levels simultaneously. The software has also been adapted for use in humans, and the techniques described here may prove useful for intra-operative monitoring of hearing thresholds during human surgery.

4.1.1 The use of LabVIEW as a programming language

LabVIEW is a graphical program-development environment based on the G programming language. Programs written using LabVIEW are called virtual instruments or VIs, and consist of "block diagrams", in which data move along wires between icons representing variables and functions. Each VI may contain other VIs, which are then called sub-VIs. The graphical user interface (GUI) of a LabVIEW program is the front panel, so-called because it represents the front panel of a traditional, or non-virtual instrument. LabVIEW was chosen as a software development tool in this project primarily because of the relative speed and ease with which the complicated programming tasks (such as data acquisition, manipulation, display, and file-handling) could be completed, and the ease with which programs could be later modified to suit changing requirements and protocols.

National Instruments also manufacture a range of data acquisition (DAQ) cards that may be used by LabVIEW to sample and produce analogue DC voltages and 5 V digital signals. One such DAQ card, the Lab-PC+ (National Instruments Corp., TX, USA), was used in a number of experiments to sample the endocochlear potential (EP), produce analogue voltages to control DC current injection equipment, and provide the power supply and control signals for a custom-built relay circuit used to direct the soundcard output to multiple speakers.

While the software was designed to operate using the Microsoft Windows version of LabVIEW, the VI could theoretically be run on the Macintosh version of LabVIEW with only slight modifications. It could not, however, operate under the UNIX version of LabVIEW, which lacks soundcard interface sub-VIs integral to the software's operation.

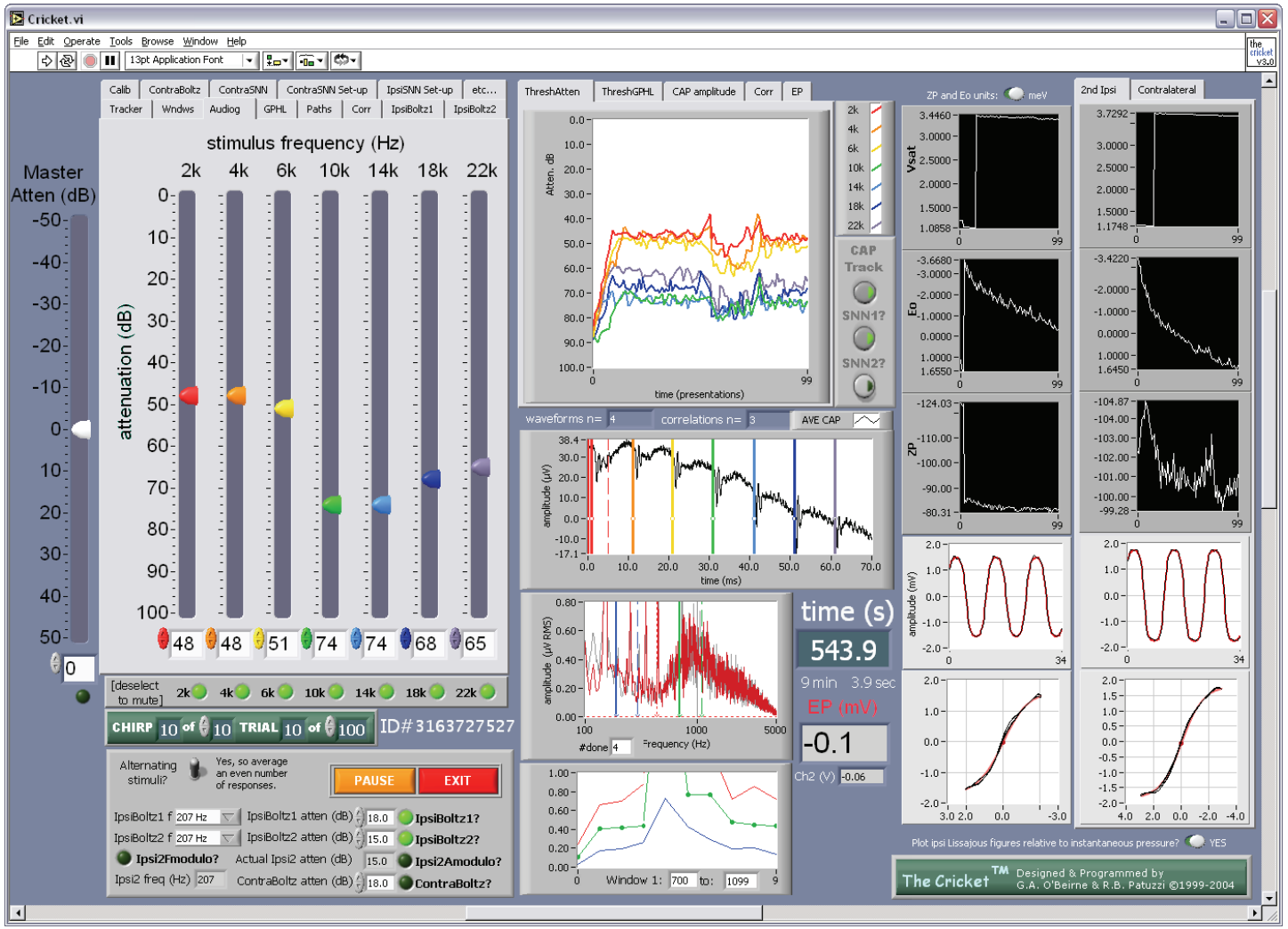

Figure 4.1: The front panel of The Cricket. Shown is a 10-minute trace recorded while setting up prior to an experiment. The tone-burst level used to evoke the left Boltzmann CM was decreased by 6 dB after the first 20s, causing changes in all three Boltzmann parameters. The round-window signal gain was increased by 10 dB to the calibrated level at 100s, causing increases in the Vsat and SNN traces, and CAP amplitude trace (not shown). EP was not measured on this occasion.

4.2 Front panel

The front panel of the VI is shown in Figure 4.1, and was designed for a 1280 x 1024 screen resolution. As shown in Figure 4.2, the more commonly used settings were placed directly on the front panel, while others were placed in a bank of tabs on the left of the screen, and are described in detail in later sections.

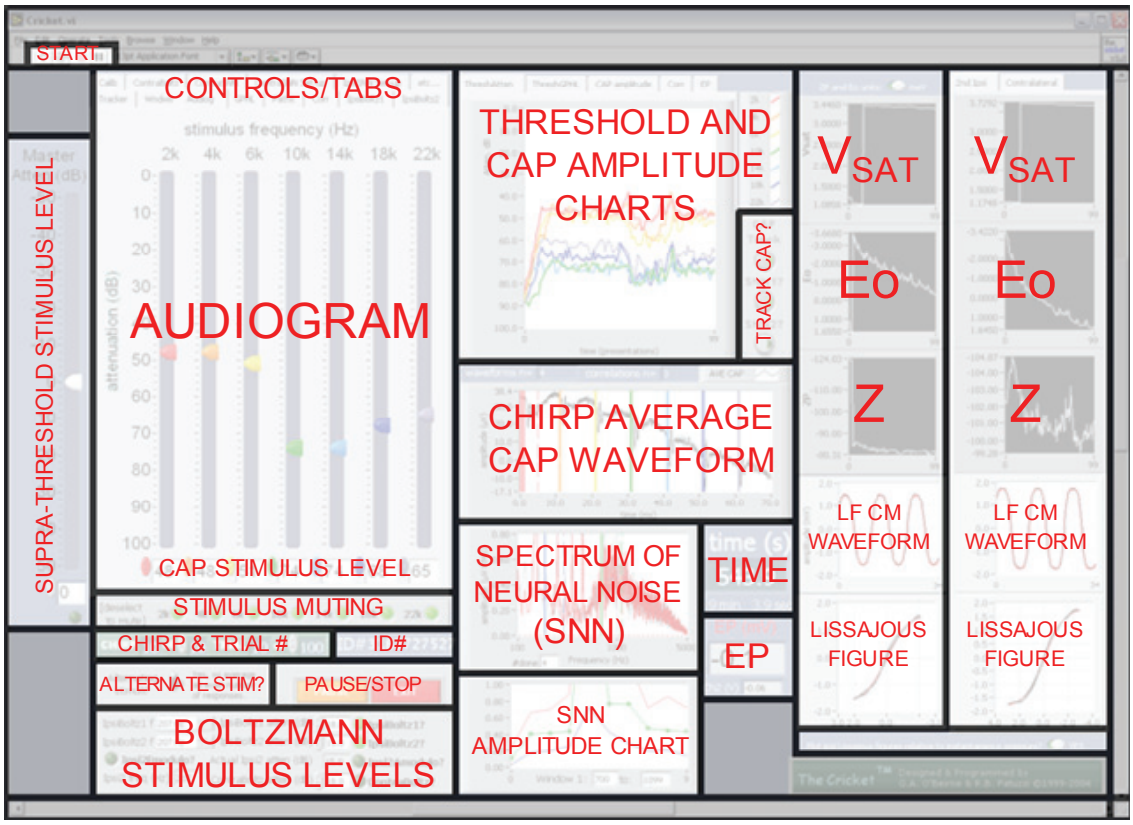

Figure 4.2: Annotated schematic diagram for the software Front Panel shown in Figure 4.1.

4.3 Measurement procedures

In its simplest configuration, the software could operate using only the soundcard of the computer to acquire waveforms and present stimuli. Indeed, it was first designed as a laptop-based evoked-response averager for measurement of the post-auricular muscle response (PAMR), requiring only a pair of headphones and a small battery-operated custom-built biological amplifier for operation (O'Beirne and Patuzzi, 2001). The present version of the software has been heavily expanded and customised for laboratory research, and in some instances assumes the presence of additional hardware for control of signal routing and measurement, as discussed later.

4.3.1 Measurement cycle

The sequence in which the measurement of physiological parameters was carried out is referred to here as the “measurement cycle”, the primary divisions of which were the

"chirp" and the "trial", as illustrated in Figure 4.3 below. These terms will be used repeatedly throughout this chapter.

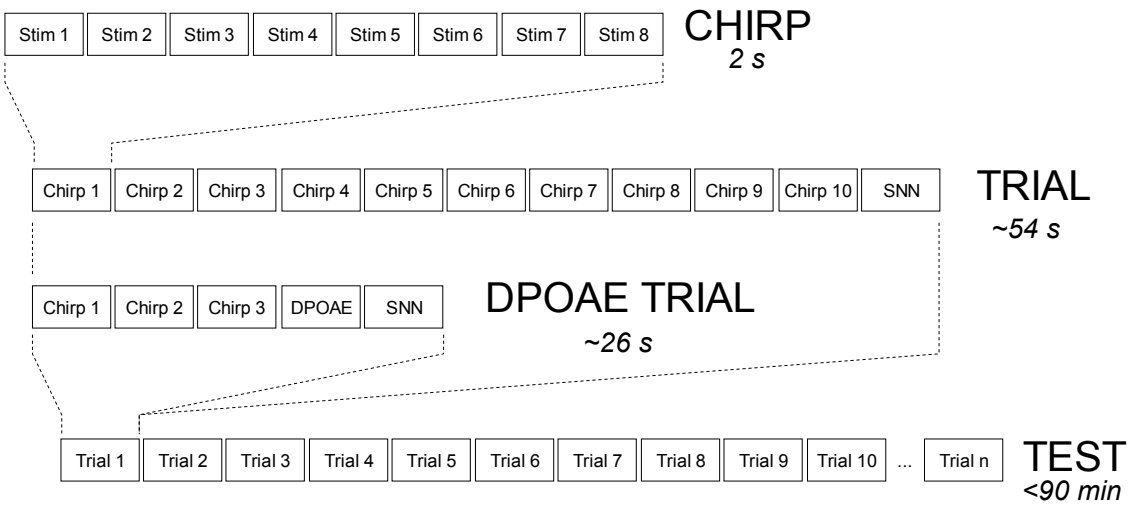

Figure 4.3: Schematic diagram of the measurement cycle carried out by the Cricket, showing both a normal trial and the alternative DPOAE trial (see text).

Measurements of the CAP threshold or CAP waveform and Boltzmann analysis of the low-frequency CM were rapidly interleaved so as to be nearly simultaneous. As shown in Figure 4.3, each set of CAP and Boltzmann stimuli was delivered in a "chirp", consisting of eight stimulus sets presented over two seconds. The stimulus set is described in greater detail in Section 4.3.2 below. The two-second chirp length was chosen because it was the longest continuous read/write duration that remained within the capabilities of our experimental computer over the course of an entire test, and also because it allowed greater temporal resolution of our time-course measurements.

A "trial" usually consisted of ten chirps followed by SNN and/or DPOAE measurements. Whereas the Boltzmann parameters and CAP data (such as peak-to-peak amplitudes or tracked thresholds) were saved to disk following each chirp, the averaged waveforms (n = 80) were saved to disk at the end of each trial. The HF tone-bursts of every alternate stimulus set were usually inverted to cancel any CM components in the averaged waveform, particularly from the 2 kHz and 4 kHz tone-bursts. The number of chirps per trial could be adjusted to allow greater resolution of the time-courses of the SNN or DPOAE measurements. For example, when recording DPOAEs within the measurement cycle, usually three chirps were presented per trial.

4.3.2 Acoustic stimuli

The software used custom-generated sound stimuli, shown in Figure 4.4. CAPs were elicited by 5 ms tone-bursts (with a 1 ms rise-fall time) at seven different frequencies. In

the majority of the experiments described here, the seven frequencies were 2, 4, 6, 10, 14, 18, and 22 kHz, but these were often varied to study particular regions of the cochlea in greater detail. While most of the tone-bursts were gated sinusoids, the 22 kHz tone-burst was instead a gated square wave at 22.049 kHz. This frequency was chosen to avoid aliasing problems with the soundcard, which used a 44.1 kHz sampling rate. The neural responses were unlikely to be affected by the use of a square-wave at this frequency, because the third harmonic of 22.05 kHz (66.15 kHz) is beyond the range of hearing for guinea pigs (Heffner et al., 1971; Prosen et al., 1978), and beyond the capabilities of the driver used.

Following the train of HF tone-bursts were two 50 ms LF tone-bursts used in the Boltzmann analysis procedure described in Section 4.5 below. The level of each component of the stimulus (the seven HF CAP tone-bursts and the two LF Boltzmann tone-bursts) was set by multiplying the "raw" (unattenuated) stimulus array by an "attenuation array" of the same length. At the end of each chirp was a trigger pulse for synchronising the data acquisition, described in Section 4.3.3 below. The seven tone-burst frequencies and wave types could be adjusted via the "on-the-fly stimulus creation" controls, shown in Figure 4.5.

The order in which frequencies were presented within a stimulus train was found to have little effect on the responses measured[3]. This was assessed by selectively omitting or rearranging tone-bursts to ensure that a change in auditory threshold at frequency did not *artefactually* change the responses at other frequencies.

4.3.3 Data acquisition hardware

Although the output of the soundcard was limited to two channels (left and right), operation of the VI required three signals to be directed to three destinations – the CAP stimuli were to be carried to the high-frequency driver (a reverse-driven Brüel & Kjær 4134 condenser microphone); the low-frequency tone-bursts for Boltzmann analysis were to be sent to the low-frequency driver; and the trigger pulse (appended to the end of the chirp stimulus) was to be directed back into the soundcard to establish the timing of the input data relative to the output stimuli. The trigger pulse was essential for synchronisation because of the latencies introduced by the Windows operating system that affected LabVIEW's control of the soundcard.

[3] On rare occasions, tracking of the first CAP response (2 kHz) was disturbed by its temporal proximity to the 207 Hz CM. However, where this occurred experimentally, the 2 kHz data was omitted from analysis.

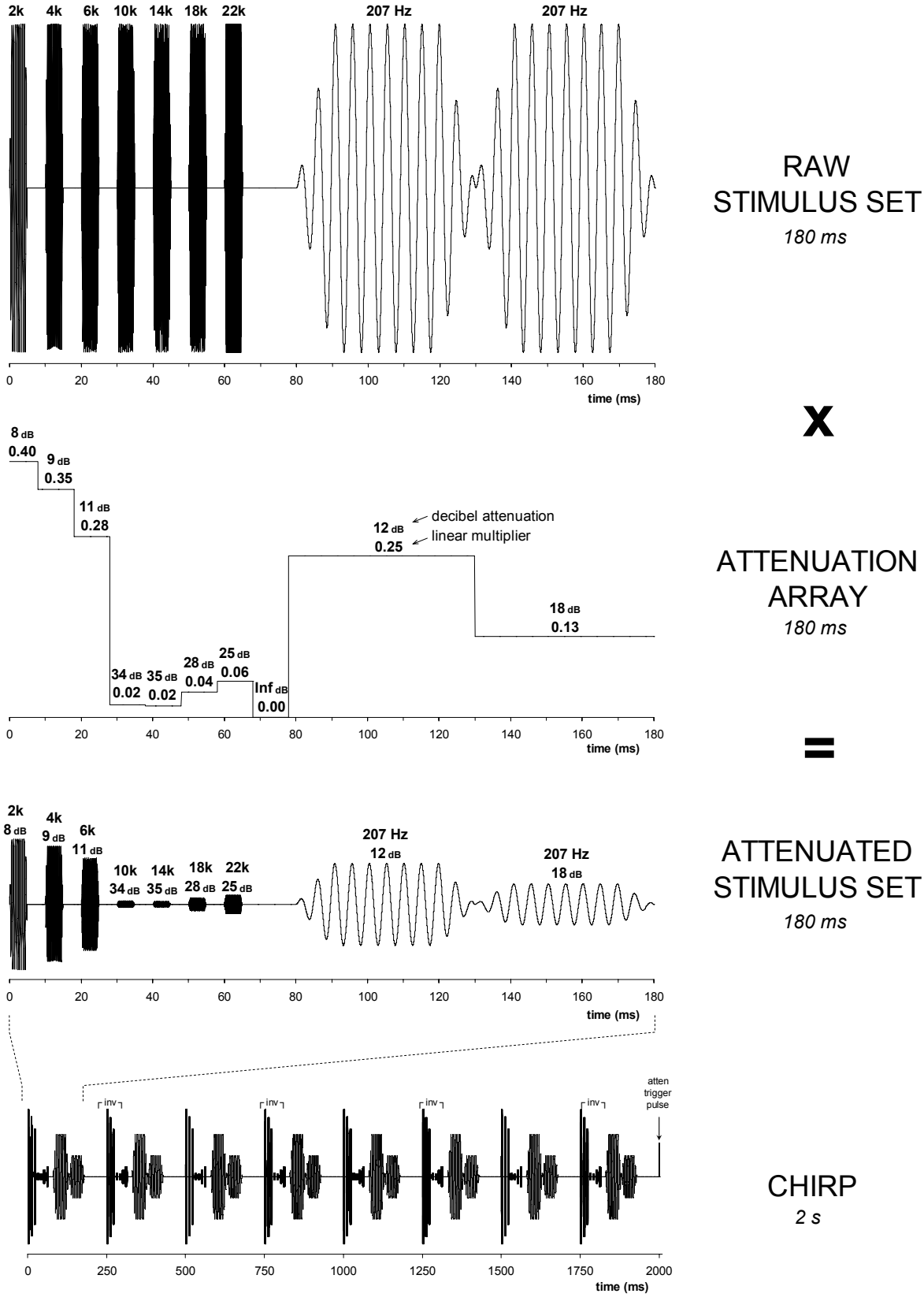

Figure 4.4: Schematic diagram showing the raw acoustic stimuli used by the software, and the generation of the "chirp" sound stimulus. Also shown is the "attenuation array" which was altered dynamically during the threshold-tracking process (see text).

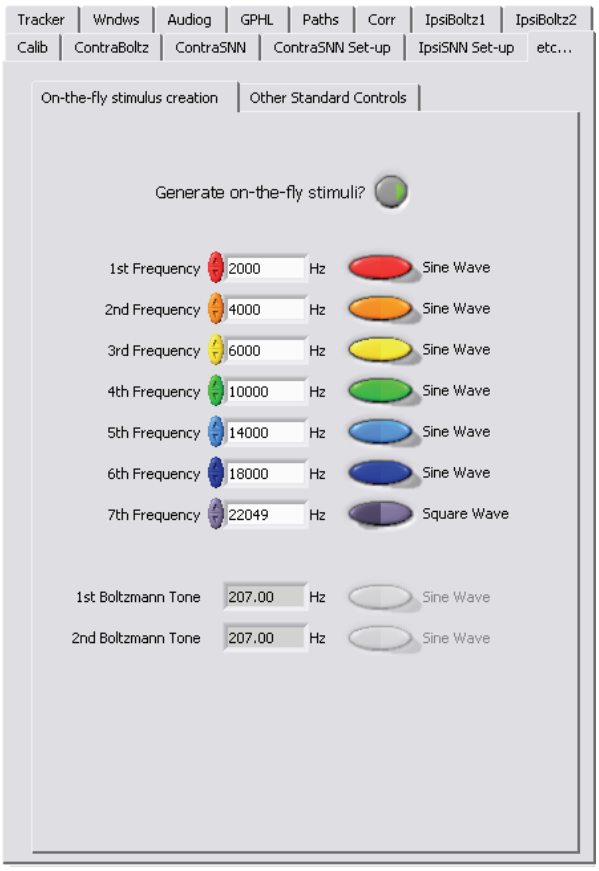

Figure 4.5: The frequencies and wave-type of the stimuli used to evoke the CAPs could be adjusted during the course of an experiment using the "On-the-fly stimulus creation" tab. Note that while sine waves are used for most frequencies, the 22 kHz tone-burst was evoked using a square wave at 22049 Hz (see text).

After trialling many variations, the configuration shown in Figure 4.6 was adopted. The CAP stimuli were carried on the right channel, while the low-frequency Boltzmann tone-bursts and the trigger pulse were carried on the left channel. The possibility of the large trigger pulse producing an audible click in the guinea-pig ear canal was reduced by attenuating and low-pass filtering the left-channel signal before sending it to the low-frequency driver, as shown in Figures 4.6. These steps also reduced the risk of high-frequency feed-through from the right soundcard channel to the left channel being fed to the low-frequency driver.

A peak-picking algorithm was used to detect the trigger pulse on the left channel of the input. Due to the trigger's position at the end of the chirp, the peak corresponding to the trigger pulse was always the last of the 113 peaks detected by the algorithm in each input. The response evoked by the chirp was divided into the eight segments to be averaged by counting back from the trigger pulse in increments of 11025 samples (250 ms).

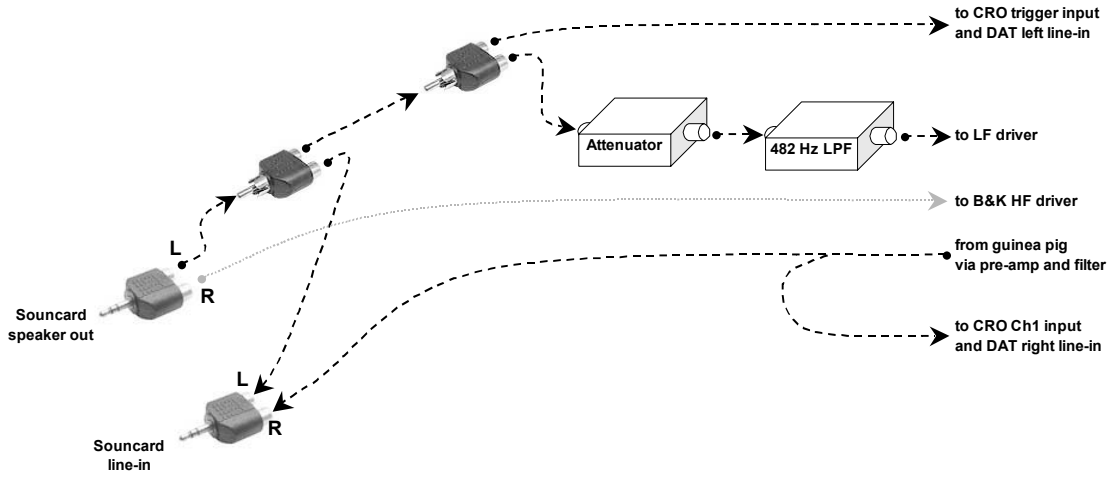

Figure 4.6: Schematic diagram illustrating the signal paths between the soundcard and the experimental setup. The DAT recording system was later replaced by another computer, which streamed the signals to hard drive during the experiment for off-line analysis.

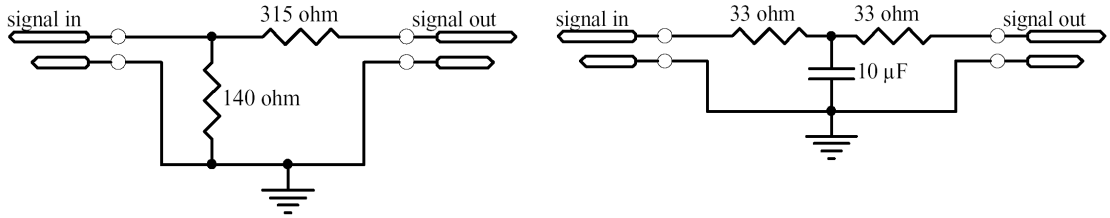

attenuator circuit 482 Hz low-pass filter circuit

Figure 4.7: Schematic diagrams illustrating attenuator and low-pass filter circuits in the signal path to the low-frequency driver.

4.4 CAP threshold estimation

The CAP threshold estimation component of the software was capable of automatically tracking the hearing threshold of an animal over the course of an entire experiment. The tracking method had greater temporal and threshold resolution than the commonly-used manual "visual detection" technique, which relied on the observer manually altering the stimulus level so that the raw (unaveraged) evoked response was just visible on the screen of a CRO amid the background biological/electrical noise (Johnstone et al., 1979; Rajan et al., 1991).

Although highly effective and accurate, the visual detection technique used a subjective measure of signal-to-noise ratio: in effect, the observer altered the stimulus level until their own subjective SNR criterion was satisfied. The software's automated method replaced this visual estimate of SNR with an objective mathematical estimate, based on the correlation between successive responses, as described in detail below.

4.4.1 Automated tracking methods

Objective methods have been used previously to determine the presence or absence of numerous evoked responses, including the auditory brainstem response (Don et al., 1984; Mason, 1988), the post-auricular muscle reflex (Fraser et al., 1978; Patuzzi and O'Beirne, 1999b), and somatosensory-evoked potentials (Cullity et al., 1976; Pratt et al., 1994). The process of objectively deciding whether a response is present or absent is often referred to as "machine scoring", and may be made by a variety of methods, such as:

i) comparing successive responses, using a mathematical score such as the variance ratio (Schimmel et al., 1975; Wong and Bickford, 1980), F_{sp} score (Don et al., 1984), difference/sum ratio (Fraser et al., 1978), or correlation (described in Section 4.4.3 below; see also O'Beirne, 1998; Patuzzi and O'Beirne, 1999b; Patuzzi and Thomson, 2000), or a combination of these, such as the ratio of the correlation to the variance ratio (Cullity et al., 1976; Stevens et al., 1980);

ii) comparing the evoked response to a template (the expected response), or comparing the averaged response amplitude to a criterion level (Salt, 2004); or

iii) using some other statistical measure, such as comparing the energies of the signal in pre- and post-stimulus windows.

The "hunting" process for threshold estimation may also be achieved in a number of ways. A variation of Békésy audiometry (von Békésy, 1947) using the correlation measure was used by O'Beirne (1998) for tracking the PAMR and the CAP. In addition to ramping of the attenuation, other methods have used fixed attenuation steps, or attenuation steps that vary as a function of time. The software used an attenuation step that varied according to how different the correlation of the response was from a target correlation level. This method of altering the stimulus level is described in Section 4.4.3 below.

4.4.2 Correlation calculations

The first step in the correlation procedure was to select the region of the waveform to compare (the "correlation window"). Although the correlation value may be "diluted" by the inclusion of lower-amplitude sections of waveform on either side of the peak, this widening of the correlation window is often warranted to accommodate any latency shifts that may occur as a function of stimulus amplitude or response filtering. The sections of the CAP waveforms enclosed by the correlation windows are shown in bold

in the averaged traces of Figure 4.8. The rationale for choosing these particular correlation windows is described in Section 4.4.4 below.

In calculating the correlation value between two successive waveforms [$x_1(t)$ and $x_2(t)$], each sample in the first waveform [$x_1(i)$] was multiplied by the corresponding sample in the second waveform [$x_2(i)$]. The sum of these products across the array [$\Sigma x_1(i) \cdot x_2(i)$] was therefore a measure of the correlation between the waveforms. Because this simple correlation measure was dependent on the absolute amplitude of the waveforms (rather than the amplitude of the CAP relative to background noise), which could change with electrode resistance, the correlation was normalised by dividing by $\sqrt{(\Sigma x_1(i)^2 \cdot \Sigma x_2(i)^2)}$. This produced a correlation measure which was around zero if the waveforms were random (uncorrelated), or around one if the waveforms were nearly identical (and exactly one if they were identical), and was unaffected by amplification of the system, or attenuation of the CAP signal due to sub-optimal electrode contact.

In summary, the correlation between the waveforms $x_1(t)$ and $x_2(t)$ was given by Equation 1 below, and was most often expressed as a percentage:

$$Corr = \frac{\left(\sum_{i=0}^{n} x_1(i) \cdot x_2(i)\right)}{\sqrt{\left(\sum_{i=0}^{n} x_1(i)^2 \cdot \sum_{i=0}^{n} x_2(i)^2\right)}}, \text{ where } n = \text{number of waveform samples.} \qquad \textbf{[1]}$$

4.4.3 Threshold estimation

While a repetitive response clearly present above the noise of the recording would result in a correlation greater than zero, the choice of which correlation level to take as the indicator of response threshold was not as obvious. Assuming the absence of any artefact that would give a spurious correlation reading, any long-term average correlation level greater than zero would indicate that a response was present. However, the noise associated with the correlation measure (for example, the standard deviation of a set of successive correlation readings) was inversely proportional to the magnitude of the reading itself, in that highly correlated signals were dominated by the signal rather than the random noise. It was therefore desirable to use a more stable indicator of response presence that was still close to threshold.

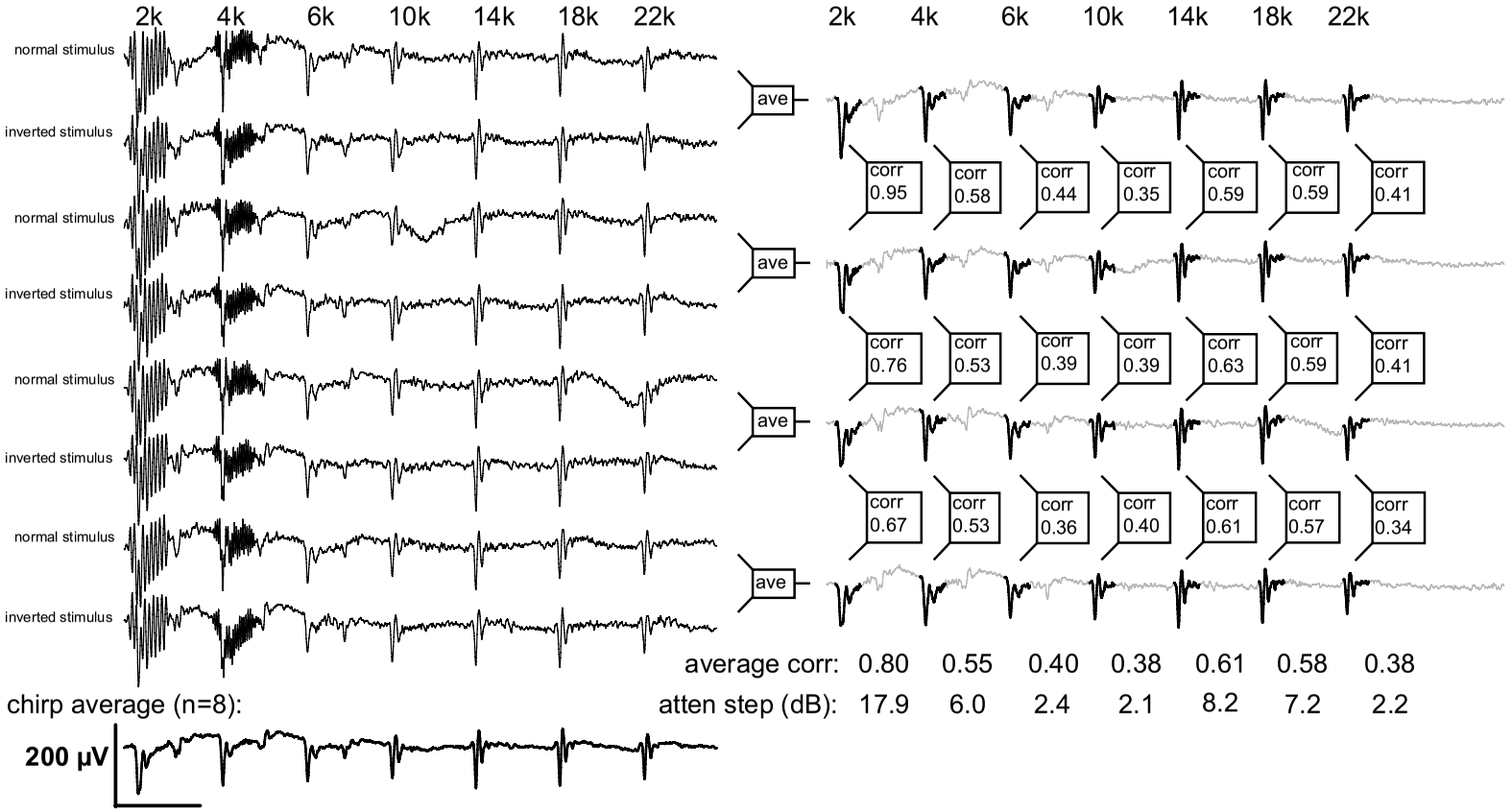

Figure 4.8: Summary of the calculation of average correlation values used in the theshold tracking process. Each pair of CAP waveform sets evoked by normal and inverted stimuli was averaged to cancel the symmetric cochlear microphonic components, resulting in four averaged (n=2) CAP waveform sets. The windowed portions of each of these averaged CAP waveforms (shown in bold) were correlated with adjacent waveforms, as shown. The average of these three correlation calculations was then used to calculate the next attenuation step for that tone-burst frequency, as defined by Equation 2 (see text). The eight raw CAP waveform sets were averaged to a single waveform which was displayed and saved to disk.

It was decided to use the tracking algorithm to adjust the stimulus attenuation to maintain an average correlation level of 25%. The 25% correlation measure provided acceptably stable threshold estimates (with standard deviations typically around 1.5 dB) that were shown by extrapolation to be around 5.5 dB higher than the stimulus level that gave a correlation of zero (as shown in Figure 4.9). Another estimate of the difference between tracked threshold and "actual" threshold was obtained from the input/output figure relating probe level (in dB above 25%-correlation-tracked threshold) to CAP amplitude (mV pp), which is shown in Figure 8.12 of Chapter 8. By extrapolation of the IO curve it was shown that the tracked threshold was 2.4 dB (± 0.9 dB) higher than the stimulus level that would have given a CAP amplitude of zero.

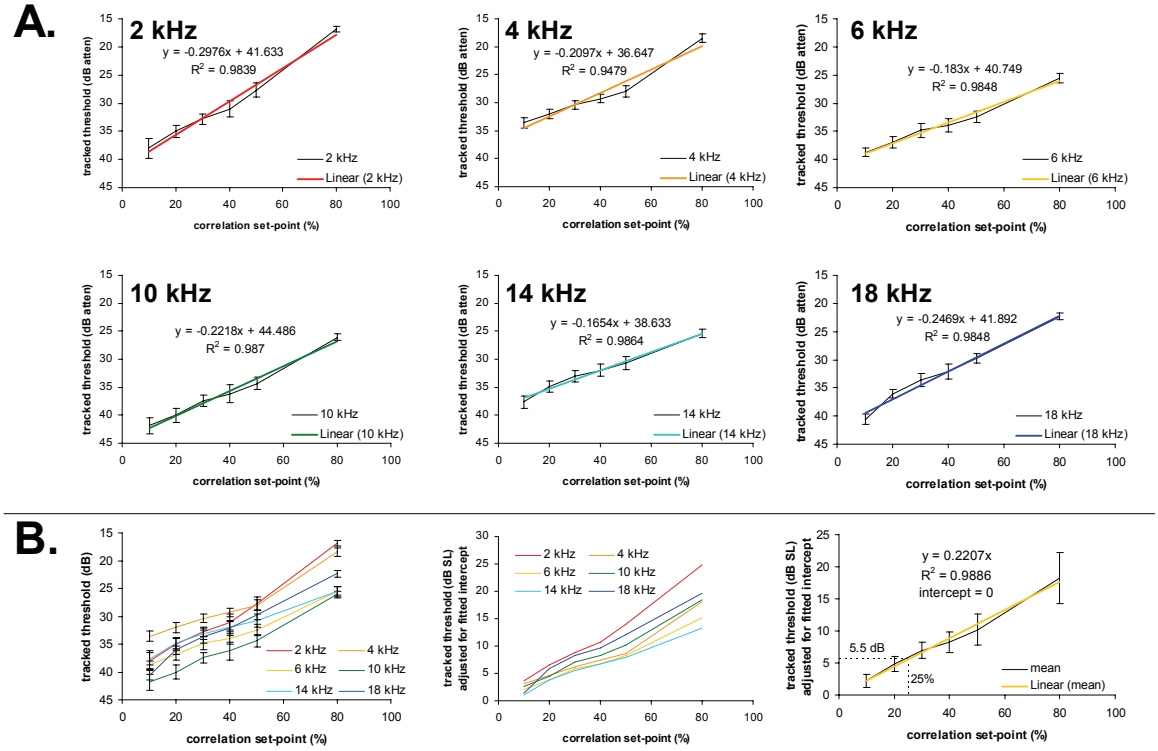

Figure 4.9: A. The mean tracked "threshold" for various frequencies decreased as correlation set-point approached zero. Representative results are presented from one animal, showing the means and standard deviations of the tracked response attenuation, and the linear regression lines describing these functions. **B.** From left to right, these three charts show i) the pooled data from each frequency in A, without regression lines, ii) the same data shifted vertically by the y-intercept of their regression lines, and iii) the mean and standard deviations of this shifted data. The data indicate that the thresholds tracked using a 25% correlation set-point were around 5.5 dB higher than the stimulus level that gave a correlation of zero, assumed (by definition) to be actual response threshold.

The rate at which the stimulus-level is ramped is generally held constant in conventional Békésy audiometry. While this enables the threshold to be estimated by averaging the excursions, rapid ramping rates can sometimes lead to subtle changes in

threshold being missed, while overly slow rates can make the system sluggish in responding to large step changes in threshold, such as those that occur with some experimental perturbations.

To counteract these problems, the software used an empirically-derived scaling procedure to change the attenuation by large steps (up to ± 30 dB) when the measured correlation was far from the target correlation, but by very small steps (a fraction of a dB) when the measured correlation was close to target. This increment was determined using Equation 2 below, and is illustrated graphically in Figure 4.10.

$$increment\ (dB\ atten)\ =\ 0.15\times(corr\text{-}target)+0.00006\times(corr\text{-}target)^3 \qquad \textbf{[2]}$$

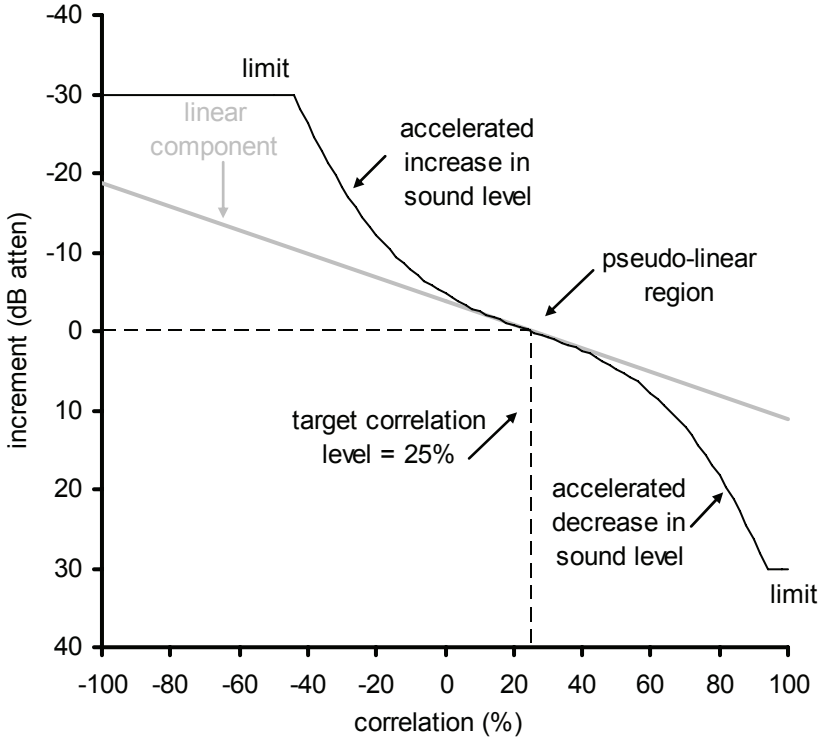

Figure 4.10: The transfer curve relating the measured correlation level, and subsequent change in stimulus level is shown in black. The linear portion of the equation that was applicable close to target correlation is shown in grey. The target correlation level in this case was 25%, and the maximum step change in attenuation was limited to ± 30 dB.

The pseudo-linear region of the curve helped ensure low-noise tracking of stable thresholds, while the cubic portion of the curve enabled more responsive change to large threshold shifts.

Although the maximum attenuation increment was limited to 30 dB, in practice it was closer to 5 dB, as this was the increment provided by Equation 2 for a correlation of zero. This was not optimal, as it could obscure the time-course of the onset of large

hearing losses. In future versions of the software, the response of the threshold tracker could be improved by increasing the slope of the tracking function in the region between the target correlation level and zero correlation.

4.4.4 Measures to increase threshold-tracking stability

The accuracy and stability of the threshold-tracking procedure was improved by measures that increased the SNR of the signal being tracked, because any reduction in asynchronous background noise would make changes in the signal more conspicuous (for example, a reduction in CAP amplitude as stimulus level approached neural threshold). Several techniques were used to increase the SNR, and therefore the stability of the threshold-tracking process. These included:

Pre-averaging of waveforms: When alternating stimuli were used, pairs of waveforms evoked using normal and inverted stimuli had to be averaged prior to correlation, so as not to cause a negative correlation reading from the inverting CM at low frequencies. This pre-averaging also had the effect of improving the signal-to-noise ratio of the waveform sent to the correlator by a factor of $\sqrt{2}$, or 3 dB, thereby improving the tracking stability.

Choice of correlation window: The portion of each waveform used in correlation calculations (the correlation window) was, in most experiments, the 5 ms period beginning 1 ms after the onset of the stimulus. The 1 ms offset was used to avoid tracking the onset of the SP rather than the CAP. However, while a 5 ms window length was suitable for most situations, it did result in tracking of the SP-offset during perturbations which diminished the CAP but which left the SP relatively unaffected, such as during perfusions of high concentrations of potassium or replacement of sodium with choline (Chapter 8). This problem was reduced in later experiments by shortening the window to 3 ms to exclude the SP-offset at the end of the tone-burst.

Removal of DC offset: The correlation method is vulnerable to DC offsets, which increase the degree of similarity between two waveforms. Because the software was designed to track neural threshold as indicated by the CAP, it was necessary to remove the influence of the DC summating potential. Two methods were used to reduce the DC offset of the waveforms: either i) the waveforms were high-pass filtered at 300 Hz using a fourth-order Butterworth filter prior to being sent to the correlator, or ii) any DC offset present in the waveform was calculated and subtracted prior to being sent to the correlator. The “Remove DC Offset” option was used in preference to the “300 Hz HPF” option, because the filter introduced a phase-roll that moved the rising

edge of any large SP inside the correlation window, thereby producing a spurious correlation.

Post-averaging of correlation values: When alternating stimuli were being used, the correlation value used to determine the step-change in attenuation level was the average correlations of four successive alternated waveforms (that is, the average of the correlations between alternated waveforms 1&2, 2&3, and 3&4), as shown in Figure 4.8. When non-alternating stimuli were used, the average correlation of eight successive non-alternated waveforms was used (that is, between non-alternated waveforms 1&2, 2&3, 3&4, 4&5, 5&6, 6&7, and 7&8).

4.4.5 Front panel "audiogram" interface

The two audiogram tabs, shown in Figure 4.11, provided both a visual display of the most-recent tracked threshold, and the means of setting the level of fixed stimuli when tracking was not used.

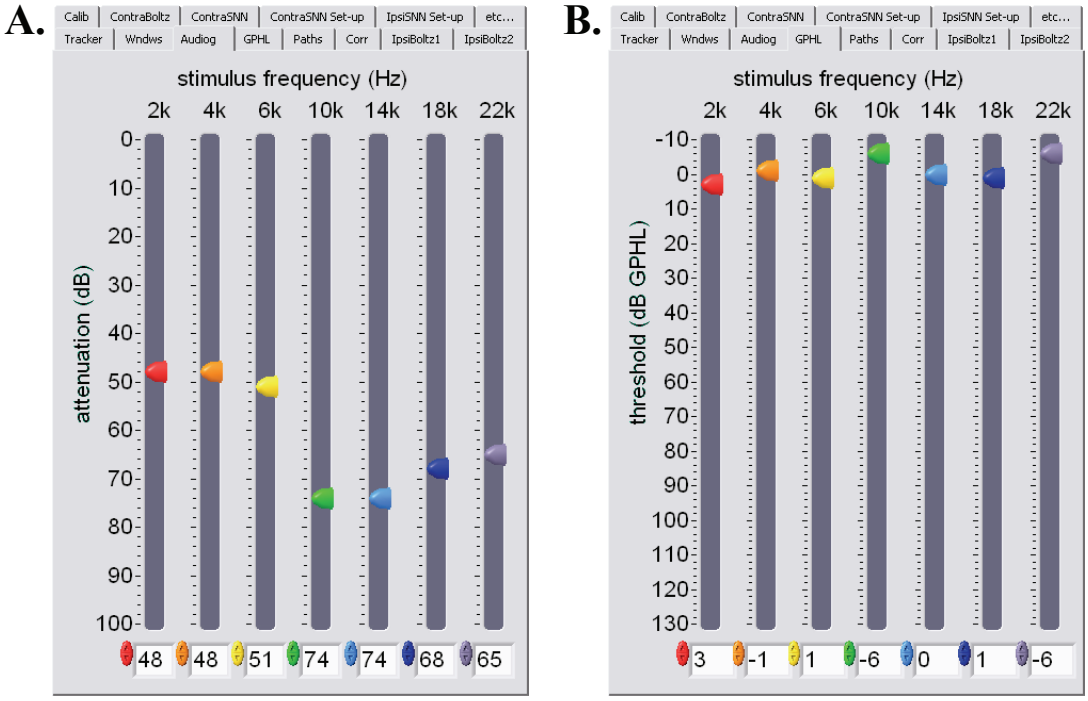

Figure 4.11: A. Stimulus levels were displayed either as attenuations relative to maximal stimulus level (0 dB attenuation), or **B.** the same levels could be expressed as standardised guinea pig hearing levels (GPHL), calculated from the ten guinea pigs with the best overall thresholds measured with that particular experimental setup (see text). Frequency colour-coding is the same as for the audiometric time-course charts.

When in threshold-tracking mode (set using the "CAP Track" button in the centre of the front panel), the audiogram displays were updated automatically between each chirp. When in fixed-stimulus mode, the sliders and numerical controls could be used to set the levels of each of the tone-bursts.

The audiogram displays on the two tabs had different references. The "Audiog" tab, shown in Figure 4.11A, displayed stimulus levels as attenuations relative to maximal stimulus level (0 dB attenuation).

Shown in Figure 4.11B is the "GPHL" tab, which expressed the same thresholds using a normalised reference: The tracked thresholds of the ten guinea pigs that had the best overall hearing levels were averaged at each frequency and were used to derive a correction factor to convert these tracked attenuation levels into "guinea pig hearing level" (dB GPHL), akin to the "hearing level" (dB HL) used in human audiometry. This reference scale simplified comparison of hearing levels between guinea pigs and allowed quicker assessment of the state of an animal during an experiment.

On the setup used for the majority of these recordings, GPHL thresholds were derived by subtracting the attenuation level (dB atten) from reference levels shown in Table 4.1 below.

Frequency (Hz)	**2 kHz**	**4 kHz**	**6 kHz**	**10 kHz**	**14 kHz**	**18 kHz**	**22 kHz**
Correction factor (dB)	51	47	52	68	74	69	59

Table 4.1: Reference attenuation levels for calculating tracked thresholds in GPHL.

The means and standard deviations of initial GPHL thresholds of 62 animals recorded on the standard setup are shown in Table 4.2 below.

Frequency (Hz)	**2 kHz**	**4 kHz**	**6 kHz**	**10 kHz**	**14 kHz**	**18 kHz**	**22 kHz**
Threshold (dB GPHL)	10 ± 9	9 ± 7	9 ± 7	8 ± 9	11 ± 10	10 ± 11	15 ± 17

Table 4.2: Average initial tracked thresholds of 62 animals in GPHL.

As mentioned above, the audiogram displays could be used to set the attenuations of the stimuli at each frequency when tracking was disengaged. Desired values were either entered in the boxes at the base of each scale, or were set by moving the relevant sliders. To present stimuli at a set level above the tracked threshold of the animal, the "Master Atten" slider was used. This was an attenuation placed in series with the audiogram

attenuators, so that that if the Master Attenuation was set to -20 dB, a stimulus shown as a 50 dB atten level would be presented at the higher level of 30 dB atten. This higher level was not displayed on the audiogram trace, but *was* shown on the time-course displays described in Section 4.4.7 below, and was saved to file.

4.4.6 CAP trace display

The chirp-average CAP trace was displayed in the centre of the front panel, as shown in Figure 4.12 below.

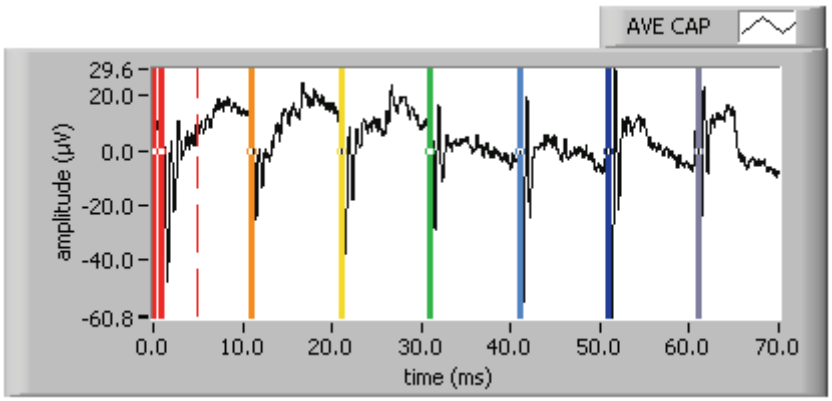

Figure 4.12: Average CAP waveforms elicited by alternating tone-bursts 20 dB above tracked threshold. From left to right, the tone-burst frequencies were 2 kHz, 4 kHz, 6 kHz, 10 kHz, 14 kHz, 18 kHz, and 22 kHz. Thick coloured bars mark onset of correlation windows. Thin dashed bar indicates correlation window width. Frequency colour-coding is the same as for CAP thresholds or amplitudes on time-course charts, and the audiogram display.

In addition to the averaged trace, a single raw trace from each chirp was visible on the "Wndws" tab, allowing the user to check for electrical artefact, or examine the waveform without cancellation of the CM by alternating stimuli. Although useful, this feature was seldom used in our experimental setup, because the raw trace from the RW was always visible on a nearby CRO. It was, however, used whenever calibration of soundcard input voltages was performed (see Section 4.10.1 below).

4.4.7 Time-course displays

Displayed in the bank of tabs at the centre of the panel were the time-courses for the tracked thresholds (expressed as either dB attenuation or dB GPHL), the amplitudes of the CAPs, the correlation values, and the EP. Shown in Figure 4.13 is a set of three of these time traces recorded during a transient hypoxia. This data was saved to file, as described in Section 4.9 below.

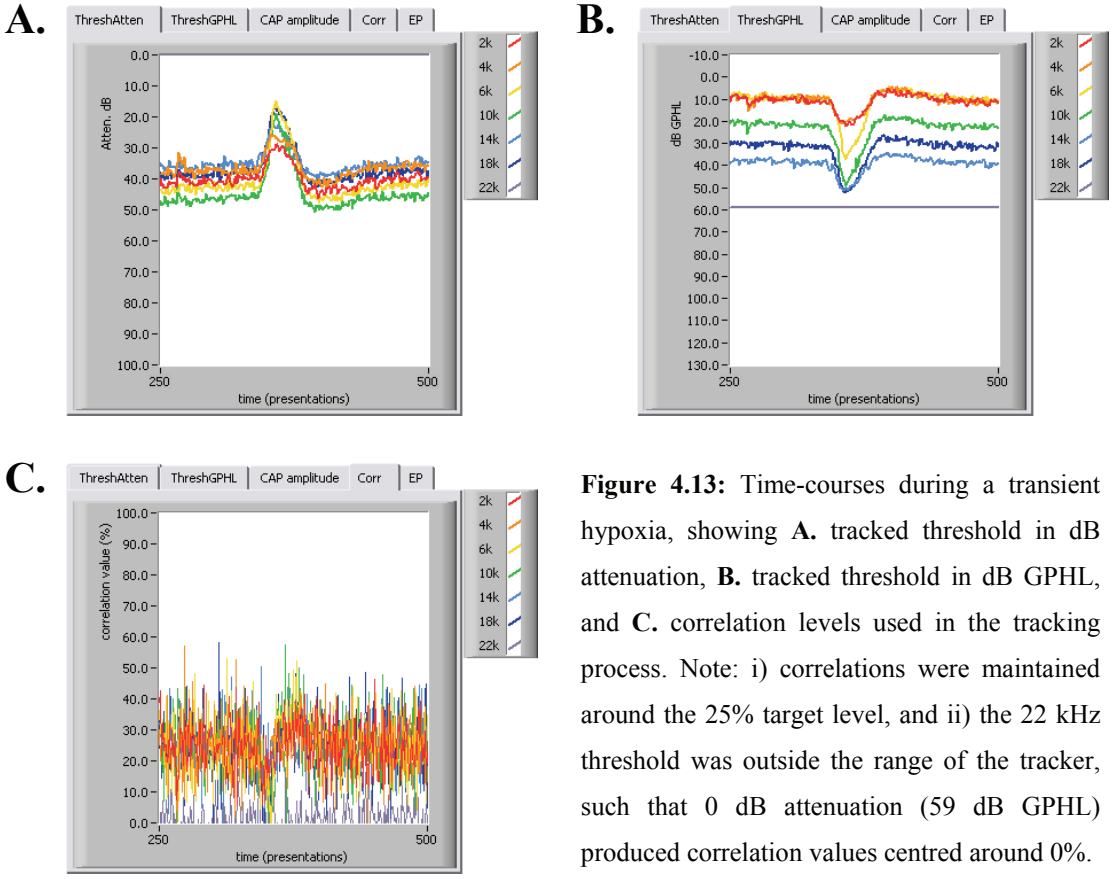

Figure 4.13: Time-courses during a transient hypoxia, showing **A.** tracked threshold in dB attenuation, **B.** tracked threshold in dB GPHL, and **C.** correlation levels used in the tracking process. Note: i) correlations were maintained around the 25% target level, and ii) the 22 kHz threshold was outside the range of the tracker, such that 0 dB attenuation (59 dB GPHL) produced correlation values centred around 0%.

4.5 Boltzmann analysis of CM waveforms – "The Boltzmatron"

The software was used to carry out Boltzmann analysis of CM waveforms, which could be measured simultaneously using probes of two different levels or frequencies, or recorded from two different locations within the same cochlea, or from opposite sides of the head. The theory behind Boltzmann analysis is described in Chapters 1 and 3.

4.5.1 Development of the Boltzmatron

Patuzzi and Rajan (1990) and Da Cruz (1993) used offline spreadsheet mathematics to derive Boltzmann parameters using a least-squares algorithm to fit the synthesised CM to the recorded CM data. This offline method was extremely time-consuming, and could not be performed fast enough to be of use during the course of an experiment. In response to this, a rapid, automated method of Boltzmann analysis was developed by Patuzzi (1995; Patuzzi and Moleirinho, 1998) using custom-built electronic circuitry. This circuitry, nicknamed the "Boltzmatron", carried out a form of adaptive signal processing – using negative feedback to minimise the error between a synthesised distorted waveform and the real CM waveform in an iterative manner. The parameters used to generate the synthesised waveform were then assumed to describe the real CM waveform. This analogue Boltzmatron allowed real-time monitoring of

mechanoelectrical transduction during an experiment (usually with a CM evoked by a continuous 200 Hz tone), and generated valuable insights into the changes in cochlear micromechanics during a range of experimental perturbations (for example, Moleirinho, 1993; Halliday, 1994; Marcon, 1995; Kirk et al., 1997).

By 1998, personal computers had become fast enough to enable the development of an online method of Boltzmann analysis using virtual instrument software to replace the analogue circuitry. The virtual instrument Boltzmatron (described in Patuzzi and O'Beirne, 1999a) used a nonlinear Levenberg-Marquardt (Lev-Mar) algorithm (Levenberg, 1944; Marquardt, 1963) to obtain a least-squares fit of the synthesised CM to the CM data recorded using a Lab-PC+ DAQ card (National Instruments Corp., TX, USA). This technique was extremely rapid, taking under a second to acquire and analyse a sample of CM data. Similar least-squares methods have been used by other authors to obtain real-time estimates of Boltzmann parameters (for example, Sirjani et al., 2004).

4.5.2 Incorporation of the Boltzmatron into the software

The modular nature of the LabVIEW development environment made it a relatively simple task to incorporate the analysis (non-linear curve-fitting) section of the Boltzmatron VI into the software, with some additional modifications to further quicken and improve the fitting process.

These modifications included a reduction in the number of free parameters, and the addition of some numerical constraints: Because the frequency of stimulus used to evoke the CM was controlled by the software, it was reasonable to fix the CM frequency parameter to that of the stimulus. CM phase was left as a free parameter. V_{off} was constrained to be a negative number, and V_{sat} and ZP were constrained to be positive and negative, respectively, as it was possible for the VI to invert these two, as the same resulting synthesised CM waveform was produced as long as they were of opposite sign to one another. To increase the speed of the fit, the waveform was down-sampled from 44.1 kHz to 11.025 kHz. This did not affect the accuracy of the fit, because the CM waveform was low-pass filtered at 5 kHz during recording, and the signals of interest were well below the 5.5 kHz Nyquist frequency for that sampling rate. A probe frequency of 207 Hz was used in order to reduce the possibility of any artefacts caused by mains interference (the harmonics of which occur at multiples of 50 Hz in Australia).

4.5.3 First-guess parameters

The non-linear Lev-Mar numerical methods used by the Boltzmatron were an iterative process, which could be sped up considerably by the provision of so-called "first-guesses" for the parameters to be fitted. The first-guess parameters were set on the "IpsiBoltz1" and "IpsiBoltz2" tabs on the front panel. They could be entered manually, or the experimenter could copy the current "best fits" to the "first guesses" by pressing a small button located underneath the first-guess parameters on each of these tabs.

4.5.4 Fitting to short-duration 50 ms tone-bursts versus continuous tones

The presence of the intense and continuous 200 Hz tone used to evoke the CM for Boltzmann analysis has been found to cause a slow scala tympani operating point shift, referred to as "probe-tone adaptation" (see Chapter 6, and Marcon, 1995; Patuzzi and Moleirinho, 1998).

In the present study, it was desirable to avoid this adaptation in order to differentiate the effects of experimental perturbations from those of the measurement process itself. To do this, the probe was presented for the minimum amount of time that still allowed accurate determination of the Boltzmann parameters. As shown in Figure 4.4, two tone-bursts of 50 ms each were presented eight times per chirp. Over the course of a standard 10-chirp trial, the Boltzmann probes were therefore present for under 15% of the time, compared to 100% for a continuous tone.

The signal-to-noise ratio of the CM was improved by around 9 dB by sending the chirp average (n = 8) CM to the Boltzmatron instead of the raw CM. The synthesised waveform was fitted to a 13.6 ms waveform segment (just under three cycles of the 207 Hz CM). To prevent any interference from onset transients, the three cycles commencing at 24.57 ms after the start of the stimulus were used, as shown in Figure 4.14.

4.5.5 Boltzmatron display

The data from the Boltzmann analysis was updated to the front panel after each chirp, and was also saved to disk. On the right of the front panel were two columns of charts displaying the Boltzmann parameters, Vsat, Eo, and ZP (which was divided by pressure to give the actual Z). The onscreen time-traces allowed the user to judge when the effects of a perturbation had subsided.

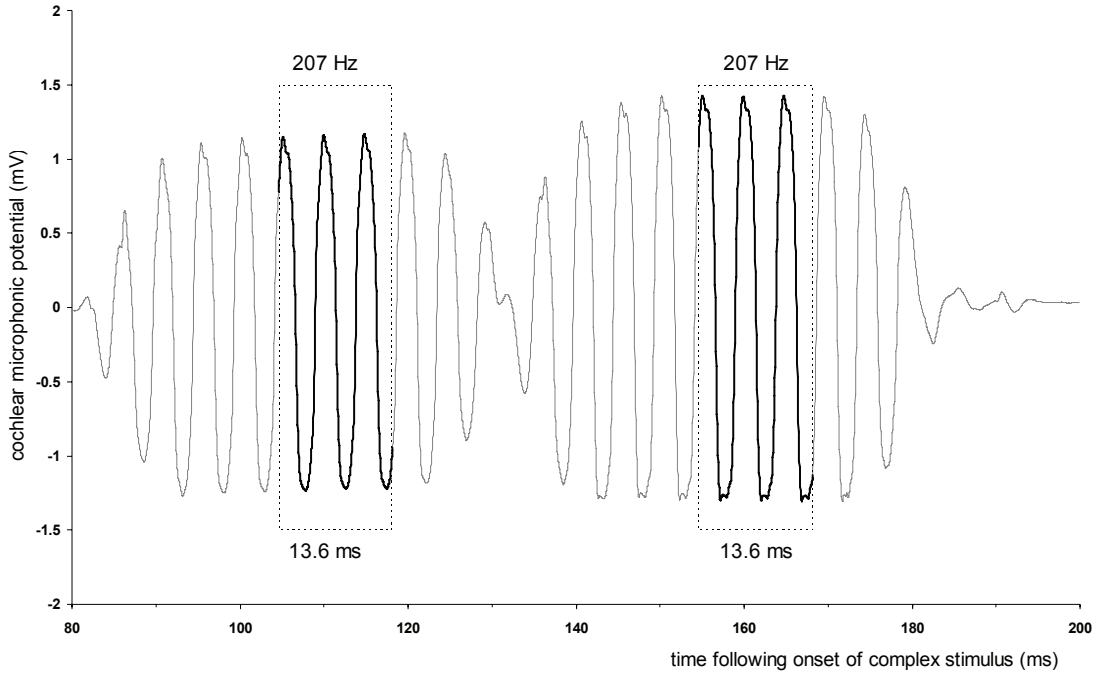

Figure 4.14: The sections of the averaged 207 Hz CM waveforms chosen for analysis were the 13.6 ms sections commencing 24.57 ms after the onset of the tone, as indicated here.

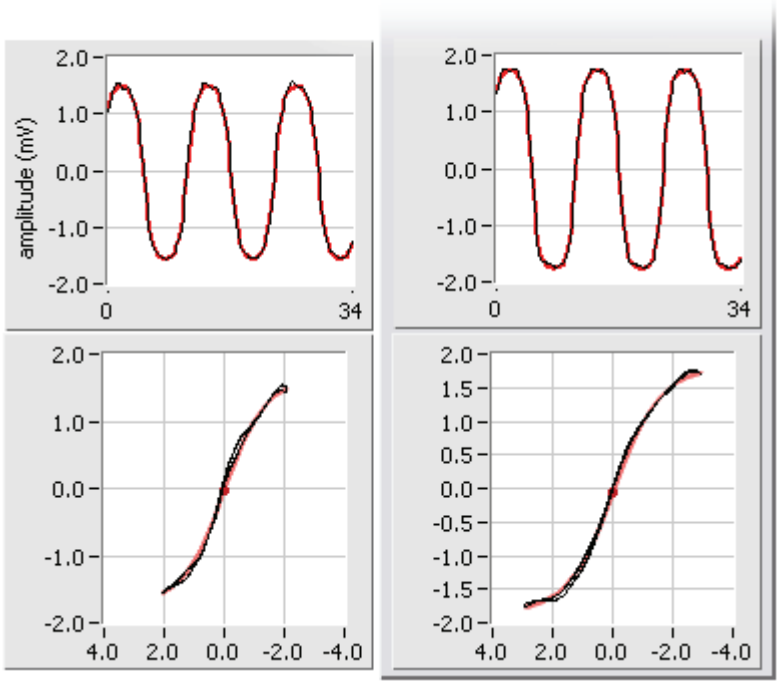

Figure 4.15: Actual (black) and fitted (red) CM waveforms and Lissajous figures were displayed on the front panel. The red dot on the Lissajous figures represents the operating point on the OHC transfer curve. The vertical axis of all four plots was potential (mV), while the horizontal axis was time (ms) for the waveform traces, and instantaneous ear-canal sound pressure (Pa) for the Lissajous transfer curves. In this example, the CMs were evoked by 50 ms 207 Hz tone-bursts at 97 dB SPL on the left trace, and 100 dB SPL on the right trace. The error of the Boltzmann fits to these curves was 65 µV RMS and 57 µV RMS respectively.

Beneath these were the actual (black) and fitted (red) CM waveforms, and the actual and fitted CM Lissajous figures (also black and red, respectively). These allowed a direct visual estimate of the "goodness of fit", which could be confirmed by the mean squared error between the actual and fitted data that was also saved to disk.

4.5.6 Boltzmann probe-level modulo function

The attenuation level of the second Boltzmann probe could be varied cyclically to examine the effects of stimulus level on the measured parameters. When the "modulo" feature was selected, the stimulus attenuation was altered in 1 dB steps with each chirp to a maximum of ±3 dB around the selected attenuation level. For example, with a selected attenuation level of 15 dB, the attenuation levels over seven chirps would be 12 dB, 13 dB, 14 dB, 15 dB, 16 dB, 17 dB, and 18 dB, before returning to 12 dB with the next chirp. The modulo function was also available for the frequency of Boltzmann probe, but these features were not used during the current project. A similar procedure was implemented for the construction of DPOAE input/output functions, described in Section 4.7 below.

4.6 Measurement of Neural Noise

The spectrum of neural noise was calculated by applying a Fast Fourier Transform (FFT) algorithm to a 318 ms period of round-window electrical activity. The RW signals were sampled at a rate of 11025 Hz, resulting in a spectrum with frequency resolution of 3.14 Hz. A Blackman-Harris window function was used in calculating the FFT to minimise "spectral splatter" or "leakage distortion" (caused by the abrupt truncation of the signal to a finite length; Norton, 1989). This sampling was repeated usually four or eight times, and the resulting spectra were averaged, displayed (see Figure 4.16A), and saved to a file for later analysis. While the most recent spectrum was plotted in red, the spectrum calculated during the previous SNN measurement was displayed in the background of the chart in grey for comparison. The mean amplitude of the spectrum (in units of μV RMS) was calculated between 700 and 1100 Hz, and displayed on a chart on the front panel, shown in Figure 4.16B.

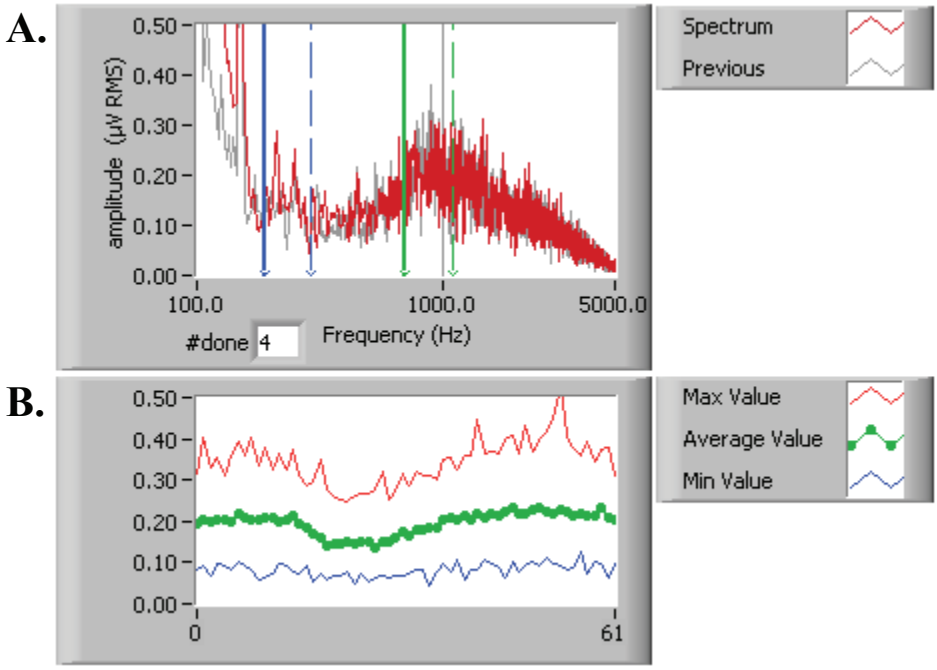

Figure 4.16: A. The average (n=4) SNN recorded from the round window, plotted with a logarithmic frequency axis. The most recent spectrum is plotted in red, with the previous measurement plotted behind in grey for comparison. Sections of the spectrum may be selected for monitoring over time – on most occasions, the region monitored was between 700 and 1100 Hz, marked by the green vertical bars. The resulting time-course is shown in **B.** Shown are the maximum (red), average (green), and minimum (blue) values of the spectrum in 700-1110 Hz region. The data presented in this figure are from a 56 minute period, during which time there was 10 min perfusion of 8 mM Na^+ choline artificial perilymph (GP#113 – ID#3144124228).

The facility was included to allow "smoothing" of the SNN display. When activated, a running average of the spectrum was calculated (using an odd number of points, usually 11, to avoid skewing the spectral data). This smoothing was for display purposes only, and did not affect the data saved to file.

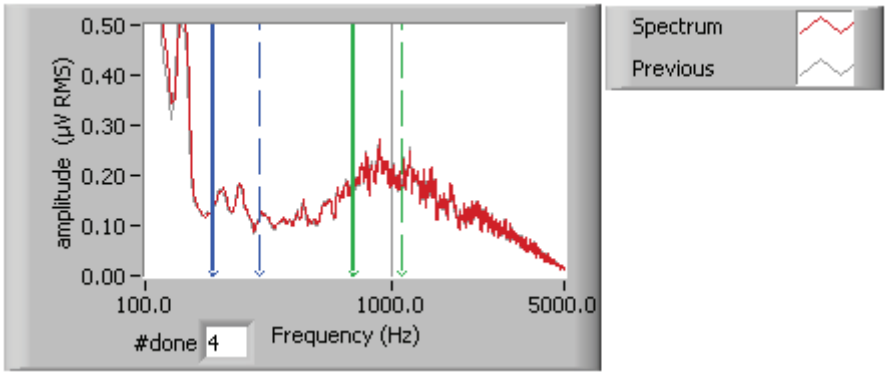

Figure 4.17: The same SNN data from Figure 4.16, but with the "smoothing" option selected, in which an 11-point running average of the spectrum data was performed.

4.6.1 Stimulus generation for "driven" neural noise measurements

The spectrum of the neural noise may be enhanced or suppressed by the simultaneous presentation of pure-tones or noises of various bandwidths and centre-frequencies (Cazals and Huang, 1996). The ability to study such modulation was included in the software and, although it did not form part of this project, it was used successfully in other studies, reported elsewhere (Brown, 2002; McMahon, 2004).

When this feature was used, customised noise-bursts of 1000 ms duration (50 ms rise/fall times) were played during each SNN measurement. To avoid creating a synchronous microphonic that would appear in the averaged spectrum, the 1000 ms samples were randomly-selected subsets of a larger noise file: Looped raw noise files of around 5 seconds duration were synthesised[4] externally using a program such as Sound Forge 6.0 (Sonic Foundry Inc.), and cross-faded in such a way that they could be played in a loop without incurring a "click" when the loop restarted. With each presentation, the raw noise loop was rotated by a random interval, and a one second segment of the loop was extracted, modified to have a 50 ms rise/fall time, attenuated, and played. In this way, the one-second noise sample played to the cochlea during the driven SNN measurements was different with each presentation.

4.7 Measurement of DPOAEs

Distortion-product otoacoustic emissions were elicited by simultaneously-presented pairs of 50 ms tone-bursts (with 5 ms rise-fall times), delivered via separate channels of the stereo soundcard output to a pair of acoustically-coupled Beyer Dynamic DT48 phones. These tone-bursts were presented in sets of 32, followed by a trigger pulse that was used to establish the timing of the data acquisition. An f_2/f_1 ratio of 1.2 was normally used (Harris et al., 1989; Gaskill and Brown, 1990), but this could be varied by the user.

The ear canal sound pressure and/or the scala media cochlear microphonic were monitored and sampled at a rate of 44.1 kHz. The recordings from the 32 tone-bursts were then synchronously averaged, which lowered the noise-floor of the recordings by around 15 dB. The FFT of a 1000-sample (22.7 ms) excerpt of this averaged response waveform was then calculated using a Blackman-Harris window, which gave a frequency resolution of 44.1 Hz. Frequency and phase information from the FFT were

[4] Examples of the noises synthesised include third-octave bandwidth noise with centre frequencies of between 500 Hz and 16 kHz, white noise, and noise high-pass filtered at 4 kHz, 8 kHz, and 12 kHz.

then saved to a file. The DPOAE measurement system was displayed in three main panels, shown in Figure 4.18.

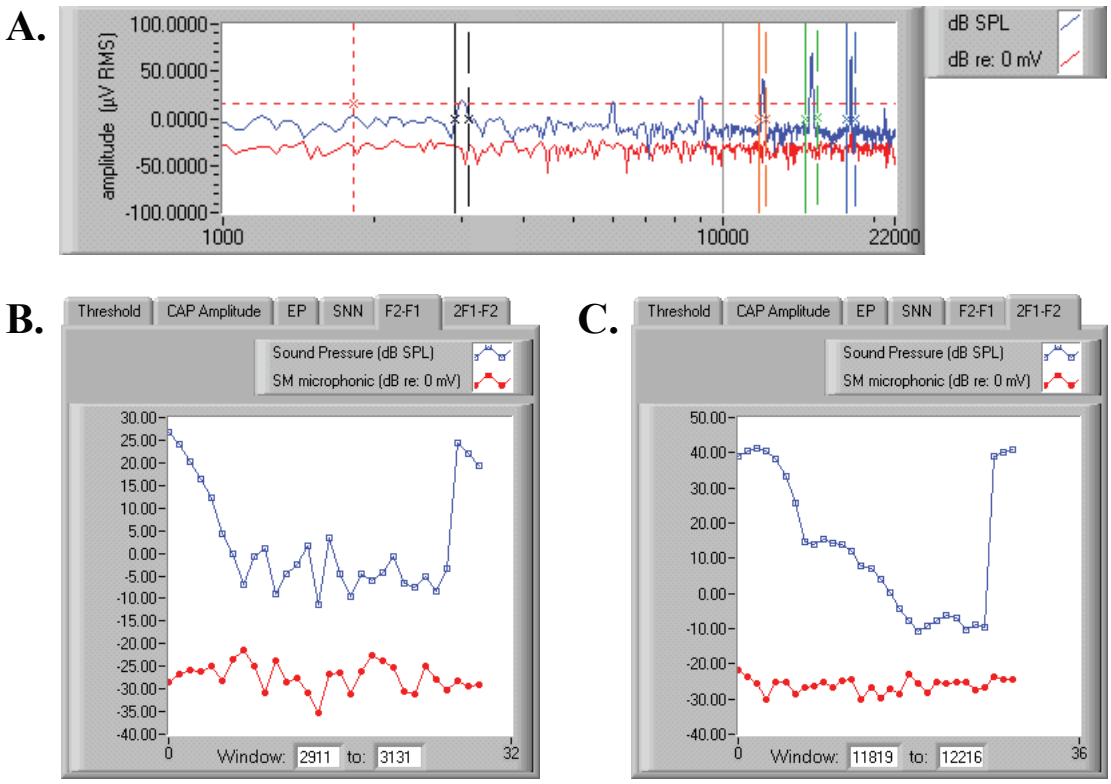

Figure 4.18: A. The spectrum of the sound pressure recorded from the ear canal (blue) and the scala media cochlear microphonic (red). The primaries used in this example were f_1 = 15 kHz and f_2 = 18 kHz. The vertical bars indicate the measurement windows set by the software around each primary frequency, and around the f_2-f_1 and $2f_1$-f_2 frequencies (3 kHz and 12 kHz respectively). The f_2-f_1 and $2f_1$-f_2 peak amplitudes are displayed as time-traces in **B.** and **C.** This particular time-trace shows a DPOAE input/output function. Again, ear-canal sound pressure is shown in blue and the scala media CM is shown in red. The sequence is shown to start again after the first 26 data points.

4.8 Measurement of DC voltages

The software used the Lab-PC+ card to monitor the EP, which was displayed on an indicator and time-trace on the front panel, and saved to disk after every chirp. Because the EP was measured relative to the scala tympani potential, the signal from the custom-built DC-amplifier was converted to scala media mV by dividing by the amount of gain, and subtracting the scala tympani offset voltage.

A second DC voltage was recorded from the channel of the Lab-PC+ card used to control the DC current injection box, described in Chapter 7. This allowed the timing and intensity of current applications to be recorded alongside the Boltzmatron and CAP threshold data, and saved to disk, as described below.

4.9 File saving

Data was saved in tab-delimited text files, which allowed analysis in most spreadsheet applications. Different measurement types were saved in separate files for logistical reasons. For example, time-course data generated with each chirp was saved in one file, while the SNN data and CAP waveforms averaged over a trial were saved in other files. The suffix `.aer` was used to denote the files as auditory evoked responses.

The base folder in which the data was to be saved was set in the Paths tab, and was confirmed each time the VI was started. The user had the option of saving each set of acquired data with a unique 10-digit identification (ID) prefix[5]. This removed the requirement to manually enter filenames, and, since the ID number represented the number of seconds that had elapsed since 12:00 am, 1st Jan 1904 (UTC), it also allowed the timestamp of acquisitions to be established accurately, which was useful when appending sequential files to one another. The ID number was displayed on the front panel for note-taking during experiments.

4.10 Calibration procedures

4.10.1 Calibration of input voltages

The input calibration settings were accessible via the "inputs" sub-tab of the main "Calib" tab, shown in Figure 4.19A below. When a voltage is sampled by a soundcard with 16-bit resolution, the voltage is expressed as one of 2^{16}, or 65536 levels. Calibrating the soundcard input involved calculating the conversion from the soundcard representation (a signed integer from -32768 to +32768) into the original source voltage, usually by comparing soundcard measurements with CRO or multimeter measurements. A further calibration step also took into account any additional amplification in the signal path.

After disengaging the previous calibration conversion factors (by deselecting the "Use calibrated input units?" button), the peak-to-peak amplitude of an externally-generated 1 kHz sine wave was measured both on a CRO and on the raw CAP trace in the "Wndws" tab. Both these values and the additional gain were entered as shown in Figure 4.19A, with provision for separate values and gains for signals from the contralateral cochlea, when applicable. In the example shown in Figure 4.19A, a 102 mV pp 1 kHz tone at the input to the soundcard was equivalent to 2091 amplitude units pp (around 3.2% of the input range). Assuming that the 102 mV pp signal had

[5] For example, 3182267580_Boltz.aer for the Boltzmatron, CAP threshold and amplitude data, 3182267580_Combined.aer for the CAP waveforms, and 3182267580_Spec.aer for the SNN.

already been amplified by 50 dB, the resulting calibration factor was: 1 amplitude unit = 0.154 µV at the round window.

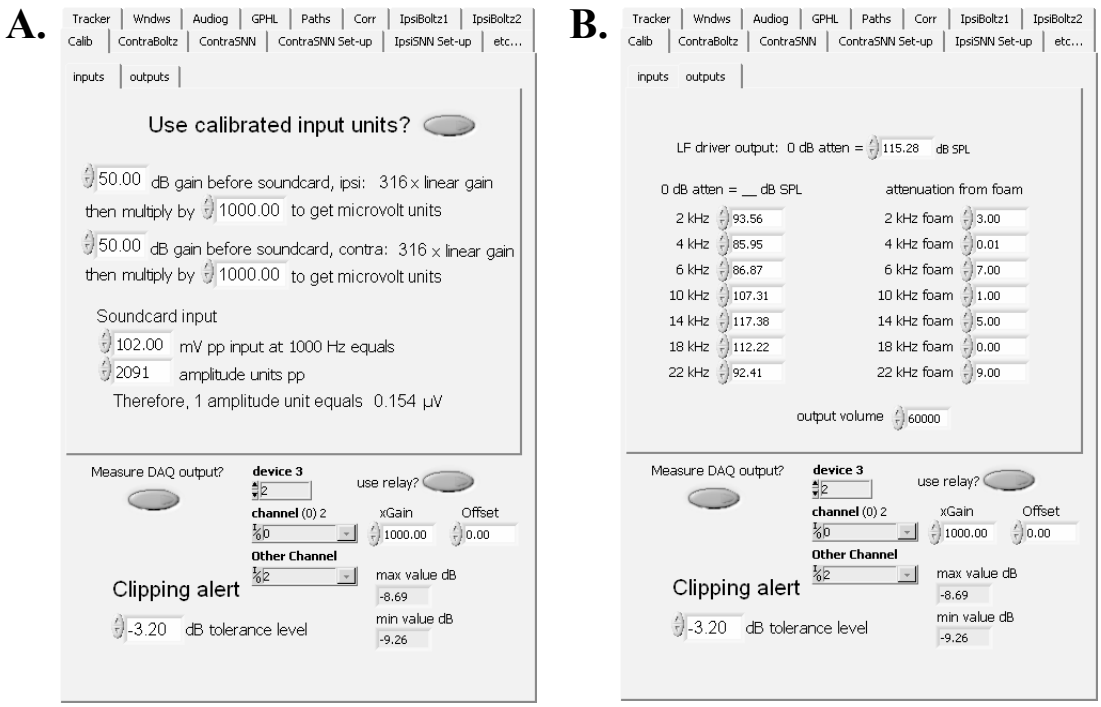

Figure 4.19: In addition to the settings for the DAQ inputs and soundcard clipping notification (see text), the calibration tabs contained **A.** the controls for the calibrating the soundcard inputs, and **B.** controls for taking into account the calibration of the output sound pressure levels.

4.10.2 Calibration of output sound levels

The calibration settings for the output sound levels were accessible via the "outputs" sub-tab of the main "Calib" tab, shown in Figure 4.19B. Unlike the "inputs" tab, the "outputs" tab was not actually used to derive the correction factors – rather, the calibration corrections derived elsewhere were entered here and were used to convert ZP to Z (for the low-frequency driver calibration).

Additional provision was made for the attenuation incurred by a small foam damper that was inserted in the tip of the B&K high-frequency driver. This damper was used to prevent any high-frequency hiss (produced by the high-voltage power supply for the driver) from interfering with the SNN measurements. Because the level of attenuation would change depending on how the foam was placed, new attenuations could be entered whenever the foam was moved or replaced. The output level of the soundcard was also set here, in order to override the settings of the Windows taskbar volume-control.

In the main “Calib” tab were also additional settings for adjusting the voltages measured by the Lab-PC+ DAQ card, and for notifying the user that the input signal was clipping at the soundcard. As shown in Figure 4.19 A and B, the alert was displayed whenever the input signal came within 3.2 dB of the maximal input level.

Chapter 5
Application of force to the cochlear wall: effect on auditory thresholds, OHC transduction, and DPOAEs

5. Application of force to the cochlear wall

5.1 Introduction

This chapter describes the changes in cochlear sensitivity and mechanoelectrical transduction observed during a novel cochlear perturbation: the application of force to the cochlear wall. The application of force (or "the push" as we call it) was hoped to be a practical method of creating a prolonged bias of the OHC operating point, which we have found difficult to create by other means. The aim of the experiments was to develop a method of delivering a large step-perturbation to the cochlea that would elicit some form of regulatory oscillation.

While numerous methods exist to create *transient* operating-point shifts, including low-frequency acoustic bias (see Chapter 6; also Patuzzi, 1983; Patuzzi et al., 1984a; Patuzzi et al., 1984b; Frank and Kössl, 1997; Choi et al., 2004; Salt, 2004), and hydrostatic bias (Salt and DeMott, 1998; Wit et al., 1999; Thalen et al., 2001), attempts to create a *prolonged* OHC operating point shift are largely thwarted by the numerous sources of AC-coupling in the auditory system, including the malleo-incudal slip joint of the middle-ear, the high-pass filtering of the helicotrema, movement of water across the basilar membrane, and the movement of endolymph through cochlear aqueduct, all of which act to prevent the transmission of DC stimuli to the hair cells.

Measured during the push were auditory thresholds, CAP magnitudes and waveshapes, and the Boltzmann parameters of the low-frequency CM waveforms recorded from the first turn of the guinea pig cochlea, and distortion-product otoacoustic emissions recorded from the ear canal. In any event, the cochlear oscillations evoked by the push technique were highly damped, and were usually limited to a single cycle, indicating that although the push caused a range of changes to numerous aspects of cochlear function, some of which were often unpredictable, it was not a particularly effective method of eliciting cochlear oscillations.

The data obtained using this technique provides ample evidence of just how resistant the cochlea is to DC mechanical stimuli, particularly that which does not cause a large pressure differential across the basilar membrane. The technique used to apply force to the cochlear wall is described below. More general methods, including surgical techniques, experimental equipment, software, stimulus delivery, and measurement techniques were presented in detail in Chapters Three and Four.

5.2 Methods

While the surgery and electrode placement in some of the experiments was carried out with Dr. Peter Sellick, the experiments were performed solely by the author. The results presented here were recorded during 15 applications of force in three animals.

Force was applied to the cochlear wall using a 1-mm-diameter insulated thoriated-tungsten rod advanced with a micromanipulator (Narishige Co. Ltd., Tokyo, Japan). Tungsten was chosen because of its rigidity and resistance to flexion during the push. The last three centimetres of the rod were insulated with nail varnish to prevent electrical contact between the micromanipulator and the cochlea.

In almost all cases, the rod was guided through the bulla opening and aligned with the first cochlear turn, posterior to the round window. Prior to recording, the rod was adjusted until it was just touching the wall of the cochlea. Force was applied by advancing the micromanipulator and reading the displacement from its Vernier scale. As shown in Figure 5.1, the rod was in series with a reinforced rubber block. The stiffness of this rod/rubber-block arrangement was measured to be 4.4 kNm^{-1} (± 0.24 kNm^{-1}; n = 6), so that a micromanipulator displacement of 1 mm produced a force of 452 g (± 25 g).

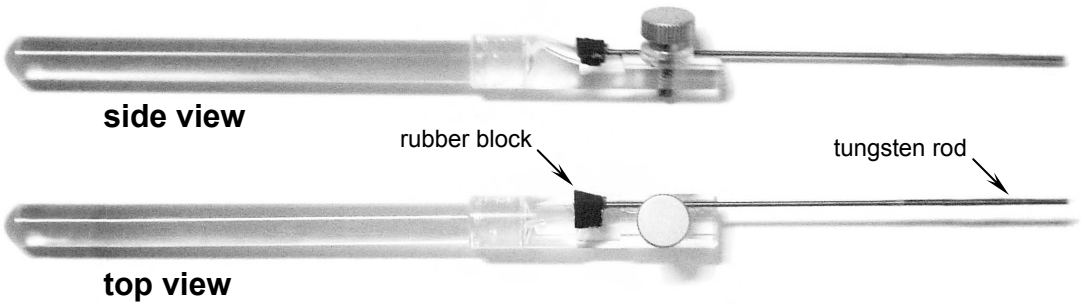

Figure 5.1: The device used to apply force to the cochlear wall.

The forces applied in these experiments were well below those required to fracture the otic capsule at the first turn. In a series of experiments with guinea pig cadavers (data not shown), the force needed to crack the wall of the cochlea at the 1st turn was found to be approximately 1600 g (± 415 g; n = 5) when using a rod of diameter 2.5 mm. As cracking of the cochlea resulted in deafness and the (premature) ending of the experiment, larger pushes were reserved for the end of any experiment so that the maximum amount of information could be obtained from each animal. Results presented here were derived from pushes of less than 320 g.

5.3 Examples of typical changes with application of force

In this section, two representative examples of the results obtained during the push are presented. In subsequent sections, further examples are shown which illustrate the range of the results produced by the perturbation.

Figure 5.2 shows a typical result for two successive applications of a 135 g force to the cochlear wall at the first turn. In this example, the two applications of force (or "pushes") took 10 s to apply or remove, and were left in place for 10 minutes and 11 minutes respectively.

Changes in OHC MET during the push were inferred from the CM. Lissajous figures were obtained by plotting the averaged instantaneous peak-to-peak potential of the CM waveform during one cycle of the 207 Hz tone against the assumed sinusoidal deflection of the OHC stereocilia, which was assumed to be phase-shifted but proportional to the ear-canal sound pressure. While the effect of the push is apparent in the changes in amplitude and slope of the Lissajous figures, the extent of the CM changes is more clearly visible in the results of the Boltzmann analysis, which revealed systematic changes in the Z and Eo parameters, but little perturbation-related changes in the V_{sat} parameter. The first push produced a stepwise 12% decrease in the Z parameter, consistent with a decrease in the overall sensitivity of the MET process. The push changed the operating point (Eo) by 11 meV in the scala vestibuli (SV) direction, moving it from a resting position of +4 meV to a peak of +15 meV. Following this initial stepwise shift, Eo returned slowly toward scala tympani (ST) with an exponential time constant (τ) of 104 seconds, reaching a new steady-state value of +11 meV within 3 minutes of the onset of the push.

In this example, distortion-product otoacoustic emissions were evoked with primary frequencies of 14.0 kHz and 16.8 kHz, at levels of 73 and 80 dB SPL respectively. The amplitude of the cubic $2f_1$-f_2 distortion product decreased by 4.2 dB within the first minute of the push, and further decreased by 0.7 dB to 4.9 dB at the end of the 10 minute application period. By contrast, the maximal decrease in the quadratic f_2-f_1 emission was only 1.2 dB at two minutes after the onset of the push, after which time the f_2-f_1 amplitude recovered to near its pre-push level.

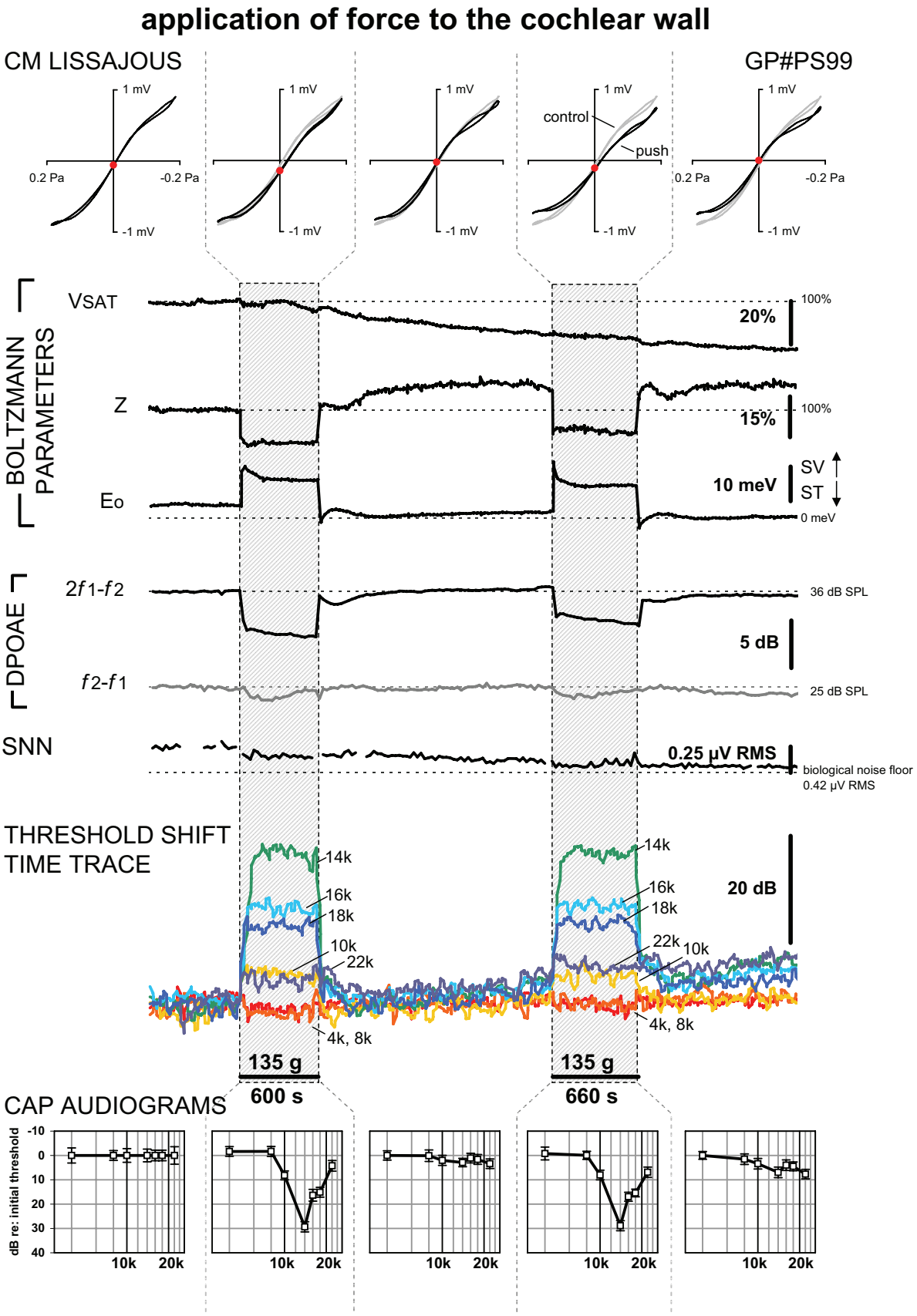

Figure 5.2: Successive applications of a 135 g force to the cochlear wall at the first turn resulted in systematic changes in i) CM Lissajous figures and corresponding Boltzmann parameters , ii) DPOAEs at $2f_1$-f_2 and f_2-f_1, iii) amplitude of the SNN between 700 and 1100 Hz, and iv) CAP threshold (shown in time series and audiogram form). The grey Lissajous figures indicate the pre-push control.
ID#3151971852. 5pt running average on threshold shift time trace.

The amplitude of the spectrum of the neural noise (SNN), measured in silence between 700 Hz and 1100 Hz, fell during the push by 13% from 0.66 ± 0.02 μV RMS to 0.57 ± 0.01 μV RMS. CAP thresholds were determined at 4, 8, 10, 14, 16, 18 and 22 kHz using the automatic threshold-tracking algorithm presented in Chapter 4. The first push produced a maximal threshold shift of 29 dB at 14 kHz, with losses of 16 dB at 16 kHz, 15 dB at 18 kHz, 8 dB at 10 kHz, and 4 dB at 22.05 kHz. The standard deviations of each of these average threshold shifts were approximately 2 dB. The effects on the CAP with applications of force were usually very rapid, as shown in the CAP amplitude data of Figure 5.3. However, in the example shown in Figure 5.2, the rate of the onset (but not the offset) of the threshold shift was limited by the maximum speed of the tracking-detection algorithm[1]. On withdrawal of the force, Eo rapidly returned toward scala tympani, undershooting the pre-push operating point. From a -1.2 meV minimum, the Eo parameter showed a post-push rebound, rising to +2.2 meV over a two minute period. A similar rebound was also observed in the Z parameter and the $2f_1$-f_2 DPOAE.

The second application of force in Figure 5.2 followed a similar pattern to the first in most parameters. The Eo parameter showed an initial step rise from 2 meV to 15 meV, followed by an exponential decay to a steady-state level of 9.5 meV. The rate of adaptation during this second force application was more rapid ($\tau = 57$ seconds) than during the first, while the phase of the Z rebound was also altered.

While the data shown in Figure 5.2 represent a result typical of those recorded during the push, responses in a number of the measures of cochlear function were by no means consistent, as illustrated by the data of Figure 5.3. Shown are the results from three consecutive 20 minute pushes, each separated by a 20 minute period during which no force was applied. The first push of 226 g caused changes that were significantly different from the two subsequent pushes of 316 g. The differences in the changes observed in the $2f_1$-f_2 and f_2-f_1 DPOAEs will be discussed in Section 5.5.1 below, while the differences in the CAP waveshapes (and peak amplitudes) will be discussed in Section 5.7.2 . The changes in the Boltzmann parameters in this example are described briefly below.

[1] Resolution of the step-wise shift in threshold following the push is likely to have been limited by the speed of the tracking algorithm used. The tracking method used at the time of these recordings effectively resulted in a maximum 4.7 dB increase in attenuation step following each measurement. In addition, the time interval between each set of three CAP measurements when using the DPOAE protocol was 24 seconds. In contrast to the increase, the decrease in attenuation was limited to 30 dB, resulting in the sharper steps in threshold at the offset of the push in Figure 5.2.

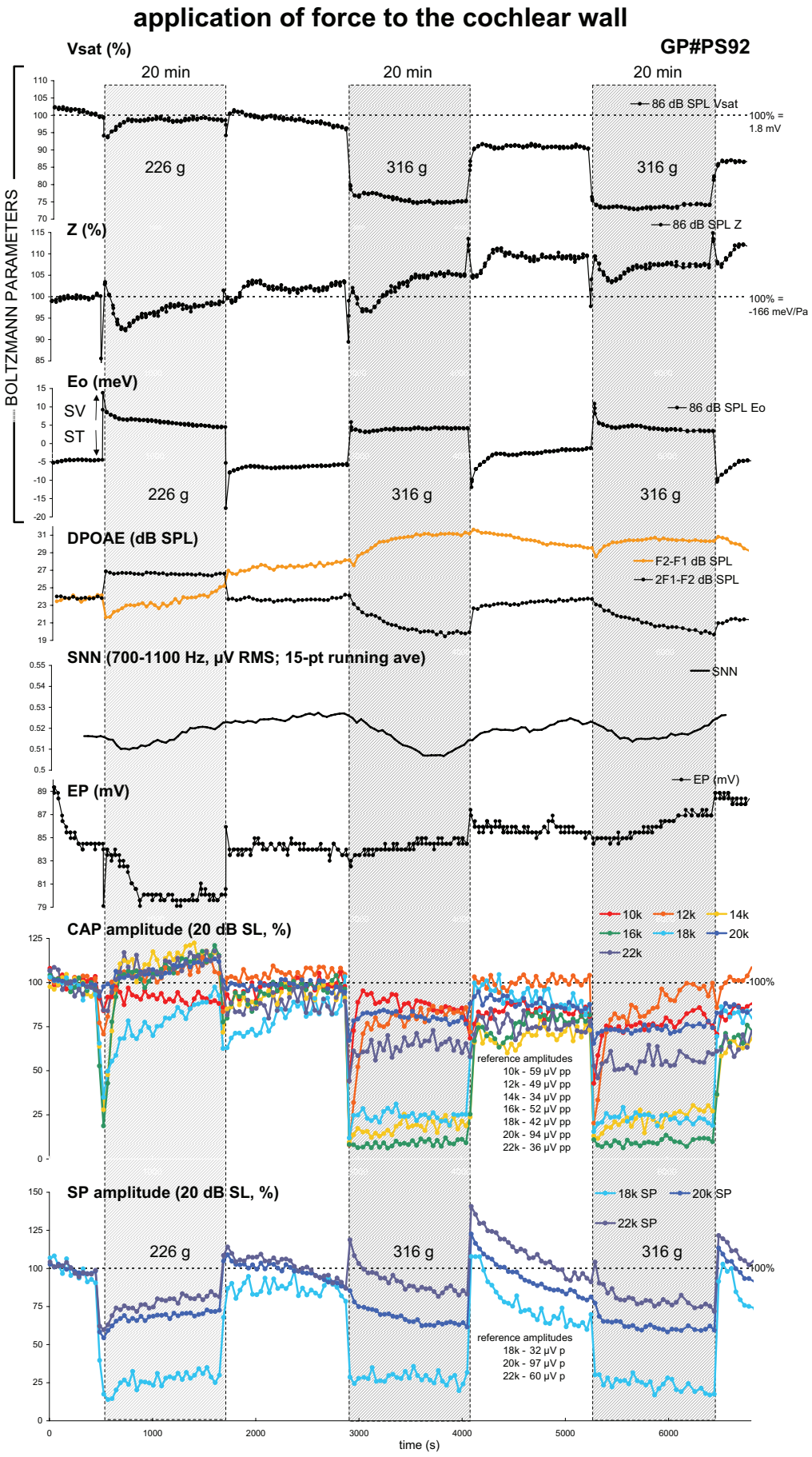

Figure 5.3: The complete data set for three consecutive 20 minute pushes of 226 g, 316 g and 316 g. The data give an indication of the variability of the changes in cochlear function observed with the push within the one animal (see text).

ID#3150166434

The first push of 226 g caused a step-decrease in Vsat of 6%, which returned to within 1% of the pre-push value after 4 minutes. In contrast to the step-change in Z that was shown in Figure 5.2, the magnitude of the Z parameter in this example was transiently reduced by 15% at the very onset of the push, before overshooting the pre-push level by 4% during the next 40 seconds. This was followed by a local minimum at 4 minutes post-push, and a slowly oscillatory recovery to within 1% of the pre-push level by the end of the 20 minute period. The pattern of the Eo changes was similar to those shown in Figure 5.2, consisting of an onset peak and a plateau phase. As mentioned earlier, the next two pushes of 316 g caused changes in some parameters that were different from those with the 226 g push. Of the Boltzmann parameters, the patterns of the Eo and Z shifts were similar during these three pushes, while the changes in Vsat were quite different: The 316 g pushes in this example caused step-shifts in Vsat of around 16 to 17% (instead of recovering during the actual perturbation), and did not recover completely on withdrawal of the force.

When comparing the changes in Figures 5.2 and 5.3, some differences in the changes in the Vsat and Z shifts are apparent. These will be discussed in depth in Section 5.6. Before this, however, the push-related changes in the spectrum of the neural noise (SNN), DPOAEs, and the EP will be presented and discussed.

5.4 Spectrum of the neural noise

5.4.1 Results - Small decreases in the SNN

In 9 of the 12 pushes for which SNN measurements were obtained, cochlear-wall force application at the first-turn produced a statistically-significant[2] decrease in the amplitude of the SNN peak. The changes in SNN with the push are shown in Figure 5.4, which presents fourteen pairs of averaged (n=4) neural noise spectra. As shown in Figure 5.5, a significant decrease in SNN was observed only when the magnitude of the SNN peak was greater than around 0.5 μV RMS.

Compared to the SNN changes that occurred with other cochlear perturbations such as hypoxia and perilymphatic choline perfusion (see Chapter 8), measurable decreases in the SNN were quite small (2.3% to 12.7%, average 6% decrease), but were of a similar order to changes measured with injection of negative direct current into scala media (for example, see Figure 6 of Patuzzi et al., 2004).

[2] $P<0.05$, unpaired one-tailed T-Test.

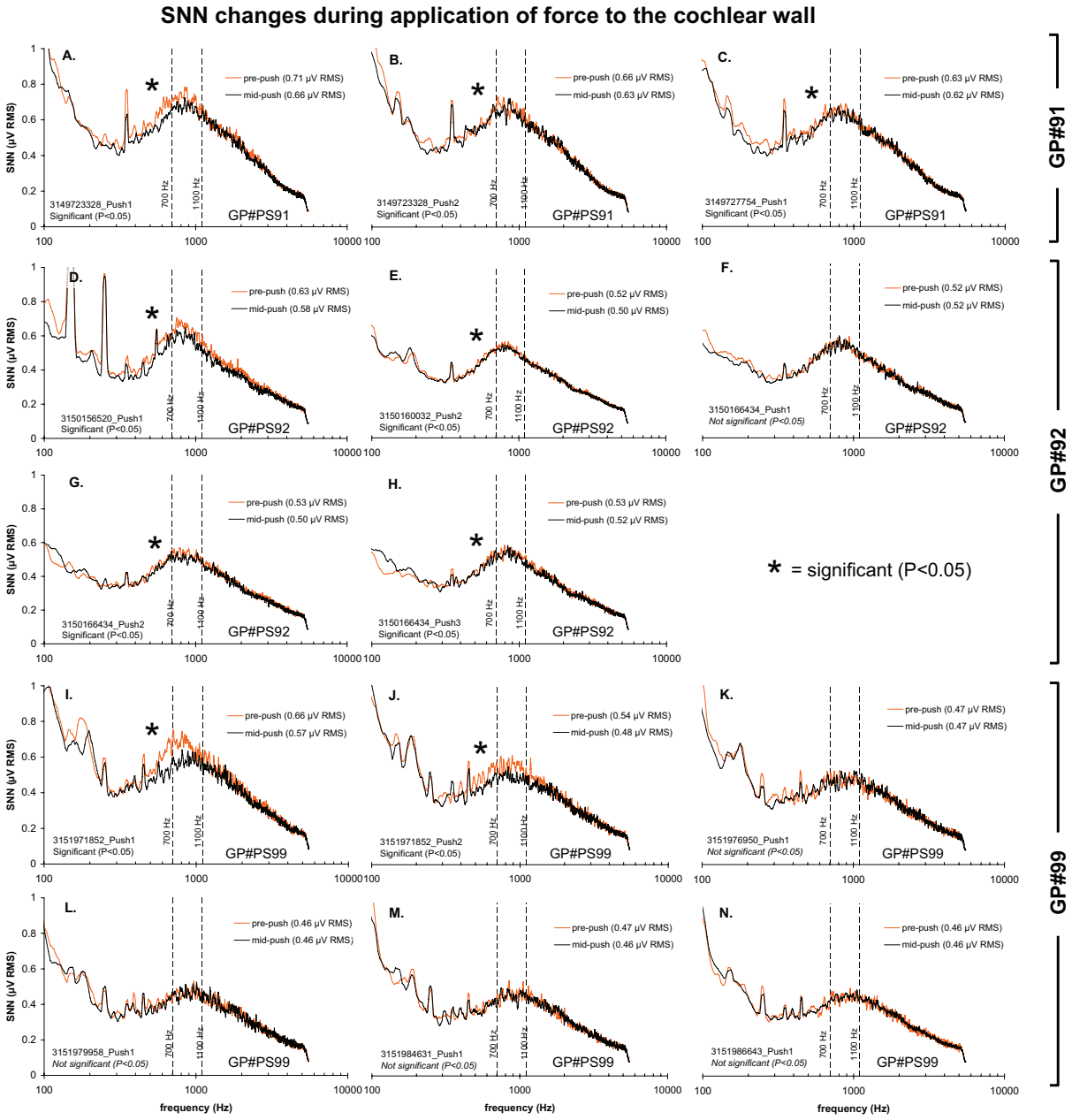

Figure 5.4: The application of force to the cochlear wall caused small but statistically-significant decreases (mean of 6%) in the amplitude of the SNN peak between 700 and 1100 Hz in 9 out of 14 pushes.

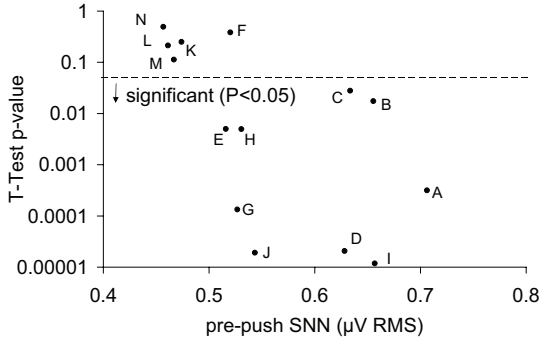

Figure 5.5: Plotting the significance of the above SNN changes (the p-value of the T-Test) against the pre-push SNN value reveals that significant decreases were only observed if the amplitude of the SNN peak was more than 0.5 µV RMS prior to the push (see text).

The SNN did not show any clear correspondence to the changes in the EP, the operating point, or Z, but did show a relationship with the Vsat parameter, as shown in the scatter-plot of Figure 5.6. When the three largest SNN decreases were excluded from the analysis (those from panels D, I, and J of Figure 5.4), the remaining data showed a significant[3] and strong correlation (R=0.98) between the changes in Vsat and the SNN during the push, which may indicate that the measures were altered via a shared mechanism. The separation of this data into two groups may reflect i) more labile contributions to the SNN from the basal-turn dendrites, and ii) the axonal components from more apical regions of the cochlea.

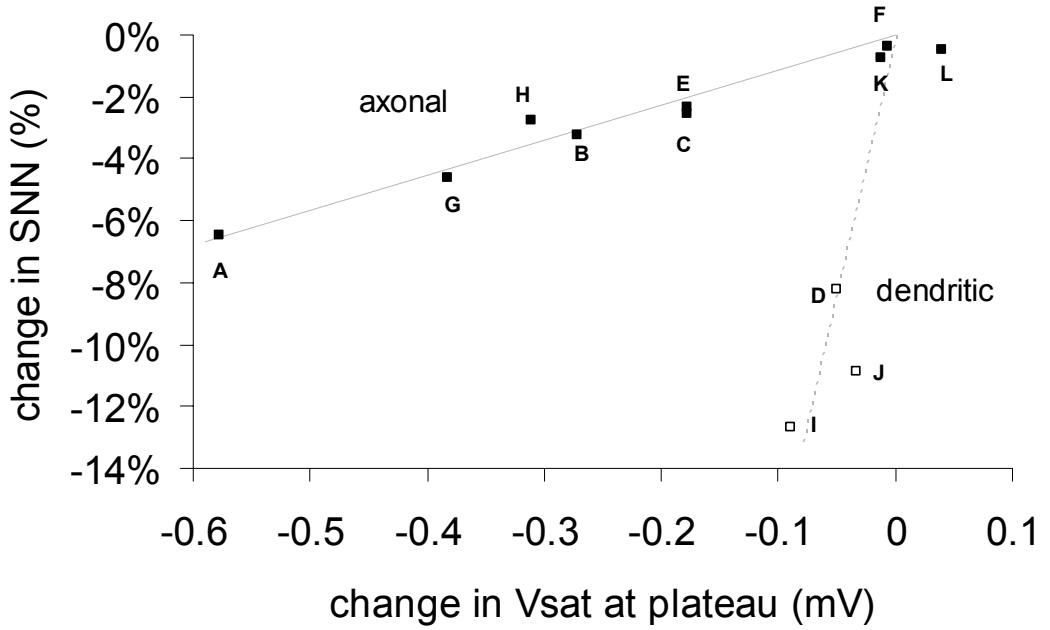

Figure 5.6: The percentage change in SNN was strongly correlated with the change in Vsat, measured during in the "plateau" phase of the push. The two data groups were putatively labelled "axonal" and "dendritic". In the axonal group, the Pearson product-moment correlation coefficient (R) between the percentage changes in SNN amplitude and the change in Vsat (mV) was 0.98.

5.4.2 Discussion - Possible origins of the small SNN changes

The SNN is a global measure of both stochastic firing rate and unitary potential resonance from some of the primary afferent neurones (Patuzzi et al., 2004). Because it contains contributions from neurones along the entire length of the cochlea, the small changes that were observed in the SNN may reflect larger rate or primary afferent resonance changes in a sub-population of cochlear neurones (Patuzzi et al., 2004), such as those in the first turn displaying a threshold shift with the push. Additionally,

[3] $p<0.0001$ (Student's two-tailed T-test).

changes in stochastic firing rate are heavily underestimated by changes in the magnitude of the SNN peak, which grows with approximately the square-root of the firing rate (Patuzzi et al., 2004).

While the underlying mechanism for the SNN decreases is not clear from the available data, the most-likely reason the observed changes were so small is that the first-turn pushes caused a reduction in those SNN components originating from first-turn neurones, while leaving intact the axonal components originating from more apical IHCs. The fact that significant decreases in SNN were observed only when the magnitude of the SNN peak was greater than around 0.5 μV RMS is consistent with the findings of Patuzzi et al. (2004) that the basal contribution to the SNN measured from the RW is relatively small under these experimental conditions. It is also consistent with the basal SNN contributions being more labile than those from apical neurones – the push may be affecting the firing rate of neurones which have already decreased in some instances (due to a falling EP, or cooling of the cochlea).

5.5 DPOAEs and the endocochlear potential (EP)

The quadratic $2f_1$-f_2 emission is thought to be an indicator of symmetric (odd-order) distortion and is often used as an indicator of active cochlear gain (Brown, 1987; Mills et al., 1993), while the f_2-f_1 emission is an indicator of asymmetric (even-order) distortion components, and is therefore sensitive to changes in operating point (Frank and Kössl, 1996; see also Shera and Guinan, 1999). Distortion-product otoacoustic emissions were recorded during the push using three sets of primary frequencies and amplitudes. Measurements in GP#PS91 and GP#PS92 were made using primary frequencies of 18.0 kHz (78 dB SPL) and 21.6 kHz (61 dB SPL). Measurements in GP#PS99 were made using primary frequencies of 14.0 kHz (73 dB SPL) and 16.8 kHz (80 dB SPL). Unfortunately, as will be discussed in Section 5.5.3 below, the primary levels used in this study may not have been the most suitable to monitor the changes in active gain with the push, because of the relative insensitivity to "cochlear insults" observed in $2f_1$-f_2 emissions produced by high-level primaries (Lukashkin et al., 2002; Avan et al., 2003). Nonetheless, with this caveat in mind, a description of the observed changes in DPOAEs follows.

In these experiments, pushes were found to cause highly variable changes in DPOAES, with either increases or decreases in the levels of the cubic and quadratic distortion products, depending on the magnitude of the push, the size of the resulting operating point shift, the EP, and the choice of primary-tone frequency and level.

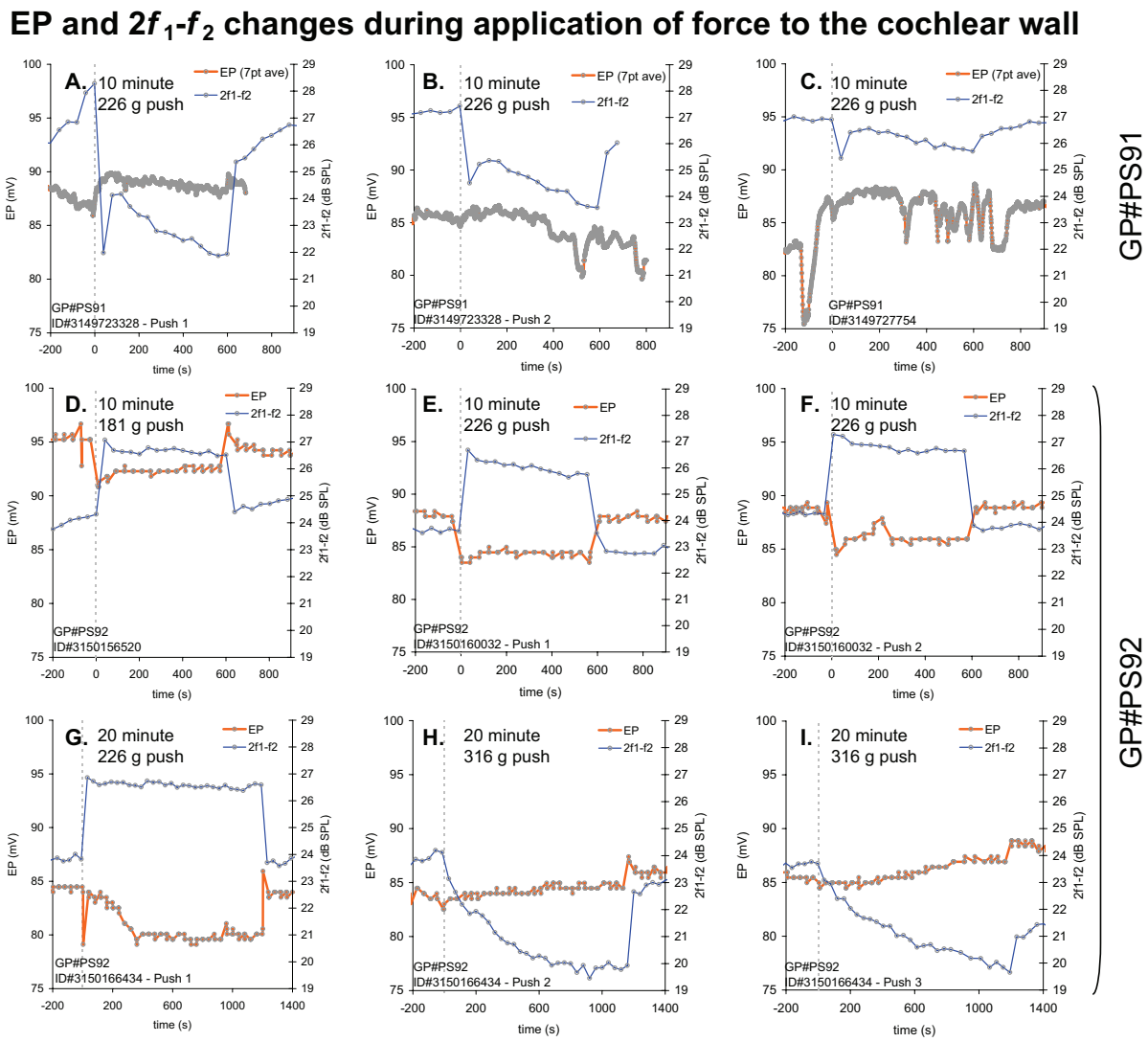

Figure 5.7: Comparison of EP data and $2f_1$-f_2 emission level in two animals displaying different responses to the push. Panels A to C were from GP#PS91, which showed a small increase in EP and a decrease in $2f_1$-f_2 level. Panels D to I were from GP#PS92, which showed either a decrease in EP and an increase in $2f_1$-f_2, or, later in the experiment, very slight changes in EP and a decrease in $2f_1$-f_2. Data is presented in chronological order. The $2f_1$-f_2 distortion product was evoked using the same primary levels and frequencies in both animals (f_1 = 18 kHz, 79 dB SPL, f_2 = 21.6 kHz, 61 dB SPL), and pushes in both animals caused hearing losses at similar frequencies (between 18 and 20 kHz). In addition to differences in the pre-push $2f_1$-f_2 levels (27 dB SPL for GP#PS91, 24 dB SPL for GP#PS92), the high-frequency hearing sensitivity of GP#PS92 (D to I) was 10 dB worse between 18 and 22 kHz than in GP#PS91 (A to C).

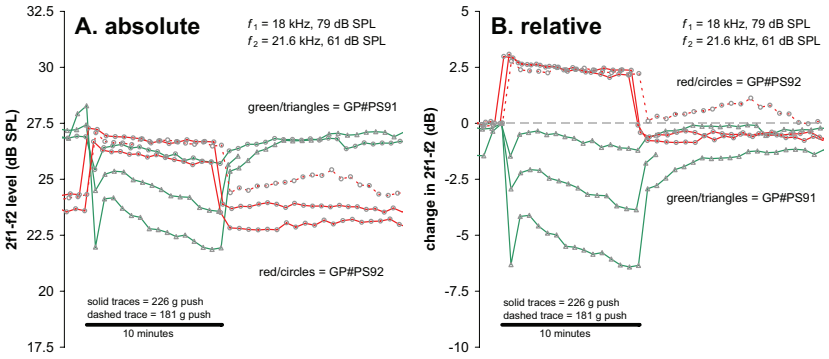

Figure 5.8: The $2f_1$-f_2 distortion product data from the 10-minute pushes of Figure 5.7 above, overlayed to illustrate the difference in the responses from the two animals. Panel A shows the absolute SPL of the emissions, while Panel B shows the change in emission level with the push.

5.5.1 Results - Relationship between $2f_1$-f_2 and the EP

The EP was measured during the push in two animals. In the first animal (GP#PS91), the push caused a rise in EP (3 pushes), while in the second animal (GP#PS92) the push caused the EP to either fall (4 pushes) or gradually rise (2 pushes). The changes in the EP were not consistent with the operating point shifts, which were *always* in the SV direction (and would therefore have been expected to decrease the EP due to increased current shunt). The only consistent relationship between the rise or fall in EP and any of the other parameters was in the level of the $2f_1$-f_2 emission. The inverse correlation between the sign of the changes in $2f_1$-f_2 and EP is shown in Figure 5.7, which presents overlaid $2f_1$-f_2 and EP traces from the two animals in which EP was measured. This inverse correlation was present across the two animals, and is visible in successive pushes within GP#PS92. Why this should have occurred is not known, and may represent an additional current shunt that was affected by the push.

While pushes in both animals had caused hearing losses at similar frequencies (between 18 and 20 kHz), the "state" of the animals was different at the time of recording, in that the high-frequency hearing sensitivity of GP#PS92 was 10 dB worse between 18 and 22 kHz than in GP#PS91 (Panels A to C of Figure 5.7). There were also differences in the pre-push Boltzmann parameters in both animals[4].

The EP traces in Panels A, B, and C of Figure 5.7 were recorded continuously, without any synchronisation with the data acquisition software (described in Chapter 4), and so show more measurement noise due to the presence of scala media CM in the EP recordings. Despite this, the rise in EP during the push is visible in each trace. The correlation between $2f_1$-f_2 and EP is also visible in Panels D to I of Figure 5.7 from GP#PS92, in which the EP was recorded in silence. In the cases where the EP was observed to rise during the push, the $2f_1$-f_2 emission fell, and vice versa. The differences in the $2f_1$-f_2 time-courses for 10-minute pushes in GP#91 and GP#92 is visible in Figure 5.8.

Panels G, H, and I of Figure 5.7 show data from the three consecutive pushes that were presented earlier in Figure 5.3. The first push of 226 g caused an increase in $2f_1$-f_2 and a decrease in EP, while the next two pushes of 316 g force caused slow decreases in

[4] In terms of the Boltzmann parameters, the pre-push operating points for GP#PS92 were all below 2.4 meV (average of 3.4 ± 1.6 meV), while those for GP#PS91 were all above 1.7 meV (average of 2.2 ± 4.1 meV). Similarly, the pre-push Z magnitudes for GP#PS92 were below 96 meV/Pa (average of 95 ± 5 meV), while those for GP#PS91 were above 104 meV/Pa (average of 113 ± 3 meV). These differences were not due to the amplitude of the 207 Hz Boltzmann probe being 2 dB SPL higher in GP#PS91, which would have tended to produce differences in the opposite direction.

$2f_1$-f_2 and similarly slow increases in EP. The pattern of results in these three pushes in this animal, including the correlation between these results and the Boltzmann and CAP waveshape changes, is discussed in Section 5.7.4 below.

5.5.2 Results – change in f_2-f_1 with transducer operating point

Figure 5.9 shows the changes in f_2-f_1 the plotted against the operating point shift produced by the push. The three pushes which caused operating point shifts towards SV of less than 6 meV also caused increases in the level of f_2-f_1 emission, while seven of the eight pushes which caused SV shifts larger than 6 meV caused f_2-f_1 level to decrease. Although the general relationship between operating point and f_2-f_1 is nonlinear (Frank and Kössl, 1996), over the range of push-induced operating point shifts shown in Figure 5.9 there was a significant correlation between the two measures, with a Pearson product-moment correlation coefficient (r) of -0.73 ($p<0.05$; Student's two-tailed T-test).

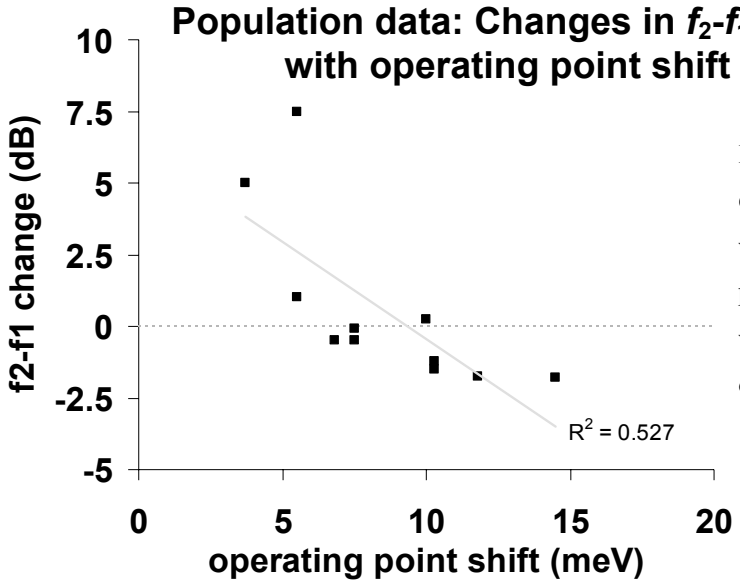

Figure 5.9: Changes in the f2-f1 emission level were correlated with the size of the operating point shift. Both measurements were taken in the "plateau phase" of the operating point shifts.

5.5.3 Discussion - Complex changes in DPOAE levels

The high-level $2f_1$-f_2 data obtained during this study did not show a close correspondence to the changes observed in other cochlear indicators during the push. The inconsistency in the $2f_1$-f_2 results (such as those shown in Figure 5.8) may be due to i) the non-linear relationship between the operating point shift and the DPOAE amplitude (as described by Frank and Kössl, 1996, and shown in Figure 5.10 below), ii) the non-monotonic input/output function of the DPOAEs, described later, or iii) a combination of both factors.

The decreases in f_2-f_1 level that were observed with increases in the operating point (shown in Figure 5.9 above) *do* show a correspondence to the schematic diagram of Frank and Kössl (shown in Figure 5.10B below), in which operating point shifts of more than +0.25 units on the horizontal axis of Figure 5.10B caused a reduction in f_2-f_1 level.

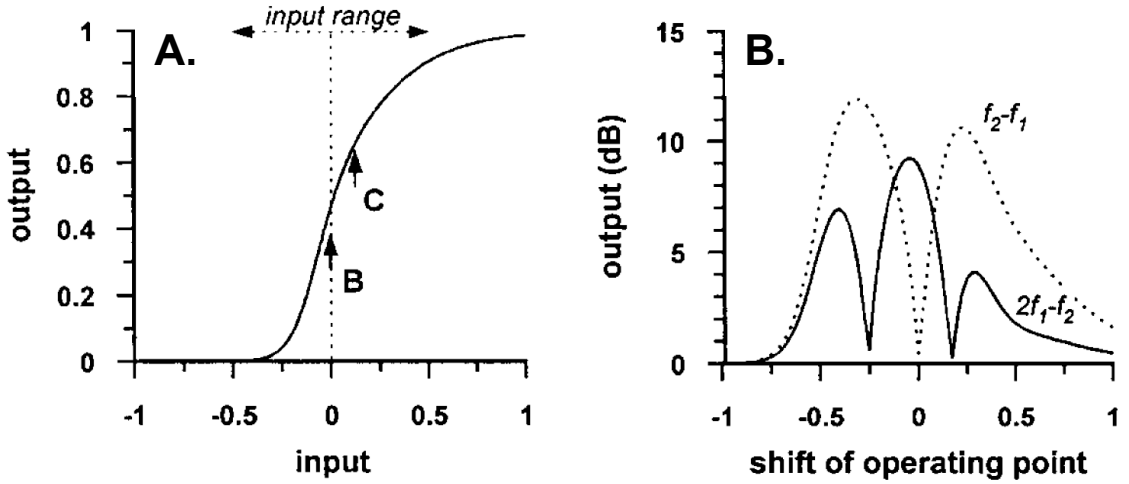

Figure 5.10: Panel A shows a 2nd-order Boltzmann function, while Panel B shows the expected changes in the $2f_1$-f_2 and f_2-f_1 emission level with movement of the operating point on this transfer curve (adapted from Frank and Kössl, 1996).

DPOAE input/output functions show monotonic growth in DPOAE amplitude at both low and high primary levels, but display a characteristic "notch" at intermediate level tones (Withnell and Yates, 1998; Lukashkin et al., 2002; Liberman et al., 2004). The notch in DPOAE amplitude corresponds to an abrupt change in the phase of the emission, because the phases of the low- and high-level emissions are opposite to each other. While DPOAE input/output functions were not obtained in the present study, it is possible that the measured variations in the $2f_1$-f_2 levels during the push were caused by a *movement* of this notch during the perturbation, similar to that which occurs with furosemide (as described below), which would have produced non-monotonic changes in $2f_1$-f_2, as demonstrated below.

Figure 5.11 (modified from Lukashkin et al., 2002) shows the change in the $2f_1$-f_2 input/output function in the guinea pig following intraperitoneal injection of furosemide. Furosemide injection has a direct effect on stria vascularis, resulting in a decrease in the EP (Sewell, 1984) and therefore a reduction in driving potential for potassium into the OHCs. *In vivo*, this causes a decrease in OHC efficiency (Da Cruz, 1993). Although the primary effect of furosemide is exerted via the EP change, direct effects on the OHCs themselves have also been noted *in vitro*, with furosemide causing

a shift in the peak OHC nonlinear capacitance toward more positive membrane potentials (Santos-Sacchi et al., 2001).

Although it is perhaps not *directly* applicable, the furosemide analogy is used here to illustrate the point that, when measured with fixed primary-tone levels, the magnitude and sign of the change in the $2f_1$-f_2 emission SPL that occurs with a reduction in cochlear amplification is dependent on both i) the size of the perturbation (drawing an analogy between a larger push and a larger furosemide effect), and ii) the chosen primary-tone levels.

To further illustrate these points, the input/output function in Figure 5.11 has been shaded to show the direction of the transition between the control state (prior to intraperitoneal injection of furosemide) and one of four other states, each at a different interval after the injection. For this particular example, the input/output function can be divided into four primary-tone-level regions:

i) Below 48 dB SPL – decreased cochlear gain resulted in a reduced $2f_1$-f_2 emission level, with larger gain decreases causing larger emission reductions;

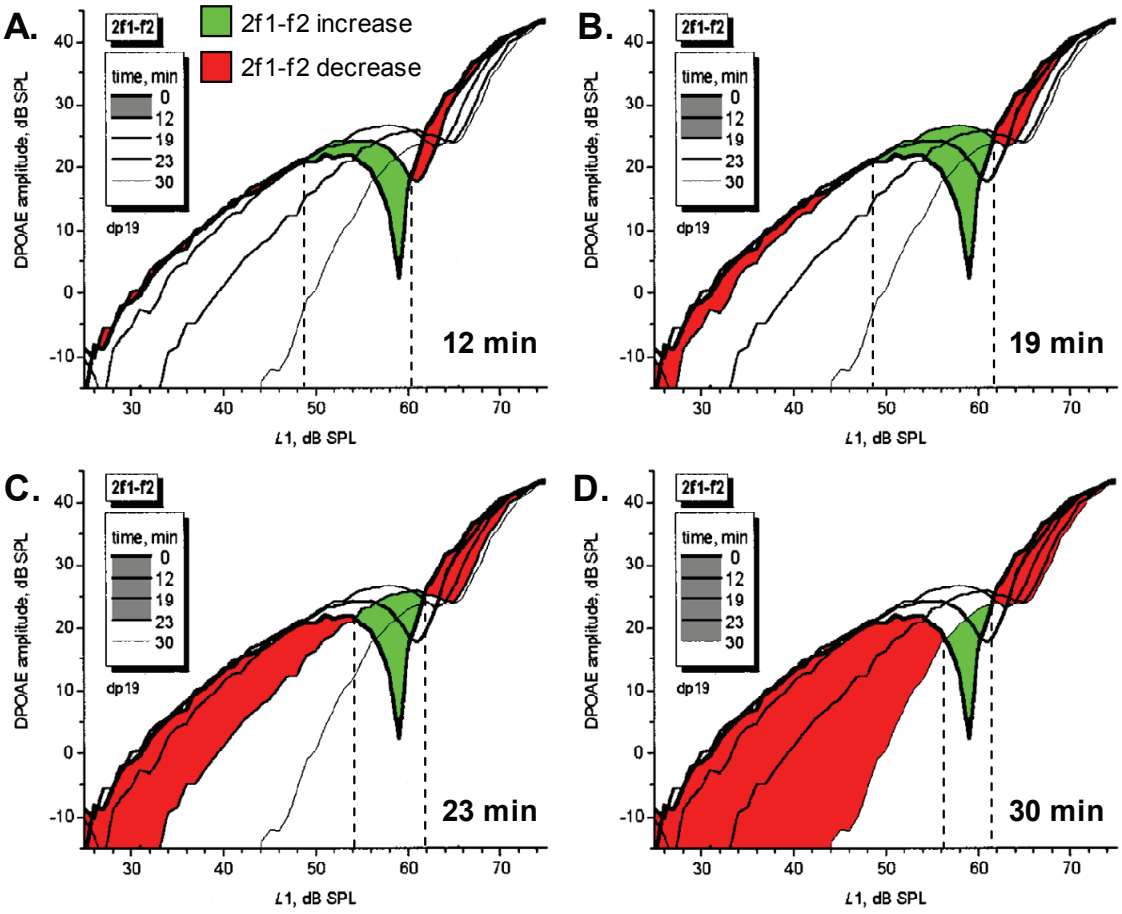

Figure 5.11: This figure (adapted from Lukashkin et al., 2002) shows the change in the $2f_1$-f_2 input/output function for different time intervals following injection of furosemide. The shaded areas show that the magnitude and sign of the change in $2f_2$-f_1 level depends on both the size of the perturbation and the chosen primary level (see text).

ii) Between 48 and 62 dB SPL – decreased cochlear gain either increased *or* decreased $2f_1$-f_2 emission level, depending on f_1 level and perturbation magnitude;

iii) Between 62 and 65 dB SPL – decreased gain caused a reduction in $2f_1$-f_2 level, but the magnitude of the emission decrease was not monotonically related to the gain decrease magnitude;

iv) Above 65 dB SPL – decreased cochlear gain resulted in a reduced $2f_1$-f_2 emission level, with larger gain decreases causing larger emission reductions;

Although the notch in these examples occurs for f_1 levels of between 60 and 68 dB SPL, a secondary notch occurs at higher levels (between 75 and 90 dB SPL), as shown in Figure 5.12. In this Figure, unpublished data from our laboratory (Sellick, personal communication) is overlaid with the data from Lukashkin et al., showing the location of the second notch relative to the first notch. The second notch is close to the L1 levels used for GP#PS91 and GP#PS92 in the experiments reported here. Further experiments are required to determine whether this second notch displays the same dynamic behaviour as the first.

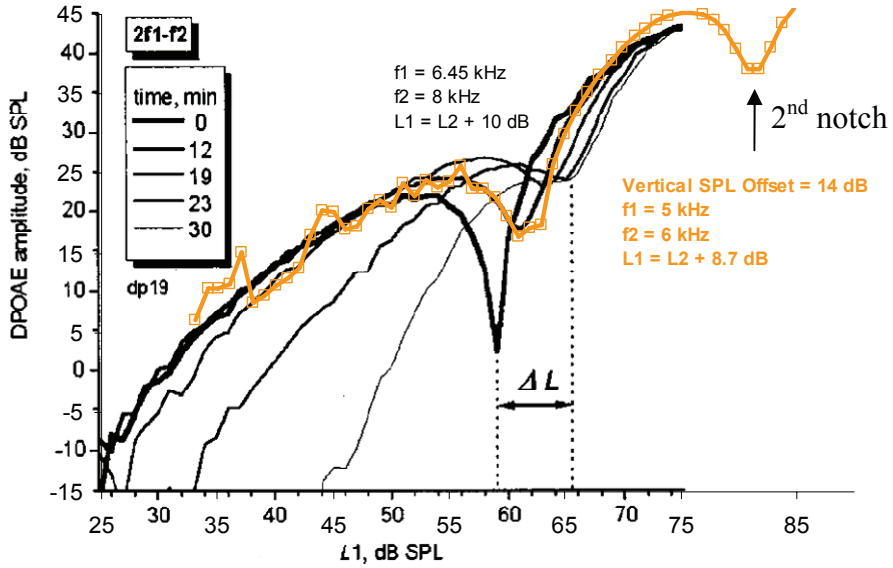

Figure 5.12: Overlaid data from Sellick (personal communication) showing a second notch in the $2f_1$-f_2 IO function with L1 levels of 75 - 90 dB SPL. The data of Lukashkin (2002) is shown for comparison. The orange trace has been vertically offset by +14 dB to account for SPL differences between the two recordings.

5.5.4 Summary of DPOAE results

In short, the DPOAE data recorded during this experimental series yielded little useful information about the changes in cochlear sensitivity and operating point with the

push, other than that it is inconsistent. The discussion above highlights the importance of using *low-level* primary tones (i.e. below approximately 45 dB SPL), or otherwise recording sets of input/output functions over a wide range of primary levels. In situations where finer resolution of the time-course of changes is required, the fixed low-level method may be preferable. For studies on novel perturbations (such as the push), a preliminary examination of the change in input/output function is warranted.

5.6 Changes in the Boltzmann parameters describing OHC MET

In this section, the changes in Boltzmann parameters observed during the push are presented. As the Boltzmann analysis technique involves curve-fitting to CM waveforms, it is important to establish that the CM waveforms were not contaminated by any neural activity evoked by the 207 Hz probe tone. Prior to describing in detail the changes that occurred in the Boltzmann parameters during the push, the issue of neural contamination is discussed below.

5.6.1 Results - Effect of neural blockade with TTX

Due to the elevation of CAP threshold and drop in CAP amplitude with the push, there was a possibility that the changes observed in the Boltzmann parameters were neural in origin, either due to an efferent-mediated effect, or due to the possible loss of any neural contamination of the CM which would alter the fit of the Boltzmann equation to the CM waveform. To examine this possibility, the push was repeated before and after the application of a 100 μM solution of the voltage-gated sodium-channel blocker tetrodotoxin (TTX; Calbiochem-Behring Corp., La Jolla, CA, USA) to the round window in one animal.

As shown in Figures 5.13 and 5.14, the application of TTX caused the elimination of neural responses at each frequency as it diffused through the cochlea. The SNN amplitude was also reduced (data not shown). The SP amplitudes were reduced by an average 24 ± 11% (ranging from 43% at 22 kHz to 9% at 14 kHz) – however this amplitude reduction was probably due to the attenuation of the electrical signal from the RW by the TTX saline solution. In terms of the Boltzmann parameters, the attenuation of the RW signal by the saline solution also reduced the Vsat parameter by 30%. Apart from this large step-change in Vsat, the Z parameter was increased by 7%, and Eo changed by less than 1 meV following application of TTX, and both these

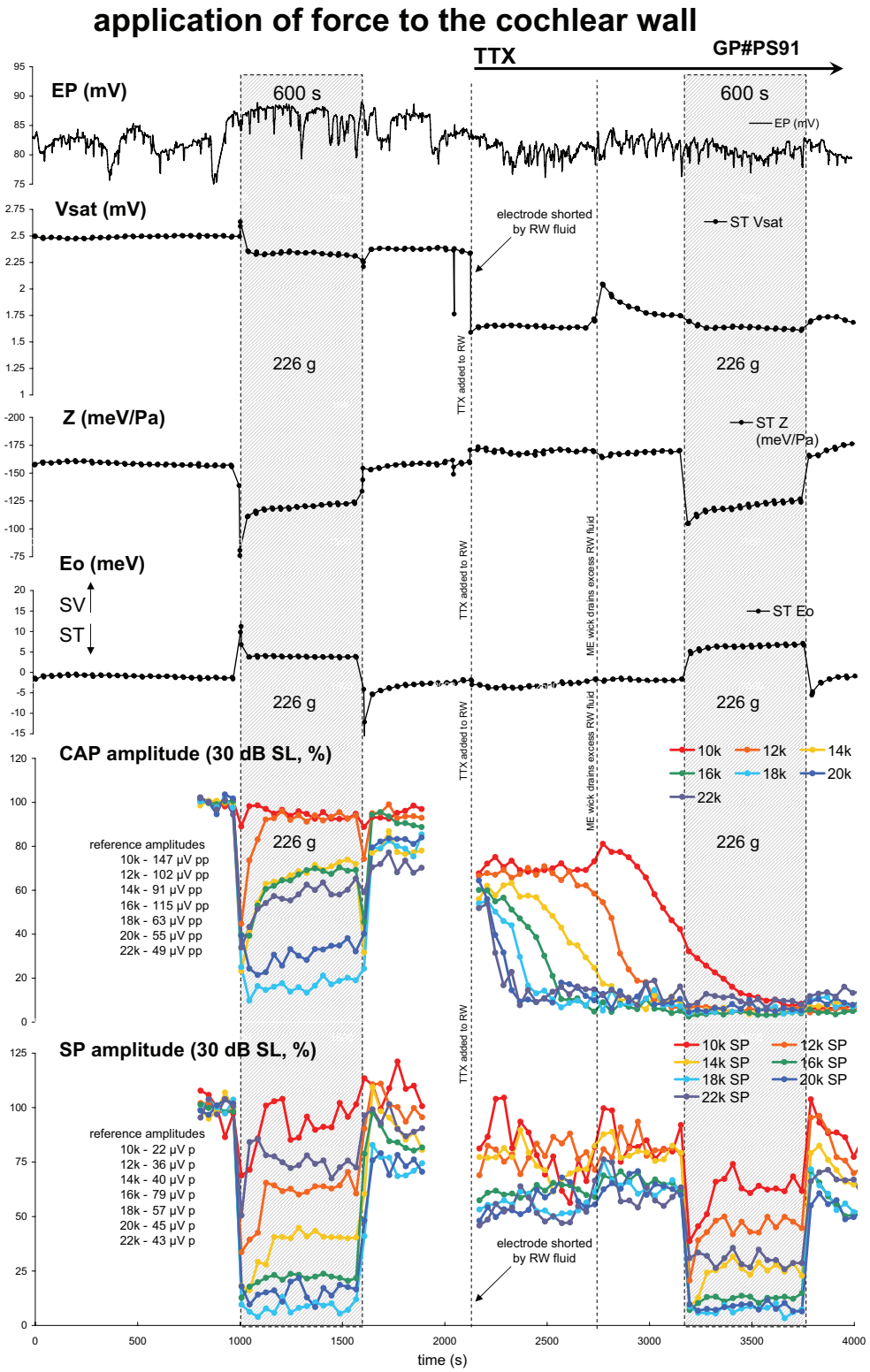

Figure 5.13: The changes in the Boltzmann parameters during the application of force to the cochlear wall were not neural in origin, as these data, and those in Figure 5.14 overleaf, demonstrate. The application of tetrodotoxin (TTX; 10 µM in saline) to the round window at 2134 s partially shorted the recording electrode, causing an immediate step-wise reduction in amplitude of the recorded signal, visible in Vsat and the neural traces, followed by the elimination of neural responses at each frequency as it slowly diffused through the cochlea. The TTX also reduced the SNN amplitude (above the biological noise floor) by 75% (data not shown), while the SP amplitudes were unaffected. The application of force some 18 minutes after the TTX dose produced Boltzmann changes similar to those with neural responses intact, as did subsequent force applications (see Figure 5.14).

ID#3149727754

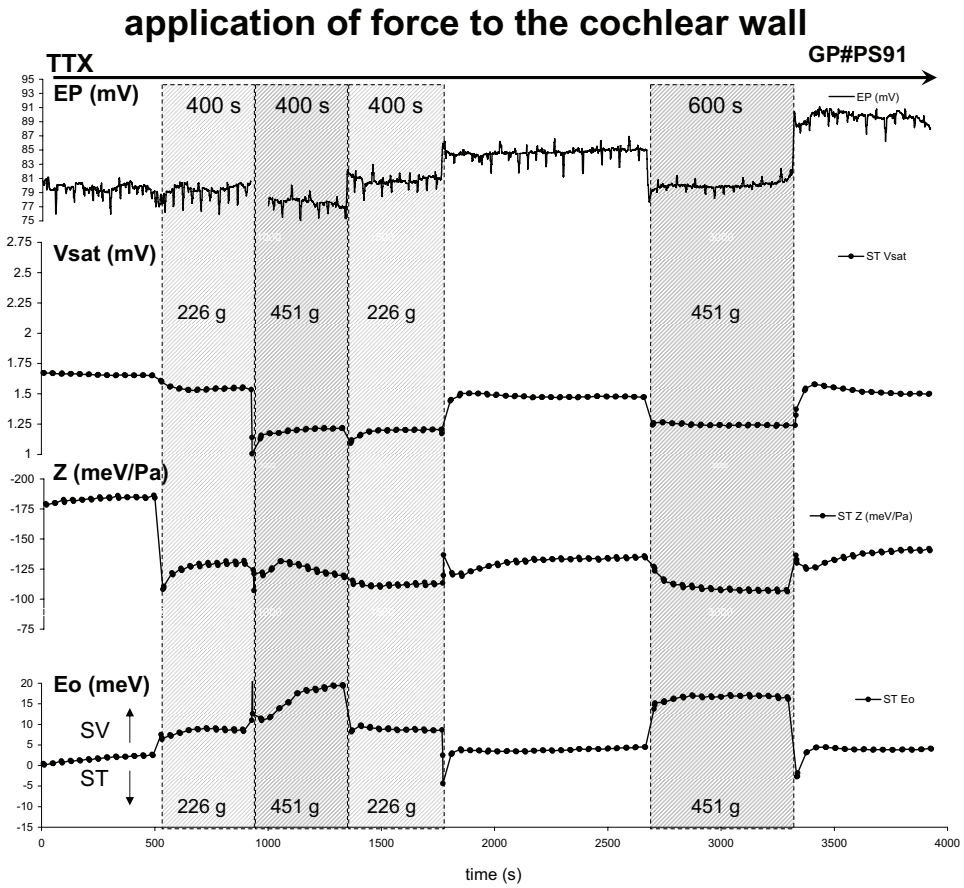

Figure 5.14: A continuation of the trace shown in Figure 5.13. Increasing the push from 226 g to 451 g caused a further decrease in Vsat, a biphasic Z change, and a further slow operating point shift toward scala vestibuli. Withdrawal to 226 g returned the operating point to the same value as during the previous 226 g push, but caused only small changes in Vsat and Z, while the next 451 g push caused a similar degree of Vsat and operating point shift as the previous 451 g push (see text).
ID#3149731856

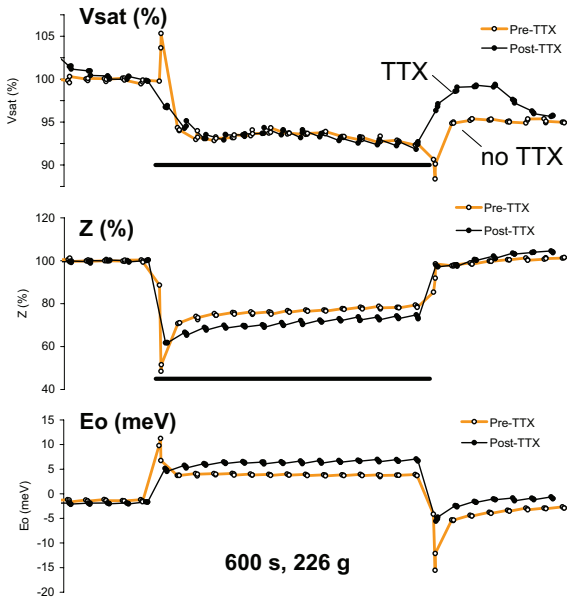

Figure 5.15: While the pre- and post-TTX Boltzmann changes with force application were similar in most respects, the post-TTX data lacked the transients seen at onset in almost all pre-TTX examples.
ID#3149727754

changes were largely reversed by removal of the excess fluid from the middle-ear cavity.

As shown in Figure 5.14, the application of force some 18 minutes after the TTX dose (when neural responses above 12 kHz had been eliminated) produced Boltzmann changes that were similar to those with neural responses intact, with the exception that i) the plateau of the operating point shift was larger by around 2.5 meV towards scala vestibuli following TTX; ii) the post-TTX push resulted in a greater decrease in the Z parameter (a 29% rather than 25% reduction); and iii) the post-TTX Boltzmann traces lacked onset transients (and in the case of Eo, the adaptation component). This is clearly visible in Figure 5.15, in which the pre- and post-TTX push traces are overlaid.

The difference in Eo traces following the TTX is interesting, because onset transients were visible in the Eo traces of almost all of the other push results. While more data is required for certainty, the absence of onset transients in the five post-TTX pushes carried out in this one animal may indicate a possible neural contribution to the onset adaptation component.

5.6.2 Results - Effects of 200 Hz probe level

The effect of the 200 Hz Boltzmann probe level on the results obtained with the push was examined in one animal. This was performed using a modified version of the Boltzmatron, which extracted Boltzmann data from CM waveforms elicited by a compound stimulus consisting of interleaved 50 ms tone-bursts at 90, 93, 99, and 105 dB SPL. The data obtained from this recording is shown in Figures 5.16 and 5.17.

An important result from this data is the confirmation that the changes observed in the Boltzmann parameters during a push are not consistent with a simple drop in stimulus level. Such a drop in stimulus level could have occurred if the push altered the transmission characteristics of the middle-ear, or the geometry of the insertion of the stapes in the oval window. While both the push and a reduction in probe tone SPL cause a reduction in Vsat and a SV operating point shift, the push causes a *decrease* in Z, whereas the stimulus level reduction causes Z to increase. The difference in the magnitude of the changes in the Boltzmann parameters measured with different probe levels is also apparent in Figure 5.17: as the probe level was increased, the size of the measured changes in Vsat and Z decreased, while the size of the changes in Eo increased. The time-constant of Eo adaptation also tended to increase with increasing probe level, but why this should be the case is not clear from the available data.

Boltzmann parameters at multiple probe-tone SPLs during application of force to the cochlear wall

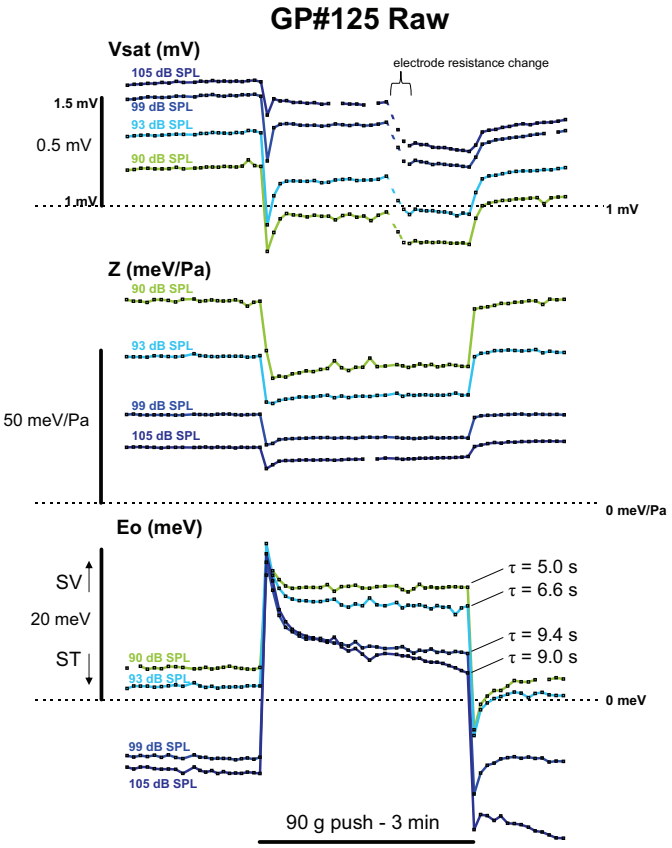

Figure 5.16: This figure shows the effect of a 90 g push on the Boltzmann parameters recorded using 200-Hz-tone levels of 90, 93, 99 and 105 dB SPL. The measurements from the four levels were recorded at the same time using an interleaved protocol.

The time-constant of adaptation of the operating point shift was largely dependent on the level of the Boltzmann tone.

The drop in Vsat (dashed line) was due to a reduction in the amplitude of the RW electrical signal due to a partial shorting of the recording electrode, but this does not affect the Z and Eo fits. It is also clear from this figure that the changes in the Boltzmann parameters observed with a push are not due to a reduction in the amplitude of the sound stimulus delivered to the cochlea, as the changes in Z were in the wrong direction.

The largest operating point shifts occurred at levels for which the resting operating point was closer to scala tympani, indicating a saturation in the effect of sound level on Eo as operating point moved toward scala vestibuli.

ID#3170308399

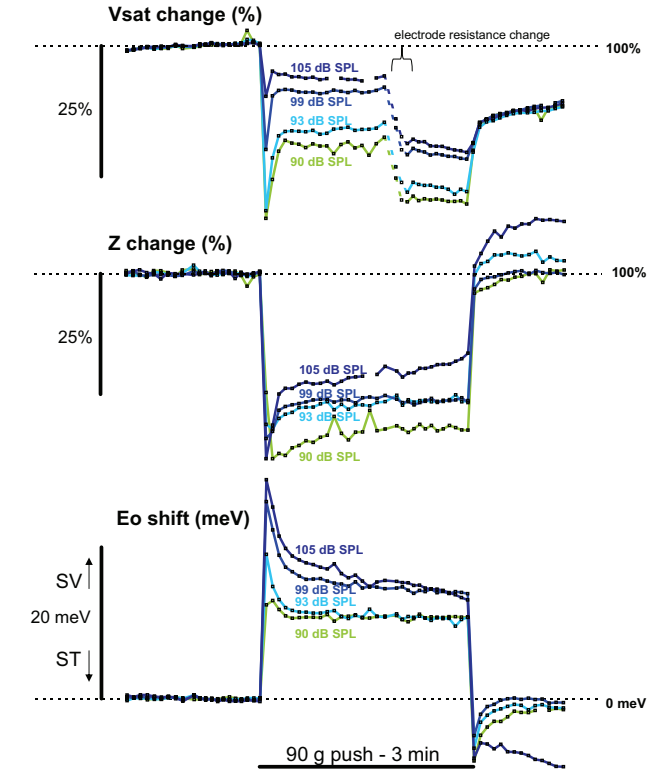

Figure 5.17: The data from Figure 5.16 above, reformatted to show the percentage changes in Vsat and Z, and the magnitude of the operating point shifts, during the push.

The percentage changes in Vsat and Z decreased with increasing probe level, while the operating point shifts increased with increasing probe level.

ID#3170308399

While the percentage change in Z with the push decreased with increasing sound level, the absolute change in the ZP parameter (in units of meV) during the push was essentially constant (averaging 35 ± 3 meV) across the four sound levels. Just why the sensitivity change imposed by the push should be proportional to the sound pressure level (in Pa) is also not clear.

The increased magnitude of the Eo changes with increasing probe-tone SPL may be a function of the initial operating point, rather than the sound level: Results obtained in other experiments (not presented here) appear to show a form of compressive nonlinearity in the *measured* operating point, such that the extent of dynamic fluctuations is reduced if the operating point is towards scala vestibuli, compared to if it were zero or towards scala tympani. This proposed dependence on operating point was derived from the very-low-frequency (VLF) modulation experiments mentioned in Chapter 6, in which the probe stimulus level remained constant, but the operating point was altered by a very-low-frequency bias tone. In those cases, the dynamic changes in Eo were also largest from ST-biased waveforms than for SV biases.

5.6.3 Results – Summary of observed changes in Boltzmann parameters

In the majority of cases, the push caused a reduction in Vsat, an increase in Z, and a SV Eo shift. As seen in the example in Figure 5.15, the Z and Eo parameters often showed a degree of "adaptation" or "decay" following a transient at the onset of the push, which may or may not have a neural basis. To differentiate between the onset values and the post-adaptation values, "plateau" measurements were also tabulated at just prior to 600 s after the push.

The Eo changes were the most consistent, with all applications of force producing a rapid operating point shift towards scala vestibuli. The adaptation component, if present, was well described by a single-exponential function in most cases (in a few cases, an additional linear component to the decay was present). The time-constants of the adaptation for a number of traces are shown in Figure 5.18. While no clear relationship between the time constant and any other parameter was observed across the population, in one animal in which multiple probe levels were used simultaneously, the time-constant of the Eo adaptation appeared to vary with the sound-level of the Boltzmann probe tone (possibly as a consequence of the different quiescent operating points), as described in Section 5.6.2 above.

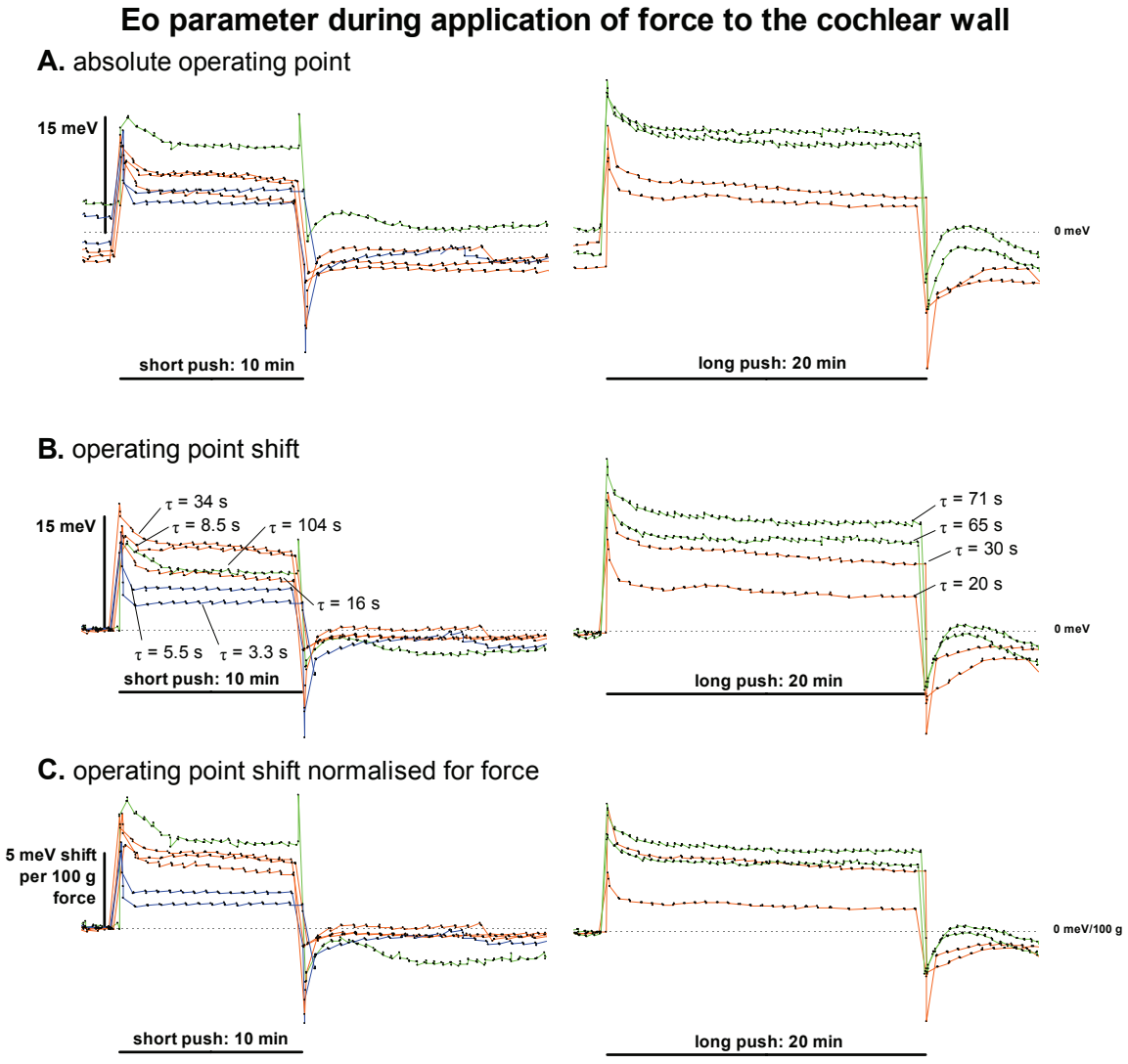

Figure 5.18: A. and **B.** Time courses of operating point (Eo) shifts in response to 10 minute and 20 minute applications of force to the cochlear wall. The time constants of the Eo adaptation varied widely, with an average τ of 38 (± 33; n = 11) seconds. The traces are colour-coded by the animal and the level of the probe tone used (green = GP#PS99, 84 dB SPL; orange = GP#PS92, 86 dB SPL, blue = GP#PS91, 88 dB SPL). The relationship between the probe-tone level and adaptation time constant is discussed in the text. **C.** The Eo shift measured was not directly dependent on the amplitude of the force applied, and dividing the Eo shifts by the level of force did not account for the variability between measurements.

The average peak operating point shift was 15 meV (± 3 meV; n = 12), adapting to 9 meV (± 3 meV; n = 12). While larger pushes caused larger operating point shifts in some cases (such as in GP#PS99, where doubling the size of the push from 136 g to 271 g increased the size of the operating point shift from 7.5 meV to 13 meV), in other cases no discernible pattern was visible. Across the population examined, the pooled data did not show a significant correlation ($R^2 < 0.01$) between the degree of operating point shift with a push and the amount of force applied. Additionally, the percentage

standard deviation of the pooled operating point shifts was not reduced by dividing the shifts by the amount of force applied: doing so gave a normalised average peak operating point shift of 7 meV per 100 g of applied force (± 2 meV; n = 12), adapting to 4 meV per 100 g of applied force (± 1 meV; n = 12). An example of this lack of correlation can be see in Figure 5.3, which showed the Boltzmann parameters recorded in one animal in which the degree of operating point shift was not correlated with the size of the push, nor with the initial absolute operating point.

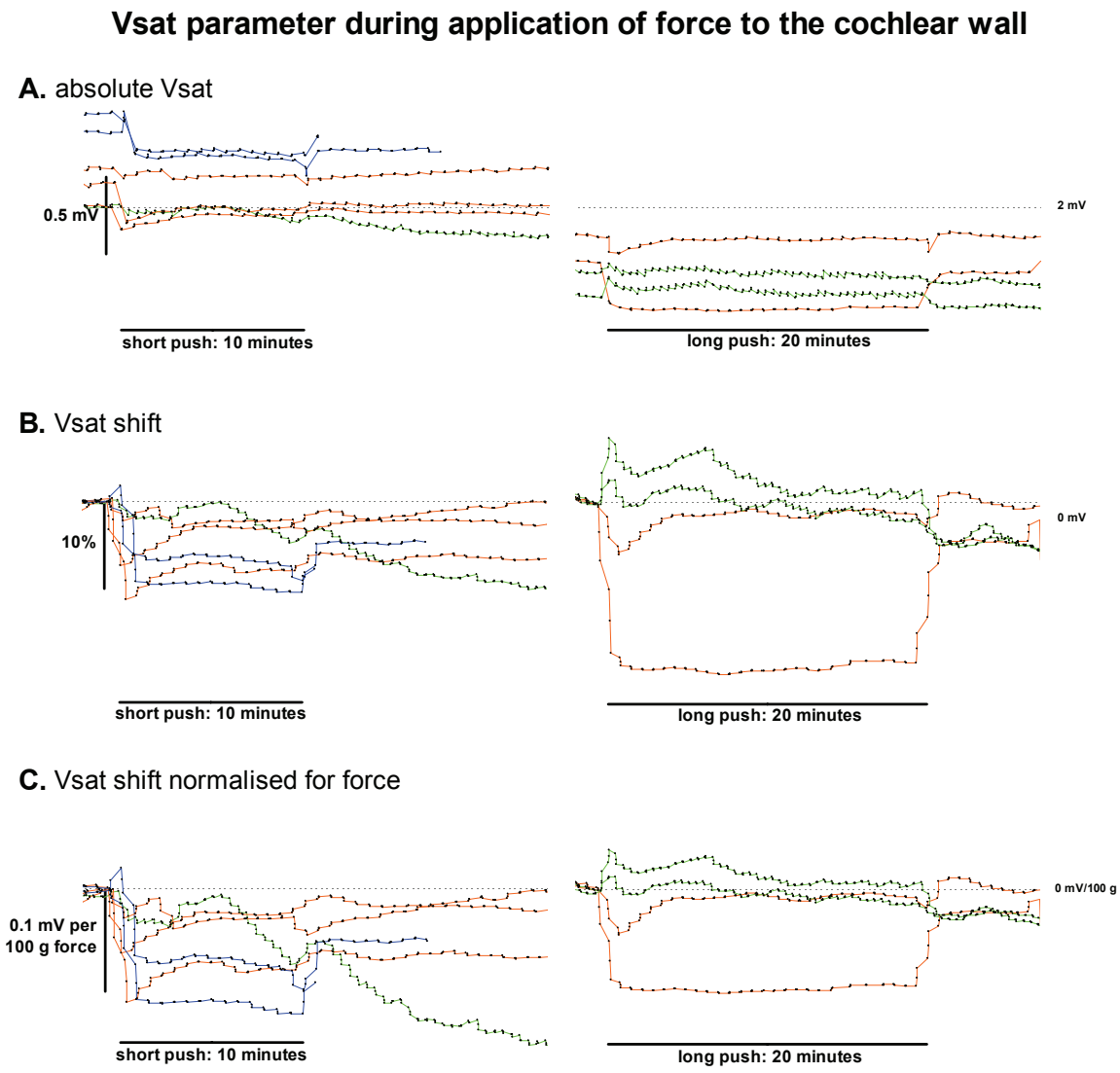

Figure 5.19: A. and **B.** Time courses of changes in the Vsat parameter in response to 10 minute and 20 minute applications of force to the cochlear wall. The traces are colour-coded by the animal and the level of the probe tone used (green = GP#PS99, 84 dB SPL; orange = GP#PS92, 86 dB SPL, blue = GP#PS91, 88 dB SPL). **C.** Dividing the Vsat shift by the amplitude of the force applied increased the variation between the green and blue 10-minute push traces. (5-point running averages on these traces).

While the changes in the operating point were always in the SV direction, the Vsat and Z changes showed more variability. As shown in Figure 5.19, Vsat was reduced immediately after onset of force application in 10 out of 15 pushes, with 14 of 15 pushes showing Vsat reductions after 600 s. The average change in Vsat was -7% (± 8%; n = 13), but reductions of up to 22% were also observed (such as that shown in Figure 5.3). Dividing the changes in Vsat by the amount of force applied also did not reduced their standard deviation.

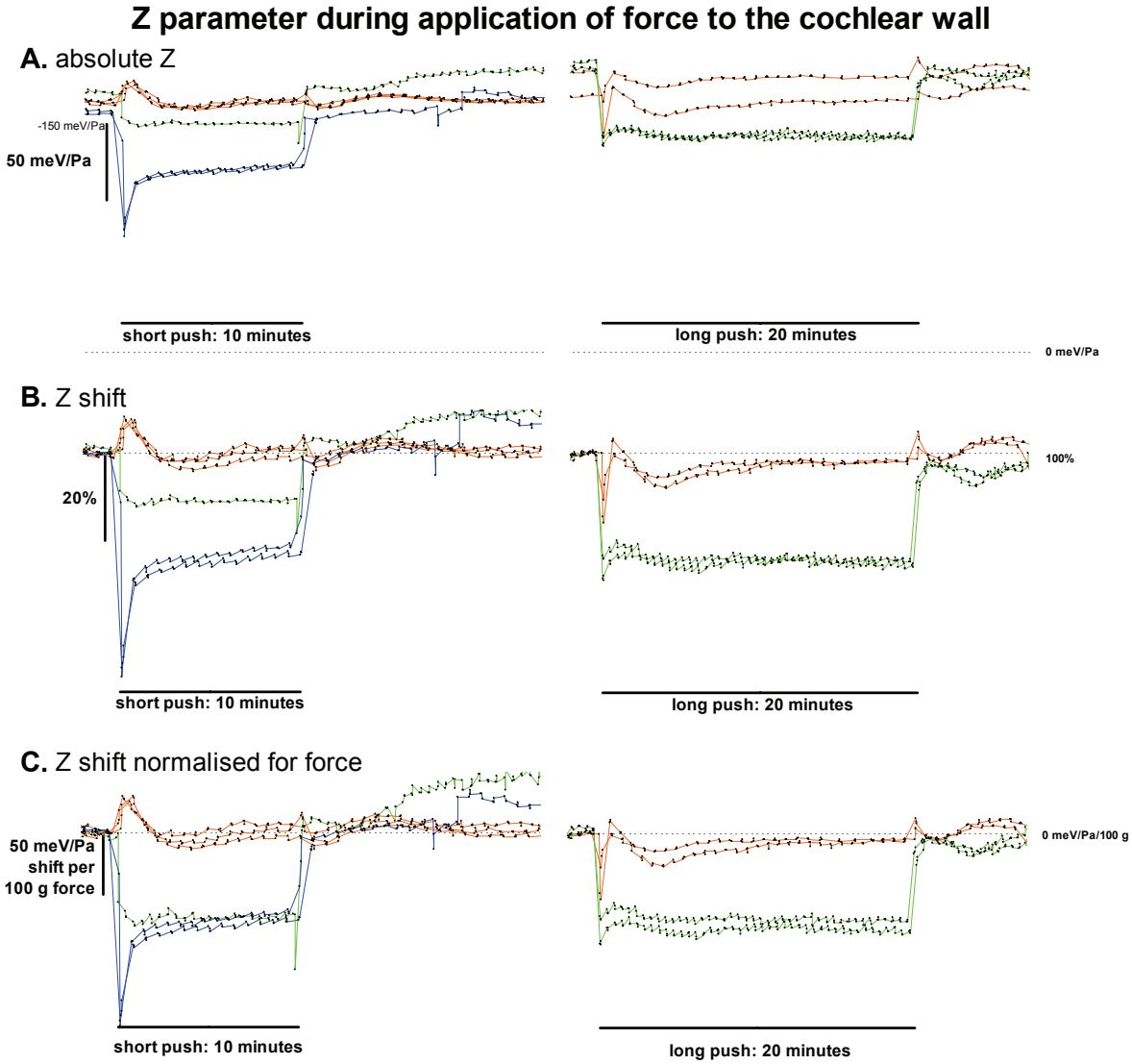

Figure 5.20: A. and **B.** Time courses of changes in the Z parameter in response to 10 minute and 20 minute applications of force to the cochlear wall. The traces are colour-coded by the animal and the level of the probe tone used (green = GP#PS99, 84 dB SPL; orange = GP#PS92, 86 dB SPL, blue = GP#PS91, 88 dB SPL). **C.** Dividing the Z shift by the amplitude of the force applied reduced the variation between the green and blue 10-minute push traces.

The changes in the Z parameter were generally larger than those in Vsat. As shown in Figure 5.20, in 12 out of 15 pushes the magnitude of the Z parameter decreased[5], indicating a reduction in the sensitivity of the MET process or an increase in the stiffness of hair-bundles or the organ of Corti. After 600 s, this proportion was increased to 13 of the 15 pushes. Of the first-turn pushes, the push caused a peak reduction in Z of 22% (± 26%; n = 13), which plateaued to 12% (± 11%; n = 13) below the original value. Unlike the operating point or Vsat parameters, the standard deviation of the pooled Z changes *was* decreased when the changes were normalised by the force applied. This is most clearly visible in Figure 5.20 by comparing the time-courses of GP#91 and GP#99 in Panel B (un-normalised) and Panel C (normalised).

In addition, the Z changes during and after the push fell into two groups – i) those which showed a step-decrease in Z with or without a front-end transient (GP#91, GP#99); or ii) an increase in Z followed by return to pre-push levels, with or without a transient decrease at the front end (GP#92). These two patterns of Z shift also differed in the direction of their off-response oscillations, as described below.

5.6.4 Results - Oscillations in Boltzmann parameters with the push

In general, the onset of the push was not very effective at causing large amplitude oscillations, although small amplitude oscillations were observed. Removal of the push caused large half-cycle oscillations in the operating point and smaller amplitude oscillations in the Z parameter that were twice the frequency of those in the Eo parameter. Interestingly, while the offset oscillations were almost always in the same direction for the operating point (as shown in Figure 5.18), the two types of Z shift shown for the 20-minute pushes in Figure 5.20B (and described above) showed offset oscillations that were in the opposite direction from each other. This is shown in Figure 5.21 below.

The possible mechanism of the differences in these Z shifts between these animals is discussed further in Section 5.6.8 below.

---

[5] Because the Z parameter is a negative number with the particular Boltzmann formula used, the magnitude is referred to here, with a decrease in magnitude meaning a change toward zero.

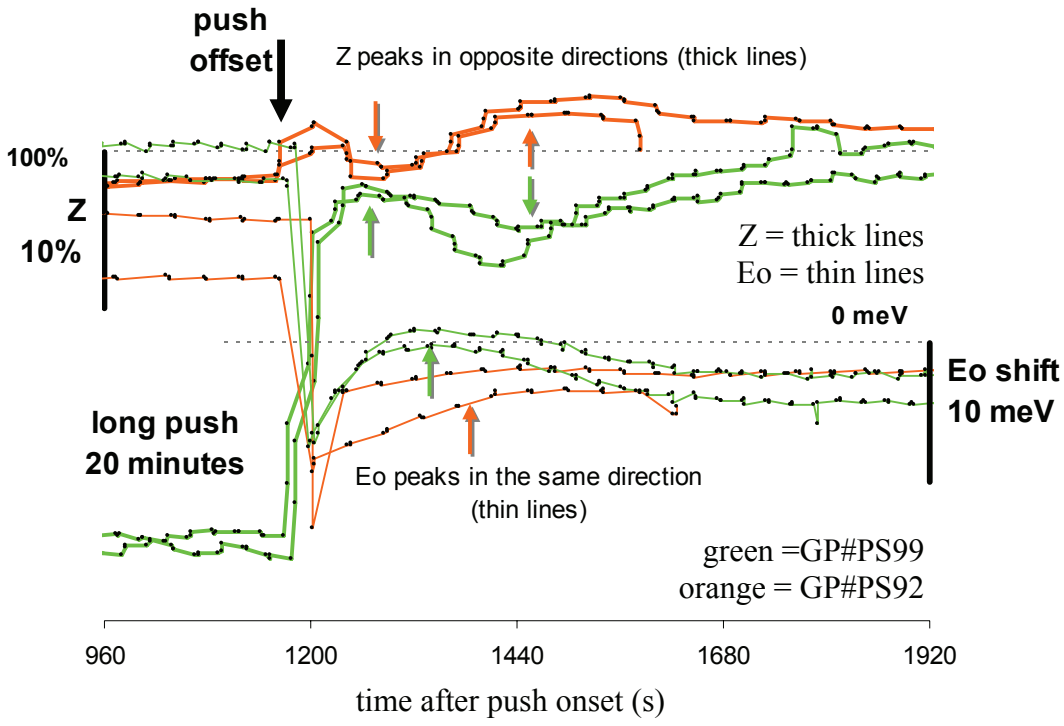

Figure 5.21: Time courses of the offset oscillations in the Z parameter (thick traces) and the operating point (thin traces) following 20-minute applications of force to the cochlear wall. The data has been replotted from Figures 5.18B and 5.20B, and shows the anti-phase oscillations in Z between the two animals, while the operating point oscillations were in the same direction.

5.6.5 Discussion - Changes in the Boltzmann parameters with the push

In summary, the application of force to the cochlear wall did not produce the simple OHC perturbation we had hoped for. Its effects were unlike those produced by any other cochlear perturbation examined during this study. Clearly, the most consistent characteristic of the changes in the Boltzmann parameters was the SV operating point shift, which occurred in every application of force, accompanied in most cases by a degree of adaptation which may be subject to a neural contribution. In most cases, a reduction in the magnitude of the Z was observed, which was in the opposite direction to the Z changes usually seen in perturbations that cause SV operating point shifts. A possible explanation for the Z shifts is discussed in Section 5.6.8 below. The changes in Vsat were also quite variable in magnitude, but with the push causing a decrease in Vsat in 8 out of 10 cases.

We have already shown (in Section 5.6.2 above) that the changes with the push were not consistent with a simple reduction in sound stimulus level. The remaining

possible mechanisms fall into two broad categories: A scala vestibuli operating point shift could be caused by at least two mechanisms – one of which involves a relaxation of OHC motility (an "active" mechanism), and one in which the SV shift was the primary perturbation (that is, a "passive" mechanism in which the basilar membrane was simply pushed towards scala vestibuli, resulting in the hair bundles moving in the direction that opens MET channels). Neither of these two mechanisms is wholly consistent with the changes observed with the push, as described below.

5.6.6 Discussion - The "active relaxation" mechanism

The "active" mechanism would be one in which the SV shift is caused by a relaxation of fast or slow OHC motility in response to an initial primary perturbation. For example, if the primary effect of the push were a reduction in electrical driving potential for potassium into the OHCs, we would expect:

i) a reduction in the current through the OHCs, resulting in a decrease in V_{sat} and CM amplitude [observed in 10 out of 15 pushes];

ii) hyperpolarisation of the OHCs, resulting in OHC elongation and a scala vestibuli operating point shift [observed in every push]; and

iii) an increase in the Z parameter (such as that observed with hypoxia or injection of positive current into scala tympani), indicating an increase in MET sensitivity and/or organ of Corti compliance [observed in 3 out of 15 pushes].

The initial trigger for such a mechanism could be a reduction in the EP, as was observed in four of nine pushes in which the EP was measured. A fall in EP might be expected by this perturbation, because the section of cochlear wall displaced was that overlying the scala tympani of the first turn: this section of cochlear wall is known to contain the collecting venules that drain the capillary areas overlying stria vascularis (Axelsson and Vertes, 1978; Jones-Mumby and Axelsson, 1984), and so their obstruction would be expected to cause a local EP reduction due to a reduced strial blood flow. Another possible mechanism is discussed below.

5.6.7 Discussion - The "passive perturbation" mechanism

The "passive" mechanism would be one in which the OHCs play no *active* part in the SV shift, such as if the primary perturbation were the upward mechanical bias of the organ of Corti, resulting in movement of the hair bundle toward the basal body and opening of MET channels. In this case, we would expect:

i) The SV operating point shift [observed in every push] to cause an increase in apical conductance, and a depolarisation of the OHCs;

ii) a decrease in the Z parameter (MET sensitivity/organ of Corti compliance) such as that observed with injection of negative current into scala tympani [observed in 12 out of 15 pushes]; and

iii) an inflow of calcium, increasing the permeability of the basolateral wall, and causing a slow rise in V_{sat} and CM amplitude [observed in 5 out of 15 pushes].

As a second-order effect, we would expect the depolarisation step to cause a subsequent fast electromotile contraction of the OHCs and/or a slow motile contraction caused by increased intracellular calcium following depolarisation, which may explain the observed "adaptation" of the operating point parameter.

Both of these mechanisms would predict changes similar to those observed experimentally, which may indicate that either one mechanism or the other is dominating in a particular push. In any case, the pattern of changes observed during the push seems odd.

If the "passive perturbation" mechanism were dominant, how could the push cause the initial SV operating point shift? We call it a scala vestibuli shift because, with the usual transverse displacement of the basilar membrane during normal functioning of the cochlea, an operating point shift in the direction that opens MET channels is usually consistent with the movement of the reticular lamina towards scala vestibuli. Such an operating point shift could, however, be brought about by other means. Figure 5.22 shows two such mechanisms, both of which would result in an operating point shift in the direction that causes opening of MET channels. The illustrated changes have been exaggerated for the sake of clarity (the observed operating point shifts would, in reality, equate to nanometre movements of the hair bundle). In Figure 5.22A, the cochlear wall push causes a movement of the reticular lamina towards scala vestibuli, causing an opening of the MET channels by the usual radial shear mechanism encountered with a pressure differential between scala tympani and scala media (for example, with sound). In Figure 5.22B, the push causes a movement of the reticular lamina toward the modiolus while leaving the osseous spiral lamina and the tectorial membrane in place, thereby causing a direct shear of the hair bundles resulting in MET channel opening. Alternatively, the changes could also result from a different mechanism not considered here.

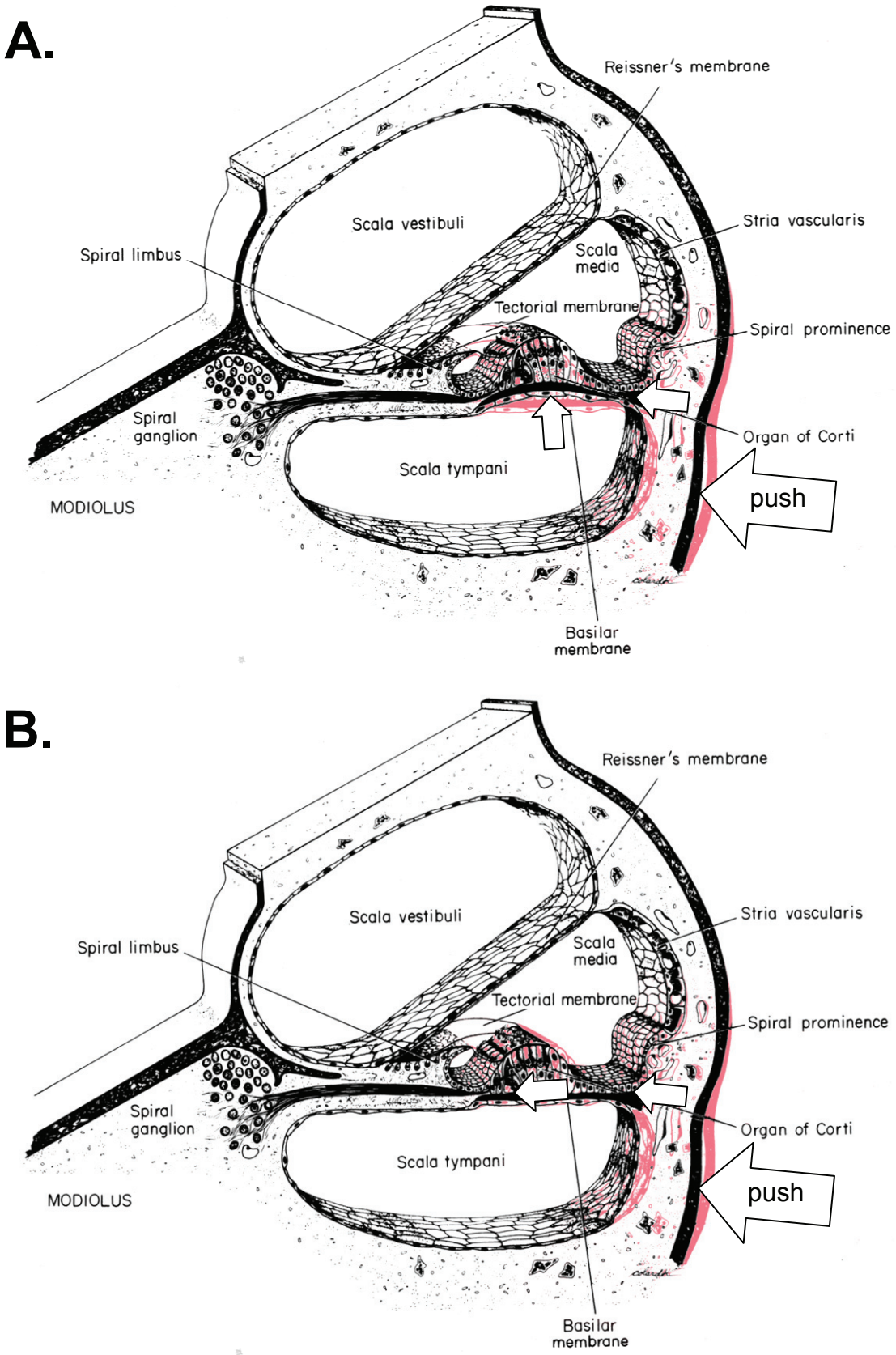

Figure 5.22: Two possible mechanisms for the operating point shift observed with the application of force to the cochlear wall. Deformation of the cochlear wall could cause a scala vestibuli displacement of the basilar membrane (**A**) or could cause a lateral compression of the basilar membrane (**B**). Note: Illustrated changes are highly exaggerated for clarity. Figure adapted from Fawcett (1986).

Although a persistent force or pressure is required in order to statically displace the BM from its resting position (Gummer et al., 1981), the long-lasting SV shift observed with the push is not likely to be produced by an increase in ST hydrostatic pressure, or a decrease in SM hydrostatic pressure. Experiments involving the injection of fluids into the cochlea have shown that such pressure differentials are rapidly dissipated within the cochlea (Takeuchi et al., 1991; Wit et al., 1999). However, the mechanism shown in Figure 5.22A could occur without a pressure differential if it were a direct consequence of the geometric changes (i.e. a "bending" or "buckling" of the BM, rather than a pressure-induced "bulge").

As it is, there does not appear to be enough information to eliminate any of these possible mechanisms – either the active mechanism or the two passive mechanisms. The underlying cause of the changes in cochlear parameters during the push is therefore unknown. However, the available evidence does point to a micromechanical (rather than neural) basis for the observed changes in cochlear sensitivity, as will be discussed in later sections.

5.6.8 Discussion - Changes in MET sensitivity and the Z parameter

As described in the above section, the main difference between the changes observed with the push and with other perturbations that cause a SV operating-point shift was in the direction of the Z changes. Two patterns of Z changes were commonly observed during the push: i) a decrease in Z accompanied by a front-end transient (GP#91, GP#99); or ii) an increase in Z followed by return to pre-push levels, with or without a transient decrease at the front end (GP#92). In addition, as shown in Figure 5.21 above, the offset oscillations in Z were twice the frequency of those in the operating point. This rectification or frequency-doubling relative to the operating point oscillations could result from some sort of movement across a bell-shaped (rather than linear or sigmoidal) transfer curve. The explanation for both i) this difference between the Z shifts during the push and those with other perturbations that cause SV shifts, and ii) the frequency-doubling of the Z oscillations, could rest with the dependence of EMT sensitivity on hair-cell loading.

While the Z parameter is a measure of the sensitivity of the mechanoelectrical transduction process, the saturation feedback model of the active process (Zwicker, 1979) holds that it will also be a measure of the sensitivity of the *electromechanical* transduction process. That is, the sensitivity of the forward transduction process is affected by the contribution to basilar membrane vibration made by the reverse

transduction process. As shown in Figure 5.23 (from Santos-Sacchi, 1992), isolated unloaded OHCs contract with depolarisation, with length changes that follow a Boltzmann function. The slope of the Boltzmann function (shown in Panel B) is such that the sensitivity of the length change to the membrane potential is higher in the depolarising direction (Santos-Sacchi, 1992; He et al., 2003). With this curve, a depolarisation of the hair cell from its resting potential to around -26 mV would result in an increase in the sensitivity of the EMT process, with larger cyclical length changes for a given AC receptor potential than would be produced at more hyperpolarised potentials.

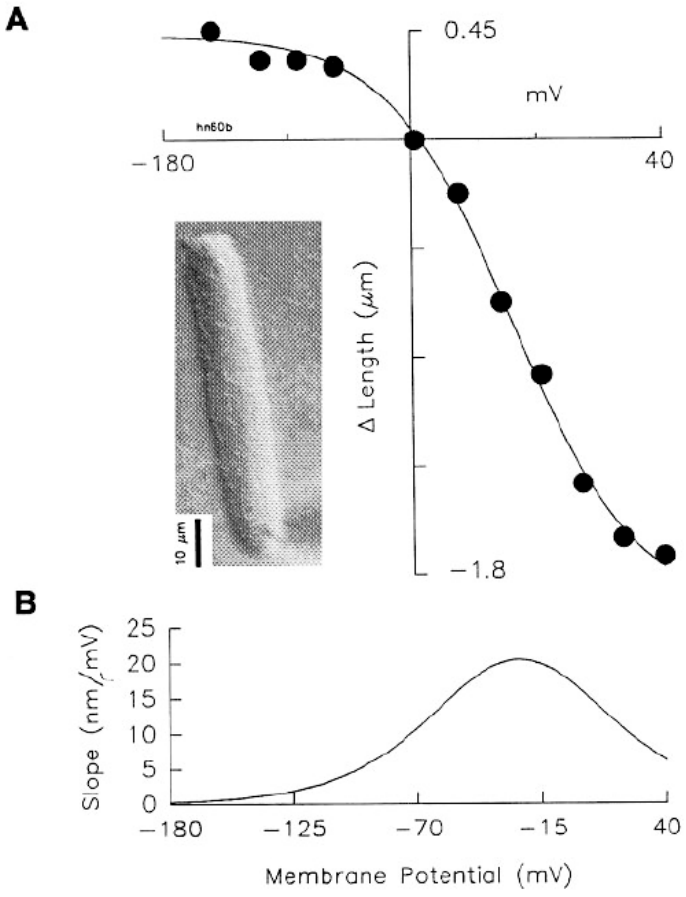

Figure 5.23: Data from Santos-Sacchi (1992) showing the **A.** the length-change of an unloaded, isolated OHC with change in membrane potential, and **B.** the slope of the Boltzmann function fitted to the length-change data. Note that depolarisation from a membrane potential of -70 mV would increase the sensitivity of the length-change to voltage, while a hyperpolarisation from -70 mV reduces this sensitivity.

In vivo, however, the hair cell is under compression between the Deiters' cells and the reticular lamina (RL), and the EMT transfer curve under these circumstances is different. By pre-compressing or pre-stretching the OHC with a stiff fibre, He (2003) showed that the sensitivity function could be altered by the mechanical load. As shown in Figure 5.24, when the cell was placed under compression, the length change saturated more in the depolarising direction. This pattern of responses is consistent with a shift of the sensitivity function towards more negative membrane potentials, as shown schematically in Figure 5.25, such that at the resting membrane potential the OHC lies

on the region of *decreasing* slope. This is likely to be the case *in vivo*, whereby a depolarisation of the hair cell results in a decrease in the sensitivity of the EMT process, resulting in the pattern of Z changes commonly observed with current injection[6].

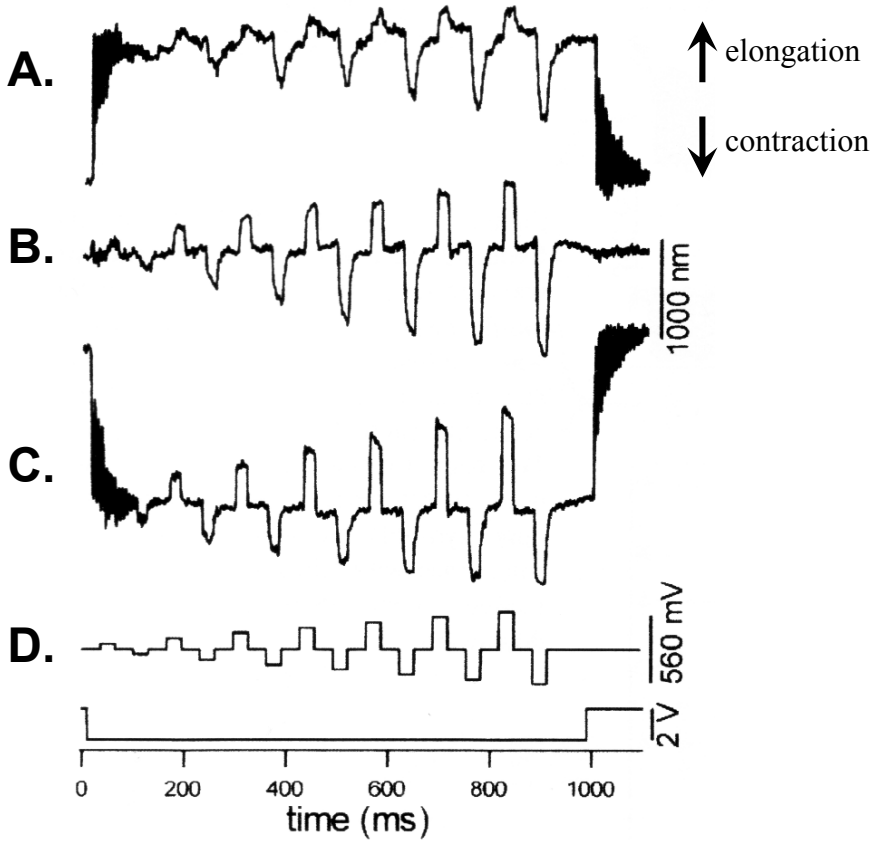

Figure 5.24: Data from He (2003) showing the length-change of an isolated OHC during conditions of **A.** pre-stretching, **B.** unloaded, or **C.** pre-compression, with **D.** change in membrane potential. Note that the under the presumed *in vivo* condition (under pre-compression), the asymmetry is reversed, with the OHC being more sensitive in the elongation direction (see text).

This is illustrated schematically in Figure 5.25. In a normally-loaded *in vivo* OHC, a depolarisation would result in a decrease in sensitivity, as shown in the middle panel, but a reduction in the degree of OHC loading during the push could cause a shift of the bell-curve to the right, as shown in the bottom panel. If we assume that the push causes a depolarisation of the OHCs (as discussed in Section 5.6.7 above), then i) the simple decreases in Z observed in GP#91 and GP#99 could be caused by a relatively *small* change in loading, while ii) a larger change in loading might be sufficient to shift the bell curve such that both an increase *and* decrease in Z is observed (GP#92) as the depolarisation moves the OHC over the peak of the curve.

[6] These current injection results will be described in full in Chapter Seven, but briefly, a ST injection of positive current causes an increase in Z, while a ST injection of negative current causes a decrease in Z).

This scheme could also explain a number of features of the offset oscillations. If we consider the example of the offset oscillations shown in Figure 5.21 above (in which the Z and Eo oscillations from GP#PS92 and GP#PS99 were compared), we can situate two cochleae on different positions on the sensitivity curve of Figure 5.25, such that one is situated on the rising phase with depolarisation (at point A) while the other is situated on the falling phase (at point B). Let us also assume that oscillations in Z are caused by an oscillation in the OHC membrane potential (V_m), while the oscillations in Eo are either also *caused by* the V_m oscillations, or are themselves the cause. Because the two cochleae are on opposite sides of the peak in the sensitivity curve, then the movements of these points along the horizontal axis during the membrane potential oscillations following the push will cause the resulting changes in sensitivity to be out of phase with each other. If the oscillations in membrane potential are large enough, they might be sufficient to move both points A and B over the peak of the sensitivity curve with each cycle, resulting in the frequency of the oscillation in Z being double that of the oscillation in V_m (or the operating point, under electromotile control).

However, while the above sequence of events may provide a possible explanation for the observed changes in Z, it is still uncertain whether or not i) there *was* any change in the loading of the OHC, or ii) any depolarisations (if present) were large enough to cause this degree of movement of the sensitivity curve.

5.6.9 Discussion - Adaptation of the Boltzmann parameters

We have theorised in Section 5.6.7 above that the observed changes in the Boltzmann parameters may have been caused by a depolarisation of the OHCs. This depolarisation would occur via the OHC voltage divider effect, due to a rapid increase in apical conductance causing an increase in the standing current into an outer hair cells.

The observed adaptation of the Boltzmann parameters to the push (particularly the operating point) was consistent with the action of the homeostatic regulation mechanisms modelled in Chapter Two:

i) The assumed depolarisation would increase the activation probability of the basolateral voltage-sensitive Ca^{2+} channels resulting in increased entry of Ca^{2+} into the cell, in accordance with the Goldman-Hodgkin-Katz (GHK) equation.

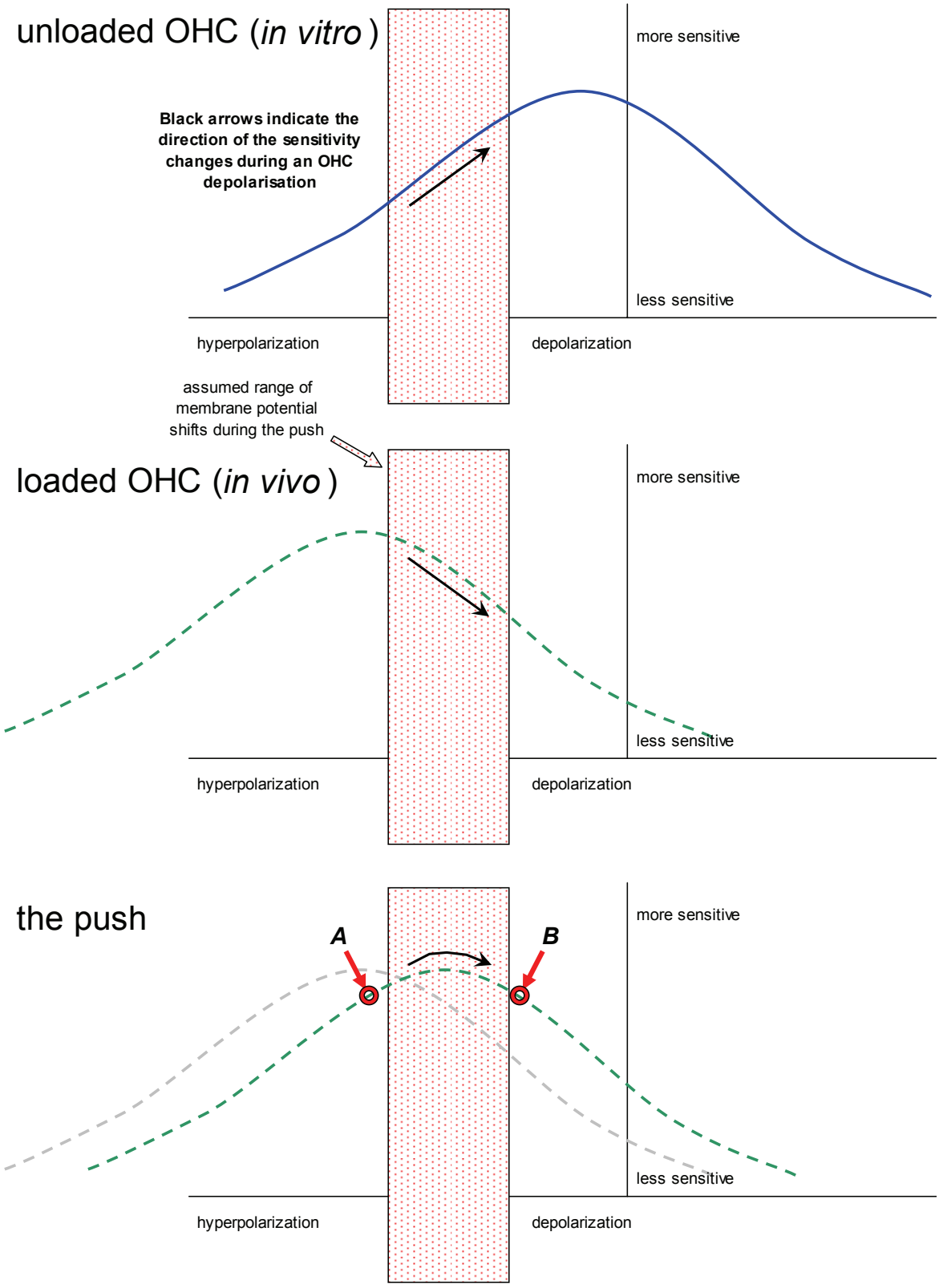

Figure 5.25: A schematic illustration of the changes in the EMT sensitivity curve with loading of the OHC, as described by He (2003). The top panel represents the unloaded situation, similar to that encountered *in vitro* and shown in Figure 5.23 above (from Santos-Sacchi, 1992). The second panel represents the situation encountered *in vitro* where the OHC is wedged between the Deiters' cells and the reticular lamina. The third panel is used to illustrate the possible shifts in this sensitivity curve that could occur with the push. Points A and B represent different cochlear states or loci that would result in different changes in sensitivity with depolarisation and/or loading (see text).

ii) This increased Ca^{2+} flux would integrate to produce an increased intracellular Ca^{2+} concentration, which would in turn produce a contraction of the cell due to the operation of the calcium-dependent slow motility mechanism.

iii) This contraction would result in a shift in operating point towards the scala tympani direction, which would thereby partially compensate for the initial scala vestibuli operating point shift.

Although the onset (but not the offset) transients appeared to be abolished following the application of the sodium channel blocker TTX, it is difficult to make a firm conclusion regarding the reliability of this result, due to the limited amount of TTX data available. Visual inspection of the CM waveforms during the transients did not reveal any obvious increases or decreases in the neural inflections to the waveforms. In any case, the TTX result suggests that the underlying step changes in the Boltzmann parameters, and the transients observed on removal of the push, were not neurally-mediated. Rather than indicating a neural contamination of the CM waveforms, the abolition of the onset transients by TTX may indicate a severing of input to the olivocochlear efferent system. To examine this possibility, the effects of push could be compared during efferent blockade and stimulation.

Although these operating point shifts were in the opposite direction, the time-constants of the observed exponential decays in the operating point were substantially longer than those obtained when artificial endolymph is injected into scala media (1 to 3 seconds; Wit et al., 1999), suggesting a different mechanism was involved.

Regardless of the presence or absence of the onset transients, a SV shift remained throughout the duration of the push. This indicates that, if they exist in mammals, any stereociliary adaptation processes present *in vivo* (Eatock, 2000) must at least have a limited range, such that they are incapable of completely counteracting the effect of this DC stimulus.

5.7 CAP threshold, amplitude, and waveshape

The application of force to the cochlear wall most commonly produced an elevation of CAP thresholds, and a reduction in SP and CAP amplitudes. However, in some cases the opposite occurred, resulting in improvements in tracked CAP threshold, and increases in the amplitudes of the SP and/or CAP.

When a hearing loss did occur, the frequency at which the maximal loss occurred was dependent on the point of contact between the tungsten rod and the otic capsule experiment, which was largely determined by the available geometry (i.e. the relative locations of the bulla hole and the otic capsule within the middle ear).

5.7.1 Results - Changes in CAP threshold and amplitude (summary data)

Panels A, B, and C of Figure 5.26 show audiometric shifts during the push in three different animals. As the rod alignment was slightly different in each animal, the degree of threshold shift and site of maximal loss also differed. Repeat pushes in the same animal with the same probe alignment caused similar-shaped threshold shifts. The threshold shifts were centred around 14 kHz in Panel A, 20-22 kHz in Panel B, and 18-20 kHz in Panel C.

In six of the eight threshold measurements, there was a small (less than 3 dB) improvement in some of the tracked CAP thresholds at frequencies lower than the site of maximal loss. Because there was a small but significant decrease in background SNN during the push (as described in Section 5.4 above), there was the possibility that this improvement in low-frequency tracked threshold may have been artefactual, due to an increase in the SNR encountered by the threshold-tracking algorithm (see Chapter 9). However, as shown in Panel D, the averaged CAP amplitude[7] at these frequencies often also increased, making it more probable that these improvements in sensitivity were not artefactual. At this point it is worth mentioning that the summary data in Figure 5.26 was measured just prior to the removal of the push in each case, and so it incorporates the effects of any homeostatic processes that occurred in the cochlea while the push was in place.

Larger force applications produced threshold shifts over a wider frequency range. As shown in Panel A, a two-fold increase in push magnitude (shown by the bold curve) did not greatly affect the degree of threshold loss at the centre frequency, but did cause larger threshold shifts at adjacent frequencies than did the two smaller pushes (lighter curves).

[7] The N1-P1 measure of CAP amplitude is used in this Chapter.

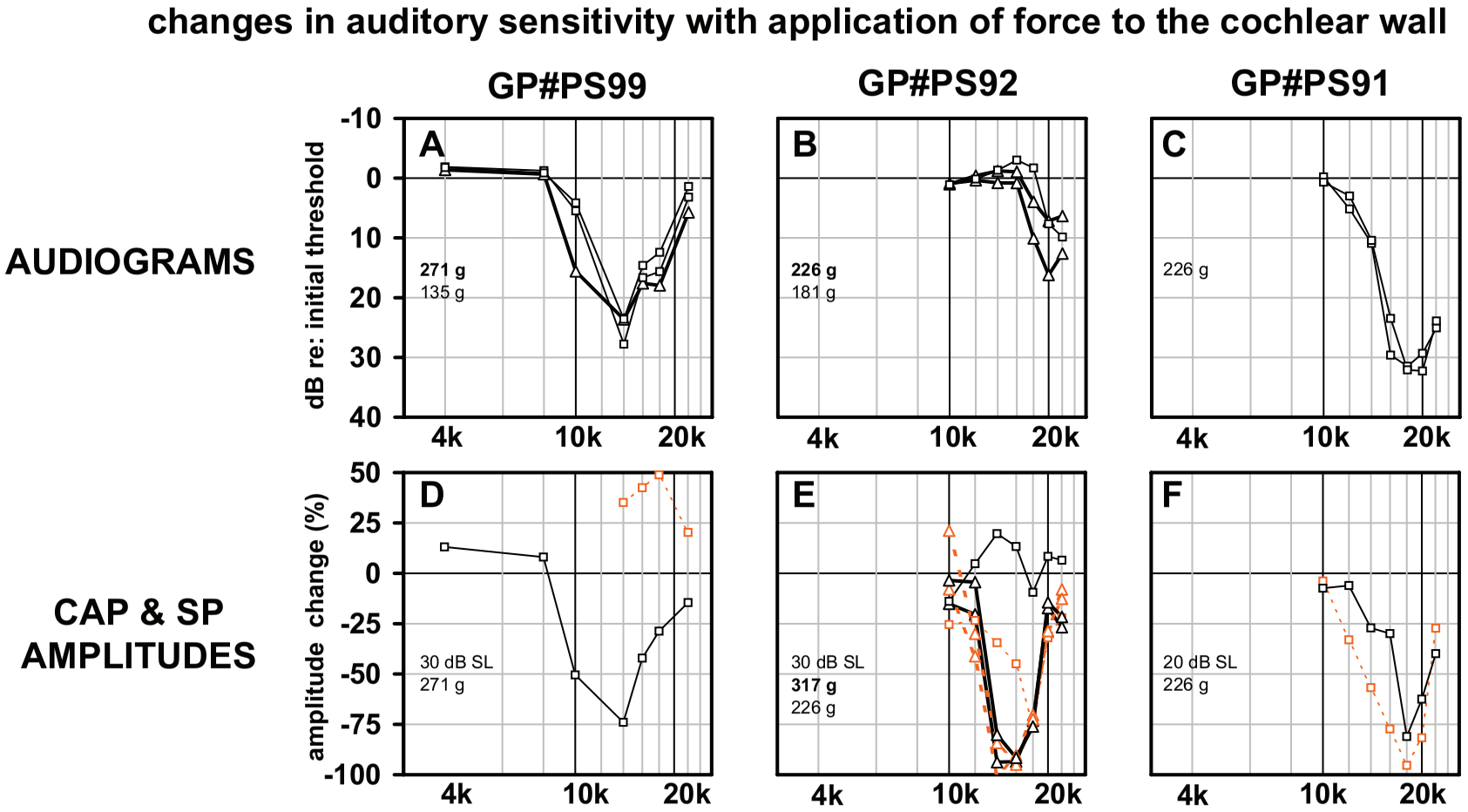

Figure 5.26: Panels **A** to **C** shows the changes in tracked CAP threshold with the push in three different animals, with three slightly different rod placements. Pushes of larger magnitude (bold traces) caused threshold shifts over a wider range. Panels **D** to **F** show the percentage change in CAP amplitude (black solid lines) and SP amplitude (orange dashed lines) in the same three animals. The pattern of the waveshape changes was quite variable - in Panel D, the push caused a decrease in CAP amplitude, but an increase in SP amplitude, while in the 226 g push in Panel E (square symbols), an *increase* in CAP amplitude and a *decrease* in SP amplitude was observed, possibly due to the contribution of a negative SP from the OHCs (see text).

Panels D, E, and F show the percentage changes in CAP amplitude (solid lines) and SP (dashed lines) in these same animals. As would be expected, the maximum hearing loss and maximum loss of CAP amplitude occurred at the same frequency when the same probe alignment was used (e.g. in Panels A and D, and C and F). In Panel E, the probe was in a different position that compared to Panel B, resulting in a different pattern of sensitivity change. In this series, three out of the five applications of force in which supra-threshold waveforms were acquired resulted in a decrease in both the SP and CAP at the region corresponding to the probe alignment. However, one of these five pushes caused a decrease in CAP amplitude but an increase in SP amplitude, while another resulted in a decrease in SP amplitude but an increase in CAP amplitude. The CAP waveforms for these three scenarios are presented in Figures 5.27 to 5.29, and are discussed below.

5.7.2 Results - Changes in CAP waveshape

Figure 5.27 is representative of the changes in CAP waveforms that occurred in three of the five pushes, and corresponds to the amplitude data summarised in Panel F of Figure 5.26. The waveforms shown were evoked at 30 dB above tracked threshold at frequencies of 10, 12, 14, 16, 18, 20 and 22.05 kHz. In previous force applications with this same animal (and with the tungsten rod aligned with the same part of the otic capsule), the maximal loss of CAP threshold was observed between 18 and 20 kHz. In this push, the maximal loss of CAP amplitude occurred at these same frequencies (81% decrease in amplitude at 18 kHz, 63% decrease at 20 kHz), and also corresponded to sites of maximal loss of SP amplitude (95% decrease in amplitude at 18 kHz, 82% decrease at 20 kHz). An increase in N1 peak latency was also observed.

By contrast, in Figure 5.28, the push resulted in an *increase* in SP amplitude and a decrease in CAP amplitude, and corresponds to the amplitude data summarised in Panel D of Figure 5.26. The amount of force applied in this case was larger than that shown in the previous figure (271 g, compared to 226 g in Figure 5.27), and the alignment of the rod was such that prior applications of force had resulted in a maximal CAP threshold loss at 14 kHz. In this instance, however, although there was still a maximal loss of CAP amplitude at this frequency (74% decrease), there was a 35% *increase* in SP amplitude. The CAP amplitudes at 4 kHz and 8 kHz increased slightly during the push, consistent with the improved thresholds at these frequencies shown in Figure 5.26A.

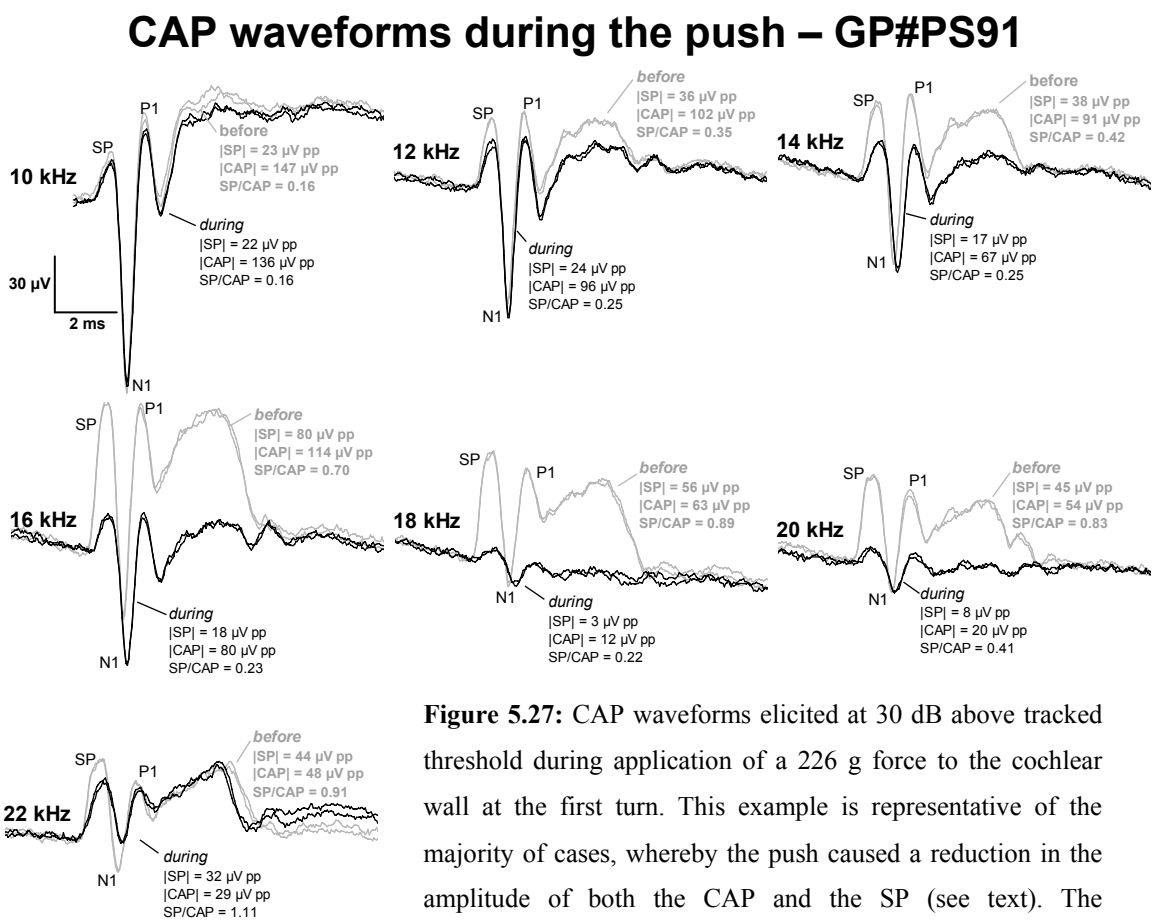

Figure 5.27: CAP waveforms elicited at 30 dB above tracked threshold during application of a 226 g force to the cochlear wall at the first turn. This example is representative of the majority of cases, whereby the push caused a reduction in the amplitude of both the CAP and the SP (see text). The amplitude data is summarised in Figure 5.26 F.
ID#3149727754 - GP#PS91

The improvement in CAP amplitude with a push was more pronounced in Figure 5.29, which shows CAP waveforms recorded before and during a 226 g push. These data correspond to those denoted by square symbols in Figure 5.26E. In this case, the push caused a decrease in CAP amplitude at 10 kHz and 18 kHz, but an increase in CAP amplitude at 12 kHz, 14 kHz, 16 kHz, 20 kHz, and 22 kHz. While a component of these CAP amplitude increases was due to the P1 peak, the amplitude of the N1 peak was increased by 3% at 12 kHz, 13% at 14 kHz and 12% at 16 kHz. The increase in N1 amplitude was also associated with a reduction in peak latency.

Whereas the SP amplitudes fell during the 226 g push at this location, a 316 g push at the same location (some 20 minutes after the withdrawal of the 226 g push) caused a transient increase in SP amplitude at 22 kHz. This is not reflected in the summary data of Figure 5.26E, which was measured just prior to the end of the push. The difference in the 22 kHz time-course between the two pushes is shown in Figure 5.3 above, and in the waveforms of Figure 5.30 below. The EP and DPOAE results of this particular experiment were discussed in Section 5.5 above.

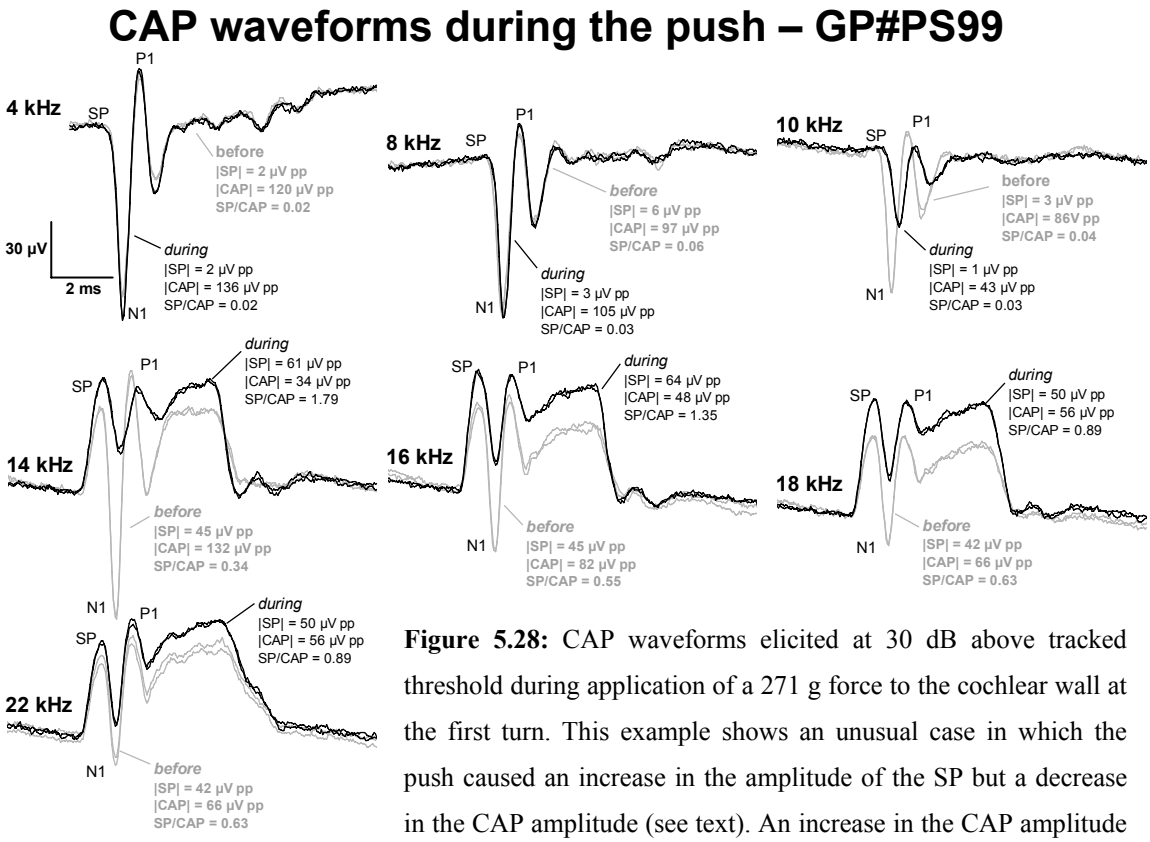

Figure 5.28: CAP waveforms elicited at 30 dB above tracked threshold during application of a 271 g force to the cochlear wall at the first turn. This example shows an unusual case in which the push caused an increase in the amplitude of the SP but a decrease in the CAP amplitude (see text). An increase in the CAP amplitude was seen at 4 kHz and 8 kHz. This amplitude data is summarised in Figure 5.26 D. ID#3151979958 - GP#PS99

5.7.3 Summary of changes in hearing sensitivity and CAP

To summarise, the push produced a fairly localised reduction in neural sensitivity, causing threshold shifts of between 15 and 30 dB. Despite some changes in SP amplitude, the CAP morphology was basically within normal limits, and the reductions in CAP amplitude were accompanied by latency shifts similar to those caused by stimulus reduction. It seems, therefore, that a large part of the CAP threshold shifts are due to mechanical causes, rather than neural changes *per se*. As discussed below, the changes in the Boltzmann parameters describing OHC MET were analysed in detail to determine what could have caused these reductions in mechanical sensitivity.

5.7.4 Discussion - Changes in SP and CAP with the push

The reduction in CAP amplitudes and loss of CAP thresholds in the region affected by the push is most simply explained with a local decrease in the amplitude of basilar membrane vibration. This is also supported by the decrease in SP amplitude in three of the five pushes where supra-threshold averaged response waveforms were obtained; by the concurrent changes in the Boltzmann parameters; and by the latency shifts of the CAP responses.

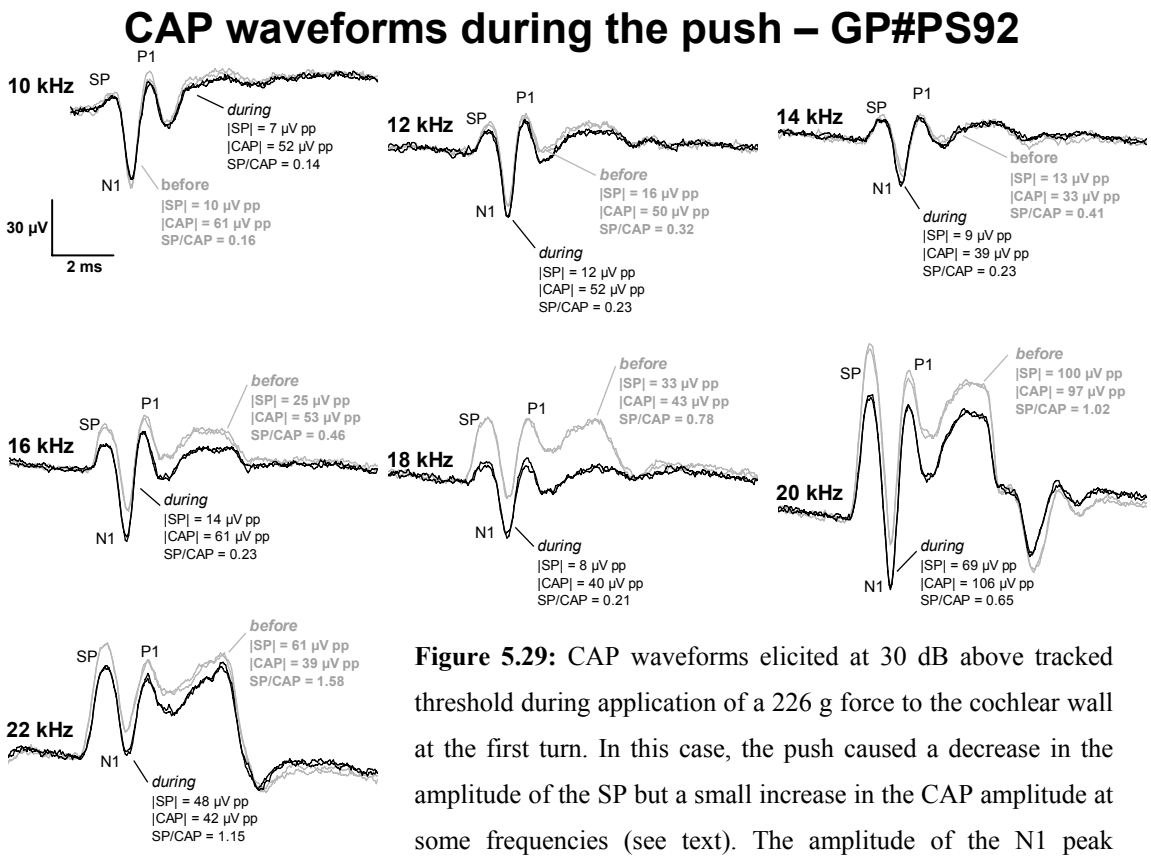

Figure 5.29: CAP waveforms elicited at 30 dB above tracked threshold during application of a 226 g force to the cochlear wall at the first turn. In this case, the push caused a decrease in the amplitude of the SP but a small increase in the CAP amplitude at some frequencies (see text). The amplitude of the N1 peak (measured from the SP) was larger during the push at 12 kHz, 14 kHz, and 16 kHz. This amplitude data is summarised in the light traces of Figure 5.26 E. ID#3150166434 - GP#PS92

The threshold shifts are not consistent with the presence of any masking noise created by the push (for example, due to any "creaking" of the otic capsule or a similar sound), which would have resulted in an increase in SNN. In the event, no significant rise in SNN was observed.

However, in the cases where an increase in CAP sensitivity is observed, the interpretation is slightly more complicated. As discussed in Chapter 2, the MET process could theoretically be improved by the SV Eo shift observed during the push if the quiescent operating point were situated on the scala tympani side of optimal. In the example shown in Figure 5.3, where both the CAP amplitude and the $2f_1$-f_2 emission were increased during the push, the measured initial pre-push operating point was more "towards scala tympani" than was usual for other animals in that series of experiments (-4.4 meV, compared to an average of -1.7 ± 2.8 meV), indicating that this "operating-point optimisation" mechanism is plausible.

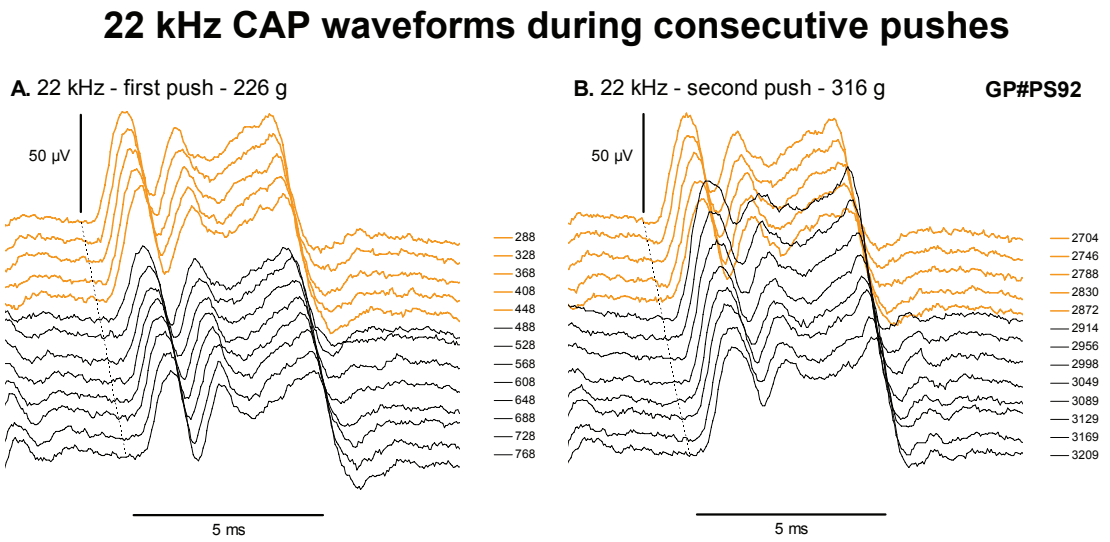

Figure 5.30: These waterfall plots show consecutive 22 kHz CAP waveforms (20 dB SL) at the onset of the push (transition from orange to black traces). The first push of 226 g caused a decrease in SP amplitude and an increase in CAP amplitude, while the second push (316 g) caused an increase in SP but a decrease in CAP (see text). The legends show the time co-ordinate (in seconds) for each trace to allow comparison with the amplitude time-traces for these waveforms shown in Figure 5.3.
ID#3150166434 - GP#PS92

Another possible explanation for the threshold improvement, and in particular the improvements seen for the low CFs in the cochlear apex during a basal turn push, is that the application of the push caused some form of release from the effects of neurotransmitter rundown. Although the SNN amplitude is proportional to both the spontaneous neural firing rate and the resonance of the primary afferent unitary response waveform (Patuzzi et al., 2004), the small drop in the SNN measured from the round window may understate a larger decrease in spontaneous activity in the apical turns. The presumed decrease in spontaneous activity may have reduced the depletion of neurotransmitter stores and increased spike security for stimuli near threshold level. However, the reduction in SNN does not appear to be correlated with EP, which also rose on occasions.

Given that the push appears to exert a mechanical, rather than solely neural, effect, and that both increases and decreases in SP and CAP were observed, what could the possible causes of the different response patterns be?

The relative changes in the detection threshold of the SP and CAP can be used as a tool to separate solely neural effects from mechanical effects: we presume that a mechanical disturbance will cause an elevation in both CAP threshold and SP detection threshold, while a neural disturbance alone will elevate CAP threshold more than SP detection threshold. As SP detection threshold was not measured during these

experiments, we are left to interpret SP amplitude, which is a more complicated measure. In addition to the dependence of SP amplitude on the amplitude of basilar membrane vibration, it can also be affected by the EP, and the membrane potential of the IHCs. The OHCs can also contribute to the RW SP if their operating point is significantly non-zero (i.e. if there is a DC component to the OHC receptor current): A scala tympani operating point will yield a RW-positive SP similar to that which originates from the IHCs. However, during the push, the operating point shifts were consistently in the scala vestibuli direction, which would contribute a negative SP to the RW waveforms. This would be consistent with the data of Klis and Smoorenburg (1985), who showed a reduction in SP amplitude during the SV phase of a low-frequency bias tone.

In short, because the sensitivity changes are most likely of a mechanical origin, the following scheme may explain the observed CAP and SP changes:

i) a decrease in both CAP and SP amplitudes may result from a reduction in BM vibration (with an additional negative-SP contribution from SV-biased OHCs);

ii) an increase in CAP amplitude but a decrease in SP amplitude may be due to improved BM vibration (due to a "more optimal" operating point, as discussed earlier) combined with a negative SP contribution from the SV-biased OHCs;

iii) a decrease in CAP amplitude but an increase in SP amplitude may be due to a reduction in BM vibration combined with a possible elevation of EP, increasing the driving potential for K^+ through IHCs. While an increase in the EP would cause an increase in SP, the EP was not measured in the case where an increase in SP amplitude was observed.

5.8 Summary

The technique of applying force to the cochlear wall was developed with the aim of producing a large mechanical step-perturbation that would elicit some sort of regulatory oscillation. In the event, the push was not a particularly effective method of eliciting cochlear oscillations. However, the other effects it produced were interesting, if somewhat unpredictable.

The application of force to the cochlear wall was found to produce a significant operating point shift towards scala vestibuli, although the means by which this occurred is unknown. However, the subsequent effects of the push are consistent with a depolarisation of the OHCs arising from the opening of MET channels in the apex of

the OHC. The push also caused very localised reduction in basilar membrane vibration, causing a threshold shift of around 15 to 30 dB. In human audiometry, a 20 dB hearing loss is enough to pass a screening test. The fact that a deformation of the wall of the cochlea using forces a quarter of that required to crack the otic capsule produces a maximal hearing loss no greater than 35 dB is surprising, and illustrates just how resilient the cochlea is to DC mechanical stimuli.

In addition, the CAP waveshape is not drastically changed during the push, despite some changes in SP. The available evidence supports a mechanical change, rather than a neural effect *per se*.

Chapter 6
The low-frequency “bounce” phenomenon

6. The low-frequency "bounce" phenomenon

6.1 Introduction

As discussed in Chapters 1 and 2, the "bounce" phenomenon is the name given to the cochlear oscillations following LF stimulation that are observed in a number of measures of cochlear function. The ability of intense low-frequency acoustic stimulation to produce oscillations in hearing sensitivity was first noted during psychophysical experiments by Hirsch and Ward (1952). This line of research has been developed and elaborated upon by other groups over the past 40 years, in both human and animal subjects (see, for example, Hughes, 1954; Hirsch and Bilger, 1955; Zwicker and Hesse, 1984; Patuzzi and Wareing, 2002; Salt, 2004). Observations by Kirk (1972) of bounce oscillations in the EP were confirmed by Kirk and Patuzzi (1997) and Salt (2004), and were found to possess temporal characteristics similar to those of psychophysical measures of transient tinnitus (Wareing, 2001; Patuzzi and Wareing, 2002; see also Hughes and Rosenblith, 1957, and Kemp, 1986). In addition to the presence of the bounce in the EP, observations of bounces in measures of hair-cell function, such as TEOAEs (Kemp, 1982; 1986), f_2-f_1 DPOAEs (Kirk and Patuzzi, 1997), and the Boltzmann parameters describing the low-frequency CM (even in the presence of the neural blocker TTX; Kirk et al., 1997), have confirmed that the bounce is cochlear, rather than neural or central, in origin.

Boltzmann analysis of the 200 Hz CM (Kirk et al., 1997) has previously shown transient decreases in Vsat following the offset of the stimulating tone, occurring concurrently with a movement of the operating point towards scala tympani. These changes in operating point were reflected in the f_2-f_1 DPOAEs, and were proposed to be the cause of the transient hypersensitivity (Kirk and Patuzzi, 1997), being produced by an osmotic imbalance or fluid disturbance. Recent work by Salt (2004) has documented the development of transient endolymphatic hydrops following intense low-frequency stimulation, but concludes that this hydrops is a consequence, rather than a cause, of the ST operating point shift.

In addition to the single cycle, or even half-cycle, of oscillation in hearing threshold commonly reported with the bounce, psychophysical studies have shown the degree of damping of the oscillation can vary between subjects and between experiments (Wareing, 2001; Patuzzi and Wareing, 2002), resulting in the prolonged oscillations that

last for many cycles. We suggest here that both phenomena are produced by the same mechanism.

This chapter reviews the above findings in the context of the mathematical model discussed in Chapter Two, and presents a small amount of new data from 3 animals. In one of these animals (GP#69), CAP threshold at multiple frequencies were monitored simultaneously with the Boltzmann parameters, while in the other two animals (GP#52 and GP#122) only one or the other of these measures was performed. The aim of this set of experiments was to determine which cochlear processes were the dominant cause of the "bounce" oscillations described above. The available evidence, presented in this chapter, suggests that the dominant mechanism for the cochlear gain changes observed with the bounce is likely to be an oscillation in the basolateral permeability of the OHCs, with the influence of operating point on the oscillations in cochlear sensitivity being limited in some cases.

6.2 Methods

6.2.1 Electrode placement

CM waveforms were recorded using a chlorided silver wire on the round window, with reference to an indifferent electrode in the temporalis muscle. As the CM produced by low-frequency tones is primarily generated in the basal turn of the cochlea (Patuzzi et al., 1989b), the round window electrode was appropriately placed to record CM waveforms from this region. Other features of the experimental setup and recording system were presented in Chapter Three.

6.2.2 Stimulus delivery and data acquisition

The custom-written data-acquisition software described in Chapter Four was used for the majority of the data collected here. In addition, the bounce was studied using modified software that was developed to allow extraction of the Boltzmann parameters from a 207 Hz CM waveform in the presence of a very-low-frequency (VLF) tone (of approximately 13 Hz). In these cases, both the 207 Hz and 13 Hz stimuli were of a longer duration than those used elsewhere in the project (1 second, as opposed to 50 ms). The modified software was written for a series of experiments (not presented here) that called for Boltzmann analysis of 207 Hz CM waveforms at different phases of a 13 Hz acoustic bias tone, and so had the capability of delivering both of these stimuli while carrying out the required analysis. Because both the prolonged probe tone and the

presence of the bias tone elicited bounce oscillations that are presented in this chapter, a brief discussion of the different stimuli and the sound system is warranted.

The acoustic stimulus consisted of a 12.94 Hz bias tone to create a slow movement of the organ of Corti, and a 207.04 Hz probe tone to elicit a cochlear microphonic for Boltzmann analysis. The frequencies were chosen so that the ratio of the bias frequency to the probe frequency was 1:16, and the periods of both the bias and the probe were integer numbers of samples (3408 and 213 points, respectively) at the sampling frequency of 44100 Hz. The stimulus produced was 1000 ms in length, and had a rise-fall time of two cycles of the bias tone (154.56 ms). The levels of the bias and probe tones could be adjusted separately, and were produced on separate channels of the soundcard output for delivery to the drivers, which are described below. A synchronisation pulse was placed on the probe tone channel to enable the timing of the data acquisition to be established.

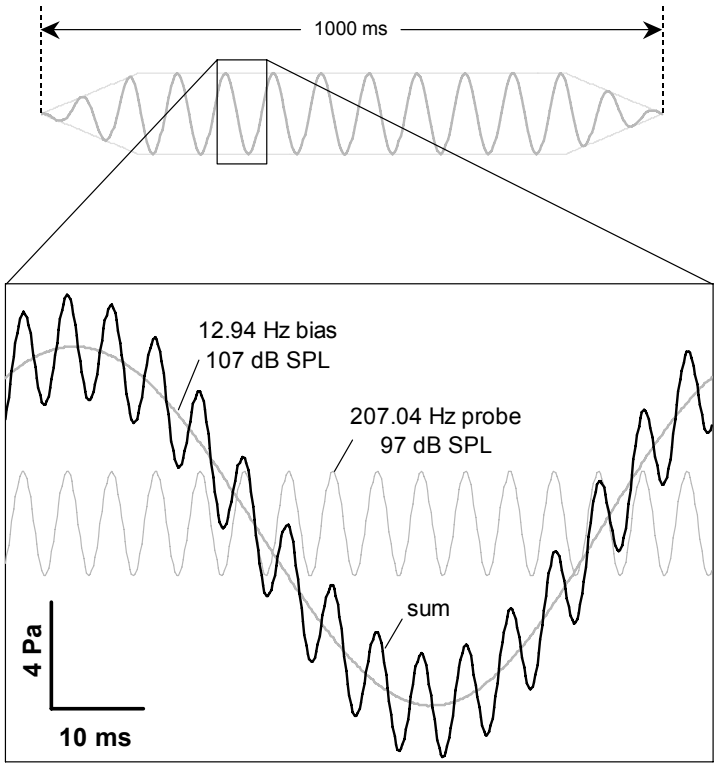

Figure 6.1: A schematic diagram of the compound acoustic stimulus used to enable measurement of the 207 Hz microphonic during very-low-frequency biasing of the cochlear partition by a 13 Hz tone.

A 12” polypropylene loudspeaker was used to produce a 12.94 Hz bias tone, while a smaller low-frequency driver was used to generate a 207.04 Hz probe tone. The signals were mixed acoustically to avoid any nonlinear interactions in the amplifiers. Air leakage was reduced by sealing the 12” loudspeaker around its edges to a thick fibreboard faceplate using silicone (RTV-102, GE Plastics, VIC, Australia). The

loudspeaker was coupled to the ear cone by a 25 cm length of tubing (5 mm outer diameter, 3 mm inner diameter) that was also sealed with silicone.

The parts of the CM waveform evoked with the rise-fall portion of the stimulus were discarded, and the remaining waveform was divided into nine segments corresponding to the nine full cycles of the bias tone. These were then averaged into a single waveform, increasing the signal-to-noise ratio by a factor of 3. Within this averaged waveform were 16 cycles of the 207.04 Hz CM, each of which were processed separately by the modified Boltzmann-analysis software, producing fitted Boltzmann parameters for each 22.5º phase interval of the bias tone. In the analyses presented here, the 22.5º segment of the 207 Hz CM waveform from which the Boltzmann parameters were extracted was the one in which the pseudo-DC bias produced by the 13 Hz tone was closest to a zero-crossing.

6.3 Results

6.3.1 Bounces in CAP thresholds and Boltzmann parameters

Oscillations in neural threshold following low-frequency acoustic stimulation were examined using custom-written data-acquisition software, enabling the oscillations in CAP threshold at multiple frequency regions to be compared with simultaneously-recorded 207 Hz Boltzmann data.

Figure 6.2 shows CAP data recorded concurrently with the Boltzmann parameters in an animal with an elevated 18 and 22 kHz thresholds. Two-minute exposures to a continuous 207 Hz tone at 101 dB SPL caused transient improvements in neural sensitivity of up to 5 dB at 14 and 22 kHz, with smaller bounces of between 2 and 3 dB occurring at frequencies down to 4 kHz. Two traces (recorded 16 minutes apart) are overlaid, demonstrating the reproducibility of the effect in this animal.

Prior to the transient hypersensitivity was an initial period of reduced sensitivity (up to 5 dB at 22 kHz), which corresponded to an elevation in Vsat of between 6% and 10%, a 5% reduction in Z, and an average 4.2 meV shift in operating point towards scala tympani. The peak of the CAP *hypersensitivity* (the “bounce” occurring at approximately 120 seconds after the end of the continuous tone) occurred concurrently with a local minimum in Vsat, and also with the point at which the operating point had recovered to the plateau level following the initial ST shift.

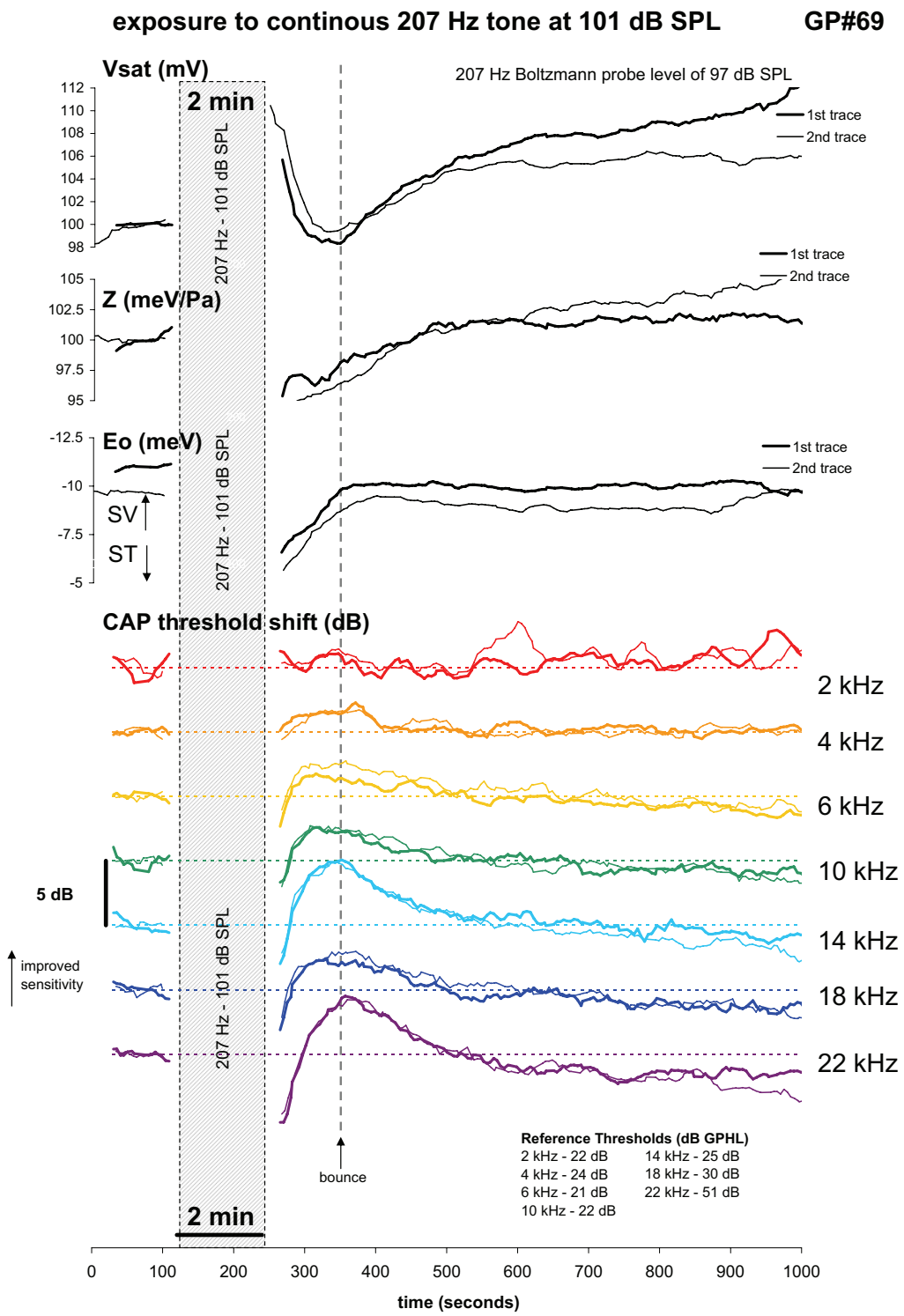

Figure 6.2: Example of the bounce in the CAP thresholds in a deteriorating animal, with the accompanying Boltzmann data. Exposure to an intense low-frequency tone caused an initial loss of hearing sensitivity (as determined by tracked CAP threshold), followed by a transient improvement in sensitivity around two minutes following the end of the exposure (indicated by the vertical dashed line). The largest bounces (approx. 5 dB) occurred at 22 kHz and 14 kHz, with smaller bounces of between 2 and 3 dB occurring at frequencies down to 4 kHz. The peak in the enhancement of CAP sensitivity corresponded to a local minimum in Vsat, and the point at which the operating point recovered to the plateau level following the tone.

ID#3118376594 - Thresholds (dB GPHL; 2 kHz to 22 kHz): 22, 24, 21, 22, 25, 30, 51.
7-point running average on Boltzmann data (97 dB SPL)

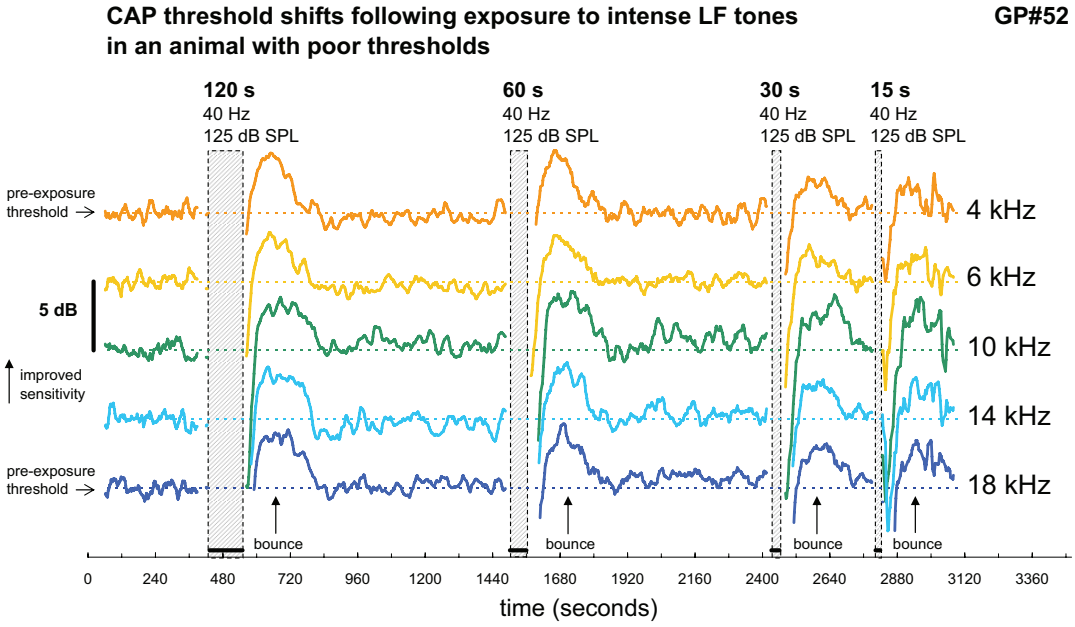

Figure 6.3: Tracked CAP thresholds during 125 dB SPL 40 Hz exposures of decreasing duration, in an animal with poor thresholds. The threshold traces are spaced apart vertically by 5 dB, with the pre-exposure threshold references indicated by the horizontal dashed lines. The "bounce" in threshold is clearly visible: Following each exposure was an initial loss of sensitivity, followed by a transient improvement in hearing thresholds peaking one minute after the end of each exposure.
ID#3108356469. 11-point running average
Thresholds (4 kHz to 18 kHz, dB GPHL): 40, 35, 53, 66, 61.

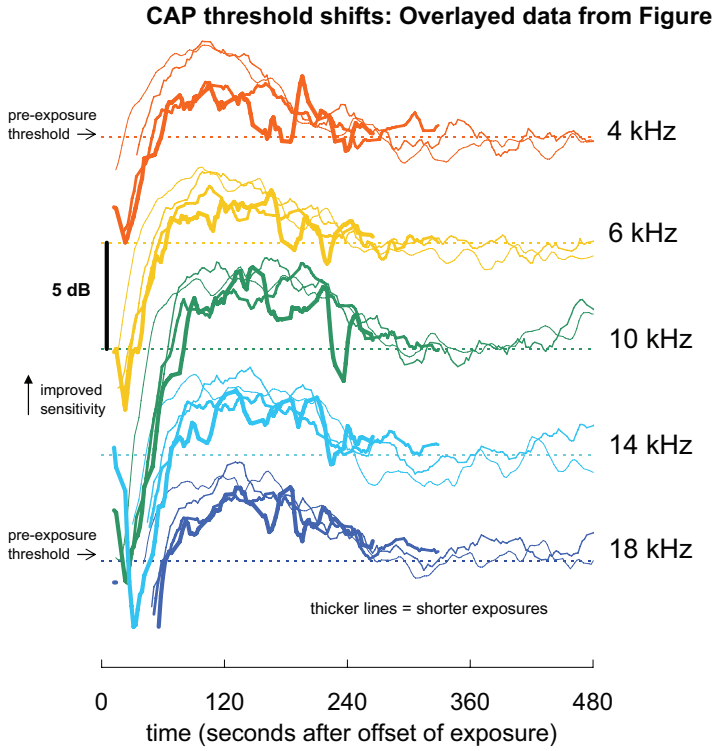

Figure 6.4: Overlaying the plots from Figure 6.3 reveals that reducing the duration of the exposure by a factor of eight did not affect the timing of the bounce, although the shorter duration exposures (thicker lines) resulted in smaller amplitude bounces at some frequencies. The timing of the bounce (the frequency of the over-damped oscillation) did appear to vary with probe frequency, with the 4 kHz and 6 kHz traces peaking before the more basal frequencies.
ID#3108356469. 11-pt running ave

A comparison of the degree of correlation between the CAP thresholds and the Boltzmann parameters revealed a closer correlation between the CAP bounces and the Vsat parameter, with Pearson product-moment correlation coefficients (r) of 0.87, 0.81, and 0.84 for 14 kHz, 18 kHz and 22 kHz. This correlation was higher than that measured between the CAP threshold shift and the Z parameter (mean r value of 0.34 ± 0.11 for those frequencies), or the CAP threshold shift and the operating point (mean r value of 0.29 ± 0.13 for those frequencies).

Further data showing a series of bounces in CAP thresholds is presented in Figure 6.3. In contrast to the previous figure, the CAP responses in this animal were recorded in the absence of a concurrent 207 Hz probe tone (i.e. no Boltzmann parameters were recorded during the experiment). Despite the animal having poor thresholds (an average hearing loss of 50 dB between 4 kHz and 18 kHz), clear bounces in CAP thresholds were produced by 125 dB SPL 40 Hz exposures of different durations: The first exposure (of 120 seconds) produced average peak improvements in thresholds of 4.2 dB (± 0.5 dB) at frequencies between 4 kHz and 18 kHz, with the peaks in neural sensitivity occurring at approximately 110 s (± 14 s) following the offset of the exposure. As shown in this Figure, and in the overlaid traces of Figure 6.4, reduction of the duration of subsequent exposures by up to a factor of eight did not significantly alter the timing of this peak in sensitivity. However, at some frequencies (such as 4 kHz), the shorter duration exposures produced bounces that were approximately half the amplitude of those caused by longer-duration exposures.

6.3.2 Bounces and oscillations in Boltzmann parameters

In contrast to the oscillations in the Boltzmann parameters shown in Figure 6.2 (which were measured using a 50-ms 207 Hz probe tone-burst), presented in this section are data recorded from one animal in which a *1-second* 207 Hz probe tone-burst was used, and in which a 13 Hz bias tone-burst was presented either intermittently or continuously. Because of the different software used for these experiments, no threshold data were recorded. The two protocols are shown in Figures 6.5 below.

Figure 6.6 shows two sets of oscillations in the Boltzmann parameters that were triggered by 1-minute exposures to the 13 Hz bias tone at 119 dB SPL. The Boltzmann parameters were extracted from a segment of CM that was closest to the zero-crossing of the CM amplitude and Eo modulation patterns (the 22.5º segment), which allowed the amplitude of the CM to be measured as if the bias tone were not present. The largest oscillations were shown in the CM amplitude and Vsat parameters, which went through

three complete cycles of a decaying oscillation following the first exposure. The second presentation caused CM amplitude to rise by 4% during the 60 second presentation period, and began to decrease before the bias tone was ceased. After the offset of the tone, the CM amplitude fell to 2% below the pre-presentation value (2.3 mV), reaching a minimum at 60 seconds post-offset, before oscillating around the pre-presentation value in a highly damped manner.

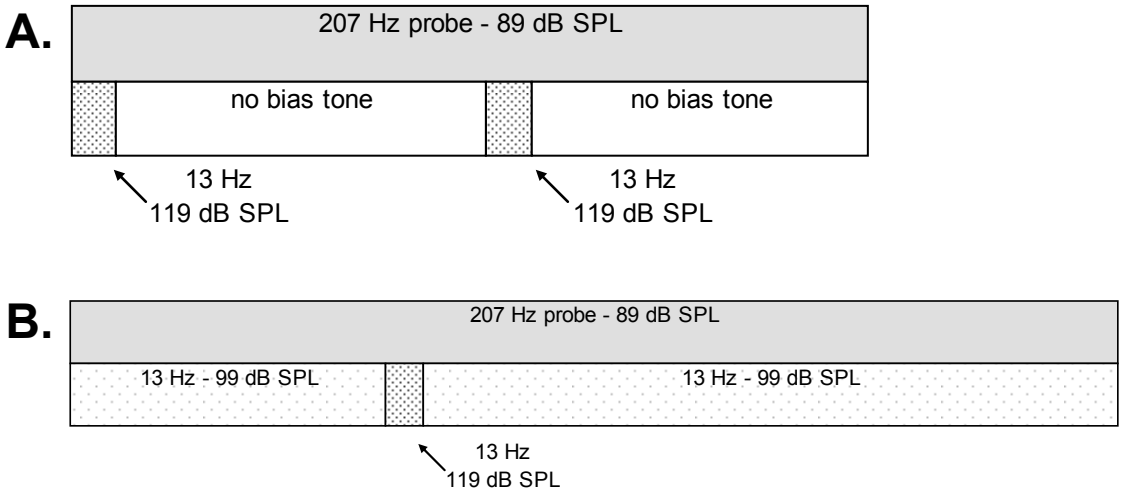

Figure 6.5: Schematic diagram of two stimulus protocols used to obtain the data presented in this section. **A.** To elicit the data shown in Figure 6.6, 1-second 207 Hz probe tone-bursts were at 89 dB SPL throughout, while 1-second 13 Hz bias tone-bursts were presented at 119 dB SPL for 1 minute periods. **B.** The data shown in Figure 6.7 were also recorded with 1-second 207 Hz probe tone-bursts at 89 dB SPL, but used a different protocol, in which 1-second 13 Hz bias tone-bursts were present throughout,. The level of the bias tone-bursts was increased from 99 dB SPL to 119 dB SPL for a 1 minute.

The operating point showed a 4 meV "adaptation" shift toward ST over a 10 minute period in response to the onset of the tones, with the oscillations superimposed on this baseline. There were also differences in the timing of the peaks in the Vsat and Eo parameters: After the first exposure of Figure 6.6, the minimum peak in Vsat occurred around 120 s, followed by a local maximum peak at around 230 s, while the SV peak in Eo occurred roughly midway between these at 180 s. Similarly, after the second exposure, the Eo SV peak occurred at 870 s, midway between the Vsat peaks at 820 and 930 s. This lag is equivalent to a (positive or negative) 90º phase shift between the two parameters.

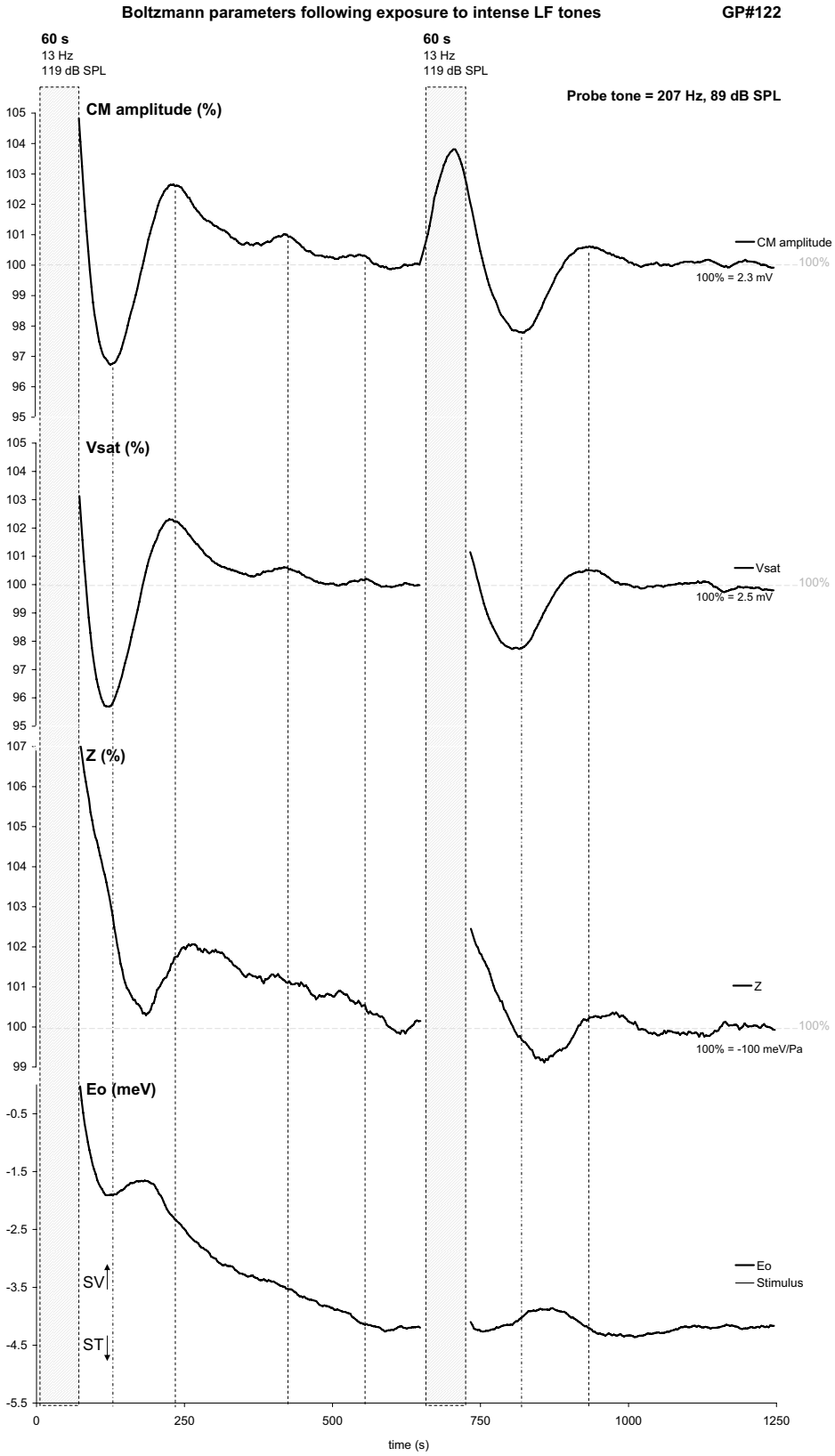

Figure 6.6: Damped oscillations in the Boltzmann parameters were observed following two 60-second exposures to 13 Hz tones of 119 dB SPL. The CM amplitude (measured at a zero-crossing of the bias tone) increased during the the presentation of the second bias tone, and began to decrease prior to the end of the bias. Measurements were not made during the first tone. The dashed vertical lines enable comparison of the peaks in the CM amplitude with those in the Boltzmann parameters. The "100%" reference refers to the level immediate prior to the *second* exposure.

ID#3167358972 - 9-point running average

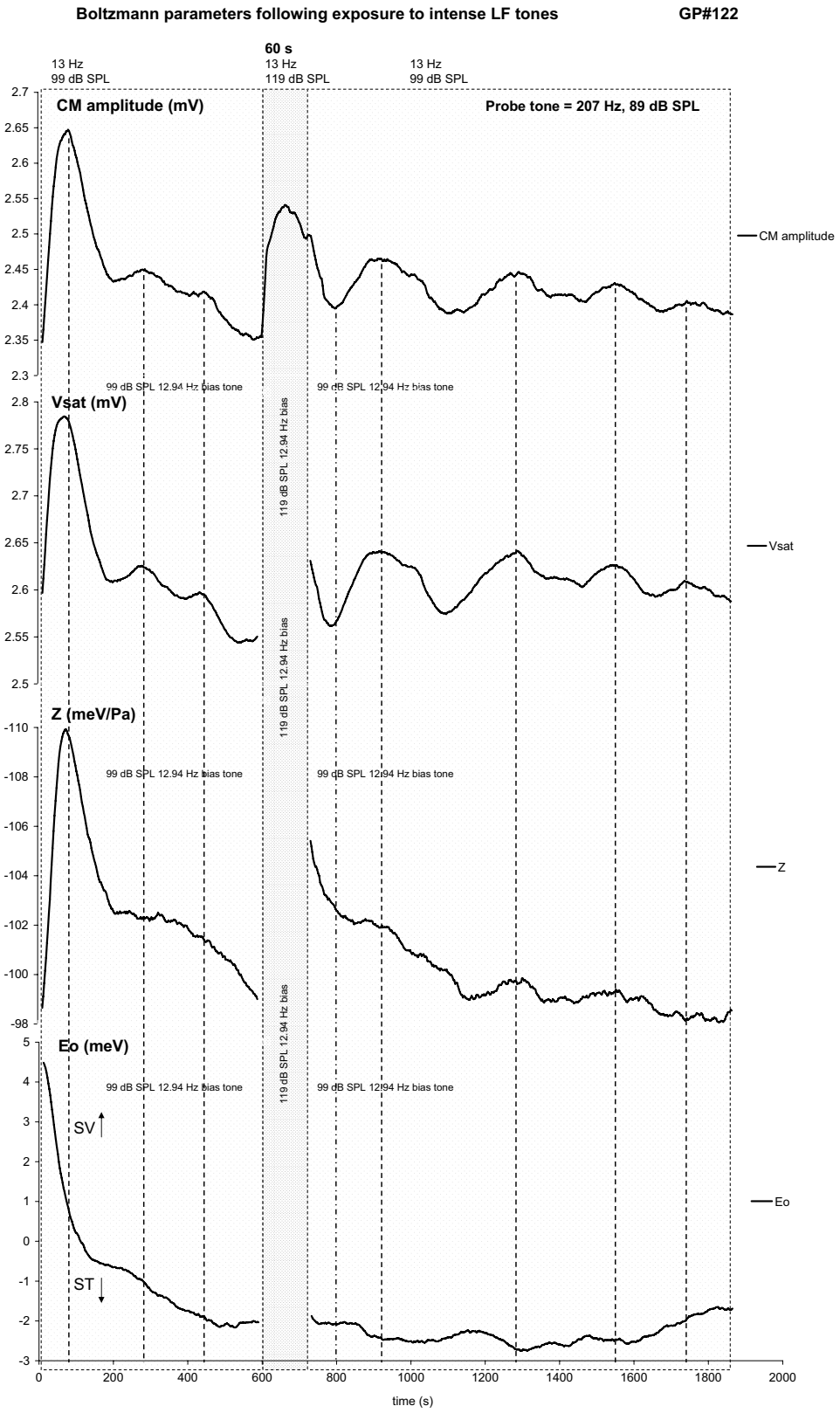

Figure 6.7: Oscillations in the Boltzmann parameters in the presence of an intense VLF tone. The oscillations were highly visible in the Vsat parameter, but were muted in Z and Eo, indicating that the oscillation mechanism was affecting the basolateral wall to a greater degree than the hair bundle. The multiple traces represent the Boltzmann parameters at 16 different phases of the bias tone. After being in silence for four minutes, the onset of the 207.04 Hz probe and the 12.94 Hz bias tone caused an operating point shift toward ST, and a transient rise in Vsat and Z, which recovered in an oscillatory manner. Increasing the VLF tone amplitude by 20 dB for two minutes caused an increase in the amplitude of the oscillations (see text).

ID#3167361573 - 9-point running average

While the oscillations in Figure 6.6 were damped, the oscillations were more prolonged and of larger amplitude in the data of Figure 6.7. In this case, the oscillations were triggered by the onset of the combined 13 Hz bias tone (99 dB SPL) and the 207 Hz probe tone (89 dB SPL). Prior to the recording, the animal had been in silence for four minutes. The onset caused an 8% increase in Vsat, peaking around 80 seconds after onset, which then recovered in an oscillatory manner to near starting values within 10 minutes. The Z parameter showed a 13% increase in magnitude that also peaked around 80 s, but was far less oscillatory during recovery, being almost monotonic after the first peak. The operating point did not peak in the same way as Vsat and Z, but moved steadily toward ST by 6 meV over 10 minutes, with slight oscillations.

At ten minutes after the bias onset, the level of the 12.94 Hz bias tone was increased by 20 dB to 119 dB SPL for two minutes. This was sufficient to trigger a larger set of oscillations in the Boltzmann parameters, most visible in Vsat, that persisted for the next 20 minutes. Note that while the peak in Vsat in the first 100 s of the trace was an *onset* effect, caused by the presentation of the combined tone, the local minimum in Vsat occurring around 800 s was an *offset* effect, caused by the reduction of the 13 Hz tone from 119 dB SPL to 99 dB SPL. Highly attenuated oscillations were also visible in Z and Eo, although the pattern of the oscillations was different in all three parameters. The difference in oscillation pattern is highlighted in Figure 6.8, in which the Vsat and Eo parameters are overlaid.

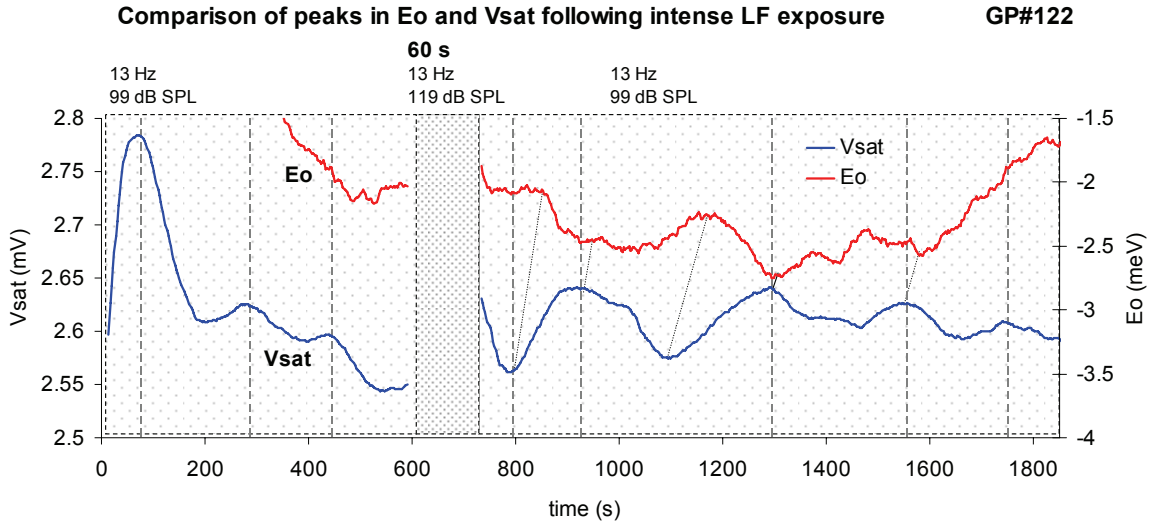

Figure 6.8: The Vsat and Eo traces from Figure 6.7 overlaid, with possible correspondences between oscillation peaks indicated by diagonal lines to show the phase delay between the two parameters.

The diagonal lines in Figure 6.8 indicate possible correspondences between the peaks in Eo and Vsat, but as the oscillations in Eo were irregular and non-sinusoidal,

these correspondences are open to interpretation. Generally, although of much lower amplitude (compared to the measurement noise), the peaks in Eo occurred midway between those of Vsat, again indicating a 90º phase shift between the two parameters. The Vsat and CM amplitude oscillations themselves were also not pure sinusoids. The dominant oscillation in the CM amplitude trace had a mean period of 181 ms (± 36 ms; n = 2) before the two-minute exposure and 270 ms (± 77 ms; n = 4) following it. The rate of decay of the oscillation amplitude was also not constant, with a rate of 6 dB per 200 s between 850 s and 1200 s, slowing to 6 dB per 820 seconds between 1200 s and 1700 s. It appears, therefore, that either the phase relationship of the loop variables or the total loop gain was changing during the period following the exposure.

6.4 Mathematical modelling of the low-frequency bounce phenomenon

A low-frequency exposure simulation was carried out to assess whether the mathematical model of OHC regulation presented in Chapter Two was capable of showing i) the "low-frequency adaptation" shift towards ST; and ii) oscillations in auditory sensitivity and, in particular, a transient hypersensitivity following LF exposure. The model perturbation used was a near-saturating 5 Hz square-wave bias that was capable of causing a ±100 meV movement of the hair bundle. The results of this exposure, using the standard set of model parameters, are presented Figure 6.9.

As will be demonstrated in Figure 6.13, the simulated LF tone caused the rapid influx of Ca^{2+} into the model OHC, as the cyclical depolarisation of the membrane potential caused the opening of voltage-gated Ca^{2+} channels. During the 10-minute presentation of the tone, the average (quiescent) operating point showed an initial 2.3 meV movement towards SV during the first 30 seconds, followed by a slower shift towards scala tympani, reaching 11 meV below the control value of -6 meV after 10 minutes. The first 30 seconds of the mean operating-point shift were dominated by a prestin-mediated electromotile movement towards SV in response to the mean hyperpolarisation of the OHC caused by the 5% increase in $[Ca^{2+}]_i$ during the first 30 seconds of the tone. The accumulated $[Ca^{2+}]_i$ triggered an increase in M4 activity, causing a slow-motile contraction which dominated the operating point shifts over the remaining 9½ minutes of the LF exposure. The increased $[Ca^{2+}]_i$ also increased the permeability of the basolateral wall of the OHC (via the Ca^{2+}-gated K^+ channels), which caused the mean quiescent EP to fall by 2 mV during the first 30 second of the exposure, after which it began to rise as the apical conductance was reduced under the influence of the ST operating point shift.

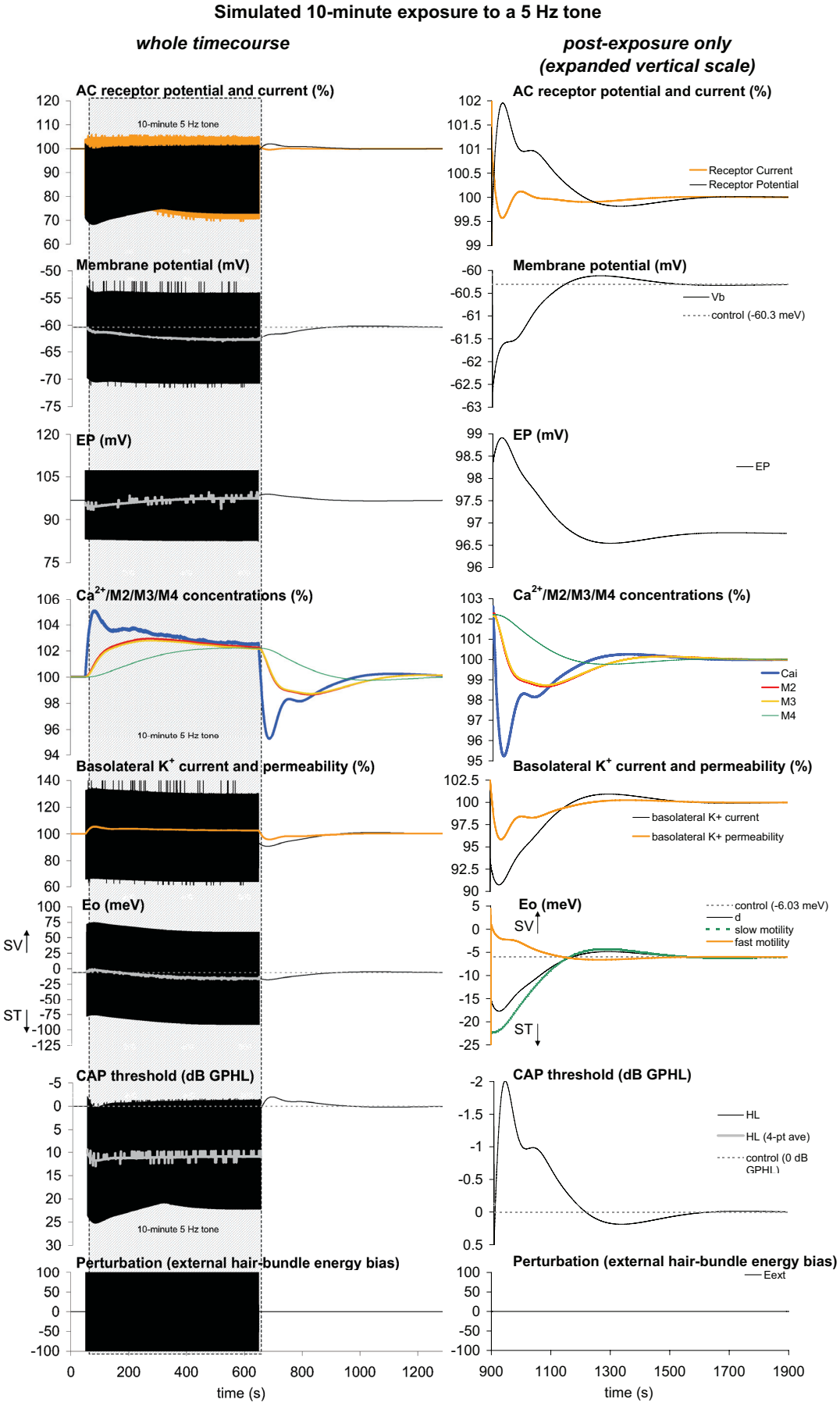

Figure 6.9: OHC model results during a simulated 10-minute exposure to a low-frequency tone (5 Hz square wave), using the standard set of model parameters. The second column presents the post-exposure changes at a larger vertical scale (see text).

On cessation of the tone, the influx of calcium through the periodic opening of the L-type calcium channels ceased, while the extrusion of calcium under the influence of the now-elevated M3 levels continued. This resulted in the $[Ca^{2+}]_i$ falling to 4.5% below control levels, which reduced the basolateral K^+ permeability by 4%, and caused the small-signal AC receptor potential to increase by 2% relative to control levels. This increase in AC receptor potential would have been even larger had the operating point been at a more sensitive part of the MET transfer curve, rather than heavily towards ST. Nevertheless, the 2% increase in small-signal receptor potential was extrapolated to a 2 dB hypersensitivity, peaking at around 45 seconds after the offset of the tone. A discussion of the differences between the model results and the experimental data follows in Section 6.5 below.

6.5 Discussion

The aim of these experiments was to obtain data that would enable inferences about the underlying mechanism of the "bounce phenomenon" to be made. In particular, it was hoped that the correspondence between the CAP threshold shifts and the Boltzmann parameters would provide further information as to the origin of the reduction in sensitivity, whether it was more correlated with changes in the operating point (consistent with the mechanism suggested by Kirk et al., 1997), or with changes in Vsat, or Z.

6.5.1 The hypothesis – the bounce and OHC basolateral permeability

To summarise, our hypothesis was that the sequence of events at the onset of low-frequency tone was as follows:

i) the low-frequency, high amplitude AC receptor potential causes cyclical opening of the voltage-sensitive calcium channels, resulting in an increase in intracellular calcium;

ii) this elevated $[Ca^{2+}]_i$ causes the opening of calcium-sensitive K^+ channels, increasing the permeability of the basolateral wall of the OHC, while also triggering a slow-motile contraction of the OHC (which would be reflected in an Eo shift towards SV);

iii) the increased basolateral permeability causes an increase in receptor current (which would be reflected in increases in CM amplitude and Vsat), a decrease in the EP (due to increased current shunt through the OHCs), a hyperpolarization of the OHC basolateral membrane potential, a decrease in

the AC receptor potential, and a reduction in contribution of prestin-based somatic electromotility to cochlear gain (Zheng et al., 2000), causing an elevation in CAP thresholds.

According to the homeostatic model presented in Chapter Two, the rise in $[Ca^{2+}]_i$ triggers an increase in the messengers M2, M3, and M4, of which M3 increases the rate of calcium sequestration by upregulation of the SERCAs in the subsurface cisternae and/or the PMCAs of the OHC basolateral membrane. The phase-delay between the steps of the messenger cascade causes oscillations in intracellular calcium level, ultimately resulting in the oscillations in neural threshold observed by Wareing and Patuzzi (Wareing, 2001; Patuzzi and Wareing, 2002) and shown in Figure 6.9.

Prior to the offset of the tone, the level of calcium is elevated, as is the levels of M2, M3, and M4. At the offset, the following sequence of events was hypothesised:

i) the cessation of the intense LF tone causes a reduction in the influx of calcium through the voltage-sensitive channels due to the receptor potential mechanism;

ii) the slower time-course of the changes in M3 concentration results in continued sequestration of calcium, despite the reduction in the calcium influx, causing a reduction of $[Ca^{2+}]_i$ to below pre-stimulation levels, peaking around 1-2 minutes after cessation of the tone;

iii) the decrease in $[Ca^{2+}]_i$ causes a reduction in basolateral permeability, which would cause a decrease in Vsat, an increase in the EP, an increase in the AC receptor potential and, therefore, an improvement in cochlear gain.

The slow decrease in M4 levels would also cause a relaxation of the slow-motile contraction, resulting in a return of the operating point towards resting levels.

In the present study, the Boltzmann parameters were measured during the bounce in two animals (GP#69 and GP#122), with the largest changes being observed in the Vsat parameter and the analogous CM amplitude. These measures are dependent on the magnitude of the saturated AC receptor current through the OHC, which (assuming the mechanical drive to the hair bundle is constant) is itself dependent on i) the permeability of the basolateral wall of the OHC, and ii) the driving potential across the organ of Corti (provided by the EP). While the resting operating point of the OHC hair bundles obviously affects cochlear transduction (as discussed in Chapter One), in Figure 6.2, the

significant[1] correlation between the time-course of the bounce in CAP thresholds and that of the Vsat parameter supports the theory that the changes in active gain following the exposure to low-frequency tones were dominated by changes in the permeability of the basolateral wall of the OHCs, and the corresponding changes in the OHCs' ability to generate an AC receptor potential. The question of whether this basolateral permeability mechanism can account for the data from other cochlear measures, however, such as the EP, the operating point, the Z parameter, and DPOAEs, is addressed below.

6.5.2 Previous data – changes in the EP during the bounce

As illustrated in Figures 6.10 to 6.12 below, previous studies in guinea pigs have shown that the EP increases transiently immediately following the offset of the tones (Kirk, 1972; Kirk and Patuzzi, 1997; Salt, 2004), and can be either elevated or depressed during the tone itself. The results of the mathematical model (Figure 6.9) bore a similarity to the guinea pig data of Salt (2004; bottom panel of Figure 6.12). In the model, the EP showed an initial decrease under the influence of the increased basolateral permeability, followed by an increase under the influence of the scala tympani operating point shift. The EP was not measured during the guinea pig experiments in the present study. However, the relative timing of the changes in the EP and those of the Vsat parameter may provide some indication of the cause of the changes in both parameters, as described below.

In the three recordings from GP#69 and GP#122 the data show that, in contrast to the EP, the Vsat parameter and CM amplitude *increased* during the LF exposure, and *decreased* transiently after the offset. A similar pattern of Vsat changes was also reported by Kirk et al. (1997). This movement of Vsat and EP in opposite directions is consistent with the basolateral permeability mechanism described above: the results of EP bias experiments (to be presented in Chapter Seven) indicate that if the causative agent were the change in the EP, the Vsat parameter would move in the *same* direction as the EP, because an increase in the EP would increase the current through the OHC[2]. However, the exact nature of such correspondences will remain somewhat speculative until further experiments provide clarification of the time-courses of CAP threshold, EP, and the Boltzmann parameters, when measured simultaneously.

---

[1] $p<0.0001$ (Student's two-tailed T-test).

[2] In addition to being in the wrong direction, the EP changes probably would have to be larger, as the current injection results of Marcon and Patuzzi (in preparation) suggest a ± 3% oscillation in Vsat would require an approximate ± 6% oscillation in EP, which is larger than those reported during the bounce.

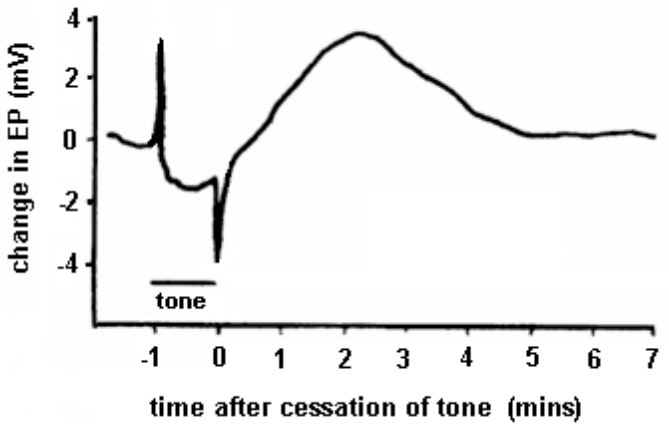

Figure 6.10: Guinea-pig data from Kirk (1972), showing the changes in the EP following a 1-minute exposure of a 115 dB SPL 200 Hz tone (horizontal bar). The EP decreases during the tone, and rises by 4 mV following the offset of the tone.

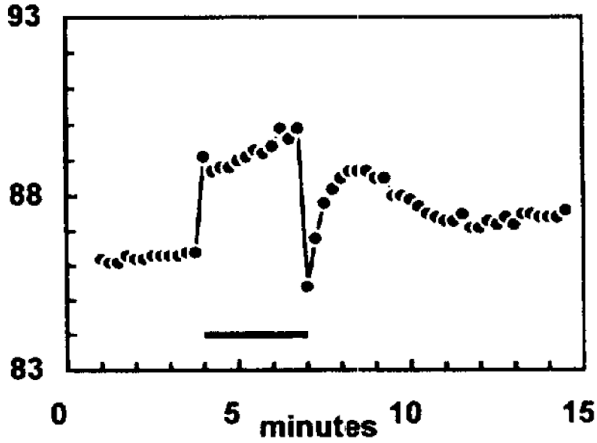

Figure 6.11: Guinea-pig data from Kirk and Patuzzi (1997), showing the changes in the EP following a 3-minute exposure of a 95 dB SPL 200 Hz tone (horizontal bar). The EP increases during the tone, but rises by 3 mV following the offset of the tone.

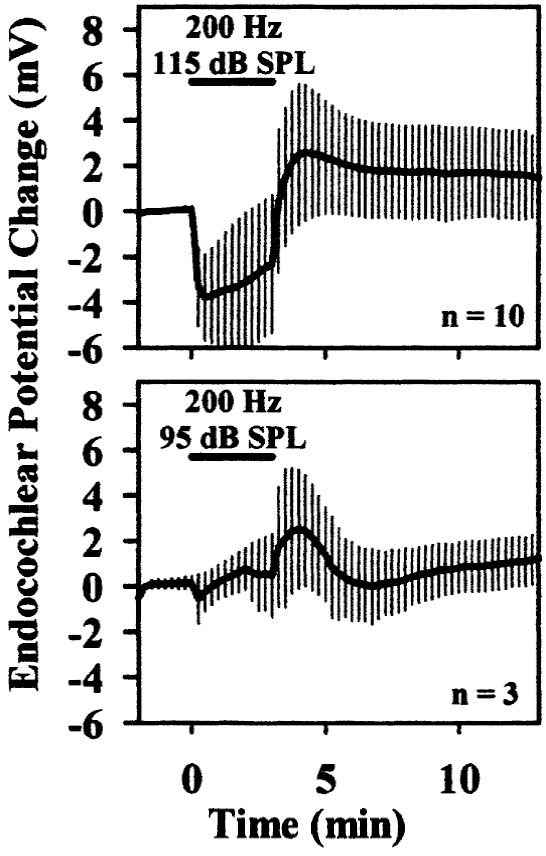

Figure 6.12 Guinea-pig data from Salt (2004) showing the mean changes in the EP for 3-minute presentations of 200 Hz tones at 115 dB SPL (top panel) and 95 dB SPL (bottom panel). Vertical bars represent standard deviations of the measurements. While the post-offset rise in EP was present, the 115 dB SPL data showed a decrease in EP during the tone (consistent with Figure 6.10 above), while the 95 dB SPL data showed a net EP rise during the tone (consistent with Figure 6.11 above).

The time-course of the changes in the EP is also relevant to the generation of transient tinnitus following the bounce, as will be discussed in Section 6.5.7 below.

6.5.3 Published changes in Eo and DPOAEs during the bounce

In the example shown in Figure 6.8, the peaks in the Eo oscillation appeared to be delayed relative to the peaks in Vsat. Although the correspondence between these peaks is open to interpretation, they indicate that the mechanisms producing the changes in Vsat and Eo are influenced by oscillations of the same loop (because they have the same oscillation frequency), but at different points in the loop (as indicated by their different phase). In the context of the homeostatic model of Chapter Two, this is consistent with a phase-delay between the accumulation of intracellular calcium and the slow-motile contraction of the OHC under the influence of the intracellular messenger M4.

While DPOAEs were not measured during the bounce in this study, they were examined by Kirk and Patuzzi (1997), who found large changes in the f_2-f_1 emission, but very small change in $2f_1$-f_2. The changes in operating point and f_2-f_1 led them to suggest that the increase in cochlear sensitivity following exposure to the LF tone was caused by the transient changes in the operating point. However, the data obtained in this study suggest that the bounce is not consistent with operating point changes alone. In all cases (both the traditional damped "bounce" and the slow oscillations), the largest[3] effect of the LF tone was seen in the Vsat parameter, and while attenuated oscillations were observed in operating point, they never occurred without a Vsat change, while Vsat oscillations could be seen with little or no Eo oscillation (see Patuzzi, 2003). In their experiments, Kirk et al. (1997) noted that the Eo changes followed a similar time-course to the Vsat parameter, which fell transiently by an average of 5 ± 5% (n = 8).

Kirk et al. (1997) suggested that the operating point shift they observed during the bounce could have resulted from an osmotic perturbation, such as a bloating of scala media. Salt (2004) derived the changes in cross-sectional area of scala media from measurements of the longitudinal movement of perilymph during low-frequency exposures, and concluded that although an increase in the cross-sectional area of scala media was observed, it was likely to be a *symptom* of the observed ST operating point shift, rather than the cause of it. The extremely low amplitude of the Eo effects observed in the present study suggests that, in our experiments at least, the bounce was not likely

[3] The term "largest" refers to the comparison between the observed changes with the bounce and with changes caused by other perturbations, and also compared to the measurement noise of the parameter.

to be due to an osmotic mechanism or fluctuations in the hydrostatic pressure of the cochlear fluids, as suggested by Kirk et al. (1997; Kirk and Patuzzi, 1997). Rather, the CAP threshold oscillations are more likely to be due to the changes in the permeability of the basolateral wall under the influence of cytosolic calcium oscillations, with any resulting operating point shift being incidental rather than crucial to the oscillation. In the modelling data presented in Section 6.4 above, the presence of the changes in operating point during the bounce actually *reduced* the magnitude of the transient hypersensitivity at the offset of the tone, due to the reduced apical permeability limiting the size of the small-signal AC receptor potential.

In the present version of the model, both the slow contraction and the changes in basolateral permeability are governed (directly or indirectly) by cytosolic calcium levels. However, as will be discussed in Chapter Nine, the division of cytosolic calcium into two functionally separate pools (one of which affects the slow contraction, and one which affects basolateral permeability) may provide a closer match to the experimental observations, and account for the difference in amplitude between the Eo and Vsat oscillations.

6.5.4 Accumulation of calcium in OHCs during LF tones – dependence on stimulus amplitude, frequency and duration.

As discussed above, the "bounce" could be produced by an oscillation in intracellular calcium levels, triggered by its accumulation in the OHCs. The cause of this accumulation is presumed to be the cyclical opening of voltage-sensitive calcium channels in response to the low-frequency receptor potential. As the opening probability for the L-type calcium channels is asymmetric around the OHC resting membrane potential (with a half-activation voltage of -45 mV; Rodriguez-Contreras and Yamoah, 2003), larger receptor potentials (produced by larger LF tones) would cause these channels to be open for a greater percentage of the time, as illustrated in Figure 6.13 below. If the density of the voltage-gated channels is substantially higher than that of the non-voltage-dependent calcium channels, larger AC receptor potential amplitudes would result in a larger influx of calcium, and a large cumulative Ca^{2+} rise during a LF tone.

Additionally, because of this dependence on large AC receptor potential amplitudes for calcium accumulation with sound, the frequency of the stimulating tone would have to be limited to below the RC cut-off frequency for the basolateral membrane, which has been estimated at around 400 Hz for a basal OHC (Housley and Ashmore, 1992;

Preyer et al., 1996). Therefore, at a constant drive to the OHC stereocilia, we would expect that the size of the calcium influx would increase with lower acoustic stimulation frequencies, because these would produce the least low-pass-filtered receptor potential. For LF stimuli delivered at a given SPL in the ear canal, the drive to the stereocilia is not constant across frequencies (due to the high-pass filtering of the helicotrema). In his studies of the hydrops induced by low-frequency tones, Salt (2004) found the hydropic effects achieved with intense 200 Hz tones to be more consistent that those produced by 50 Hz, 500 Hz or 1000 Hz stimulation. The fact that 200 Hz tones produced larger effects than 50 Hz stimulation at the same SPL may simply be due to the helicotrema acoustic high-pass filtering mentioned above.

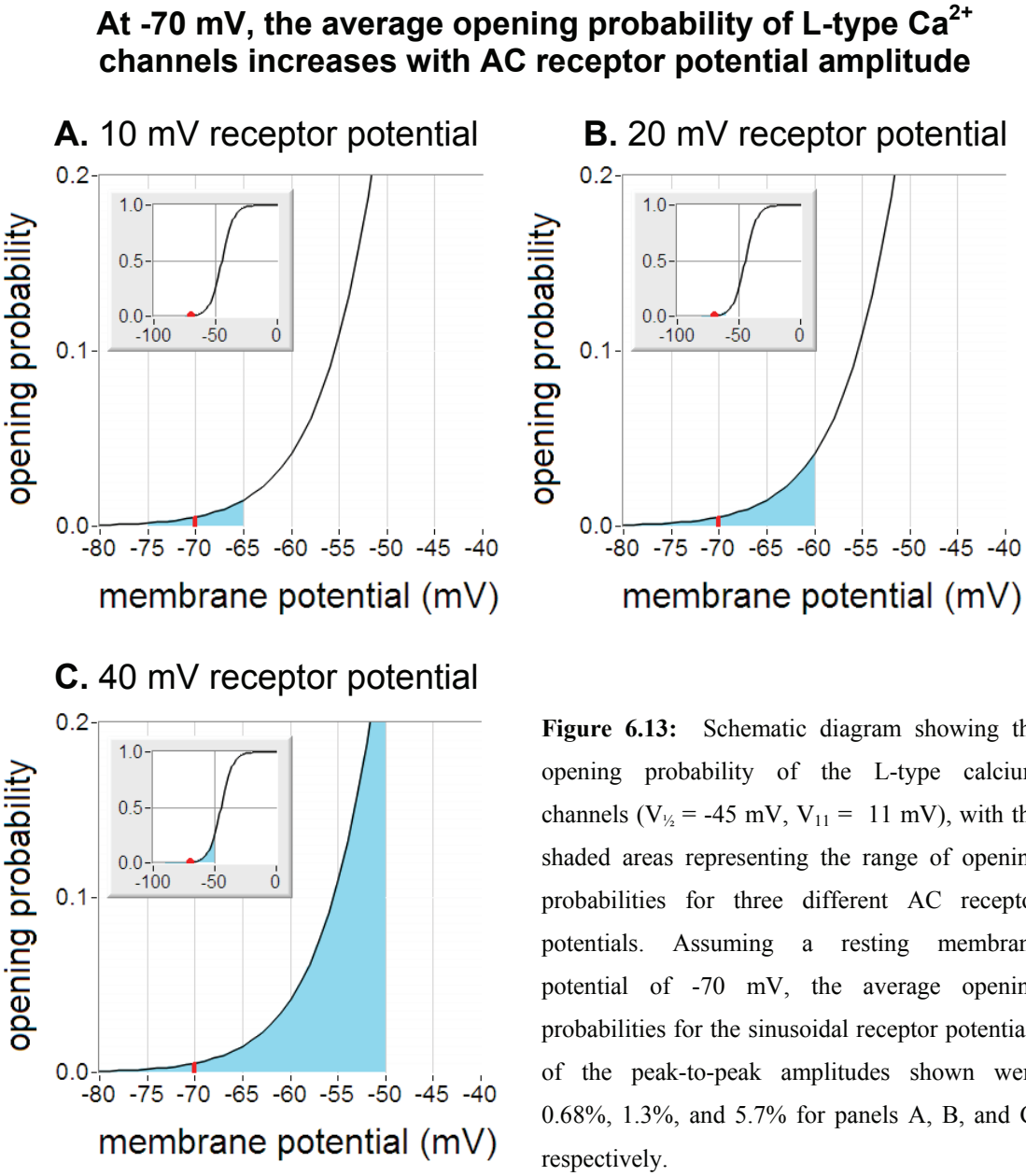

Figure 6.13: Schematic diagram showing the opening probability of the L-type calcium channels ($V_{½}$ = -45 mV, V_{11} = 11 mV), with the shaded areas representing the range of opening probabilities for three different AC receptor potentials. Assuming a resting membrane potential of -70 mV, the average opening probabilities for the sinusoidal receptor potentials of the peak-to-peak amplitudes shown were 0.68%, 1.3%, and 5.7% for panels A, B, and C, respectively.

For continuous tones, the calcium accumulation would be dependent on the amplitude and frequency of the LF tone, but for intermittent tones, such as those used in many of the examples presented here, the mark/space ratio of the presentation protocol is also likely to influence the size of the calcium effect. As described in Chapter 4, the custom-written data-acquisition software used during most of the other recordings carried out during this project used 50 ms 207 Hz tone-bursts for the Boltzmann analysis of CM waveforms. This short-tone-burst analysis was equivalent to having the LF tone on for just under 15% of the time, which was intended to limit the amount of Ca^{2+} entry to the OHC. However, the modified Boltzmatron analysis software used in these experiments used 1-second tone-bursts that were presented (on average) every 2.6 seconds, resulting in the tone being on for approximately 64% of the time. This four-fold increase in the presence of the tone is the most likely cause for the increased oscillatory behaviour observed with the multi-phase recording procedure used in Figures 6.6 and 6.7.

In Figures 6.6 and 6.7, the operating point moved slowly towards scala tympani over the first 10 minutes of the tone. As shown in Figure 6.14 below, this equivalent contraction has been reported previously by Marcon (1995) and Patuzzi and Moleirinho (1998), who referred to it as "low-frequency adaptation". This slow contraction was also visible in the results of the mathematical model, shown in Figure 6.9.

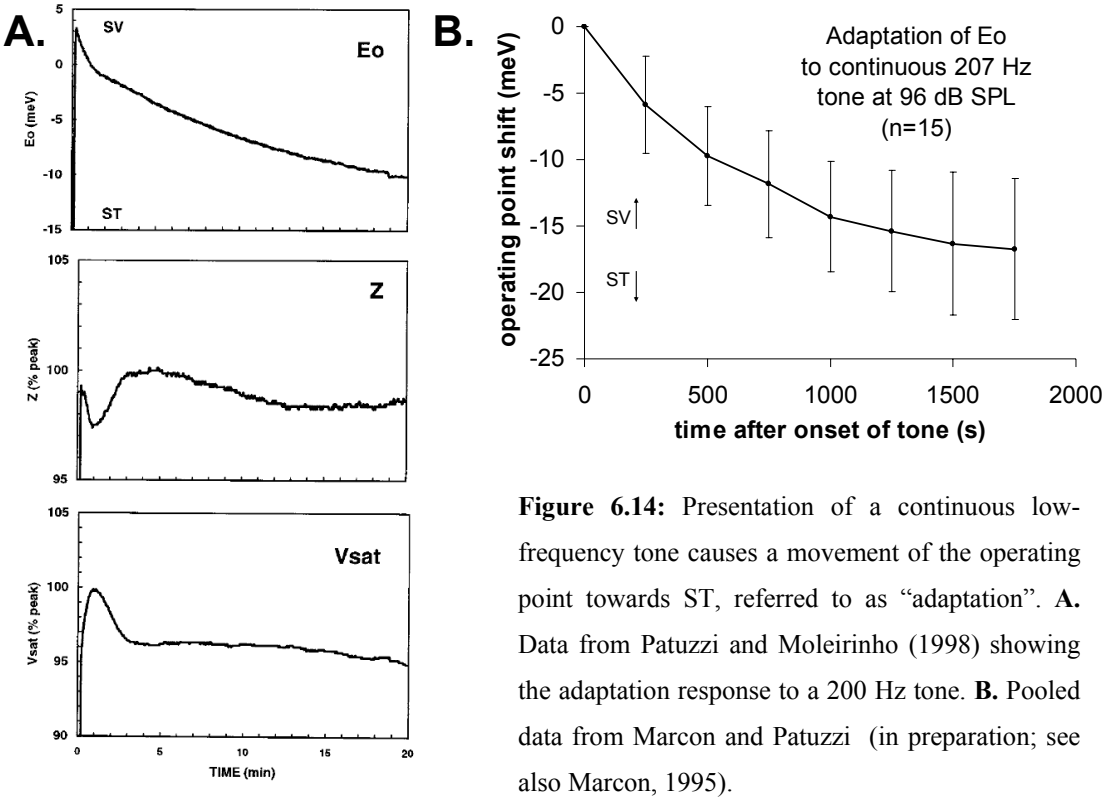

Figure 6.14: Presentation of a continuous low-frequency tone causes a movement of the operating point towards ST, referred to as "adaptation". **A.** Data from Patuzzi and Moleirinho (1998) showing the adaptation response to a 200 Hz tone. **B.** Pooled data from Marcon and Patuzzi (in preparation; see also Marcon, 1995).

This low-frequency adaptation was not often observed in the experiments of the present study (presented in Chapters Five, Six, Seven, and Eight) because the custom-written data-acquisition software (described in Chapter Four) was specifically designed to avoid it, by the use of 50 ms tone-bursts to evoke the 207 Hz CM, rather than continuous tones. Ironically, this resulted in the observation of far fewer instances of oscillatory behaviour than previous researchers using the continuous-tone Boltzmann analysis technique, such as Marcon and Patuzzi (in preparation).

6.5.5 Duration of exposure and CAP threshold bounce

As shown in Figure 6.4, decreasing duration of the LF stimulus by eightfold did not affect the timing of the bounce, but did result in smaller bounces at lower frequencies. This result was consistent with the data of Wareing and Patuzzi (in preparation), who demonstrated a similar trend in psychophysical threshold fluctuations in humans. As shown in Figure 6.15 from Wareing (2001), exposures of one minute or more produced relatively constant amplitude off-effects, while amplitudes were reduced for decreasing exposure durations below one minute.

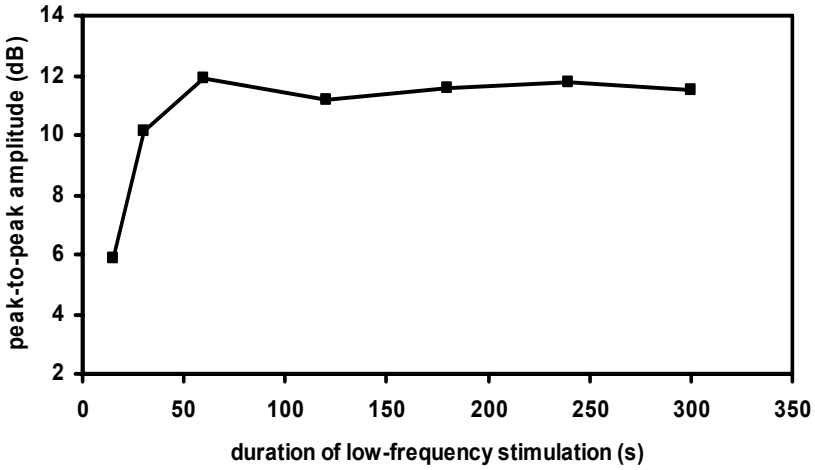

Figure 6.15:. Data from Wareing (2001) showing the effect of LF stimulus duration on the peak-to-peak amplitude of the bounce in psychophysical thresholds in human subjects.

The fact that i) the frequency and phase of the oscillations did not markedly alter, and ii) the changes in oscillation amplitude were not *proportional* to exposure duration, are indicators that i) the process initiating the bounce at the offset was subject to some form of saturation; and/or ii) that there was a high-pass filter element in the loop, such that the bounce was initiated by the transients at onset or offset.

In Figures 6.3 and 6.4, the timing of the bounce appeared to vary slightly with the probe frequency, with the hypersensitivity at 4 kHz and 6 kHz peaking just before the

more basal frequencies. This result is *not* consistent with the human data of Wareing and Patuzzi (in preparation), who found that the period of psychophysical threshold oscillation in humans following a 40 Hz exposure was *decreased* for increasing frequencies above 3 kHz. As shown in Figure 6.16, the period of their off-effect oscillations decreased from a relatively constant 225 s below 3 kHz to 205 s at 5 kHz, and 155 s at 10 kHz. The peaks in the CAP data from the guinea pig shown in Figure 6.3 show much less of a frequency dependence, but the cause of this discrepancy is not known.

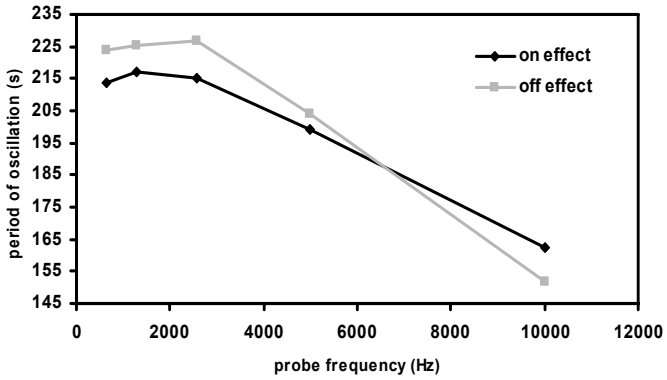

Figure 6.16:. Data from Wareing (2001) showing that the period of the psychophysical-threshold oscillations in human subjects decreased for increasing probe-frequencies.

In the present experimental series, the guinea-pig data presented in Figure 6.2 showed a larger amplitude bounce in the higher frequencies, with the bounce almost absent at 2 kHz, possibly reflecting the reduced contribution of the active process at the more apical regions of the cochlea. This result is consistent with the data of Salt (2004; Figure 6.17 below), which appears to show a larger amplitude oscillation at 8 kHz than at 4 kHz and 2 kHz.

Interestingly, the guinea-pig CAP data in Figures 6.2 and 6.3 showed large amplitude bounces at frequencies at which there were large hearing losses. It is not certain what proportion of the pre-exposure hearing loss was conductive in those cases, but an increased oscillation amplitude might be expected if the cause of the hearing loss was a chronic elevation cytosolic calcium levels in the OHCs. Such an elevation would not only limit the generation of the AC receptor potential required for somatic motility, but could result in increased oscillatory behaviour as the voltage-gated Ca^{2+} channels becomes less important in the regulation of cytosolic calcium (see discussion in Section 2.9.1 of Chapter Two).

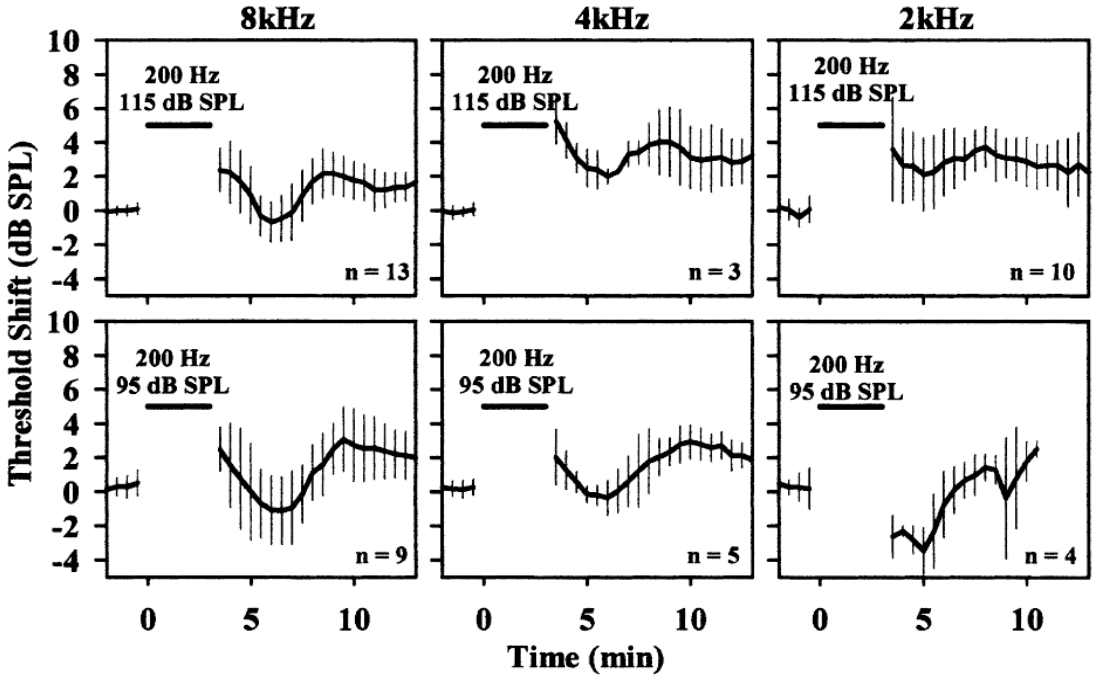

Figure 6.17: Guinea-pig data from Salt (2004) showing the mean threshold shifts at 8 kHz, 4 kHz, and 2 kHz for 3-minute presentations of 200 Hz tones at 115 dB SPL (top row) and 95 dB SPL (bottom row). Vertical bars represent standard deviations of the measurements.

6.5.6 The single bounce versus the slow oscillations

The data presented in Figures 6.2 and 6.7 are consistent with the traditional "bounce" being the first cycle of the slow oscillations observed in the Boltzmann parameters. This is supported by the fact that both phenomena share the same characteristics (initial Eo movement toward scala tympani, and reduction in Vsat and Z magnitude), and display a similar 90º phase relationship between Vsat and Eo. The most parsimonious explanation is that both phenomena are produced by the same mechanism, but that they differ in the degree of damping: while the guinea-pig data of Kirk and Patuzzi (1997) shown in Figure 6.18 below showed only a single half-cycle of hypersensitivity, the human psychophysical data of Wareing (2001) shown in Figure 6.19 displayed two or more hypersensitivities (indicated by the black and grey arrows). A further decrease of this damping would therefore be expected to cause the multi-cycle oscillations observed in the Boltzmann parameters in Figures 6.6 and 6.7.

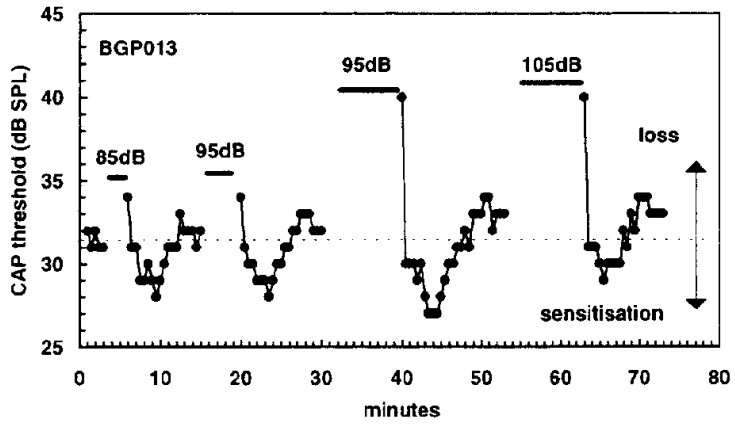

Figure 6.18: Guinea-pig data from Kirk and Patuzzi (1997) showing bounces in the 4 kHz CAP threshold in response to 200 Hz exposures of differing durations, at 85, 95, and 105 dB SPL (see text).

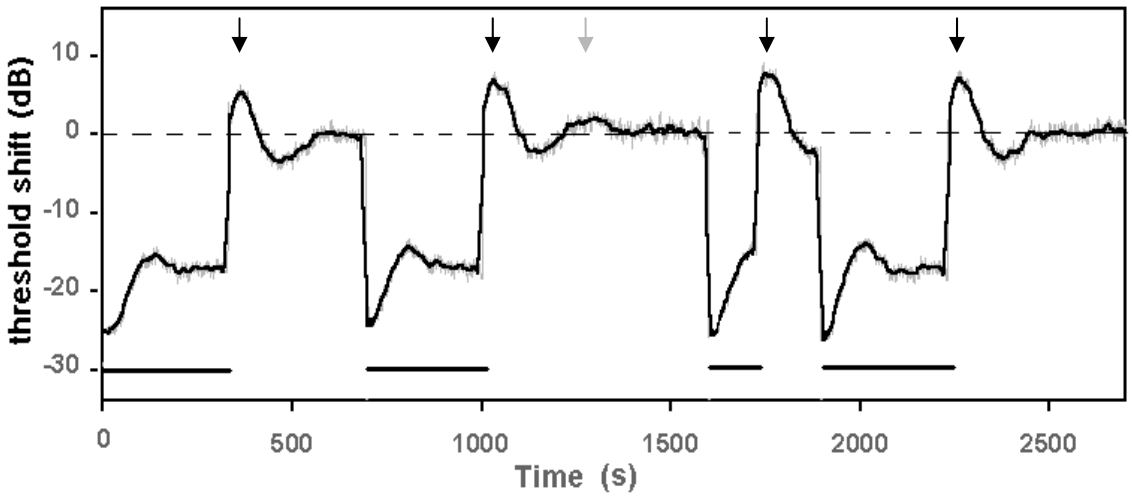

Figure 6.19: Damped sinusoidal oscillations in human audiometric threshold (tracked with Békésy audiometry) at onset and offset of exposures (black bars) to a 126 dB SPL 40 Hz tone. Transient hypersensitivities (bounces) are marked with an arrow. Figure adapted from Wareing (2001).

6.5.7 Transient tinnitus during the bounce

Patuzzi and Wareing (2001; 2002) studied the bounce phenomenon in human subjects using Békésy audiometry to track psychophysical threshold, and to match the loudness of a synthesised "tinnitus" in the contralateral ear to that of the transient tinnitus evoked by the LF tone. Comparison of the time-course of the threshold shifts and the tinnitus revealed significant phase delays between the two measures, with the peak of the tinnitus loudness occurring around 30-40 seconds after the peak threshold enhancement, as shown in Figure 6.20.

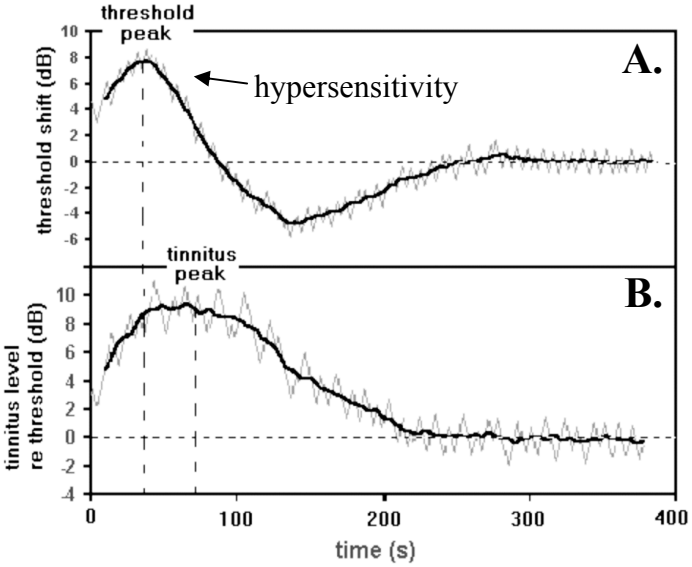

Figure 6.20: Békésy audiometry results from Patuzzi and Wareing (2002) showing **A.** psychophysical threshold oscillations and **B.** the contralaterally-matched loudness of transient tinnitus following 3 minute exposures to 116 dB SPL 100 Hz tones in a single subject.

In the case of the tinnitus observed during the bounce (Hughes and Rosenblith, 1957; Kemp, 1986; Wareing, 2001; Patuzzi and Wareing, 2002), the form of tinnitus is probably "rate tinnitus" - the result of an increase in the spontaneous firing rate of the primary afferent neurons that occurs with depolarisation of the IHCs during transient increases in the EP (Patuzzi, 2002). As discussed in Section 6.5.2 above, the EP has been found to increase transiently following the offset of the LF tone. However, there may be evidence to suggest that the *timing* of the peaks is different in humans and guinea-pigs. In guinea-pig experiments, Salt (2004) noted that the time-course of threshold changes following LF exposure was *slower* than that of EP changes[4]. However, the human data shown in Figure 6.20 indicated that the hypersensitivity occurred *before* the tinnitus peak. The cause of this discrepancy is unknown, however, a greater range of relative timings for these peaks would be possible if basolateral permeability and operating point were controlled by separated calcium pools, as will be discussed in Chapter Nine.

6.6 Summary

The conclusions drawn from the experimental data and modelling results presented here are:

i) the bounce phenomenon and the slow oscillations in the Boltzmann parameters most likely arise from the same mechanism, and differ only in the degree to which the oscillations are damped;

[4]Similar results were produced by our mathematical model in Figure 6.9.

ii) the threshold oscillations observed during the bounce are likely to arise from changes in the permeability of the basolateral wall of the OHC under the influence of cytosolic calcium concentration; and

iii) the mathematical model is capable, using the standard set of parameters, of reproducing the "low-frequency adaptation" of operating point during the LF tone, and the EP changes, and the transient hypersensitivity following LF exposures.

Along with positive EP bias, the bounce is one of the few cochlear perturbations that can transiently enhance cochlear sensitivity. The bounce phenomenon is interesting in that it indicates that active gain is *not* the only "goal" of cochlear regulation, for if it were regulated at the expense of everything else, it would not be maintained at a sub-optimal level. Because the period of threshold hypersensitivity coincides with an elevation of the endocochlear potential that is likely to produce a rate tinnitus (produced by the excessive release of neurotransmitter from the IHCs), the regulation mechanisms of the cochlear may be a compromise between hearing sensitivity and spontaneous neural firing rate, with evolutionary pressures deciding whether the increased hearing sensitivity or decreased tinnitus contribute most to the survival chances of the organism. These points, and the proposed two-pool model of cytosolic calcium in the OHCs, will be discussed further in Chapter Nine.

Chapter 7
Effect of direct-current bias on cochlear potentials

7. Scala tympani direct-current injection

7.1 Introduction

The dependence of the OHC receptor current on the driving potential provided by the EP may be assessed by the injection of positive or negative direct current (DC) into scala media or scala tympani. Both methods alter the potential difference across the cochlear partition, affecting the hair cells, but also modulate the neural currents responsible for action potentials in the primary afferent neurones (Schreiner et al., 1986; Brown et al., 2004).

This chapter describes the changes observed in a number of cochlear parameters during both short-term and long-term injection of negative and positive DC current[1] into scala tympani. These are compared with the results of Marcon and Patuzzi (in preparation) for scala media current injection. The responses examined in the present study included CAP thresholds and CAP waveforms, low-frequency cochlear microphonic (CM) waveforms, and spontaneous neural noise recorded from the first turn of the guinea pig cochlea.

The duration of the current injections reported here range from "short-term" (under 2 minutes) to "long-term" (5 minutes to 90 minutes). The "short-term" injections were several orders of magnitude longer than those of other authors (e.g. Parthasarathi et al., 2003), who have used injection periods of 5 ms or less. The difference between the two approaches lies in the time-course of the effects under investigation: the aim of our experiments was to characterise the slower regulatory changes that happen in the cochlea within minutes, as well as the first-order effects that occur within seconds.

Although we had originally assumed that the injection of negative current into scala tympani would be equivalent to the injection of positive current into scala media, there are clear differences between the results reported in this chapter and those of Marcon and Patuzzi (in preparation), as will be discussed in later sections.

7.2 Methods

Details of animal preparation, acoustic stimulation, and data acquisition were presented in Chapter Three.

---

[1] Despite the obvious linguistic redundancy, the term "DC current" will be used here for convenience.

Injection of DC current into scala tympani was carried out through a first-turn cochleostomy (described in Chapter Three), initially using an Ag/AgCl electrode similar to that used for round-window recordings. However, electrolysis of this injection electrode resulted in excessively noisy recordings, particularly when ST-positive currents were injected. To minimize this electrolysis, the electrode was placed in a saline-filled micropipette inserted into ST through the cochleostomy. The saline-filled micropipette functioned as a salt-bridge, reducing current density at the electrode and therefore the degree of electrolysis. The silver-wire electrodes were later replaced with less reactive platinum-iridium wire (0.003" bare wire diameter; A-M Systems, Inc., WA, USA).

DC current was delivered to the injection electrodes via an Analogue Stimulus Isolator Box (A-M Systems Model 2200, SDR Clinical Technology, NSW). The control signal for the current injection was a DC voltage output from a Lab-PC+ card (National Instruments, TX, USA) controlled by the custom-written data acquisition software described in Chapter 4. To prevent large transient currents overloading the recording apparatus, the control signal was "ramped" up or down by the software over a period of 6 seconds, and was also externally low-pass filtered with an RC time constant of 1.38 seconds (f_c = 0.72 Hz). Using the 10 μA/V setting of the Analogue Stimulus Isolator Box, a 5 V control voltage resulted in a 56 μA current injection into ST.

7.3 Results – short-term current injection

The short-term injection of DC current into scala media had a number of effects within the cochlea, including modulation of cochlear gain, CAP waveshape, and the cochlear microphonic (as indicated by changes in CM amplitude and the Boltzmann parameters describing OHC MET). These changes are described below.

7.3.1 Effects on Boltzmann parameters

Figure 7.1 shows typical results for injections of positive and negative currents of increasing magnitude (from ±11 to ±56 μA) into scala tympani. Injections were approximately 60 s in duration, and were separated by 60 s periods during which no current was injected.

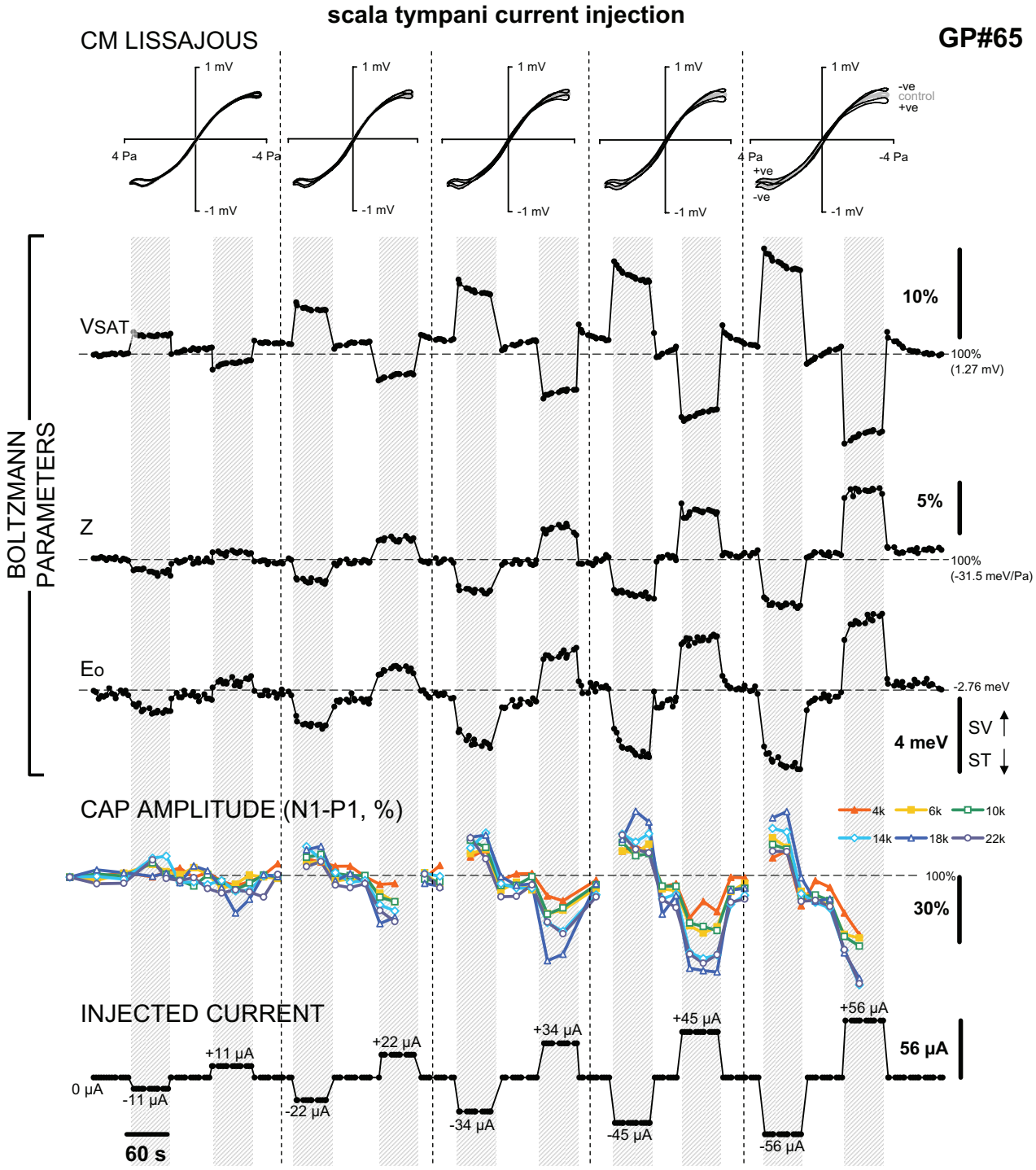

Figure 7.1: Successive injections of positive and negative DC current into scala tympani resulted in systematic changes in the 207 Hz CM Lissajous figures and the corresponding Boltzmann parameters describing OHC transduction. Also shown are the percentage changes in CAP amplitude (measured between the N1 and P1 peaks), which were generally larger for more basal frequencies.

ID#3116319946 102 dB SPL Boltzmann probe. 14k, 18k, & 22k CAP responses elicited by square waves.

The effects of the current injection on the 207 Hz CM were large enough to be visible in the Lissajous figures themselves, but are more clearly seen in the results of the Boltzmann analysis, which revealed systematic changes in all three parameters. Beginning with the injection of -11 μA, the injections of negative current into scala tympani caused increases in Vsat (and CM amplitude), presumably due to an elevated driving potential causing an increase in potassium current through the OHCs. The size of the step-change in Vsat was proportional to the amplitude of the current injection, with an approximate 10% increase in Vsat per 50 μA of negative current injected. The Vsat changes were accompanied by simultaneous operating point shifts towards scala tympani. The ST shifts were consistent with a net hair-bundle movement in the direction that causes closure of the MET channels, equivalent to a step-change of approximately 3.6 meV per 50 μA of negative current injected. A decrease in the Z parameter, consistent with a reduction in compliance of the organ of Corti, was also observed.

The injections of negative current into scala tympani were interleaved with injections of positive current, which caused changes in the Boltzmann parameters that were approximately equal and opposite to the changes with negative current injection. This is shown clearly in Figure 7.2, in which the responses to negative and positive current injection are overlaid. The Vsat and Eo shifts overlie closely, while the Z parameter was found to be more sensitive to injections of positive current than to negative current (positive current injections caused Z changes of approximately 5.5% per 50 μA of injected current, compared to changes of only 3% per 50 μA of negative current injected).

The changes in the Boltzmann parameters during the short-duration current injection shown in Figures 7.1 and 7.2 could be separated into fast and slow components. The fast components were rapid step-changes in the value of each parameter at onset and offset, while slow components were more gradual shifts that were either in the same direction as the fast onset (for Z and Eo), or in the opposite direction of the fast onset (for Vsat). Following each current injection, Vsat and Eo did not return immediately to the pre-injection baseline, but were instead transiently offset by an amount similar to the magnitudes of the slow components. Given that the fast component onset and offset were of approximately equal magnitude, these observations suggested that i) the fast and slow components were due to separable processes, and ii) the process responsible for the fast component responded to the intracellular potential changes with a sensitivity

independent of the short-term intracellular concentration changes presumed to cause the slow components.

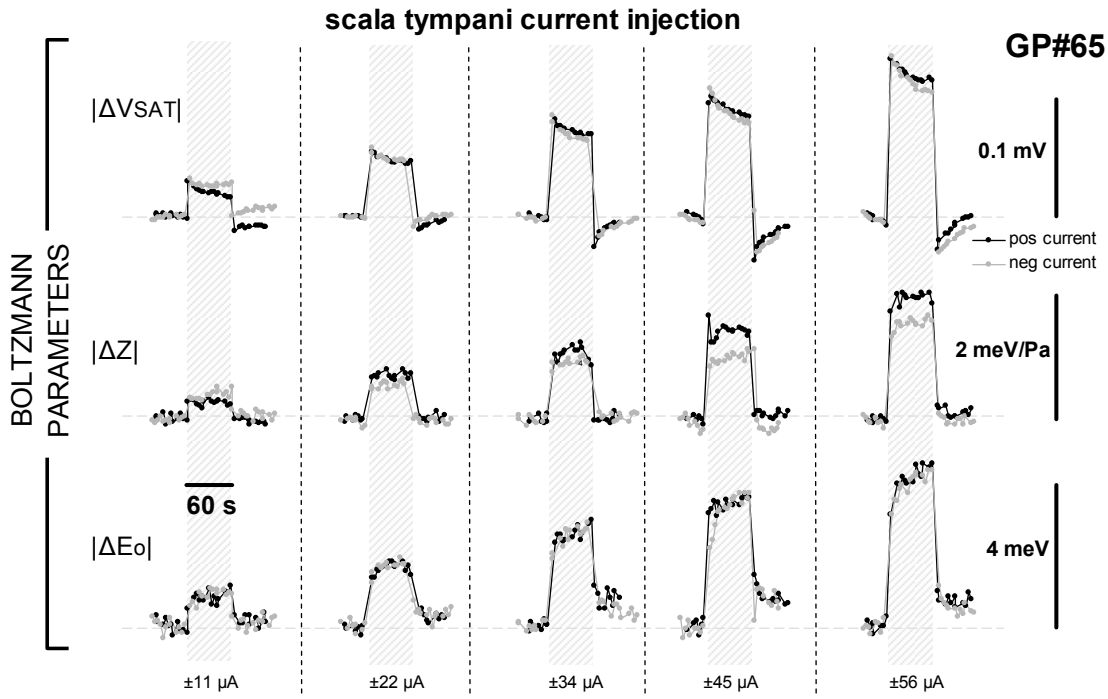

Figure 7.2: The data from Figure 7.1 re-plotted to show that the effects on the Boltzmann parameters of positive and negative DC current injection into ST were approximately equal and opposite. Inversion and superimposition of the positive current injection data over the negative injection reveals particularly close correspondence between the Vsat and Eo changes. Smaller changes in the Z parameter were observed with negative current than with positive current (see text).

ID#3116319946 102 dB SPL Boltzmann probe. 14k, 18k, & 22k CAP responses elicited by square waves.

7.3.2 Neural effects: Asymmetric threshold shifts

While the negative current injections used in the present study were large enough to cause measurable changes in the Boltzmann parameters and CAP waveshape, *they did not result in significant threshold shifts in the short-term*. By contrast, injection of positive current into scala tympani, which reduced the driving potential for potassium through the organ of Corti, did cause high-frequency threshold shifts over a five-minute period.

This asymmetry in threshold shifts is visible in Figure 7.3, which shows the effect of 5-minute ±56 µA current injections into scala tympani.

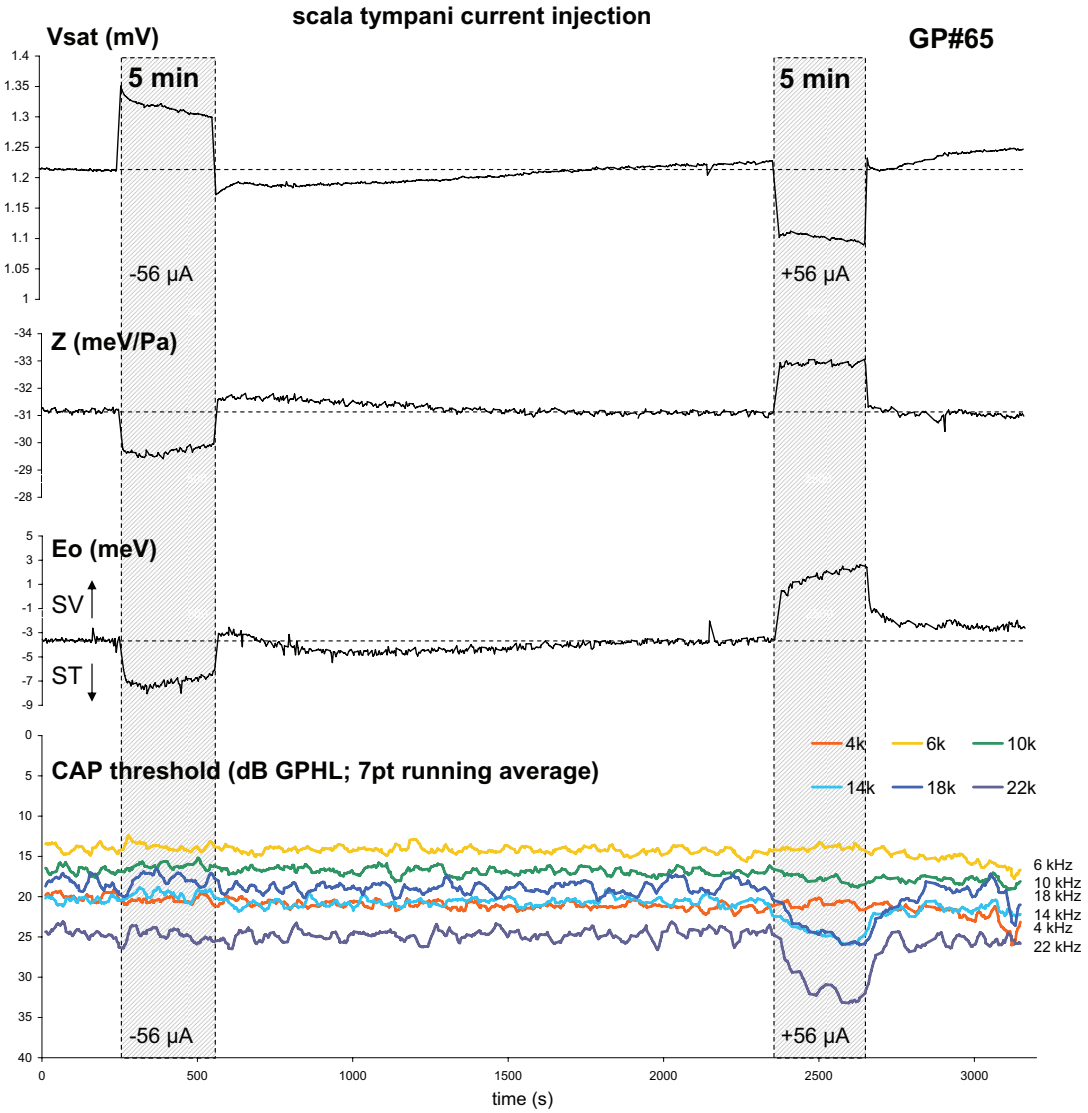

Figure 7.3: While injection of negative and positive DC current into scala tympani caused roughly symmetrical changes in Boltzmann parameters, only the postive injection resulted in significant shifts in tracked CAP threshold, causing threshold losses at 10, 14, 18, and 22 kHz of 2, 5, 7 and 9 dB respectively.
ID#3116314749

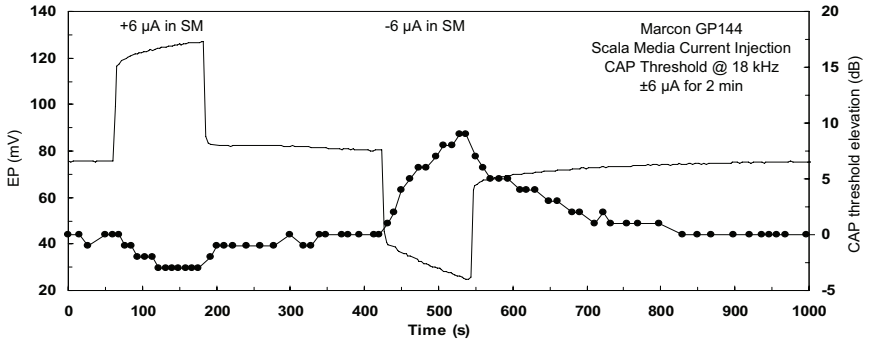

Figure 7.4: Data from Patuzzi (2002) showing changes in the endocochlear potential and CAP threshold (manually tracked using the visual-detection threshold) during injection of ±6 µA current into scala media. As with the example shown in Figure 7.3 above, increasing the driving potential caused insignificant changes in 18 kHz threshold (if anything, a slight improvement), while reduction in driving potential caused a slow-onset 10 dB threshold shift.

As with the data presented in Figure 7.1, the Boltzmann effects were relatively symmetric: the negative current injection caused a 10% increase in Vsat, a 5% decrease in Z, and a 4 meV maximal operating-point shift towards scala tympani, while the positive current injection caused a 10% decrease in Vsat, a 6% increase in Z, and a 4 meV step operating-point shift towards scala vestibuli (which increased to 6 meV over the 5-minute injection period). However, while there was no significant shift in CAP threshold during the negative current injection, the positive current injection caused elevation of high-frequency thresholds with a time-course that lacked a fast component (i.e. thresholds increased over the 5 minute injection period, but did not show a step change at onset or offset). Of the frequencies assessed, the threshold elevation was greatest around 22 kHz (up to 9 dB elevation), decreasing to around 2 dB at 10 kHz, with no detectable elevation at lower frequencies.

The slow temporal onset of this threshold shift was not due to the ramp-rate of the threshold tracking algorithm, which was capable of responding to very fast changes in CAP threshold (see Chapter Four). Indeed, similar results were found by Marcon and Patuzzi for current injections into scala media (reported in Patuzzi, 2002), using the visual detection technique to manually track CAP thresholds (Johnstone et al., 1979; Rajan et al., 1991). As shown in Figure 7.4, injection of ±6 μA via a micro-electrode in scala media produced a ±50 mV EP modulation, but only the negative injection (causing a reduction in EP and driving potential) produced a significant threshold shift at the frequency measured (18 kHz). The time-course of the EP change recorded by Marcon and Patuzzi also showed the fast and slow components found in the Boltzmann parameters. In the case of EP, the slow component was in the same direction as the fast component. The probable mechanism behind such changes, derived from the modelling work of Chapter Two, is discussed in Section 7.6.2 below.

7.3.3 Neural effects: greater modulation of P1 amplitude

The effect of current bias on CAP waveforms evoked by supra-threshold stimuli was also examined. The changes in waveshape were quantified by measurement of the amplitude of the neural peaks: As the SP was presumed to last for the entire 5 ms duration of the tone-burst, the amplitude of N1 was measured from the SP peak where present, and from the pre-stimulus baseline for more apical frequencies (further from the recording location). The P1 amplitude was measured from the N1 peak (rather than the SP or the pre-stimulus baseline), which ensured its amplitude was always positive.

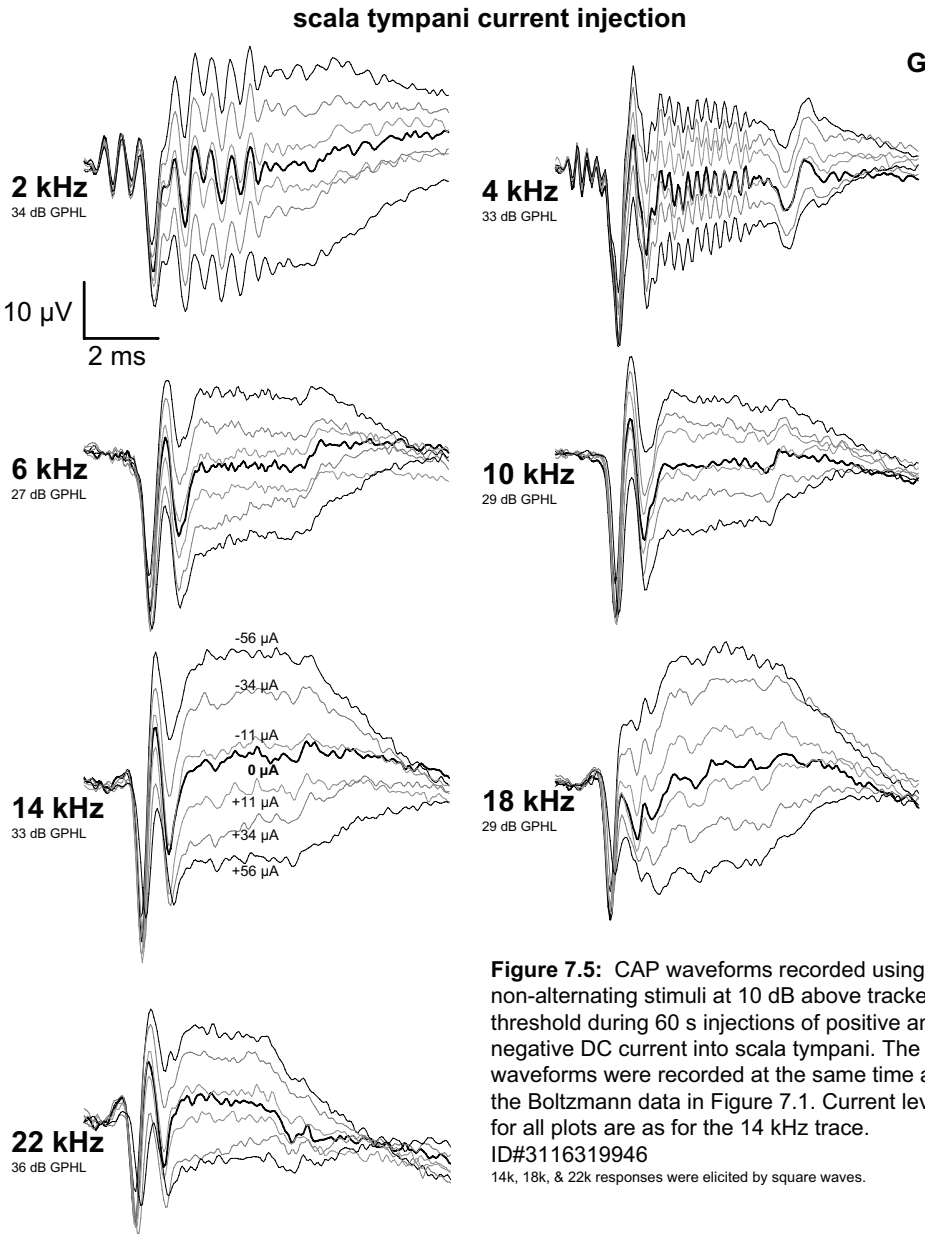

Figure 7.5: CAP waveforms recorded using non-alternating stimuli at 10 dB above tracked threshold during 60 s injections of positive and negative DC current into scala tympani. The waveforms were recorded at the same time as the Boltzmann data in Figure 7.1. Current levels for all plots are as for the 14 kHz trace.
ID#3116319946
14k, 18k, & 22k responses were elicited by square waves.

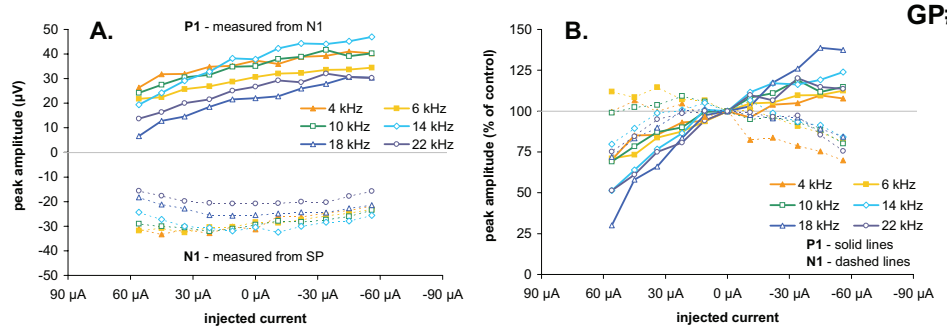

Figure 7.6: The N1 and P1 amplitudes of waveforms in the series shown in Figure 7.5 above, shown in absolute amplitude (**A**) and as percentages of the control amplitude (**B**). The injection of DC current into scala tympani modulated P1 amplitude (solid traces) greater than N1 amplitude (dash traces), with the largest P1 modulation occurring at high frequencies. Also visible in B. is the non-monotonicity of the the N1 modulation (discussed in the text).
ID#3116319946 14k, 18k, & 22k responses were elicited by square waves.

Figure 7.5 shows CAP waveforms elicited by non-alternating stimuli at 10 dB above tracked threshold during scala tympani current injection. The waveforms were recorded during the current injection series shown in Figure 7.1, where current was presented at levels of ±11, ±22, ±34, ±45, and ±56 μA[2]. The largest changes with injection were observed in the amplitudes of P1, and in the baseline shift occurring between the N2 peak and the end of the stimulus. The N1 amplitude was also modulated, but to a lesser extent than P1. The change in the neural baseline shift (which was in the same direction as the P1 shift) is discussed in Section 7.7.5 below.

The amplitudes of the N1 and P1 peaks are shown in Figure 7.6. As these waveforms were evoked using non-alternating stimuli, the 2 kHz waveforms were excluded from the analysis due to the difficulty of measuring the neural peaks amid the uncancelled CM. For the remaining frequencies, it can be seen that the P1 amplitudes were inversely proportional to the current amplitude, with the largest percentage modulation occurring for the higher frequencies that were closer to the injection site than the lower frequencies (Figure 7.6B). Unlike P1 modulation, the N1 amplitude function was non-monotonic at higher frequencies, decreasing for both positive and negative injections. For the low-frequency CAPs (4 kHz, 6 kHz and 10 kHz), the amplitude fluctuations appeared roughly proportional to current injected.

The changes in the SP amplitudes at 14, 18, and 22 kHz recorded during this one experiment are shown in Figure 7.7 below. The 14 and 22 kHz SP amplitudes showed a significant[3] inverse correlation with amplitude of the current injection. The modulation data for SP amplitude at 18 kHz was somewhat noisier in this animal. The change in SP amplitude is consistent with a change in driving potential for K^+ through the inner hair cells, and possibly the modulation of cochlear gain.

To summarise, the short-term injection of DC current of up to ±56 μA in scala tympani did not markedly distort the morphology of the CAP waveforms, but caused a graded change of the N1 and P1 peak amplitudes, SP amplitude, and neural baseline shift. A discussion of the probable causes of the observed neural effects appears in Section 7.7.5 below.

---

[2] In Figure 7.5, the traces for ±22 μA and ±45 μA were omitted for clarity.

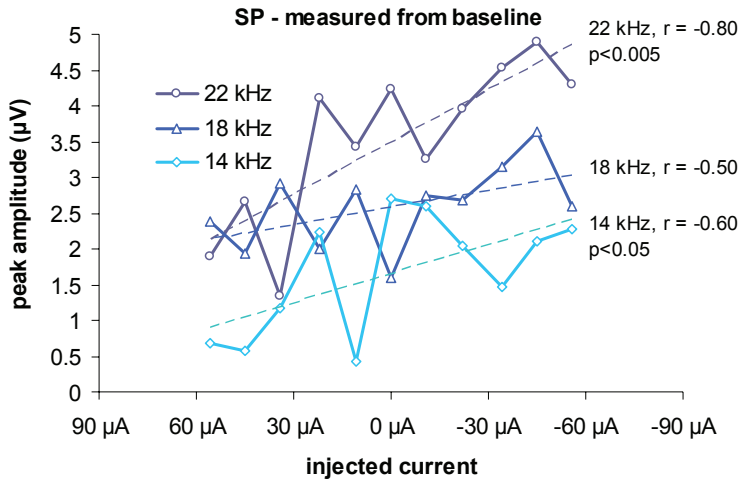

Figure 7.7: The amplitude of the 14 kHz and 22 kHz SPs were inversely proportional to the injection of DC current into scala tympani. The small amplitude of these SPs is due to the low stimulus level used (10 dB above tracked threshold). ID#3116319946

7.4 Results - extended injection of negative current

While the previous section presented data for current injections of 5 minutes or less, the effect of injecting *negative* current for 10 minutes or longer was examined in three animals. As with the shorter injections, the Boltzmann parameters, CAP threshold, CAP waveshape, and SNN were measured. Results for the prolonged injection of *positive* current are not presented here, because recordings of injections of more than a few minutes were disrupted by excessive electrolysis noise.

In the three long-duration negative current injections reported here, the "slow-component" of the Vsat change referred to in the previous section (that is, the decrease in Vsat following the step-increase at the onset of the injection in Figure 7.2) was followed by a slow oscillation that included a broad increase in Vsat between 7 and 11 minutes after onset of the injection that was indicative of an increase in basolateral permeability.

7.4.1 Extended injection of DC current without collapse of thresholds

In some cases, such as that shown in Figure 7.8, injection of 56 µA of negative current for periods as long as 85 minutes caused relatively minor amounts of deterioration, while in other cases, the rundown was much more severe, causing either a temporary threshold shift of at least 20 dB (as shown in Figure 7.12), or in one case a loss of hearing sensitivity that showed no signs of recovery two hours after the injection was stopped (data not shown).

---

[3] Student's two-tailed T-test, $p<0.005$ for 22 kHz, $p<0.05$ for 14 kHz.

Shown in Figure 7.8 is the former case, in which negative current was injected for an 85 minute period with only a mild elevation of high-frequency thresholds. The first two minutes of the injection showed the same fast and slow components of the Eo and Vsat changes that were described in Section 7.3.1 above. After this initial period, Vsat, Eo, and the SP amplitudes showed a highly-damped oscillation. Although the peaks of this oscillation were relatively broad, the operating point peaked toward ST at around 1000 s, followed by a local Vsat maximum at around 1150 s, with the SP amplitudes reaching maximal values broadly between these two. Estimates of the phase-shift between the Eo and Vsat were difficult to calculate because the period of the oscillations increased with time, with the second peak being much broader than the first. However, given that the next SV peak in Eo occurred at around 2250 s, it can be roughly calculated that Vsat peak lagged the first Eo peak by around 22º. The latter stages of the recording were affected by condensation on the recording electrodes: the resulting artefactual changes are marked with asterisks in Figure 7.8. Changes in the N1 and SP amplitudes during this experiment are shown in the bottom two traces of this figure, and are discussed in Section 7.4.2 below.

A second example of a prolonged current injection is shown in Figure 7.9. Although the current injection lasted 40 minutes, only data from the first 20 minutes of the injection are shown, as the remainder of the recording was excessively noisy. Nevertheless, the figure clearly shows the onset effects of the -56 μA ST injection, with the Boltzmann parameters, SNN, and CAP peak amplitudes showing changes that were qualitatively similar to those that occurred during the first 20 minutes of the injection shown in Figure 7.8 above: After the initial 5.5% step-rise in Vsat at the onset (the "fast component"), there was the same "slow component" decrease to around 2.5% above the pre-injection level after 90 seconds. After this time, Vsat slowly increased to 4.8% above baseline, reaching a broad maximum between 7 – 11 minutes after commencement of the injection before falling to within 2% of baseline levels. Over the same period, the Eo trace showed a more monotonic shift towards scala tympani, moving by 7 meV over the 20 minute period shown. Z showed a more complex pattern, with an initial step-decrease of 3%, followed by a further decrease to 5% below baseline that peaked prior to the Vsat peak. After an initial increase, the SNN fell gradually by 20% over the 20 minute period.

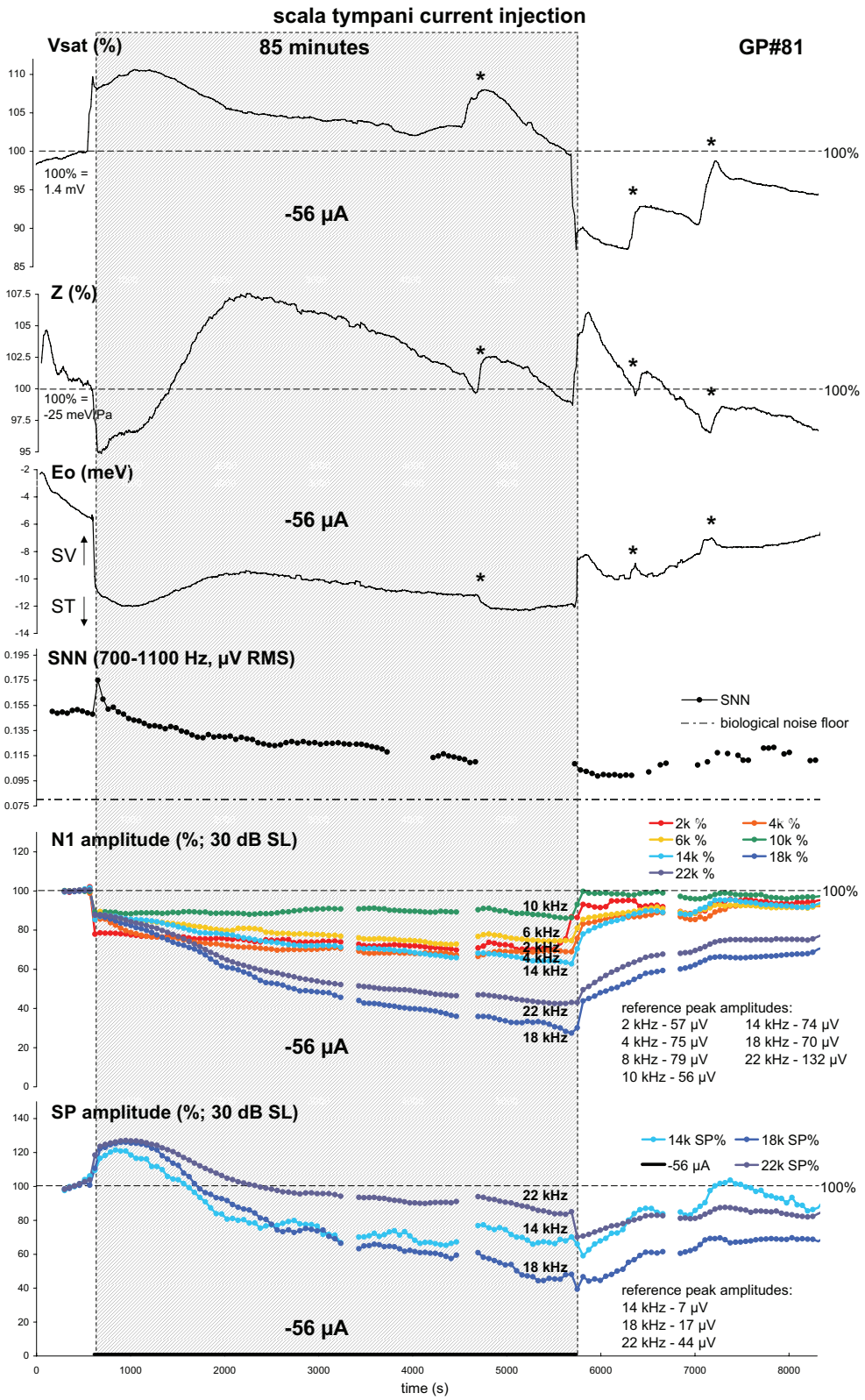

Figure 7.8: Prolonged injection of negative DC current into scala tympani resulted in systematic changes in the CM Lissajous figures and the corresponding Boltzmann parameters describing OHC transduction. Also shown are the percentage changes in N1 peak amplitudes (rather than CAP amplitudes, as shown in previous examples), which were generally larger for more basal frequencies, and the changes in SP amplitudes: After the initial increase in SP, amplitudes fell to below pre-injection levels, indicating active gain changes. Waveforms are presented in Figures 7.10 and 7.11. The asterisks indicate changes due to condensation between the injection and recording electrodes.

ID#3122427905 - Thresholds (2 kHz to 22 kHz; dB GPHL): 9, 9, 9, 3, 8, 5, 19.
103 dB Boltzmann probe level
9-pt running average on Boltzmann traces (excluding onset and offset of injection)
5-pt running average on other traces (excluding onset and offset of injection)
The recording was stopped for 15 seconds at 3330 s and 6764 s to change files.

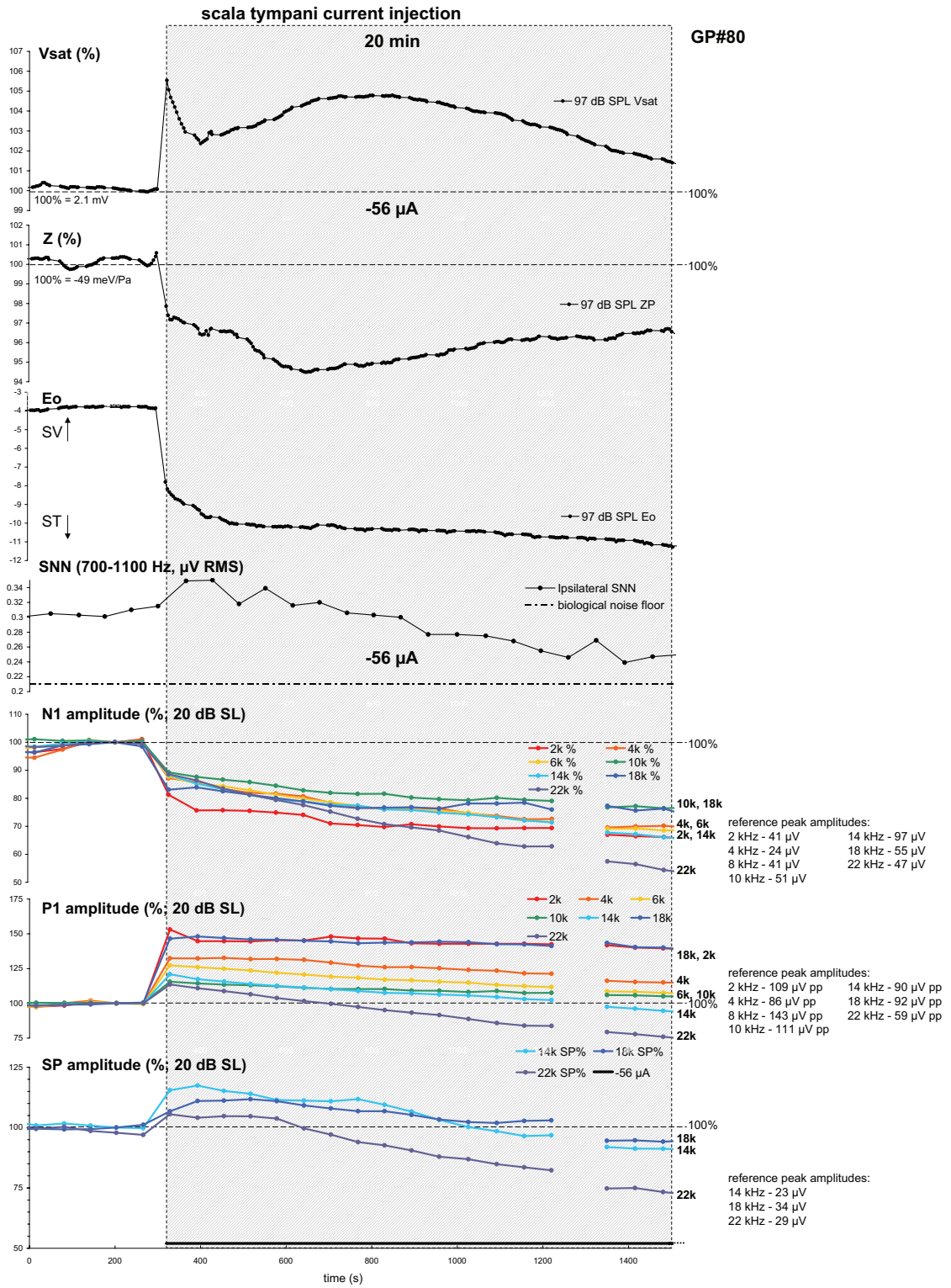

Figure 7.9: The effect of negative DC current injection on Boltzmann parameters, SNN, and CAP peak amplitudes. Following the initial step-increase at the onset of the injection due to the increased driving potential, the Vsat parameter decreased over the first 90 seconds, before subsequently oscillating, reaching a broad peak between 7 and 10 minutes after injection onset. In contrast, the Eo parameter showed a more monotonic 5 meV step-shift towards ST, followed by a slower further ST shift over the 20 minute period shown. N1 amplitudes were reduced at all frequencies, while P1 and SP amplitudes showed an initial increase, followed by a gradual decrease (to below baseline at some frequencies).
ID#3121821019 - Thresholds (2 kHz to 22 kHz; dB GPHL): 22, 8, 0, 3, 6, 10, 20.
9-pt running average on Boltzmann traces (excluding onset of the injection)

Changes in the N1, P1, and SP amplitudes during this experiment are shown in the bottom three traces of Figure 7.9, and showed similar changes to those from Figure 7.8, which are discussed in the section below.

7.4.2 Changes in CAP waveshape during prolonged current injection

The time-course of the changes in the N1 and SP amplitudes during the 85-minute current injection experiment were shown in the bottom two traces of Figure 7.8. Including the initial step-increase, SP amplitudes[4] increased by 25% over the first 7 minutes, after which time they decreased, reaching control levels between 17 and 28 minutes after the start of the current injection. The onset of the current injection caused N1 amplitudes (measured from the SP peak where available) to decrease instantaneously by 12% (± 1%) at all measured frequencies except 2 kHz, which decreased by 24%. After this initial step-decrease, the 18 kHz and 22 kHz N1 amplitudes decreased steadily over the first 30 minutes, after which time their rate of decrease slowed by a factor of five. N1-amplitudes for frequencies below 18 kHz decreased at a much slower rate, with some frequencies (such as 10 kHz) not decreasing at all. Although the time-course was not shown in that figure, the P1 amplitudes showed an initial increase of 25 ± 15% during the first two minutes, with the largest increases occurring at the more apical frequencies (45% at 2 kHz and 4 kHz), and the smallest increases at 14 kHz and 18 kHz (9 and 12%, respectively). After this initial increase, P1 amplitudes fell by 21 ± 22% over the following 60 minutes of the injection, with the largest decreases observed at 18 and 22 kHz (56 and 45%, respectively).

The waveforms from that experiment are shown in Figures 7.10 and 7.11. Figure 7.10 compares the control CAP waveforms with those recorded during the first two minutes of the injection, while Figure 7.11 compares the two-minute stage waveforms with those recorded after 63 minutes of injection (prior to the first of the artefactual condensation-related changes). As shown in Figure 7.10, the increase in SP and P1 amplitudes and the corresponding decrease in N1 amplitude at the onset of the current injection occurred without any significant changes in peak latencies. Over the 85 minutes of the current injection, however, there was a decrease in the peak-amplitudes of the 14, 18, and 22 kHz CAP waveforms, which was accompanied by an elongation of peak latencies of approximately 0.1 to 0.2 ms.

---

[4] As the summating potential is produced by the IHC receptor current in the vicinity of the recording electrode, SP amplitude data was only available for the 14, 18, and 22 kHz tone-bursts.

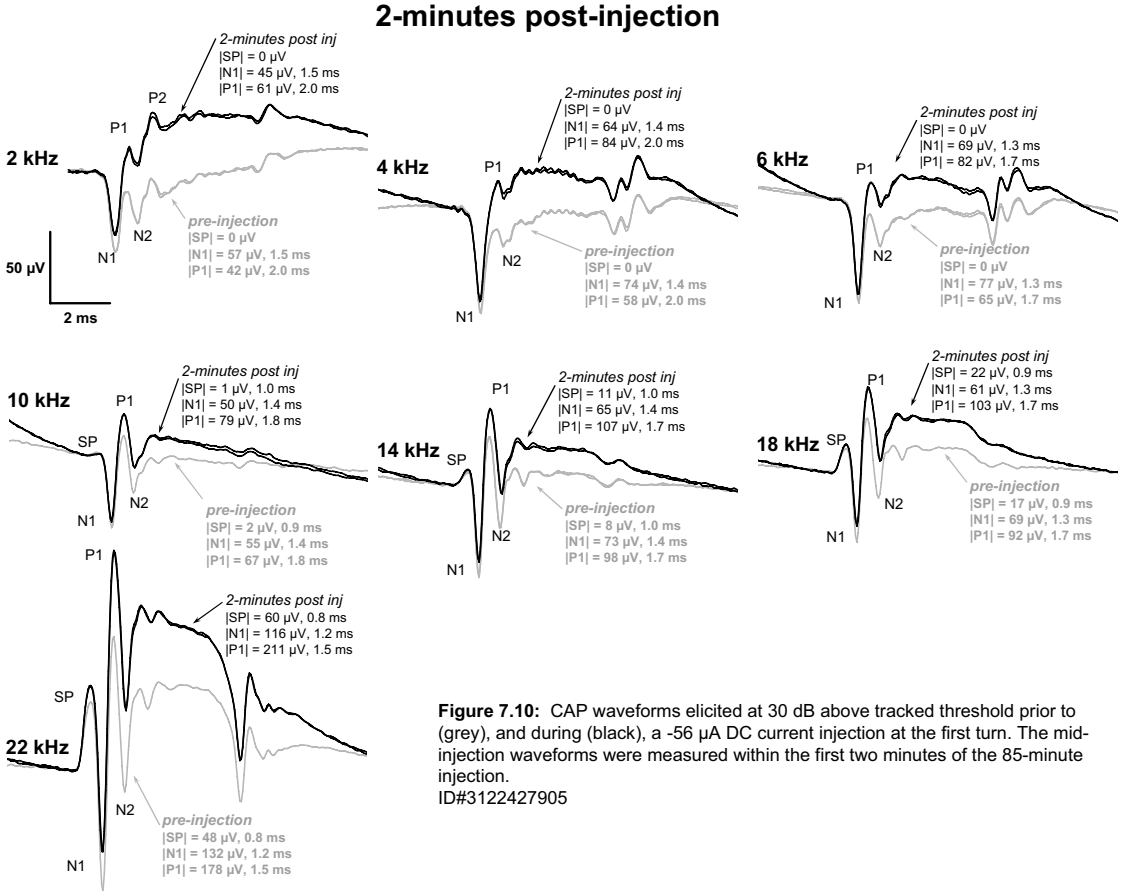

Figure 7.10: CAP waveforms elicited at 30 dB above tracked threshold prior to (grey), and during (black), a -56 µA DC current injection at the first turn. The mid-injection waveforms were measured within the first two minutes of the 85-minute injection.
ID#3122427905

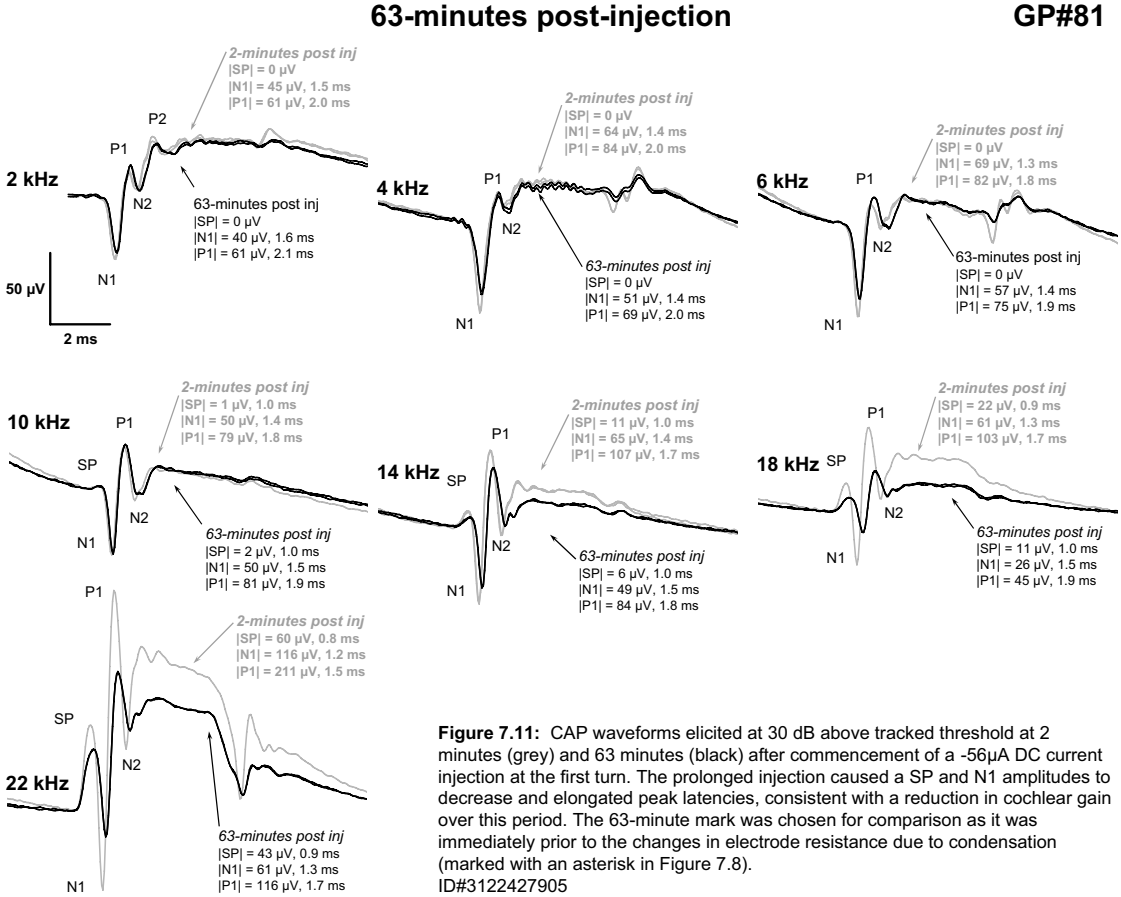

Figure 7.11: CAP waveforms elicited at 30 dB above tracked threshold at 2 minutes (grey) and 63 minutes (black) after commencement of a -56µA DC current injection at the first turn. The prolonged injection caused a SP and N1 amplitudes to decrease and elongated peak latencies, consistent with a reduction in cochlear gain over this period. The 63-minute mark was chosen for comparison as it was immediately prior to the changes in electrode resistance due to condensation (marked with an asterisk in Figure 7.8).
ID#3122427905

These changes were consistent with a decrease in cochlear gain over this period. In addition, the percentage change in P1 amplitude at each frequency was not significantly different from the percentage change in N1 amplitude. Following a step-increase at the onset of the current, the amplitude of the SNN also decreased by 25% during the first 60 minutes of the injection period.

7.4.3 Prolonged injection of DC current with loss of threshold

In contrast to the prolonged injections of the previous section, Figure 7.12 shows an instance where a -56 μA ST current injection of only 10 minutes duration caused a threshold loss of at least 20 dB in the high frequencies, and unusual changes in the Boltzmann parameters.

The first five minutes of the injection showed changes in Eo, SNN, and CAP amplitude[5] that were not dissimilar to those seen during previous injections. However, the initial step-shift in Vsat was unusually large (approximately 10%), while the Z parameter did not change significantly. The directly-measured peak-to-peak CM amplitude (not shown) showed a similar 11% step-increase at the onset of injection.

After the five minutes of the injection, the Vsat parameter continued to increase, reaching a maximum of 13% above pre-injection levels, while the peak-to-peak CM amplitude grew to a maximum increase of 20%. Operating point moved towards scala vestibuli, while the Z parameter showed a 16% slow *increase*, which was in the opposite direction from that seen with the other negative current injections.

The initial CAP amplitude changes were not abnormal for this magnitude injection, with the exception of the 22 kHz CAP, which continued to increase in amplitude (due to an increasing P1). After five minutes of the injection, the CAP amplitudes began to collapse, beginning with 22 kHz, 14 and 18 kHz, and then more apical frequencies. The CAP amplitudes were reduced to zero for frequencies above 6 kHz, indicating a threshold loss of at least 20 dB. On cessation of the injection, the 2 kHz and 4 kHz CAP amplitudes were restored almost immediately, while the more basal responses took between 10 and 12 minutes to recover completely. The 14 and 22 kHz CAP amplitudes were elevated relative to the pre-injection baseline.

---

[5] The measure of CAP amplitude used in this figure was the peak-to-peak amplitude (N1-P1), equivalent to the measures of P1 amplitude from the figures above.

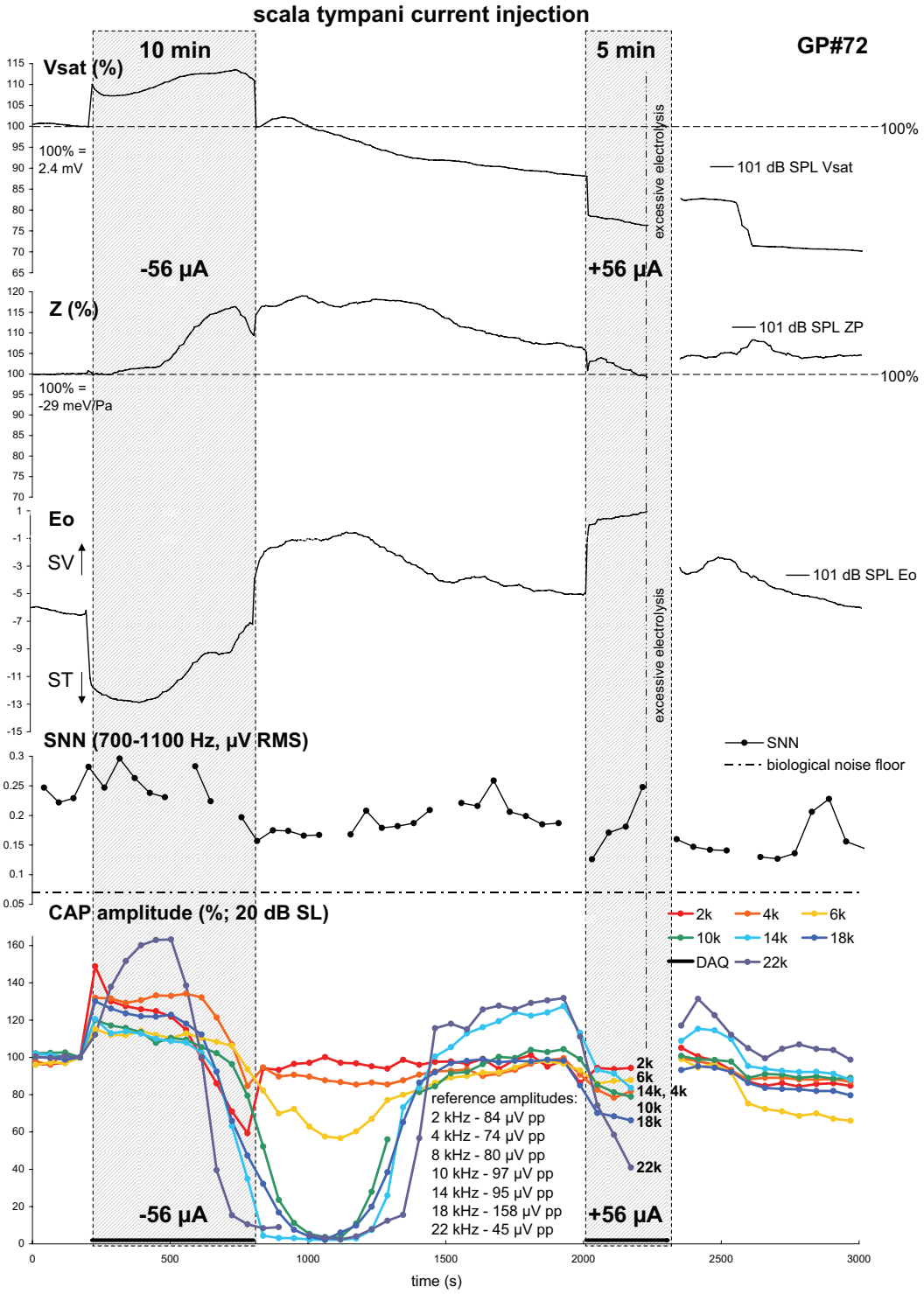

Figure 7.12: The effect of negative and positive DC current injection on Boltzmann parameters, SNN, and CAP amplitudes. In contrast to the 85 minute current injection shown in Figure 7.8, the injection of negative current for only 10 minutes in this animal caused a threshold loss of at least 20 dB in the high frequencies, and marked changes in the Boltzmann parameters, including a 16% slow increase in Z. This Z change was in the opposite direction to that commonly seen with negative current injection. On cessation of the injection, the CAP amplitudes recovered completely within 10 - 12 minutes. A subsequent injection of positive current into scala tympani caused a reduction in CAP amplitudes, a reduction in Vsat, and a scala vestibuli operating point shift, but caused a *reduction* in the magnitude of the Z parameter, again in the opposite direction to that seen with most current injections. The positive injection also caused excessive electrolysis, resulting in loss of data and prompting the termination of the injection after only five minutes. ID#3119924998 - Thresholds (2 kHz to 22 kHz; dB GPHL): 21, 10, 1, 1, 5, 10, 19. 9-pt running average on Boltzmann traces (excluding onset and offset of injections)

A subsequent injection of positive current into scala tympani caused a reduction in CAP amplitudes, a reduction in Vsat, and a scala vestibuli operating point shift, but caused a reduction in the magnitude of the Z parameter, again in the opposite direction to that seen with most current injections. The positive injection also caused excessive electrolysis, resulting in loss of data and prompting the termination of the injection after only five minutes.

The cause of the large threshold shift seen with this negative current injection is not entirely clear, but is likely to be mechanical in origin. It is not likely to reflect transmitter run-down caused by prolonged depolarisation of the inner hair cells, as the SNN was not entirely abolished. The recovery of thresholds on cessation of the injection would argue against any ototoxicity arising from electrolysis of the stimulating electrode, or would indicate that it was short-lived if it occurred.

7.4.4 Summary of Boltzmann changes during negative current injection

In summary, the systematic changes in the Boltzmann parameters for the short current injections (shown in Figures 7.1 and 7.2) were the first phases of slow oscillations (albeit highly damped ones). This point is illustrated in Figure 7.13, in which the responses to 1-minute, 5-minute, and 85-minute current injections were overlaid.

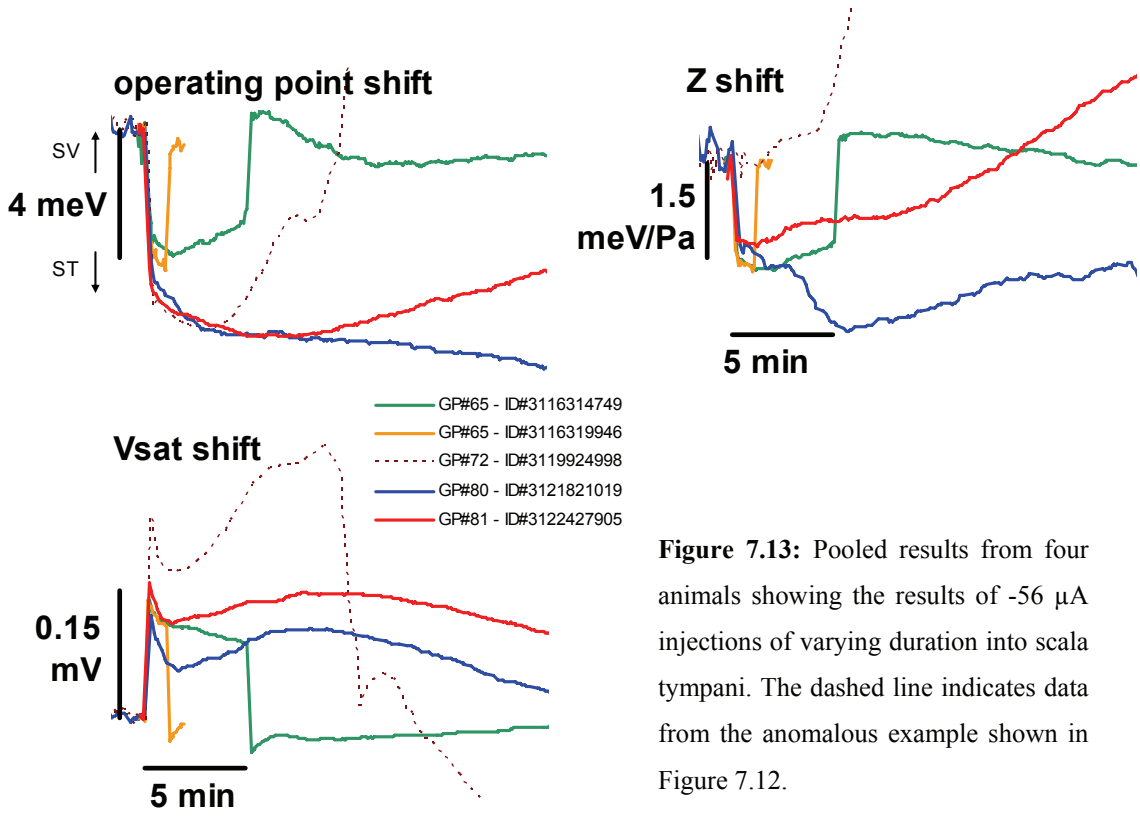

Figure 7.13: Pooled results from four animals showing the results of -56 µA injections of varying duration into scala tympani. The dashed line indicates data from the anomalous example shown in Figure 7.12.

Although they are of different durations, the five results shown in Figure 7.13 indicate some of the common features of the negative current injections. The Vsat traces all showed an initial step-increase that was followed by a smaller transient decrease lasting at least one to two-minutes. The longer injections showed slow oscillatory increases in Vsat afterwards between 7 and 10 minutes after onset. The operating point shifts were characterised by an initial step-shift in Eo towards ST, followed by a further shift towards ST that during 3 of the 4 longer injections moved back towards SV after a variable interval. With the exception of the data from GP#72 (dashed trace), the -56 μA injection into ST caused a step-decrease in Z of between 1.2 and 1.6 meV/Pa (mean 4.6 ± 1.3%), with variable longer-term changes. The possible mechanisms of these time-courses are discussed in Section 7.7.1 below.

7.5 Results - Comparison with the SM results of Marcon and Patuzzi

The current injection experiments carried out in the present project were performed under the assumption that the primary effect of the current injection was the change in the driving potential across the organ of Corti, such that the injection of current of one polarity into scala tympani would produce the same results as the injection of current of the opposite polarity into scala media. However, comparison of the ST current injections described above with the SM injection data of Marcon and Patuzzi (in preparation) revealed a number of systematic differences between the two sets of results. These differences, discussed below, may arise from the different injection locations (SM versus ST), or may be due to the presence of a continuous LF tone for Boltzmann analysis during the Marcon and Patuzzi SM-injection experiments[6], which may have increased the calcium concentration in the OHCs, thereby altering the mechanical responses to electrical stimulation.

In the SM injections, the operating point shift still consisted of a fast component and a slow component, but the ratio of the size of the components (which we will call the "fast:slow ratio") differed from those during ST injections. In the SM injections of positive current shown in Figure 7.14, the fast:slow ratio was 0.4:1 after five minutes, whereas over the same duration in the ST injections the fast:slow ratio was significantly higher, at approximately 2:1.

---

[6] Marcon and Patuzzi used an analogue computer to perform real-time Boltzmann analysis(the device is described in Patuzzi, 1995; Patuzzi and Moleirinho, 1998). As the analogue and digital Boltzmann analysis methods are directly comparable, the mark/space ratio of the LF tones (continuous versus intermittent) is the only significant difference between the two forms of measurement.

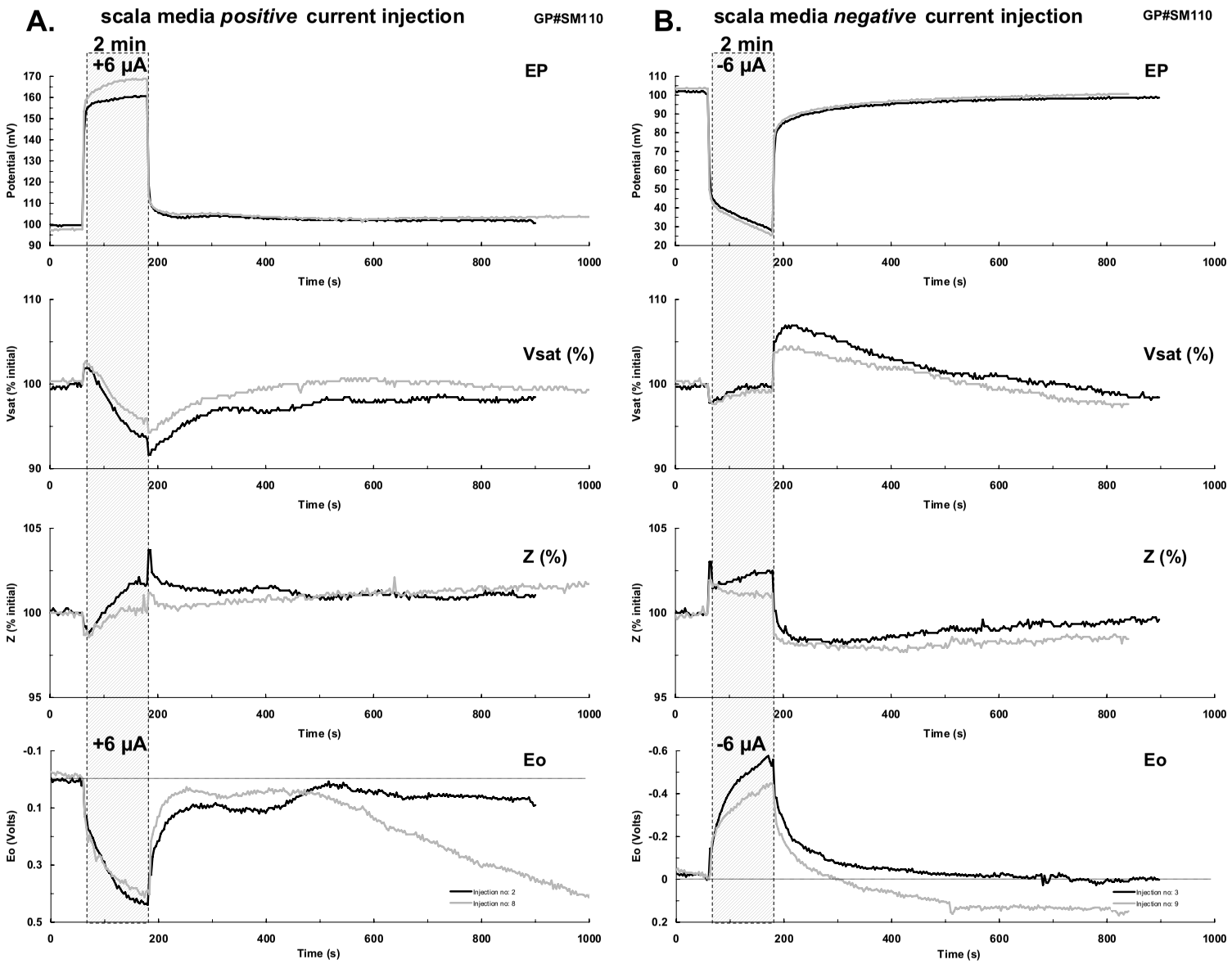

Figure 7.14: Data from Marcon and Patuzzi (in preparation) showing overlayed data for two injections of positive and negative DC current into scala media. Shown are the changes in the EP and Boltzmann parameters. **A.** Injection of positive current into scala media increased the driving potential provided by the EP, causing a 2.2% step-increase in Vsat at the onset of injection, followed by a large decrease to 5% below pre-injection levels, an increase in Z, and a further movement of the operating point towards ST. **B.** Scala media injection of negative current reduced the EP, causing a 2.1% step-decrease in Vsat, followed by an increase to within 0.4% of the pre-injection baseline. The step-changes in Z were larger than for the positive current injections, while the Eo traces were roughly equal and opposite to those for positive injection.

The Z parameter showed an initial 1.4% decrease, followed by a slow increase to baseline in one case, or to 1.72% above the pre-injection baseline. The Vsat traces for the positive SM current injection showed an initial average 2.2% step-increase, followed by a large decrease to 5% below pre-injection level. The EP trace also showed fast and slow components that were both in the same direction.

Marcon and Patuzzi's two-minute SM injections of negative current (shown in Figure 7.14B) did not produce the "equal-and-opposite" changes in Vsat that were observed for one-minute ST current injections of opposite polarities in the present set of experiments (shown in Figure 7.1), although this pattern was observed for the EP and Eo traces. The step-shifts in Z were larger for the negative SM injections than for the positive SM injections of Figure 7.14B, and for some reason the two similar injections in that figure produced slow changes in Z that were in opposite directions.

To summarise, the SM-injection results of Marcon and Patuzzi showed Vsat changes that were markedly different from the pattern of results observed in the present series of ST-injections, and operating point changes that had a much larger slow-component compared to the fast component. The differences will be discussed in Section 7.8 below.

7.6 Results - Modelling of SM current injection effects

The mathematical model of OHC homeostasis presented in Chapter Two was used to simulate the effects of current injection. The modelling of current injection effects had proceeded on the assumption that the scala media and scala tympani DC current injections were equivalent, and so the data of Marcon and Patuzzi were used as the template against which the success or failure of the modelling simulations were judged.

In this model, the injection of DC current into scala media was simulated by the systematic alteration of the open-circuit EP (see Chapter Two). Figure 7.15 shows the results from two five-minute EP biases, equivalent to injections of positive and negative current into scala media respectively, of magnitude sufficient to raise and lower the EP by 20 mV. The reader is encouraged to compare the results from the model output presented in this figure with guinea-pig data recorded by Marcon and Patuzzi for similar duration current injections, presented in Figures 7.14 (which contains EP traces and Boltzmann data) and 7.4 (which contains EP traces and CAP threshold).

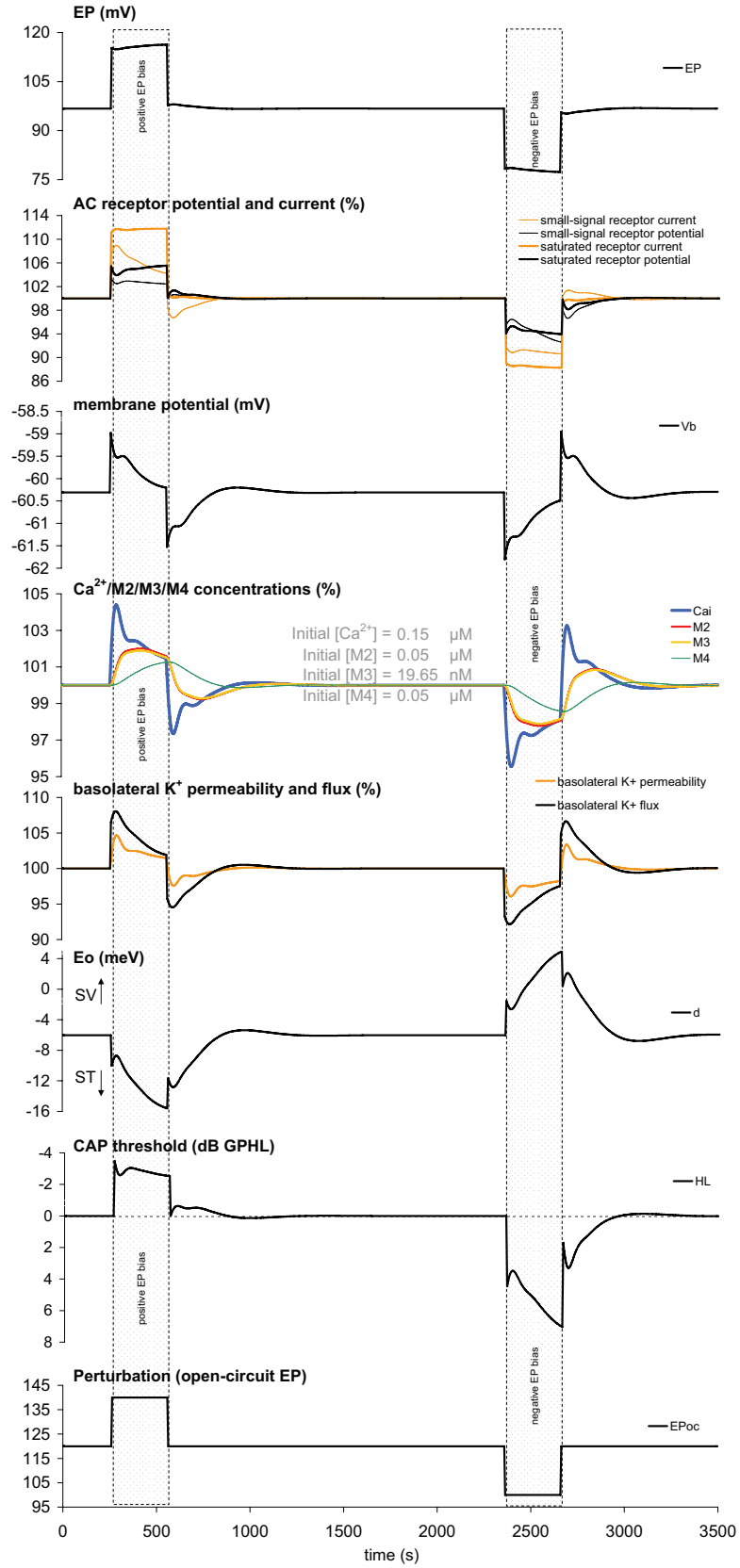

Figure 7.15: OHC model parameters during consecutive five-minute EP bias perturbations. Key features of the model output resemble the experimental data for DC current injections, shown in Figures 7.4 and 7.14. These include the slow increase in the EP perturbation (positive or negative) during the plateau phase of each injection, the correspondence between the 12% change in saturated receptor current and the measured 10% change in Vsat, the 4 meV step-shifts in operating point, and the asymmetric changes in hearing sensitivity (with larger changes observed with EP reduction).

7.6.1 Model responses to positive SM current injection

In Figure 7.15, the positive EP bias increased the driving potential for potassium into the OHC from 157 mV to 177 mV, which increased the flux of potassium into the cell by 6.5%. This resulted in step-changes in a number of parameters, including a depolarisation of 1.3 mV, an electromotile contraction of 4.0 meV toward scala tympani, and increase in the saturated AC receptor current by 11%, and an increase in the saturated AC receptor potential of 5.4%. Using the empirical relationship presented in Equation 8, the observed 3.3% increase in small-signal receptor potential was extrapolated to a 3.5 dB improvement in CAP thresholds.

The step-changes described above were followed by slower changes that were mediated by changes in intracellular ionic concentrations (particularly in intracellular calcium) that were triggered by the change in membrane potential with current injection. The 1.3 mV step-depolarisation increased the opening probability of the L-type voltage-dependent calcium channels by 30%, causing an influx of calcium into the hair cell down its electrochemical gradient[7]. The intracellular calcium level increased by 4.5% over the first 30 seconds of the injection, causing a 4.6% increase in basolateral permeability (via the opening of SK-type calcium-sensitive potassium channels). This caused the efflux of potassium to increase further, and caused a 0.5 mV repolarisation of the cell during this first 30 seconds.

The 4.5% rise in $[Ca^{2+}]_i$ caused the levels of the intracellular messengers M2 and M3 to also increase, which potentiated the sequestration of Ca^{2+} into the subsurface cisternae. The $[Ca^{2+}]_i$ then began to decrease, reducing the permeability of the basolateral wall, reducing the K^+ efflux and causing a slow increase in the EP (due to the decreased shunt-current). After the initial step-shift towards ST, the operating point showed a small 1.1 meV inflection toward scala vestibuli (due to the sharp reduction in the degree of depolarisation of the membrane potential caused by the influx of calcium), which has not been observed experimentally. Nevertheless, this was followed by a further 6.7 meV shift towards scala tympani under the influence of the increasing M4 concentration on slow-motility.

At the end of the injection, there was a step-shift in a number of parameters due to the reduction in driving potential: the membrane potential showed a step-

---

[7] The presence of these voltage-controlled channels is a requirement for this influx to occur: If the basolateral calcium conductance were fixed, the first-order effect of this depolarisation would be a decrease in intracellular Ca^{2+} concentration, due to the reduced electrical gradient for Ca^{2+} entry.

hyperpolarisation of 1.3 mV, the operating point moved towards scala vestibuli by 3.9 meV, and the K^+ flux fell by 6%. These parameters then showed a gradual and, in some cases oscillatory, return to pre-injection levels, driven by the return to calcium to steady-state levels.

The results of the negative EP bias were roughly equal and opposite to the changes with the positive bias, but were of larger magnitude: The step-change in operating point was 2% larger for the negative bias than for the positive bias, increasing to 13% larger by the end of the injection period. The threshold shift during the negative EP bias was 0.6 dB larger at the onset of the injection, which increased to 4.5 dB larger at the end of the injection. The difference between the threshold shifts during negative and positive injections was due to the magnitude of the AC receptor potential increasing by 4.2% during the positive injection, but decreasing by 7.4% during the negative current injection – the mechanisms of this asymmetry are discussed further in Section 7.7.3 below.

7.6.2 Correspondences between the model results and experimental data

A number of the features of the model results are similar to those observed with scala media current injection. The fact that these similarities occur concurrently, and occur with one set of parameters, provides some validation of the model's ability to replicate the experimental findings. It is important to consider that the size and duration of the current injection were chosen so as to create a generic EP increase and decrease, not to specifically match the data shown in Figure 7.14, and so the absolute magnitude of the changes of some parameters will differ.

Many characteristics of the EP trace match those observed experimentally – after the initial step-increase in simulated EP of the model, it continued to rise over the five-minute injection period by approximately 6% of the size of the step-increase under the influence of the growing ST operating point shift and the corresponding reduction in apical permeability. The SM injection data of Marcon and Patuzzi also show a continued EP rise, albeit slightly larger at 10-14%. At the offset of the injection, the model EP fell to a level that was above the pre-injection baseline, before slowly returning to the baseline level over 1 minute, again under the influence of the operating point. The experimental data also shows the EP returning to an elevated baseline (again, a larger degree of elevation - around 8%), but in this case the baseline remained elevated, indicating a longer term change that was outside the functioning of the model.

The model Eo showed an initial fast-electromotile step-shift towards ST, followed by a continued slow-motile shift in the same direction, with a fast:slow ratio of 0.6:1. The data of Marcon and Patuzzi showed a similar pattern, with an average fast:slow ratio of 0.4:1 (which, as mentioned earlier, contrasts with the ST injection results of the present study, which showed a 2:1 fast:slow ratio).

In the mathematical model, the CAP threshold shift was estimated according to the OHCs ability to generate a small-signal receptor potential (for details of these calculations, see Chapter Two). The modelled CAP threshold shift showed a 2.5 dB threshold improvement by the end of the 5-minute positive current injection, but was elevated by 7.4 dB by the end of negative current injection. A similar asymmetry was also observed during scala media and scala tympani current injections in the guinea-pig, as shown in Figures 7.3 and 7.4 The slow components of the modelled threshold-shift time-courses show a reasonable match to the experimental data, but the step-shifts in threshold at the onset and offset of the modelled injection are not observed experimentally.

The Vsat parameter was approximated by the saturated AC receptor current. Whereas the experimental data showed a 2% increase in Vsat, followed by a decrease to 5% below baseline, the saturated receptor current showed an 11% step increase which remained elevated throughout the injection period. The *small-signal* receptor current showed slightly more similarity to the experimental Vsat results, showing a 7% increase, followed by a slow decrease to 4% above baseline.

In short, the mathematical model of the OHC presented in Chapter Two was capable of reproducing many of the changes observed during current-injection experiments in the guinea-pig. The development and fine-tuning of the model was carried out using the scala media current injection results as a guide, and provides a better match to these results than to the scala tympani injection results presented in this chapter. Whether this was just due to the fine-tuning of the model, to the different Boltzmann measurement processes used, or to some intrinsic difference in the underlying mechanism of the changes observed at the two injection locations, is unclear. In terms of the experimental data, it is difficult to use the ST injection results presented here to assess the differences between ST current injection and SM current injection, primarily because of the systematic differences in the way that our study and that of Marcon and Patuzzi was carried out. The greatest of these was the use of an intermittent Boltzmann probe-tone in this study instead of the continuous tone used by Marcon and Patuzzi. As shown in

Chapter Six, it is likely that the presence of a continuous LF tone leads to an elevation of cytosolic calcium which changes the motile responses of the OHCs. This is supported by the different ratio of the fast and slow motile components to the operating point shifts observed in the two studies. To resolve this issue, the effects of scala media and scala tympani current injection will have to be compared under the same experimental conditions.

7.7 Discussion

7.7.1 Explanation of observed changes in Boltzmann parameters

This section summarises the changes observed during injection of direct current into the cochlea in the context of the mechanisms implied by the OHC mathematical model. Scala media DC current injection was simulated using the mathematical model of OHC homeostasis described in Chapter 2. Based on the similarities between the experimental data and the results of this simulation (presented in Section 7.6 above), it seems plausible that the fast and slow changes in the Boltzmann parameters were caused by instantaneous driving potential changes and slower changes in intracellular calcium concentration, respectively. The changes in Eo and Vsat are described below, while the changes in the Z parameter changes are discussed in Section 7.7.4 below.

Based on the modelling work presented in Section 7.6 above, the observed changes in the Boltzmann parameters with *negative* DC current injection into scala tympani appear to be well accounted for by the following sequence of events:

- At the onset of the injection of negative current into scala tympani, there would be an increase in the driving potential for potassium through the OHCs causing an increase in the flow of potassium ions through the OHC and a rapid depolarisation of the basolateral membrane potential.
- In the presence of sound, this increase in the potassium driving potential would cause a step-increase in the AC receptor current that would be reflected in a sharp Vsat increase.
- The rapid depolarisation would cause a conformational change in prestin, the OHC motor protein, causing an electromotile contraction of the hair cell that is reflected in the step-shift in operating point towards ST. Such an effect could occur within fractions of a millisecond, as fast electromotility must function at audio frequencies in order to be the cochlear amplifier (Frank et al., 1999).

- The initial depolarisation is then presumed to trigger subsequent slow changes in OHC function: the step-depolarisation would open voltage-dependent L-type calcium channels, causing an influx of calcium into the hair cell down its electrochemical gradient. The intracellular calcium rise, which is presumed to have a finite time-constant (Allbritton et al., 1992), would cause an increase in basolateral permeability (via the opening of SK-type calcium-dependent potassium channels; Dulon et al., 1998) which would then begin to repolarise the cell.

- While the repolarisation would reduce the extent of the prestin-meditated contraction, the ST operating point changes we observed are consistent with the rise in intracellular calcium causing a *further* contraction of the hair cell via the calcium-mediated slow motility process, indicating that the operating point shifts are dominated by calcium in this phase of the current injection.

It might be expected that such an increase in basolateral permeability would cause an increase in Vsat and CM amplitude, due to the expected increase in receptor current. Indeed, this is observed in the results from the mathematical model. Experimentally, however, we actually observe an initial decrease in Vsat, for both scala-media-positive and scala-tympani-negative current injections, over the first 90-120 seconds. In three of the four ST-negative current injections that lasted more than five minutes (shown in the summary Figure 7.13), the initial decrease was followed by a transient Vsat rise that peaked after 7-10 minutes, which is consistent with the behaviour of the model. The circumstances surrounding the observed *initial reduction* in Vsat, and the incompatibility of this behaviour with the homeostatic model, is explored further in the "Two-Pool Theory of OHC Calcium Control" discussions in Chapter 9.

Before that, however, let us briefly discuss the OHC changes at the offset of the injection. Again, based on the modelling work presented in Section 7.6 above, the observed changes in the Boltzmann parameters at the *offset* of the negative DC current injection into scala tympani appear to be well accounted for by the following sequence of events:

- At the offset of the injection, there would be a decrease in the driving potential for potassium through the OHCs causing a reduction in the flow of potassium ions through the OHC and a rapid hyperpolarisation (or repolarisation) of the basolateral membrane potential.

- In the presence of sound, this reduction in the potassium driving potential would cause a step-decrease in the AC receptor current and therefore Vsat.
- The hyperpolarisation would cause a step-shift in operating point towards SV, due to a relaxation of the prestin-mediated electromotile contraction. Experimentally, the magnitudes of the fast contractions at onset and offset were found to be equal (Figure 7.2), which implies that the electromotile shifts were not markedly affected by the slower changes in intracellular ionic concentrations that occurred during the injection.
- The repolarisation would then trigger a partial closure of the L-type calcium channels, leading to i) a reduction in the calcium influx, ii) a closure of calcium-dependent potassium channels, and iii) a slight depolarisation towards the pre-injection baseline.

The changes that occur at offset of the scala-tympani-negative current injections are essentially the same as those observed at the *onset* of scala-tympani-*positive* current injections.

7.7.2 Small operating point shifts with current injection.

The Eo shifts seen with current injection were distinct and reproducible, but were relatively small, yielding only a 3.6 meV step-shift for a 50 μA injection, compared to much larger shifts with other perturbations (for example, the approximately 20 meV ST shift with perilymphatic perfusion of 50 mM K^+ (see Chapter 8).

Although the 200 Hz CM recorded at the round window is produced primarily in the basal turn (Patuzzi et al., 1989b) with only minor contributions from more apical regions, the current injected at site near the round window may affect a much smaller area, decaying exponentially with an estimated length constant of around 1 mm. These two processes could, in combination, lead to a "dilution" of the measurement of the current injection effects. To counter the additivity of these two effects, a less focal stimulus could be used (such as current injection from a line source close to the basilar membrane), and/or a more focal response could be analysed. The modulation of a more place-specific response than the low-frequency CM, such as a tone-burst evoked CAP, would give a clearer indication of the magnitude of the current effect at that location, if it were not complicated by the effect of the injection on the axonal currents. As discussed by Brown et al. (2004), only 1% of the current injected at the round window

would reach the 2 kHz place[8], and yet a significant modulation of the round-window CAP is observed at that frequency due to axonal modulation. Preliminary attempts to introduce a long wire electrode into the cochlea as a means of stimulating a larger length of the organ of Corti were not successful, and were not pursued further.

7.7.3 Asymmetric threshold shifts – contributing factors

The threshold shifts produced by both scala tympani and scala media current injection were asymmetric, with the loss of threshold with ST-positive/SM-negative current injection being larger than the improvement in threshold for injections of the opposite polarity. This behaviour was also reproduced by the mathematical model of the OHC. In the model, the threshold shifts were calculated empirically from the small-signal AC receptor potential, which is itself dependent on processes occurring at the apex and the base of the cell. As mentioned earlier, hair cell capacitance was not included in the model calculations.

The AC receptor potential is inversely proportional to the slope of the basolateral IV-curve: If the apical IV curves intercept the basolateral IV curve at a region of shallower slope, the receptor potential will increase, whereas if they intercept at a steeper section of the basolateral IV curve, the receptor potential will decrease. As described by the GHK equation, the basolateral wall IV-curve is non-linear, with the slope of the curve decreasing with hyperpolarisation. At the step-shift onset of the simulated negative EP bias (which causes hyperpolarisation of the model OHC), the point of intersection of the IV curves changed such that the slope of the new point on the basolateral IV curve was 3.7% lower than the control value. Taken in isolation, this change in the slope of the basolateral IV curve would have acted to increase the small-signal AC receptor potential, and decrease the small-signal receptor current, thereby partially counteracting the changes in receptor potential and receptor current that did arise from the changes in apical conductance, described below. An interesting implication of this nonlinearity is that if the basolateral IV-curve were sufficiently tightly-curved, the first-order effects of EP change on receptor potential could be nulled completely and instantaneously. While this nullification does not occur in the model, the results of EP bias are at least slightly minimised by this mechanism.

---

[8] This assumes a length constant for the current spread of 1 mm, and a guinea pig place/frequency slope of 2.5 mm/octave.

Another EP-buffering mechanism arises from the changes in transducer operating point during the current injection. This can be illustrated by an examination of the IV-curves of the mathematical model during the simulation of positive and negative EP biases presented in Section 7.6 above. The IV curve of the mathematical model at the end of both five-minute current injections is shown in Figure 7.16. In this figure, the apical IV curves for a saturated stimulus are shown, as the differences in the small-signal apical IV curves would not be visible on this scale, while the control IV curves are shown in grey. Comparison of Panels A and B of this figure shows that the positive EP bias caused an increase in small-signal receptor potential of 2% (re: control), while the reduction in small-signal receptor potential during negative EP bias was 7%. For the approximately 20 mV increase in EP, the near-instantaneous prestin-mediated contraction with depolarisation caused an operating point shift of 4 meV towards scala tympani. As the quiescent operating point was situated on the ST side of the symmetrical point, the -4 meV shift moved the apex of the cell to a less sensitive part of the transfer curve, causing a 4% step-reduction in apical conductance. By contrast, the 20 mV decrease in EP caused an Eo shift of 4.5 meV toward scala vestibuli, which moved the apex to a *more sensitive* part of the transfer curve, increasing the apical conductance by 4.5%. These conductance changes can be seen at a glance in Figure 7.16 by comparing the slopes of the control (grey) and mid-injection (red) apical IV curves. It can be seen from the above example that possessing a resting operating point that is on the scala-tympani side of the mid-point (the point of maximal sensitivity) provides a small degree of "buffering" against changes in the EP, by increasing the apical conductance when the EP falls and reducing it when the EP rises.

7.7.4 Asymmetric changes in the Z Boltzmann parameter

As shown in Figure 7.2, the effect of the current bias on the Vsat and Eo Boltzmann parameters was remarkably symmetric, in that positive and negative current injections caused equal but opposite effects for both the fast and slow components of the changes. However, the changes in Z were visibly asymmetric, with the reduction in Z with negative current injection (3% per 50 μA) being of smaller magnitude than the increase in Z with positive current injection (5.5% per 50 μA). The Z parameter is a measure of the sensitivity of the mechanoelectrical transduction process to displacement or pressure in the ear canal, and is proportional to the compliance of the organ of Corti: An increase in the stiffness of the organ of Corti will result in a reduction in the amount of hair-bundle displacement for a given ear-canal pressure stimulus.

A. IV curves – 5 min positive SM current injection

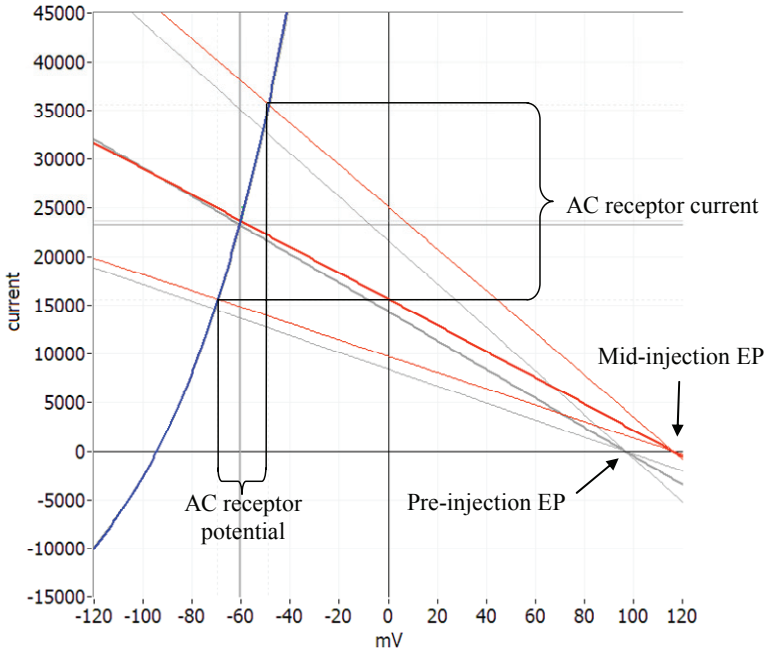

EP: 116 mV

Saturated:
receptor current: + 12%
receptor potential: + 6%

Small signal (not shown)**:**
receptor current: + 4%
receptor potential: + 2%

Threshold elevation:
-2.5 dB

B. IV curves - 5 min negative SM current injection

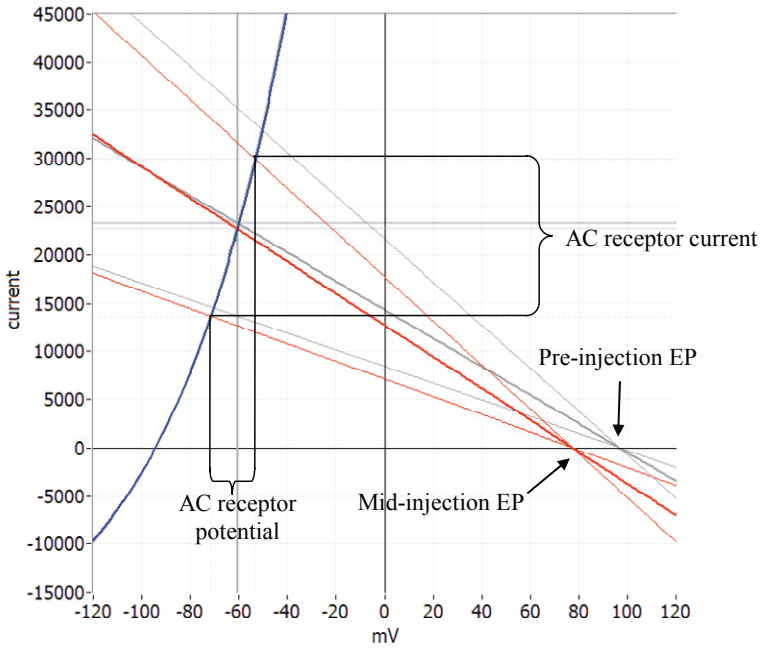

EP: 77 mV

Saturated:
receptor current: - 12%
receptor potential: - 6%

Small signal (not shown)**:**
receptor current: - 9%
receptor potential: - 7%

Threshold elevation:
7 dB

Figure 7.16: The effect of 5-minute positive scala media current injection on the IV curves of the model OHC. IV-curves are shown in grey for the pre-injection condition, and in colour for the condition after 5 minutes of current injection. The IV curves for the basolateral wall (blue curves) had returned to within 2% of the pre-injection condition after five minutes, while the set of apical of curves (red lines) remained considerably shifted to the right or left for positive current injection (**A.**) and negative current injection (**B.**), respectively. The changes in EP, CAP thresholds, and the percentage changes (re: baseline) of the saturated and small-signal receptor currents and receptor potentials are also shown.

The asymmetric changes in Z parameter during current injection raise two questions: The first is "what is the explanation for the *direction* of the changes in Z?", and the second is "why was the *magnitude* of the Z reduction smaller than the Z increase?". The answers to both of these questions may be found in the relationship between the mechanical loading of the OHCs and their electromotile responses.

As discussed in Chapter Five, isolated unloaded OHCs contract *in vitro* on depolarisation with length changes following a Boltzmann function that saturates more in the hyperpolarising direction than in the depolarising direction, thereby favouring contraction (Santos-Sacchi, 1992; He, 2003). This was illustrated in Figure 5.23 of Chapter Five. In a series of experiments involving either pre-compressing or pre-stretching the OHC with a stiff fibre, He (2003) showed that the degree of the asymmetry could be altered, and indeed reversed, by the mechanical load. As was shown in Figure 5.24 of Chapter Five, the length change saturated more in the depolarising direction (favouring elongation) when the cell was placed under compression. More importantly, the magnitude of the length changes with voltage was also increased when the cell was placed under compression.

The OHCs *in situ* are likely to be under compression, with the intracellular turgor pressure pushing outward along the long axis of the OHC against the compressive forces imposed by the reticular lamina and the Deiters' cells. When the cell is in a steady-state (not contracting or expanding) the compressive forces of the cell and the intracellular turgor are equal. When the OHCs contract with a depolarising current injection (as indicated by the ST operating point shift), the amount of *extrinsic* compression the OHCs are under would decrease (that is, the compressive force imposed by the reticular lamina and the Deiters' cells would become a smaller proportion of the total compression of the cell). If the key variable in the data of He (shown in Figure 5.24 of Chapter Five) is *extrinsic compression*, then the observed decrease in Z (MET sensitivity) during the depolarising current injections is therefore explicable by the decrease in motile sensitivity when the compression of the cell is reduced. Conversely, when the cell elongates during a hyperpolarising current injection (indicated by the SV operating point shift), the amount of extrinsic compression supplied by the reticular lamina and the Deiters' cells would *increase*, thereby increasing the electromotile sensitivity, and producing the observed increase in Z. The attempt that has been made here to use characteristics of electromechanical transduction (EMT) to explain changes in mechanoelectrical transduction (MET) is not entirely

unreasonable, as both MET and EMT are multiplicative components of the active process (as illustrated in Figure 2.4 of Chapter Two).

7.7.5 Effect of DC current injection on CAP waveshape

The greater modulation of the P1 peak was consistent with observations by Brown et al. (2004), who used DC current injection (and other techniques) to determine the origin of P1. They concluded that i) the P1 was produced by the efflux of potassium from the primary afferent neurones during the repolarisation following the depolarisation caused by the Na^+ influx that produces the N1 peak, and ii) the fact that injection of DC current appeared to modulate P1 amplitude to a greater extent than N1 amplitude was most likely due to the resting potential of the neurones being closer to the highly-negative K^+ equilibrium potential than the positive Na^+ equilibrium potential (Siegel and Dallos, 1986).

Figure 7.6 showed that while the modulation of P1 was monotonic, the modulation of the N1 amplitude at higher frequencies was non-monotonic, with reductions in N1 amplitude occurring for both positive and negative current injections. The non-monotonic behaviour of N1 could be the combined result of two processes: i) the modulation of peak amplitude with changes in driving potential, and ii) the reduction in cochlear gain with positive current injection into scala tympani. If the injection of negative current into scala tympani caused a depolarisation of the primary afferent resting potential, the driving potential for sodium into the neurone would be reduced, thereby reducing the amplitude of the N1 peak, while hyperpolarisation with positive current injection would increase N1 amplitude, as it does for the frequencies below 10 kHz in Figure 7.6. The fact that this does not occur for high frequencies (the N1 amplitude decreases) is consistent with the high-frequency CAP threshold elevation demonstrated in Figure 7.3. That is, the reduction in N1 amplitude with large positive current injection into scala tympani may be a consequence of decreased BM vibration, rather than arising from a modulation of neural current only.

7.8 Summary

The effects of short-term and long-term scala tympani current injection were assessed in guinea pigs using Boltzmann analysis of the low-frequency CM and measurements of CAP amplitude, threshold, and waveshape at multiple frequencies. We conclude that:

i) injection of current into scala tympani causes changes in the Boltzmann parameters on two time-scales, with step-changes at the onset and offset of the injection caused by changes in driving potential for potassium through the OHCs and associated electromotile effects, and slower, often oscillatory, changes most likely to be caused by changes in cytosolic calcium;

ii) the observed changes in the Boltzmann parameters were largely equal and opposite for positive and negative current injections, with the exception of the Z parameter, which displays asymmetries that *may* be caused by changes in OHC-compression-related EMT sensitivity;

iii) extended injections of DC current produce deleterious effects on cochlear function, most likely mechanical in origin, that can sometimes cause sudden threshold elevations of as much as 20 dB.

Our mathematical model of OHC regulation, using the standard set of model parameters, successfully accounted for many of the effects of scala media current injection, including changes in the EP, AC receptor current (reflected in the CM and Vsat), operating point, and small-signal AC receptor potential (reflected in auditory thresholds).

Chapter 8
Perilymphatic perfusions

8. Perilymphatic perfusions

8.1 Introduction

This chapter presents the results of perilymphatic ion substitution experiments designed to examine the contribution of particular extracellular ions to hair cell and neural function. The perilymphatic perfusion technique allowed the perturbation of hair cells and neurones by the replacement of endogenous perilymph with artificial perilymph that had been altered in a controlled manner.

As discussed in Chapters One and Two, the membrane potential and electrical environment of the primary afferent neurones and the hair cells are greatly affected by the ionic composition of the extracellular fluid surrounding them. The basolateral wall of the outer hair cell, for example, contains at least a dozen different channel types, regulating the flow of potassium, calcium, sodium, water, and to a lesser extent, chloride.

In the present study, scala tympani of the guinea pig cochlea was perfused with artificial perilymphs with i) reduced sodium concentrations; ii) increased osmotic pressures; and iii) elevated potassium concentrations. In addition to these three main avenues of investigation, blockade of the medial olivocochlear efferent receptor by hexamethonium was also performed. A substantial portion of this chapter is concerned with results of simulated perfusions carried out in the mathematical model. The perfusion simulations were designed to allow comparison between the model behaviour and the experimentally-observed results recorded from the guinea pig. The results of these experiments provided valuable information about the validity of the schematic model of OHC homeostasis implemented in the mathematical model, some of which challenged our original hypothesis, and which lead to the development of a revised theory (the “two-pool” model, which will be discussed in Chapter Nine).

8.1.1 Ionic composition of perilymph and endolymph

The primary difference between perilymph and endolymph is that perilymph has a high sodium content, whereas endolymph is high in potassium. Additional differences are also found in the calcium concentration of the two fluids, which is 25 - 50 times higher in perilymph than in endolymph. A summary of the ionic composition of the inner ear fluids are shown in Table 8.1 below. The data, taken from Wangemann and Schacht (1996), are averages of measurements (assembled from various references) obtained in guinea pigs and rodents.

Component	SM endolymph (mM)	ST perilymph (mM)	SV perilymph (mM)
Na^+	1.3	148	141
K^+	157	4.2	6.0
Ca^{2+}	0.023	1.3	0.6
Cl^-	132	119	121
HCO^{3-}	31	21	18
Aspartate	0.015	0.002	0.003
Glutamate	0.053	0.007	0.008
Glutamine	0.054	0.625	0.645
Glycine	0.071	0.322	0.289
Alanine	0.040	0.321	0.367
Glucose	0.6	3.6	3.8
Urea	4.9	5.0	5.2
Protein (mg/100 mL)	38	178	242
pH	7.4	7.3	7.3

Table 8.1: Composition of inner ear fluids (Wangemann and Schacht, 1996).

The mean osmolalities (n = 8) of SM endolymph, ST perilymph, and SV perilymph in the guinea pig were found by Konishi et al. (1984) to be 304.2 ± 6.8, 292.9 ± 5.7, and 293.5 ± 5.2 mOsm/kg H_2O respectively, indicating that the osmolality of endolymph is significantly higher (p = 0.01) than that of perilymph.

8.2 Methods

Details of animal preparation, acoustic stimulation, and data acquisition were presented in Chapter Three.

Perfusions in this experimental series were performed by hand-drilling a fine hole through the otic capsule at the first turn, and using a custom-made perfusion pipette to pump artificial perilymph into scala tympani. Another hole was made at the apex to allow this fluid to drain into the middle-ear cavity, where it was absorbed by fine tissue-wicks. The two types of perfusion pipette used in these experiments are shown in Figure 8.1 below.

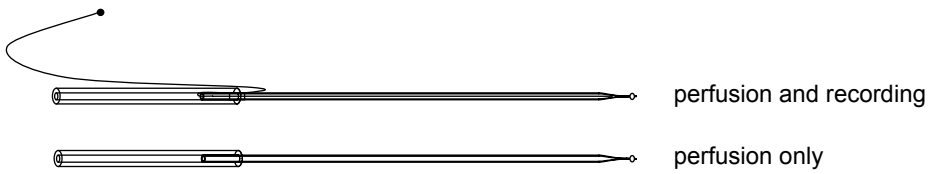

Figure 8.1: The design of the perfusion pipettes used in these experiments. In some cases. the pipettes incorporated an etched silver recording electrode running down the lumen to near the tapered tip of the pipette (top diagram), with the artificial perilymph forming a salt-bridge to the scala tympani fluid.

Perfusion pipettes made from borosilicate glass were pulled to a tip-diameter of 0.1 mm. A bead of silicone (RTV-734, Dow Corning, MI, USA; RTV-102, GE Plastics, VIC, Australia) was placed around the shank of the pipette approximately 0.5-0.7 mm from the end of the pipette to seal the cochleostomy, preventing leakage of cochlear fluids and shunting of perfusion pressure. A Silastic sleeve was attached with silicone to the opposite end of the pipette for connection to the Teflon tube carrying the perfusate from the perfusion pump located outside the soundproof room. The Teflon tube was earthed by a metal insert shortly after its entry to the room to prevent the transmission of electrical interference through the perfusate into the cochlea. The perfusates were delivered at a rate of 3 μL/min by a syringe pump (Harvard Apparatus model 55-1111, MA, USA). Pipettes were placed with the aid of a micromanipulator (Narishige Co. Ltd., Tokyo, Japan).

In all perfusion experiments, the perfusion pipette was removed, rinsed, and refilled between applications of different solutions. The artificial perilymph used in these experiments was based on a formulation by Bobbin (Jenison et al., 1985; Bobbin et al., 1990), which is shown in Column I of Table 8.2. The solutions were divided into 10 mL aliquots before being frozen for later use. To avoid precipitation of calcium salts, the solutions were made without the addition of the $CaCl_2$, which was added after defrosting the aliquot on the morning of experimentation. The solutions were then warmed to 38° C and adjusted to a pH of 7.4 using HCl or NaOH.

The osmolalities of the perfusates used were measured by freezing-point depression using a Fiske One-Ten osmometer (Fiske Associates, MA, USA). The osmolalities of the artificial perilymphs were 302 ± 6 mOsm/kg H_2O, unless they were designed to create an osmotic perturbation. This control value was close to the perilymph osmolality of 292.9 ± 5.7 mOsm/kg H_2O measured by Konishi et al. (1984). Solutions which were unintentionally hypotonic when produced, such as the N-methyl-D-glucamine$^+$ ($NMDG^+$) or 50 mM K^+ constant-[K][Cl]-product artificial perilymphs, were corrected by addition of sucrose.

8.2.1 Control perfusions

Control perfusions were carried out using the artificial perilymph described in Column I of Table 8.2. Examples of the time-course of changes in the Boltzmann parameters and thresholds during control perfusions are shown in Figure 8.4 of Section

8.3.3 , while CAP waveforms recorded during control perfusions are shown in Section 8.3.8 .

	I	II	III	IV	V	VI	VII
Reagent	Control	Low-Na^+ (Choline)	Low-Na+ (Choline) plus Hexamethonium	Low-Na+ ($NMDG^+$)	Hexamethonium	Sucrose Hyperosmotic	50 mM K^+ Const. KCl Product
NaCl	137	0	0	0	137	137	4.4
KCl	5	0	0	0	5	5	4.4
$NaHCO_3$	12	8	8	8	12	12	12
Glucose	11	11	11	11	11	11	11
$CaCl_2.2H_2O$	2	2	2	2	2	2	2
$MgCl_2.6H_2O$	1	1	1	1	1	1	1
$NaH_2PO_4.H_2O$	1	0	0	0	1	1	1
Choline Chloride	0	142	142	0	0	0	0
Na Gluconate	0	0	0	0	0	0	87.6
K Gluconate	0	0	0	0	0	0	45.6
Sucrose	0	0	0	38.4	0	45	15.7
$KHCO_3$	0	4	4	4	0	0	0
KH_2PO_4	0	1	1	1	0	0	0
Hexamethonium Chloride	0	0	0.75	0	0.75	0	0
NMDG Chloride	0	0	0	142	0	0	0

Ion/Sugar	Control	Low-Na^+ (Choline)	Low-Na^+ (Choline) plus Hexamethonium	Low-Na^+ ($NMDG^+$)	Hexamethonium	Sucrose Hyperosmotic	50 mM K^+ Const. KCl Product
Na^+	150	8	8	8	150	150	105
Cl^-	148	148	148.8	148	148.8	148	14.8
HCO_3^-	12	8	8	8	12	12	12
Glucose	11	11	11	11	11	11	11
K^+	5	5	5	5	5	5	50
Ca^{2+}	2	2	2	2	2	2	2
Mg^{2+}	1	1	1	1	1	1	1
PO_4	1	1	1	1	1	1	1
Choline	0	142	142	0	0	0	0
$NMDG^+$	0	0	0	142	0	0	0
Gluconate	0	0	0	0	0	0	133.2
Sucrose	0	0	0	38.4	0	45	15.7
Hexamethonium	0	0	0.75	0	0.75	0	0
$[K^+]$ $[Cl^-]$ product (mM^2)	740	740	743.8	740	743.8	740	740

Calculated Osmolarity (mOsm/L)	330	326	327.5	364.4	331.5	375	346
Measured Osmolality (mOsm/kg H_2O)	303 ± 6 (n = 21)	298 ± 6 (n = 3)	299 (n = 1)	298 ± 6 (n = 3)	298 (n = 1)	349 ± 1 (n = 3)	299 ± 11 (n = 2)

Table 8.2: The composition of the perfusates used in the experiments reported here, listed by reagent and ion/sugar concentration, excluding contributions from the small amounts of HCl or NaOH used to adjust the solution pH. Values different from the control artificial perilymph are highlighted. Means and standard deviations of osmolality measurements are shown.

8.3 Results - Reduction in perilymphatic sodium

The aim of this part of the study was to determine the functional significance of the sodium-transport mechanisms of the OHC by examining the degree to which OHC function is affected by extracellular sodium concentration. OHC function was assessed through Boltzmann analysis of the low-frequency CM, and measurement of the high-frequency summating potential, recorded from the round window.

As discussed in Chapter Two, the three main sodium transport mechanisms present in the basolateral walls of mammalian cochlear hair cells are the Na^+/Ca^{2+} and Na^+/H^+

antiports, and the Na^+/K^+/ATPase pump. At the apical face of the OHC, both inner and outer hair cells are permeable to Na^+ via the MET channel (Lumpkin et al., 1997) and the ATP-sensitive P2X receptor (Housley et al., 1998). An additional TTX-sensitive voltage-dependent sodium channel found in tall hair cells of the alligator lizard cochlea (Evans and Fuchs, 1987), if present in mammalian hair cells, is unlikely to be open under physiological conditions: perilymphatic perfusion of TTX (which would block these channels, if present) does not substantially affect CM responses (Patuzzi and Moleirinho, 1998).

The Na^+/Ca^{2+} antiport does not appear to be present in IHCs (Kennedy, 2002), but may play a role in the regulation of intracellular calcium in OHCs (Ikeda et al., 1992a), with the extrusion of Ca^{2+} being coupled to the flow of Na^+ into the cell down its electrochemical gradient from perilymph. A Na^+/H^+ exchange (NHE) antiport, consisting mostly of the NHE-1 isoform, has been localised to the many tissue of the cochlea, including IHCs and OHCs (Bond et al., 1998; Goto et al., 1999). The intracellular sodium concentration of hair cells is decreased by the action of the ubiquitous Na^+/K^+/ATPase pump, which is present in the basolateral wall of the OHCs but is believed to have a relatively low activity (Sunose et al., 1992; Sunose et al., 1993).

When isolated OHCs are examined *in vitro*, the removal of sodium from the extracellular solution caused a large increase in intracellular calcium (Ikeda et al., 1992a). Sunose et al. (1992) reported that reduction of extracellular Na^+ to $1/10^{th}$ of control levels caused a small hyperpolarisation (of around 2 mV) in isolated OHCs. However, isolated OHCs generally display higher intracellular Na^+ concentrations than would be expected *in vivo* (Kros, 1996), and are under electrical and ionic conditions that are different from those of *in vivo* OHCs, and so the significance and extent of this hyperpolarisation in the living animal is uncertain.

In addition to monitoring of the OHC effects via the Boltzmann parameters, neural thresholds and waveforms were monitored at multiple frequencies. The effect of reduced perilymphatic sodium on cochlear potentials was investigated by perfusion of scala tympani with a modified artificial perilymph, shown in column II of Table 8.2. The sodium concentration of the artificial perilymph was reduced by almost 95%, from the normal value of around 150 mM (Wangemann and Schacht, 1996) to 8 mM, by substitution with choline (Evans and Fuchs, 1987; Offner et al., 1987). As will be shown in Section 8.4 below, it is likely that this solution produced an 80% reduction in

perilymphatic sodium on perfusion through scala tympani. The measured osmolality of the reduced-Na^+ choline perilymph (298 ± 6 mOsm/kg H_2O) was similar to that of the control perilymph (303 ± 6 mOsm/kg H_2O).

To ensure that the effects observed with choline perfusion were due to the reduced sodium concentration rather than direct action of choline on the cholinergic outer-hair-cell efferent synapse, experiments were conducted that employed i) pre- and co-perfusion with the nicotinic acetylcholine receptor antagonist, hexamethonium chloride (Rajan, 1990), and ii) the use of $NMDG^+$ instead of choline to replace sodium (Ikeda et al., 1992a; Chabbert et al., 1995; Surin et al., 2000). The osmolality of the $NMDG^+$ perilymph was corrected to 297 ± 6 mOsm/kg H_2O using sucrose. The results of the hexamethonium and $NMDG^+$ experiments are described in Sections 8.3.6 and 8.3.7 , respectively.

8.3.1 Time-course of effects of reduced-Na^+ choline perfusion

Choline perfusions were performed in three animals, with representative results shown in Figures 8.2 to 8.8. The usual time-course for reduced-Na^+ perfusions was separable into two components: a set of transient changes that occurred during the first 2-3 minutes of the perfusion, followed by either a sustained perturbation or a return towards pre-perfusion values. The pattern of onset transients was particularly visible in the operating point shifts, which were the most consistent of the Boltzmann parameters in the five examples shown here. In four of the five examples, following an initial brief ST shift, the operating point usually showed a larger movement towards SV that was sustained until the end of the perfusion.

The first example is Figure 8.2, which shows the time-course of the effects of a 10-minute perfusion of reduced-Na^+ choline perilymph on the Boltzmann parameters, spectrum of the neural noise (SNN), and N1 and SP amplitudes.

During the first two minutes of the perfusion, the 80% reduction in perilymphatic sodium concentration caused a 6% increase in Vsat (consistent with an increase in the permeability of the basolateral wall of the OHC), a 15% increase in the magnitude of Z, and a 1.3 meV Eo shift toward ST followed a reversal towards SV, resulting in a sustained operating point shift that was 1.7 meV more towards SV than the pre-perfusion value.

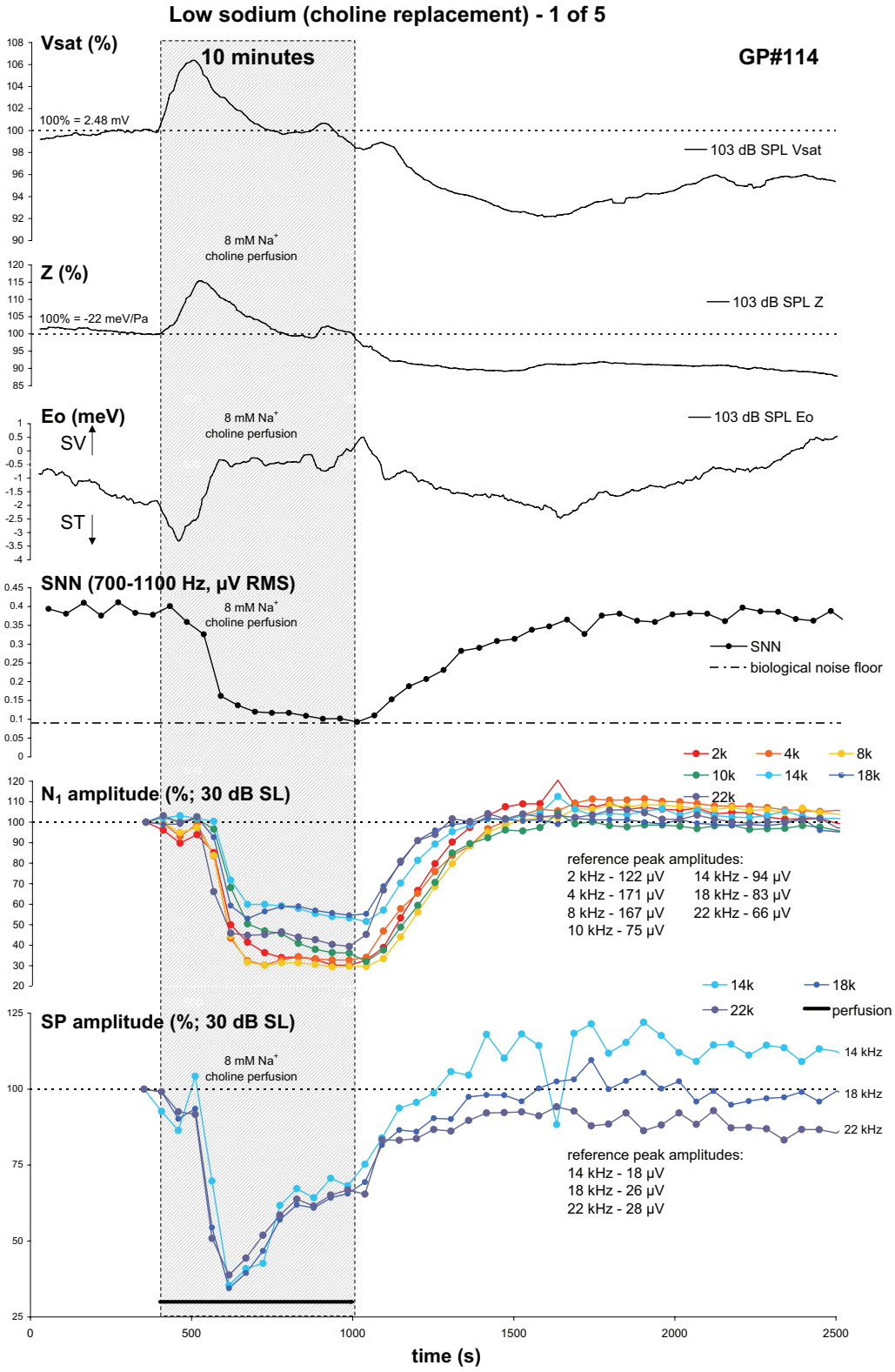

Figure 8.2: Boltzmann parameters, SNN, N1 & SP amplitudes during a 10 minute perfusion of 8 mM Na^+ choline artificial perilymph. The perfusion caused large decreases in neural measures (a 72% reduction in SNN, and an average 55% reduction in N1 amplitude). While an average maximum 64% reduction in SP was also observed, the SP amplitudes began to recover before the N1 amplitudes. The changes in the Boltzmann parameters are discussed in the text.

ID#3146112153. Thresholds (2 kHz to 22 kHz, dB GPHL): 13, 6, 4, -4, 1, -3, -10. (Boltzmann parameters 7-pt running average)

The changes in neural indicators were more marked than those of the Boltzmann parameters: SNN fell by approximately 74% from around 0.39 μV RMS to a low of 0.10 μV RMS[1] at the end of the perfusion, while N1 amplitudes fell by an average of 55%. SP amplitudes also fell by an average of around 65%.

That the reduced sodium perfusion clearly had an IHC or neural effect in addition to the motor effect was indicated by the Boltzmann parameters: while the CAP and SNN amplitudes remained depressed throughout the perfusion, the Boltzmann parameters had almost recovered by the end of the perfusion period (Vsat and Z returned to within 2%, and Eo was within 2 meV, of their pre-perfusion values). The amplitude of the SPs followed a similar time-course to the Boltzmann parameters, recovering to within 33% of pre-perfusion values, unlike the SNN or N1 amplitude time-courses. Interestingly, the neural effects occurred some time after the Boltzmann parameters began to change, with the large decreases in N1 amplitude and SNN amplitude occurring almost two minutes after Vsat began to increase. It is not clear whether this indicates some delay in the perfusate reaching the neurones, or that the hair cells are more sensitive to small changes in the ionic environment before manifesting them as a threshold elevation.

8.3.2 Reproducibility and the effect of perfusion duration

An earlier set of consecutive perfusions in this same animal (GP#114) highlighted how reversible and reproducible the effects of the reduced-Na^+ choline perfusions could be. Shown in Figure 8.3 is the time-course of changes in the Boltzmann parameters, SNN, tracked CAP thresholds, and supra-threshold CAP amplitudes. Although the two measurements were taken 76 minutes apart, and show results from perfusions of different durations (20 minutes and 10 minutes), the reproducibility of the onset and offset effects of the perturbation in the Boltzmann parameters is remarkable. To allow comparison of both the onset and offset of the perfusion, a 10-minute period has been excised from the 10-minute perfusion at the point indicated by the vertical bar.

The Boltzmann parameters show a set of onset features within the first 2.5 minutes, followed by a relatively static response during the remaining 7.5 minutes of the perfusion (or 17.5 minutes for the longer perfusion). The first component of the onset features (occurring 60-70 seconds after commencement of the perfusion) involved a 2-5% decrease in Vsat and Z, and a 0.5 to 1.5 meV operating point shift towards ST.

[1] This value was close to the typical biological noise floor of between 0.08 and 0.09 μV RMS recorded in deafened, but live, guinea pigs.

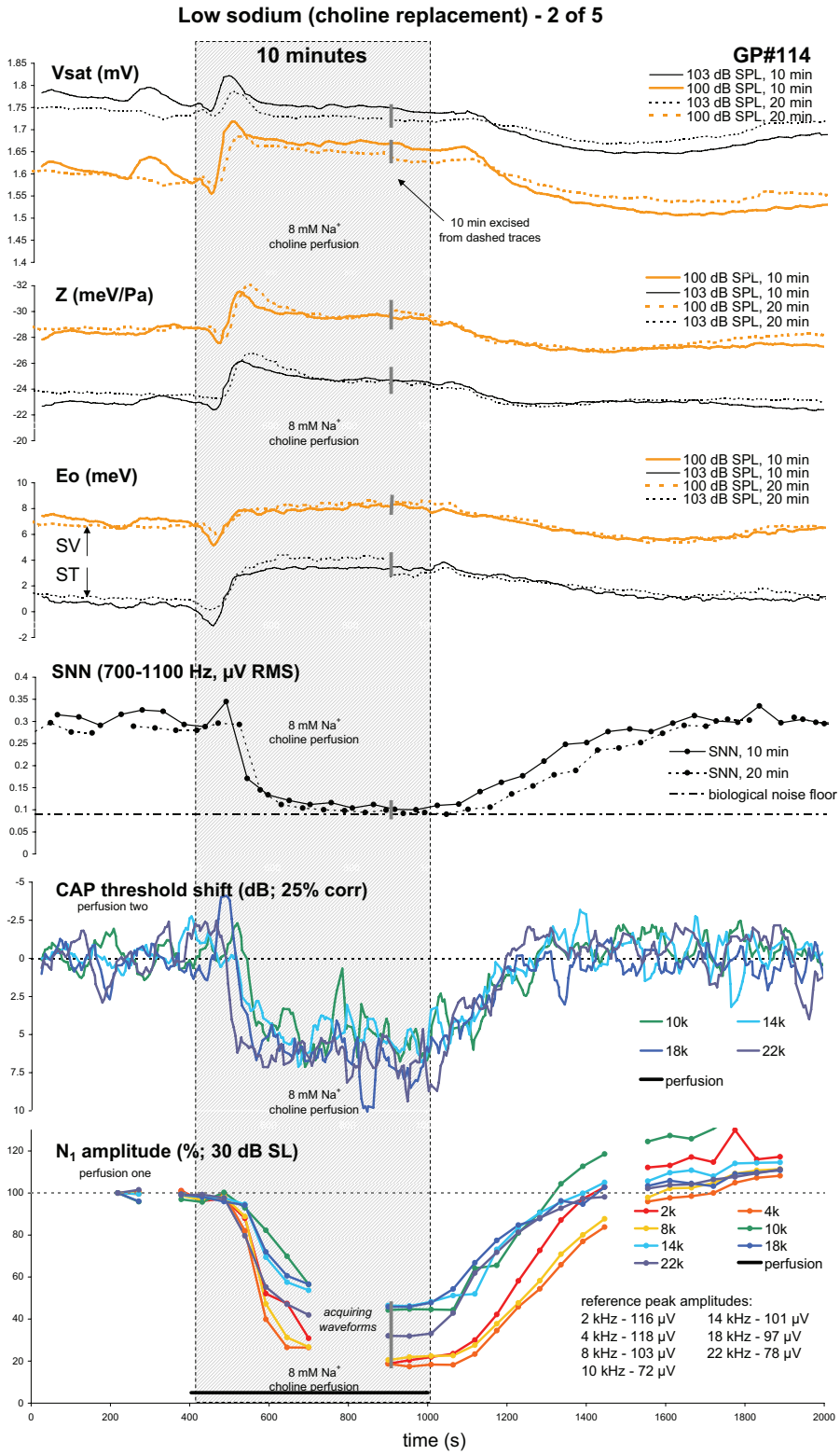

Figure 8.3: Measures of cochlear function recorded during consecutive perfusions (76 minutes apart) of 8 mM Na^+ choline artificial perilymph. While the first perfusion (dashed traces and N1 amplitude data) was 20 minutes in duration, the second perfusion (solid traces and CAP threshold data) was 10 minutes duration. To allow comparison of these traces, ten minutes of data has been excised from the first perfusion at the 900 second mark (grey bars). It is assumed the high reproducibility of the Boltzmann and SNN data permits direct comparison of tracked CAP thresholds and N1 amplitudes: The perfusion caused an average 6 ± 1 dB shift in tracked threshold at frequencies from 10 kHz to 22 kHz, and an average 58 ± 6% reduction in CAP amplitude at those frequencies (68 ± 12% overall).

ID#3146117193 (dash). Thresholds (2 kHz to 22 kHz, dB GPHL): 12, 2, -2, -5, 2, 1, -6.
ID#3146121272 (solid). Thresholds (2 kHz to 22 kHz, dB GPHL): 6, 1, -1, -5, 1, -3, -6.
(Boltzmann parameters and CAP threshold shift 7-pt running average)

This initial component was followed during the next 60 seconds by a larger 4-8% transient increase in Vsat, a 10-13% increase in Z, and a 3-4 meV shift in operating point towards SV. While remaining unchanged during the first component of the Boltzmann changes, the neural measures (i.e. the SNN peak amplitude during both perfusions, the N1 amplitudes during the 1st perfusion, and the tracked CAP thresholds during the 2nd perfusion) showed the effects of the perfusion at around 1.5 minutes after the onset of the perfusion, roughly corresponding to the start of the second component of the Boltzmann changes.

During the remainder of the perfusion, the Z parameter remained at approximately 2-6% above the pre-perfusion value. The Vsat parameter measured using a 103 dB SPL 207 Hz probe tone reached a plateau within 1% of the pre-perfusion level, while that measured with the 100 dB SPL probe tone produced a Vsat 3-4% above the pre-perfusion level. The plateau Eo shifts towards SV were 1.5 meV and 3 meV for the 100 and 103 dB SPL probes respectively.

The similarities between the results from these two consecutive perfusions indicate very little lasting difference between the pre- and post-perfusion cochleae, and that the ability of the cochlea to recover from this perturbation was not different for 10-minute and 20-minute perfusions.

8.3.3 Comparison of control and choline perfusions

Figures 8.4 and 8.5 are presented on facing pages for comparison, and show the results of consecutive perfusions of control perilymph and reduced-Na^+ choline perilymph in GP#115. The control perfusion of artificial perilymph caused a 15% decrease in Vsat, a 2% rise in Z followed by a 9% fall, and a relatively static Eo shift of 1.9 ± 0.18 meV towards SV. By contrast, the data for the choline perfusion immediately afterwards (shown in Figure 8.5 on the facing page) share many of the characteristics of the choline perfusion in GP#114 that was presented in Figure 8.2: In particular, the Boltzmann parameters showed a peak 5% rise in Vsat after 2.5 minutes, an increase in Z of 10% after 2 minutes, and a 3 meV Eo shift towards SV broadly peaking between 340 and 500 s after perfusion onset. As will be discussed in later sections, the ionic composition of the perilymph is presumed to remain relatively constant during the second half of the sustained perfusion. Despite this, the Boltzmann parameters began to return towards their pre-perfusion values before the end of the perfusion.

Comparison of the CAP amplitude data for the control and choline perfusions shows the largest difference between the two Figures. The measure of evoked neural firing

used in Figures 8.4 and 8.5 was the peak-to-peak CAP amplitude (N_1-P_1) in response to tone-bursts presented at 30 dB above tracked threshold. During the control perfusion, the maximum reduction in CAP amplitude was 40% at 6 kHz, with a 26 ± 1% reduction for frequencies between 10 and 22 kHz. During the first five minutes of the choline perfusion, however, a 75 ± 1% reduction in CAP amplitudes was observed for frequencies from 2 kHz to 10 kHz, with percentage reductions of 67%, 54%, and 64%, for 14 kHz, 18 kHz, and 22 kHz respectively. The waveforms acquired during this period are shown in Section 8.3.8 below.

8.3.4 Examples of reduced perfusate clearance and reduced perfusion rate

While the previous three examples of choline perfusion showed a rapid onset to the perfusion and slower offset, two examples were obtained in which either the rate of onset or offset were reduced. The likely cause of the reduced rate of offset may be a reduction in the clearance of the perfusate from the cochlea by the bulk flow of endogenous perilymph, perhaps due to a reduction in CSF pressure.

The data in Figure 8.6 were recorded from GP#115 approximately 4.5 hours after those shown in Figure 8.5. Despite the animal having good CAP thresholds at the commencement of this recording, the neural parameters did not show the same recovery from the perfusion as was seen previously. Following the end of the perfusion. the SNN amplitude remained near the biological noise floor of the recording, while the recovery of the CAP amplitudes was very slow, increasing by an average of 12% of the pre-perfusion CAP amplitude every 10 minutes. A possible explanation for this is that the apical cochleostomy became partially blocked, thereby reducing the flow of endogenous perilymph to replace the experimental perfusate (Ohyama et al., 1988).

Figure 8.7 represents an example of a low-sodium choline perfusion carried out in an animal with a perforated round-window membrane. The ability of the perfusate to reach the apical turns was therefore greatly reduced, resulting in the neural effects being primarily limited to the basal turn. Reductions in N1 amplitude (at 20 dB above tracked threshold) of 77%, 58%, and 38% were observed at 22 kHz, 18 kHz, and 14 kHz respectively, with an average 15 ± 2% reduction in N1 amplitude observed at the lower frequencies.

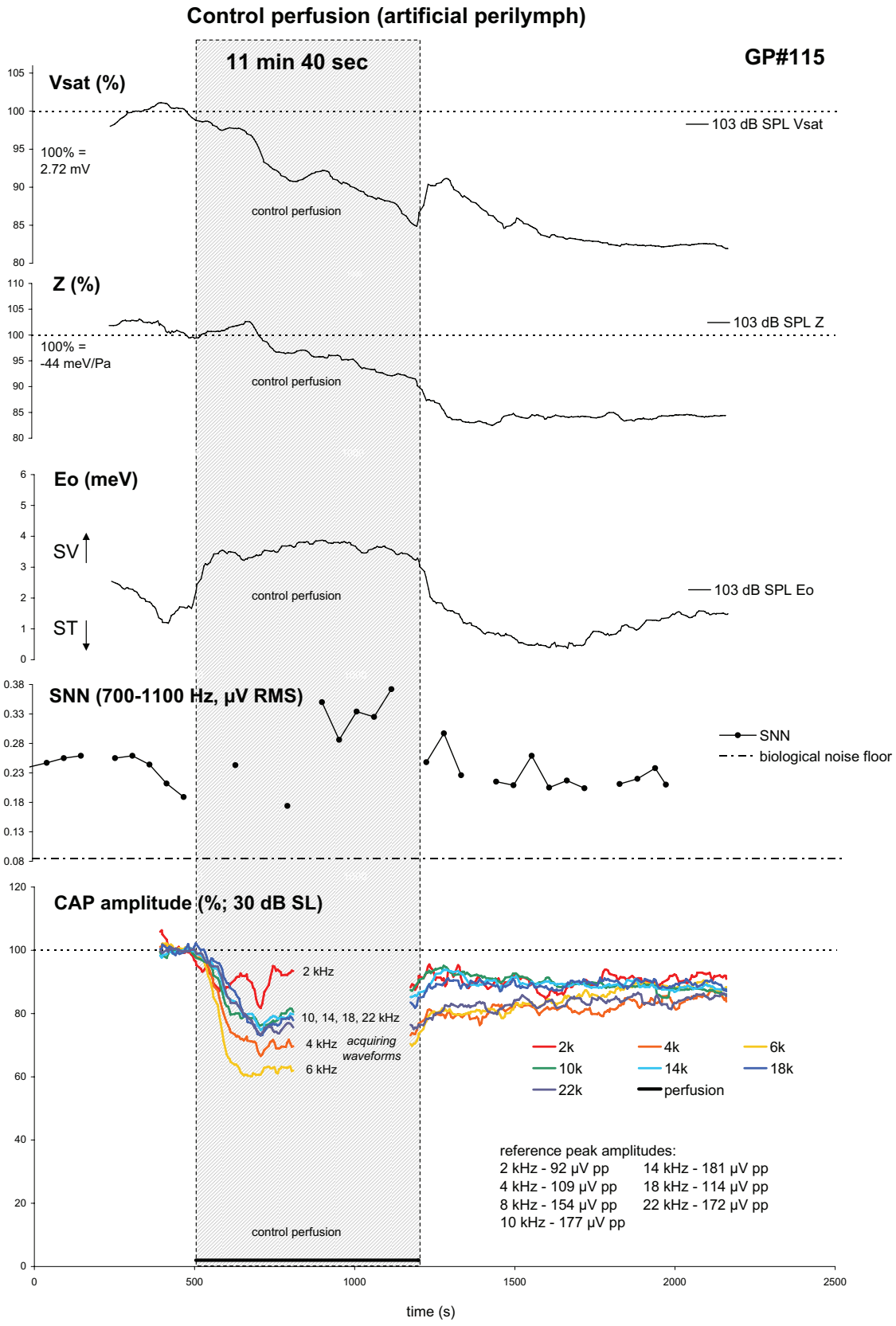

Figure 8.4: Boltzmann parameters, SNN, and peak-to-peak CAP amplitudes during an 11 minute 40 second control perfusion of artificial perilymph.
ID#3147920670. Thresholds (2 kHz to 22 kHz, dB GPHL): 2, 0, 5, 4, 5, 3, 5.
(Boltzmann parameters & CAP amplitudes 7-pt running average)

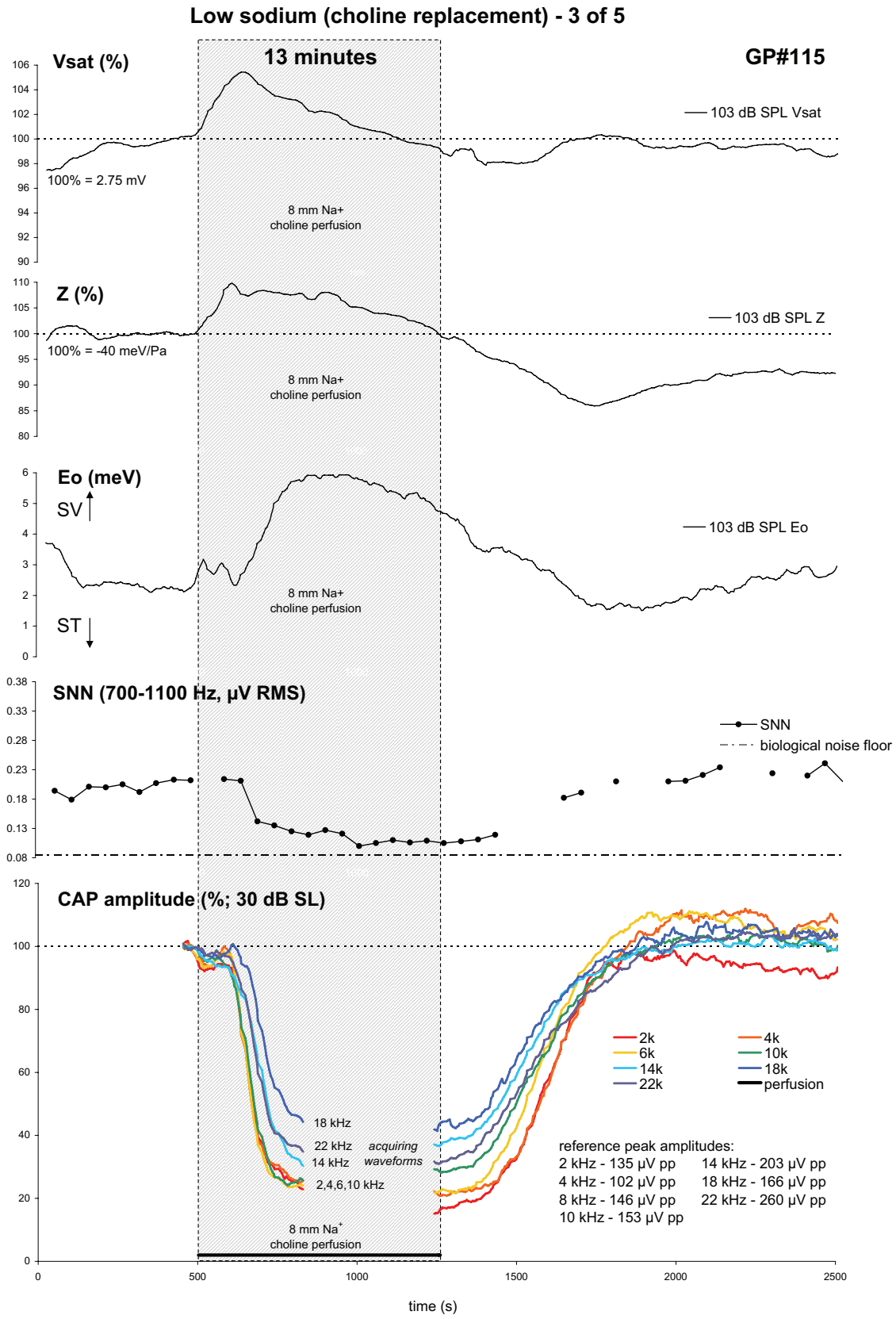

Figure 8.5: Boltzmann parameters, SNN, and peak-to-peak CAP amplitudes during a 13 minute perfusion of 8 mM Na^+ choline artificial perilymph (see text).
ID#3147923796. Thresholds (2 kHz to 22 kHz, dB GPHL): 3, -2, 4, 2, 7, 4, 8.
(Boltzmann parameters & CAP amplitudes 7-pt running average)

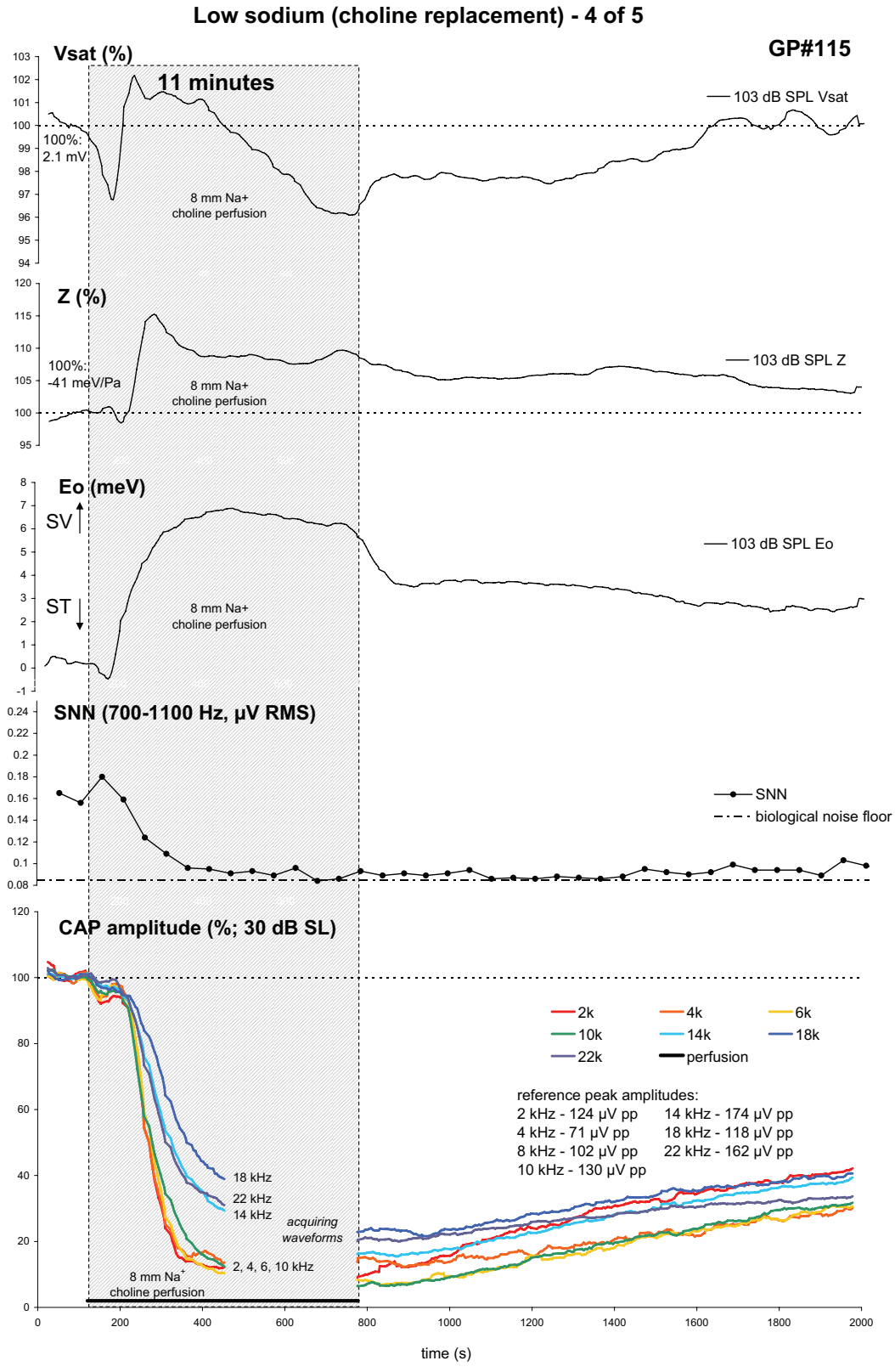

Figure 8.6: Boltzmann parameters, SNN, and peak-to-peak CAP amplitudes during an 11 minute perfusion of 8 mM Na^+ choline artificial perilymph, recorded over 4.5 hours after the data presented in Figure 8.5 (see text). The rate of recovery of the neural parameters after the perfusion is greatly reduced.

ID#3147940664. Thresholds (2 kHz to 22 kHz, dB GPHL): 5, -4, 3, 2, 8, 2, 11.
(Boltzmann parameters & CAP amplitudes 7-pt running average)

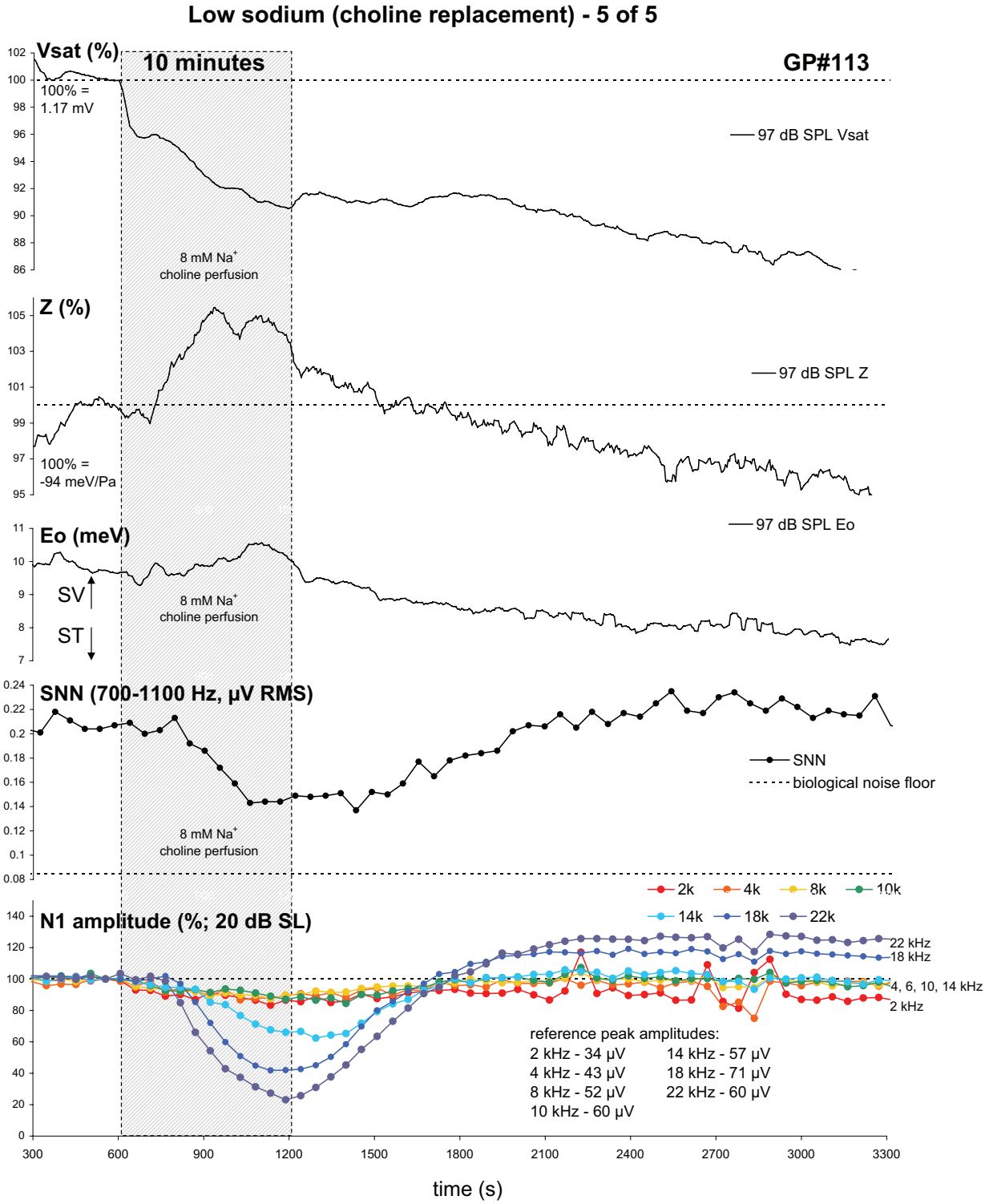

Figure 8.7: Boltzmann parameters, SNN, N1 amplitudes during a 10 minute perfusion of 8 mM Na^+ choline artificial perilymph. In this case, the round-window membrane was perforated, presumably reducing the ability of the perfusate to reach the apical turns, with effects of the perfusion primarily limited to the basal turn. The largest threshold shifts were observed from 14 kHz to 22 kHz (see text).

ID#3144124228. Thresholds (2 kHz to 22 kHz, dB GPHL): -3, -8, -5, -1, 3, 19, 25. (Boltzmann parameters 7-pt running average)

A 30% reduction in SNN amplitude (equivalent to over 50% of the SNN activity above the noise floor of the recording) was observed during this perfusion. This decrease indicates the large basal contribution to the recorded activity: as the largest N1 reductions were observed at 14 kHz and above, the remaining SNN activity is likely to be the result from axonal contributions from the apical regions, which were not greatly affected by the perfusion. The Boltzmann parameters showed a 9.5% decrease in Vsat, a 5% increase in Z, and a 1 meV Eo shift towards SV. While the decrease in Vsat was unlike the changes observed in the other choline perfusions, the changes in Z and Eo were not significantly different.

8.3.5 Summary figure – Boltzmann parameters and SNN during choline perfusions

Figure 8.8 shows overlaid choline perfusion data from the two animals with intact round-window membranes (i.e. excluding GP#113). Because the perfusions were of different durations (all above 10 minutes), the focus of the figure is in the changes that occurred at the onset of the perfusion. To enable better comparison, all of the traces shown in Figure 8.8 were recorded with 207 Hz probe tones at the same level (103 dB SPL). The trend that emerges is a 2-6% increase in Vsat peaking around 90-105 s after the onset of perfusion, occasionally preceded by a slight drop in Vsat around 50-60 s after onset, with all 5 perfusions showing Vsat at or below the pre-perfusion level after 10 minutes of the perfusion. The change in Z was similar to the Vsat time-course, but larger in amplitude, with a 6-15% increase peaking around 110-160s. In 4 of the 5 perfusions shown, the Z parameter remained above the pre-perfusion baseline after 10 minutes. Similarly, in 4 of the 5 perfusions the pattern of operating point shifts showed a small 0.5 – 1.5 meV shift towards ST at around 60 seconds, with all 5 perfusions showing a lasting SV shift of 2-6 meV after 10 minutes. Also shown in Figure 8.8 are the SNN traces from those five perfusions, which all showed a decrease to near the biological noise floor by the end of the perfusion period. The commencement of the decrease in SNN corresponded roughly with the main changes in Boltzmann parameters after 90 seconds of perfusion (i.e. the Vsat increase, Z increase, and SV operating point shift).

8.3.6 Choline perfusions with concurrent efferent blockade

The neurotransmitter of the outer hair cell efferent synapse is acetylcholine (for reviews, see Klinke, 1981; Guinan, 1996). However, as in other systems, the pre-cursor choline may also be an agonist of the receptor (see, for example, Alkondon et al., 1997).

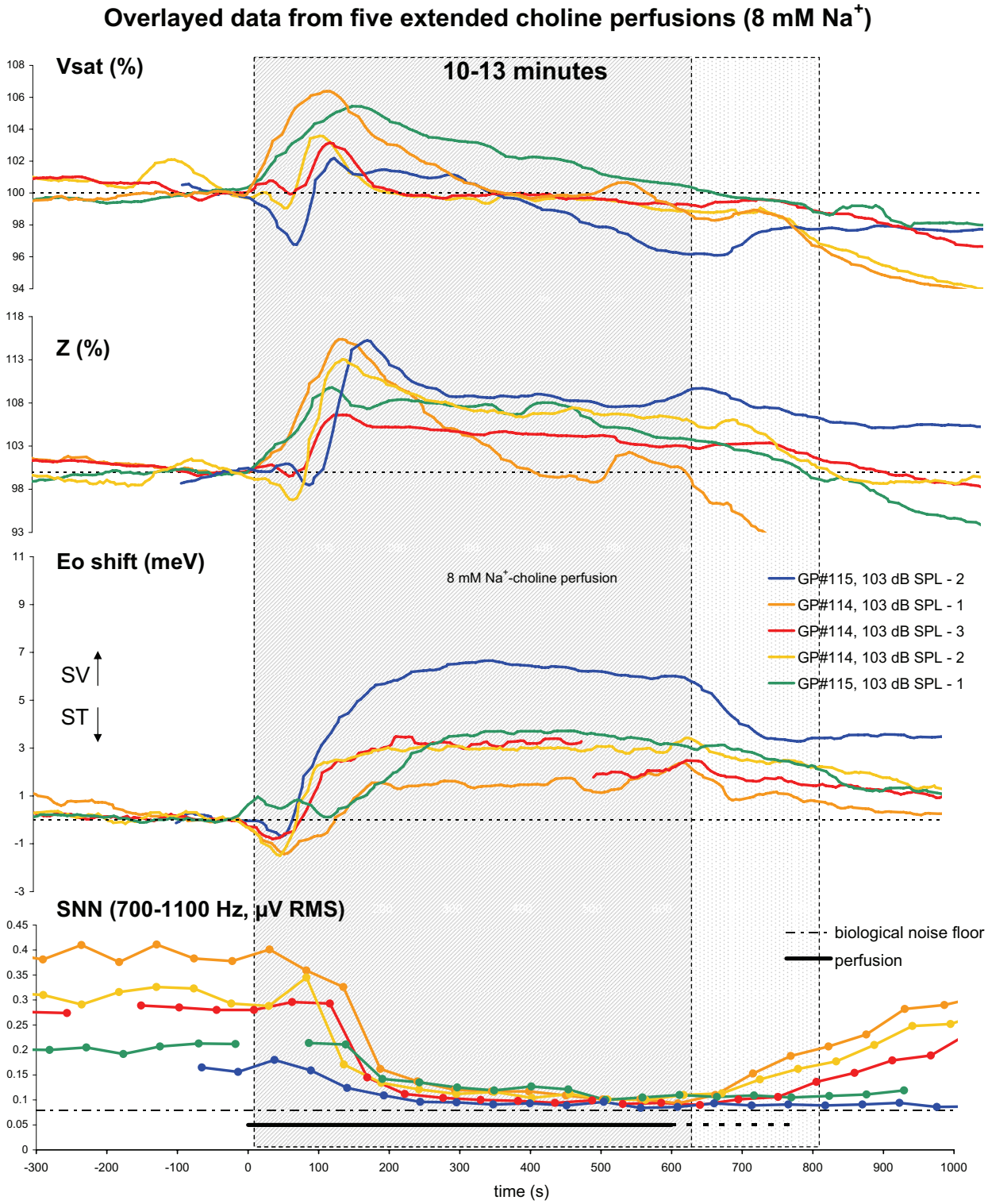

Figure 8.8: Boltzmann parameters and SNN amplitude recorded during five extended perfusions of 8 mM Na^+-choline artificial perilymph in four animals. The blue traces were recorded from GP#115 at a time when the recovery from the perfusion took longer than usual. Boltzmann traces (103 dB SPL) - 7-pt running average

To eliminate the possibility that the effects observed with choline perfusion were due to direct action of the choline on the cholinergic outer hair cell efferent synapse, two choline perfusions in one animal (GP#115) were performed with pre- and co-perfusion with the nicotinic acetylcholine receptor antagonist, hexamethonium chloride (Rajan, 1990). The measured osmolalities of the hexamethonium containing perilymphs were 298 mOsm for hexamethonium control and 299 mOsm for choline plus hexamethonium. These values were similar to that of the control perilymph (303 ± 6 mOsm).

Figure 8.9 shows the Boltzmann parameters, SNN, and CAP amplitudes during a control perfusion of artificial perilymph containing 750 μM hexamethonium. The hexamethonium perfusion caused a lasting 15% reduction in Vsat. Taken in isolation, this result is consistent with a blockade of tonic efferent activity, causing a reduction in OHC calcium influx, and therefore a reduction in basolateral potassium permeability. However, the time-course of the Vsat changes during this perfusion was similar to that of the control perfusion performed earlier in that animal (shown in Figure 8.4), and so more data is required to confirm the first-order effects of hexamethonium on the Boltzmann parameters.

The perfusion which followed, shown in Figure 8.10, contained both the 8 mM Na^+ choline perilymph with 750 μM hexamethonium. The pattern of changes observed with this perfusion was not significantly different to those with the hexamethonium-free choline shown in the Summary Figure 8.8. The Vsat parameter showed a 5% increase peaking at 150 seconds post-perfusion, followed by a decrease to 4% below pre-perfusion levels after 10 minutes, and 8% after the 12.5 minutes of the perfusion. The Z parameter showed an 8-11% increase over the duration of the perfusion, while the operating point showed a 1.5 meV SV step-shift at the immediate onset of the perfusion (most likely a perfusion artefact), followed by a further 2.5 meV shift towards SV. The neural effects of this combined hexamethonium and choline perfusion were also not significantly different from those of the choline perfusions, with a 91 ± 2% fall in CAP amplitudes observed at frequencies from 2 to 10 kHz, and a 75 ± 5% decrease in amplitudes from 14 to 22 kHz.

Figure 8.11 shows another example of the combined hexamethonium/choline perfusion. The results of this perfusion were similar to those in Figure 8.10, with the exception that the recovery of the neural parameters was impaired. To assess whether this was due to a reduced clearance of the perfusate from the cochlea (such as would

occur with a reduction in bulk flow of endogenous perilymph), the perilymphatic compartment was flushed with control artificial perilymph. This resulted in the SNN and 30 dB SL CAP amplitudes recovering rapidly to within an average of 12 ± 7% of the pre-perfusion values. The effectiveness of this washout in restoring CAP amplitudes is shown further in Figure 8.12, which compares input/output functions recorded from GP#115 prior to the choline/hex perfusion, during the perfusion, and following the washout.

In summary, in the two perfusions carried out in GP#115, the choline perfusions containing hexamethonium did not differ significantly from those without hexamethonium, indicating that the results obtained with 8 mM Na^+ perfusions were due to the effect of the low-sodium, rather than the choline.

8.3.7 Replacement of sodium with N-methyl-D-glucamine$^+$

To eliminate further the possibility of a choline-related efferent effect, perfusion of 8 mM Na^+ artificial perilymph in which N-methyl-D-glucamine$^+$ ($NMDG^+$) was used as the replacement ion, was performed in one animal (GP#120). $NMDG^+$ is often used as a substitute ion for potassium or sodium (for example, Housley and Ashmore, 1992; Ikeda et al., 1992b; Chabbert et al., 1995), and is not reported to have an efferent effect.

Figure 8.13 shows data from a 15 minute perfusion of 8 mM Na^+ artificial perilymph described in Column IV of Table 8.2. The asterisks and dashed line in that Figure indicate an unknown event that occurred at around 500 seconds after the onset of the perfusion that triggered changes in the recorded parameters[2]. Nevertheless, analysis of the 500 seconds of perfusion data before this point showed an 18% increase in Vsat during the first minute, followed by a reduction of the increase to 7% after two minutes, and finally reaching a plateau at 13% above the pre-perfusion value. The Z parameter was transiently decreased by 25% during the first minute, and then increased to a plateau level 16% above the pre-perfusion value.

[2] These changes were not consistent with an attenuation of the sound stimuli, as this would have caused an increase in the Z parameter and changes in the 10 kHz SP. A blockage of the apical cochleostomy may have been the cause, which may explain the reduced recovery of the N1 and SNN amplitude.

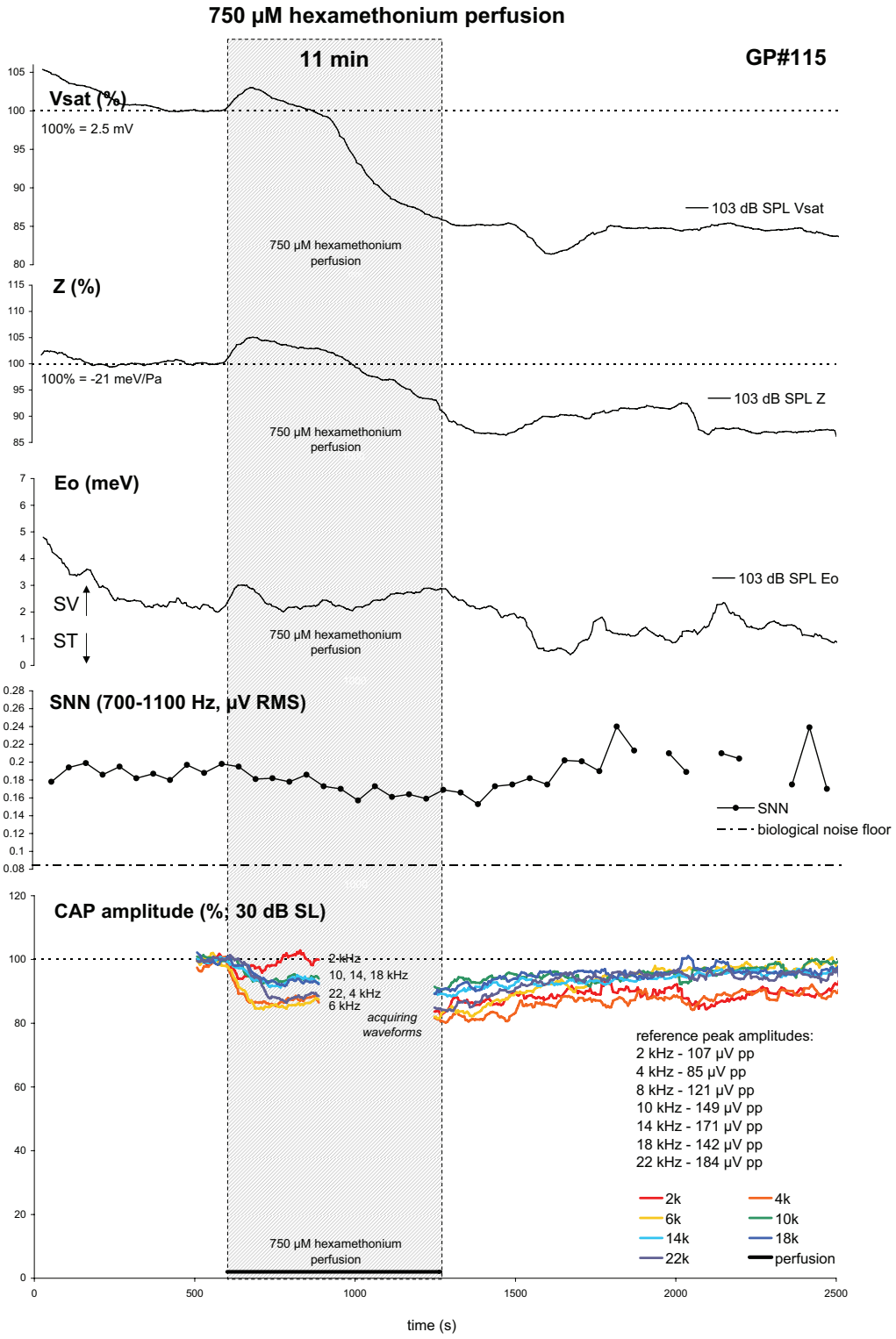

Figure 8.9: Boltzmann parameters, SNN, and CAP amplitudes during a typical 11 minute perfusion of artificial perilymph containing 750 µM hexamethonium chloride. Following initial small increases, the hexamethonium perfusion caused a 14% reduction in Vsat, a net 1 meV Eo shift towards SV, and a 5% increase and 8% decrease in Z. The neural parameters showed a 13% reduction in SNN, and an average 14% reduction in CAP amplitude. The perfusion of artificial perilymph containing hexamethonium served as a control for the reduced-Na^+ plus hexamethonium perfusion presented in Figure 8.10.

ID#3147927309. Thresholds (2 kHz to 22 kHz, dB GPHL): -2, 2, -4, -1, -6, -3, -6. (Boltzmann parameters & CAP amplitudes 7-pt running average)

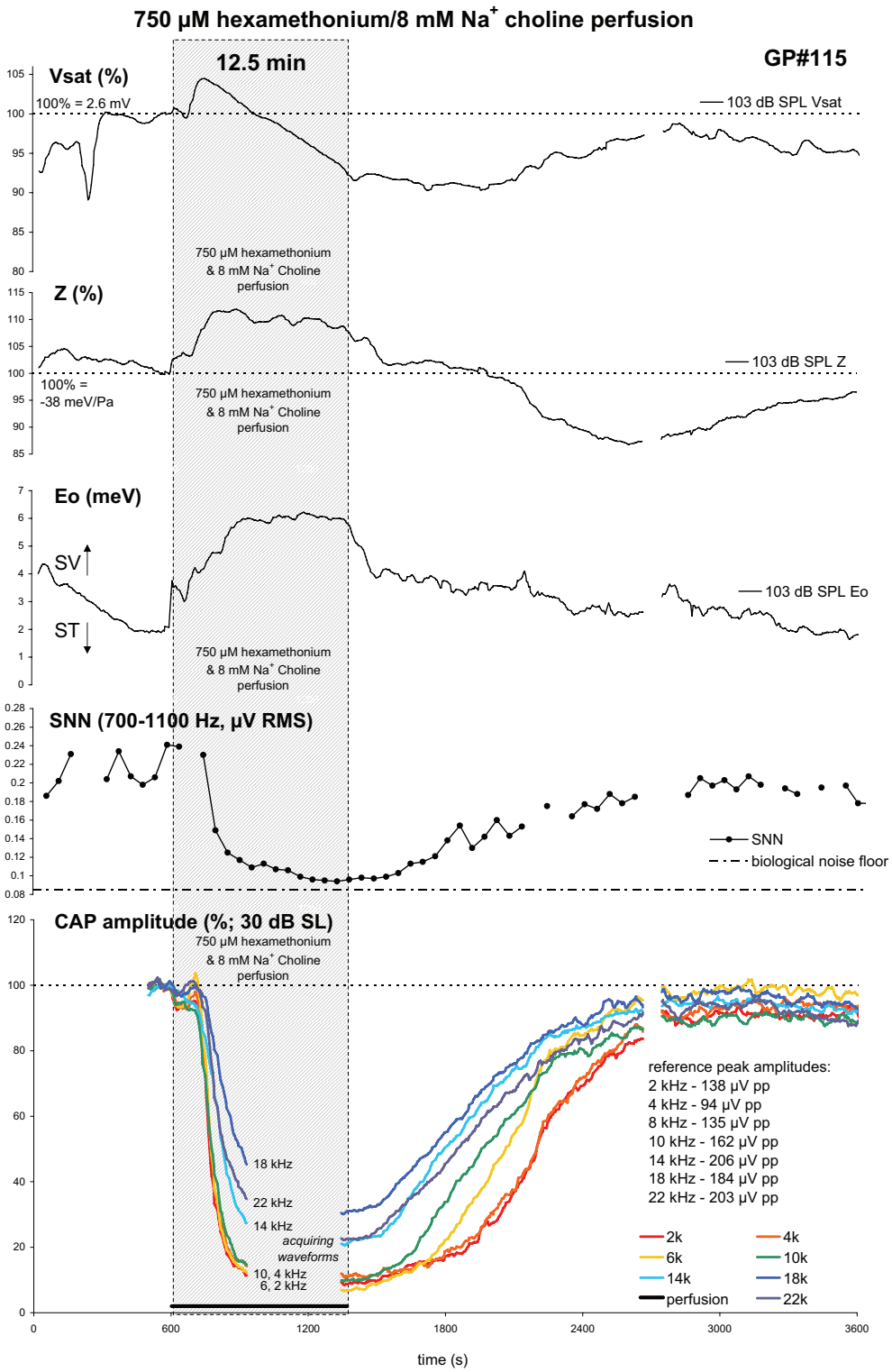

Figure 8.10: Boltzmann parameters, SNN, & CAP amplitudes during a 12.5 minute perfusion of 750 µM hexamethonium & 8 mM Na^+ choline perilymph. After a 4% increase in Vsat during the first 90 seconds of the perfusion, it decreased by 8% over the next 11 minutes. There was also a net 4 meV Eo shift towards SV, and a 9-11% increase in Z. The neural parameters showed a reduction in SNN to near the noise-floor, and an average 84 ± 9% reduction in CAP amplitude. ID#3147930552. Thresholds (2 kHz to 22 kHz, dB GPHL): 3, -4, 3, 3, 6, 5, 9. (Boltzmann parameters & CAP amplitudes 7-pt running average)

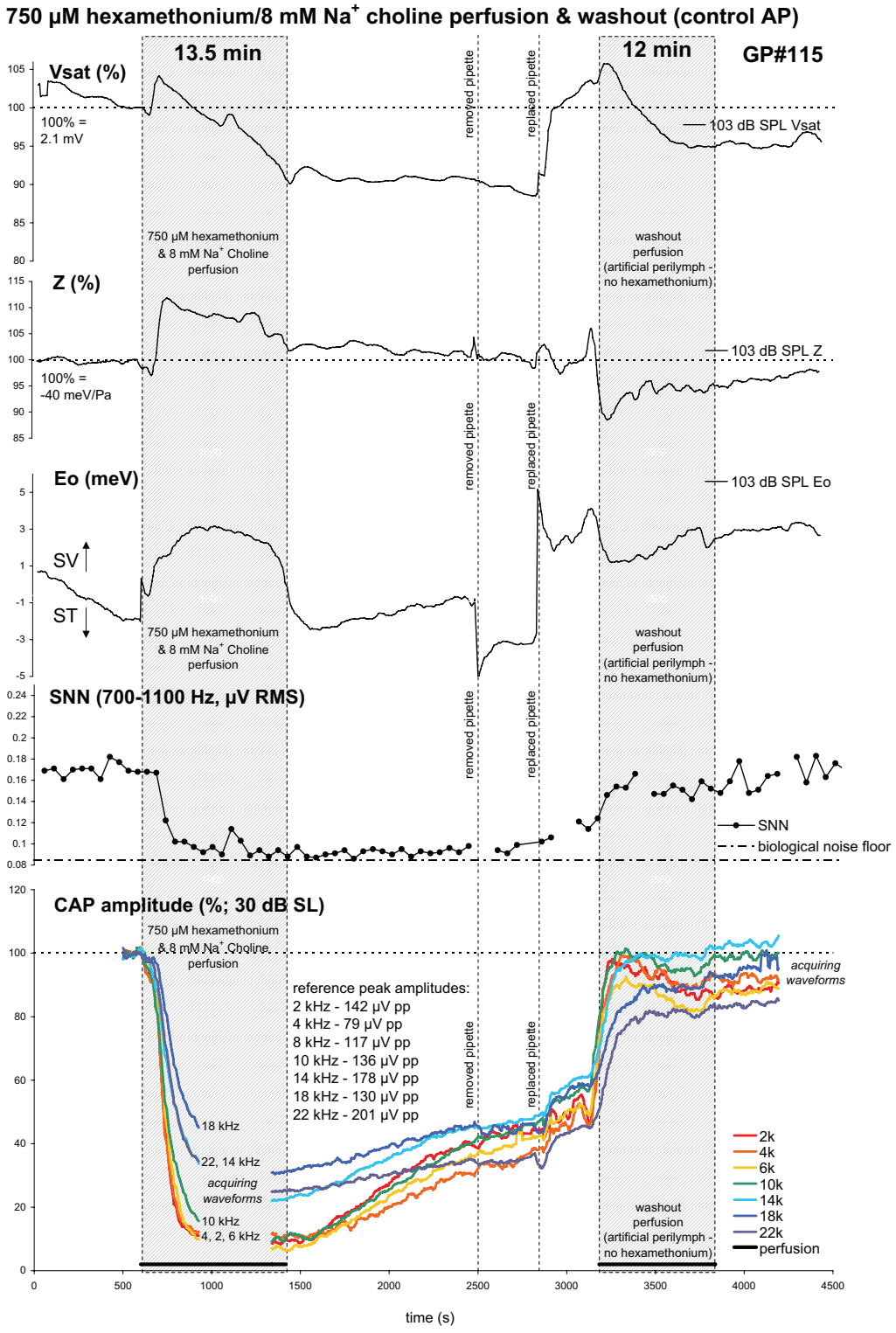

Figure 8.11: Boltzmann parameters, SNN, & CAP amplitudes during a 13.5 minute perfusion of 750 µM hexamethonium & 8 mM Na^+ choline perilymph, followed 30 minutes later by a 10.9 minute perfusion of 150 mM Na^+ control artificial perilymph.
ID#3147935495. Thresholds (2 kHz to 22 kHz, dB GPHL): 2, -3, 4, 3, 7, 5, 10.
(Boltzmann parameters & CAP amplitudes 7-pt running average)

CAP input/output functions before and during 750 µM hexamethonium/ 8 mM Na^+ choline perfusion, & and following washout with control AP.

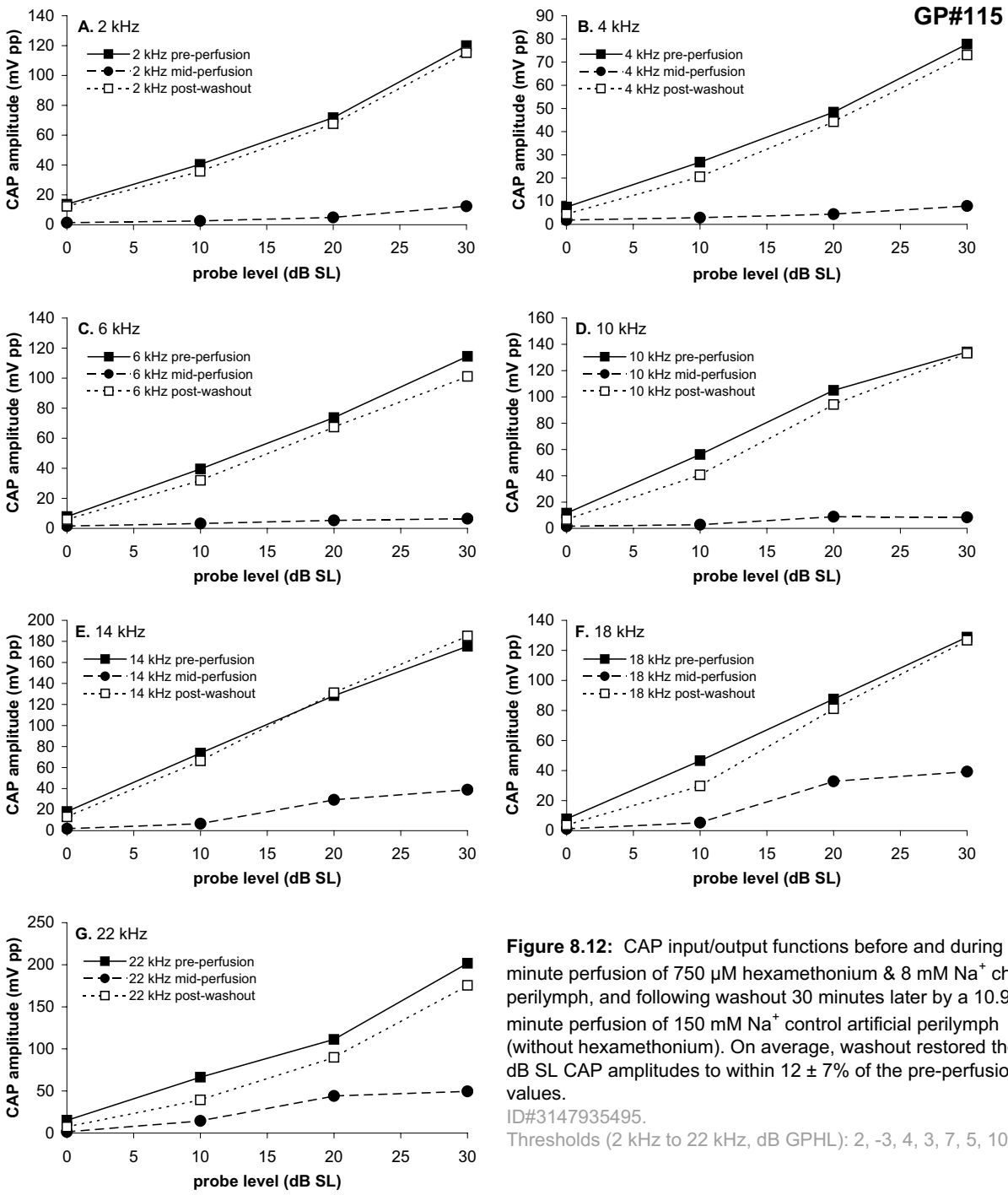

Figure 8.12: CAP input/output functions before and during a 13.5 minute perfusion of 750 µM hexamethonium & 8 mM Na^+ choline perilymph, and following washout 30 minutes later by a 10.9 minute perfusion of 150 mM Na^+ control artificial perilymph (without hexamethonium). On average, washout restored the 30 dB SL CAP amplitudes to within 12 ± 7% of the pre-perfusion values.

ID#3147935495.

Thresholds (2 kHz to 22 kHz, dB GPHL): 2, -3, 4, 3, 7, 5, 10.

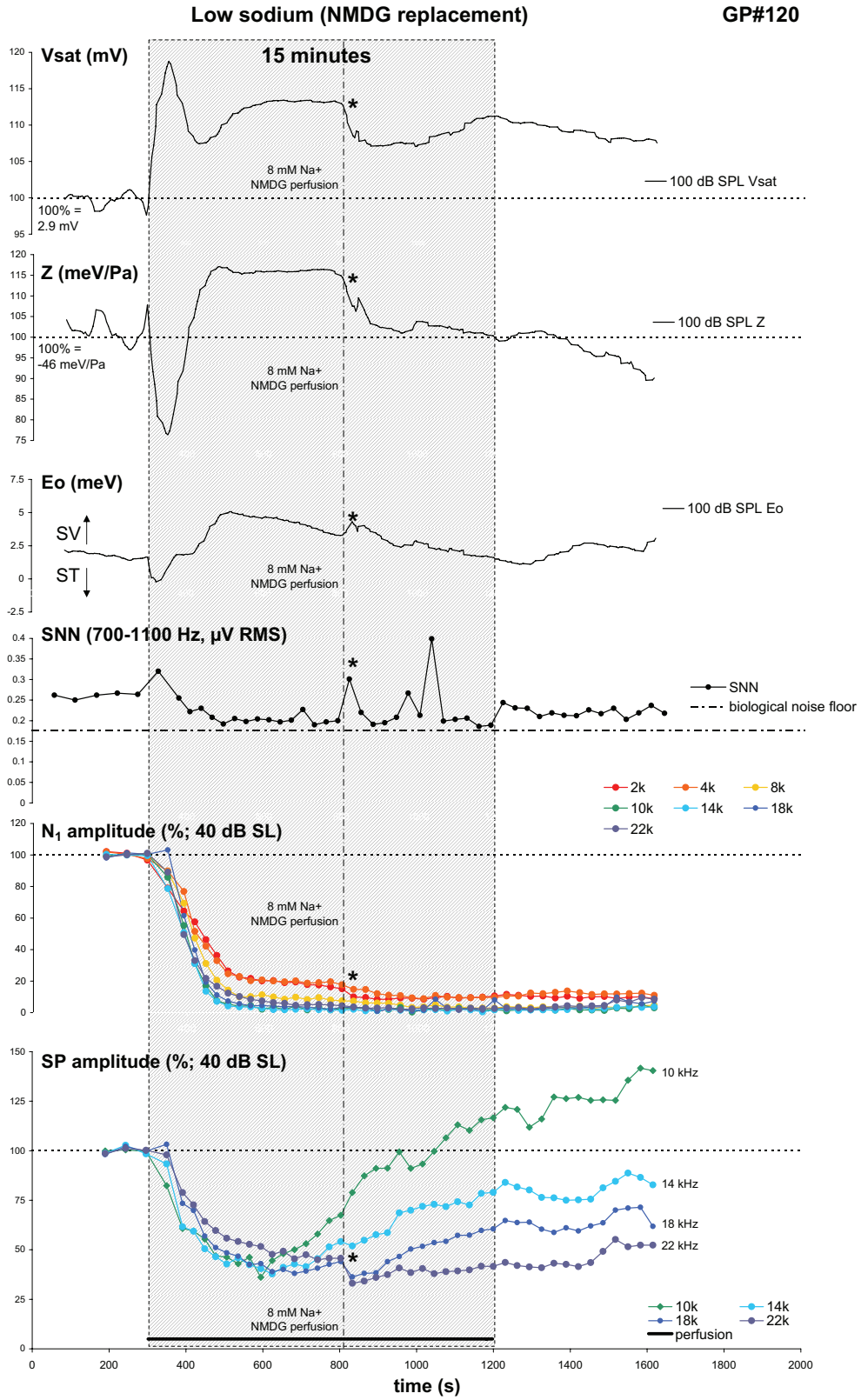

Figure 8.13: Boltzmann parameters, SNN, N1 & SP amplitudes during a 15 minute perfusion of 8 mM Na^+ $NMDG^+$ artificial perilymph. The asterisks and dashed line indicate an unknown event that caused changes in all measured parameters. Despite this, at the onset of perfusion it is clear that the low-Na^+ perilymph containing $NMDG^+$ caused larger changes in the Boltzmann parameters and the CAP responses (above 10 kHz) than the choline perfusions: an average 97% reduction in N1 amplitude, and an average 48% reduction in the SP, an indicator of basilar membrane vibration amplitude, was observed (see text).
ID#3164943094. Thresholds (2 kHz to 22 kHz, dB GPHL): -3, -5, 3, -3, 3, -2, -3.

The operating point showed an initial 1.8 meV shift toward ST (peaking just prior to the peaks in Vsat and Z), followed by a larger shift towards SV that moved back towards the pre-perfusion value over the next five minutes.

N1 amplitude at 40 dB SL was reduced by an average of 97% at frequencies 10 kHz and above, indicating a threshold loss of around 40 dB at those frequencies. At more apical frequencies, there was a 90% decrease in N1 amplitude at 6 kHz, and an average 82% loss at 2 and 4 kHz.

The SP amplitudes (above 10 kHz) were reduced by 48% over the first 5.5 minutes, after which time they began to recover in order of increasing frequency (from 10 kHz to 22 kHz). At 20 minutes after the onset of the perfusion (i.e. 5 minutes after the offset) the 10 kHz SP had increased to 40% larger than its pre-perfusion magnitude, while the 14 kHz, 18 kHz, and 22 kHz SPs had recovered to 50%, 70%, and 85% of their pre-perfusion magnitudes. However, the N1 amplitudes remained suppressed for at least 20 minutes following the onset of the perfusion.

Because further perfusions of $NMDG^+$ were not carried out, it is uncertain whether this lack of recovery is a characteristic effect of this perfusate, or that the clearance of the perfusate was impaired by reduced bulk perilymph flow, as was presumed to have occurred in Figures 8.6 and 8.11.

8.3.8 Observed changes in CAP waveforms

The effect of perilymph sodium concentration on CAP waveforms was assessed in GP#114 and GP#115 during perfusions of choline-substitution perilymph, and in GP#120 using the $NMDG^+$-substitution perilymph.

Figure 8.14 shows CAP waveforms recorded from GP#115 during the 13 minute perfusion of 8 mM Na^+ choline perilymph shown in Figure 8.5. These are overlaid with waveforms recorded during a perfusion of control artificial perilymph in the same animal, 52 minutes earlier. The waveforms shown were recorded at 30 dB above tracked threshold, but because the tracked threshold baseline ("0 dB SL") was different for the two recordings, the SP amplitudes may differ at some frequencies because of the higher absolute sound levels used[3], rather than any effect of the low-Na^+ perfusion.

[3] That is, they are "iso-SL", but not "iso-SPL".

Effect of low-sodium choline perfusion on CAP waveforms (30 dB SL) GP#115
[asterisks indicate near-identical SPLs]

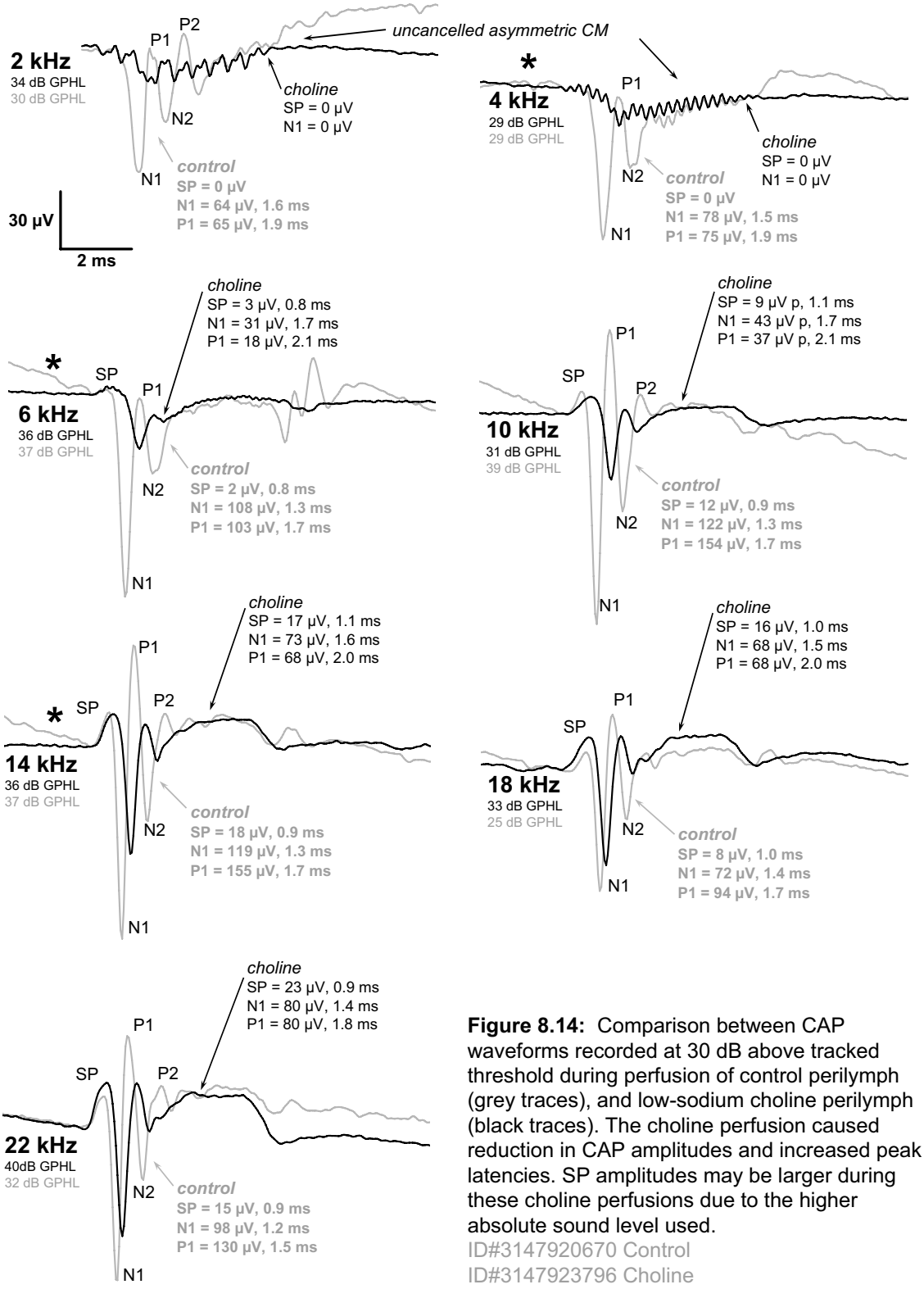

Figure 8.14: Comparison between CAP waveforms recorded at 30 dB above tracked threshold during perfusion of control perilymph (grey traces), and low-sodium choline perilymph (black traces). The choline perfusion caused reduction in CAP amplitudes and increased peak latencies. SP amplitudes may be larger during these choline perfusions due to the higher absolute sound level used.
ID#3147920670 Control
ID#3147923796 Choline

However, at 6 and 14 kHz the absolute sound levels differed by only 1 dB, allowing direct comparison of these waveforms, and assessment of the effect of the low-sodium choline perfusion on the SP: While the SP amplitudes were essentially unchanged at these two frequencies with the perfusion, the peaks were broader with the SP-peak latency at 14 kHz being delayed by 0.2 ms. The N1 peak amplitudes (measured from the SP peak) at these two frequencies were decreased by around 72% at 6 kHz and 39% at 14 kHz, with latency shifts of 0.4 and 0.3 ms respectively. At other frequencies, comparison of results obtained at the same level above tracked threshold (but at different absolute SPLs) showed N1 peak amplitudes to be decreased by around 64% at 10 kHz, 6% at 18 kHz, and 18% at 22 kHz (relative to control perfusions), with latency shifts of between 0.1 and 0.4 ms. The amplitude of the P1 wave was diminished by around 83% relative to the control perfusion level at 6 kHz, 76% at 10 kHz, 56% at 14 kHz, 61% at 18 kHz, and 38% at 22 kHz. The N1-P1 intervals in Figure 8.14 were essentially unchanged at lower frequencies, and were slightly elongated at the high frequencies (0.05 ms at 18 kHz and 0.27 ms at 22 kHz).

In addition to the above changes in peak amplitude and latency, changes in the number of peaks in the waveform and the off-response were also observed. In the same figure (Figure 8.14), comparison of the choline-perfusion data and the iso-SPL control perfusion waveforms at 14 kHz shows that while an N1, P1, and N2 peak are visible in both the low-Na^+ and control waveforms, the control waveform also has P2, N3, P3, and N4 peaks that are absent from the low-Na^+ waveform. This reduction of later peaks is also visible at the iso-SL waveforms of that Figure at 10 kHz, 18 kHz and 22 kHz. Off-responses were present in the control waveforms at frequencies from 6 kHz to 22 kHz, but these were also absent from the choline responses.

Figure 8.15 shows waveforms from the same animal during perfusions of control artificial perilymph and choline artificial perilymph, both of which contained hexamethonium. As with Figure 8.14, changes in peak amplitude and latency were observed, but the reductions were of larger magnitude: At 6 kHz, the choline + hexamethonium perfusion has caused total spike failure, leaving only a dendritic potential. At other frequencies, reductions in N1 amplitude and elongated peak latencies were observed. The reductions in peak amplitude during this perfusion were visible in the time-series shown in Figure 8.10.

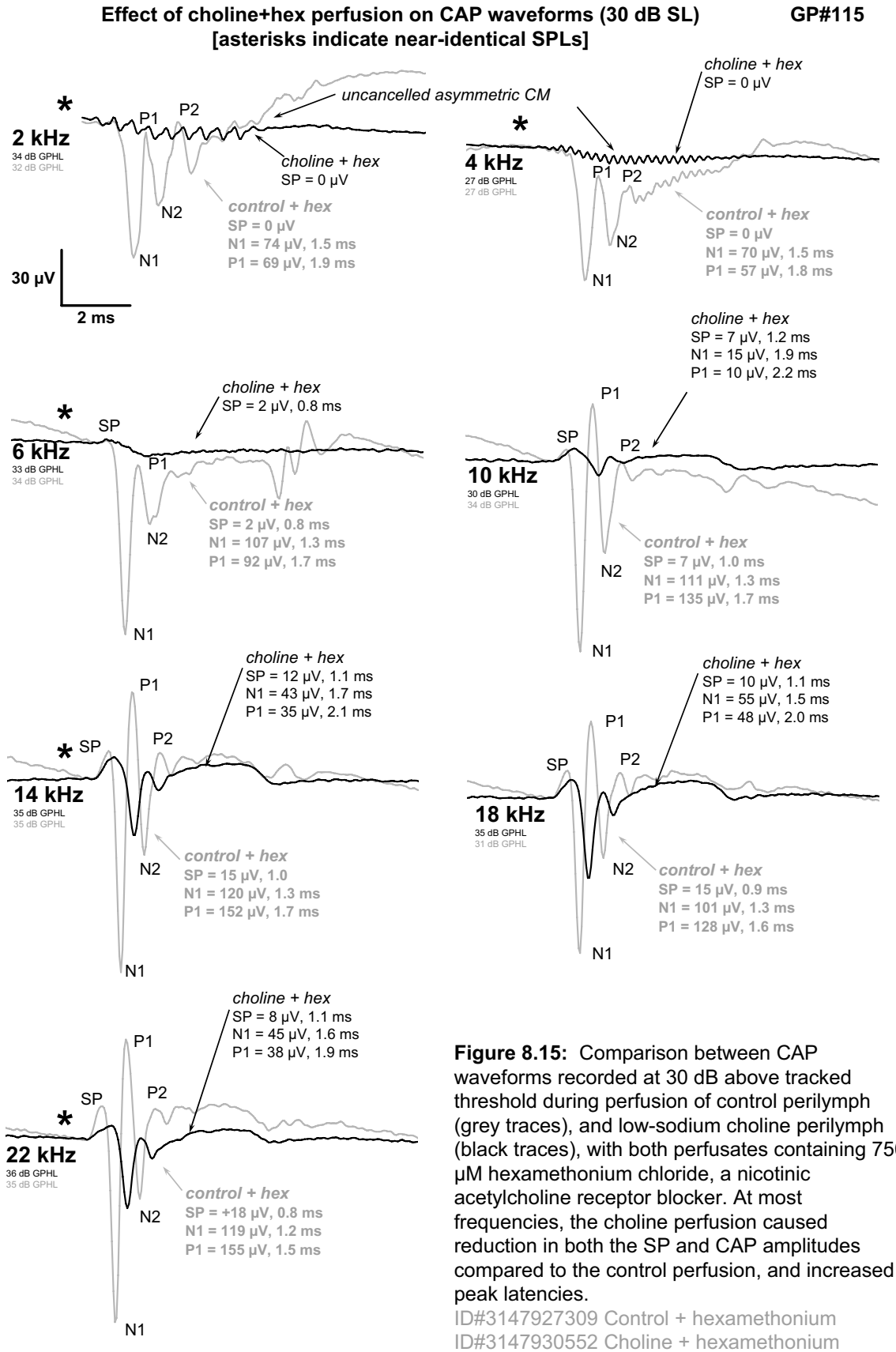

Figure 8.15: Comparison between CAP waveforms recorded at 30 dB above tracked threshold during perfusion of control perilymph (grey traces), and low-sodium choline perilymph (black traces), with both perfusates containing 750 µM hexamethonium chloride, a nicotinic acetylcholine receptor blocker. At most frequencies, the choline perfusion caused reduction in both the SP and CAP amplitudes compared to the control perfusion, and increased peak latencies.

ID#3147927309 Control + hexamethonium
ID#3147930552 Choline + hexamethonium

In addition to comparing CAP waveforms during low-Na^+ perfusions with those during control perfusions, the onset of these changes may be seen in time-series, such as that of Figure 8.16, which shows the transition from the normal 22 kHz CAP waveform to that observed during the low-Na^+ $NMDG^+$-substitution perilymph perfusion. The waveforms were elicited at a constant SPL (40 dB above pre-perfusion tracked threshold), and show the reduction in peak amplitudes and increases in peak latency over a 4.5 minute period following commencement of the perfusion. While the SP amplitude was reduced by 52% in the waveform labelled "565 s", the N1 and P1 amplitudes (measured from the SP and N1 respectively) were reduced by 92% and 95%. The reduction of the later waveform peaks is also visible in Figure 8.16, as is the elimination of the off-response.

The observed changes in CAP waveforms are not explicable by a simple decrease in cochlear gain, because comparison of low-sodium waveforms with control waveforms evoked at lower sound levels (to mimic lower amplitude BM vibration) highlights several remaining differences. Figure 8.17 shows a CAP waveform (black trace) evoked by a 14 kHz waveform at 30 dB above tracked threshold during a perfusion of low-sodium choline perilymph. In the Iso-SP panel of the figure, the waveform is compared to a control CAP waveform (grey trace) recorded in the same animal, at almost the same SPL, during a perfusion of control artificial perilymph.

The SP amplitudes in these two traces are the same, which could be taken as an indicator that the amplitude of basilar membrane vibration has not changed. However, the N1 amplitude of choline CAP trace was reduced by almost 40%, while P1 amplitude was reduced by 55%, with significant latency shifts of both peaks. This reduction of peak amplitude and elongation of latency is similar to that which occurs with a 10 dB reduction in sound level, as indicated by the comparison of waveforms in the "Iso-N1" panel of that figure. In this example, the N1 amplitudes of the 30 dB SL choline waveform and the 20 dB SL control waveform are the same, and the N1 latencies are more similar. A key difference between the Iso-N1 waveforms is that the P1 amplitude was reduced by an additional 28% during the choline perfusion, despite being evoked at a level 10 dB higher than the control perfusion waveform. A similar reduction in P1 amplitude was observed during the scala-tympani-positive DC current injection experiments of Chapter Seven.

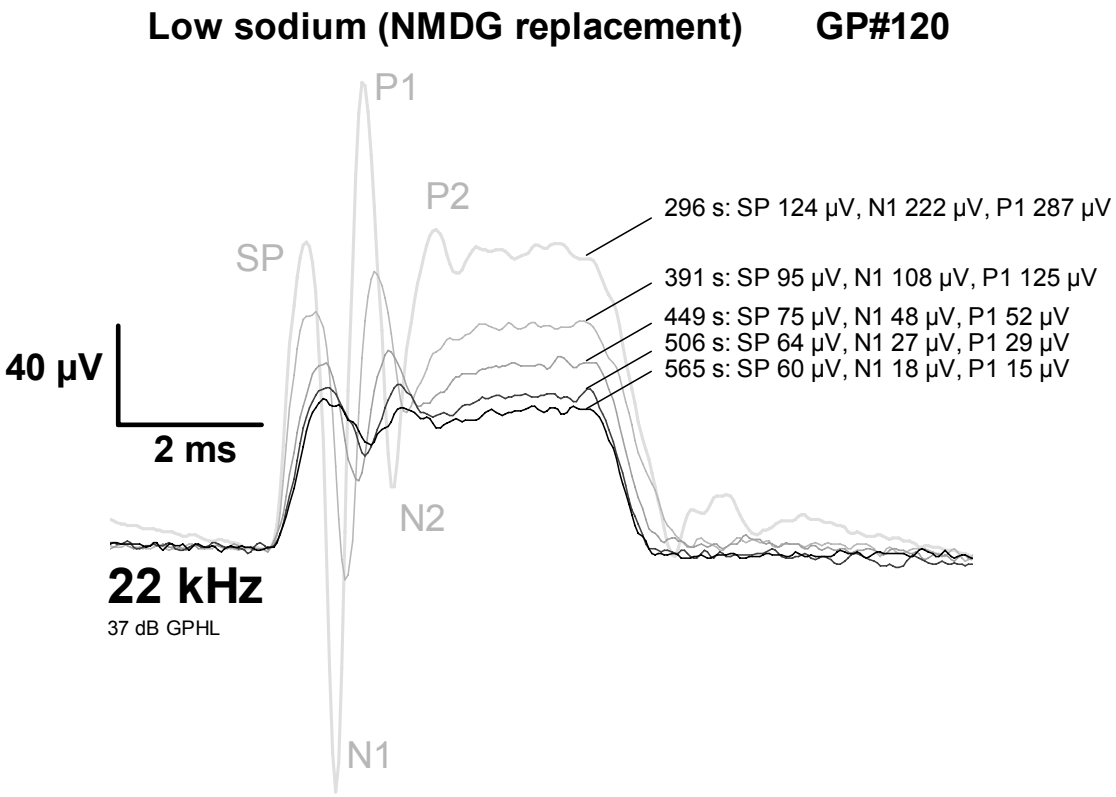

Figure 8.16: CAP waveforms recorded 30 dB above tracked threshold during the first 4.5 minutes of a 15 minute perfusion of 8 mM Na^+ NMDG artificial perilymph shown in Figure 8.13. The time-code is the same as in Figure 8.13 – the reduced-sodium perfusion commenced at 300 s, and caused reduction of peak amplitudes, and increases in peak latencies.

ID#3164943094

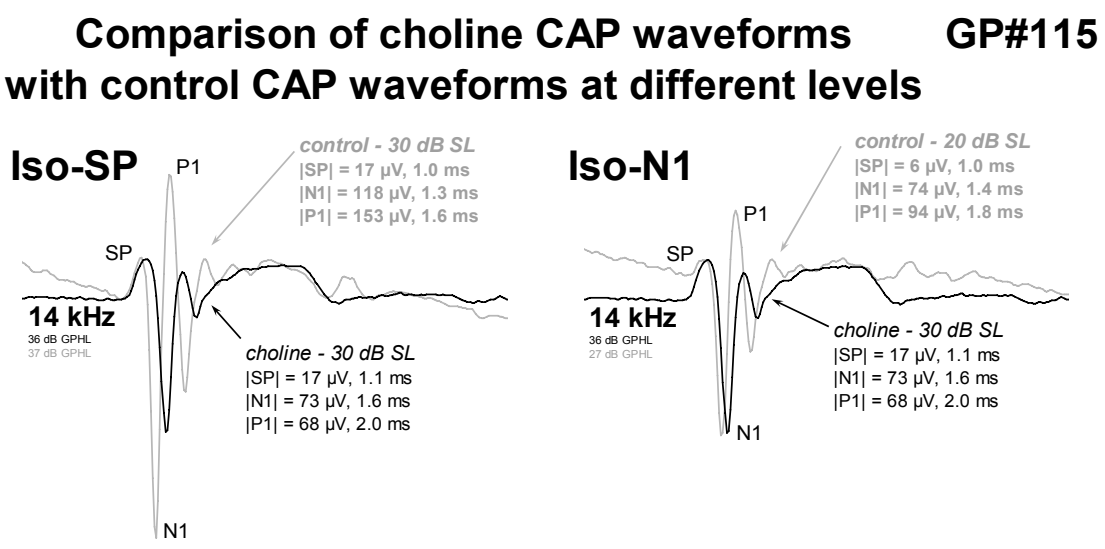

Figure 8.17: Comparison between CAP waveforms recorded at 30 dB above tracked threshold during perfusion of low-sodium choline perilymph (black traces), and CAP waveforms recorded during perfusion control perilymph (grey traces), reveal a neural effect of the reduced-sodium perfusion in addition to any mechanical effect due to the OHCs.

ID#3147920670 Control. ID#3147923796 Choline

8.3.9 The choline perfusions of Moleirinho and Patuzzi

Shown in Figure 8.18A are data from Moleirinho and Patuzzi (unpublished) for perfusions of low-sodium choline perilymph, similar to that used in the present study. Visual-detection threshold tracking of the CAP and SP showed that both the CAP and SP follow similar recovery time-courses following the 90 second perfusion, with thresholds for the two measures differing by a maximum of 6 dB.

The effect of strychnine on the choline perfusions is shown in Figure 8.18B, which compares 90-second perfusions of low-sodium artificial perilymph containing choline, before and after co-perfusion with strychnine, a blocker of cholinergic neurotransmission. The data show little difference in the pre- and post-strychnine CAP threshold time-courses, providing further evidence that the results of low-sodium perfusions using choline as a substitution ion were not efferent-mediated.

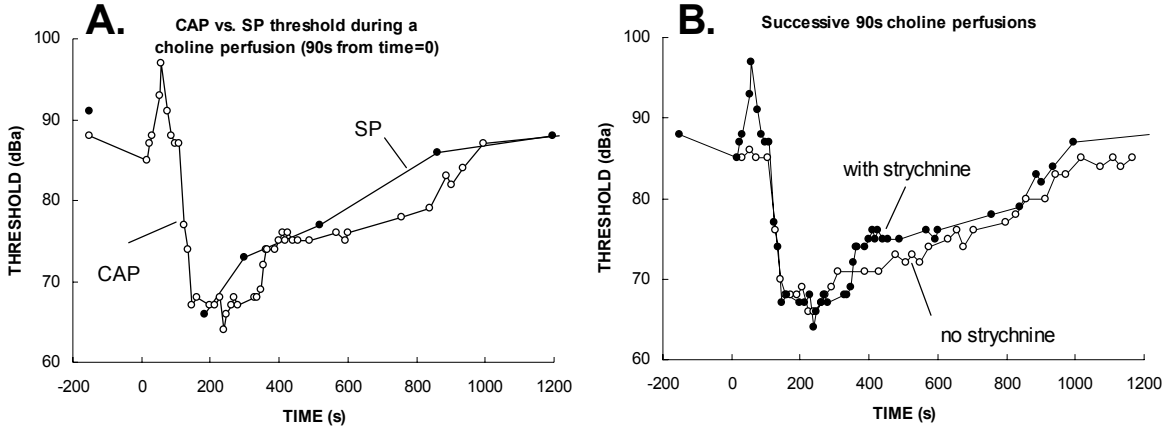

Figure 8.18: A. Data from Moleirinho and Patuzzi (unpublished) showing the similar recovery time-courses of CAP and SP threshold shifts recorded during a 90-second perfusion of reduced-sodium choline artificial perilymph, similar to that used in the present study. **B.** Treatment of the animal with strychnine did not significantly affect the time-course of the threshold shifts observed with successive 90 second perfusions of the reduced-sodium choline perilymph (Moleirinho and Patuzzi, unpublished).

8.4 Results – Mathematical modelling of reduced-sodium perfusions

The mathematical model described in Chapter Two was used to carry out simulations of reduced-sodium perilymphatic perfusions. Unless stated otherwise, simulations presented here were carried out using the standard set of OHC model parameters that were listed in Chapter Two. In contrast to other perfusion simulations presented in this chapter, the time-course of the perfusion was simulated as the *absence* of sodium, rather than a perfusion of either choline or NMDG.

8.4.1 Ten-minute perfusion of 8 mM sodium AP

The time-course of the perfusate concentration was derived from the Washington University Cochlear Fluids Simulator (v1.6h; Salt, 2002), using the settings listed in the legends of the figures presented in this section. Perfusate concentrations were calculated for the 22 kHz place, according to the place-frequency map of Tsuji and Liberman (1997). The "perfusion of the absence of sodium" was simulated by subtracting the calculated concentration time-course for a sodium perfusion from the baseline sodium level, rather than adding to it, as was usually the case. In this way, the passive diffusion characteristics of sodium that were included in the Fluid Simulator time-course were preserved (namely, the diffusion co-efficient). One important implication of this method of calculating the simulated time-course is that, despite the perfusate solution containing only 8 mM Na^+, the minimum Na^+ concentration reached during the perfusion was around 28 mM. In this sense, it is likely that the intended "severity" of the perturbation was reduced in the cochlea (i.e. an 80% reduction in $[Na^+]_i$, instead of 95%).

Figure 8.19 shows the results of a simulated 10-minute perfusion of 8 mM Na^+ in scala tympani. The time-course of the perfusate concentration is shown in the bottom panel. During the first 75 s of the perfusion, the scala tympani Na^+ concentration fell from 148 mM to 30 mM. This caused a 12% increase in $[Ca^{2+}]_i$, due to a 35% reduction in antiport flux. Predictably, the potassium influx through the Na^+/K^+/ATPase was reduced by only 0.02% by the reduced sodium, while the potassium efflux through the calcium-sensitive K^+ channels increased by 5%, causing a net hyperpolarisation of the basolateral membrane potential by 2.2 mV and a reduction in the EP by 1.2 mV. The hyperpolarisation caused a 4.6 meV SV electromotile operating-point shift.

The increased basolateral permeability caused the small-signal AC receptor potential to increase by 4.5%, which was extrapolated to a modest 4 dB threshold shift. The saturated AC receptor current, analogous to CM amplitude or the Vsat Boltzmann parameter, increased by 2.4% during this time. Over the remainder of the perfusion, the increasing $[Ca^{2+}]_i$ also caused the concentrations of the second messengers M2, M3 and M4 to rise. While the Ca^{2+}-induced hyperpolarisation had caused a SV electromotile operating point shift, the increasing concentration of M4 initiated a slow-motile contraction toward scala tympani which exceeded the electromotile contraction and caused a net operating point shift of -24 meV. Once the $[Ca^{2+}]_i$ had begun to decrease (due to increased sequestration under the influence of the messenger M3), the basolateral K^+ current began to decrease also.

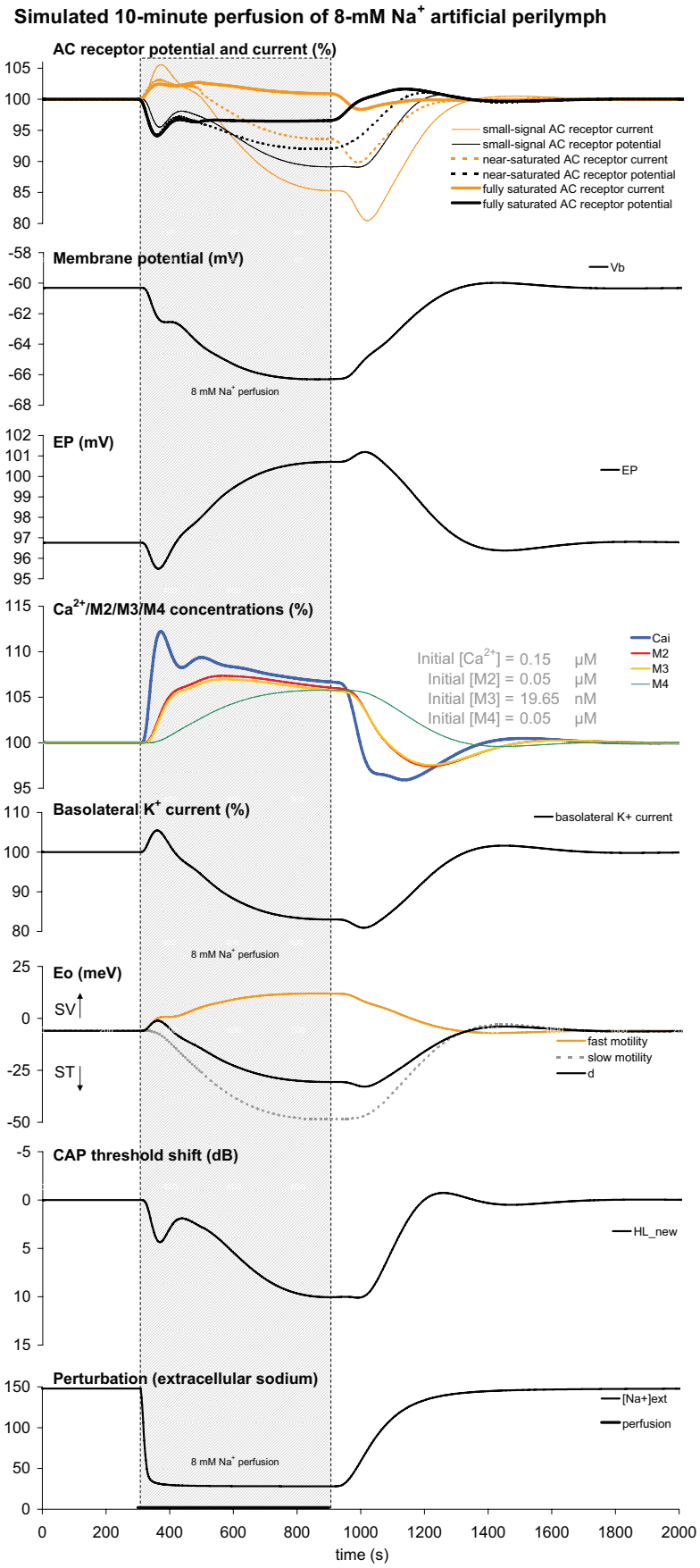

Figure 8.19: OHC model parameters during a simulated 10-minute perfusion of reduced Na^+ (8 mM) artificial perilymph (see text). Washington University Cochlear Fluids Simulator v.1.6h settings: Guinea pig cochlea. Ten-minute perfusion of Na^+ (1.99×10^{-5} cm^2/s diffusion coefficient) at 3 µL/min, perfusate entry at 2 mm, exit at 16.2 mm. Radial ST-SV communication half-time normalized to 0.1 mm^2 cross-sectional area. Cochlear aqueduct enters at 1.1 mm. Apical perilymph communication enabled - 0.03 mm^2 helicotrema area. Perilymph leak of 0.5 µL/min at 16.2 mm location. Recording locations chosen assuming 22 mm guinea-pig cochlea and the 22 kHz location, according to the place-frequency map of Tsuji and Liberman, 1997.

This reduced basolateral permeability caused the small-signal receptor potential to increase, before it fell further under the influence of the slow contraction towards ST and the reduction in apical permeability. Consequently, the calculated threshold shift showed a similar pattern, with a slight improvement giving way to a further loss which reached a maximum of 10 dB. At the offset of the perfusion, the parameters which were most directly influenced by intracellular calcium (namely, the basolateral permeability, EP, the membrane potential, and operating point) showed mildly oscillatory recovery time-courses due to the interplay between the concentrations of Ca^{2+} and the messenger M3 controlling its sequestration. In particular, the CAP threshold showed a very slight bounce of under 1 dB.

Comparison of the above simulation output to those observed experimentally revealed a number of significant differences. Firstly, it must be remembered that the threshold shift predicted by the model only refers to that component that was due to changes in active gain, and so any component of the threshold shift due to the effect of the sodium on the neurones themselves was not calculated. A number of features of the changes in saturated AC receptor current were similar to the Vsat changes in the guinea pig: the model predicted a 2% increase in saturated AC receptor current after around 105 seconds followed by a gradual decrease. This was consistent with the summary of the experimental data shown in Figure 8.8, although the decreases in recorded Vsat often fell below baseline. [Note: In this respect, the near-saturated[4] AC receptor current (dashed line) showed a better match to the experimental data]. However, the operating point shifts were in the *opposite* direction to those observed experimentally: the experimental Eo data during the low-sodium perfusions (summarised in Figure 8.8) showed a small ST shift during the first 60 seconds, followed by a sustained SV shift, while the model predicted the opposite pattern[5]. This is discussed further in Section 8.5.2 below. In the meantime, to provide an indication of how the results of the above model perfusion were affected by the *magnitude* of the sodium reduction, a series of simulations were carried out in which the extracellular sodium concentration was reduced from the control level of 148 mM to levels of 128, 64, 32, 16, and 8 mM, with this last level being the same as that used in the guinea-pig experimental perfusions presented in Section 8.3 above. The overlaid results are shown in Figure 8.20.

[4] The AC signal magnitudes used in the model load-line calculations were ±1 meV for small-signal, ±100 meV for near-saturated, and ±150 meV for fully saturated AC stimulation.
[5] The magnitude of the operating point shifts was also much smaller than those of the model, but seeing as they were in the opposite direction, this is essentially irrelevant.

Simulated 10-minute perfusion of Na^+ artificial perilymphs of different concentrations

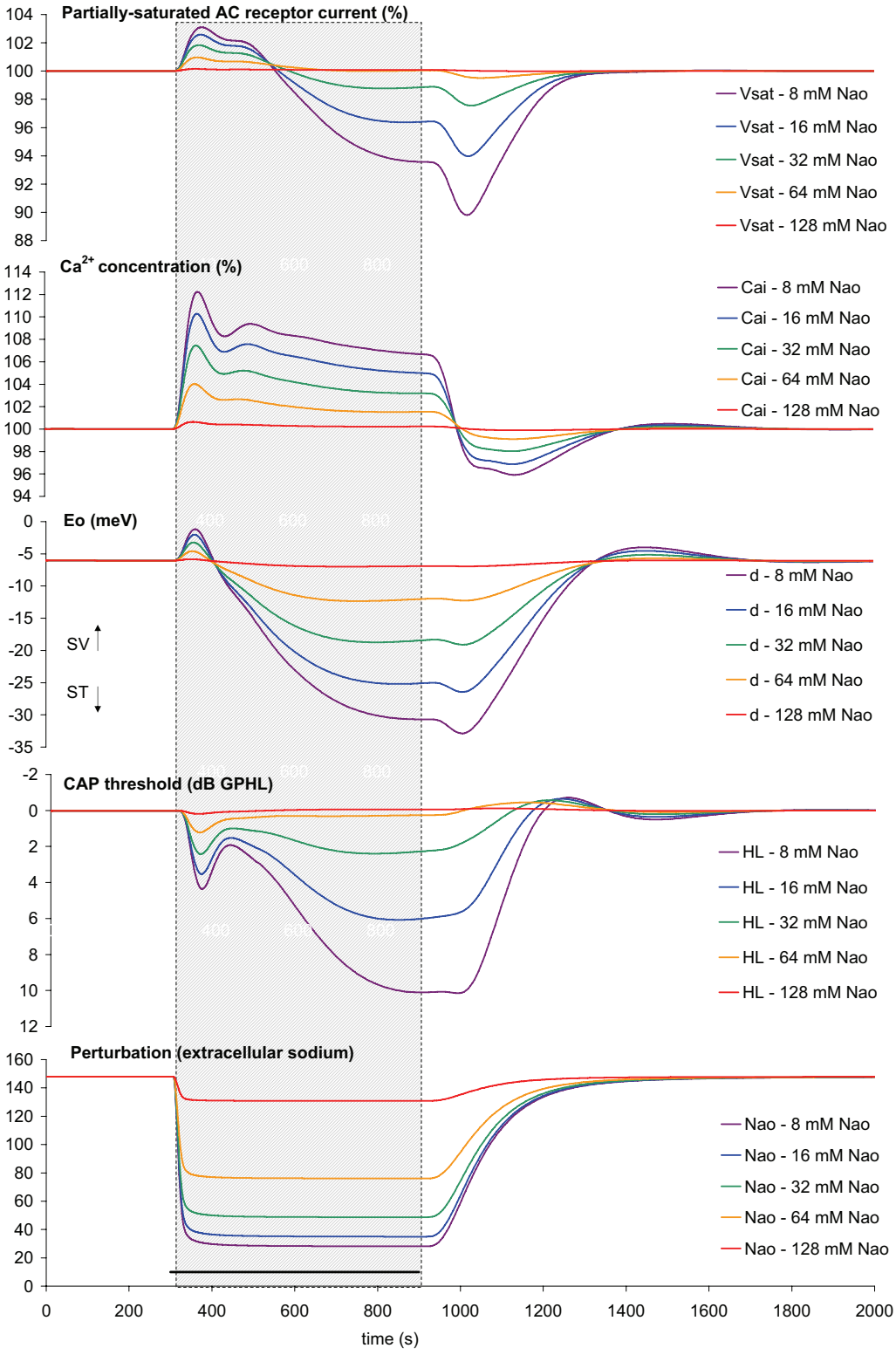

Figure 8.20: OHC model parameters during simulated 10-minute perfusions of reduced Na^+ artificial perilymphs (see text).

Washington University Cochlear Fluids Simulator v.1.6h settings: Guinea pig cochlea. Inverted ten-minute perfusion of Na^+ (1.99 x 10^{-5} cm^2/s diffusion coefficient) at 3 µL/min, perfusate entry at 2 mm, exit at 16.2 mm. Radial ST-SV communication half-time normalized to 0.1 mm^2 cross-sectional area. Cochlear aqueduct enters at 1.1 mm. Apical perilymph communication enabled - 0.03 mm^2 helicotrema area. Perilymph leak of 0.5 µL/min at 16.2 mm location. Recording locations chosen assuming 22 mm guinea-pig cochlea and the 22 kHz location, according to the place-frequency map of Tsuji and Liberman, 1997.

8.5 Discussion - Reduction in perilymphatic sodium

The reduction of perilymphatic sodium clearly had a neural effect in addition to the observed effect on the OHCs: this was indicated by the large reductions in SNN amplitude, and the large percentage reduction in CAP amplitude in cases where the changes in the Boltzmann parameters were relatively minor. These results are consistent with those of Salt and Konishi (1982), who found that both intravenous injection and perilymphatic perfusion of the sodium channel blocker amiloride caused a 65% reduction in the CAP responses, but little or no change in the CM or EP compared to the control perfusion of Ringer's solution. Amiloride is also known to block the Na^{+}/Ca^{2+} antiport (Ikeda et al., 1992a), which was the ionic transporter in the model that initiated the observed hair cell effects, discussed further in Section 8.5.2 below.

8.5.1 Onset and offset of perfusion effects correspond to predicted time-course of perfusate concentration

The rate of changes in cochlear parameters differed at the onset and offset of the perfusions. For the results presented in Figures 8.3, the average ratio of the onset to the offset was 3.7 for the neural measures of cochlear function (5.0 for SNN, and cross-frequency averages of 3.1 for CAP threshold shift and 2.8 for CAP amplitude. The calculation of these ratios for the CAP threshold shift is illustrated in Figure 8.21). This average ratio of 3.7 was presumably due to the rate with which the perfusates were delivered to scala tympani being considerably faster than the bulk flow of endogenous perilymph that was responsible for "washing out" the experimental perfusate.

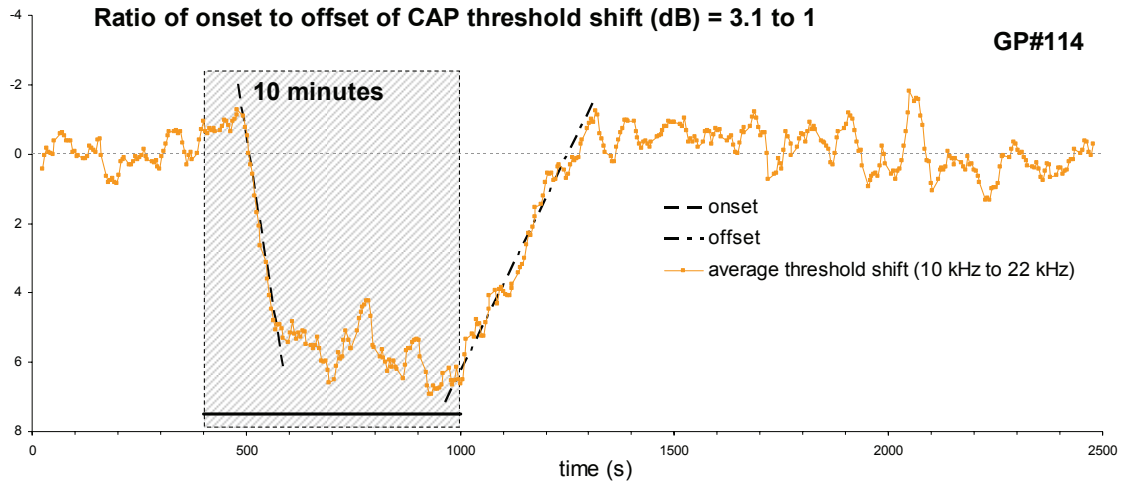

Figure 8.21: The ratio of onset to the offset of neural responses, including CAP threshold shift (shown here), N1 amplitude, and SNN peak amplitude, corresponded to the ratio of the perfusion flow rate to the estimated bulk flow rate of endogenous perilymph in perforated cochleae (Ohyama et al., 1988; Salt et al., 1991).

ID#3146121272. Thresholds (2 kHz to 22 kHz, dB GPHL): 6, 1, -1, -5, 1, -3, -6.

While the rate of perilymph flow in a sealed cochlea is extremely low (around 1.6 nL/min from base to apex; Ohyama et al., 1988), the flow of perilymph in perforated cochleae has been measured at between 0.49 μL/min and 1.0 μL/min (Ohyama et al., 1988; Salt et al., 1991). Given a perfusion rate of 3 μL/min, the calculated onset/offset ratio of 3.7 corresponds to a passive perilymph flow rate of 0.8 μL/min – a value consistent with the published flow rates.

In GP#115, the passive perilymph flow rate appeared to be reduced (see, for example, Figure 8.6), resulting in a prolonged depression of neural responses following the perfusion. As was demonstrated in Figure 8.11, the rate of recovery from the perfusion could be accelerated by active replacement of artificial perilymph by using the perfusion pump. Consistent use of this washout technique (with a simple valve in the perfusion line) would most likely remove much of the variability in the post-perfusion time-courses, and may be warranted in future studies.

8.5.2 Mechanism of hair cell changes with extracellular sodium reduction

The primary effects of the reduced-sodium perfusions appear to be largely consistent with an increase in cytosolic calcium concentration due to a reduction in Ca^{2+} efflux through the Na^{+}/Ca^{2+} antiport. However, as mentioned earlier, the major difference between the experimental results and the model predictions was in the direction of the operating point shift. As will be discussed in detail in Chapter Nine, *this operating point shift is not explicable within the current model framework.* This particular simulation result is more likely to indicate a more significant difference between the model mechanisms and those encountered in the real OHC than a simple "fine-tuning" problem of the model: at the concentrations required for calcium to produce the observed increases in basolateral permeability, the slow-motile contraction exceeds any fast-motile expansion due to the hyperpolarisation of the OHC. While altering the model parameters for the relative sensitivities of the fast and slow motile processes would correct this operating point shift *for this perturbation*, it would result in the production of less realistic simulation results during other perturbations. This issue will be discussed further in Chapter Nine.

In comparison, the observed changes in basolateral permeability were well explained by the model. Patuzzi and Rajan (1990) calculated that a 15% increase in CM amplitude (during efferent stimulation) was equivalent to a doubling of the conductance of the basolateral wall of the OHC. The maximal percentage increase in Vsat observed during our low-sodium choline perfusions was 6%, which would presumably therefore have

arisen from an approximate 40% increase in basolateral conductance. An increase in $[Ca^{2+}]_i$ and basolateral potassium conductance is also seen with medial olivocochlear (MOC) efferent stimulation or pharmacological activation of MOCs receptors (Housley and Ashmore, 1991; Fuchs and Murrow, 1992; Blanchet et al., 1996; Evans, 1996). However, a firing of the medial olivocochlear (MOC) neurones is unlikely to be responsible for the changes observed during our perfusions, because the reduced extracellular sodium would also hyperpolarise the MOCs neurones, decreasing their tonic activity.

While the observed changes in the Vsat and Eo Boltzmann parameters have already been analysed with reference to the schematic and mathematic model of the OHC in Section 8.4.1 above, the Z parameter, on the other hand, does not have a ready analogue in the model. The increases in Z were the most consistent of the changes in the Boltzmann parameters during the low-sodium perfusions, showing 6-15% increases. Increases in Z would be observed if the axial stiffness of the OHC was reduced. The axial stiffness of OHCs has been shown to be voltage-dependent: in isolated *unloaded* OHCs, axial stiffness increases with hyperpolarisation and decreases with depolarisation (He and Dallos, 1999; He and Dallos, 2000). In *loaded* OHCs (more similar to the *in vivo* situation), this voltage-dependent stiffness change is reversed (He, 2003), with axial stiffness decreasing with hyperpolarisation and increasing with depolarisation (see discussion in Chapters Five and Seven). The mathematical model predicted a hyperpolarisation during the low-sodium perfusion (Figure 8.19), which would therefore have caused a reduction in axial stiffness, and the experimentally observed increase in the Z parameter. The axial stiffness of the OHCs is also calcium-dependent (decreasing with increasing cytosolic calcium; Frolenkov et al., 2003): the increase in intracellular calcium produced by a reduction in Na^+/Ca^{2+} antiport activity would also therefore produce the observed increase in the Z parameter.

8.5.3 Neural susceptibility to extracellular sodium reduction

Large reductions in CAP and SNN amplitude were seen with the reduction in perilymphatic sodium concentration. While the SP amplitude remained relatively unchanged in some cases (such as in Figure 8.14), there was a broadening of the SP peak, which was most likely due to the longer latency of the N1 peak (described below). The unchanged SP amplitudes could suggest that the amplitude of the BM vibration and functioning of the IHC may not have been significantly affected, at least at these frequencies. The reduction in peak amplitude is consistent with the reduced

concentration gradient for the influx of sodium required for an action potential. This reduced Na^+ entry would hyperpolarise the primary afferent neurones and increase the N1 peak latency, presumably because each excitatory post-synaptic potential would take longer to reach threshold. The same mechanism would account for the large changes in the SNN that were also observed. The SNN, recorded in silence, is a measure of both the stochastic neural firing rate, and of the degree of sub-threshold resonance in the unitary potential of the primary afferent dendrites (Dolan et al., 1990; McMahon and Patuzzi, 2002). This resonance is also visible in the averaged CAP waveform, and also affects the amplitude of the spectrum of the averaged CAP waveform (the SAW; McMahon and Patuzzi, 2002). As shown in Figures 8.14 and 8.15, the presence of later peaks in the CAP waveforms was greatly reduced with the reduction in extracellular sodium, with the P2 peak being lost. Another perturbation that resulted in the loss of the later peaks of the CAP waveform was the injection of DC negative current into scala tympani (see Chapter 7, and also Patuzzi et al., 2004), presumably due to the associated changes in the membrane potential of the primary afferent neurones.

Brown et al. (2004) suggest that the N1-P1 measure of CAP amplitude is a useful indicator of the K^+ current. If the loss of extracellular sodium results in a hyperpolarisation of the neuronal membrane potential, we would expect a reduction of the gradient for K^+ entry, which is consistent with the reduction in P1 amplitude shown in the Iso-N1 panel of Figure 8.17. As with the DC current injection results of Chapter Seven, this results is consistent with the resting potential of the neurones being closer to the highly-negative K^+ equilibrium potential than the positive Na^+ equilibrium potential (Siegel and Dallos, 1986).

8.5.4 Correspondence between tracked thresholds and CAP amplitudes

The reproducibility of the perfusion shown in Figure 8.3 permitted a comparison between the automatically-tracked CAP thresholds and the N1 amplitudes for supra-threshold stimuli in this animal.

If the only effect of the reduced perilymphatic sodium were a reduction in basilar membrane vibration, it would be expected that the relationship between CAP amplitude and CAP threshold, and between SP and CAP amplitudes and latencies, would be the same as for a reduction in sound level. To demonstrate, the pre-perfusion traces of Figure 8.12 show CAP input/output (IO) functions relating the reduction in CAP amplitude as the sound stimulus was reduced. In this case, the CAP amplitude is shown to increase linearly with decibel stimulus level (up to 30 dB SL at least), and so when

applied to the CAP changes with choline perfusion, the average 65 ± 8% decrease in CAP amplitude with choline perfusion would correspond to an average 21 ± 3 dB threshold shift if the loss were purely a motor one. However, as shown in Figure 8.3, the tracking algorithm detected only a 6 dB threshold shift. Measurement of CAP threshold during choline perfusion posed particular problems for the correlation-based threshold tracking method used in this study (described in Chapter 4). Because correlation is dependent on signal-to-noise ratio (SNR), it is only effective in tracking changes in CAP threshold if the level of background electrical noise (such as the SNN) is relatively constant. However, because concurrent decreases were observed in both CAP and SNN during choline perfusion, the magnitude of any changes in threshold were likely to have been underestimated by the automated tracking method. If the loss in sensitivity were only 6 dB, this would indicate that the Na^+/Ca^{2+} antiport is simply not the dominant calcium efflux mechanism *in vivo*.

8.5.5 Effects of hexamethonium perfusion

The hexamethonium perfusion caused a lasting 15% reduction in Vsat. Taken in isolation, this result is consistent with a blockade of tonic efferent activity, causing a reduction in OHC calcium influx, and therefore a reduction in basolateral potassium permeability. Amazingly, this occurred with no discernable change in operating point: this point will be discussed in further detail in Chapter Nine. However, the time-course of the perfusion was similar to that of the control perfusion performed earlier in that animal, shown in Figure 8.4, and so it is difficult to draw any firm conclusions as to the effect of hexamethonium perfusion on the Boltzmann parameters. There was, however, a small but measurable increase in SNN following the hexamethonium perfusion, which would be consistent with the predicted increase in EP due to the reduced shunt.

8.5.6 Lack of a cholinergic effect from choline

We have already mentioned that the efferent neurones of the MOCs would be hyperpolarised by the reduced extracellular sodium, and would therefore show reduced activity. However, the possibility remained that the choline used as the substitution ion for sodium could affect the cholinergic MOCs synapse directly. Fortunately, in the experiments presented here, i) the blockade of the ACh-sensitive Ca^{2+} channels by hexamethonium or strychnine produced no difference in the effects observed, ii) the use of a different substitution in ($NMDG^+$) also produced similar effects.

One possible explanation for this lack of a choline effect is that choline is simply not effective in stimulating the efferent synapse. Another is that the observed lack of a

cholinergic effect was due to the suppression of the efferent synapse by one or more of the drugs used in the anaesthetic regime – in particular, the muscarinic antagonist atropine, and the nicotinic antagonist, pancuronium. Atropine is a cholinergic antagonist with a high affinity for muscarinic receptors, that was used in this experimental series as a pre-medication to dry mucosal secretions and to counteract the bradycardia associated with barbiturate anaesthesia. As mentioned in Chapter Three, guinea pigs were injected subcutaneously with 0.1 mL atropine sulphate (0.6 mg/mL; Apex Laboratories, NSW) prior to every experiment described here. In isolated chick hair cells, the presence of 100 μM atropine blocked the intracellular Ca^{2+} increase observed with extracellular application of 100 μM ACh (Vetter et al., 1999; Elgoyhen et al., 2001), but whether the 0.06 mg of atropine sulphate injected would result in similar concentrations in the cochlear fluids is not clear. Another possibility is that the efferent synapse could have been blocked by the intramuscular injection of 0.1 mL pancuronium bromide (2 mg/mL; AstraZeneca, NSW, Australia) that was used to eliminate middle-ear muscle activity and myogenic electrical noise. Pancuronium is a competitive nicotinic antagonist, and a member of the same curarimimetic family, d-tubocurarine, was found to block the ACh effect in chick hair cells (Wangemann and Schacht, 1996).

Although these possibilities do exist, they are unlikely to have had a significant effect on the guinea pig experiments presented here, as these premedication protocols have been used routinely in our laboratory for many years, during which time dozens of efferent-related experiments have been successfully performed.

8.6 Results – Hyperosmotic perfusions

In four animals, scala tympani was perfused with artificial perilymph that had been made hyperosmotic by the addition of sucrose. The perilymph osmolarity was increased with the aim of causing a movement of water down its concentration gradient into scala tympani, to allow the effects of osmotic bias on the Boltzmann parameters, neural noise, and auditory thresholds, to be examined. It was expected that the primary effect of an increase in perilymph osmolarity would be the movement of water down its concentration gradient into scala tympani, which would result in a movement of the basilar membrane toward scala vestibuli, and a corresponding operating point shift. However, the operating point shifts were quite variable, with the most consistent change in the Boltzmann parameters being the increase in the Z parameter, an indicator of the overall sensitivity of the MET process.

The mean osmolality of the sucrose artificial perilymph was 349 ± 1 mOsm/kg H_2O, compared to mean osmolality of 303 ± 6 mOsm/kg H_2O for control artificial perilymphs used in the present study, and 293 ± 6 mOsm/kg H_2O for endogenous guinea pig perilymph (Konishi et al., 1984).

8.6.1 Two-minute perfusions of 350 mOsm artificial perilymph

Figure 8.22 shows the results for a two minute perfusion of 350 mOsm artificial perilymph. During the perfusion there was a 2 meV operating point shift toward SV peaking around 1 minute into the perfusion, after which time Eo returned toward ST before oscillating around the pre-perfusion value. The Vsat parameter also showed a transient 3% increase during the perfusion, before falling to below its starting level and showing a damped oscillation. This oscillation was also visible in the Z parameter, which had shown a 25% increase during the perfusion, peaking 140 to 160 s after perfusion onset. SNN amplitude decreased during the hyperosmotic perfusion by around 20%.

The hyperosmotic perfusion caused threshold shifts up of 20 dB at 4 kHz, increasing to 32 dB at 18 kHz. The onset of the threshold shifts was most rapid in the higher frequencies, which also showed the quicker recovery of sensitivity following offset of the perfusion. As will be demonstrated in Section 8.8 below, this is most likely due to the time-course of the perfusate concentration along the cochlea.

Figure 8.23 shows overlaid results for two identical and consecutive perfusions, delivered 47 minutes apart in the same animal (GP#93). The Vsat traces for both perfusions showed a slight decrease at the onset of the perfusion (larger during the second perfusion), followed by a broad peak at 110 – 150 s that reached 11% during the first perfusion and 5% during the second. The Z parameters for both perfusions shared a near-identical time-course over the first 40 seconds of the perfusion, after which time both showed a peak of 9-10% above the pre-perfusion values, with the Z peak in the second perfusion peaking earlier and showing a slower recovery than during the first perfusion. Although the Eo changes for the second perfusion were double the amplitude of those from the first perfusion, both perfusions shared a similar time-course, showing a transient SV peak followed by a smaller ST undershoot that were both superimposed on a much more gradual SV shift.

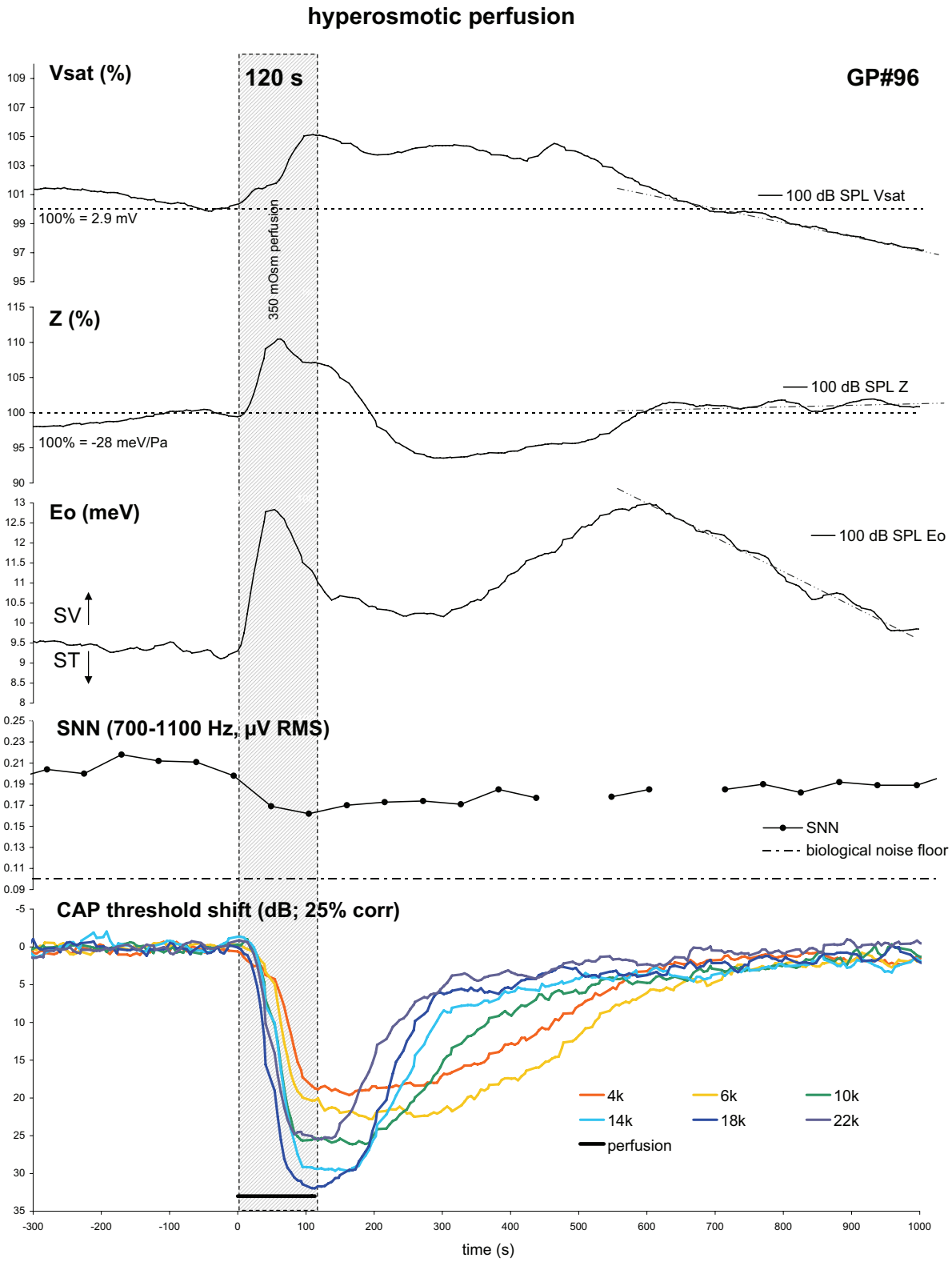

Figure 8.22: Boltzmann parameters, SNN, and tracked CAP thresholds recorded during a two-minute perfusion of 350 mOsm artificial perilymph. Stippled lines in the Boltzmann traces from 400 s act as linear references against which small oscillations in the parameters can be seen. ID#3129169817. Thresholds (4 kHz to 22 kHz, dB GPHL): 9, 9, 8, 12, 13, 23. 7-pt running average

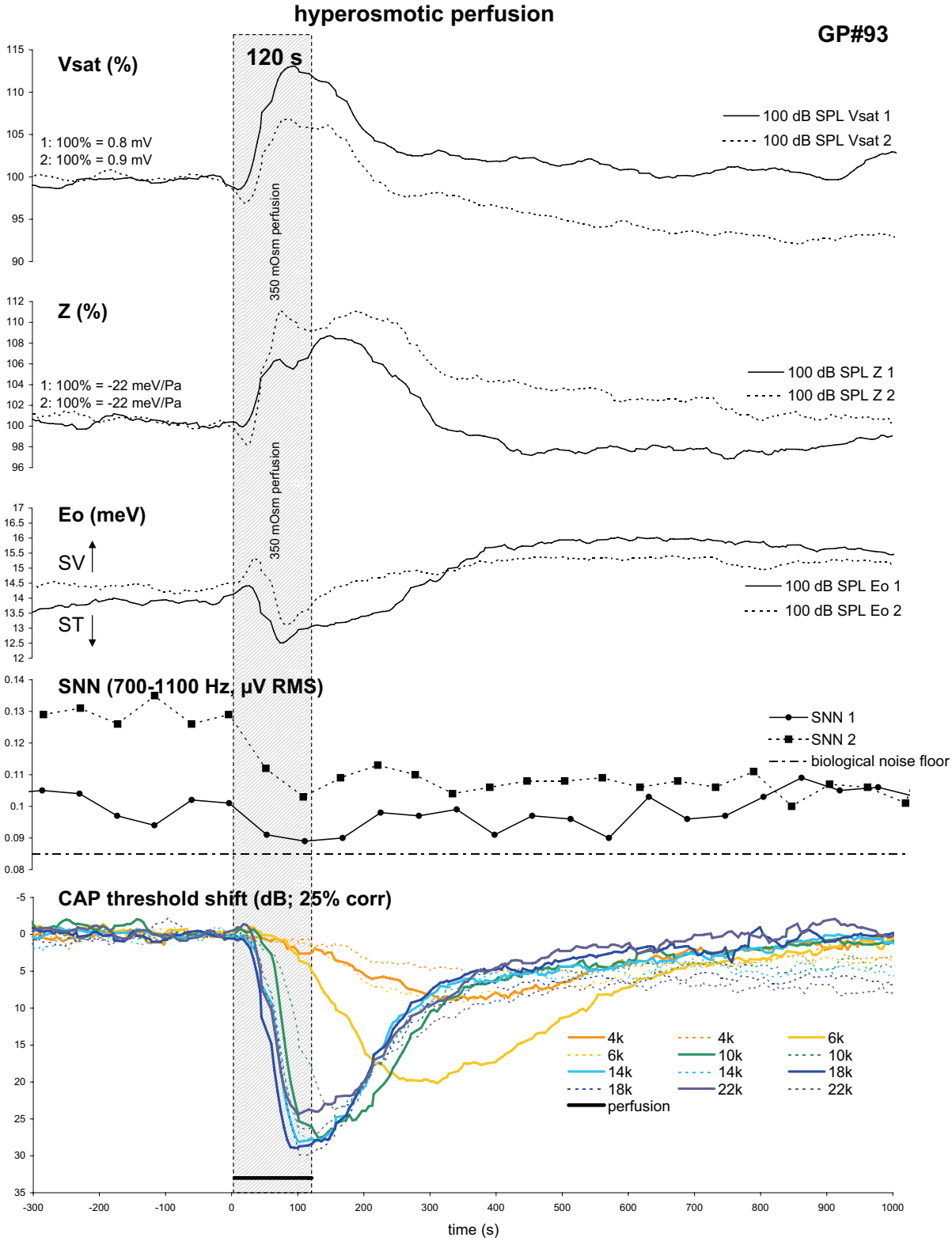

Figure 8.23: Boltzmann parameters, SNN, and tracked CAP thresholds recorded during consecutive two-minute perfusions (47 minutes apart) of 350 mOsm artificial perilymph. The traces are overlayed to illustrate the reversible and reproducible nature of this perturbation. ID#3127961347 (solid). Thresholds (2 kHz to 22 kHz, dB GPHL): 13, 10, 7, 9, 15, 13, 20. ID#3127964168 (dash). Thresholds (2 kHz to 22 kHz, dB GPHL): 11, 11, 7, 9, 15, 14, 22. 7-pt running average

While the SNN fell by approximately 12% during the first perfusion, and by 20% during the second. The CAP threshold traces for the first perfusion (solid lines) showed that the thresholds at frequencies from 10 kHz to 22 kHz followed a similar time-course to each other, with more elongated time-courses for the 6 kHz and 4 kHz traces. All thresholds had recovered to within 2 dB of their pre-perfusion thresholds by the time of the second perfusion. This second perfusion (dashed lines) displayed more elongated time-courses for the 10 kHz, 6 kHz, and 4 kHz traces.

The first-turn threshold shifts were more closely correlated to the changes in basolateral permeability than the operating point changes: the Pearson correlation coefficients (r) between the 22 kHz CAP threshold and the Vsat and Z parameters were 0.91 and 0.85 respectively, compared to 0.48 for Eo.

Two further examples of hyperosmotic perfusions are shown in Figures 8.24 and 8.25. While the results in Figure 8.24 from GP#94 were similar to those from GP#96 (Figure 8.22), the results from GP#95 (Figure 8.25) are another example of the presumed effects of a reduced clearance of perfusate. Although the animal had only a 30 dB hearing loss at 22 kHz at the start of the perfusion shown here, the condition of the animal was generally poor, and its heart rate had begun to decrease markedly. Following the hyperosmotic perfusion, the CAP thresholds took a much longer time to recover to normal levels. Additionally, the operating point shift towards SV was much larger, and did not show the same rapid recovery observed in other animals of this experimental series. The differences between the results of this perfusion and the others in the hyperosmotic series are clearly visible in Figure 8.26.

Figure 8.26 shows the overlaid traces for the hyperosmotic perfusions presented in Figures 8.22 to 8.25. To enable better comparison, all of the traces shown in Figure 8.26 were recorded with 207 Hz probe tones at the same level (100 dB SPL). In all five traces, Vsat was elevated by the end of the 120 second perfusion period, showing a mean increase of 6 ± 4%. The most consistent of the Boltzmann parameters during these perfusions was the Z parameter, with the five hyperosmotic perfusions showing a mean 8 ± 1% increase in Z by the end of perfusion. The operating point shifts showed more variability: With the exception of GP#95 (the blue trace in Figure 8.26) which showed a large SV shift, the hyperosmotic perfusions caused initial operating point shifts towards scala vestibuli of around 1-2 meV that peaked around 40-50 seconds into the perfusion, that were either followed by a brief undershoot towards scala tympani (GP#93 and 96) or initiated a longer-lasting ST operating point shift (GP#94).

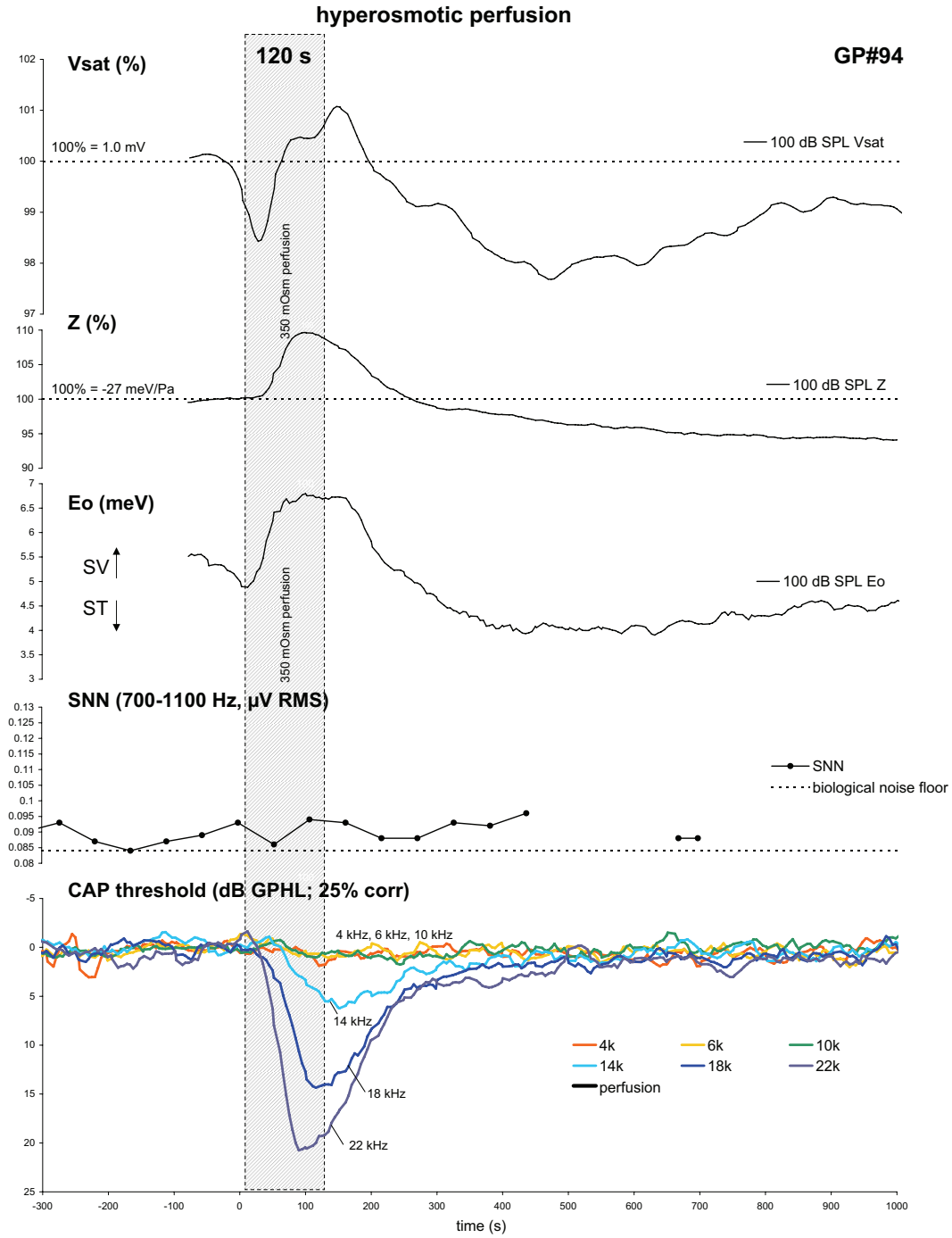

Figure 8.24: Boltzmann parameters, SNN, and tracked CAP thresholds recorded during a two-minute perfusion of 350 mOsm artificial perilymph. In this example, the perfusion only affected thresholds at 14 kHz, 18 kHz, and 22 kHz, and the changes in the Boltzmann parameters were smaller than for other similar perfusions (see text).
ID#3128406137. Thresholds (4 kHz to 22 kHz, dB GPHL): 16, 23, 25, 22, 20, 21.
7-pt running average

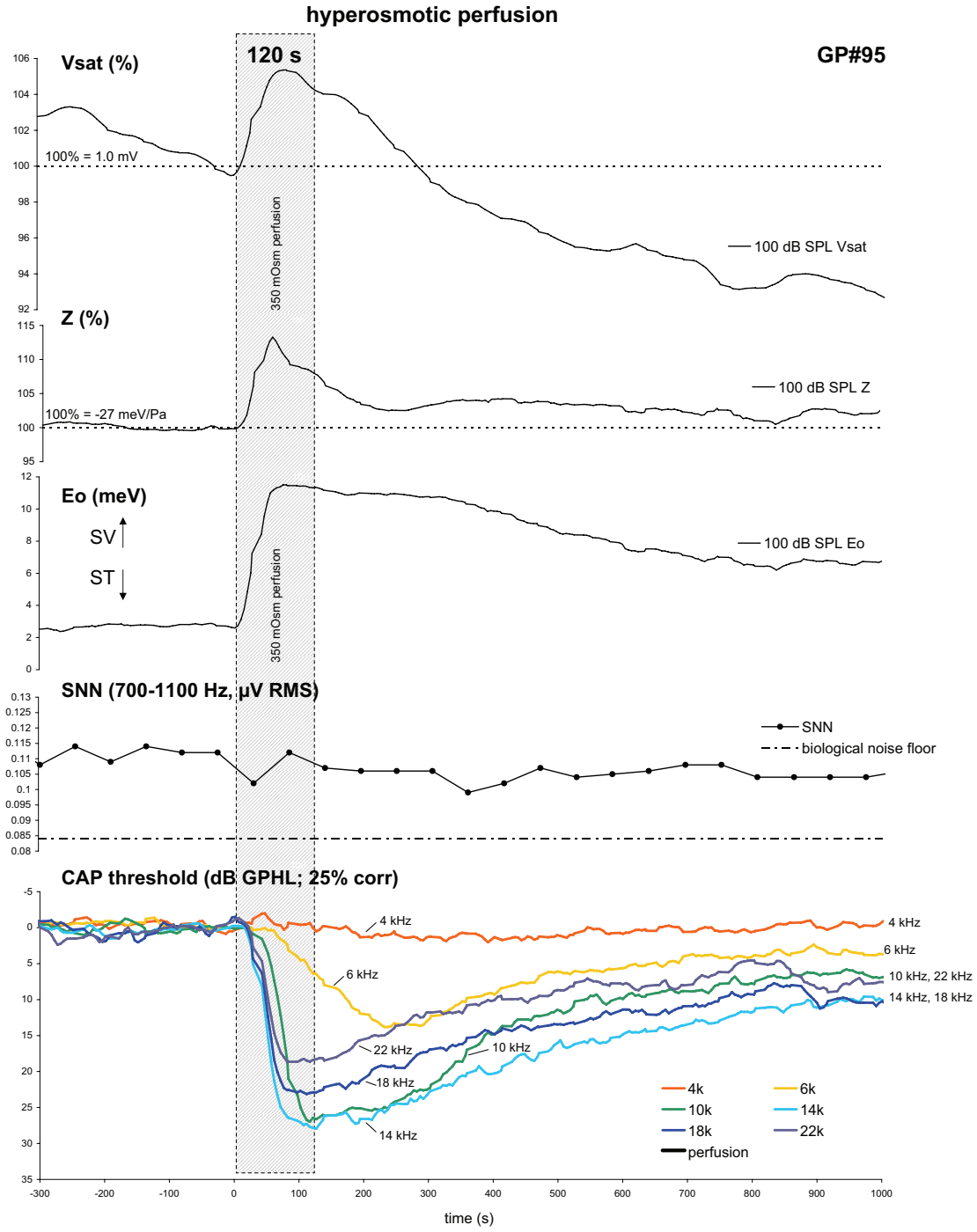

Figure 8.25: Boltzmann parameters, SNN, and tracked CAP thresholds recorded during a two-minute perfusion of 350 mOsm artificial perilymph, in a deteriorating animal. The lack of a quick recovery from this perfusion may be due to the decreased clearance of the perfusate from the cochlea as the animal deteriorated, heart rate decreased, and CSF pressure presumably fell. ID#3128566589. Thresholds (4 kHz to 22 kHz, dB GPHL): 13, 13, 16, 20, 19, 30. 7-pt running average

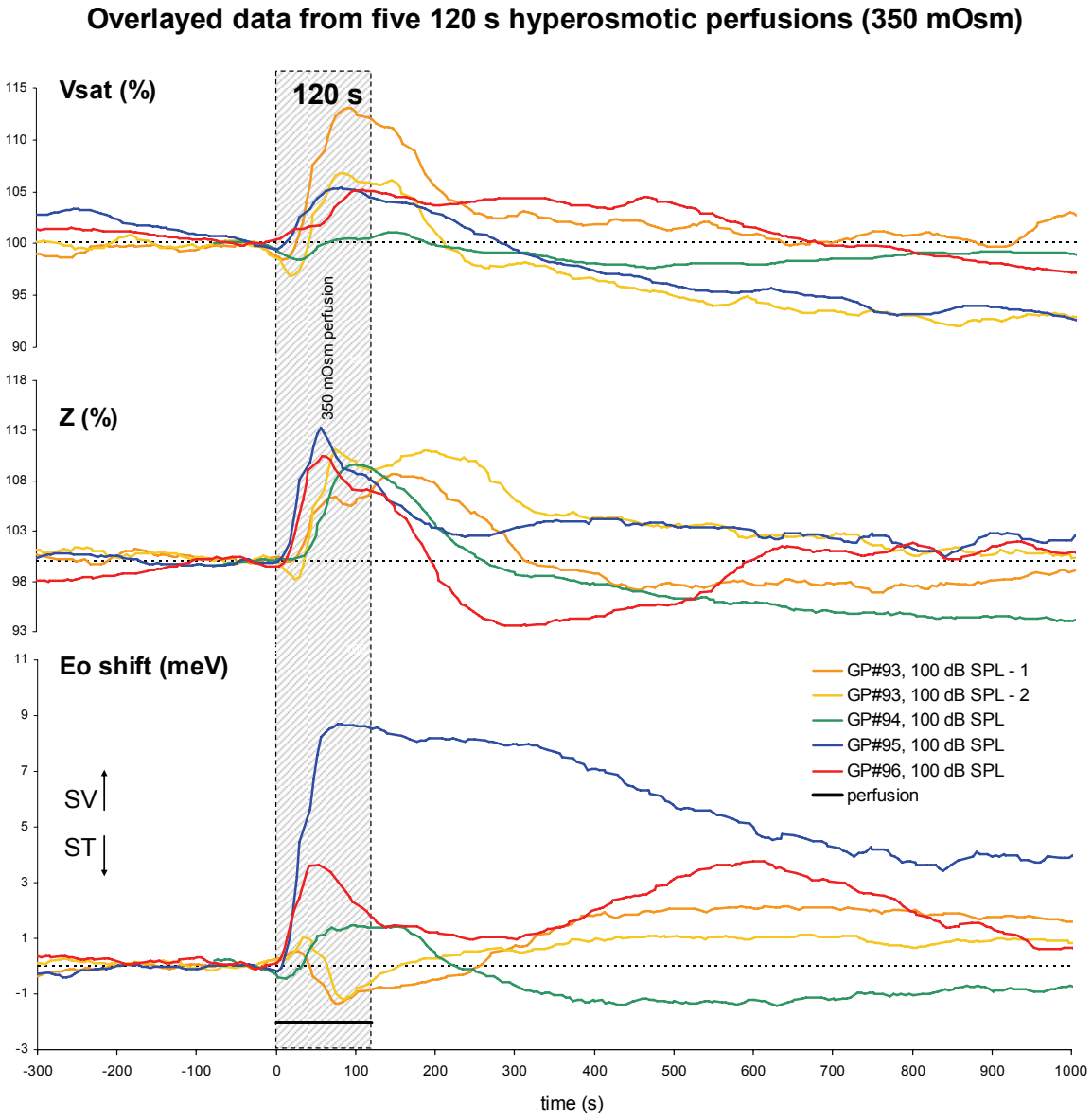

Figure 8.26: Boltzmann parameters recorded during five two-minute perfusions of 350 mOsm artificial perilymph in four animals. The blue traces were recorded from GP#95, which was in poor condition at the time of the perfusion.

Boltzmann traces (100 dB SPL) - 7-pt running average

However, in the three perfusions shown for GP#93 and 94, the operating point did not shift more than ± 2 meV away from the pre-perfusion point.

Figure 8.27 shows CAP and SP threshold data recorded by Marcon and Patuzzi (in preparation) during two-minute perfusions of 60 mM and 120 mM sucrose. The time-courses of the CAP and SP thresholds were almost identical, indicating that the cause of the threshold shift was likely to be of mechanical (i.e. hair-cell) origin, rather than disproportionately neural. Although the concentrations of sucrose used in Marcon and Patuzzi's experiments were higher than the 45 mM sucrose used in the present

experiments, the threshold shifts (of between 30 and 35 dB) were of similar magnitude to those recorded in GP#93, GP#94 and GP#96.

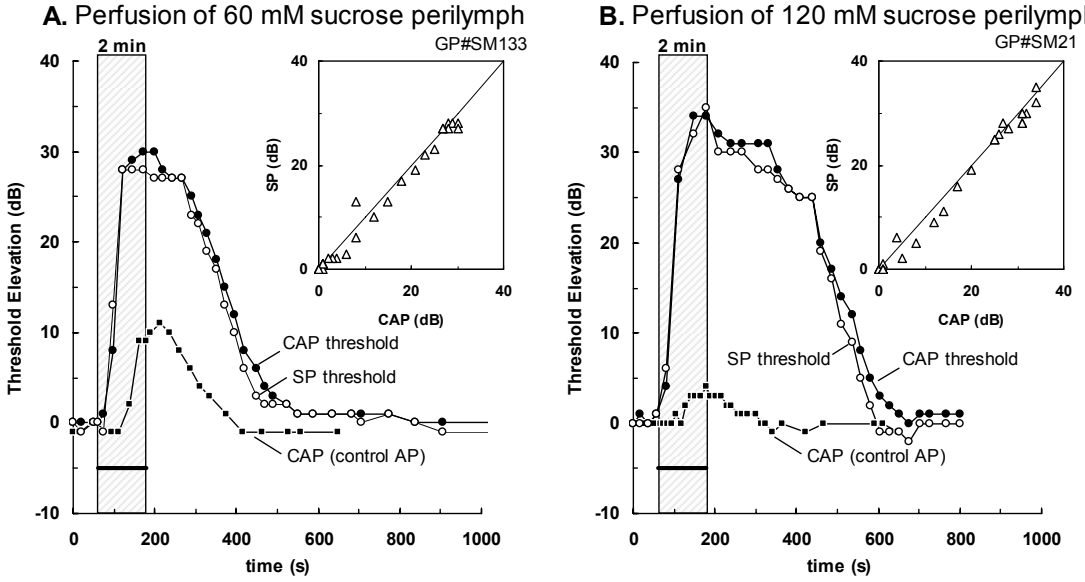

Figure 8.27: CAP and SP thresholds recorded by Marcon and Patuzzi (in preparation) during 2-minute perfusions of **A.** 60 mM and **B.** 120 mM sucrose artificial perilymphs. The insets in each figure show that the SP thresholds were proportional to the CAP thresholds, indicating a mechanical (rather than solely neural) basis for the loss of threshold.

8.7 Results – Mathematical modelling of hyperosmotic perfusions

With regard to the mathematical model of OHC regulation presented in Chapter Two, it was initially envisaged that the hyperosmotic perilymphatic perfusions would be able to be simulated by replicating the operating point shift that would occur from the movement of water from scala media into scala vestibuli. While water movement is not included explicitly in the model, the presumed effects of the perfusion on the operating point may be simulated by calculating the time-course of a 45 mM sucrose perfusion using the Washington University Cochlear Fluids Simulator, scaling it by the presumed magnitude of the resulting hydrostatic shift, and using it to alter the "external energy bias" parameter of the OHC model. In this way, the results of the operating point changes on the OHC ionic concentrations and permeabilities could be compared to the observations made during the experimental perfusions presented above. In the event, the experimentally-measured changes in the operating point were the least consistent of the Boltzmann parameters during the hyperosmotic perfusions, for reasons which will be discussed in Section 8.8 below, and so the aforementioned method of simulating them was unlikely to prove entirely successful. Nevertheless, the results of such perfusions are presented in Figures 8.28 and 8.29, to illustrate the changes in the other hair cell

parameters that would be expected from an operating point bias of a duration similar to that of the perfusion.

Figure 8.28 shows the results for a simulated perfusion of hyperosmotic sucrose artificial perilymph of a concentration sufficient to cause an external energy bias of 43 meV towards scala vestibuli. The external energy bias towards scala vestibuli (assumed to have been caused by the movement of water down its concentration gradient into scala tympani) caused the opening of MET channels and a 3 mV depolarisation of the basolateral cell membrane. This depolarisation caused a prestin-mediated electromotile contraction which partially limited the SV operating-point shift. The depolarisation also caused an opening of voltage-gated Ca^{2+} channels and a 13% increase in intracellular calcium, which caused a 16% increase in the opening probability of the Ca^{2+}-sensitive K^{+} channels (data not shown). This increased the small-signal slope of the basolateral IV curve by 21% (data not shown), which would have increased the receptor current had there not been a concurrent reduction in the apical MET sensitivity of 24% due to the operating point shift. In the event, these two factors combined to cause a net *decrease* in the small-signal receptor current of 15%, and a corresponding decrease in the saturated receptor current (equivalent to Vsat) of 4.5%. The reduced apical MET sensitivity also caused a 30% decrease in the small-signal receptor potential, which resulted in a threshold shift of 24 dB. The increase in intracellular calcium caused a staggered rise in the messengers M2 and M3, which acted on the SERCA Ca^{2+}-ATPase to increase the rate of sequestration of calcium into the subsurface cisternae, causing a mildly oscillatory decrease in intracellular calcium towards resting levels, while the increased M4 concentration caused a slow contraction of the OHC, resulting in a reduction of the magnitude of the SV operating point shift.

To create a *rise* in the AC receptor current (to match the experimental Vsat rise) required an operating point shift small enough to move from the resting operating point (6 meV towards ST) to a point closer to 0 meV, the point of maximum sensitivity on the apical MET transfer curve. Figure 8.29 shows the results for a simulated perfusion of sucrose artificial perilymph at a concentration sufficient to cause an external energy bias of 4.3 meV towards scala vestibuli (that is, a tenth of the external energy bias shown in Figure 8.28). This resulted in the partially-saturated AC receptor current (dashed orange line in the top panel of Figure 8.29) showing an extremely slight decrease (0.02%), followed by an increase of 0.1%.

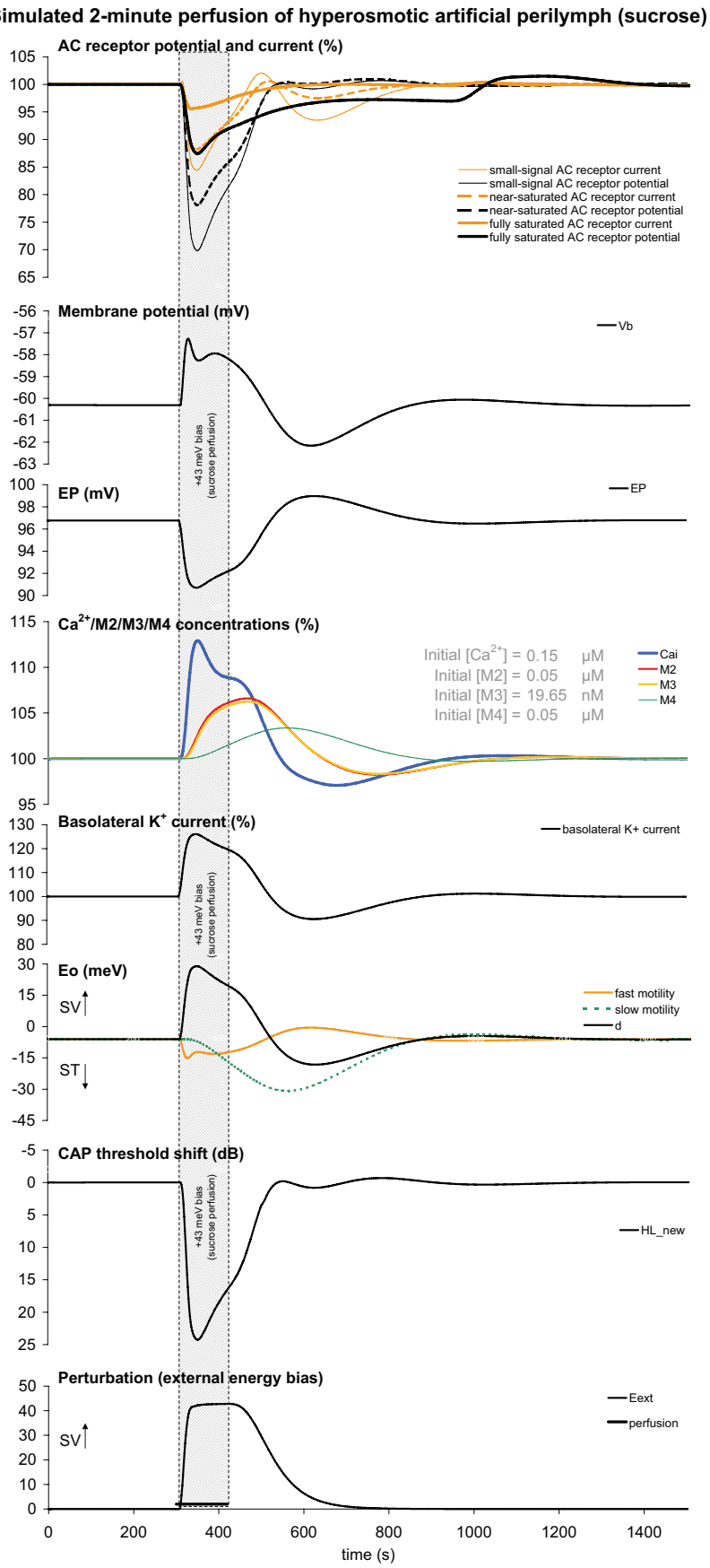

Figure 8.28: OHC model parameters during a simulated 2-minute perfusion of hyperosmotic sucrose AP of a concentration sufficient to cause a maximal +43 meV hair bundle external energy bias (see text).

Washington University Cochlear Fluids Simulator v.1.6h settings: Guinea pig cochlea. Two-minute perfusion of sucrose (0.71 x 10^{-5} cm^2/s diffusion coefficient) at 3 µL/min, perfusate entry at 2 mm, exit at 16.2 mm. Radial ST-SV communication half-time normalized to 0.1 mm^2 cross-sectional area. Cochlear aqueduct enters at 1.1 mm. Apical perilymph communication enabled - 0.03 mm^2 helicotrema area. Perilymph leak of 0.5 µL/min at 16.2 mm location. Recording locations chosen assuming 22 mm guinea-pig cochlea and the 22 kHz location, according to the place-frequency map of Tsuji and Liberman, 1997.

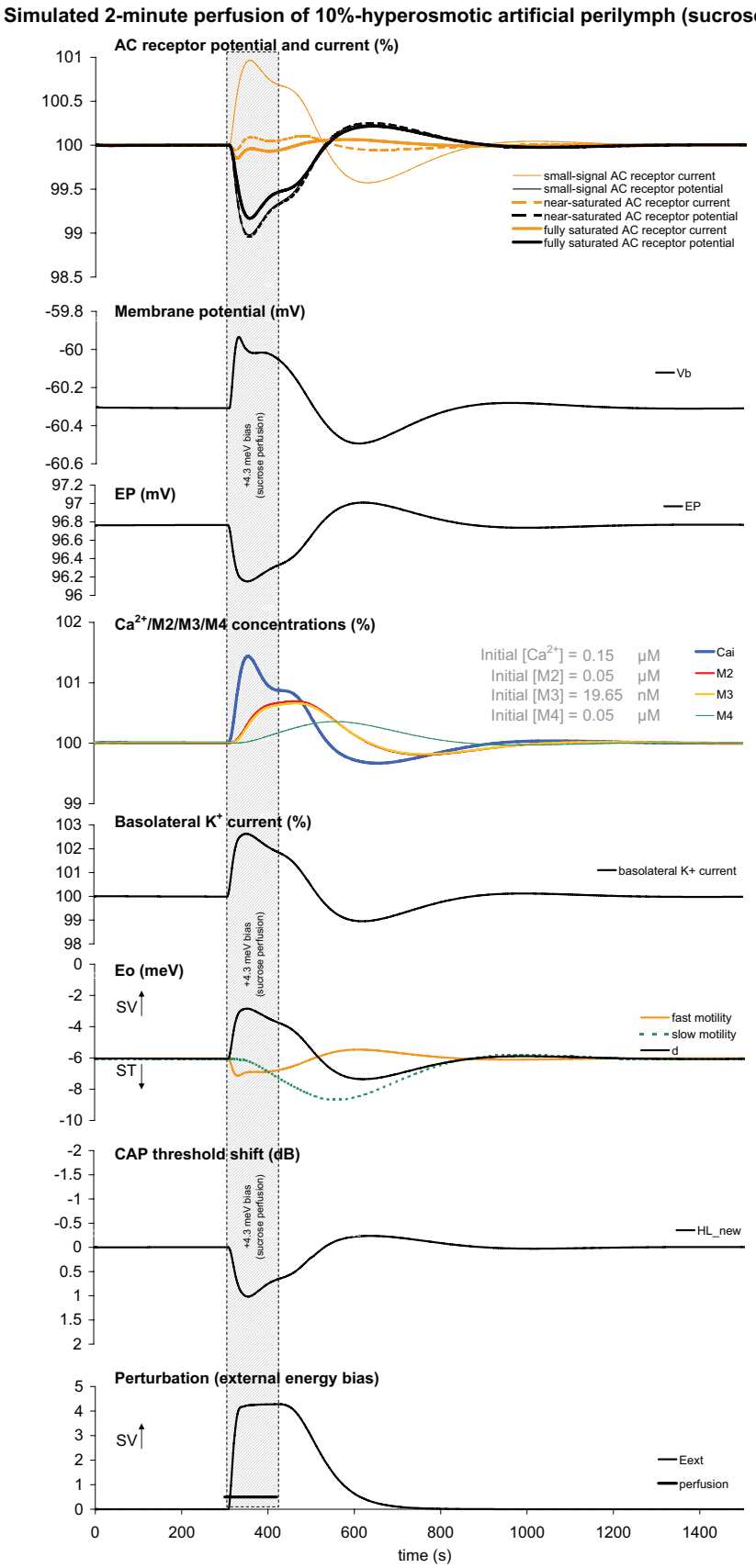

Figure 8.29: OHC model parameters during a simulated 2-minute perfusion of hyperosmotic sucrose AP of a concentration sufficient to cause a maximal +4.3 meV hair bundle external energy bias (see text).

Washington University Cochlear Fluids Simulator v.1.6h settings: Guinea pig cochlea. Two-minute perfusion of sucrose (0.71 x 10^{-5} cm^2/s diffusion coefficient) at 3 µL/min, perfusate entry at 2 mm, exit at 16.2 mm. Radial ST-SV communication half-time normalized to 0.1 mm^2 cross-sectional area. Cochlear aqueduct enters at 1.1 mm. Apical perilymph communication enabled - 0.03 mm^2 helicotrema area. Perilymph leak of 0.5 µL/min at 16.2 mm location. Recording locations chosen assuming 22 mm guinea-pig cochlea and the 22 kHz location, according to the place-frequency map of Tsuji and Liberman, 1997.

These simulated Vsat changes were around one-tenth of those recorded experimentally, but were in the same direction as the changes observed in GP#94, and indeed, followed a similar time-course. The time-course of the simulated operating point shifts was also similar to those recorded in GP#94, with the model producing operating point shifts toward SV that were of a similar order (3 meV, compared to the experimentally measured 2 meV). The time-courses of these two perfusions are compared in Figure 8.30 below.

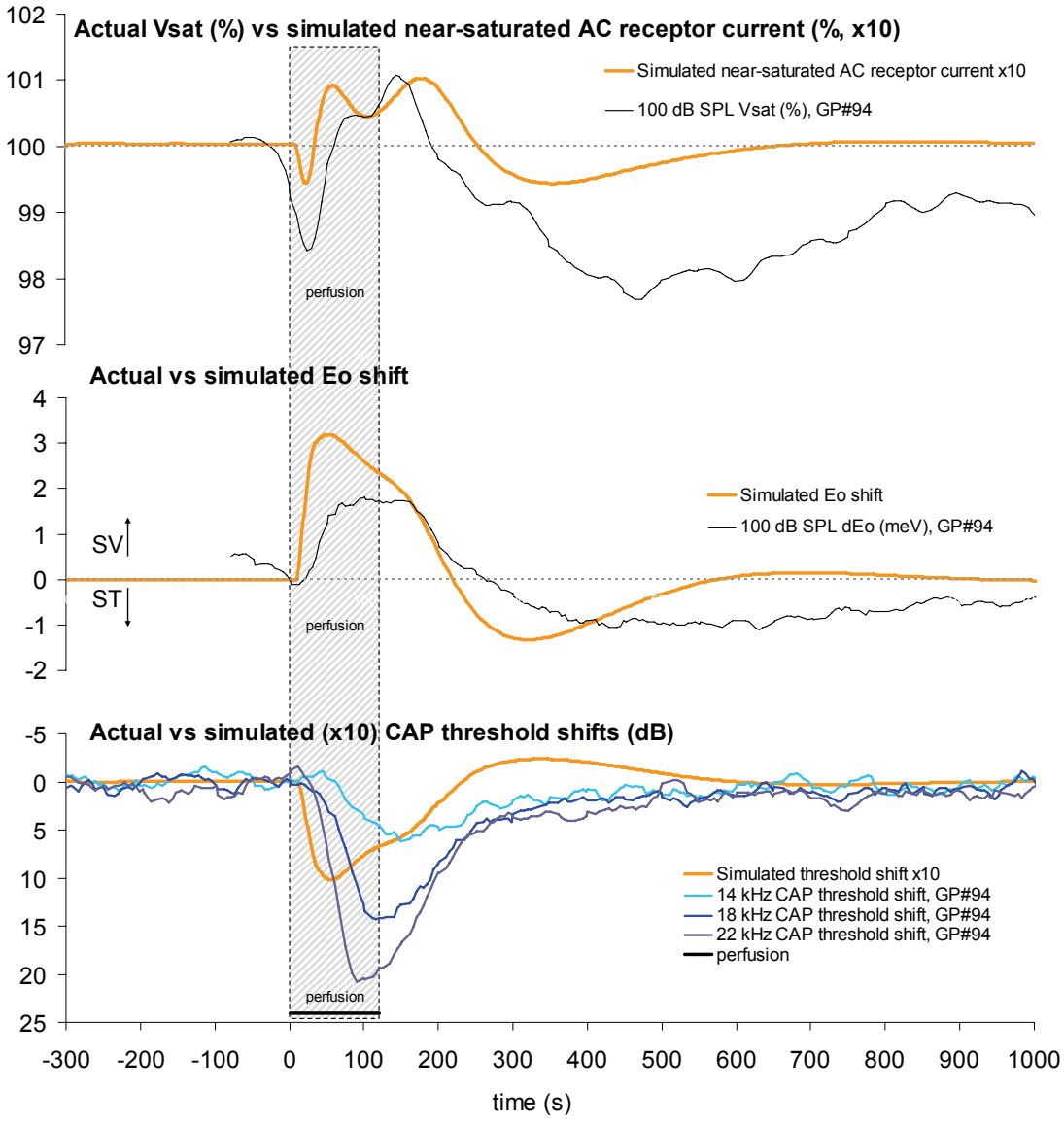

Figure 8.30: Results from the mathematical model of the OHC compared to experimental data recorded from the guinea-pig (GP#94) for a hyperosmotic perfusion. The model results were produced using the standard set of parameters, but the magnitudes of the simulated AC receptor current change and the simulated CAP threshold shift have been scaled by a factor of 10. The full simulation result was shown in Figure 8.29, while the full experimental result was shown in Figure 8.24 (see text).

The discrepancies between the experimental data and the simulation results are discussed further in Section 8.8 below.

To compare the changes observed during simulations of hyperosmotic perfusions with those during *hypo*-osmotic perfusion, Figure 8.31 shows the overlaid results for simulated hydrostatic perfusions for both SV and ST biases. The changes in operating point and cytosolic calcium level were reasonably symmetric, while the changes in the saturated AC receptor current were larger for the ST biases. The correspondingly larger changes in small-signal receptor potential during the ST biases resulted in asymmetric threshold shifts, resulting in small hypersensitivities with ST biases, compared to slightly larger threshold *losses* during SV biases. As shown in Figure 8.32, when a similar parameterisation was performed with larger biases (to ±43 meV), no hypersensitivity was recorded, and there were no increases in saturated AC receptor current. This was due to the operating point shifts in both directions causing hair-bundle movement to less sensitive parts of the apical MET transfer curve, as described above.

8.8 Discussion – Hyperosmotic perfusions

The available evidence suggests that the 20-35 dB elevation of CAP thresholds observed during hyperosmotic perfusions was mechanical, rather than neural, in origin. This is supported by the large increases in Vsat and Z, the lack of a large decrease in the spontaneous neural noise, and the similar elevation magnitudes and time-courses of the CAP and SP thresholds.

The time-course of the measured CAP threshold shifts were significantly different for basal and apical frequencies, with the first-turn frequencies showing larger and more rapid threshold shifts. Rather than being a characteristic of the cochlear regions themselves, this difference in time-courses was well accounted for by the predicted concentration of the perfused sucrose. This is illustrated in Figure 8.33, which shows results from the Washington University Cochlear Fluids Simulator (v1.6h; Salt, 2002) for a matched perfusion in the guinea-pig, the full data from which was shown in Figure 8.22. In this case, there is a very close match between the differences in the onset of the sucrose concentration (and therefore, relative osmolarity) at the 22 kHz and 6 kHz sites (using the place-frequency map of Tsuji and Liberman, 1997), and the threshold elevation and recovery at those frequencies. The examples of hyperosmotic perfusions shown here also demonstrated the lack of a lasting effect of the perfusion. In most cases (including those of Marcon), the thresholds returned to pre-perfusion levels with a time-course similar to that predicted for the wash-out of the perfusate.

Simulated 2-minute perfusions of slightly hyper- and hypo-osmotic artificial perilymphs (sucrose)

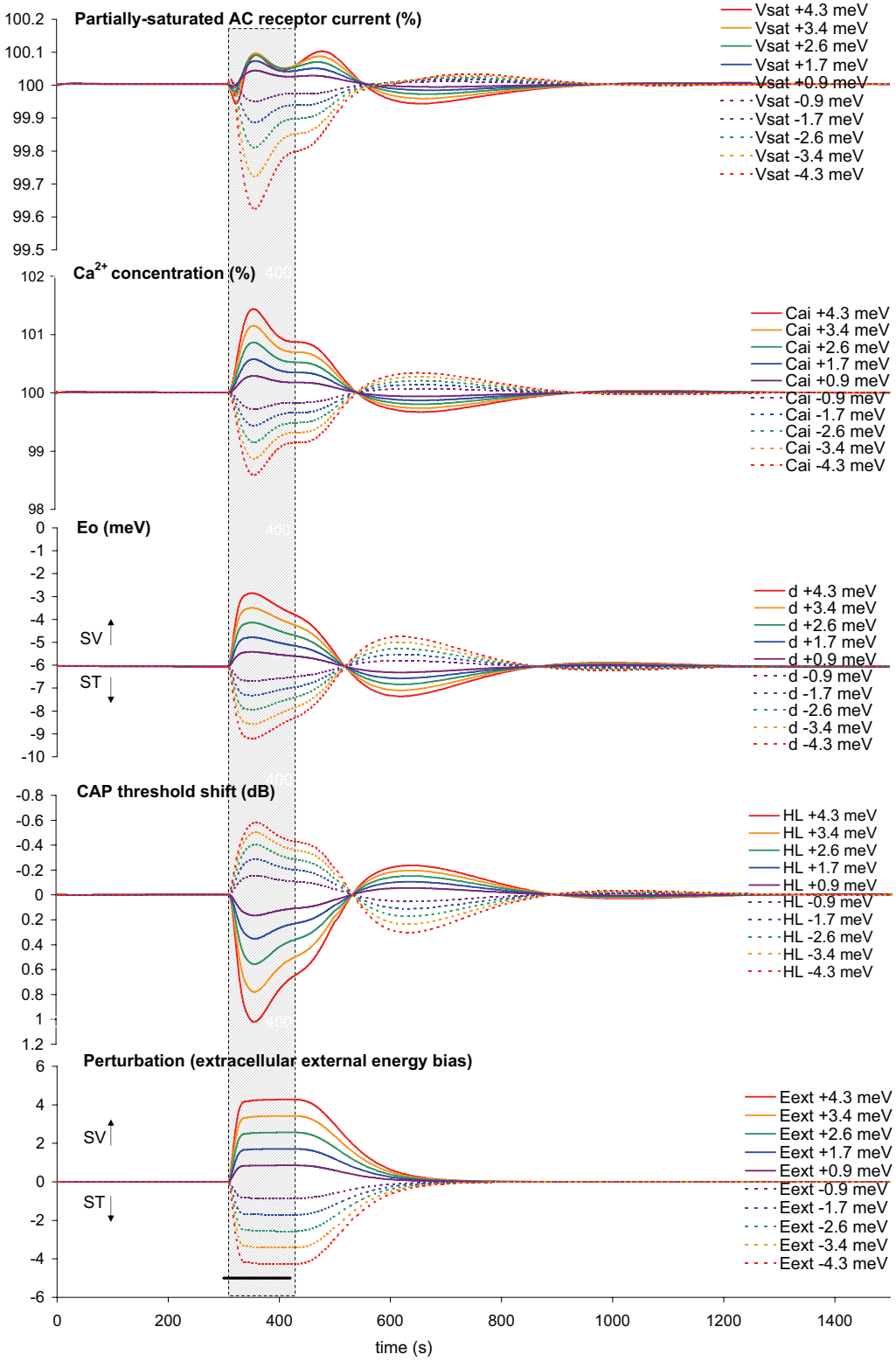

Figure 8.31: OHC model parameters during simulated 2-minute perfusions of slightly hypo- and hyper-osmotic sucrose artificial perilymphs (see text).

Washington University Cochlear Fluids Simulator v.1.6h settings: Guinea pig cochlea. Simulated two-minute perfusion of sucrose (0.71×10^{-5} cm^2/s diffusion coefficient) at 3 µL/min, perfusate entry at 2 mm, exit at 16.2 mm. Radial ST-SV communication half-time normalized to 0.1 mm^2 cross-sectional area. Cochlear aqueduct enters at 1.1 mm. Apical perilymph communication enabled - 0.03 mm^2 helicotrema area. Perilymph leak of 0.5 µL/min at 16.2 mm location. Recording locations chosen assuming 22 mm guinea-pig cochlea and the 22 kHz location, according to the place-frequency map of Tsuji and Liberman, 1997.

Simulated 2-minute perfusions of highly hyper- and hypo-osmotic artificial perilymphs (sucrose)

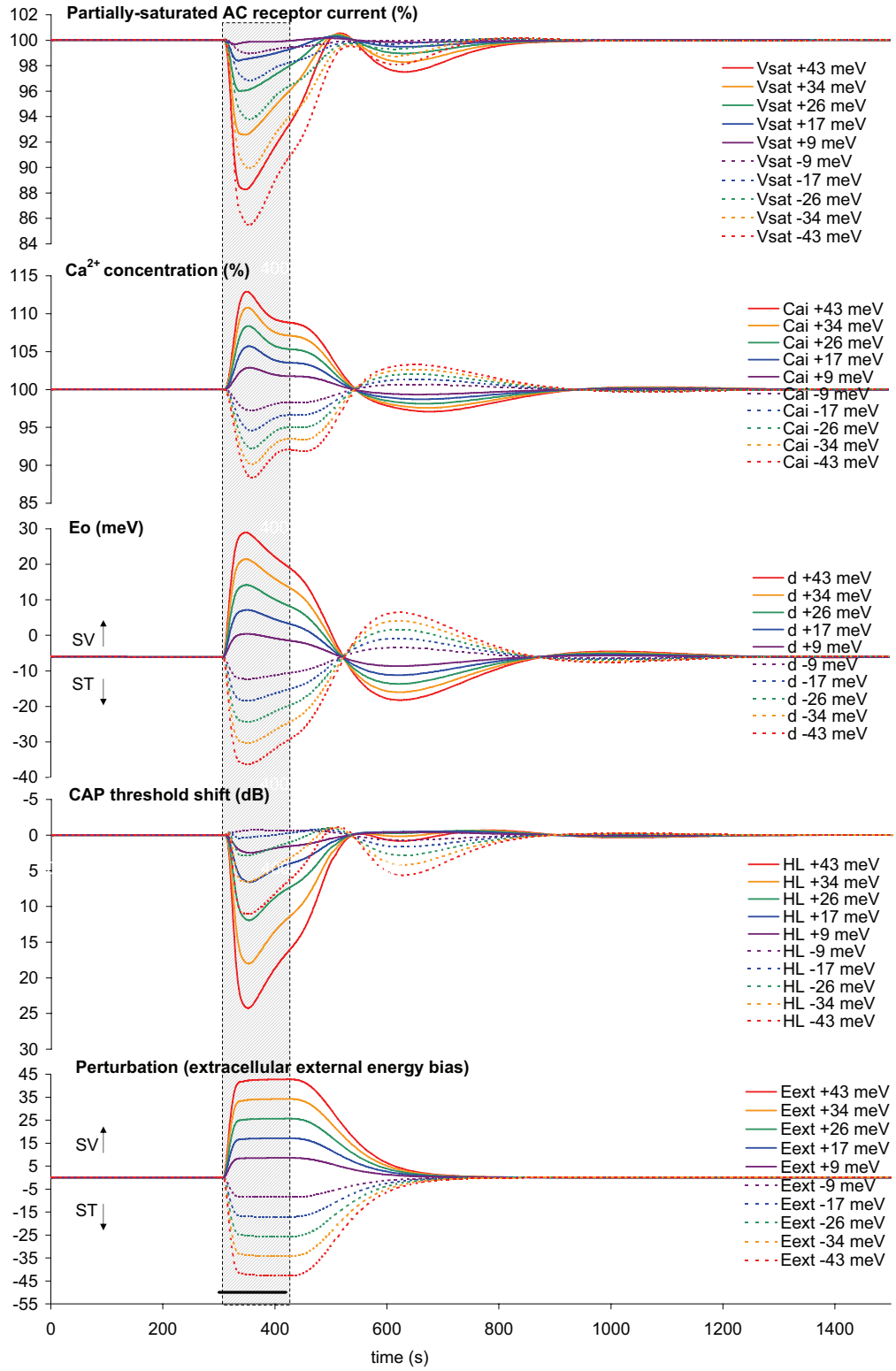

Figure 8.32: OHC model parameters during simulated 2-minute perfusions of highly hypo- and hyper-osmotic sucrose artificial perilymphs (see text).

Washington University Cochlear Fluids Simulator v.1.6h settings: Guinea pig cochlea. Simulated two-minute perfusion of sucrose (0.71×10^{-5} cm^2/s diffusion coefficient) at 3 µL/min, perfusate entry at 2 mm, exit at 16.2 mm. Radial ST-SV communication half-time normalized to 0.1 mm^2 cross-sectional area. Cochlear aqueduct enters at 1.1 mm. Apical perilymph communication enabled - 0.03 mm^2 helicotrema area. Perilymph leak of 0.5 µL/min at 16.2 mm location. Recording locations chosen assuming 22 mm guinea-pig cochlea and the 22 kHz location, according to the place-frequency map of Tsuji and Liberman, 1997.

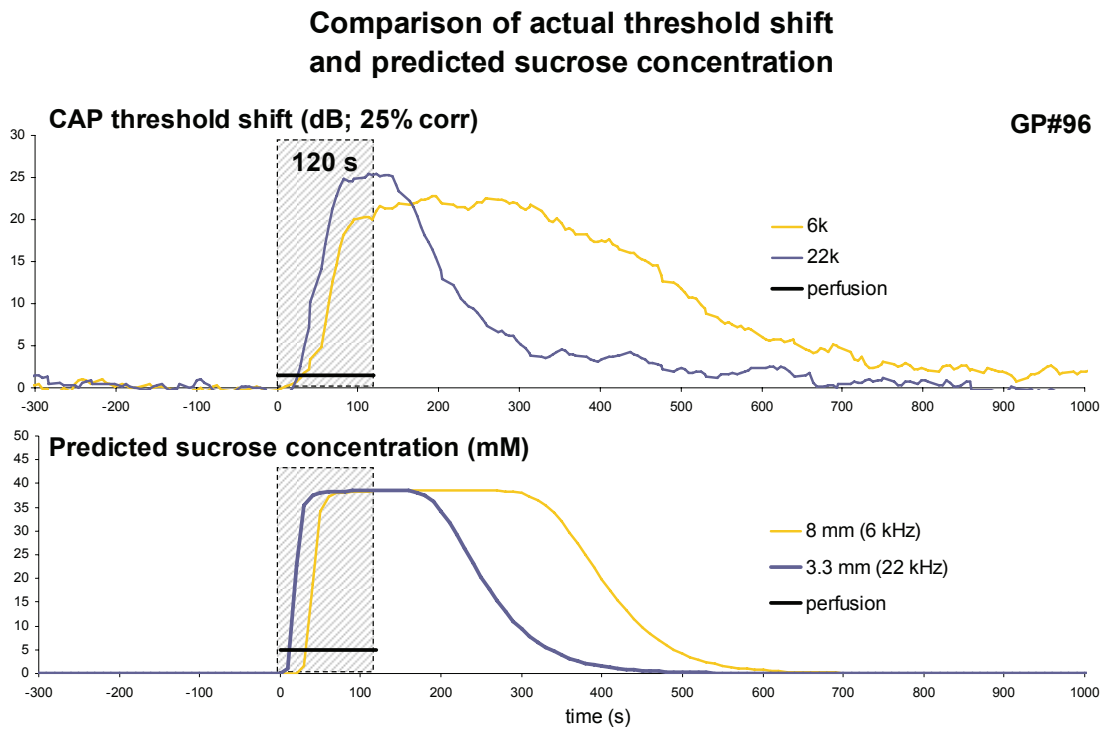

Figure 8.33: The difference between the CAP threshold time-courses at 22 kHz and 6 kHz was at least partially accounted for by the predicted concentration of the sucrose at the scala tympani locations roughly corresponding to the 22 kHz and 6 kHz sites.

Washington University Cochlear Fluids Simulator v.1.6h settings: Guinea pig cochlea. 120 second perfusion of sucrose (0.71×10^{-5} cm^2/s diffusion coefficient) at 3 µL/min, perfusate entry at 2 mm, exit at 16.2 mm. Radial ST-SV communication half-time normalized to 0.1 mm^2 cross-sectional area. Cochlear aqueduct enters at 1.1 mm. Apical perilymph communication enabled - 0.03 mm^2 helicotrema area. Perilymph leak of 0.5 µL/min at 16.2 mm location. Recording locations chosen assuming 22 mm guinea-pig cochlea and place-frequency map of Tsuji and Liberman (1997).

Three of the five hyperosmotic perfusions shown here did not result in large operating point shifts. The lack of an operating point shift may indicate an inability of the osmotic bias to cause a large static movement of the basilar membrane, due to the equalisation of pressure between scala tympani and scala vestibuli by the helicotrema. As Reissner's membrane is considerably more compliant than the basilar membrane (except in the extreme apex of the cochlea; von Békésy, 1960), this pressure difference is likely to cause a larger movement of Reissner's membrane than of the basilar membrane, thereby minimising the operating point shifts observed.

According to our mathematical model, the observed operating point changes were not the major cause of the OHC disruption. Simulations which replicated similarly small operating point shifts did not cause large enough changes in basolateral permeability (reflected experimentally in the Vsat measure), and consequently did not produce threshold shifts as large as those observed experimentally. Indeed, perturbations which

cause larger changes in operating point than those measured here (such as DC current injection) do not produce threshold shifts anywhere near as large.

The Z parameter was the most consistent of the Boltzmann parameters measured here. It is possible that the average 8% increase in Z during these hyperosmotic perfusions reflects a decrease in axial stiffness. Chan and Ulfendahl (1997) noted that small percentage changes in osmotic pressure surrounding isolated OHCs caused large changes in axial stiffness. Such a decrease in axial stiffness may be caused by the increase in intracellular calcium predicted by our model, as the effect of cytosolic calcium on OHC stiffness has been observed previously (Frolenkov et al., 2003).

The large increases in Vsat observed during the hyperosmotic perfusions was an indicator of a large increase in the permeability of the OHC basolateral membrane. As mentioned during the discussion of the choline-perfusion results, Patuzzi and Rajan (1990) calculated that a 15% increase in CM amplitude (during efferent stimulation) was equivalent to a doubling of the conductance of the basolateral wall of the OHC, which could equate to a roughly 40% increase in basolateral permeability during the hydrostatic perfusions, and would certainly produce the 25 dB hearing losses observed experimentally and during the simulations of larger operating point shifts presented in Figure 8.32 above. However, the means by which this increase in basolateral permeability was initiated is not explained by the present version of the model.

8.9 Results – Increase in perilymphatic potassium

The effects of increased perilymphatic potassium on cochlear potentials were investigated in three animals by perfusion of scala tympani the artificial perilymph shown in column VII of Table 8.2, in which the potassium concentration of the artificial perilymph was increased from the normal value of around 4.2 mM (Wangemann and Schacht, 1996) to 50 mM. The chloride concentration of the artificial perilymph was lowered from 148 mM to approximately 14.8 mM to maintain a constant [K][Cl] product of 740 mM^2, thereby minimising chloride movement and osmotic effects on cochlear structures (Boyle and Conway, 1941). In a fourth animal, in which a perfusion of artificial perilymph containing 20 mM potassium was performed, the chloride concentration altered to 37 mM to maintain this same [K][Cl] product.

8.9.1 10-minute perfusion of 50 mM K^+ artificial perilymph

Figure 8.34 shows the changes in Boltzmann parameters, SNN, and tracked CAP thresholds in GP#98 for a 10-minute perfusion of 50 mM K^+ artificial perilymph (291 mOsm).

The perfusion caused an initial 6% rise in Vsat over the first 60 seconds, followed by a reduction over the next 300 seconds to 55% of its pre-perfusion value, after which time it recovered slowly to reach a steady state at 86% of the pre-perfusion level. The Z parameter showed an initial 18% decrease during the first 160 seconds of the perfusion, before increasing to pre-perfusion value by 380 seconds post-onset, and then overshooting this pre-perfusion Z by 8% before returning to normal. The changes in the operating point were large compared to other cochlear perturbations – on commencement of the perfusion, Eo moved toward scala tympani by 39 meV, reaching a minimum of -31 meV after 140 seconds. This rapid ST shift was followed by a more gradual return towards SV at a rate that was 10% of that of the onset ST shift. The "recovery" of the Boltzmann parameters toward their normal values began while the perfusion was occurring, and while the perilymphatic K^+ concentration was presumably still at its most elevated. It is possible that this result reflects some sort of increased physiological clearance of the perfusate from scala tympani.

The perfusion caused a reduction in SNN amplitude to below the biological noise floor (at least a 58% reduction), and a CAP threshold shift of more than 30 dB at 22 kHz was also observed before the threshold measurements were dominated by the tracking of the SP rather than CAP[6]. As will be discussed further in Section 8.9.3 below, the SP threshold and CAP threshold were found by Marcon and Patuzzi (in preparation) to not differ significantly during high-potassium perfusions. The SP threshold was elevated further to a loss of 42 dB at 22 kHz and 47 dB at 18 kHz. After the 10 minute perfusion period, the thresholds at frequencies below 14 kHz recovered to within 6 dB of pre-perfusion levels over the next 40 minutes, while the 22 kHz threshold remained suppressed by around 30 dB for the duration of the experiment. However, like the Boltzmann parameters, the tracked SP thresholds at many frequencies (particularly 14 and 18 kHz) had begun to improve during the period of the perfusion itself.

[6] As discussed in Chapter 4, a change in the "correlation window" setting of the tracking software was implemented after this experiment to prevent this occurrence.

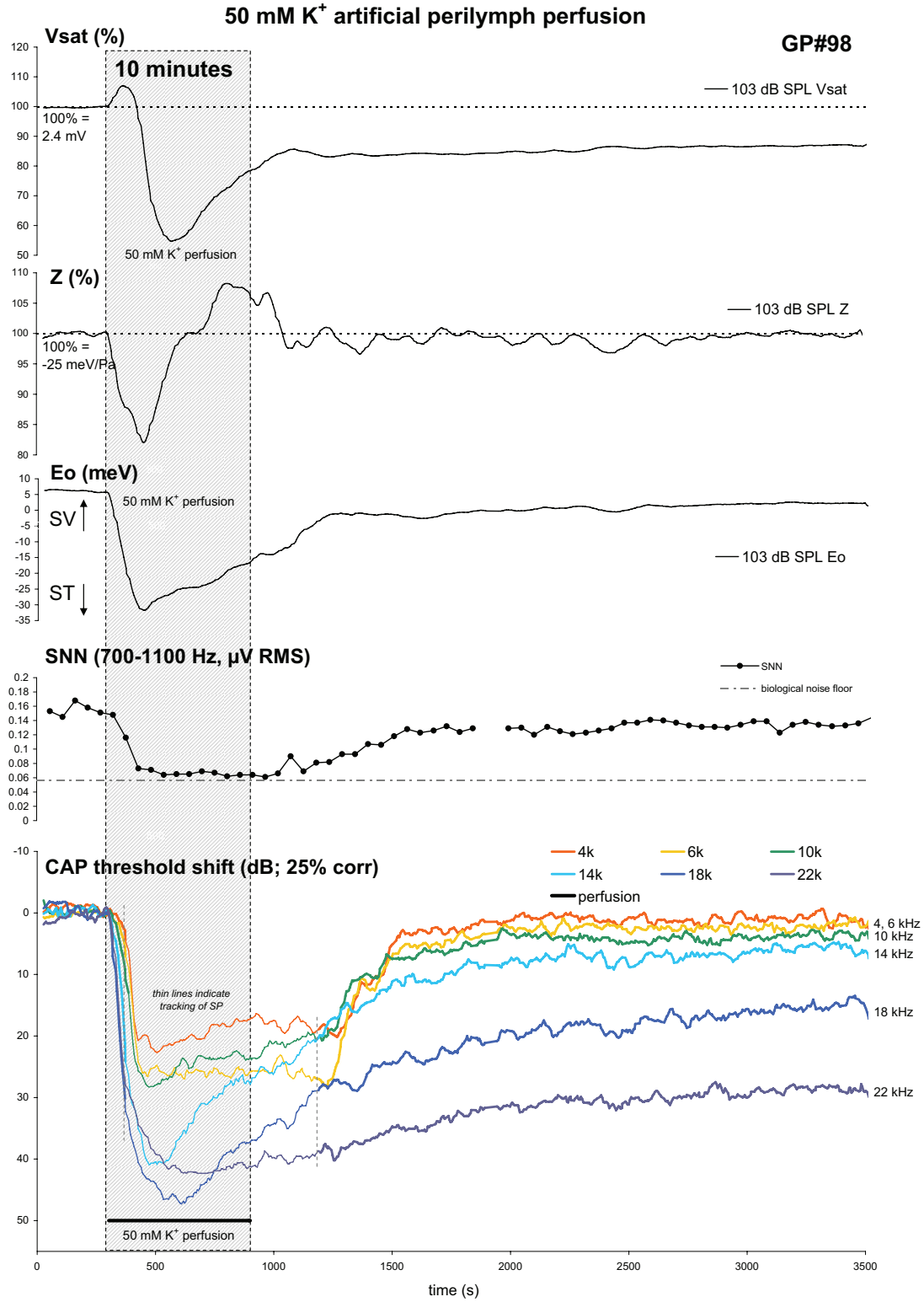

Figure 8.34: Boltzmann parameters, SNN, and tracked CAP threshold shifts recorded during a 10 minute perfusion of 50 mM K^+ artificial perilymph (291 mOsm). Following an initial average 7% rise, the perfusion caused a maximal 45% reduction in Vsat. As with Vsat, the sharp Eo shift toward scala tympani (-17 meV/min) was followed by a slower recovery toward scala vestibuli (+1.8 meV/min) that occurred despite the continuation of the perfusion. A 58% reduction in SNN amplitude, and threshold shifts of more than 40 dB at frequencies above 14 kHz were also observed.

ID#3130470120. Thresholds (2 kHz to 22 kHz, dB GPHL): 13, 15, 17, 14, 15, 10, 17. Boltzmann and CAP traces 7-pt running average

8.9.2 Shorter perfusions of 50 mM K^+ artificial perilymph

While the time-course of the CAP threshold shift during the perfusion in Figure 8.34 consisted of a reasonably monotonic loss and recovery, the pattern of threshold shifts observed during short (0.5 – 2 minute) perfusions of elevated potassium perilymph was often non-monotonic.

Figure 8.35 shows the changes in the Boltzmann parameters, SNN, and tracked CAP thresholds for a 30-second perfusion of 50 mM K^+ artificial perilymph (306 mOsm). At the onset of the perfusion, Vsat showed an 8% decrease, while Z increased by 4% and Eo moved by 14 meV towards scala tympani. The first peak of the hearing loss (as indicated by the 26% decrease in CAP amplitude at 14, 18, and 22 kHz) corresponded to both the minimum in Vsat and the maximal operating point shift. At the point at which the CAP amplitude had transiently improved, the operating point had reached its post-perfusion plateau, while Vsat was in the region of a local maximum, and Z was close to its pre-perfusion value. The second peak of the hearing loss, occurring between 120 and 140 seconds after the commencement of the perfusion, corresponded to a local minimum in Vsat, a local maximum in Z, while the operating point was still at 5 meV below the pre-perfusion value.

Figure 8.36 shows the changes in the Boltzmann parameters, SNN, and tracked CAP thresholds for a 40-second perfusion of 50 mM K^+ artificial perilymph (250 mOsm). While this potassium perfusion was complicated by a concurrent hypo-osmolarity, the results of the perfusion were similar in most respects to those shown for the iso-osmotic potassium perfusion in Figure 8.35: At the onset of the perfusion, Vsat decreased by 11%, Z decreased by 10% and Eo moved by 17 meV towards scala tympani. These peaks in the Boltzmann parameters occurred at around 56, 94, and 78 seconds (respectively) after perfusion onset. The first peak of the hearing loss consisted of threshold elevations of 11, 14 and 22 dB at 14, 18, and 22 kHz respectively. These occurred first at 22 kHz at 73 seconds after perfusion onset, then at 18 kHz at 78 s, and 14 kHz at 93 s post-onset. The thresholds below 14 kHz did not show this oscillatory pattern, and remained within ± 2 dB of their pre-perfusion levels (data not shown).

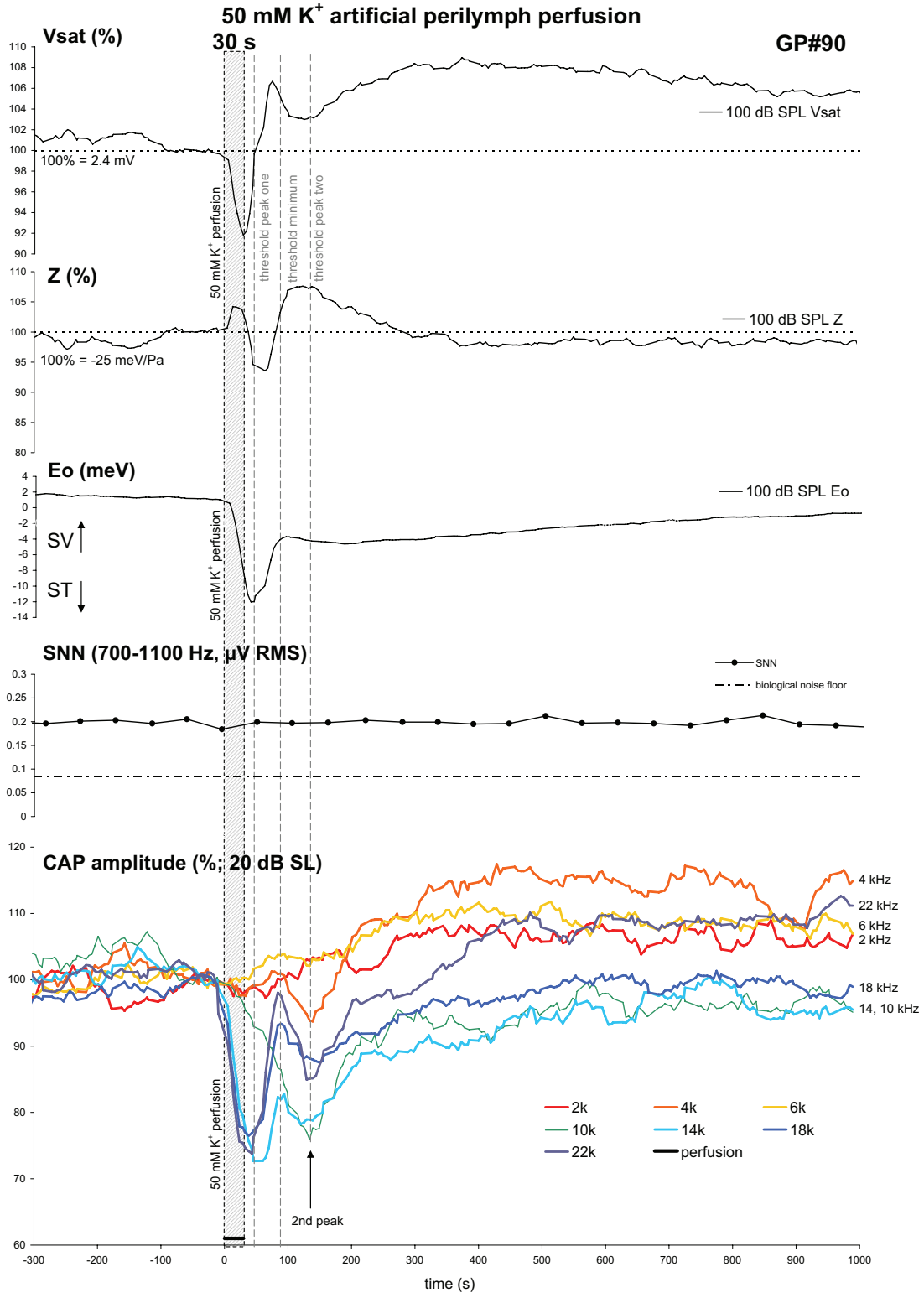

Figure 8.35: Boltzmann parameters, SNN, and tracked CAP threshold shifts recorded during a 30-second perfusion of 50 mM K^+ artificial perilymph (306 mOsm). The onset of the perfusion caused an 8% decrease in Vsat, a 4% increase in Z, and a sharp 13 meV Eo shift toward scala tympani. The SNN amplitude was not affected, but the CAP amplitudes (20 dB SL) at frequencies above 14 kHz showed a decrease of 24-26%, followed by a non-monotonic recovery (see text).

ID#3127184788. Thresholds (2 kHz to 22 kHz, dB GPHL): 20, 22, 24, 19, 26, 25, 30. Boltzmann and CAP traces 7-pt running average

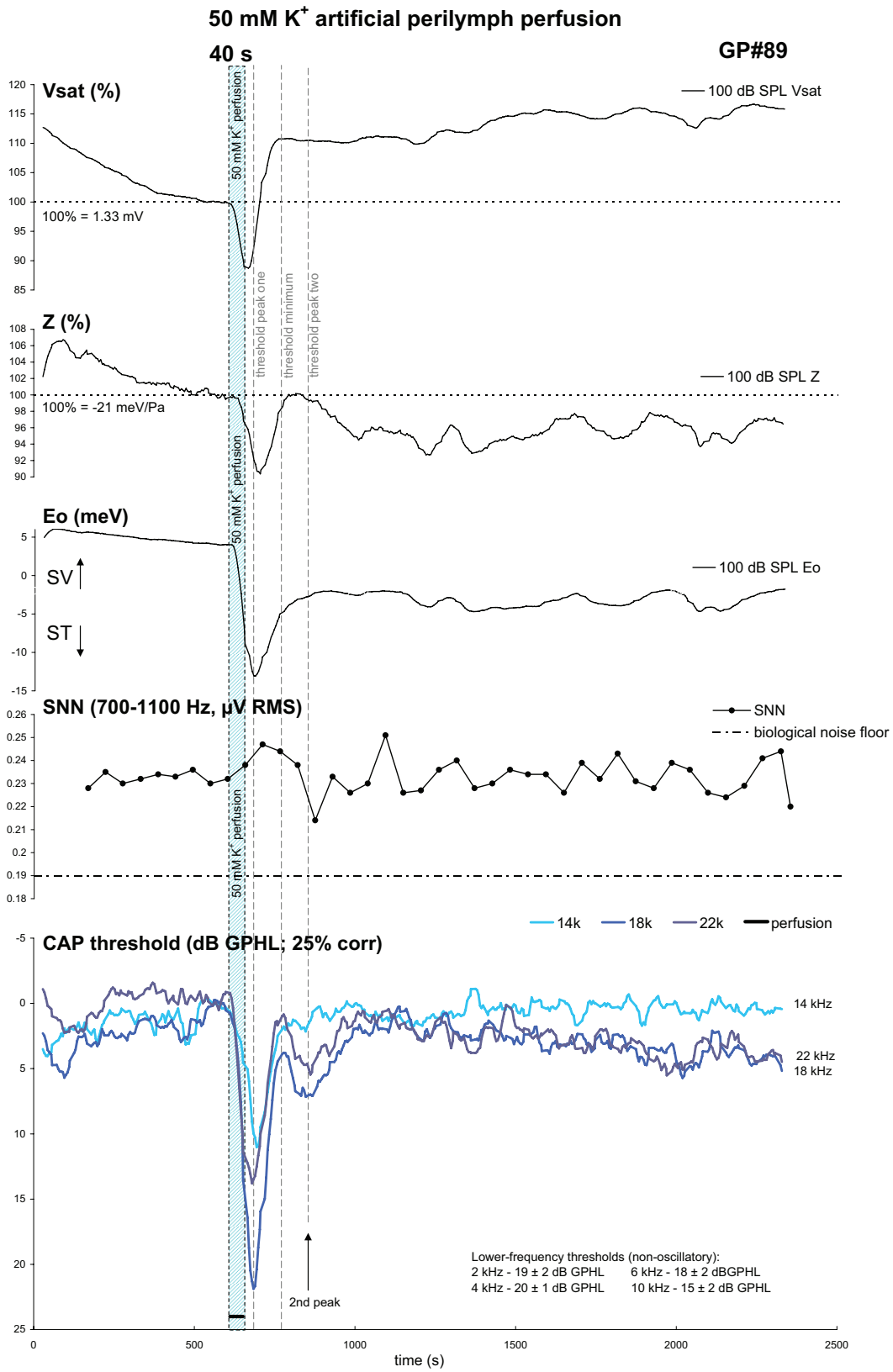

Figure 8.36: Boltzmann parameters, SNN, and tracked CAP thresholds recorded during a 40-second perfusion of a hypo-osmotic (250 mOsm) 50 mM K^+ artificial perilymph (constant [K][Cl] product). Note the oscillations in high-frequency CAP thresholds following the initial 15-20 dB loss with the perfusion.

ID#3126844793. Thresholds (2 kHz to 22 kHz, dB GPHL): 19, 22, 20, 17, 22, 22, 34. Boltzmann and CAP traces 7-pt running averages

This first threshold peak corresponded to the both the minimum in Vsat and the maximal operating point shift. At the point at which the CAP amplitude had transiently improved, the operating point had reached its post-perfusion plateau, while Vsat was in the region of a local maximum, and Z was close to its pre-perfusion value. A second threshold peak occurring 240 s after the onset of perfusion did not appear to correspond to any peaks in the Boltzmann data. In fact, when the Boltzmann parameters at the threshold minimum (i.e. an improved sensitivity) and at the second threshold peak (at 240 s) are compared, the Vsat and Z parameters were almost identical, but the operating point had moved closer to the midpoint during the second threshold peak. This is intriguing, as it might be expected that an operating point shift *towards the region of maximum sensitivity* on the apical MET transfer curve would improve matters, rather than worsen them.

This multi-phasic or non-monotonic pattern of threshold loss and recovery was also observed by Marcon (Marcon, 1995; Marcon and Patuzzi, in preparation). Figure 8.37 compares the threshold loss from the 40-second perfusion shown in Figure 8.36 above to the results of three *hyperosmotic* perfusions of 30 mM K^+ artificial perilymph, each of two-minute duration. While both the first and second threshold shifts were larger during the perfusions of Marcon, the timing of the peaks was similar in all four perfusions. The influence of the osmotic component to the perfusion is discussed in Section 8.10.3 below.

8.9.3 Changes in CAP waveforms during perfusions of 50 mM K^+ AP

In addition to the changes in the Boltzmann parameters and neural threshold, changes in the CAP waveforms were also observed. Figure 8.38 shows the changes in 20 dB SL CAP waveforms recorded between 1 and 2 minutes after the onset of a 30 s perfusion of 50 mM K^+. As with the waveforms presented in Figures 8.14 and 8.15, the waveforms are iso-SL, rather than iso-SPL, and so comparison of the SP amplitudes may be complicated by the different absolute SPLs used. However, the control and 50 mM K^+ waveforms were evoked at levels within 2 dB of each other at 2 kHz, 10 kHz, and 14 kHz, enabling a comparison of pre- and post-perfusion waveforms to be made at these frequencies. The N1 amplitudes decreased by $40 \pm 17\%$ at these frequencies, while P1 amplitudes decreased by $44 \pm 16\%$. The SP amplitudes remained constant, but rather than indicating that the magnitude of BM vibration amplitude was unchanged, this result may have been caused by the IHC SP being supplemented by an outer hair cell SP produced by the large ST operating point shift.

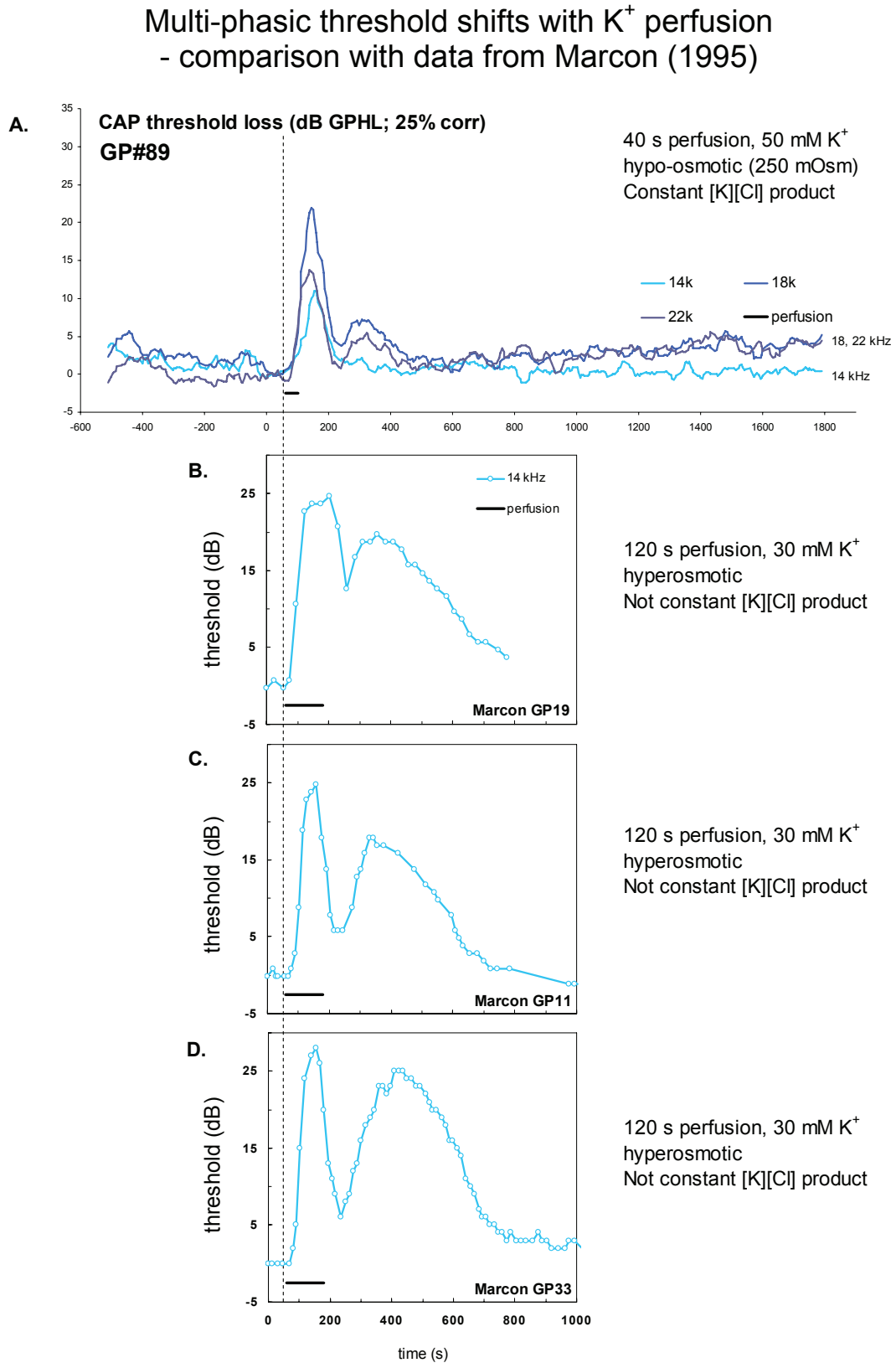

Figure 8.37: Comparison of **A.** the oscillations in tracked CAP thresholds of Figure 8.36 for a 40 second perfusion of hypo-osmotic 50 mM K^+ artificial perilymph (constant [K][Cl] product) with **B. C.** & **D.** data from Marcon (1994) showing CAP thresholds for *two-minute* perfusions of *hyperosmotic 30 mM* K^+ in artificial perilymph (*non-constant* [K][Cl] product). Data are presented at the same scale in all four panels.

Effect of 50 mM K^+ artificial perilymph perfusion on CAP waveforms (20 dB SL)
[asterisks indicate near-identical SPLs] **GP#90**

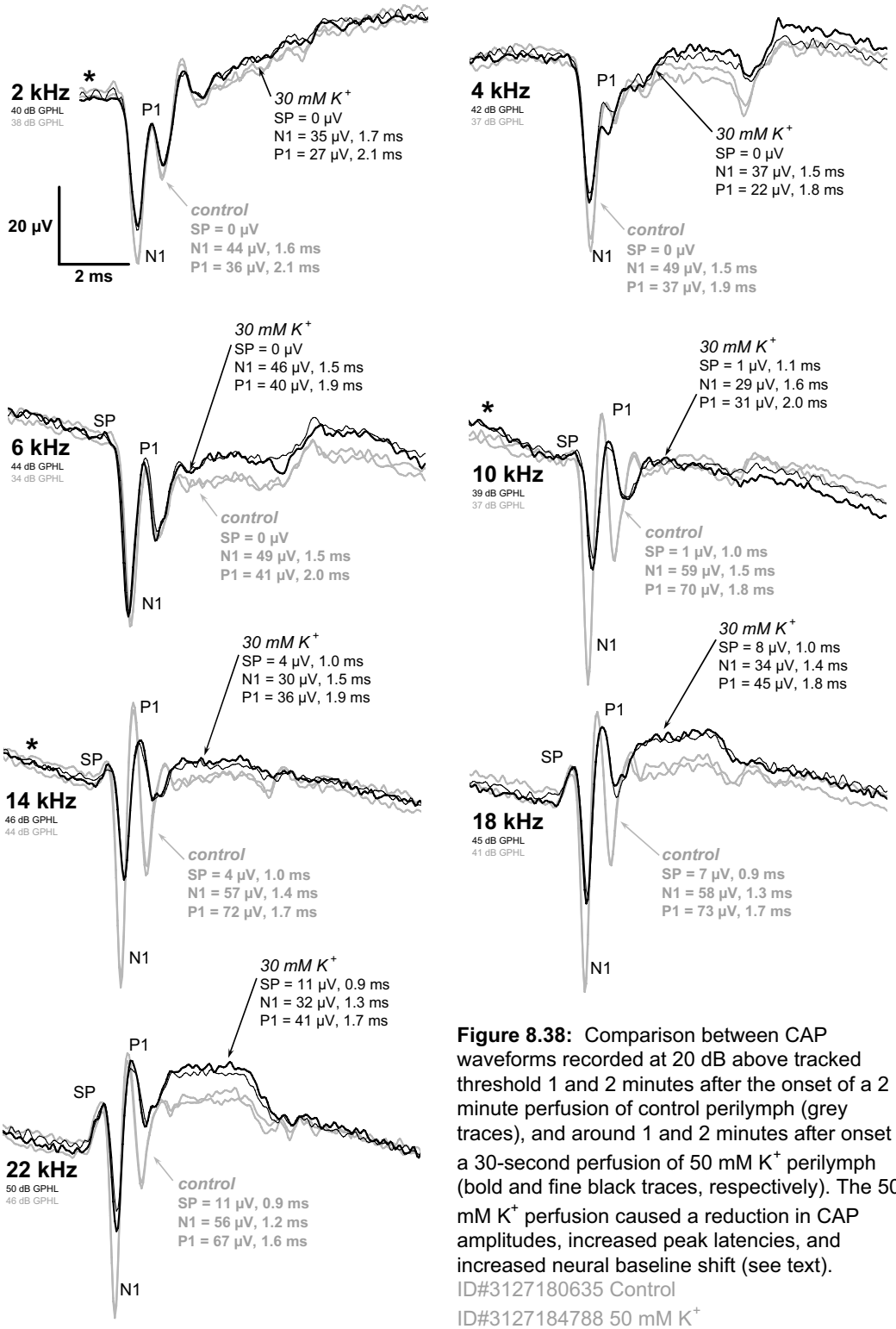

Figure 8.38: Comparison between CAP waveforms recorded at 20 dB above tracked threshold 1 and 2 minutes after the onset of a 2 minute perfusion of control perilymph (grey traces), and around 1 and 2 minutes after onset of a 30-second perfusion of 50 mM K^+ perilymph (bold and fine black traces, respectively). The 50 mM K^+ perfusion caused a reduction in CAP amplitudes, increased peak latencies, and increased neural baseline shift (see text).
ID#3127180635 Control
ID#3127184788 50 mM K^+

As shown in Figure 8.39 the changes in SP threshold recorded by Marcon (1995) during a 2-minute perfusion of 30 mM K^+ artificial perilymph showed similar multi-phasic patterns before and after neural blockade by TTX. This result may indicate that a large part of the effects of the potassium perfusion was not neurally-mediated. However, as with the previous example, the possibility remains that the SP may have been influenced by the operating point shifts.

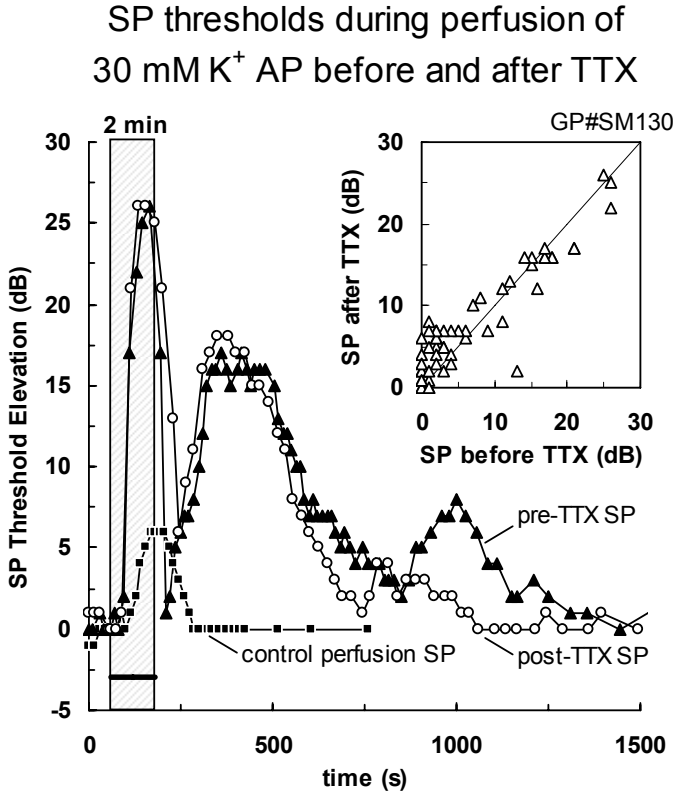

Figure 8.39: The pattern of SP threshold elevation during perfusion of 30 mM K^+ artificial perilymph was not significantly different after the application of TTX, which may indicate that a large part of the effects of the potassium perfusion was not neurally-mediated. Data from Marcon and Patuzzi (in preparation).

8.10 Results – Mathematical modelling of elevated-potassium perfusions

High-potassium perilymphatic perfusions were simulated using the mathematical model of the OHC presented in Chapter Two. The time-course of the perfusate concentration was derived from the Washington University Cochlear Fluids Simulator (v1.6h; Salt, 2002), using the settings listed in the legends of the figures presented in this section. The perfusate concentrations were calculated for the 22 kHz place, according to the place-frequency map of Tsuji and Liberman (1997). Unless stated otherwise, simulations presented here were carried out using the standard set of model parameters listed in Chapter Two.

8.10.1 Two-minute perfusion of 10 mM potassium AP

Figure 8.40 shows the results of a simulated 2-minute perfusion of 10 mM K^+ in scala tympani. The time-course of the perfusate concentration is shown in the bottom panel. During the first 40 s of the perfusion, the scala tympani K^+ concentration increased from 4.2 mM to 8.9 mM, causing a 10% reduction in the efflux of potassium across the basolateral wall of the OHC. During these 40 s, the basolateral membrane potential was depolarised by 3.4 mV from -60 mV to -57 mV, while the EP rose by 2.5 mV. The depolarisation caused an electromotile operating-point shift of 10 meV toward scala tympani. At 40 seconds after the onset of the perfusion, the depolarisation was stemmed by the increasing basolateral K^+ permeability caused by the rising intracellular Ca^{2+} concentration: Over the first 60 seconds, the $[Ca^{2+}]_i$ had increased by 18%, which caused a 25% increase in basolateral K^+ permeability, and increased the slope of the basolateral wall IV-curve at the membrane potential by almost 50%. This change in the slope of the IV-curve caused the small-signal AC receptor current to increase by 11%, while the small-signal AC receptor potential fell by 22%, which was extrapolated to a 19 dB threshold shift. The saturated AC receptor current, analogous to CM amplitude or the Vsat Boltzmann parameter, increased by 4% during this time.

During the perfusion, the increasing $[Ca^{2+}]_i$ also caused the concentrations of the second messengers M2, M3 and M4 to rise. While the Ca^{2+}-induced repolarisation had relaxed the electromotile operating point shift, the increasing concentration of M4 caused a further slow-motile contraction toward scala tympani, reaching a maximum operating point of -40 meV. This caused a further decrease in the small-signal AC receptor potential (to 35% below control), which increased the threshold shift to 27 dB.

At the offset of the perfusion, the calcium-dependent parameters (such as basolateral permeability, EP, and membrane potential) showed slightly oscillatory recoveries due to the interplay between the concentrations of Ca^{2+} and the messenger M3 controlling its sequestration. The effects of the *duration* of the simulated perfusion were visible during 10-minute and 30-second perfusions, shown in the following sections.

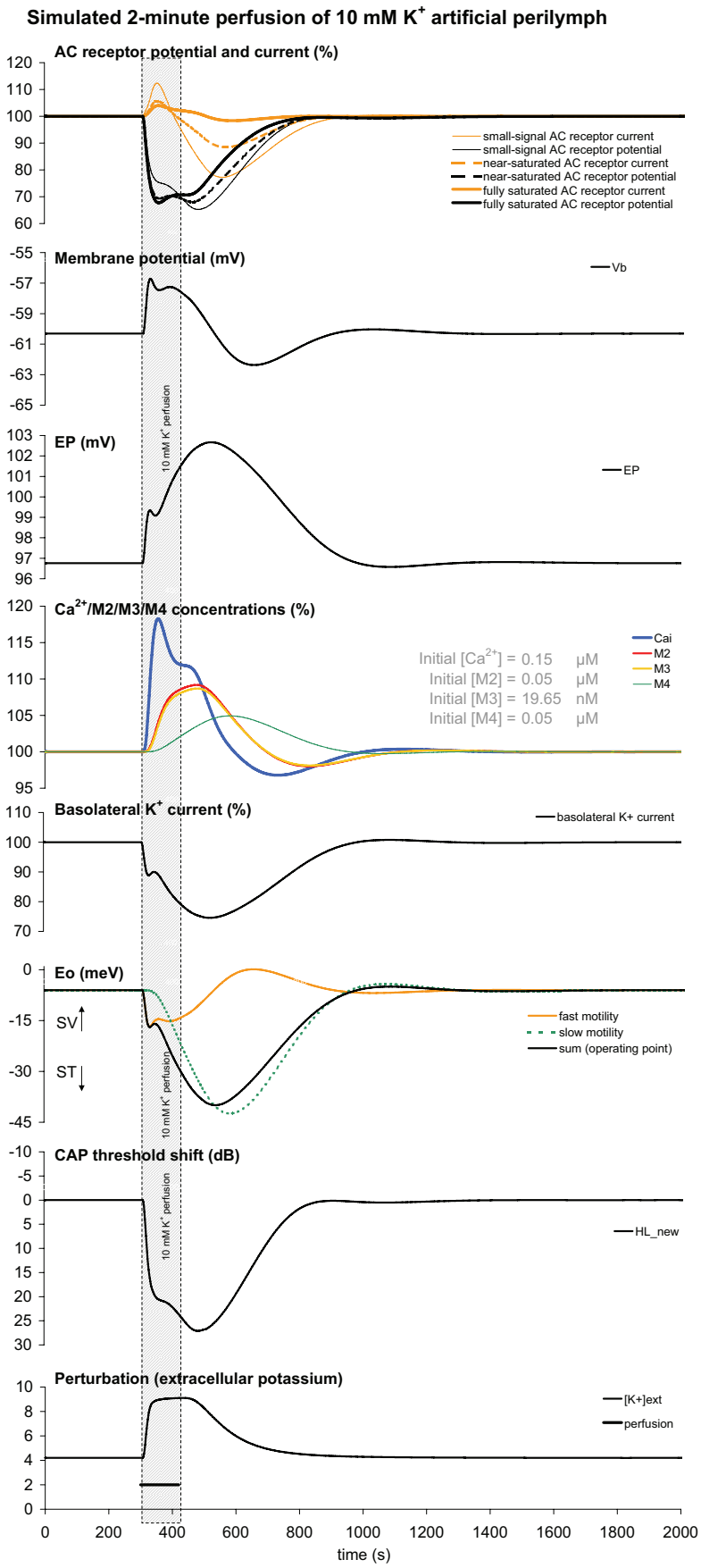

Figure 8.40: OHC model parameters during a simulated 2-minute perfusion of 10 mM K^+ artificial perilymph (see text). Washington University Cochlear Fluids Simulator v.1.6h settings: Guinea pig cochlea. Two-minute perfusion of K^+ (2.47 x 10-5 cm^2/s diffusion coefficient) at 3 µL/min, perfusate entry at 2 mm, exit at 16.2 mm. Radial ST-SV communication half-time normalized to 0.1 mm^2 cross-sectional area. Cochlear aqueduct enters at 1.1 mm. Apical perilymph communication enabled - 0.03 mm^2 helicotrema area. Perilymph leak of 0.5 µL/min at 16.2 mm location. Recording locations chosen assuming 22 mm guinea-pig cochlea and the 22 kHz location, according to the place-frequency map of Tsuji and Liberman, 1997.

8.10.2 Ten-minute perfusion of 10 mM potassium AP

Figure 8.41 shows the results of a simulated 10-minute perfusion of 10 mM K^+ in scala tympani. The results of the first two-minutes of the perfusion were identical to those shown in Figure 8.40, but while the perfusate concentration began to decrease after two-minutes during that perfusion, the perfusate concentration remained elevated for a further 8 minutes.

Over the 10-minute perfusion, the concentrations of Ca^{2+} and the intracellular messengers M2, M3, and M4 were able to come close to reaching a steady state. This resulted in many of the other parameters reaching a plateau level by the end of the perfusion. These plateau values were as follows: V_m – -59.3 mV; EP – 104.6 mV; $[Ca^{2+}]_i$ – 108%; $[M2]_i$ – 107%; $[M3]_i$ – 107%; $[M4]_i$ – 107%; Basolateral K^+ current – 66%; Eo – -59 meV; CAP threshold shift – 39 dB.

While a longer perfusion might be assumed to result in a perturbation of larger magnitude, this was not the case for all of the model parameters: the concentrations of Ca^{2+}, M2, and M3 were all lower at the end-point of the 10-minute perfusion than at the end of the 2-minute perfusion. The only intracellular messenger whose concentration was increased during the longer-duration perfusion was M4, due to the longer integration time for that messenger (as shown in Figure 2.8 of Chapter 2). This resulted in a much larger slow contraction relative to the shorter perfusions, with the ST operating-point shift causing a greater reduction in small-signal AC receptor potential, and a larger threshold shift. The ten-minute perfusion simulation also provides a comparison to the experimental results for the perfusion of the same duration shown in Figure 8.34.

8.10.3 30-second perfusion of 10 mM potassium AP

Figure 8.42 shows the results of a simulated 30-second perfusion of 10 mM K^+ in scala tympani. This perfusion duration was chosen in order to provide a comparison to those results obtained in the guinea-pig experiments presented in Section 8.9.2 above. However, using the standard set of model parameters, the results of the perfusion did not provide a very close match to the one example of a 30-second K^+ perfusion of normal osmolarity that was shown in Figure 8.35. A slightly longer perfusion of 40 seconds was also performed in the guinea pig (Figure 8.36), but the solution used was hypo-osmotic, which may have contributed an osmotic component to the result in addition to the effects due to the potassium itself.

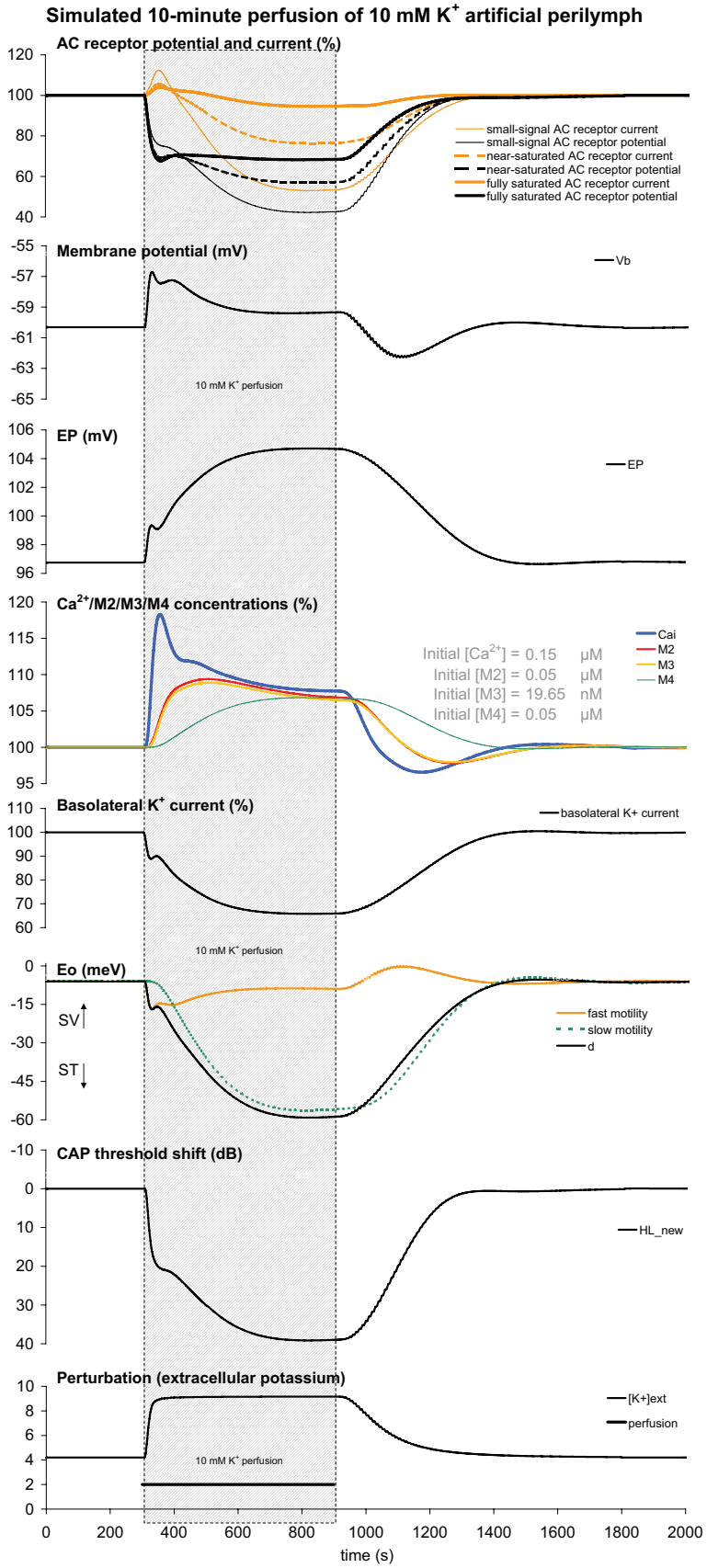

Figure 8.41: OHC model parameters during a simulated 10-minute perfusion of 10 mM K^+ artificial perilymph (see text).

Washington University Cochlear Fluids Simulator v.1.6h settings: Guinea pig cochlea. Ten-minute perfusion of K^+ (2.47×10^{-5} cm^2/s diffusion coefficient) at 3 µL/min, perfusate entry at 2 mm, exit at 16.2 mm. Radial ST-SV communication half-time normalized to 0.1 mm^2 cross-sectional area. Cochlear aqueduct enters at 1.1 mm. Apical perilymph communication enabled - 0.03 mm^2 helicotrema area. Perilymph leak of 0.5 µL/min at 16.2 mm location. Recording locations chosen assuming 22 mm guinea-pig cochlea and the 22 kHz location, according to the place-frequency map of Tsuji and Liberman, 1997.

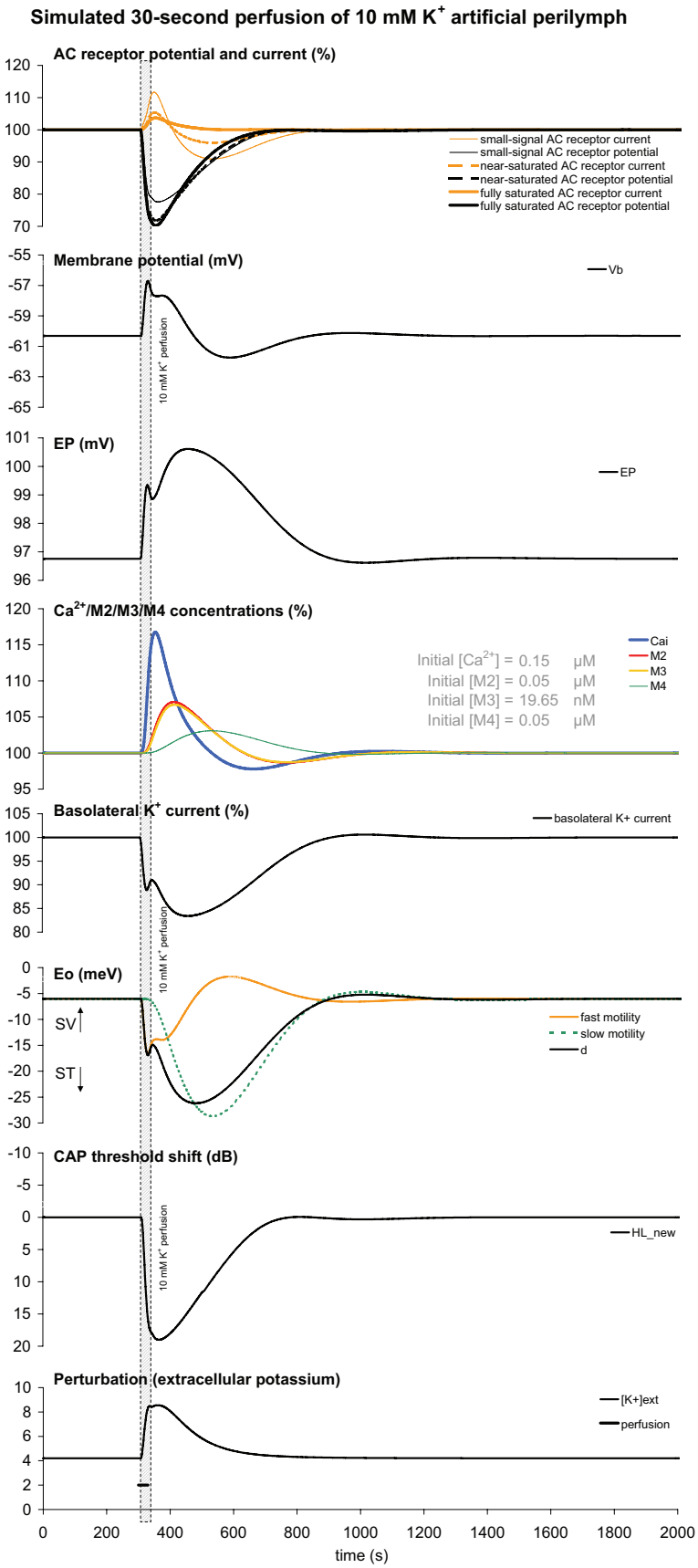

Figure 8.42: OHC model parameters during a simulated 30-second perfusion of 10 mM K^+ artificial perilymph (see text).

Washington University Cochlear Fluids Simulator v.1.6h settings: Guinea pig cochlea. Thirty-second perfusion of K^+ (2.47 x 10^{-5} cm^2/s diffusion coefficient) at 3 µL/min, perfusate entry at 2 mm, exit at 16.2 mm. Radial ST-SV communication half-time normalized to 0.1 mm^2 cross-sectional area. Cochlear aqueduct enters at 1.1 mm. Apical perilymph communication enabled - 0.03 mm^2 helicotrema area. Perilymph leak of 0.5 µL/min at 16.2 mm location. Recording locations chosen assuming 22 mm guinea-pig cochlea and the 22 kHz location, according to the place-frequency map of Tsuji and Liberman, 1997.

Given that the simulated effects of 50 mM K^+ were much larger than those observed experimentally, a 10 mM perfusate concentration was simulated here, so as to provide a better match to the experimental time-courses. In this section, simulations are presented for 30-s perfusions of 10 mM K^+ AP of normal osmolarity with the standard model-parameter settings, and with a set of altered parameters.

For the simulated perfusion of 10 mM K^+ AP using standard model settings, the first 30 s were identical to the longer simulations shown above. However, the short duration of the perfusion meant that the maximal K^+ concentration reached at the 22 kHz site was around 13% lower than that reached during a 10-minute perfusion (as discussed further in Section 8.11 below). During this simulation, the model OHC showed a net 20 meV ST operating point shift that was dominated by the slow-contraction, reaching a peak at 3 minutes after perfusion onset. By comparison, the guinea pig data shown in Figure 8.35 showed a 14 meV ST shift, reaching a peak at 90 s post-onset.

However, the largest difference was in the Vsat changes: In the guinea-pig, the Vsat parameter decreased by 8% at 30 s post-onset, before increasing to a plateau level of 10% above control at 160 s post-onset. These results contrast with the model predictions: In the model, the saturated AC receptor current, analogous to the Vsat Boltzmann parameter, showed an *increase* rather than a decrease. The 40-s, hypo-osmotic K^+ perfusion example (shown in Figure 8.36) also showed a Vsat decrease of a similar pattern (albeit slightly slower in its time-course), reaching its minimum of 11% below control at 70 s post-onset, and reaching a plateau at 10% above control levels at 400 s post-onset. Because the onset of the short-term and longer-term K^+ perfusions showed different Vsat changes (a decrease during the short-term perfusion, compared to an increase during the longer-term perfusion), it is clear that more data is required.

In addition to the Vsat changes, the simulations presented above did not produce the multi-phasic hearing loss observed with the short-duration K^+ perfusions shown in this Chapter, and the experiments of Patuzzi and Marcon. However, with some alteration of the model parameters, a multi-phasic hearing loss could be produced. Shown in Figure 8.43 are the results from simulated 30-second perfusions of artificial perilymphs containing pipette concentrations of K^+ that were between 1 and 5 times larger than perilymphatic potassium concentration. This simulated perfusion was not carried out with the standard model parameters: the magnitude of the slow contraction was increased by changing the slow-motility sensitivity parameter (S_{Slow}) from 15000 to 35000.

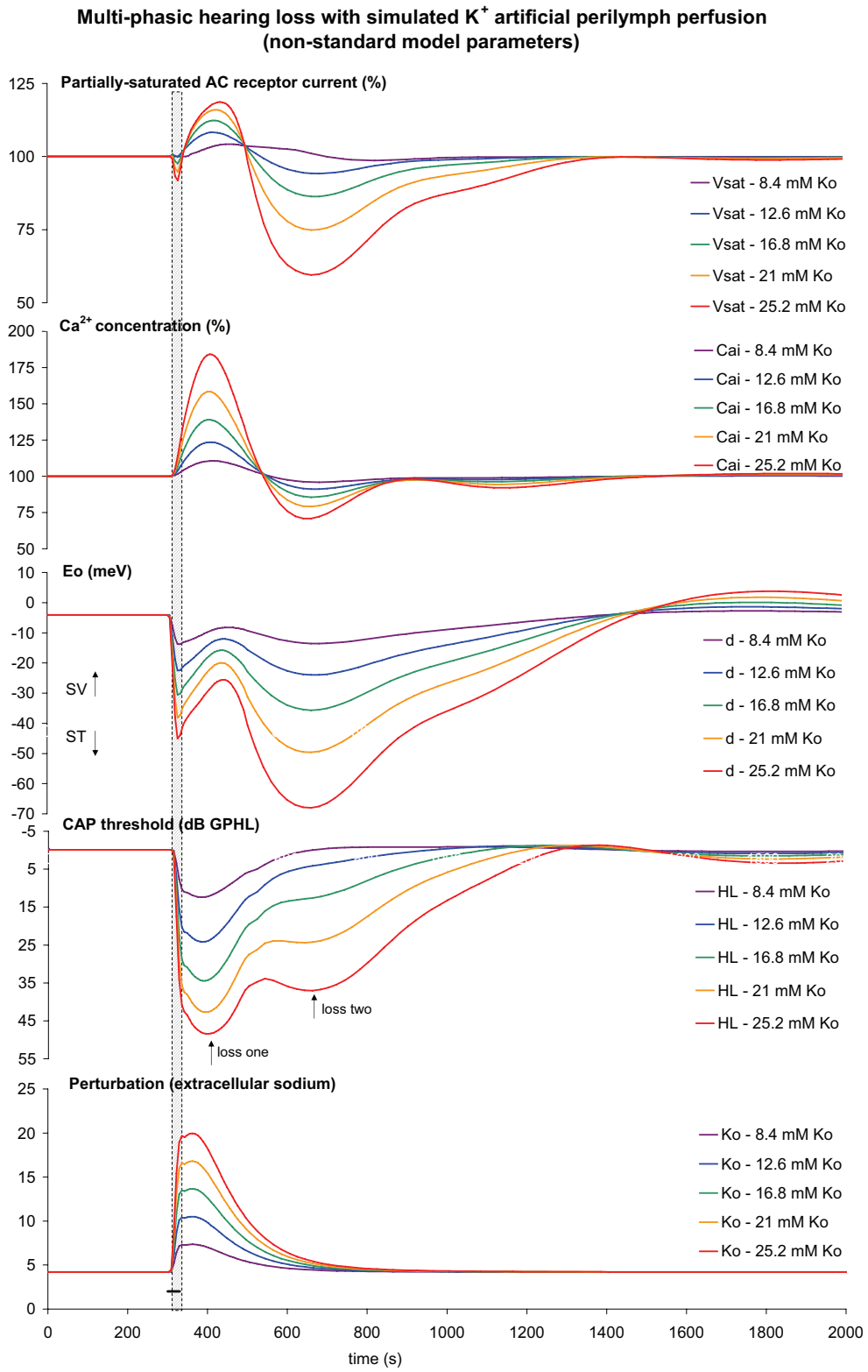

Figure 8.43: OHC model parameters during simulated 30-seconds perfusions of elevated K^+ artificial perilymphs (see text). This perfusion was *not* carried out with the standard model parameters: the slow contraction sensitivity (S_{Slow}) was increased from 15000 to 35000, and the intracellular turgor was increased from 100 to 1100 to compensate for the resulting ST shift. The time-scale of the model was also increased 5-fold.

Washington University Cochlear Fluids Simulator v.1.6h settings: Guinea pig cochlea. Simulated 30-second perfusion of K^+ (0.71×10^{-5} cm^2/s diffusion coefficient) at 3 µL/min, perfusate entry at 2 mm, exit at 16.2 mm. Radial ST-SV communication half-time normalized to 0.1 mm^2 cross-sectional area. Cochlear aqueduct enters at 1.1 mm. Apical perilymph communication enabled - 0.03 mm^2 helicotrema area. Perilymph leak of 0.5 µL/min at 16.2 mm location. Recording locations chosen assuming 22 mm guinea-pig cochlea and the 22 kHz location, according to the place-frequency map of Tsuji and Liberman, 1997.

Because this change resulted in a larger tonic ST shift, the intracellular turgor was increased from 100 to 1100 to compensate. The time-scale of the model was also increased 5-fold to alter the dynamics of the 2nd-messenger cascade. As shown in the "CAP threshold" panel of Figure 8.43, the largest concentration of K^+ used (25.2 mM K^+) resulted in a hearing loss of 48 dB at 2-minutes post-onset, followed by a recovery and a hearing loss of 37 dB at 8-minutes post-onset. The first hearing loss was caused by a peak in cytosolic calcium, which increased the permeability of the basolateral wall and caused a large reduction in the small-signal AC receptor potential. The second hearing loss was caused by the large 62 meV operating point shift towards scala tympani, which reduced the apical MET sensitivity by 74%. The local minimum in hearing loss at 6-minutes post-onset represented the crossover point between these two different types of hearing losses.

While this result is unlikely to represent the actual physiological mechanism of the multi-phasic hearing loss in the guinea pig, it does yield some useful information. It is clear from the modelling required to generate this result that, in order to produce the inflection in the hearing loss recovery trace, there is a need to temporally separate the hearing losses produced by the action of Ca^{2+} on basolateral permeability, and by the action of M4 on the operating point. In the multi-phasic simulation result shown above, the phase delay between the Ca^{2+} parameter and the M4 parameter was greater than 180º (compared to around 135º during the standard-parameter-set 30-second K^+ simulation result), but the size of the M4 peak was greatly reduced compared to the large calcium increase, necessitating the increase in slow-motility sensitivity parameter to compensate for this reduction in loop gain. An alternative possibility is that the one of the two hearing losses could be produced by some other mechanism, such as a concurrent osmotic bias, that operates at a different time-scale to the K^+ induced mechanism. While the hypo- and hyper-osmotic K^+ perfusions presented in Figure 8.37 did have just such an osmotic component to their perturbation, the same cannot be said of the example shown in Figure 8.35, which had an osmolality of 306 mOsm, and yet still produced a multi-phasic hearing loss.

In any case, it is possible that this problem in generating large temporal separations while maintaining adequate motility could be resolved by separating the intracellular calcium into two distinct pools. This "two-pool model" of OHC calcium, and its implications for these perfusion results. is discussed further in Chapter Nine.

8.11 Discussion – Increase in perilymphatic potassium

The perfusions of elevated potassium artificial perilymph produced a number of interesting results, including a multi-phasic elevation and recovery of CAP and SP thresholds that was also visible in measures of CAP amplitude, and some extremely large and rapid operating point shifts. In fact, the 50 mM K^+ perfusion shown in Figure 8.34 resulted in the largest operating point shift observed for a perturbation in this study. In that particular case, the observed changes in threshold and the Boltzmann parameters were not likely to have been caused by an osmotic mechanism (at least to a first-order), because a constant [K][Cl] product was maintained, and the osmolality of the solution used in Figure 8.34 (291 mOsm) was not significantly different from the 292.9 ± 5.7 mOsm average recorded in ST perilymph by Konishi et al. (1984).

The TTX results of Marcon and Patuzzi, shown in Figure 8.39, indicated that the observed multi-phasic threshold shift was mechanical in origin. The CAP waveforms shown in Figure 8.38 showed latency shifts and peak reductions that would be expected from a reduction in active gain, but looked relatively normal, despite the large concentrations of K^+ in the perfused artificial perilymph. This apparent lack of a separate neural effect may indicate that the primary afferent neurones are in some way sheltered from extreme fluctuations in the potassium concentration of the perilymph and "Cortilymph".

Although the multi-phasic loss is likely to be mechanical in origin, attempts to reconcile the Boltzmann data with the phases of the hearing loss were not successful, most likely because of the extremely rapid nature of the threshold shifts, and possibly because of the spatial difference between the generators of the basal turn low-frequency CM and the individual frequencies. In this case, it seemed that the results of the modelling enabled greater insight into what was required to achieve the multi-phasic hearing loss than did the Boltzmann data.

Results of the potassium perfusion differed markedly depending on the duration of the perfusion. Apart from the duration of the perfusion affecting the length of exposure of the hair cells to the perfusate, it also affected the *size* of the effective potassium perturbation, producing a smaller perturbation for the shorter-duration perfusions than for the longer ones. As illustrated in Figure 8.44, modelling of expected perfusate concentration using the Washington University Cochlear Fluids Simulator (v1.6h; Salt, 2002) showed that when using a perfusion rate of 3 μL/minute under conditions matching these experiments, the maximal perilymphatic K^+ concentration at the 22 kHz

site was predicted to reach only 75% of the pipette concentration during a 30-second perfusion (and 80% for a 40-second perfusion), compared to 85-86% of the pipette concentration for perfusions over two-minutes duration.

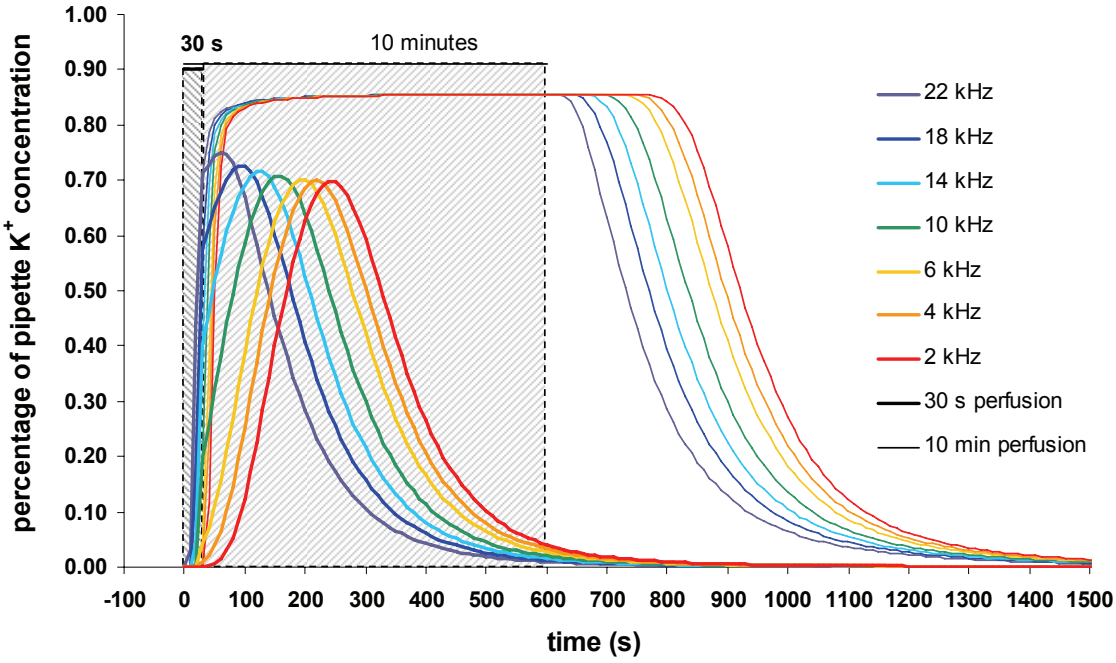

Figure 8.44: The predicted maximum concentration of K+ reaching various cochlear locations was assumed to depend on the duration of the perfusion, with 30-second perfusions (bold traces) resulting in lower perfusate concentrations throughout the cochlea than 10-minute perfusions (lighter traces).

Washington University Cochlear Fluids Simulator v.1.6h settings: Guinea pig cochlea. 30-second and 10-minute perfusions of K^+ (2.47 x 10^{-5} cm2/s diffusion coefficient) at 3 µL/min, perfusate entry at 2 mm, exit at 16.2 mm. Radial ST-SV communication half-time normalized to 0.1 mm^2 cross-sectional area. Cochlear aqueduct enters at 1.1 mm. Apical perilymph communication enabled - 0.03 mm^2 helicotrema area. Perilymph leak of 0.5 µL/min at 16.2 mm location. Recording locations chosen assuming 22 mm guinea-pig cochlea and place-frequency map of Tsuji and Liberman (1997).

Aside from this duration effect, the results of the mathematical model of the OHC for perfusion of a given potassium concentration were much larger than those observed experimentally. It was, in most cases, necessary to simulate these potassium perfusions using a lower concentration of potassium than that which was assumed to reach the hair cells. This is either an indicator that the density of potassium (and other) channels in the model requires some adjustment, or that the concentration of perfusate that bathes the basolateral membrane of the hair cells *in situ* is different from that in the body of scala tympani, such that the concentration of perfusate that reaches the basolateral wall may be significantly lower than that in the perilymph on the other side of the basilar membrane.

8.12 Summary

Results were presented for perilymphatic perfusions of three main types – reduced sodium, elevated osmolarity, and elevated potassium. Mathematical modelling of the effects of each of these perturbations on the OHC was carried out, both as a means of testing the accuracy of the model, but also as a means of explaining the changes that were observed experimentally. In general, the model was successful in replicating many characteristics of the perturbations, but there were a number of aspects of the experimental data that *were not* accurately reproduced by the model. This information was extremely valuable, in that it has prompted revision of the schematic model of OHC regulation that was presented in Chapters One and Two. A brief synopsis of this revised model is presented in Chapter Nine.

To summarise, the reduced sodium perfusions had a distinct neural effect in addition to the mechanical effects revealed by the Boltzmann analysis of the CM. The observed changes in the Boltzmann parameters (except for the operating point – see below) were consistent with an increase in cytosolic calcium concentration. This Ca^{2+} increase was more likely to be due to a reduction in Ca^{2+} efflux through the Na^{+}/Ca^{2+} antiport, rather than any efferent-like effect caused by the pharmacological action of choline on the ACh-sensitive Ca^{2+} channel in the basolateral wall. The consistently-observed prolonged operating point shift towards scala vestibuli was not consistent with the action of the schematic model of OHC regulation, which predicted a slow-motile operating point shift towards scala tympani. However, the predicted changes in basolateral permeability *were* consistent with the experimental data. This will be discussed further in Chapter Nine. The neural effects were consistent with a reduction of the concentration gradient for the influx of Na^{+} required for an action potential.

The mechanism of the hyperosmotic perfusions is not known, but its effects were *not* consistent with a simple movement of the reticular lamina towards scala vestibuli. The threshold shifts produced by the hyperosmotic perfusions were often of the order of 30 dB, and were most likely to be mechanical in origin. The most consistent changes in the Boltzmann parameters were increases in Vsat and the Z parameter. The modelling task was more difficult for this type of perfusion, as it was not clear what the actual causative perturbation was: an attempt to model the hyperosmotic perfusions using a scala-vestibuli operating point shift as the perturbation resulted in discrepancies between the experimental data and the model results, particularly with respect to the

relative magnitudes of the changes in the operating point and Vsat. This, too, will be discussed in Chapter Nine.

The elevated potassium perfusions caused extremely large and rapid operating point shifts towards scala tympani that were accompanied by threshold elevations that showed a multi-phasic recovery pattern. This recovery pattern was shown to be mechanical in origin. Indeed, the CAP waveshape was relatively normal during this perturbation, indicating that the primary afferent neurones may be in some way sheltered from the large increases in perilymphatic potassium during these perfusions. The multi-phasic pattern of hearing loss was not reproduced by the mathematical model using the standard set of model parameters. However, by adjusting the sensitivity of the slow-contraction in the model, and speeding up the model time-scale, an appropriately multi-phasic hearing loss was produced, indicating that *temporal separation* of the calcium hearing loss (i.e. the increased basolateral permeability) and the operating-point hearing loss (i.e. movement to a less-sensitive part of the MET transfer curve) was required for its production.

The time-course of the effects of the sodium and sucrose perfusions followed the estimated time-course of the concentrations of the perfusates in scala tympani, indicating little *lasting* effects of these perfusions. It was also shown that physiological clearance of perfusates (by the bulk flow of perilymph) can be impaired under certain conditions, which suggests that controlled washout of experimental perfusates by post-perfusion with control AP may be warranted.

Chapter 9
General discussion

9. General discussion

The aim of the present study was to develop methods to investigate and characterise the homeostatic mechanisms within the OHCs of the organ of Corti. Building upon Patuzzi's conceptual model of OHC homeostasis (Patuzzi, 2003), a mathematical model of the electrophysiological and mechanical interactions within the OHCs was developed and refined over a number of years, using as a template the data of Marcon and Patuzzi (Marcon, 1995; Marcon and Patuzzi, in preparation) and later the results of electrophysiological experiments in guinea pigs conducted by the present author. The hypothesis underlying the development of the homeostatic model was that oscillatory phenomena such as the bounce were produced in the cochlea by oscillations in the cytosolic calcium concentration of the outer hair cells.

The electrophysiological experiments were designed to obtain a "panoramic view" of cochlear regulation during a range of cochlear perturbations, and were facilitated by the development of custom-written software that enabled the interleaved and near-simultaneous measurement of multiple indicators of cochlear function, including CAP threshold, amplitude and waveshape at multiple frequencies, Boltzmann analysis of the low-frequency CM, cubic and quadratic DPOAEs, the SNN, and the EP. The simultaneous monitoring of these cochlear potentials yielded a great deal of information about the time-courses and interaction between the functional components of the OHCs.

The most useful application of the mathematical model came from the process of comparing the experimental data to the results of matched simulations. In this process, a number of shortcomings of the present conceptual model were revealed. Some of these differences between the experimental data and the model were due to choice of particular values for model parameters: as described in Chapter Two, a number of these choices were made in the absence of solid physiological data describing the characteristics of the particular ionic transport mechanisms. However, some of the other discrepancies were probably due to more fundamental limitations of the schematic model itself. We now believe that many of these differences can be at least partially resolved by: i) the inclusion of the prestin nonlinearity into cell model; and ii) the separation of the cytosolic calcium concentration into two functionally-separate "pools" – one of which controls basolateral permeability, and one which is responsible for the slow-motile contraction.

In this discussion chapter, an overview of the experimental findings is presented, followed by a brief description of the two-calcium-pool model.

9.1.1 Overview of experimental and modelling results

A major impetus for the creation of the hair cell model was to develop an understanding of the cochlear processes responsible for the so-called "bounce phenomenon", where cochlear gain slowly oscillates (usually displaying a transient improvement in sensitivity) following exposure to a low-frequency (LF) tone. In Chapter Six it was shown that the bounce in CAP thresholds and Boltzmann parameters following exposure to an intense LF tone was probably produced by the same mechanism that produced the slow oscillations in the Boltzmann parameters observed by Marcon and Patuzzi (Marcon, 1995; Marcon and Patuzzi, in preparation), but differed in the degree to which the oscillations were damped. In this case, the threshold oscillations observed probably arise from changes in the permeability of the basolateral wall of the OHC under the influence of cytosolic calcium concentration.

Results from the application of force to the cochlear wall were presented in Chapter Five. The technique of applying force to the cochlear wall was developed with the aim of producing a large mechanical step-perturbation that would elicit a regulatory oscillation that could be examined by mathematical modelling. Ultimately, the push was *not* a particularly effective method of achieving this. It was, however, a method of generating *small* sustained scala vestibuli operating point shifts: after an initial period of "adaptation", a residual operating point shift remained in place *for the duration of the push* (over 20 minutes). As discussed in Chapter One, the cochlea possesses numerous high-pass filter mechanisms to limit the influence of DC mechanical stimuli. The "push" experiments provided an example of just how efficient some of these mechanisms were: when the cochlear wall was deformed using very large forces (around one-quarter of those required to actually crack the otic capsule), the resulting hearing loss was no greater than 35 dB[1]. On the basis of our measurements, these threshold elevations were most likely mechanical in origin, and were perhaps produced by some sort of change in the geometry of the organ of Corti.

The results of scala tympani current injection experiments were presented in Chapter Seven. Short-term injection of DC current into scala tympani produced changes in the Boltzmann parameters that consisted of step-shifts at the onset and offset of the injection that were probably caused by changes in driving potential for potassium

through the OHCs and electromotility, which then initiated slower, oscillatory changes that were consistent with the changes in cytosolic calcium predicted by the single-pool model. The ST current injection results of this study, and the SM current injection results of Marcon and Patuzzi (in preparation), provided a good indication of the relative magnitudes and time-courses of the electromotile (i.e. prestin-mediated) and slow-motile contractions. The mathematical modelling of this perturbation produced results that matched most features of the experimental data (see, for example, Section 7.6.2 and Figure 7.15 on Page 228).

The results of perilymphatic ion-substitution experiments were presented in Chapter Eight. These experiments provided the largest amount of information regarding the ability of the single-pool model to account for the observed OHC responses. Reduction of sodium concentration of artificial perilymph from 148 mM to 8 mM produced both neural and hair-cell effects: the OHC effects were probably caused by an increase in cytosolic calcium concentration, resulting in an increase in Vsat, but there were also operating point shifts *toward scala vestibuli* that were *not* consistent with the single-pool model and an increase in OHC calcium. Hyperosmotic perfusions were found to result in very small operating point shifts (of less than ± 2 meV on most occasions), but produced consistent increases in Z and Vsat, and resulted in CAP threshold shifts of around 30 dB. A mechanical (rather than neural) origin for the threshold elevations was suggested by hyperosmotic sucrose perfusion results from Marcon and Patuzzi (in preparation), showing that the SP threshold shifts followed a near-identical time-course to the CAP thresholds. Brief perfusions of 50 mM potassium AP were found to cause rapid operating point shifts (of almost 40 meV) towards scala tympani, and a rapid elevation of threshold that exhibited a multi-phasic recovery. Modelling using a *non-standard* set of model parameters (see Section 8.10.3) showed that this complex pattern is likely to arise from the temporal separation of two types of motor hearing loss: those due to intracellular calcium (and its effect on basolateral conductance) and those due to operating point shifts. The effects produced by the model for elevations of extracellular potassium were far greater in magnitude than those observed experimentally. One possibility explanation for this disparity is that the model accurately reflects the *in vivo* situation because the K^+ fluctuations reaching the Cortilymph surrounding the OHCs were (due to some sort of diffusion barrier) smaller than those in the perilymph in the body of scala tympani. Alternatively, it may indicate that the sensitivity of the model

[1] A human with a 35 dB hearing loss is often not even provided with a hearing aid.

hair cell to extracellular potassium was simply too great, and that a reduction in the density of the basal (and apical) K^+ conductances is required.

9.1.2 Model successes and shortcomings

The model, using the *standard set of parameters* presented in Chapter Two, was capable of reproducing a number of key features of the experimental data. These were:

i) the "low-frequency adaptation" phenomenon, whereby the operating point of the OHC moves towards scala tympani during an intense LF tone;

ii) the transient hypersensitivity of the "bounce phenomenon", and the associated EP changes, following LF exposures;

iii) the changes in EP and operating point (both fast and slow components, both mid- and post-injection, during both positive and negative EP biases);

iv) the asymmetric changes in CAP threshold during positive and negative current injection;

v) the increase in Vsat during the low-sodium choline perfusions.

It was *unable* to replicate (using the standard set of parameters):

i) the initial *decrease* in Vsat during the first 90-120 seconds of SM-positive and ST-negative current injections (where the OHC model would predict an *increase* in AC receptor current due to the action of the elevated cytosolic calcium on Ca^{2+}-sensitive K^+ channels);

ii) the operating point shifts during the low-sodium choline perfusions, which showed a small ST shift during the first 60 seconds, followed by a sustained SV shift. The model predicted the *opposite* pattern, with an initial hyperpolarisation-induced relaxation of electromotility, followed by a large slow-motile contraction under the influence of the second-messenger M4;

iii) the *decrease* in Vsat during the first 30 seconds of the elevated-K^+ perfusion. The model predicted an *increase* in AC receptor current due to the increase in cytosolic calcium with depolarisation of the OHC;

iv) the multi-phasic time-course of the threshold shifts observed during brief perfusions of elevated potassium.

Many of these discrepancies concerned the direction of the slow-motile operating point shifts in the model. Another example of these discrepancies in the operation point

shifts was the hexamethonium perfusions of Chapter Eight, that produced a large reduction in Vsat, but virtually no operating point shift. This was not consistent with the single-pool model, which predicted the reduction in cytosolic calcium would cause a relaxation of any tonic slow-motile contraction, producing an operating point shift towards scala vestibuli.

With reference to the modelling of the hyperosmotic perfusion experiments, it was found that when the size of the simulated perturbation was adjusted so that the magnitude of the operating point shifts matched the experimental data, the temporal characteristics of the simulation time-course showed quite a close match to the experimental data (as shown in Figure 8.30 of Chapter Eight), with the exception that that the *magnitudes* of the changes in AC receptor current and CAP threshold were approximately *one-tenth* of those observed experimentally. This indicated that, for the hyperosmotic perfusions, the changes in cytosolic calcium concentration required to cause the observed slow-motile shifts were too large for the observed changes in basolateral permeability.

The third observed discrepancy between changes in the basolateral permeability and the operating point was during the slow oscillations of Chapter Six, which were manifested primarily in Vsat. These LF-induced Vsat oscillations indicated large changes in basolateral permeability that were most likely to be caused by cytosolic calcium oscillations. These oscillations were not always manifest in the operating point, or were of very low magnitude (compared to other operating point shifts).

9.2 The two-calcium-pool model of outer hair cell regulation

The above observations provided a clear indication that something was wrong with the relationship between the basolateral permeability and the operating point. In an intermediate stage of the modelling, an attempt was made to rectify this: whereas both the slow contraction and the calcium sequestration had been controlled by M3 in earlier versions of the homeostatic model (see, for example, O'Beirne and Patuzzi, 2002; Patuzzi, 2003), an additional second messenger (M4) was included, as a means of "decoupling" the operating point shifts from the basolateral permeability changes. While this inclusion improved the ability of the single-pool model to account for the observed experimental changes, the above discrepancies remained.

Upon examination of the above data, it became clear that despite the inclusion of M4, a further separation of the effects of cytosolic calcium was required. One possible solution was to divide the cytosolic calcium into two separate pools: the **contraction**

control pool (CCP) and the **basolateral permeability control pool** (BPCP), as described below. The rationale behind the separation of calcium into two pools was, in part, based on the observations of the spatial distribution of the synaptic cisternae and the sub-surface cisternae that is responsible for the fast and slow efferent effects (Sridhar et al., 1995; Sridhar et al., 1997; Yoshida et al., 1999; Cooper and Guinan Jr, 2003), shown in Figure 9.1 below.

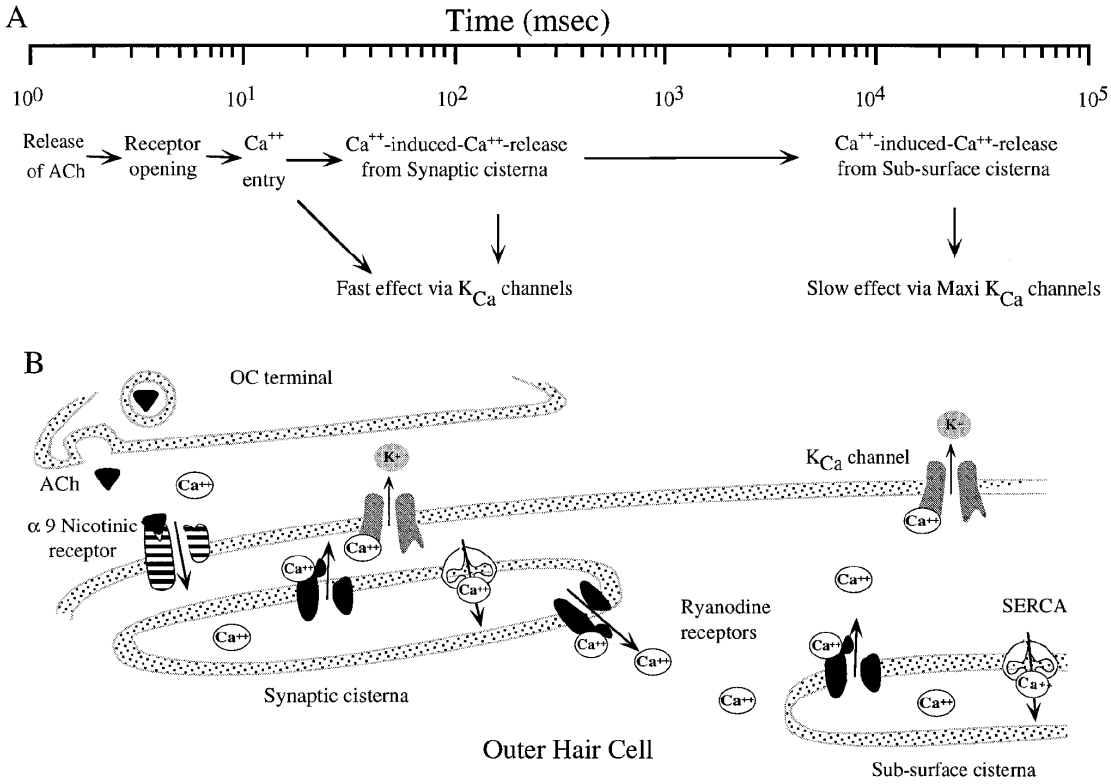

Figure 9.1: Schematic diagram (from Sridhar et al., 1997) showing **A.** the time-course of the fast and slow olivocochlear efferent effects, and **B.** the cellular components responsible for the release of Ca^{2+}. (Note: only the spatial arrangement of the synaptic cleft, the SC, and the SSC are to scale).

The application of this spatial separation to the OHC model is shown schematically in Figure 9.2. For our purposes, let us assume that the BPCP has the standard OHC calcium-transport components: L-type voltage-sensitive Ca^{2+} channels and Ca^{2+}-ATPases (either PMCAs or SERCAs), Na^{+}/Ca^{2+} antiports, ACh-sensitive Ca^{2+} channels, and Ca^{2+}-sensitive K^{+} channels. Let us also assume, however, the BPCP does not have access to the slow-motility mechanism of the OHC. In contrast, the CCP *does* have access to the slow-motility machinery, but does *not* have the Na^{+}/Ca^{2+} antiport, ACh-sensitive Ca^{2+} channels, or Ca^{2+}-sensitive K^{+} channels. This leaves the L-type voltage-sensitive Ca^{2+} channels and Ca^{2+}-ATPases as the only remaining Ca^{2+} transport mechanisms in that pool.

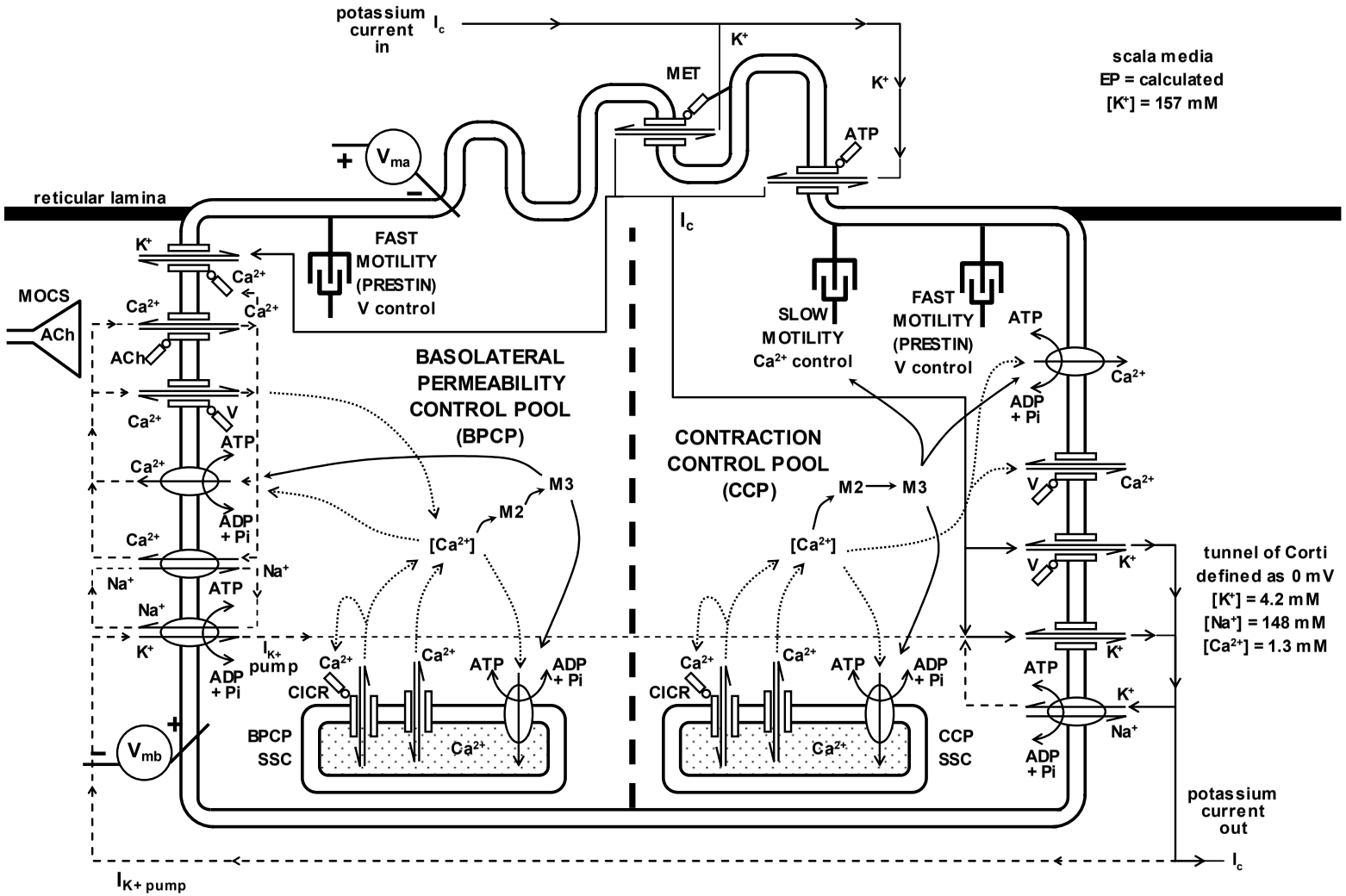

Figure 9.2: A schematic representation of the "two-pool" model of the outer hair cell (see text).

The implication of this topology is that although the distribution of ion transport mechanisms is heterogeneous, the voltage across the basolateral membrane (and therefore the activity of prestin) is assumed to be shared by both compartments. Due to the limited diffusion of calcium through the cytosol (Allbritton et al., 1992), the degree to which any "cross-talk" between the two calcium pools of our hair cell model might occur is unclear.

In any case, to examine the effects of this proposed calcium separation, we can consider the results of thought experiments for model simulations of some of the experimental perturbations carried out during this project.

9.2.1 Hypothetical two-pool results for low-sodium perfusions

For the low-sodium choline perfusions, the two-pool model would predict the following changes. The reduction in perilymphatic sodium would cause an increase in the cytosolic calcium in the BPCP, due to a lack of substrate for the Na^+/Ca^{2+} antiport, producing a reduction in calcium extrusion. This increase in BPCP calcium concentration would increase the opening probability of the Ca^{2+}-sensitive K^+ channels, causing an increase in basolateral K^+ flux and an increase in Vsat. This increase in basolateral conductance would also hyperpolarise the basolateral cell membrane and cause a prestin-mediated *expansion* of the OHC, resulting in the experimentally-observed operating point shift *towards scala vestibuli*. The calcium concentration in the CCP would not be altered by any first-order effects of the sodium reduction, but the subsequent hyperpolarisation of the basolateral cell membrane would cause a *reduction* in calcium entry to the CCP, due to the closure of the L-type channels. This hyperpolarisation would also contribute to the operating point shift towards scala vestibuli (mediated by prestin), again predicting a result consistent with those observed experimentally (for example, Figure 8.26 on Page 290).

That is, the two-pool model could account for *both* the increase in Vsat and the scala vestibuli operating-point shift observed experimentally, whereas the single-pool model has been shown to predict the opposite operating-point shift.

9.2.2 Hypothetical two-pool results for hexamethonium perfusions

Considering the two-pool model, the blockade of the MOCS receptor with a perilymphatic perfusion of hexamethonium would cause a reduction in the tonic entry of calcium via the ACh-sensitive calcium channels in the BPCP. The reduction of calcium in BPCP would cause a reduction in the opening probability of the Ca^{2+}-

sensitive K^+ channels, causing a decrease in basolateral K^+ flux and a drop in Vsat. The resulting depolarisation of the OHC basolateral membrane may cause a prestin-mediated electromotile contraction and a small operating point shift towards scala tympani. The hexamethonium would not cause any first-order changes in calcium entry to the CCP (which lacks the ACh-sensitive channels), and so would not produce the large *slow-motile* contraction predicted by the single-pool model, but not observed experimentally.

This increase in basolateral permeability without a large slow-motile contraction would be consistent with the ability of the MOCs to alter the standing current through the OHCs causing large changes in the EP and CM amplitude (equivalent to a halving of basolateral membrane resistance; Patuzzi and Rajan, 1990), but *without* a corresponding operating point shift.

9.2.3 Hypothetical two-pool results for DC current injections

The existing mathematical single-pool model was capable of replicating most of the results of DC current injection, as shown in Chapter Seven, and the separation of cytosolic calcium into two pools would not significantly affect these results, for the following reasons: The injection of negative current into scala tympani would cause a depolarisation that would result in an electromotile contraction of the OHC, *and* because both the CCP and the BPCP have voltage-sensitive Ca^{2+} channels, the Ca^{2+} concentration in both pools would increase, with the rise in the CCP Ca^{2+} levels causing an M2/M3/M4 increase and slow-motile contraction. That is, because the only difference between the pools is the lack of the Na^+/Ca^{2+} antiport and the presence of ACh-sensitive Ca^{2+} channels in the CCP, perturbations that are driven by membrane potential changes should act on both compartments in a similar manner, and produce similar results in the one-pool and two-pool models.

9.2.4 Hypothetical two-pool results for the low-frequency bounce

As shown in Chapter Six, the presentation of an intense low-frequency continuous tone resulted in large oscillations in Vsat, but limited oscillations in the operating point. The modelling results confirmed that one contributor to oscillatory behaviour was the voltage-sensitive and ACh-sensitive calcium channels, with voltage-sensitive Ca^{2+}-channels acting to dampen cytosolic calcium oscillations. This stifling of oscillations in the model occurs because, when elevated calcium increases the permeability of the basolateral wall and hyperpolarises the cell, the voltage-gated Ca^{2+} channels close, which counteracts the causative increase in calcium: effectively, a minor feedback loop

(Loop III of Figure 1.7 on Page 22) is damping an oscillation due to a major feedback loop (Loop IV of that Figure). Similarly, when low calcium decreases the permeability of the basolateral wall and depolarises the cell, the voltage-gated Ca^{2+} channels would open, allowing an increase in intracellular calcium, which counteracts the causative decrease. This negative feedback does not occur when calcium-transport is dominated by the ACh-sensitive channels (or indeed, any calcium leakage channels) rather than the voltage-controlled Ca^{2+} channels: instead, the hyperpolarisation caused by elevated intracellular calcium would result in a *further* influx of calcium, due to the increased electrochemical gradient for calcium entry into the OHC. This positive feedback may be sufficient to prolong the oscillatory behaviour that we predict is due to the action of the M2/M3/M4 intracellular messenger cascade.

In the two-pool model, the BPCP contains the ACh-sensitive Ca^{2+}-channels, but these are lacking in the CCP. This would mean that the CCP calcium levels would be far less likely to oscillate than those of the BPCP. This may account for the observations of oscillations in Vsat without corresponding oscillations in operating point (see Figure 1.4 of Chapter One, and Chapter Six).

9.2.5 Slow-contraction under the influence of M4

As illustrated schematically in Figure 1.8 of Chapter One, the calcium-dependent slow-motile contraction was assumed in the model to occur at the end of a 4-stage process: Ca^{2+} entry, Ca^{2+} to M2, M2 to M4, M4 to contraction.

While we can be certain that elevated intracellular calcium results in hair cell length changes, the exact mechanism by which this occurs is not yet known. Based on their own work, and that of Dulon et al. (1990), Pou et al. (1991), and Puschner and Schacht (1997), Coling et al. (1998) proposed a possible biochemical mechanism for slow-motile effects, reproduced in Figure 9.3.

As shown in the Figure 9.3, this mechanism involves both the calcium-calmodulin complex and CaM-kinase II in the initial steps. As discussed in Section 1.5.4 of Chapter One, the calcium-calmodulin complex and CaM-kinase II are candidates for the homeostatic model's second-messengers M2 and M3, respectively. If we now assume that the cytosolic calcium is separated into two pools, we have effectively removed the requirement for the slow contraction to be controlled by M4 rather than M3, because the separation between operating point and basolateral permeability now occurs at the level of calcium itself. That is, each of the two pools can be controlled by a simpler 3-stage feedback process.

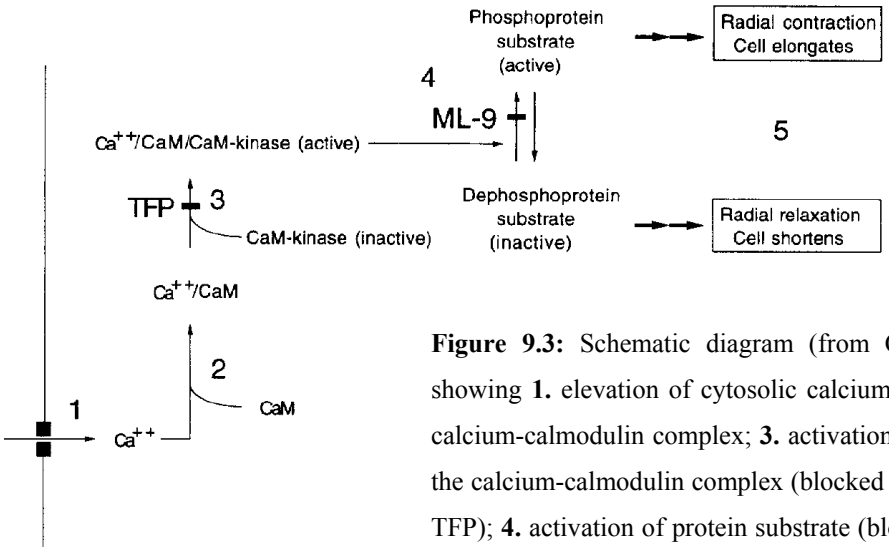

Figure 9.3: Schematic diagram (from Coling et al., 1998) showing **1.** elevation of cytosolic calcium; **2.** formation of the calcium-calmodulin complex; **3.** activation of protein kinase by the calcium-calmodulin complex (blocked by trifluoperazine, or TFP); **4.** activation of protein substrate (blocked by ML-9); and **5.** initiation and maintenance of slow motility.

9.3 Prestin and basolateral impedance

The modelling results suggest that the short-circuiting of the AC receptor potential by a low-impedance basolateral wall would be sufficient to account for the reduction of the active gain. This result would suggest that the mechanical activity of prestin was *not* affected by the 400 Hz low-pass filter in the basolateral wall (such as that measured by Housley and Ashmore, 1992, discussed below), or, at least, that the amplitude of the AC receptor potential at very high audio frequencies (e.g. around 22 kHz) is still sufficient to drive the active process adequately, because *reduction* of the AC receptor potential magnitude by an increase in basolateral permeability still had the ability to decrease active gain. It may be that the previous estimates of OHC capacitance and/or the corner frequency of the OHC membrane low-pass filter are incorrect. Measurements on *isolated, mechanically-unloaded* outer hair cells by Housely and Ashmore (1992) indicated a corner frequency of around 400 Hz. However, in mechanically-loaded OHCs *in situ*, the corner frequency may extend to frequencies many times higher than this. This could occur from a restriction of gating charge movement of prestin when the OHCs are constrained between the reticular lamina and the Deiters cells. In this case, the restriction of prestin movement would reduce the capacitance it imparts to the cell membrane and allow high-frequency receptor potentials sufficient to drive somatic motility. This would therefore allow for the subsequent reduction in cochlear sensitivity by cochlear perturbations that increase basolateral permeability.

In addition to the importance of the magnitude of the AC receptor potential, the DC membrane potential is also important in determining the sensitivity of the OHC length to these AC receptor potential changes. The mathematical model presented in Chapter

Two used a simple linear approximation to the voltage-length function of prestin (see Equation 7 on Page 39), whereas the voltage-length function of the OHC has been shown to be nonlinear (Santos-Sacchi, 1992). For the model presented here, the inclusion of this nonlinearity is the next step in the modelling process: as discussed in Section 5.6.8 of Chapter Five, Section 7.7.4 of Chapter Seven, and Section 8.5.2 of Chapter Eight, this nonlinear sensitivity may account for many of the changes observed experimentally (particularly those of the Z parameter of the Boltzmann analysis). When this EMT nonlinearity is included in the cell model, the magnitudes of both the DC membrane potential *and* the AC receptor potential become increasingly important in determining the overall functioning of the model hair cell.

9.3.1 Somatic motility versus stereociliary motility

As described in Chapter One, stereociliary motility was excluded from the model from the outset, because one goal of the modelling process was to examine how well the experimental data could be explained by the effect of cytosolic calcium on basolateral permeability, and the effect of AC receptor potential changes on *somatic* motility. The discussion presented in this thesis proceeded from a somatic-motility viewpoint, and most of the results were well explained by this, or by a modified two-pool version of the model. However, we must also ask whether the experimental results were, in any way, consistent with the motor being located in the hair bundle? In short, none of the experimental results were *more* consistent with the active process being located in the stereocilia than in the soma, while the reverse often appeared to be true. However, none produced results that eliminated the possibility of a contribution from stereociliary motility.

As described in Section 6.5 of Chapter Six, exposure to intense LF tones was presumed to reduce cochlear sensitivity by causing an increase in cytosolic calcium and basolateral permeability, thereby reducing the amplitude of the AC receptor potential required to drive the conformational changes of prestin. However, adaptation processes in stereocilia are also calcium-mediated (for a review, see Eatock, 2000; Fettiplace and Ricci, 2003), and the entry of calcium into the stereocilia during MET is likely drive the contribution of adaptation motors to vibration in lower vertebrates. Because some also ascribe this behaviour to apical hair cells of the mammalian cochlea (for example, Chan and Hudspeth, 2005), could the changes in cytosolic calcium during LF exposure modulate stereociliary calcium concentrations and cause oscillations in the sensitivity of a stereociliary motor? In our experiments, measurement of the CM waveforms from the

base of the cochlea during the bounce were consistent with an *increase* in cochlear sensitivity when the CM amplitude was at its *lowest* (indicating a reduced receptor current, but increased receptor potential). If the component of the receptor current carried by Ca^{2+} was also modulated in this way, we could expect a reduction in cochlear sensitivity in-phase with the *decrease* of the CM amplitude, rather than the *increase* we observed. However, such considerations must await further experimental data to show whether fast adaptation occurs in the base of the mammalian cochlea.

9.4 What is being regulated?

In considering the schematic model of OHC regulation, we can ask the question "what exactly is being regulated in the cochlea?". From the experimental and modelling results presented here, and from the work of Patuzzi (2002), it seems that the "regulatory" mechanisms described here achieve a compromise between the maintenance of active gain and spontaneous neural firing rate.

Active gain is maintained by i) using both calcium-dependent slow motility and slow-acting electromotility to keep the hair bundle upright; and ii) extruding calcium to lower the permeability of the basolateral wall. In this way, a large AC receptor potential can be generated, resulting in a greater contribution to active gain from prestin. Spontaneous neural firing rate is probably determined by the release of neurotransmitter from the IHCs[2]. However, the rate of neurotransmitter release is dependent on the membrane potential of the IHCs. This is in turn influenced by the EP, which is subject to a degree of regulation by the OHC current shunt (Patuzzi, 2002).

The bounce phenomenon provides clear evidence that active gain is *not* maintained at the expense of everything else, for if it were, it would not be maintained at a sub-optimal level. Because the period of threshold hypersensitivity coincides with an elevation of the endocochlear potential that is likely to produce a rate tinnitus (produced by the excessive release of neurotransmitter from the IHCs), the regulation mechanisms of the cochlear may be a compromise between hearing sensitivity and spontaneous neural firing rate, with evolutionary pressures deciding on the balance between absolute hearing sensitivity and peripheral signal-to-noise ratio.

9.5 Directions for future research

There are many aspects of the present work which would benefit from further investigation, and preliminary work has begun on some of these. The concurrent

measurement of the EP, Vsat, and CAP thresholds during the bounce phenomenon (in short, adding concurrent CAP measurements to the results of Kirk et al., 1997) would provide additional information that would help in determining the exact nature of the relationship between these variables. In particular, it would allow an assessment of whether the basolateral permeability mechanism proposed for the Bounce phenomenon (see Section 6.5 of Chapter Six) is valid.

The revised "two-pool" model described above has now been created (not reported here), and also incorporates the nonlinear voltage-length relationship discussed in Section 9.3 above. As discussed above, these two modifications should provide a better match to the experimental data, and the gross-adjustment of the model parameters to achieve this has commenced. What we have not considered in the model thus far is the *phase* of the AC receptor potential necessary to impart energy into cochlear vibration and cancel viscous forces (Geisler, 1986; Geisler and Sang, 1995; Nilsen and Russell, 2000) – membrane capacitance may be considered in a future version of the model.

The software developed during the current project for the electrophysiological monitoring of cochlear regulation (presented in Chapter Four) has been used extensively within our laboratory and elsewhere. The tone-burst method of Boltzmann analysis has proved successful in allowing measurement of OHC MET from the low-frequency CM without inducing a transient hydrops that disturbs the normal functioning of the cochlea (see, for example, Salt, 2004). The multi-frequency threshold-tracking method described in that chapter has proved particularly useful in allowing the effects of perturbations to be examined across the frequency range of the cochlea, and the modifications to the tracking process discussed in Section 4.4.3 are underway.

---

[2] The role of the lateral olivocochlear system (LOCS) was not included in the present model, which was concerned with OHC function.

References

10. References

Alberts, B., Johnson, A., Lewis, J., Raff, M., Roberts, K., Walter, P., 2002. Molecular Biology of the Cell. Garland Science, New York.

Alkondon, M., Pereira, E.F., Cortes, W.S., Maelicke, A., Albuquerque, E.X., 1997. Choline is a selective agonist of alpha7 nicotinic acetylcholine receptors in the rat brain neurons. Eur. J. Neurosci. 9(12):2734-2742.

Allbritton, N.L., Meyer, T., Stryer, L., 1992. Range of messenger action of calcium ion and inositol 1,4,5-trisphosphate. Science 258(5089):1812-1815.

Allen, J.B., 2003. Meeting discussion session. In: Gummer A.W. (Ed.), Biophysics of the Cochlea. World Scientific, Singapore, pp. 563-592.

Anniko, M., Lim, D., Wroblewski, R., 1984. Elemental composition of individual cells and tissues in the cochlea. Acta Otolaryngologica 98(5-6):439-453.

Ashmore, J.F., 1987. A fast motile response in guinea-pig outer hair cells: the cellular basis of the cochlear amplifier. J. Physiol. (Lond.) 388:323-347.

Ashmore, J.F., Meech, R.W., 1986. Ionic basis of membrane potential in outer hair cells of guinea pig cochlea. Nature 322(6077):368-371.

Assad, J.A., Hacohen, N., Corey, D.P., 1989. Voltage dependence of adaptation and active bundle movement in bullfrog saccular hair cells. Proc. Nat. Acad. Sci. USA. 86(8):2918-2922.

Avan, P., Bonfils, P., Gilain, L., Mom, T., 2003. Physiopathological significance of distortion-product otoacoustic emissions at 2f1-f2 produced by high- versus low-level stimuli. J. Acoust. Soc. Am. 113(1):430-441.

Avan, P., Legouix, J.P., 1988. Effect of elevated potassium concentration in the perilymph on the nonlinearity of cochlear microphonics in the guinea-pig cochlea. Hear. Res. 35(2-3):159-164.

Axelsson, A., Vertes, D., 1978. Vascular histology of the guinea pig cochlea. Acta Otolaryngol. 85(3-4):198-212.

Barrett, J.N., Magleby, K.L., Pallotta, B.S., 1982. Properties of single calcium-activated potassium channels in cultured rat muscle. J. Physiol. (Lond.) 331:211-230.

Beagué, L., 1984. Hodgkin-Huxley: Thirty years after. In: Kleinzeller A., Baker P. (Eds.), Current topics in mebranes and transport. Vol.22 - The squid axon. Academic Press, Orlando, p. 154.

Belyantseva, I.A., Frolenkov, G.I., Wade, J.B., Mammano, F., Kachar, B., 2000. Water permeability of cochlear outer hair cells: characterization and relationship to electromotility. J. Neurosci. 20(24):8996-9003.

Berridge, M.J., 1998. Neuronal calcium signaling. Neuron 21(1):13-26.

Blanchet, C., Erostegui, C., Sugasawa, M., Dulon, D., 1996. Acetylcholine-induced potassium current of guinea pig outer hair cells: its dependence on a calcium influx through nicotinic-like receptors. J. Neurosci. 16(8):2574-2584.

Bobbin, R.P., Ceasar, G., Fallon, M., 1990. Potassium induced release of GABA and other substances from the guinea pig cochlea. Hear. Res. 46(1-2):83-93.

Bobbin, R.P., Parker, M., Wall, L., 2003. Thapsigargin suppresses cochlear potentials and DPOAEs and is toxic to hair cells. Hear. Res. 184(1-2):51-60.

Bobbin, R.P., Salt, A.N., in press. ATP-gamma-S shifts the operating point of outer hair cell transduction towards scala tympani. Hearing Research.

Bond, B.R., Ng, L.L., Schulte, B.A., 1998. Identification of mRNA transcripts and immunohistochemical localization of Na/H exchanger isoforms in gerbil inner ear. Hear. Res. 123(1-2):1-9.

Bosher, S.K., Warren, R.L., 1978. Very low calcium content of cochlear endolymph, an extracellular fluid. Nature 273(5661):377-378.

Boyle, P.J., Conway, E.J., 1941. Potassium accumulation in muscle and associated changes. J. Physiol. (Lond.) 100:1-63.

Brown, A.M., 1987. Acoustic distortion from rodent ears: a comparison of responses from rats, guinea pigs and gerbils. Hear. Res. 31(1):25-37.

Brown, D.J., 2002. Cochlear potentials: Their origin, use in tinnitus research, and modification by DC current injection. Honours Thesis, Department of Physiology, University of Western Australia, Nedlands.

Brown, D.J., McMahon, C.M., Patuzzi, R.B., 2004. K(+) currents produce P(1) in the RW CAP: evidence from DC current bias, K(+) channel blockade and recordings from cochlea and brainstem. Hear. Res. 190(1-2):60-74.

Brown, M.C., Smith, D.I., Nuttall, A.L., 1983. The temperature dependency of neural and hair cell responses evoked by high frequencies. J. Acoust. Soc. Am. 73(5):1662-1670.

Cazals, Y., Huang, Z.W., 1996. Average spectrum of cochlear activity: a possible synchronized firing, its olivo-cochlear feedback and alterations under anesthesia. Hear. Res. 101(1-2):81-92.

Chabbert, C., Canitrot, Y., Sans, A., Lehouelleur, J., 1995. Calcium homeostasis in guinea pig type-I vestibular hair cell: possible involvement of an Na(+)-Ca2+ exchanger. Hear. Res. 89(1-2):101-108.

Chambard, J.M., Ashmore, J.F., 2005. Regulation of the voltage-gated potassium channel KCNQ4 in the auditory pathway. Pflugers Arch. 450(1):34-44.

Chan, D.K., Hudspeth, A.J., 2005. Ca(2+) current-driven nonlinear amplification by the mammalian cochlea in vitro. Nat. Neurosci.

Chan, E., Ulfendahl, M., 1997. Relationship between stiffness, internal cell pressure and shape of outer hair cells isolated from the guinea-pig hearing organ. Acta Physiol. Scand. 161(4):533-539.

Chen, C., Nenov, A., Norris, C.H., Bobbin, R.P., 1995. ATP modulation of L-type calcium channel currents in guinea pig outer hair cells. Hear. Res. 86(1-2):25-33.

Chertoff, M.E., Brownell, W.E., 1994. Characterization of cochlear outer hair cell turgor. Am. J. Physiol. 266(2 Pt 1):C467-479.

Chertoff, M.E., Lerner, D., Amani-Taleshi, D., Nagai, Y., 2000. Characterizing non-linearity in the cochlear microphonic using the instantaneous frequency. Hear. Res. 145(1-2):190-202.

Choi, C.H., Chertoff, M.E., Bian, L., Lerner, D., 2004. Constructing a cochlear transducer function from the summating potential using a low-frequency bias tone. J. Acoust. Soc. Am. 116(5):2996-3007.

Clack, R.L., Patuzzi, R.B., 2001. The Post-auricular Muscle Response in Objective Threshold Estimation. Master of Clinical Audiology Thesis, Department of Physiology, University of Western Australia, Nedlands.

Cody, A.R., Russell, I.J., 1987. The response of hair cells in the basal turn of the guinea-pig cochlea to tones. J. Physiol. (Lond.) 383:551-569.

Coling, D.E., Bartolami, S., Rhee, D., Neelands, T., 1998. Inhibition of calcium-dependent motility of cochlear outer hair cells by the protein kinase inhibitor, ML-9. Hear. Res. 115(1-2):175-183.

Cooper, N.P., Guinan Jr, J.J., 2003. Separate mechanical processes underlie fast and slow effects of medial olivocochlear efferent activity. J. Physiol. (Lond.).

Corey, D.P., Garcia-Anoveros, J., Holt, J.R., Kwan, K.Y., Lin, S.Y., Vollrath, M.A., Amalfitano, A., Cheung, E.L., Derfler, B.H., Duggan, A. and others. 2004. TRPA1 is a candidate for the mechanosensitive transduction channel of vertebrate hair cells. Nature.

Crawford, A.C., Evans, M.G., Fettiplace, R., 1989. Activation and adaptation of transducer currents in turtle hair cells. J. Physiol. (Lond.) 419:405-434.

Crawford, A.C., Evans, M.G., Fettiplace, R., 1991. The actions of calcium on the mechano-electrical transducer current of turtle hair cells. J. Physiol. (Lond.) 434:369-398.

Crawford, A.C., Fettiplace, R., 1985. The mechanical properties of ciliary bundles of turtle cochlear hair cells. J. Physiol. (Lond.) 364:359-379.

Cullity, P., Franks, C.I., Duckworth, T., Brown, B.H., 1976. Somatosensory evoked cortical responses: detection in normal infants. Dev. Med. Child Neurol. 18(1):11-18.

Da Cruz, M.J., 1993. Quantification of the fundamental mechanisms leading to cochlear hearing loss. Masters Thesis, Department of Physiology, University of Western Australia, Nedlands.

Dallos, P., 1970. Low-frequency auditory characteristics: Species dependence. J. Acoust. Soc. Am. 48(2):489-499.

Dallos, P., 1973. The Auditory Periphery. Academic Press, Inc., New York.

Dallos, P., Evans, B.N., Hallworth, R., 1991. Nature of the motor element in electrokinetic shape changes of cochlear outer hair cells. Nature 350(6314):155-157.

Dallos, P., He, D.Z., Lin, X., Sziklai, I., Mehta, S., Evans, B.N., 1997. Acetylcholine, outer hair cell electromotility, and the cochlear amplifier. J. Neurosci. 17(6):2212-2226.

Dallos, P., Santos-Sacchi, J., Flock, Å. 1982. Intracellular recordings from cochlear outer hair cells. Science 218(4572):582-584.

Ding, J.P., Salvi, R.J., Sachs, F., 1991. Stretch-activated ion channels in guinea pig outer hair cells. Hear. Res. 56(1-2):19-28.

Dolan, D.F., Nuttall, A.L., Avinash, G., 1990. Asynchronous neural activity recorded from the round window. J. Acoust. Soc. Am. 87(6):2621-2627.

Don, M., Elberling, C., Waring, M., 1984. Objective detection of averaged auditory brainstem responses. Scandinavian Audiology 13(4):219-228.

Dulon, D., Luo, L., Zhang, C., Ryan, A.F., 1998. Expression of small-conductance calcium-activated potassium channels (SK) in outer hair cells of the rat cochlea. Eur. J. Neurosci. 10(3):907-915.

Dulon, D., Schacht, J., 1992. Motility of cochlear outer hair cells. Am. J. Otol. 13(2):108-112.

Dulon, D., Zajic, G., Schacht, J., 1990. Increasing intracellular free calcium induces circumferential contractions in isolated cochlear outer hair cells. J. Neurosci. 10(4):1388-1397.

Eatock, R.A., 2000. Adaptation in hair cells. Annual Review of Neuroscience 23:285-314.

Eatock, R.A., Corey, D.P., Hudspeth, A.J., 1987. Adaptation of mechanoelectrical transduction in hair cells of the bullfrog's sacculus. J. Neurosci. 7(9):2821-2836.

Elgoyhen, A.B., Vetter, D.E., Katz, E., Rothlin, C.V., Heinemann, S.F., Boulter, J., 2001. alpha 10: A determinant of nicotinic cholinergic receptor function in mammalian vestibular and cochlear mechanosensory hair cells. Proc. Nat. Acad. Sci. USA. 98(6):3501-3506.

Ernst, A., Zenner, H.P., 1995. Acute hyperpolarization and elongation of cochlear outer hair cells on superfusion with cis-platinum. Eur. Arch. Otorhinolaryngol. 252(3):163-166.

Evans, M.G., 1996. Acetylcholine activates two currents in guinea-pig outer hair cells. J. Physiol. (Lond.) 491(Pt 2):563-578.

Evans, M.G., Fuchs, P.A., 1987. Tetrodotoxin-sensitive, voltage-dependent sodium currents in hair cells from the alligator cochlea. Biophys. J. 52(4):649-652.
Fawcett, D.W., 1986. A Textbook of Histology. W.B. Saunders, Philadelphia.
Fettiplace, R., Ricci, A.J., 2003. Adaptation in auditory hair cells. Curr. Opin. Neurobiol. 13(4):446-451.
Frank, G., Hemmert, W., Gummer, A.W., 1999. Limiting dynamics of high-frequency electromechanical transduction of outer hair cells. Proc. Nat. Acad. Sci. USA. 96(8):4420-4425.
Frank, G., Kössl, M., 1996. The acoustic two-tone distortions 2f1-f2 and f2-f1 and their possible relation to changes in the operating point of the cochlear amplifier. Hear. Res. 98(1-2):104-115.
Frank, G., Kössl, M., 1997. Acoustical and electrical biasing of the cochlea partition. Effects on the acoustic two tone distortions f2-f1 and 2f1-f2. Hear. Res. 113(1-2):57-68.
Fraser, J.G., Conway, M.J., Keene, M.H., Hazell, J.W., 1978. The post-auricular myogenic response: a new instrument which simplifies its detection by machine scoring. J Laryngol Otol 92(4):293-303.
Frolenkov, G.I., Mammano, F., Kachar, B., 2003. Regulation of outer hair cell cytoskeletal stiffness by intracellular Ca(2+): underlying mechanism and implications for cochlear mechanics. Cell Calcium 33(3):185-195.
Fuchs, P.A., Murrow, B.W., 1992. Cholinergic inhibition of short (outer) hair cells of the chick's cochlea. J. Neurosci. 12(3):800-809.
Furuta, H., Luo, L., Hepler, K., Ryan, A.F., 1998. Evidence for differential regulation of calcium by outer versus inner hair cells: plasma membrane Ca-ATPase gene expression [published erratum appears in Hear Res 1998 Dec;126(1-2):214]. Hear. Res. 123(1-2):10-26.
Gadsby, D.C., Kimura, J., Noma, A., 1985. Voltage dependence of Na/K pump current in isolated heart cells. Nature 315(6014):63-65.
Garrahan, P.J., Glynn, I.M., 1967a. Factors affecting the relative magnitudes of the sodium:potassium and sodium:sodium exchanges catalysed by the sodium pump. J. Physiol. (Lond.) 192(1):189-216.
Garrahan, P.J., Glynn, I.M., 1967b. The incorporation of inorganic phosphate into adenosine triphosphate by reversal of the sodium pump. J. Physiol. (Lond.) 192(1):237-256.
Gaskill, S.A., Brown, A.M., 1990. The behavior of the acoustic distortion product, 2f1-f2, from the human ear and its relation to auditory sensitivity. J. Acoust. Soc. Am. 88(2):821-839.
Geisler, C.D., 1986. A model of the effect of outer hair cell motility on cochlear vibrations. Hear. Res. 24(2):125-131.
Geisler, C.D., 1998. From Sound To Synapse. Physiology of the Mammalian Ear. Oxford University Press, New York.
Geisler, C.D., Sang, C., 1995. A cochlear model using feed-forward outer-hair-cell forces. Hear. Res. 86(1-2):132-146.
Gillespie, P.G., Cyr, J.L., 2004. Myosin-1c, the hair cell's adaptation motor. Annu. Rev. Physiol. 66:521-545.
Gitter, A.H., Fromter, E., Zenner, H.P., 1992. C-type potassium channels in the lateral cell membrane of guinea-pig outer hair cells. Hear. Res. 60(1):13-19.
Goto, S., Oshima, T., Ikeda, K., Takasaka, T., 1999. Expression and localization of the Na+-H+ exchanger in the guinea pig cochlea. Hear. Res. 128(1-2):89-96.
Guinan, J.J., Jr., 1996. Physiology of olivocochlear efferents. In: Dallos P., Popper A.N., Fay R.R., Popper A. (Eds.), The Cochlea. Springer-Verlag, New York, NY, pp. 435-502.

Gummer, A.W., Johnstone, B.M., Armstrong, N.J., 1981. Direct measurement of basilar membrane stiffness in the guinea pig. J. Acoust. Soc. Am. 70(5):1298-1309.
Halliday, A.F., 1994. Short-term threshold shift: An investigation of its cause and recovery following acoustic overstimulation. Honours Thesis, Department of Physiology, University of Western Australia, Nedlands.
Harada, N., Ernst, A., Zenner, H.P., 1993. Volume regulation in guinea pig outer hair cells and the role of intracellular calcium. Acta Otolaryngol. Suppl. 500:39-41.
Harris, F.P., Lonsbury-Martin, B.L., Stagner, B.B., Coats, A.C., Martin, G.K., 1989. Acoustic distortion products in humans: systematic changes in amplitudes as a function of f2/f1 ratio. J. Acoust. Soc. Am. 85(1):220-229.
He, D.Z., 2003. Mechanical responses of cochlear outer hair cells. In: Gummer A.W. (Ed.), Biophysics of the Cochlea. World Scientific, Singapore, pp. 181-184.
He, D.Z., Dallos, P., 1999. Somatic stiffness of cochlear outer hair cells is voltage-dependent. Proc. Nat. Acad. Sci. USA. 96(14):8223-8228.
He, D.Z., Dallos, P., 2000. Properties of voltage-dependent somatic stiffness of cochlear outer hair cells. J. Assoc. Res. Otolaryngol. 1(1):64-81.
He, D.Z., Jia, S., Dallos, P., 2003. Prestin and the dynamic stiffness of cochlear outer hair cells. J. Neurosci. 23(27):9089-9096.
Heffner, R., Heffner, H., Masterton, B., 1971. Behavioral measurements of absolute and frequency-difference thresholds in guinea pig. J. Acoust. Soc. Am. 49(6):1888-1895.
Heller, S., Bell, A.M., Denis, C.S., Choe, Y., Hudspeth, A.J., 2002. Parvalbumin 3 is an abundant Ca2+ buffer in hair cells. J. Assoc. Res. Otolaryngol. 3(4):488-498.
Hille, B., 1992. Ionic Channels of Excitable Membranes. Sinauer Associates Inc., Sunderland.
Hirsch, I.J., Bilger, R.C., 1955. Auditory threshold recovery after exposures to pure tones. J. Acoust. Soc. Am. 27:1186-1194.
Hirsch, I.J., Ward, W.D., 1952. Recovery of the auditory threshold after strong acoustic stimulation. J. Acoust. Soc. Am. 24:131-141.
Hodgkin, A.L., Katz, B., 1949. The effect of sodium ions on the electrical activity of the giant axon of the squid. J. Physiol. (Lond.) 108:37-77.
Holley, M.C., 1996. Outer hair cell motility. In: Dallos P., Popper A.N., Fay R.R., Popper A. (Eds.), The Cochlea. Springer-Verlag, New York, NY, pp. 386-434.
Holt, J.R., Gillespie, S.K., Provance, D.W., Shah, K., Shokat, K.M., Corey, D.P., Mercer, J.A., Gillespie, P.G., 2002. A chemical-genetic strategy implicates myosin-1c in adaptation by hair cells. Cell 108(3):371-381.
Holton, T., Hudspeth, A.J., 1986. The transduction channel of hair cells from the bull-frog characterized by noise analysis. J. Physiol. (Lond.) 375:195-227.
Housley, G.D., Ashmore, J.F., 1991. Direct measurement of the action of acetylcholine on isolated outer hair cells of the guinea pig cochlea. Proc. R. Soc. Lond. B. Biol. Sci. 244(1310):161-167.
Housley, G.D., Ashmore, J.F., 1992. Ionic currents of outer hair cells isolated from the guinea-pig cochlea. J. Physiol. (Lond.) 448:73-98.
Housley, G.D., Greenwood, D., Ashmore, J.F., 1992. Localization of cholinergic and purinergic receptors on outer hair cells isolated from the guinea-pig cochlea. Proc. R. Soc. Lond. B. Biol. Sci. 249(1326):265-273.
Housley, G.D., Raybould, N.P., Thorne, P.R., 1998. Fluorescence imaging of Na+ influx via P2X receptors in cochlear hair cells. Hear. Res. 119(1-2):1-13.
Howard, J., Ashmore, J.F., 1986. Stiffness of sensory hair bundles in the sacculus of the frog. Hear. Res. 23(1):93-104.

Hudspeth, A.J., Kroese, A.B.A., 1983. Voltage-dependent interaction of dihydrostreptomycin with the transduction channels in bullfrog sensory hair cells. J. Physiol. (Lond.) 345:66P.

Hughes, J.R., 1954. Auditory sensitization. J. Acoust. Soc. Am. 26:1064-1070.

Hughes, J.R., Rosenblith, W.A., 1957. Electrophysiological evidence for auditory sensitisation. J. Acoust. Soc. Am. 29:275-280.

Ikeda, K., Saito, Y., Nishiyama, A., Takasaka, T., 1992a. Na(+)-Ca2+ exchange in the isolated cochlear outer hair cells of the guinea-pig studied by fluorescence image microscopy. Pflugers Arch. 420(5-6):493-499.

Ikeda, K., Saito, Y., Nishiyama, A., Takasaka, T., 1992b. Intracellular pH regulation in isolated cochlear outer hair cells of the guinea-pig. J. Physiol. (Lond.) 447:627-648.

Iwasa, K.H., Li, M.X., Jia, M., Kachar, B., 1991. Stretch sensitivity of the lateral wall of the auditory outer hair cell from the guinea pig. Neurosci. Lett. 133(2):171-174.

Jenison, G.L., Bobbin, R.P., Thalmann, R., 1985. Potassium-induced release of endogenous amino acids in the guinea pig cochlea. J. Neurochem. 44(6):1845-1853.

Johnstone, B.M., Patuzzi, R., Syka, J., Sykova, E., 1989. Stimulus-related potassium changes in the organ of Corti of guinea-pig. J. Physiol. (Lond.) 408:77-92.

Johnstone, J.R., Alder, V.A., Johnstone, B.M., Robertson, D., Yates, G.K., 1979. Cochlear action potential threshold and single unit thresholds. J. Acoust. Soc. Am. 65(1):254-257.

Jones-Mumby, C.J., Axelsson, A., 1984. The vascular anatomy of the gerbil cochlea. Am. J. Otolaryngol. 5(2):127-137.

Kemp, D.T., 1982. Cochlear echoes - implications for noise induced hearing loss. In: Hamernik R.P., Henderson D., Salvi R. (Eds.), New Perspectives in Noise Induced Hearing Loss. Raven Press, New York, pp. 189-207.

Kemp, D.T., 1986. Otoacoustic emissions, travelling waves and cochlear mechanisms. Hear. Res. 22:95-104.

Kennedy, H.J., 2002. Intracellular calcium regulation in inner hair cells from neonatal mice. Cell Calcium 31(3):127-136.

Kennedy, H.J., Evans, M.G., Crawford, A.C., Fettiplace, R., 2003. Fast adaptation of mechanoelectrical transducer channels in mammalian cochlear hair cells. Nat. Neurosci. 6(8):832-836.

Kimitsuki, T., Nakagawa, T., Hisashi, K., Komune, S., Komiyama, S., 1993. Cisplatin blocks mechano-electric transducer current in chick cochlear hair cells. Hear. Res. 71(1-2):64-68.

Kimitsuki, T., Nakagawa, T., Hisashi, K., Komune, S., Komiyama, S., 1996. Gadolinium blocks mechano-electric transducer current in chick cochlear hair cells. Hear. Res. 101(1-2):75-80.

Kirk, D.L., 1972. Post-stimulatory changes in the guinea pig endocochlear potential: a possible physiological basis of auditory sensitisation. Honours Thesis, Department of Physiology, University of Western Australia, Nedlands.

Kirk, D.L., Moleirinho, A., Patuzzi, R.B., 1997. Microphonic and DPOAE measurements suggest a micromechanical mechanism for the 'bounce' phenomenon following low-frequency tones. Hear. Res. 112(1-2):69-86.

Kirk, D.L., Patuzzi, R.B., 1997. Transient changes in cochlear potentials and DPOAEs after low-frequency tones: the 'two-minute bounce' revisited. Hear. Res. 112(1-2):49-68.

Klinke, R., 1981. Neurotransmitters in the cochlea and the cochlear nucleus. Acta Otolaryngologica 91(5-6):541-554.

Klis, J.F., Smoorenburg, G.F., 1985. Modulation at the guinea pig round window of summating potentials and compound action potentials by low-frequency sound. Hear. Res. 20(1):15-23.

Konishi, T., Hamrick, P.E., Mori, H., 1984. Water permeability of the endolymph-perilymph barrier in the guinea pig cochlea. Hear. Res. 15(1):51-58.

Konishi, T., Nielsen, D.W., 1978. The temporal relationship between basilar membrane motion and nerve impulse initiation in auditory nerve fibers of guinea pigs. Jpn. J. Physiol. 28(3):291-307.

Kroese, A.B., Das, A., Hudspeth, A.J., 1989. Blockage of the transduction channels of hair cells in the bullfrog's sacculus by aminoglycoside antibiotics. Hear. Res. 37(3):203-217.

Kros, C.J., 1996. Physiology of mammalian cochlear hair cells. In: Dallos P., Popper A.N., Fay R.R., Popper A. (Eds.), The Cochlea. Springer-Verlag, New York, NY, pp. 318-385.

Kros, C.J., Crawford, A.C., 1990. Potassium currents in inner hair cells isolated from the guinea-pig cochlea. J. Physiol. (Lond.) 421:263-291.

Kros, C.J., Rusch, A., Richardson, G.P., 1992. Mechano-electrical transducer currents in hair cells of the cultured neonatal mouse cochlea. Proc. R. Soc. Lond. B. Biol. Sci. 249(1325):185-193.

Kubisch, C., Schroeder, B.C., Friedrich, T., Lutjohann, B., El-Amraoui, A., Marlin, S., Petit, C., Jentsch, T.J., 1999. KCNQ4, a novel potassium channel expressed in sensory outer hair cells, is mutated in dominant deafness. Cell 96(3):437-446.

Lacampagne, A., Gannier, F., Argibay, J., Garnier, D., Le Guennec, J.Y., 1994. The stretch-activated ion channel blocker gadolinium also blocks L-type calcium channels in isolated ventricular myocytes of the guinea-pig. Biochim. Biophys. Acta 1191(1):205-208.

Levenberg, K., 1944. A method for the solution of certain nonlinear problems in least squares. Q. Appl. Math. 2:164-168.

Liberman, M.C., Zuo, J., Guinan, J.J., Jr., 2004. Otoacoustic emissions without somatic motility: can stereocilia mechanics drive the mammalian cochlea? J. Acoust. Soc. Am. 116(3):1649-1655.

Lioudyno, M., Hiel, H., Kong, J.H., Katz, E., Waldman, E., Parameshwaran-Iyer, S., Glowatzki, E., Fuchs, P.A., 2004. A "synaptoplasmic cistern" mediates rapid inhibition of cochlear hair cells. J. Neurosci. 24(49):11160-11164.

Lukashkin, A.N., Lukashkina, V.A., Russell, I.J., 2002. One source for distortion product otoacoustic emissions generated by low- and high-level primaries. J. Acoust. Soc. Am. 111(6):2740-2748.

Lumpkin, E.A., Marquis, R.E., Hudspeth, A.J., 1997. The selectivity of the hair cell's mechanoelectrical-transduction channel promotes Ca2+ flux at low Ca2+ concentrations. Proc. Nat. Acad. Sci. USA. 94(20):10997-11002.

Lytton, J., MacLennan, D., 1992. Sarcoplasmic reticulum. In: Fozzard H., Haber E., Jennings R., Katz A., Morgan H. (Eds.), The Heart and Cardiovascular System. 2nd ed. Raven, New York, pp. 1203-1221.

Marcon, S., 1995. The influence of the perilymphatic potassium concentration on the mammalian cochlea. Honours Thesis, Department of Physiology, University of Western Australia, Nedlands.

Marcotti, W., Kros, C.J., 1999. Developmental expression of the potassium current IK,n contributes to maturation of mouse outer hair cells. J. Physiol. (Lond.) 520(Pt 3):653-660.

Marquardt, D.W., 1963. An algorithm for the least-squares estimation of nonlinear parameters. J. SIAM 11(2):431-441.

Mason, S.M., 1988. Automated system for screening hearing using the auditory brainstem response. Br. J. Audiol. 22(3):211-213.

McMahon, C.M., 2004. The mechanisms underlying normal spike activity of the primary afferent synapse in the cochlea and its dysfunction: an investigation of the possible mechanisms of peripheral tinnitus and auditory neuropathy. PhD Thesis, Physiology, School of Biomedical and Chemical Sciences, University of Western Australia, Nedlands.

McMahon, C.M., Patuzzi, R.B., 2002. The origin of the 900 Hz spectral peak in spontaneous and sound-evoked round-window electrical activity. Hear. Res. 173(1-2):134-152.

Meyer, J., Furness, D.N., Zenner, H.P., Hackney, C.M., Gummer, A.W., 1998. Evidence for opening of hair-cell transducer channels after tip-link loss. J. Neurosci. 18(17):6748-6756.

Mills, D.M., Norton, S.J., Rubel, E.W., 1993. Vulnerability and adaptation of distortion product otoacoustic emissions to endocochlear potential variation. J. Acoust. Soc. Am. 94(4):2108-2122.

Moleirinho, A., 1993. An investigation into the mechanism of salicylate ototoxicity in the guinea pig. Honours Thesis, Department of Physiology, University of Western Australia, Nedlands.

Monteith, G.R., Roufogalis, B.D., 1995. The plasma membrane calcium pump--a physiological perspective on its regulation. Cell Calcium 18(6):459-470.

Mulders, W.H., Robertson, D., 2005. Noradrenergic modulation of brainstem nuclei alters cochlear neural output. Hear. Res. 204(1-2):147-155.

Munoz, D.J., Kendrick, I.S., Rassam, M., Thorne, P.R., 2001. Vesicular storage of adenosine triphosphate in the guinea-pig cochlear lateral wall and concentrations of ATP in the endolymph during sound exposure and hypoxia. Acta Otolaryngol. 121(1):10-15.

Nakagawa, T., Kakehata, S., Akaike, N., Komune, S., Takasaka, T., Uemura, T., 1991. Calcium channel in isolated outer hair cells of guinea pig cochlea. Neurosci. Lett. 125(1):81-84.

Nenov, A.P., Norris, C., Bobbin, R.P., 1996. Acetylcholine response in guinea pig outer hair cells. II. Activation of a small conductance Ca(2+)-activated K+ channel. Hear. Res. 101(1-2):149-172.

Nicholls, D., 1982. Bioenergetics: An introduction to the chemiosmotic theory. Academic Press, London.

Nieder, P., Nieder, I., 1971. Determination of microphonic generator transfer characteristic from modulation data. J. Acoust. Soc. Am. 49(2):478-492.

Nilsen, K.E., Russell, I.J., 2000. The spatial and temporal representation of a tone on the guinea pig basilar membrane. Proc. Nat. Acad. Sci. USA. 97(22):11751-11758.

Nilsson, T., Zwiller, J., Boynton, A.L., Berggren, P.O., 1988. Heparin inhibits IP3-induced Ca2+ release in permeabilized pancreatic beta-cells. FEBS Letters 229(1):211-214.

Norton, M., 1989. Fundamentals of Noise and Vibration Analysis for Engineers. Cambridge University Press, Cambridge, pp. 361-364.

Nyquist, H., 1932. Regeneration Theory. Bell Syst. Tech. J. 11:126-147.

O'Beirne, G.A., 1998. The post-auricular muscle reflex (PAMR): its detection, analysis, and use as an objective hearing test. Honours Thesis, Department of Physiology, University of Western Australia, Nedlands.

O'Beirne, G.A., Patuzzi, R.B. 2001. The post-auricular muscle response (PAMR): Basic properties, measurement techniques, and use in hearing screening. Poster presented at the IUPS Auditory Satellite Symposium, Auckland, New Zealand, 20th - 22nd August 2001.

O'Beirne, G.A., Patuzzi, R.B. Modelling the role of outer hair cells in cochlear regulation and tinnitus. In: Patuzzi R., editor. Proceedings of the Seventh International Tinnitus Seminar; 2002; Fremantle, Western Australia. University of Western Australia. p 62-67.

O'Beirne, G.A., Patuzzi, R.B., 2003. Mathematical modelling of the role of outer hair cells in cochlear homeostasis. In: Gummer A.W. (Ed.), Biophysics of the Cochlea. World Scientific, Singapore, pp. 434-435.

Oesterle, E.C., Dallos, P., 1989. Intracellular recordings from supporting cells in the guinea-pig cochlea: AC potentials. J. Acoust. Soc. Am. 86(3):1013-1032.

Offner, F.F., Dallos, P., Cheatham, M.A., 1987. Positive endocochlear potential: mechanism of production by marginal cells of stria vascularis. Hear. Res. 29(2-3):117-124.

Ogata, K., 1997. Modern control engineering. Prentice Hall, London.

Ohyama, K., Salt, A.N., Thalmann, R., 1988. Volume flow rate of perilymph in the guinea-pig cochlea. Hear. Res. 35(2-3):119-129.

Oliver, D., Klocker, N., Schuck, J., Baukrowitz, T., Ruppersberg, J.P., Fakler, B., 2000. Gating of Ca2+-activated K+ channels controls fast inhibitory synaptic transmission at auditory outer hair cells. Neuron 26(3):595-601.

Oliver, D., Knipper, M., Derst, C., Fakler, B., 2003. Resting potential and submembrane calcium concentration of inner hair cells in the isolated mouse cochlea are set by KCNQ-type potassium channels. J. Neurosci. 23(6):2141-2149.

Ospeck, M., Dong, X.X., Iwasa, K.H., 2003. Limiting frequency of the cochlear amplifier based on electromotility of outer hair cells. Biophys. J. 84(2 Pt 1):739-749.

Pack, A.K., Slepecky, N.B., 1995. Cytoskeletal and calcium-binding proteins in the mammalian organ of Corti: cell type-specific proteins displaying longitudinal and radial gradients. Hear. Res. 91(1-2):119-135.

Parthasarathi, A.A., Grosh, K., Zheng, J., Nuttall, A.L., 2003. Effect of current stimulus on in vivo cochlear mechanics. J. Acoust. Soc. Am. 113(1):442-452.

Patuzzi, R., 1995. Monitoring cochlear homeostasis with automatic analysis of the low-frequency cochlear microphonic. In: Flock Å., Ottoson D., Ulfendahl M. (Eds.), Active Hearing. Pergamon, Elsevier, Oxford.

Patuzzi, R., 1998. The Goldman-Hodgkin-Katz equation and graphical 'load-line' analysis of ionic flow through outer hair cells. Hear. Res. 125(1-2):71-97.

Patuzzi, R. Outer hair cells, EP regulation and tinnitus. In: Patuzzi R., editor. Proceedings of the Seventh International Tinnitus Seminar; 2002; Fremantle, Western Australia. University of Western Australia. p 16-24.

Patuzzi, R., Moleirinho, A., 1998. Automatic monitoring of mechano-electrical transduction in the guinea pig cochlea. Hear. Res. 125(1-2):1-16.

Patuzzi, R., Rajan, R., 1990. Does electrical stimulation of the crossed olivo-cochlear bundle produce movement of the organ of Corti? Hear. Res. 45(1-2):15-32.

Patuzzi, R., Rajan, R., 1992. Additivity of threshold elevations produced by disruption of outer hair cell function. Hear. Res. 60(2):165-177.

Patuzzi, R., Sellick, P.M., Johnstone, B.M., 1984a. The modulation of the sensitivity of the mammalian cochlea by low frequency tones. I. Primary afferent activity. Hear. Res. 13(1):1-8.

Patuzzi, R., Sellick, P.M., Johnstone, B.M., 1984b. The modulation of the sensitivity of the mammalian cochlea by low frequency tones. III. Basilar membrane motion. Hear. Res. 13(1):19-27.

Patuzzi, R., Wareing, N. Generation of transient tinnitus in humans using low-frequency tones and its mechanism. In: Patuzzi R., editor. Proceedings of the Seventh

International Tinnitus Seminar; 2002; Fremantle, Western Australia. University of Western Australia. p 71-73.

Patuzzi, R.B., 1983. Cochlear frequency selectivity and nonlinearity. PhD Thesis, Department of Physiology, University of Western Australia, Nedlands.

Patuzzi, R.B., 2003. Low-frequency oscillations in outer hair cells and homeostatic regulation of the organ of Corti. In: Gummer A.W. (Ed.), Biophysics of the Cochlea. World Scientific, Singapore, pp. 292-299.

Patuzzi, R.B., Brown, D.J., McMahon, C.M., Halliday, A.F., 2004. Determinants of the spectrum of the neural electrical activity at the round window: transmitter release and neural depolarisation. Hear. Res. 190(1-2):87-108.

Patuzzi, R.B., O'Beirne, G.A., 1999a. Boltzmann analysis of CM waveforms using virtual instrument software. Hear. Res. 133(1-2):155-159.

Patuzzi, R.B., O'Beirne, G.A., 1999b. A correlation method for detecting the sound-evoked post-auricular muscle response (PAMR). Hear. Res. 138(1-2):147-162.

Patuzzi, R.B., Thomson, S.M., 2000. Auditory evoked response test strategies to reduce cost and increase efficiency: the postauricular muscle response revisited. Audiol. Neuro-otol. 5(6):322-332.

Patuzzi, R.B., Yates, G.K., Johnstone, B.M., 1989a. The origin of the low-frequency microphonic in the first cochlear turn of guinea-pig. Hear. Res. 39(1-2):177-188.

Patuzzi, R.B., Yates, G.K., Johnstone, B.M., 1989b. Changes in cochlear microphonic and neural sensitivity produced by acoustic trauma. Hear. Res. 39(1-2):189-202.

Pollice, P.A., Brownell, W.E., 1993. Characterization of the outer hair cell's lateral wall membranes. Hear. Res. 70(2):187-196.

Pou, A.M., Fallon, M., Winbery, S., Bobbin, R.P., 1991. Lowering extracellular calcium decreases the length of isolated outer hair cells. Hear. Res. 52(2):305-311.

Pratt, H., Mittelman, N., Geva, A.B., 1994. Machine scoring of somatosensory evoked potentials. Electroencephalography and Clinical Neurophysiology 92(1):89-92.

Preyer, S., Renz, S., Hemmert, W., Zenner, H.-P., Gummer, A.W., 1996. Receptor potential of outer hair cells isolated from base to apex of the adult guinea-pig cochlea: Implications for cochlear tuning mechanisms. Aud. Neurosci. 2:145-157.

Prosen, C.A., Petersen, M.R., Moody, D.B., Stebbins, W.C., 1978. Auditory thresholds and kanamycin-induced hearing loss in the guinea pig assessed by a positive reinforcement procedure. J. Acoust. Soc. Am. 63(2):559-566.

Pujol, R., Zajic, G., Dulon, D., Raphael, Y., Altschuler, R.A., Schacht, J., 1991. First appearance and development of motile properties in outer hair cells isolated from guinea-pig cochlea. Hear. Res. 57(1):129-141.

Purdy, S., Agung, K., Hartley, D., Patuzzi, R., O'Beirne, G., 2001. Objective hearing screening in diagnosis using the postauricular muscle response (PAMR). National Acoustic Laboratories Research & Development Annual Report 2000/2001. Australian Hearing, Chatswood, pp. 6-7.

Purdy, S., Agung, K., Hartley, D., Patuzzi, R., O'Beirne, G., in press-a. The post-auricular muscle response: an objective electrophysiological method for evaluating hearing sensitivity. Int. J. Audiol.

Purdy, S., Agung, K., Patuzzi, R., O'Beirne, G., 2002. The post auricular muscle response in adults and infants. National Acoustic Laboratories Annual Report 2001/2002. Australian Hearing, Chatswood, pp. 7-8.

Purdy, S., Agung, K., Patuzzi, R., O'Beirne, G., Newall, P., in press-b. Rising-frequency chirps and earphones with an extended high frequency response enhance the post-auricular muscle response. Int. J. Audiol.

Puschner, B., Schacht, J., 1997. Calmodulin-dependent protein kinases mediate calcium-induced slow motility of mammalian outer hair cells. Hear. Res. 110(1-2):251-258.

Rajan, R., 1990. Electrical stimulation of the inferior colliculus at low rates protects the cochlea from auditory desensitization. Brain Res. 506(2):192-204.

Rajan, R., Irvine, D.R., Cassell, J.F., 1991. Normative N1 audiogram data for the barbiturate-anaesthetised domestic cat. Hear. Res. 53(1):153-158.

Ricci, A.J., Fettiplace, R., 1997. The effects of calcium buffering and cyclic AMP on mechano-electrical transduction in turtle auditory hair cells. J. Physiol. (Lond.) 501 (Pt 1):111-124.

Rodriguez-Contreras, A., Yamoah, E.N., 2003. Effects of permeant ion concentrations on the gating of L-type Ca2+ channels in hair cells. Biophys. J. 84(5):3457-3469.

Ruggero, M.A., Robles, L., Rich, N.C., 1986. Basilar membrane mechanics at the base of the chinchilla cochlea. II. Responses to low-frequency tones and relationship to microphonics and spike initiation in the VIII nerve. J. Acoust. Soc. Am. 80(5):1375-1383.

Russell, I.J., Sellick, P.M., 1983. Low-frequency characteristics of intracellularly recorded receptor potentials in guinea-pig cochlear hair cells. J. Physiol. (Lond.) 338:179-206.

Rybalchenko, V., Santos-Sacchi, J., 2003. Cl- flux through a non-selective, stretch-sensitive conductance influences the outer hair cell motor of the guinea-pig. J. Physiol. (Lond.).

Salt, A.N., 2002. Simulation of methods for drug delivery to the cochlear fluids. Adv. Otorhinolaryngol. 59:140-148.

Salt, A.N., 2004. Acute Endolymphatic Hydrops Generated by Exposure of the Ear to Nontraumatic Low-Frequency Tones. J. Assoc. Res. Otolaryngol.

Salt, A.N., DeMott, J.E., 1998. Longitudinal endolymph movements induced by perilymphatic injections. Hear. Res. 123(1-2):137-147.

Salt, A.N., DeMott, J.E., 1999. Longitudinal endolymph movements and endocochlear potential changes induced by stimulation at infrasonic frequencies. J. Acoust. Soc. Am. 106(2):847-856.

Salt, A.N., Inamura, N., Thalmann, R., Vora, A.R., 1991. Evaluation of procedures to reduce fluid flow in the fistulized guinea-pig cochlea. Acta Otolaryngol. 111(5):899-907.

Salt, A.N., Konishi, T., 1982. Functional importance of sodium and potassium in the guinea pig cochlea studied with amiloride and tetraethylammonium. Jpn. J. Physiol. 32(2):219-230.

Santos-Sacchi, J., 1992. On the frequency limit and phase of outer hair cell motility: effects of the membrane filter. J. Neurosci. 12(5):1906-1916.

Santos-Sacchi, J., Wu, M., Kakehata, S., 2001. Furosemide alters nonlinear capacitance in isolated outer hair cells. Hear. Res. 159(1-2):69-73.

Schacht, J., Zenner, H.P., 1987. Evidence that phosphoinositides mediate motility in cochlear outer hair cells. Hear. Res. 31(2):155-159.

Scherer, M.P., Gummer, A.W., 2004. Vibration pattern of the organ of Corti up to 50 kHz: evidence for resonant electromechanical force. Proc. Nat. Acad. Sci. USA. 101(51):17652-17657.

Schimmel, H., Rapin, I., Cohen, M.M., 1975. Improving evoked response audiometry. Results of normative studies for machine scoring. Audiology 14(5-6):466-479.

Schreiner, C.E., Snyder, R.L., Johnstone, B.M., 1986. Effects of extracochlear direct current stimulation on the ensemble auditory nerve activity of cats. Hear. Res. 21(3):213-226.

Schulte, B.A., 1993. Immunohistochemical localization of intracellular Ca-ATPase in outer hair cells, neurons and fibrocytes in the adult and developing inner ear. Hear. Res. 65(1-2):262-273.

Searchfield, G.D., Munoz, D.J., Thorne, P.R., 2004. Ensemble spontaneous activity in the guinea-pig cochlear nerve. Hear. Res. 192(1-2):23-35.

Seidler, N.W., Jona, I., Vegh, M., Martonosi, A., 1989. Cyclopiazonic acid is a specific inhibitor of the Ca2+-ATPase of sarcoplasmic reticulum. J. Biol. Chem. 264(30):17816-17823.

Sellick, P.M., Patuzzi, R., Johnstone, B.M., 1982. Measurement of basilar membrane motion in the guinea pig using the Mossbauer technique. J. Acoust. Soc. Am. 72(1):131-141.

Sen, A.K., Post, R.L., 1964. Stoichiometry and Localization of Adenosine Triphosphate-Dependent Sodium and Potassium Transport in the Erythrocyte. J. Biol. Chem. 239:345-352.

Sewell, W.F., 1984. The effects of furosemide on the endocochlear potential and auditory-nerve fiber tuning curves in cats. Hear. Res. 14(3):305-314.

Shera, C.A., Guinan, J.J., Jr., 1999. Evoked otoacoustic emissions arise by two fundamentally different mechanisms: a taxonomy for mammalian OAEs. J. Acoust. Soc. Am. 105(2 Pt 1):782-798.

Shigemoto, T., Ohmori, H., 1991. Muscarinic receptor hyperpolarizes cochlear hair cells of chick by activating Ca(2+)-activated K+ channels. J. Physiol. (Lond.) 442:669-690.

Siegel, J.H., Dallos, P., 1986. Spike activity recorded from the organ of Corti. Hear. Res. 22:245-248.

Sirjani, D.B., Salt, A.N., Gill, R.M., Hale, S.A., 2004. The influence of transducer operating point on distortion generation in the cochlea. J. Acoust. Soc. Am. 115(3):1219-1229.

Slepecky, N., 1989. Cytoplasmic actin and cochlear outer hair cell motility. Cell Tissue Res. 257(1):69-75.

Slepecky, N., Ulfendahl, M., Flock, Å. 1988. Effects of caffeine and tetracaine on outer hair cell shortening suggest intracellular calcium involvement. Hear. Res. 32(1):11-21.

Soh, H., Park, C.S., 2001. Inwardly rectifying current-voltage relationship of small-conductance Ca2+-activated K+ channels rendered by intracellular divalent cation blockade. Biophys. J. 80(5):2207-2215.

Spector, A.A., Brownell, W.E., Popel, A.S., 2003. Effect of outer hair cell piezoelectricity on high-frequency receptor potentials. J. Acoust. Soc. Am. 113(1):453-461.

Sridhar, T.S., Brown, M.C., Sewell, W.F., 1997. Unique postsynaptic signaling at the hair cell efferent synapse permits calcium to evoke changes on two time scales. J. Neurosci. 17(1):428-437.

Sridhar, T.S., Liberman, M.C., Brown, M.C., Sewell, W.F., 1995. A novel cholinergic "slow effect" of efferent stimulation on cochlear potentials in the guinea pig. J. Neurosci. 15(5 Pt 1):3667-3678.

Stevens, J.C., Brown, B.H., Franks, C.I., Turner, D.J., 1980. Detection of auditory evoked potentials by using a personal computer. Clin. Phys. Physiol. Meas. 1(4):285.

Strassmaier, M., Gillespie, P.G., 2002. The hair cell's transduction channel. Curr. Opin. Neurobiol. 12(4):380-386.

Sugasawa, M., Erostegui, C., Blanchet, C., Dulon, D., 1996. ATP activates non-selective cation channels and calcium release in inner hair cells of the guinea-pig cochlea. J. Physiol. (Lond.) 491(Pt 3):707-718.

Sunose, H., Ikeda, K., Saito, Y., Nishiyama, A., Takasaka, T., 1992. Membrane potential measurement in isolated outer hair cells of the guinea pig cochlea using conventional microelectrodes. Hear. Res. 62(2):237-244.

Sunose, H., Ikeda, K., Saito, Y., Nishiyama, A., Takasaka, T., 1993. Sodium extrusion mechanism in mammalian cochlear outer hair cell. Jpn. J. Physiol. 43(Suppl 1):S175-177.

Surin, A.M., Reimann-Philipp, U., Fechter, L.D., 2000. Simultaneous monitoring of slow cell motility and calcium signals of the guinea pig outer hair cells. Hear. Res. 146(1-2):121-133.

Sziklai, I., Szonyi, M., Dallos, P., 2001. Phosphorylation mediates the influence of acetylcholine upon outer hair cell electromotility. Acta Otolaryngol. 121(2):153-156.

Takeuchi, S., Takeda, T., Saito, H., 1991. Pressure relationship between perilymph and endolymph associated with endolymphatic infusion. Ann. Otol. Rhinol. Laryngol. 100(3):244-248.

Thalen, E.O., Wit, H.P., Segenhout, J.M., Albers, F.W., 2001. Dynamics of inner ear pressure change caused by intracranial pressure manipulation in the guinea pig. Acta Otolaryngol. 121(4):470-476.

Tsuji, J., Liberman, M.C., 1997. Intracellular labeling of auditory nerve fibers in guinea pig: central and peripheral projections. J. Comp. Neurol. 381(2):188-202.

Tucker, T.R., Fettiplace, R., 1996. Monitoring calcium in turtle hair cells with a calcium-activated potassium channel. J. Physiol. (Lond.) 494(Pt 3):613-626.

van den Abbeele, T., Teulon, J., Huy, P.T., 1999. Two types of voltage-dependent potassium channels in outer hair cells from the guinea pig cochlea. Am. J. Physiol. 277(5 Pt 1):C913-925.

Verkman, A.S., van Hoek, A.N., Ma, T., Frigeri, A., Skach, W.R., Mitra, A., Tamarappoo, B.K., Farinas, J., 1996. Water transport across mammalian cell membranes. Am. J. Physiol. Cell Physiol. 270(1 Pt 1):C12-30.

Vetter, D.E., Liberman, M.C., Mann, J., Barhanin, J., Boulter, J., Brown, M.C., Saffiote-Kolman, J., Heinemann, S.F., Elgoyhen, A.B., 1999. Role of alpha9 nicotinic ACh receptor subunits in the development and function of cochlear efferent innervation. Neuron 23(1):93-103.

von Békésy, G., 1947. A new audiometer. Arch. Otorhinolaryngol. 35:411-422.

von Békésy, G., 1960. Experiments in Hearing. McGraw-Hill, New York.

Walker, R.G., Hudspeth, A.J., Gillespie, P.G., 1993. Calmodulin and calmodulin-binding proteins in hair bundles. Proc. Nat. Acad. Sci. USA. 90(7):2807-2811.

Wang, J.C., Raybould, N.P., Luo, L., Ryan, A.F., Cannell, M.B., Thorne, P.R., Housley, G.D., 2003. Noise induces up-regulation of P2X2 receptor subunit of ATP-gated ion channels in the rat cochlea. Neuroreport 14(6):817-823.

Wangemann, P., Schacht, J., 1996. Homeostatic mechanisms in the cochlea. In: Dallos P., Popper A.N., Fay R.R., Popper A. (Eds.), The Cochlea. Springer-Verlag, New York, NY, pp. 130-185.

Wareing, N., 2001. Slow oscillations in auditory sensitivity evoked by low-frequency tones: An indicator of cochlear homeostasis. Honours Thesis, Department of Physiology, University of Western Australia, Nedlands.

Wit, H.P., Thalen, E.O., Albers, F.W., 1999. Dynamics of inner ear pressure release, measured with a double-barreled micropipette in the guinea pig. Hear. Res. 132(1-2):131-139.

Withnell, R.H., Yates, G.K., 1998. Onset of basilar membrane non-linearity reflected in cubic distortion tone input-output functions. Hear. Res. 123(1-2):87-96.

Witt, C.M., Hu, H.Y., Brownell, W.E., Bertrand, D., 1994. Physiologically silent sodium channels in mammalian outer hair cells. J. Neurophysiol. 72(2):1037-1040.

Wong, P.K., Bickford, R.G., 1980. Brain stem auditory evoked potentials: the use of noise estimate. Electroencephalography and Clinical Neurophysiology 50(1-2):25-34.

Wu, K.D., Bungard, D., Lytton, J., 2001. Regulation of SERCA Ca2+ pump expression by cytoplasmic Ca2+ in vascular smooth muscle cells. Am. J. Physiol. Cell Physiol. 280(4):C843-851.

Wu, Y.C., Ricci, A.J., Fettiplace, R., 1999. Two components of transducer adaptation in auditory hair cells. J. Neurophysiol. 82(5):2171-2181.

Xia, X.M., Fakler, B., Rivard, A., Wayman, G., Johnson-Pais, T., Keen, J.E., Ishii, T., Hirschberg, B., Bond, C.T., Lutsenko, S. and others. 1998. Mechanism of calcium gating in small-conductance calcium-activated potassium channels. Nature 395(6701):503-507.

Xu, A., Narayanan, N., 1999. Ca2+/calmodulin-dependent phosphorylation of the Ca2+-ATPase, uncoupled from phospholamban, stimulates Ca2+-pumping in native cardiac sarcoplasmic reticulum. Biochem. Biophys. Res. Commun. 258(1):66-72.

Xu, A., Narayanan, N., 2000. Reversible inhibition of the calcium-pumping ATPase in native cardiac sarcoplasmic reticulum by a calmodulin-binding peptide. Evidence for calmodulin-dependent regulation of the V(max) of calcium transport. J. Biol. Chem. 275(6):4407-4416.

Yoshida, N., Liberman, M.C., Brown, M.C., Sewell, W.F., 1999. Gentamicin blocks both fast and slow effects of olivocochlear activation in anesthetized guinea pigs. J. Neurophysiol. 82(6):3168-3174.

Yoshida, N., Liberman, M.C., Brown, M.C., Sewell, W.F., 2001. Fast, but not slow, effects of olivocochlear activation are resistant to apamin. J. Neurophysiol. 85(1):84-88.

Zenner, H.P., 1986a. Motile responses in outer hair cells. Hear. Res. 22:83-90.

Zenner, H.P., 1986b. [Active movements of the hair cells: a new mechanism in hearing]. HNO 34(4):133-138.

Zenner, H.P., Zimmermann, U., Schmitt, U., 1985. Reversible contraction of isolated mammalian cochlear hair cells. Hear. Res. 18(2):127-133.

Zhang, Y.H., Hancox, J.C., 2000. Gadolinium inhibits Na(+)-Ca(2+) exchanger current in guinea-pig isolated ventricular myocytes. Br. J. Pharmacol. 130(3):485-488.

Zheng, J., Shen, W., He, D.Z., Long, K.B., Madison, L.D., Dallos, P., 2000. Prestin is the motor protein of cochlear outer hair cells. Nature 405(6783):149-155.

Zine, A., Schweitzer, L., 1996. Development of intracellular Ca-ATPase in the gerbil outer hair cell lateral wall. Brain Res. 721(1-2):1-10.

Zwicker, E., Hesse, A., 1984. Temporary threshold shifts after onset and offset of moderately loud low-frequency maskers. J. Acoust. Soc. Am. 75(2):545-549.

Zwislocki, J.J., Kletsky, E.J., 1979. Tectorial membrane: a possible effect on frequency analysis in the cochlea. Science 204(4393):639-641.